Edited by
G. Mamantov, M. Blander, and G. P. Smith
THIRD INTERNATIONAL SYMPOSIUM

MOLTEN SALTS

PV 81-9

PROCEEDINGS OF THE THIRD
INTERNATIONAL SYMPOSIUM ON

MOLTEN SALTS

Edited by

Gleb Mamantov
Department of Chemistry
University of Tennessee
Knoxville, Tennessee

Milton Blander
Chemical Engineering Division
Argonne National Laboratory
Argonne, Illinois

G. P. Smith
Chemistry Division
Oak Ridge National Laboratory
Oak Ridge, Tennessee

PHYSICAL ELECTROCHEMISTRY DIVISION

Proceedings Volume 81-9

THE ELECTROCHEMICAL SOCIETY, INC., 10 South Main St., Pennington, NJ 08534

PROCEEDINGS OF THE THIRD
INTERNATIONAL SYMPOSIUM ON

MOLTEN SALTS

Edited by

Gleb Mamantov
Department of Chemistry
University of Tennessee
Knoxville, Tennessee

Milton Blander
Chemical Engineering Division
Argonne National Laboratory
Argonne, Illinois

G. P. Smith
Chemistry Division
Oak Ridge National Laboratory
Oak Ridge, Tennessee

PHYSICAL ELECTROCHEMISTRY DIVISION

Proceedings Volume 81-9

THE ELECTROCHEMICAL SOCIETY, INC., 10 South Main St.. Pennington, NJ 08534

Library of Congress Catalog Number: 81-69548
Printed in the United States of America

PREFACE

The Third International Symposium on Molten Salts was held October 6 - 9 1980, at the Fall Meeting of the Electrochemical Society, Hollywood, Florida. This volume contains forty-two papers presented at that Symposium. Five additional papers were presented at the Symposium, however, these manuscripts were not received by the Editors. The papers at this Symposium covered a very broad range of topics ranging from theory and structure of melts to numerous applications, such as batteries, solar energy, thermal energy storage, and applied electrochemistry using molten salt systems.

The number of papers presented at the Third Symposium on Molten Salts was approximately the same as those presented at the First and Second Symposia in Washington in 1976 and Pittsburgh in 1978, respectively. It is worth noting, however, that the Molten Carbonate Fuel Cell Technology Symposium was held concurrently with the Third Symposium. Thus it would appear that the interest in various aspects of molten salt chemistry is increasing.

I am grateful to the Physical Electrochemistry Division for the sponsorship of this Symposium as well as for the financial assistance with the registration expenses of most of the foreign speakers. I would also like to express my thanks to Milt Blander and Sam Yosim for the assistance in organizing this Symposium and to Drs. Blander and G. P. Smith for their help with the editing of this volume.

Finally I would like to thank the participants in the Symposium who really made this Symposium possible.

Gleb Mamantov
June 1981

CONTENTS

DOI: 10.1149/198109.0001PV

MOLTEN SALTS : RECENT PROGRESS IN DETERMINING THEIR STRUCTURE

J.E. Enderby

H.H. Wills Physics Laboratory, University of Bristol, Royal Fort, Tyndall Avenue, Bristol BS8 1TL, U.K.

Abstract

The structure of this paper is as follows. We shall first briefly review the basic principles of structural studies on multi-component systems and consider in particular the application of neutron diffraction techniques. It will be shown that the quantity which can be extracted from a single diffraction experiment on a liquid containing two ionic species, + and -, is the total structure factor $F_T(k)$ defined by

$$F_T(k)=c_+^2 f_+^2 (S_{++}(k)-1)+c_-^2 f_-^2 (S_{--}(k)-1)+2c_+c_-f_+f_-(S_{+-}(k)-1)$$

Until recently, this was all the experimental information available and it turns out to be very misleading. Quantities like near neighbour distances or coordination numbers derived directly from $F_T(k)$ represent gross averages and because of special properties associated with molten salts (i.e. charge cancellation and penetration of like species into the first coordination shell) may bear little reality to the microscopic structure. We shall describe new experiments which have allowed the individual structure factors S_{++}, S_{--}, S_{+-}, to be obtained directly.

INTRODUCTION

We label each component by the dummy suffices α and β which may take values 1,2,.....,j for a liquid containing j ion-types. The atomic fraction of the α ion-type is denoted by c_α and is subject to the sum rule

$$\sum_{\alpha=1}^{j} c_\alpha = 1. \qquad (1)$$

If any type of radiation is incident on a mixed assembly of ions, a measure of the amplitude of the scattered waves is given by

$$\sum_\alpha f_\alpha \sum_{i(\alpha)} \exp(-i\underset{\sim}{k}.\underset{\sim}{r}_i(\alpha)), \qquad (2)$$

where f_α is an appropriate scattering factor and $\underset{\sim}{r}_i(\alpha)$ denotes the

position of the ith ion of α-type. The mean intensity, which we denote $d\sigma/d\Omega$ becomes

$$\sum_{\alpha\beta} f_\alpha f_\beta^* \sum_{i(\alpha)} \sum_{i(\beta)} \exp\left(i\underset{\sim}{k}.(\underset{\sim}{r}_j(\beta)-\underset{\sim}{r}_i(\alpha))\right) \tag{3}$$

$$= \sum_{\alpha\beta} f_\alpha f_\beta^* N c_\alpha \delta_{\alpha\beta} + \sum_{i\neq j} \cos \underset{\sim}{k}.\underset{\sim}{r}_{ji} \quad , \tag{4}$$

where N is the total number of ions in the sample.

Let us now introduce partial structure factors $S_{\alpha\beta}(k)$ defined by

$$S_{\alpha\beta}(k) = 1 + \frac{4\pi N}{kV} \int_0^\infty dr(g_{\alpha\beta}(r) - 1)r \sin kr, \tag{5}$$

where V is the volume of the sample. In (5) $g_{\alpha\beta}(r)$ is the partial pair distribution function which measures the average distribution of type β ion observed from an α ion at the origin and tends, as in the one-component case, to unity at large values of r. If there is an α ion at r=0, the number of β ions at the same instant with their centres in a small element of thickness dr is

$$4\pi(N/V)c_\beta g_{\alpha\beta}(r)r^2 dr. \tag{6}$$

In terms of $S_{\alpha\beta}$, we can rewrite (4) as

$$\frac{d\sigma}{d\Omega} = \sum_\alpha N c_\alpha f_\alpha f_\alpha^* + \sum_{\alpha\beta} N c_\beta c_\alpha f_\beta f_\alpha^* (S_{\alpha\beta}-1) \tag{7}$$

and for those cases where f is real, more simply as

$$\frac{d\sigma}{d\Omega} = N \sum_\alpha c_\alpha f_\alpha^2 + F_T(k) \quad . \tag{8}$$

where

$$F_T(k) = \sum_{\alpha\beta} c_\alpha c_\beta f_\alpha f_\beta (S_{\alpha\beta}(k)-1). \tag{9}$$

If we perform scattering experiments on ionic systems, the quantity which can be extracted - and even then not directly - is $F_T(k)$. In practice, the intensity I of either neutrons, X-rays or electrons is measured as a function of a scattering angle θ in the geometry typified by fig. 1.

Quite generally,

$$I(\theta) = \alpha(\theta) \left\{ \frac{d\sigma}{d\Omega} + \delta(\theta) \right\} \qquad (10)$$

and the challenge which faces experimentalists is the determination by theory, experiment or both, of the calibration parameters $\alpha(\theta)$ and $\delta(\theta)$.

In table 1 we show the physical origins of $\alpha(\theta)$ and $\delta(\theta)$ for two principal types of radiation used, X-rays and neutrons. We shall not dwell on the determination of the calibration parameters, except to point out that it is not a trivial matter.

2. The Experiments

We focus now on simple molten salts of the form MX_n. The experimental method together with the algorithm for extracting g_{++}, g_{--} and g_{+-} have been fully described in our earlier papers (ref. 1).

The quantity which can be obtained from a single neutron diffraction experiment on a liquid containing two species, + and -, is given (eqn 9) by

$$F_T(k) = c_+^2 f_+^2 (S_{++}-1) + c_-^2 f_-^2 (S_{--}-1) + 2c_+ c_- f_+ f_- (S_{+-}-1),$$

where c_+ and c_- are the atomic fractions of the two species, f_+ and f_- are the neutron scattering lengths. To separate out $S_{\alpha\beta}$ $(\alpha,\beta=+,-)$ f_- was changed by isotopic substitution of the chlorine. The isotopes used in this work, together with the degree of enrichment and the relevant scattering lengths are shown in table 2.

Once $S_{\alpha\beta}(k)$ has been obtained, the two-body radial distribution functions (i.e. g_{++} etc) can be obtained by standard procedures (ref. 1). An example of these functions is shown in figure 2.

3. Discussion

The results shown in figure 2 serve to illustrate the important features of the structure of molten salts. These are

(i) charge cancellation: the phasing of $g_{++}(r)$, $g_{+-}(r)$ and $g_{--}(r)$ ensure that essentially complete charge cancellation occurs beyond 5Å

(ii) penetration: a substantial probability exists that an anion will find another anion as its near neighbour. The penetration of like ions into the first coordination shell will clearly have important thermodynamic consequences for mixtures of molten salts.

(iii) coordination numbers: these are invariably close to their solid state counterparts.

A summary of the experimental situation is given in table 3.

The very recent work on molten $ZnCl_2$ deserves special mention. The evidence provided by Biggin and Enderby (7) shows that the unusual structural properties of this liquid arise from the smallness of Zn^{2+} when compared with Cl^-. Specific chemical effects do not play a major role in determining the structural properties of molten $ZnCl_2$. Furthermore, the structure closely resembles that of the γ-form solid. A full discussion of the structural properties of molten $ZnCl_2$ can be found in reference 7.

Acknowledgments

The experimental work described here has been supported by the U.K. Science Research Council. My collaborator, Dr. Sue Biggin, is to be thanked for allowing me access to experimental data and many useful conversations. The samples necessary for this work have been prepared in an expert way by Mrs. Sue Langron.

REFERENCES

(1) Edwards, F.G., Enderby, J.E., Howe, R.A., and Page, D.I., 1975, J.Phys. C, 8, 3483.
(2) Derrien, Y., and Dupuy, J., 1975, J. Phys., Paris, 36, 191.
(3) Mitchell, E.W.J., Poncet, P.E.J., and Stewart, R.J., 1976, Phil. Mag., 34, 721.
(4) Page, D.I., and Mika, K., 1971, J. Phys. C, 4, 3034.
(5) Derrien, Y., and Dupuy, J., 1976, Phys. Chem. Liquids, 5, 71.
(6) Edwards, F.G., Howe, R.A., Enderby, J.E., and Page, D.I., 1978, J. Phys. C. 11, 1053.
(7) Biggin, S., and Enderby, J.E., 1981, J. Phys. C (submitted).

Table 1. Contributions to the calibration parameters.

	$\alpha(\theta)$	$\delta(\theta)$
X-rays	Sample geometry Apparatus geometry Polarization corrections Absorption in the sample	Compton scattering Multiple scattering
Neutrons	Sample geometry Apparatus geometry Absorption in the sample Absorption by the sample container	Multiple scattering Scattering by the sample container Incoherent scattering Placzek (inelastic) effects

Table 2.

Isotope	Enrichment	Coherent scattering length ($\times 10^{-12}$ cm)
^{35}Cl	99.3%	1.18
^{37}Cl	90.4%	0.349
Cl (mixture)	(37)41%-(35)59%	0.799
Ba	(natural)	0.351
Na	(natural)	0.363
Zn	(natural)	0.570

Table 3. Structural properties of molten salts derived from neutron diffraction experiments

Salt	Ref.	Position of 1st max.			Position of 1st min.			Coordination numbers			Temp. (°C)
		+-	++	--	+-	++	--	n_{+-}	n_{++}	n_{--}	
NaCl	[1]	2.6	3.9	3.9	3.9	6.0	5.8	5.8	13.0	13.0	875
KCl	[2]	3.1	4.8	4.8	4.9	7.0	7.0	6.1	16.0	16.0	800
RbCl	[3]	3.2	4.9	4.8	5.3	7.4	7.2	6.9	13.0	14.0	750
CsCl	[2]	3.4	3.9	3.9	5.4	4.3	4.3	6.0	1.5	1.5	700
CuCl	[4]	2.3	3.4	3.8	3.0	-	5.2	-	-	-	460
AgCl	[5]	2.6	3.4	-	3.4	3.9	-	4.3	3.1	-	510
		2.6	3.2	3.2	3.1	3.9	3.7	2.7	4.1	2.7	850
$BaCl_2$	[6]	3.1	4.9	3.9	4.1	7.7	5.1	7.7	14.0	7.0	1025
$ZnCl_2$	[7]	2.3	3.8	3.7	3.2	4.8	4.7	4.3	4.7	8.6	300

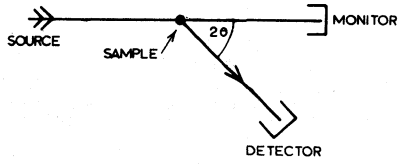

Figure 1. Conventional layout for diffraction studies.

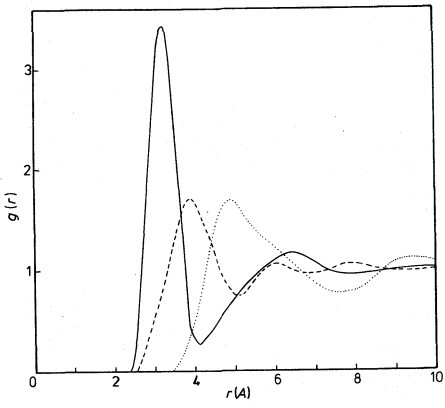

Figure 2. The radial distribution functions for molten $BaCl_2$: full curve, g_{BaCl}: broken curve, g_{ClCl}; dotted curve g_{BaBa}.

DOI: 10.1149/198109.0009PV

STATISTICAL THEORIES OF MOLTEN SALTS

Bjørn Hafskjold*)

Institute of Inorganic Chemistry
University of Trondheim
N-7034 TRONDHEIM-NTH
Norway

*)Previously Bjørn Larsen

Abstract. Recent work on statistical theories of ionic fluids are discussed. The theories are of two kinds: perturbation theories and integral equations. The statistical-mechanical basis and computational method for thermodynamic and structural properties are described. Specific theories such as the ionic virial expansion, hyper-netted chain equation, and mean spherical approximation are outlined. A charged hard-sphere model is used for illustration, and its thermodynamic and structural properties are briefly discussed.

1. INTRODUCTION

Statistical theories are tools in the bridge-building between microscopic - or intermolecular - properties on one side and macroscopic - thermodynamic and transport - properties on the other. This is illustrated in Fig. 1.

The intermolecular potential is input to the theory in the form of a numerical table or a mathematical model. Macroscopic properties are output, obtained either directly or via correlation functions that give information about the system's structure. In a true molecular theory, we want the structural information to be a result of the theory, not an input to it.

Since a statistical theory is essentially a computation of averages, it represents a one-way connection from microscopic to macroscopic properties. However, by systematic variations of the input, it is also possible to establish a two-way relation.

In this paper, we shall consider statistical theories for the equilibrium properties of molten salts. For a given potential model $u_{ij}(r)$ describing the interaction between ions i and j a distance r apart, the problem is to compute structural and thermodynamic properties.

It is convenient to start with the grand canonical partition function,

$$\Xi(\mu,V,T) = \sum_{N=0}^{\infty} \frac{z^N}{N!} \int e^{-U(\underline{r}^N)/kT} \, d\underline{r}^N \,, \qquad (1)$$

which is a function of the chemical potential μ, volume V, and temperature T of the system. The thermodynamic properties are related to Ξ by

$$PV = -kT \ln \Xi , \tag{2}$$

where P is the pressure. In eq. (1), z is the fugacity,

$$z = e^{\mu/kT} \cdot \Lambda^{-3} , \tag{3}$$

with $\Lambda = (h^2/2\pi mkT)^{\frac{1}{2}}$, the de Broglie thermal wavelength. The total potential energy of a system of N ions,

$$U(\underline{r}^N) = \sum_{i<j=2}^{N} u_{ij}(r) \tag{4}$$

is a function of the positions $\underline{r}^N$ of all the ions. Other thermodynamic properties can be obtained once the equation-of-state (2) is known.

An alternative route can be taken via the correlation functions, such as the radial distribution function g(r) given by

$$\rho^2 g(r) = \frac{1}{\Xi} \sum_{N=2}^{\infty} \frac{z^N}{(N-2)!} \int e^{-U(\underline{r}^N)/kT} d\underline{r}_3 d\underline{r}_4 \ldots d\underline{r}_N , \tag{5}$$

where ρ is the average number density.

Three different routes lead from the correlation functions to the thermodynamic properties, the energy, pressure, and compressibility equations /1/. They provide a possibility of choosing the most convenient relation or a test of the thermodynamic self-consistency of the theory.

The correlation functions also provide information about the system's structure.

The crux of a statistical theory is to evaluate integrals of the kind given in eqs. (1) and (5). To do this, one either has to use computer simulation methods or introduce approximations that facilitate

the evaluation. The two approaches complement one another in that a theory provides a more transparent relationship between microscopic and macroscopic properties whereas a simulation provides exact results.

The theories in consideration can be divided into two groups, perturbation theories and integral equations. A convenient initial approach can be taken through cluster expansions. This is shown schematically in Fig. 2.

The principles of the cluster-expansion basis, perturbation theories, and integral - equation theories will be described in the following sections. Some examples of applications to molten salts will be given.

2. CLUSTER EXPANSIONS

The common approach to a derivation of cluster expansions starts with the grand canonical partition function, eq. (1). General derivations are given by Morita and Hiroike /2/ and by Stell /3/. The Boltzmann factor, $\exp[-U(\underline{r}^N)/kT]$, is expressed in terms of Mayer f-functions, defined as

$$f_{ij}(r) = e^{-u_{ij}(r)/kT} - 1 \; . \tag{6}$$

This leads to an expansion of the partition function and the thermodynamic and structural functions derived from it.

The virial expansion,

$$P = \rho kT \sum_{i=0}^{\infty} B_i \rho^i \; , \tag{7}$$

is the result of one such expansion.

Applied to ionic systems, the virial expansion needs some modification because the normal virial coefficients, B_i, diverge. Since the sum (7) represents a finite physical quantity, there must be singular

contributions to the B_i's that cancel each other. Mayer /4/ showed how to resum the virial expansion for ionic systems in a way that removes these singularities. A comprehensive account of this technique is given by Friedman /5/.

The "ionic" virial expansion contains an ideal gas term, a Debye-Hückel term, second and higher-order ionic virial coefficients. It is well known that the Debye-Hückel term shows a concentration (density) dependence that is linear in $c^{\frac{1}{2}}$. An illustration of this is given in Fig. 3, which shows the internal electrostatic energy of an aqueous 2-2 electrolyte solution model as function of the square root of the concentration. The figure also shows that the second ionic virial coefficient of the energy is negative for small concentrations. This negative deviation from the Debye-Hückel limiting law is related to the system's tendency to form ion pairs /6/.

The ionic virial expansion is of little use for molten-salt densities because the convergence is too slow in that regime. A related perturbation theory that converges quickly even in the molten-salt regime will be discussed in the following section.

3. PERTURBATION THEORIES

The principle of a perturbation theory is to decompose the potential $u_{ij}(r)$ into a reference potential $u^o_{ij}(r)$ and a perturbation $\delta u_{ij}(r)$, and expand the quantity of interest, *e.g.* the free energy F, in $\delta u_{ij}(r)$. The $u^o_{ij}(r)$ defines the reference system, for whixh all properties (F^o, $g^o(r)$, etc.) must be known. The choice of u^o and δu depends, therefore, on the availability of reference-system properties. It also depends on the convergence of the resulting expansion in δu, which is an important point because it is, in practice, possible to obtain numerical values for the first few terms of the expansion only.

The general procedure for a perturbation-theory development is the following:

1. Expand the Mayer f-function in δu
2. Order terms in F
3. Compute numerical values term-by-term.

An expansion for equal-diameter charged hard spheres that was developed by Stell and Larsen /7/ illustrates the perturbation-theory approach. They considered the hard-sphere reference potential,

$$u^{o}_{ij}(r) = \begin{cases} \infty & \text{for} \quad r<R \\ 0 & \text{for} \quad r>R \end{cases} , \tag{8}$$

where R is the hard-sphere diameter. The properties of hard-sphere systems are now known in great detail /1/, a fact that makes such systems natural and convenient reference systems in perturbation theories. The model studied by Stell and Larsen is the so-called restricted primitive model (RPM). The perturbation

$$\delta u_{ij}(r) = e_i e_j / r \quad \text{for} \quad r>R \tag{9}$$

added to the reference potential makes up the RPM's total potential. For $r<R$, δu may be any finite function of r, but Andersen and Chandler /8/ have found that a special choice will optimize convergence of the free-energy expansion. This leads to

$$\frac{F}{VkT} = \left(\frac{F}{VkT}\right)_{\text{hard spheres}} + F_1(x) + \sum_{n\geq 1} F_{2,n}(x)(1/kT)^n + \sum_{n\geq 1} F_{3,n}(x)\rho^n \tag{10}$$

where $x = 4\pi\rho(eR)^2/kT$. The coefficients $F(x)$ depend on ρ and T combined through x, but not on ρ and T separately.

The leading contribution to F_1 is

$$F_1(x) \approx -[3x^2 + 6x + 2 - 2(1+2x)^{3/2}]/12\pi R^3 . \tag{11}$$

The coefficients $F_{2,n}(x)$ are rather complicated functions of x that are discussed by Stell and Larsen /7/, whereas the leading term in the last sum is simple,

$$F_{3,1}(x)\cdot\rho \approx -\frac{\rho}{128}\{\frac{5}{3}p^3 - 3p^2 + 3p + 4 - [4(2p+1) + (2p+1)\sin p - 2p\cos p]e^{-p}\}, \quad (12)$$

with $p = (1+2x)^{\frac{1}{2}} - 1$. At typical molten-salt densities and temperatures, the approximation

$$\frac{F}{VkT} = \left(\frac{F}{VkT}\right)_{\text{hard spheres}} + F_1(x) + F_{3,1}(x)\rho , \quad (13)$$

with the last two terms approximated by (11) and (12), turns out to be excellent.

The sum $\sum_{n\geq 1} F_{2,n}(x)(1/kT)^n$ is not negligible in the critical region of ionic salts, but it may there be fairly well approximated by /7/

$$\sum_{n\geq 1} F_{2,n}(x)(1/kT)^n \approx -\frac{2\pi}{R^3}\int_1^\infty \{\cosh[q(r)] - 1 - q(r)^2/2\}r^{*2}\,dr^* \quad (14)$$

Here, r* equals r/R, and

$$q(r) = -\frac{e^2}{kTr}e^{-xr^*} \quad (15)$$

The rhs of eq. (14) is the second ionic virial coefficient for the RPM.

Although the theory leading to eqs. (10) - (14) is rather complicated, the end result is fairly simple and can be programmed on a pocket calculator.

One application of the perturbation theory is illustrated in Fig. 4, which shows part of the liquid-gas coexistence curve for the RPM

compared with the experimental curve for KCl /9/. The hard-sphere model is found to predict a reasonable value for the critical temperature of KCl, whereas the critical density is off by a factor of ten. More detailed aspects of the critical behaviour of molten salts have been discussed by Larsen and Stell /10/.

For unequal-diameter charged hard spheres one can consider two types of perturbation theories, one based on a mixture of unequal-diameter (neutral) hard spheres and the other based on the RPM as reference system. In the latter case, the reference potential is

$$u_{ij}^{o}(r) = \begin{cases} \infty & \text{for} \quad r<R \\ e_i e_j/r & \text{for} \quad r>R \end{cases}, \tag{16}$$

and the perturbation is such that when added to u^o, the total is

$$u_{ij}(r) = \begin{cases} \infty & \text{for} \quad r<R_{ij} \\ e_i e_j/r & \text{for} \quad r>R_{ij} \end{cases}. \tag{17}$$

The function

$$\delta e_{ij}(r) = \exp[-\delta u_{ij}(r)/kT] \tag{18}$$

is a more convenient expansion parameter than δu in this case. The zeroth-order perturbation theory is simply

$$F^{o} = F_{RPM}, \tag{19}$$

which is the familiar law of corresponding states /11/. At this level, there is only one characteristic interionic distance, R. A natural choice of R is the sum of anion and cation radii. This choice also leads to a vanishing first-order term of the theory. The main correction to the law of corresponding states turns out to be of second order in the ion-diameter disparity /12/.

4. INTEGRAL EQUATIONS

An analysis of the cluster expansion leads to a relation between the direct correlation function $c_{ij}(r)$, the total correlation function $h_{ij}(r) \equiv g_{ij}(r) - 1$, and the potential /2,13/;

$$c_{ij}(r) = -u_{ij}(r)/kT + h_{ij}(r) - \ln[1+h_{ij}(r)] + B_{ij}(r). \quad (20)$$

The direct correlation function is defined by the Ornstein-Zernike equation,

$$h_{ij}(r) = c_{ij}(r) + \sum_{k}^{\text{all species}} \rho_k \int h_{ik}(r')c(|\underline{r} - \underline{r}'|)d\underline{r}' \quad (21)$$

The function $B_{ij}(r)$ is a sum of terms in the cluster expansion that belong to a certain class. Due to the topology of these term's graphical representations, B is called the sum of "bridge" diagrams /1/. In the approximations discussed here, we shall assume that $B \equiv 0$.

Eq. (21) contains two functions and their convolution (integral), which is why this approach is called integral equations.

The method of solution is:

1. Supplement the Ornstein-Zernike equation with a closure relation.
2. Solve for $h_{ij}(r)$ and $c_{ij}(r)$.
3. Compute thermodynamic properties.

A closure relation is a second relation between h and c that makes the set of equations complete. Neglecting $B_{ij}(r)$ in eq. (20) leads to a closure called the hyper-netted chain (HNC) equation. Different numerical techniques have been used to solve the HNC integral equation /14/; no analytical solution has yet been found.

A typical result for the equal-diameter charged hard-sphere system (the RPM) is given in Fig. 5, which shows the radial distribution function in a molten-salt like state. The corresponding results of a Monte Carlo computer simulation are included for comparison. Since the RPM is a hard-core model, g(r) is identically zero for $r/R < 1$, and this part

of the curve is not shown.

There is a good overall agreement between HNC and the exact MC results. The only significant discrepancy is found in g(r) between like ions ($g_{++}(r) \equiv g_{--}(r)$ for the RPM) for $1 < r/R < 2$. Moreover, the model calculations give structural features that are typical for molten salts /15/, *viz.* a high anion-cation correlation between nearest neighbors; g_{++} and g_{+-} oscillating up to several ion diameters, but in such a way that their average does not oscillate beyond $r/R \approx 3$; a significant penetration of like ions into the first coordination shell.

A somewhat simpler integral equation is obtained by neglecting all but the most dominant term of eq. (20),

$$c_{ij}(r) = -u_{ij}(r)/kT \ . \tag{22}$$

This closure is called the mean spherical approximation (MSA). For a hard-core system, eq. (22) applies to r>R since the region r<R is determined by the exact relation h(r) = -1.

The MSA must, in general, be solved numerically like the HNC equation, but in some important cases analytic solutions have been found. One such case is the RPM, for which the MSA was solved by Waisman and Lebowitz /16/. They found analytic expressions for the Laplace transform of $g_{ij}(r)$ and for the thermodynamic properties. (The Laplace transform can be inverted analytically, but is easier done numerically). In fact, we have already made use of the result for the free energy, which is

$$\left(\frac{F}{VkT}\right)_{MSA} = \left(\frac{F}{VkT}\right)_{\text{hard spheres}} + F_1(x)_{MSA} \tag{23}$$

with $F_1(x)_{MSA}$ given by eq. (11). This result was obtained via the energy equation, which has been found most accurate of the three routes from correlation functions to thermodynamic properties for the RPM.

A comparison between the MSA result for the RPM's internal energy and the experimental result for KCl(l) is shown in Fig. 6. The experimental point is taken at 1 atm. pressure. The agreement must be con-

sidered good in light of the fact that no adjustable parameters have been used (R was taken to be the sum of Pauling's anion and cation radii).

5. CONCLUSIONS

There are several statistical theories today that apply to molten-salt models, and lead to numerical as well as formal results for thermodynamic and structural properties. Some of these theories yield simple, analytic expressions that are sufficiently accurate to provide a meaningful comparison with experimental data. Interpretations of results for the structure of molten salts have already been made in terms of charged hard-sphere models /17/.

The theories are of two basic types; perturbation theories and integral equations. They complement computer simulation methods in the sense that they often provide an analytic relation between the potential parameters and the bulk properties at the cost of being less accurate than simulations.

In this paper we have discussed the basic principles of these theories and given some examples that illustrate the kind of results they lead to.

ACKNOWLEDGEMENT

Acknowledgement is made to the Norwegian Council for Science and the Humanities for support of this work.

REFERENCES

/1/ See *e.g.* J.P. Hansen and I.R. McDonald, *Theory of Simple Liquids* (Academic Press, London, 1976).

/2/ T. Morita and K. Hiroike, Progr. Theor. Phys. 25, 537 (1961).

/3/ G. Stell, in *The Equilibrium Theory of Classical Fluids*, edited by H.L. Frisch and J.L. Lebowitz (Benjamin, New York, 1964).

/4/ J.E. Mayer, J. Chem. Phys. 18, 1426 (1950).

/5/ H.L. Friedman, *Ionic Solution Theory* (John Wiley, New York, 1962).

/6/ N. Bjerrum, Kgl. Danske Vidensk. Selskab 7, No. 9 (1926).

/7/ G. Stell and B. Larsen, J. Chem. Phys. 70, 361 (1979).

/8/ H.C. Andersen and D. Chandler, J. Chem. Phys. 57, 1918 (1972).

/9/ A.D. Kirshenbaum, J.A. Cahill, P.J. McGonigal, and A.V. Grosse, J. Inorg. Nucl. Chem. 24, 1287 (1962).

/10/ B. Larsen and G. Stell, in *Studies in Statistical Mechanics*, edited by J.L. Lebowitz and E.W. Montroll (North Holland, Amsterdam, in preparation).

/11/ H. Reiss, S.W. Mayer, and J.L. Katz, J. Chem. Phys. 35, 820 (1961).

/12/ B. Hafskjold (unpublished results).

/13/ J.M.J. Van Leeuwen, J. Groeneveld, and J. DeBoer, Physica (Utrecht) 25, 792 (1959).

/14/ R.O. Watts, in *Statistical Mechanics*, A Specialist Periodical Report, edited by K. Singer (The Chemical Society, London, 1973), Vol. 1.

/15/ J.E. Enderby and G.W. Neilson, Adv. Physics 29, 323 (1980).

/16/ E. Waisman and J.L. Lebowitz, J. Chem. Phys. 56, 3086 (1972); *ibid.* 56, 3093 (1972).

/17/ M.C. Abramo, C. Caccamo, G. Pizzimenti, M. Parrinello, and M.P. Tosi, J. Chem. Phys. 68, 2889 (1978).

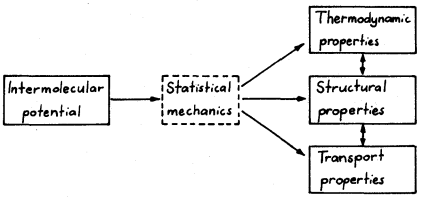

Figure 1. Schematic illustration of the relation between microscopic and macroscopic properties through statistical mechanics.

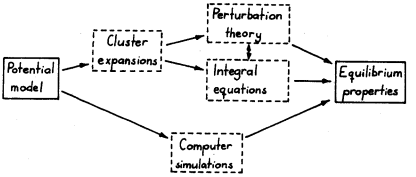

Figure 2. Schematic illustration of the division into perturbation theories and integral equations. Computer simulations provide an independent and exact route from the potential model to the equilibrium properties.

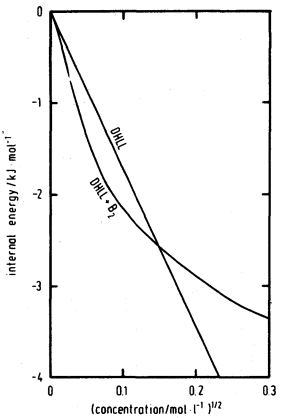

Figure 3. Internal energy for an aqueous 2-2 electrolyte solution model at 25°C as function of the square root of the concentration. The two curves were obtained from the Debye-Hückel limiting law (DHLL) and the ionic virial expansion truncated after the second term.

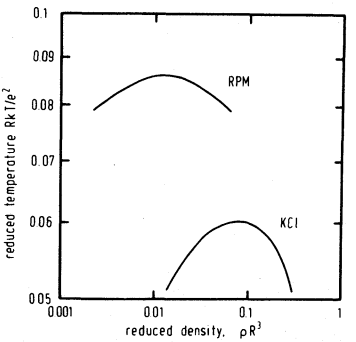

Figure 4. Liquid-gas coexistence curves for equal-diameter charged hard spheres (restricted primitive model, RPM) and KCl.

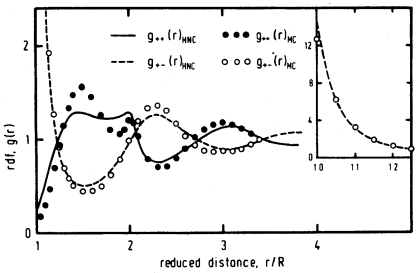

Figure 5. Radial distribution functions for the RPM in a typical molten-salt state ($RkT/e^2 = 0.0282$, $\rho R^3 = 0.669$). The results were obtained from the hyper-netted chain (HNC) equation and Monte Carlo (MC) computer simulations.

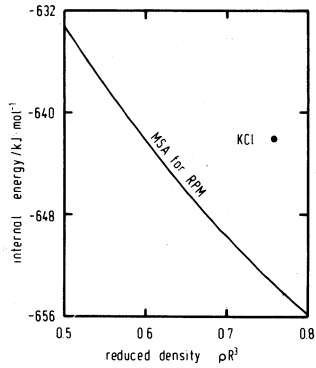

Figure 6. Internal energy for the RPM and KCl at 800°C. The result for RPM was obtained from the mean spherical approximation (MSA). The hard-sphere diameter R was set equal to the sum of Pauling's ionic radii for K^+ and Cl^-. The point for KCl represents the experimental value at 1 atm.

DOI: 10.1149/198109.0023PV

ADVANCES IN THEORIES OF MOLTEN SALT SOLUTIONS

M. L. Saboungi and M. Blander
Chemical Engineering Division
Argonne National Laboratory
Argonne, Illinois 60439

ABSTRACT

Recent advances in theories of molten salt solutions have provided fundamental insights and have expanded our ability to calculate solution properties a priori. Monte Carlo and molecular dynamics calculations for binary solutions have been used to investigate the relative importance of different ionic interactions on solution properties. The thermodynamic properties of a multicomponent system are related directly to those of the binary subsystems and of the pure components by equations derived from statistical mechanics. In dilute solutions, the phenomenon of ionic association in a binary solvent is examined; the energetics of the associations are shown to depend upon the solution properties of the lower-order subsystems. Finally, a recent study of slag exchange equilibria by the coordination cluster theory is reviewed; the results have led to a physical interpretation of the concentration dependence of these equilibria.

I. INTRODUCTION

In the last decade, advances in theories of molten salt solutions have been made which are interesting not only from a fundamental point of view but also from a practical point of view. The purpose of this paper is to review progress in molten salt solution chemistry. For clarity, concentrated and dilute solutions are discussed separately.

In concentrated solutions, advances in binary solutions have been accomplished mostly by the use of numerical simulations-Monte Carlo (MC) or molecular dynamics (MD). In ternary and higher-order solutions, statistical mechanics has been used to calculate the thermodynamic mixing properties; the interesting aspect of the derived equations is that one can perform calculations of solution properties a priori from data on lower-order systems.

In dilute solutions, ionic asociations, as well as the solubility products of relatively insoluble solids in a multicomponent solvent, have been studied. Recently, exchange equilibria between ionic solutions (including slags) and metallic solutions have been studied by taking preferential solvation into consideration.

II. CONCENTRATED MOLTEN SALT SOLUTIONS

In what follows, we start by examining advances accomplished in the simplest kind of systems, those containing monovalent ions. The binary and the ternary and higher-order solutions are considered separately, with special emphasis on the fundamental approaches used in different theories or models. We then discuss progress made in the study of systems containing ions of different valences.

A. Binary Solutions

As mentioned above, the use of numerical simulations (1-4) proved to be a unique and powerful means of gaining further insights into solution structure and into the relative importance of different ionic interactions.

Using MC calculations, the mixing process of liquid NaCl-KCl solutions has been investigated at 1083 K by Larsen et al. (1). Two hundred sixteen ions interacting with an additive pair potential of the Huggins-Mayer form were contained inside a cubic box with the well-known periodic boundary conditions. The coulombic, repulsive, dipole-dipole, and dipole-quadrupole contributions to the internal energies were evaluated for an equimolar mixture ($X_{NaCl} = X_{KCl} = 0.5$). The MC results seem to indicate that the dispersion energy is relatively important and that nearest and next-nearest neighbor interactions make equal contributions to the energy of mixing of the NaCl-KCl system (1) (Table I). However, the authors concluded by pointing out that the thermodynamic changes on mixing are calculated as small differences between large quantities and thus have large relative errors. No useful detailed information (such as a possible explanation of the measured negative excess entropy of mixing) on the mixing process was obtained.

Recently, Lantelme and Turq (4) followed the same procedure as Larsen et al., (1) to numerically simulate LiBr-KBr liquid solutions. Starting with the same number of particles, their MD results led to an evaluation of the various contributions to the internal energy. Even though the excess quantities are each obtained from small differences between two large numbers, the authors conclude that the main contribution to the enthalpy of mixing comes from a balance between (1) the negative coulomb contributions and (2) the short-range influence (which is positive and of less importance). They also computed the coordination number, n, as a function of the composition of the solution. Their study shows that the local environment depends strongly on the nature of the cations and does not depend solely on the composition of the system. In Table II, this last conclusion is illustrated by the values of the coordination number as well as the values of those of the equivalent number defined by n/X_i where X_i is the mole fraction of i for different solution compositions (4). Such information should be accounted for in any solution model to accurately represent the solution behavior.

In another aspect, computer simulations of binary solutions have been used to test the validity of some theories (2,3). Adams and McDonald (2) used MC computations in ionic liquid mixtures to discuss the

Table I. Repulsion $\langle\Phi_r\rangle$, dispersion $\langle\Phi_d\rangle$, and coulomb energy $\langle\Phi_c\rangle$ contributions from the different pairs at 1083 K and zero pressure in an equimolar NaCl-KCl liquid mixture to the energy of mixing $\langle\Delta\Phi\rangle_{mix}$ (All energies are in kcal mol^{-1} and values are taken from Reference 1).

	$\langle\Phi_r\rangle$			$\langle\Phi_d\rangle$			$\langle\Phi_c\rangle$
	+ +	+ -	- -	+ +	+ -	- -	
NaCl(l)	0.17	23.20	1.36	-0.03	-2.11	-2.12	-193.08
KCl(l)	0.39	21.85	0.55	-0.24	-4.70	-1.26	-172.75
(Na,K)Cl(l)	0.25	22.44	0.89	-0.11	-3.33	-1.65	-182.08
$\Delta\langle\Phi\rangle$mix	-0.03	-0.09	-0.07	0.03	0.08	0.04	0.84

Table II. Coordination numbers n and equivalent coordination numbers eq.n in LiBr-KBr mixtures at 1020 K (4). Plasma parameter: $\Gamma = e^2/(2kTr_{Br}) = 47.7$; Radius ratio: $R_{LiBr} = 0.476$, $R_{KBr} = 0.853$.

Mole Fraction	Br-Li			Br-K		Li-Li		K-K		Li-K		Br-Br		
of LiBr	Temp.,/K	n	eq.n	n	eq.n	n	eq.n	n	eq.n	n	eq.n	n	eq.n	n
1	1020	4.27	4.27	--	--	11.47	11.47	--	--	--	--	--	--	12.07
0.898	1020	3.89	4.33	0.65	6.37	9.98	11.11	1.70	16.66	1.54	15.1	13.54	15.1	11.92
0.5	1020	2.06	4.12	3.00	6.00	4.87	9.74	7.90	15.80	7.10	14.20	7.10	14.20	10.92
0.5	1685	1.84	3.68	2.46	4.92	4.06	8.12	6.71	13.42	5.15	10.30	5.15	10.30	10.80
0.102	1020	0.41	4.01	5.11	5.69	0.99	9.71	13.02	14.5	10.51	11.68	1.19	11.68	14.22
0	1020	--	--	5.67	5.67	--	--	15.50	15.50	--	--	--	--	15.44

eq. $n \equiv n/X_I$ where X_I is the ion fraction of the second ion of the pair.

application of dimensional methods in the statistical mechanics of pure salts. The thermodynamic properties of a binary solution can be evaluated from those of a reference salt, using perturbation calculations according to the conformal ionic solution (CIS) theory (5,6). One starts with a reference salt characterized by a single size parameter d_o, and the components of the mixture are generated from the reference salt by appropriate changes of d_o to $d_i (i = 1,2)$. These perturbations affect the configurational integrals and thus the Helmholtz free energy. Finally, the excess Helmholtz free energy of mixing ΔA_m^E is given (up to the second-order expansion) by:

$$\Delta A_m^E = a(T,V) \left(\frac{d_o}{d_1} - \frac{d_o}{d_2} \right)^2 X_1 X_2 \qquad (1)$$

where a(T,V) is a collection of multiple integrals which depends solely on the reference salt properties and X_1 and X_2 are the mole fractions of the salts of the mixture. From experiments (7,8), it appears that the coulomb contribution to the enthalpy of mixing of alkali-metal salts has a form similar to Eq. 1; it was shown that the ratio $\Delta H_m / X_1 X_2$ is proportional to the square of the difference $(1/d_2 - 1/d_2)$ where ΔH_m is the enthalpy of mixing. The proportionality factor is negative for nitrate, fluoride, and chloride mixtures; its magnitude is a function of the class of salts studied. Adams and McDonald (2) used a pair potential suggested by Blander (9) to describe the interactions between the ions. Their computations were made for binary systems having a common anion, with the ratio d_1/d_2 ranging from 1.2 to 2.0, and with all mixtures generated from the same reference salt. It is obvious that rather poor values of (d_1/d_2) were selected since (1) a much wider range of diameters is implied than those found for monovalent salts and (2) Eq. 1 does not rigorously hold since in its derivation only second-order terms in (d_o/d_i) were included, implying that d_o/d_i is assumed to be very close to unity. Their MC results on ΔH_m for the nitrate mixtures were surprisingly consistent with the predictions of the second-order perturbation theory but the sign was in disagreement with experiments. In the case of alkali-metal nitrates Kleppa and Hersh (7) reported at the equimolar concentration:

$$4\Delta H_m = -85 \left(\frac{1}{d_1} - \frac{1}{d_2} \right)^2 \text{ (kcal mol}^{-1}\text{)} \qquad (2)$$

while the MC results (2) yielded:

$$4\Delta H_m = 55 \left(\frac{1}{d_1} - \frac{1}{d_2} \right)^2 \text{ (kcal mol}^{-1}\text{)} \qquad (3)$$

This disagreement on the sign of the coefficient could result either from unrealistic size parameters being used for the salts of the numerically generated solutions or from the form of the pair potential used for the interacting particles. Another possible explanation is that due to the high density of the system, the solution might have remained solid.

More recently, a more direct test of Eq. 1 and its validity was accomplished (3) by evaluating a(T,V) by MD techniques. This quantity can be expressed, using the CIS theory as:

$$a(T,V) = \frac{N^2}{2kT(N-1)} \left\{ \frac{\langle E^2 \rangle - \langle E \rangle^2}{N} - [\langle E_c^2 \rangle - \langle E_c \rangle^2] \right\} \qquad (4)$$

where N is the total number of moles and E_c and E are defined as:

$$E_c = \sum_{a=1}^{N} \left(\frac{\partial u_{ca}}{\partial \lambda_i} \right)_{\lambda=1} \qquad (5)$$

and

$$E = \sum_{c=1}^{N} E_c$$

where a refers to the anions, c to the cations present in the binary chloride mixture, u_{ca} is the potential energy of the pair c-a and λ_i is the perturbation parameter defined as $\lambda_i = d_o/d_i$ (i = 1,2). Finally for any function Q, <Q> refers to:

$$\langle Q \rangle = \frac{1}{Z_o (N!)^2} \int \cdots \int Q \exp(-U_o/kT)(d\tau)^{2N} \qquad (6)$$

where Z_o is the configurational part of the classical partition function for the reference salt, and U_o is the potential energy of the reference salt. In this work, two pair potentials were used to represent the interactions between the 216 particles, namely the Tosi-Fumi potential (10) and a somewhat harder repulsive potential suggested by Michielsen et al. (11). The computed values for a(T,V) have a negative sign, in agreement with the experiment, but their magnitude is strongly dependent on the repulsive part of the pair potential as can be seen from Table III. This could partly explain the positive sign for a(T,V) obtained by Adams and McDonald (2).

Thus far, numerical simulations have provided information on the mixing process which permits a careful examination of ad hoc assumptions on the relative importance of different ionic interactions. The pair potentials used in these computations are empirical, and the softness seems to have a major influence on mixing properties. Thus, in order to take full advantage of the powerful numerical simulations, improved pair potentials derived, perhaps, from quantum mechanical considerations are needed, as well as criteria to test their validity and their range of application. Even though the influence of ion polarizability on the dynamics of the pure molten salts has been shown to be negligible, (13) it would be important to examine its contribution to the thermodynamics of binary mixtures.

Table III. Values of a(T,V) and relevant correlations in binary chloride mixtures for two different pair potentials (3).

Source	a(T,V) (kcal mol^{-1})	T (K)	$\frac{\langle E_c^2 \rangle}{\langle E_c \rangle^2}$	$\langle E_c \rangle$ $\langle 10^{-12}$ erg$\rangle$	$N\left(\frac{\langle E^2 \rangle}{\langle E \rangle^2} - 1\right)$
Tosi-Fumi potential (10)	-460±50	1115	1.132	14.48	0.086±0.005
Michielsen et al. potential (11) (m = 1, n = 6)	-44±4	1107	1.102	4.973	0.064±0.004
Experiment	-37 (7,8);-130 (12)				

B. Ternary and Higher-Order Solutions

In this section, advances made by statistical mechanical models are reviewed. In recent developments, emphasis has been placed on the a priori calculations of the thermodynamic properties of multicomponent systems from those of the binary subsystems and of the pure compounds. Other nonstatistical mechanical models have been suggested ad hoc, assuming some empirical means of combining properties of binary systems to perform calculations for ternary systems; these models are not included.

In ionic systems, there are two different classes of multicomponent solutions. A system is referred to as additive when all the constituents have a common anion or a common cation e.g., $(A_1^+,\ldots,A_m^+/X^-)$ or $(A^+/X_1^-,\ldots,X_p^-)$, respectively. A systems is referred to as reciprocal when all the constituents do not have a common anion or cation e.g., $(A_1^+,\ldots,A_m^+/X_1^-,\ldots,X_p^-)$ where m and p do not necessarily have the same value.

1. Additive Ionic Systems

Only ternary systems have been examined using the CIS theory (14). The expansion of the partition function, Z_m, and of the thermodynamic functions have been carried out up to the fourth-order. The final results yielded the following expression for the excess Helmholtz free energy of mixing ΔA^E_m of the ternary [AX(=1)-BX(=2)-CX(=3)] system

$$\Delta A^E_m = \sum_{i<j}\sum a_{ij}X_iX_j + \sum_{i\neq j}\sum b_{ij}X_i^2X_j + \sum_{i<j}\sum c_{ij}X_i^2X_j^2 + A\,X_1X_2X_3 + \sum_{\substack{i\\ i\neq j<k}} B_iX_i^2X_jX_k \qquad (7)$$

where X_i is the mole fraction of the i^{th} component. The coefficients a_{ij}, $b_{ij}(=-b_{ji})$ and c_{ij} are determined from the binary subsystem (i-j). For example, the Helmholtz free energy of mixing of the binary AX-BX is given by:

$$\Delta A^E_m(1\text{-}2) = a_{12}\,x_1x_2 + b_{12}\,x_1x_2\,(x_1-x_2) + c_{12}\,x_1^2x_2^2 \qquad (8)$$

where x_1 and x_2 are the mole fractions in the binary system. The coefficients A and B_i (i = 1,2,3) are ternary coefficients and can be calculated directly from the binary data using the following relations:

$$A \simeq (b_{12}^{1/3} + b_{13}^{1/3})(b_{21}^{1/3} + b_{23}^{1/3})(b_{13}^{1/3} + b_{23}^{1/3}) \qquad (9)$$

and

$$B_i = 2(c_{ij}^{1/2}\,c_{ik}^{1/2}) \qquad i\neq j\neq k \qquad (10)$$

Thus, using Eqs. 7-10, one can calculate ΔA^E_m for a ternary solution solely from information on the binary subsystems. The validity of these equations and their extensions has been tested on a variety of real systems having a wide range of complexity e.g., systems of interest for carbonate-fuel cells, high-temperature batteries, and cryolite-based systems (15,16). The CIS equations appear to provide an accurate description of the experimental data. In some cases, the equations were used to generate phase diagrams for systems where no measurements of the ternary solutions exist.

2. Reciprocal Ionic Systems

The CIS theory has been expanded (17) to study the general case of multicomponent systems schematically represented by $(A_1^+,..,A_m^+/X_1^-,...,X_p^-)$. Up to the second-order expansion, the Helmholtz free energy of the mixture is given by:

$$A_m = RT(\sum_a X_a \ln X_a + \sum_c X_c \ln X_c) + \sum_a \sum_c A^\circ_{ca}$$
$$+ \sum_a \sum_{a'<a} \sum_c \sum_{c} X_a X_{a'} X_c \lambda(ca\text{-}ca') + \sum_a \sum_c \sum_{c'<c} X_a X_c X_{c'} \lambda(ca\text{-}c'a)$$
$$- \sum_a \sum_{a'<a} \sum_c \sum_{c'<c} X_a X_{a'} X_c X_{c'} [\Delta A^\circ(a,a',c,c')]^2/2ZRT \qquad (11)$$

where X_a is the anionic fraction, X_c is the cationic fraction, A°_{ca} is the standard Helmholtz free energy of the pure compound ca, $\lambda(ca\text{-}ca')$ represents the interaction coefficient in the binary ca-ca' system having a common cation, $\lambda(ca\text{-}c'a)$ represents the interaction coefficient in the binary ca-c'a system having a common anion, Z is parameter usually taken as 6 and $\Delta A^\circ(a,a',c,c')$ is the standard Helmholtz free energy change accompanying the following metathetical reaction between the liquid salts:

$$ca + c'a' \rightleftharpoons c'a + ca' \qquad (12)$$

The properties of the multicomponent systems can be calculated from those of the binary subsystems and the pure compounds. Eq. 11 should prove to be useful in calculating liquid-solid equilibria, activities, and activity coefficients in higher-order systems.

Finally, reciprocal quaternary systems such as $(A_1^+,A_2^+,A_3^+/X_1^-,X_2^-)$ or $(A_1^+,A_1^+/X_1^-,X_2^-,X_3^-)$ have been studied by the surrounded ion model (SIM) (18). In this model, significant problems are present because the "binary" contributions [terms containing $\lambda(ca\text{-}ca')$ or $\lambda(ca\text{-}c'a)$] are introduced in an ad hoc manner and the second-order terms (the terms analogous to the last summation in Eq. 11) are incomplete. For example, Eq. 11 reduces to the correct expressions for all lower-order systems such as ternary reciprocal systems; this is not the case for the equations derived using the SIM (18).

C. Systems Containing Ions of Different Valences

Theoretical or numerical simulation studies of the solution properties of systems containing cations of different valences have not been published. So far, empirical extensions of the equations derived for monovalent multicomponent systems have been used for such asymmetrical systems. These extensions consist of either keeping the same formalism or of substituting equivalent fractions for mole fractions in the equations for the thermodynamic functions of mixing (19). The advantages of such formalisms are purely mathematical since one uses ionic or equivalent fractions only to simplify the analytical representation of data for different thermodynamic functions, e.g., ΔH_m, G_m^E, and S_m^E (16).

Fundamental studies of the influence of the difference in ionic charges on the properties of the system should be initiated.

III. DILUTE SOLUTIONS

In dilute ionic solutions, associations of ions and solubilities of relatively insoluble solids have been studied. Preferential solvation and its influence on exchange equilibria between slags and metallic solutions has also been examined.

A. Ionic Associations and Solubilities

In dilute solutions, the deviations from Henry's law are explained in terms of associations between solute ions. For example, if the solvent is referred to as BY-CY and the solute as AX, when X_A and $X_X \to 0$, the presence of associated species might be postulated:

$$A^+ + X^- \rightleftharpoons (AX) \qquad K_{11} \tag{13}$$

$$AX + A^+ \rightleftharpoons (A_2X)^+ \qquad K_{21} \quad \text{etc.} \tag{14}$$

where K_{11}, K_{21}, etc. are the association constants of AX, $(A_2X)^+$, etc., respectively. A typical case of such associations is when the solute is AgCl and the solvent is $LiNO_3$-KNO_3.

Recently, the coordination cluster theory (20) has been applied to correlate and understand the energetics of association in dilute reciprocal ternary systems (21) (e.g., the solute is AX and the solvent is BY). It was shown that to a first approximation, the specific bond free energy of association is related to $\Delta A°(A,B,X,Y)$ and to the thermodynamics of the four binary subsystems, AX-AY, BX-BY, AX-BX, and AY-BY. Thus, one could predict when associations may occur and the stabilities of the species formed as well as the factors which influence these stabilities.

For a solvent that is a binary solution and a system that is a quaternary reciprocal system, Bombi and Sacchetto (22) have examined the influence of the solvent composition on the energetics of the associations

by use of the quasichemical theory. Their results indicate a nonlinear dependence on solvent composition; the energy change ΔE_{11} associated with reaction 13 to form (AX) is given by:

$$\Delta E_{11} = RT \ln[X_B \exp(\Delta E_B/RT) + X_C \exp(\Delta E_C/RT)] \qquad (15)$$

where ΔE_B and ΔE_C are defined as the energy changes for reaction 13 to form (AX) in the solvents BY and CY, respectively. The above equation is particularly useful in the case where ΔE_B and ΔE_C are very different.

The conclusions reached from the quasi-chemical theory (22) that ΔE_{11} is not a linear combination of ΔE_B and ΔE_C were corroborated by the use of the CIS theory (17); however, from the CIS theory, it becomes evident that the interactions between the solvent ions B^+, C^+, Y^- have an influence on ΔE_{11} and should be taken into account (17). Furthermore ΔE_B and ΔE_C could be identified through the CIS theory with measurable quantities in the binary subsystems. Thus a more complicated equation than Eq. 15 appears to be needed to represent the contributions of other interactions such as that of the solvent, to ΔE_{11}(17).

Finally, within the framework of the CIS theory, the solubility product of relatively insoluble solids in a multicomponent solvent can be calculated by using an exact chemical cycle. The cycle consists of three steps:

$$AX(s) + (BY\text{-}CY) \rightleftharpoons AY + (BX\text{-}CX) \qquad \text{I}$$

$$AY \rightleftharpoons AY(\infty \text{ dln in BY-CY}) \qquad \text{II}$$

$$(BX\text{-}CX) \rightleftharpoons (BX\text{-}CX)(\infty \text{ dln in BY-CY}) \qquad \text{III}$$

The notation (∞ dln in BY-CY) means that the species on the right-hand side is at infinite dilution in the solvent (BY-CY). The standard Helmoltz free energy associated with each step is ΔA°_α (α = I, II, III) and is directly related to the solubility product, K_{SP} by the equation:

$$-RT \ln K_{SP} = \Delta A^\circ_I + \Delta A^\circ_{II} + \Delta A^\circ_{III} \qquad (16)$$

where ΔA°_I, ΔA°_{II}, and ΔA°_{III} can be estimated from the CIS equations for A_m (Eq. 11) (17) taking into account the nonrandom mixing of the B, C, X, and Y ions in solution.

B. Exchange Equilibria Between an Ionic Solution and a Metallic Solution

In this context, ionic solutions include slags. In a recent study (22), a consideration of preferential solvation has been incorporated into an examination of the exchange equilibria between an ionic and a metallic solution. An equilibrium involving exchange of components C and D between a binary slag A-B and a metallic phase can be expressed by:

$$M_C^{+n}(\text{ionic sol.}) + M_D(\text{metal}) \rightleftharpoons M_C(\text{metal}) + M_D^{+n}(\text{ionic sol.}) \qquad (17)$$

where M_C^{+n} and M_D^{+n} refer to the cations contained in the C and D components of the slag. The equilibrium quotient K is related to the equilibrium constant K_e by:

$$K = K_e \, (\gamma_C/\gamma_D) \tag{18}$$

where γ_C and γ_D are the activity coefficients of C ad D, respectively in the slag. It can be seen that for a given metal phase, the ratio of the activity coefficients (γ_C/γ_D) governs the ratio of the concentrations of the ions in the slag phase.

If random mixing is assumed, it can be shown that $\ln (\gamma_C/\gamma_D)$ is expressed by:

$$\ln(\gamma_C/\gamma_D)^* = X_A \ln[\gamma_{C(A)}/\gamma_{D(A)}] + X_B \ln [\gamma_{C(B)}/\gamma_{D(B)}] \tag{19}$$

where $\gamma_{M(N)}$ refers to the limiting activity coefficient of M at infinite dilution in pure N (M ≡ C,D; N ≡ A,B) and the designation * means that random mixing has been assumed. Eq. 19 was first proposed by Flood and Grjotheim. From the coordination cluster theory (20), it was shown that (23):

$$\ln(\gamma_C/\gamma_D) = \ln(\gamma_C/\gamma_D)^* + \sum_A \tag{20}$$

where $\sum_A$ is a collection of terms which are mostly corrections due to preferential solvation and are significant in a large fraction of cases. It was shown that preferential solvation leads to large deviations from the linear dependence predicted by Flood and Grjotheim.

IV. CONCLUDING REMARKS

Significant advances which have been made in the development of solution theories have an impact on several technological applications such as high-temperature batteries, fuel cells, aluminum electrolysis and solar energy. A better understanding of the ionic structures as well as of the relative importance of different ionic interactions is developing using sophisticated numerical methods. The results of such calculations should be incorporated into models of ionic solutions. However, theories are still lacking for solutions containing ions of different charges as well as for metal-salt solutions.

ACKNOWLEDGMENTS

This work was supported by the Division of Basic Sciences of the U.S. Department of Energy. We thank Ms. P. L. McBride for her diligence in typing this manuscript.

REFERENCES

1. B. Larsen, T. Førland, and K. Singer, Mol. Phys. 26(6), 1521 (1973).

2. D. J. Adams and I. R. McDonald, Physica (Utrecht) B79, 159 (1975).

3. M. L. Saboungi and A. Rahman, J. Chem. Phys. 65(6), 2393 (1976); J. Chem. Phys. 66(6), 2773 (1977).

4. F. Lantelme and P. Turq, Mol. Phys. 38(4), 1003 (1979)

5. H. Reiss, J. Katz, and O. J. Kleppa, J. Chem. Phys. 36, 144 (1962).

6. M. Blander, J. Chem. Phys. 36, 1092 (1962).

7. O. J. Kleppa and L. S. Hersh, J. Chem. Phys. 34, 351 (1961).

8. L. S. Hersh and O. J. Kleppa, J. Chem. Phys. 42, 1309 (1965).

9. M. Blander, Adv. Chem. Phys. 11, 82 (1967).

10. F. G. Fumi and M. P. Tosi, J. Phys. Chem. Solids 21, 31 (1964); M. P. Tosi and M. G. Fumi, J. Phys. Chem. Solids 21, 45 (1964).

11. J. Michielsen, P. Woerlee, F. V. D. Graaf, and J. A. A. Ketelaar, J. Chem. Soc. Faraday Trans. 2 71, 1730 (1975).

12. M. Blander (unpublished calculations, 1975).

13. G. Jaccuci, I. R. McDonald, and A. Rahman, Phys. Rev. A, 13, 1581 (1976).

14. M. L. Saboungi and M. Blander, J. Chem. Phys. 63(1), 212 (1975).

15. M. L. Saboungi, P. L. Lin, P. Cerisier, and A. D. Pelton, Met. Trans. 11B, 493 (1980).

16. P. L. Lin, A. D. Pelton, and M. L. Saboungi (submitted for publication).

17. M. L. Saboungi, J. Chem. Phys. (in press).

18. M. Gaune-Escard, CALPHAD 3(2), 119 (1979).

19. M. L. Saboungi and M. Blander, J. Am. Ceram. Soc. 58, 1 (1975).

20. M. Blander, M. L. Saboungi and P. Cerisier, Met. Trans. 10B, 613 (1979).

21. M. Blander and M. L. Saboungi, Acta Chem. Scand. (in press).

22. G. G. Bombi and G. A. Sacchetto, J. Electroanal. 34, 319 (1972).

23. M. L. Saboungi and M. Blander, Can. Met. Quat. (in press).

DOI: 10.1149/198109.0036PV

FIRST PEAK POSITIONS OF RADIAL DISTRIBUTION FUNCTION IN MOLTEN ALKALI HALIDES

Kazuo Furukawa and Hideo Ohno

Molten Materials Laboratory
Japan Atomic Energy Research Institute
Tokai-mura,Ibaraki 319-11
Japan

ABSTRACT

The small difference between the first peak positions in the radial distribution function of molten alkali halides from x-ray or neutron diffraction experiments and those from computer simulations exceeds the experimental error. It seems to be due to the deformation of the electron shell. In computer simulation, the shell model which has the spherical deformation was expected to have a closer value of the first peak position to the experimental one than the rigid ion model because it takes into account the polarization of ions. However, no change in the first peak position was found. Therefore, the non-spherical deformation of the electron shell at the point where ions are in contact with each other have to be taken into account.

I. Introduction

Furukawa has summarized the structure of molten alkali halides near the melting points and reported the following conclusions[1][2]:

(a) The nearest ionic distance r_1^{ℓ} in the liquid is smaller than that of the crystal r_1^{s} at the melting point.
(b) The first coordination number n_1^{ℓ} decreases from 6 in the crystal to 4-5 at fusion. These values agree with the n_1^{ℓ}(cal) calculated from the next proportional relationship using the experimental values of the other quantities,

$$V_m^s/V_m^{\ell}=[r_1^s/r_1^{\ell}]^3 n_1^{\ell}/n_1^s, \quad (1)$$

in which V_m^s and V_m^{ℓ} are the volumes of solid and liquid at the melting points.
(c) n_1^{ℓ} may be a little larger at the larger ionic radius ratio of cation and anion, r_c/r_a, in each series of halides.
(d) The second peaks in the smaller r_c/r_a of 0.3-0.5 are

sharp and definite and their maximum positions r_2^{ℓ} are near to $(1.52\text{-}1.56)r_1^{\ell}$. When r_c/r_a is larger (0.7-1.0), the second peaks are broader.

The following three are the most important factors which affect the molten structure of alkali halides;(i) the summation of the ionic radii of cation and anion, r_c+r_a, (ii) the radius ratio r_c/r_a and (iii) the deformation of ions due to the unsymmetrical local field. (iii) is characteristic of liquid and is not observed in the crystalline state. We have already pointed out that factor (iii) is important compared with factor (ii) by the analysis of the volume change in fusion and the activation energy of electrical conductivity at the melting point[3].

Recently, computer simulation by Monte Carlo(MC) or molecular dynamics(MD) has been applied to many molten alkali halides[4],[5]. The interionic potentials based on the corresponding solid state are employed for the simulation and the thermodynamical and structural properties are reported to be in good agreement with those of experiments. However, the first peak positions of the radial distribution functions of molten alkali halides calculated by computer simulation are always shorter than those of experiments by x-ray and neutron diffraction. The differences are 0.1-0.3Å and exceed the experimental error(less than 0.1Å).

In this paper, we summarize the results of x-ray and neutron diffraction experiments on molten alkali halides in which some data of our experiments by x-ray diffraction are included and the differences of the first peak position of the radial distribution function between experiments computer simulation are discussed. Some comments on the neutron diffraction method with isotopic substitution are also made.

II. Experimentals

X-ray diffraction measurements were carried out on a θ-θ x-ray diffractometer. MoKα(λ=0.711Å) was diffracted at the surface of the sample and then monochromatized by reflection on the curved graphite crystal. Slit systems of 1/2°-1/2° and 1°-1° were employed in the low($3^\circ \leq \theta \leq 10^\circ$) and high ($8^\circ \leq \theta \leq 45^\circ$) scattering angles,respectively, where θ is the scattering angle.

The samples were placed on a flat Pt tray(35x25x3mm) and heated in a small electric furnace made of Pt wire. The sample-heater assembly was enclosed under a He atmosphere by putting it in an air-tight chamber with a window

of Al foil of thickness 10μm to allow passage of the x-ray beam. The temperature was controlled within 20°C above the melting point to avoid the vaporization of the sample.

The measured intensities were corrected for polarization and absorption in the sample by the usual method[1]. The background was subtracted from the measured intensities, so that the difference between the scaling factors derived both by the high angle region method and by Krogh-Moe and Norman's method is within 0.01%. The radial distribution function D(r), the correlation function g(r) and the reduced intensity S·i(S) are given by the following expressions.

$$D(r)=4\pi r^2 g_0+\sum_m(\bar{K}_m)\,2r/\pi\int_0^{S_{max}} S\cdot i(S)\sin(rS)\,dS, \quad (2)$$

$$g(r)=D(r)/4\pi r^2 g_0 , \quad (3)$$

$$S\cdot i(S)=S[I_{eu}^{coh}(S)/\sum_m f_m^2(S)-1], \quad (4)$$

$$g_0=(\sum_m \bar{K}_m)^2\rho_0 , \quad (5)$$

and

$$S=4\pi\sin\theta/\lambda . \quad (6)$$

Where ρ_0 is the number of stoichiometric units per $\mathring{A}^3$, $\bar{K}_m$ the effective electron number in the atom m, $f_m(S)$ the independent atomic scattering intensity, $I_{eu}^{coh}(S)$ the total coherent intensity.

III. Results and Discussion

(A) First peak positions r_1 of the radial distribution function

The reduced intensity curves of molten LiCl[6] and NaCl[7] at 650°C and 810°C are shown in Fig.1 and Fig.2. The radial distribution function D(r), the correlation function g(r) and the function D(r)/r of these two molten salts are shown in Fig.3 and Fig.4. r_1 value depends on the choice of D(r), D(r)/r, or g(r). For example, r_1 values of these three curves in molten NaCl were $r_1(D)=2.81$, $r_1(D/r)=2.77$ and $r_1(g)=2.73\mathring{A}$ as shown in Fig.5.

The r_1 values reported in computer simulation are the first maximum position in g(r), and we have to compare the position from computer simulation and x-ray or neutron diffraction experiment using the same function. The reported r_1 values in x-ray and neutron diffraction experiments are almost the first maximum position in D(r). Therefore, we calculated g(r) from the reported D(r) and determined the r_1 values in g(r). The results are shown in Table 1.

The r_1 values of molten alkali halides calculated by computer simulation are always shorter than those of experiments by x-ray and neutron diffraction. The differences are 0.1-0.3Å. At least two possible reasons for the difference should be considered; (a) the experimental error including the termination effect and (b) the polarization of ions in the unsymmetrical electric field in the molten state.

(a) Error due to termination effect

Furukawa[31] and Clayton et al.[32] have already discussed how r_1 values depend on S_{max} in simple liquids. According to them, the termination effect is not significant as far as $S_{max}>7$ and does not exceed 0.05Å. We have also done a similar analysis on molten NaCl. Table 2 shows the r_1 values of molten NaCl at various S_{max} values in Fig.2. The result shows that the effect due to the termination seems to be less than 0.01Å even if the reduced intensities were truncated at $S_{max}=7.5Å^{-1}$.

To check the termination effect more precisely, the computational g(r) values of molten KCl[8] were transformed according to

$$S\cdot i(S)=4\pi g_0(\Sigma_m \bar{K}_m)^2/\Sigma_m \bar{K}_m^2 \int_0^{r_{max}=10Å} r[g(r)-1]\sin(Sr)dr. \quad (7)$$

Since $g(r)=1$ beyond $r\simeq 9Å$, r_{max} is safely replaced by infinity. Fig.6 shows the computational and experimental $S\cdot i(S)$ values. The experimental g values were obtained by using $S_{max}=7.38Å^{-1}$. The results were shown in Fig.7. The height of the first peaks of the correlation function proved to be approximately equal to that experimentally determined and the position of the first peak shifts to 3.00Å from 2.95Å. This shows that the exact r_1 should be a little shorter than 3.05Å, which was found by x-ray diffraction.

Therefore, the difference between observed r_1 value and calculated one exceeds the error due to the termination effect.

(b) Polarization of ions

According to the analysis of volume change in fusion and activation energy of electrical conductivity at the melting point[3], the electronic polarizability α, is important comparable with the radius ratio r_c/r_a to the physical properties of molten alkali halides.

Dixon and Sangster[9],[10],[11],[12] have tried to bring the polarization effect into computer simulation by the electron shell model. In order to compare experimental

results with theoretical ones in molten KCl, we have also carried out computer simulation with both the rigid ion model and the shell model[8]. In computer simulations, the partial correlation functions, g_{++}, g_{+-} and g_{--} were histogrammed into 200 divisions between r=0 and r=10Å . These histograms were accumulated over 400 steps for each simulation. Computational correlation functions can then be calculated by

$$g^*(r)=(n_+ + n_-)^{-2}[n_+^2 g_{++}(r)+2n_+ n_- g_{+-}(r)+n_-^2 g_{--}(r)], \quad (8)$$

where n is the number of electrons of each ion. Fig.8 shows the experimental and computational correlation function. Although r_1 value by the shell model was expected to be more distant than that by the rigid ion model because of taking into account the polarizability of ions, no change in r_1 was found. The computational r_1 values are shorter than that found by x-ray diffraction by 0.1Å.

Fig.9 shows partial correlation functions of the shell model and the rigid ion model in molten KCl[8]. Significant kinks around the first peaks of g_{++} and g_{--} appeared in the shell model and such kinks vaguely perceived in g_{++} and g_{--} by the rigid ion model. Unfortunately, we can not compare directly the results by computer simulation with those by neutron diffraction analysis in molten KCl[14], because the neutron diffraction experiment had too much error. But, these kinks are observed in g_{++} and g_{--} of molten NaCl[13] and RbCl[15] by neutron diffraction with isotopic substitution.

Therefore, the shell model gives qualitatively a more satisfactory agreement of the radial distribution function between calculated values and experimental ones than does the rigid ion model. However, even the shell model gave a significant, though slight, difference in the position of the first peak of the radial distribution function compared with experimental ones.

These results indicate that in the model employed in the computer simulation the polarization of the ion has not been sufficiently taken into account. It seems to be due to the non-spherical deformation of the electron shell at the area where ions are in contact with each other as shown in Fig.10.

(B) Comments on neutron diffraction method with isotopic substitution

Neutron diffraction methods with isotopic substitution permits one to get the partial structure factors which are difficult to get by the x-ray diffraction method and can

compare directly with the results of the computer simulation, in general. The partial correlation functions of some molten salts, such as NaCl[13], KCl[14], CsCl[14] and RbCl[15] were obtained by this method. However, for example in molten NaCl, there is a clear difference between the first peak position of $_{o}g(r)$ by neutron diffraction with isotopic substitution, 2.6A, and that by x-ray diffraction, 2.73Å.

Zarzycki[16] studied the structure of molten NaCl at 820°C by x-ray diffraction and reported that the distance of the nearest Na-Cl pair was 2.9Å by the analysis of the first peak in D(r). On the other hand, the distance of Na-Cl pair was reported to be 2.6Å by the neutron diffraction analysis with isotopic substitution. The first peak position of g(r) in our experiment by x-ray diffraction was 2.73Å as shown in Fig.5. This is close to the value of Zarzycki's experiment, 2.75Å, which is calculated by us using the reported results.

The first peak position, 2.6Å, obtained by the neutron diffraction with isotopic substitution was purely contributed by the un-like ion pair, $g_{+-}(r)$, and the first peak position of the mean value of the correlation function, $g_m(r)$, might become longer than 2.6Å if the contribution of like-ion pairs, $g_{++}(r)$ and $g_{--}(r)$, was considered. However, the positions of cut-off of $g_{++}(r)$ and $g_{--}(r)$ were 2.7Å and 3.0Å, respectively. Therefore, the first peak position of $g_{+-}(r)$ will not be affected by these contributions and is essentially the same as that of $g_m(r)$. These things are also supported by the computer simulation. This means that the first peak position obtained by a neutron diffraction with isotopic substitution should be the same as that obtained by x-ray diffraction. Therefore, we think that there is something yet to improve on accuracy in measurements or correction of data of the neutron diffraction with isotopic substitution.

IV. Conclusion

The small difference between first peak positions of the radial distribution function of molten alkali halides by x-ray or neutron diffraction experiments and these by computer simulations exceeds the experimental error and is essential. It seems to be due to the deformation of electron shell. Although, r_1 value in computer simulation by the shell model was expected to be more distant than that by the rigid ion model because of taking into account the polarization of ions, no change in r_1 was found. These results indicate that in the model employed in the computer simulation the polarization of ion has not been

sufficiently taken into account. It seems to be due to the non-spherical deformation of the electron shell at the area where ions are in contact with each other.

Neutron diffraction method with isotopic substitution permits one to get the partial correlation functions which are difficult to get by the ordinary x-ray diffraction method and can compare directly with the results of the computer simulation, in general. But, improvements in accuracy in measurements and corrections of data would be useful.

References

(1) K.Furukawa:Rept.Progr.Phys.,25(1962)395.
(2) H.A.Levy and M.D.Danford:Molten Salt Chemistry,Ed.by M.Blander,Interscience Publishers,John Wiley and Sons, Inc.,1963.
(3) K.Furukawa:Discuss.Faraday Soc.,32(1961)53.
(4) M.J.L.Sangster and M.Dixon:Adv.Phys.,25(1976)247.
(5) L.V.Woodcock:Advances in Molten Salt Chemistry,Ed.by J.Braunstein et al.,Plenum,New York,1975.
(6) H.Ohno,M.Yoroki,K.Furukawa,Y.Takagi and T.Nakamura: J.Chem.Soc.Faraday Transactions I,74(1978)1861.
(7) H.Ohno and K.Furukawa:J.Chem.Soc.Faraday Transactions I,77(1981) in press.
(8) R.Takagi,H.Ohno and K.Furukawa:J.Chem.Soc.Faraday Transactions I,75(1979)1477.
(9) M.Dixon and M.J.L.Sangster:J.Phys.C;Solid State Phys., 8(1975)L8.
(10) M.Dixon and M.J.L.Sangster:ibid,9(1976)909.
(11) M.Dixon and M.J.L.Sangster:ibid,9(1976)L5.
(12) M.Dixon and M.J.L.Sangster:Phys.Chem.Liquids,5(1976) 221;Phil.Mag.,35(1977)1049.
(13) F.G.Edwards,J.E.Enderby,R.A.Howe and D.I.Page:J.Phys.C; Solid State Phys.,8(1975)3483.
(14) J.Y.Derrien and J.Dupuy:J.Phys.,36(1975)191.
(15) E.W.J.Mitchell,P.F.J.Poncet and R.J.Stewart:Phil.Mag., 34(1976)721.
(16) J.Zarzycki:J.Phys.Radium,19(1958)13A.
(17) F.Vaslow and A.Narten:J.Chem.Phys.,59(1973)4949.
(18) H.A.Levy,P.A.Agron,M.A.Bredig and M.D.Danford:Ann. New York Acad.Sci.,79(1960)762.
(19) J.Krogh-Moe,T.Ostvold and T.Forland:Acta Chem.Scand., 23(1969)2421.
(20) L.V.Woodcock:Chem.Phys.Letters,10(1971)257.
(21) I.Okada,R.Takagi and K.Kawamura:Z.Naturforsh.,35a (1980)493.

(22) R.Takagi,I.Okada and K.Kawamura;Bull.Tokyo Inst.Technol.,127(1975)45.
(23) J.W.E.Lewis,K.Singer and L.V.Woodcock:J.Chem.Soc. Faraday Transactions II,71(1975)301.
(24) J.Michielsen,P.Woerlee,F.v.d.Graaf and J.A.A.Ketelaar: J.Chem.Soc.Faraday Transactions II,71(1975)1730.
(25) F.Lantelme,P.Tung,B.Quentrec and J.W.E.Lewis:Mol. Phys.,28(1974)1537.
(26) J.W.E.Lewis and K.Singer:J.Chem.Soc.Faraday Transactions II,71(1975)41.
(27) D.J.Adams and I.R.McDonald:J.Phys.C,Solid State Phys., 7(1974)2761.
(28) L.V.Woodcock and K.Singer:Trans.Faraday Soc.,67(1971) 12.
(29) S.Romano and I.R.McDonald:Physica,67(1973)625.
(30) C.Margherities and C.Sinistri:Z.Naturforsch.,30a(1975) 83.
(31) K.Furukawa:Sci.Rept.RITU,A-Vol.12,No.4(1960)368.
(32) G.T.Clayton and L.Heaton:Phys.Rev.,121(1961)649.

Table 1 First peak position $r_1(g)$ of correlation function g(r).

	Radius-sum (Pauling-Shannon)	Experiment X-ray	Neutron	Difference	Computer Simulation
LiF	1.96-1.92	1.85[17]		0.1	1.75[4] (MD)
LiCl	2.41-2.40	2.43[18]	2.37[18]	0.0	2.40[19] (MC)
		2.37[6]		0.4	2.00[20] (MD)
				0.2	2.21[21] (MD)
				0.4	2.03[23] (MD)
				0.1	2.3[23] (MC)
LiI	2.79-2.76	2.83[18]		0.2	2.6[23] (MC)
				0.1	2.73[24] (MD)
NaCl	2.76-2.83	2.75[7]		0.1	2.65[25] (MD)
		2.73[16]		0.05	2.7[26] (MD,MC)
				0.15	2.6[24] (MD)
				0.1	2.65[11] (MD*)
NaI	3.11-3.22	3.10[18]		0.1	3.01[10] (MD*)
				0.1	3.0 [9] (MD,MD*)
KF	2.69-2.71	2.65[16]		0.15	2.35[27] (MC)
				~0.3	~2.5
KCl	3.14-3.19	3.05[8]	3.03[18]	0.1	2.96[28] (MC)
		3.05[18]		0.15	2.9 [29] (MC)
				0.1	2.95[8] (MD,MD*)
CsBr	3.64-3.63	3.5[18]	3.5[18]	0.35	3.15[30] (MC)

MC:Monte Carlo method,MD:molecular dynamics method(rigid ion model),MD*:molecular dynamics method(shell model).

Table 2 S_{max} dependence of r_1 value of molten NaCl

$S_{max}/\mathring{A}^{-1}$	$r_1/\mathring{A}$
8.0	2.73
9.0	2.73
10.0	2.73

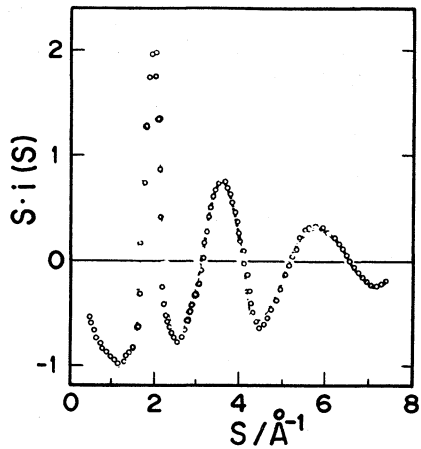

Fig.1 Reduced intensity S·i(S) of Molten LiCl at 650°C[6].

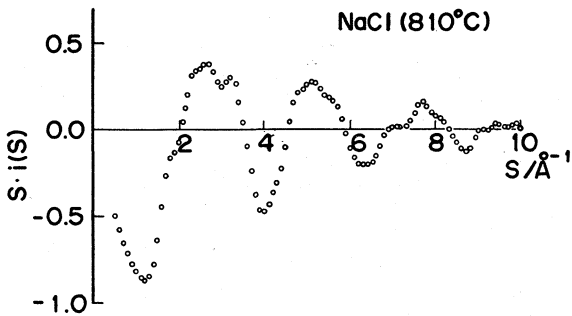

Fig.2 Reduced intensity S·i(S) of molten NaCl at 810°C[7].

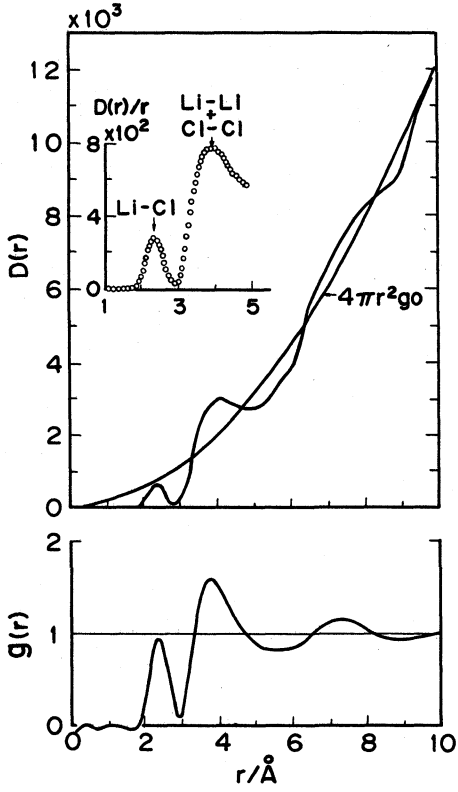

Fig.3 Radial distribution function D(r) and correlation function g(r) of molten LiCl at 650°C[6].

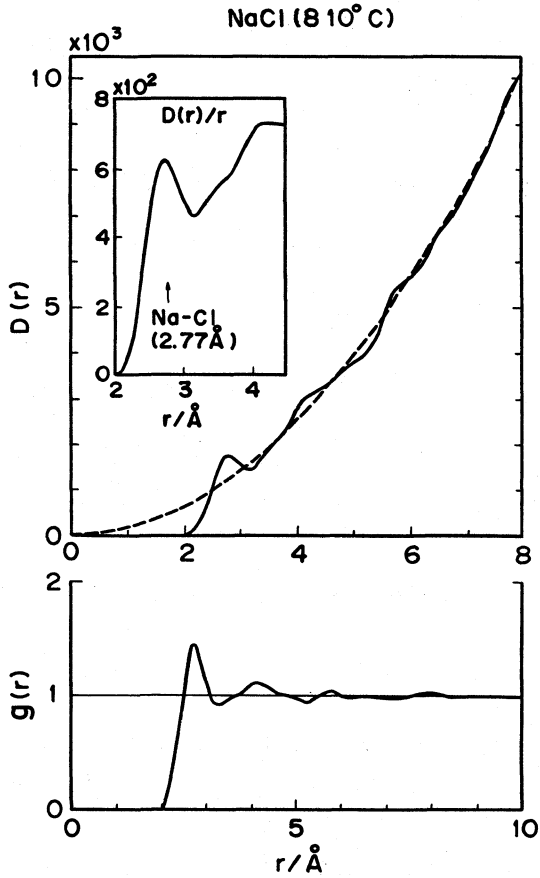

Fig.4 Radial distribution function D(r) and correlation function g(r) of molten NaCl at 810°C[7].

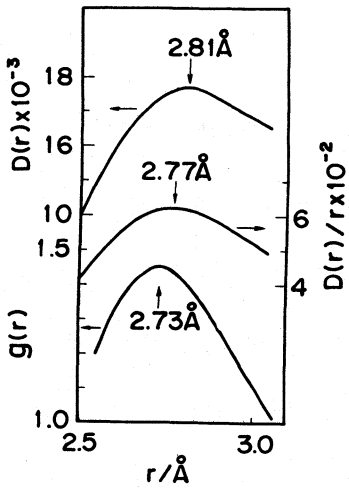

Fig.5 First peak positions of D(r),g(r) and D(r)/r of molten NaCl[7].

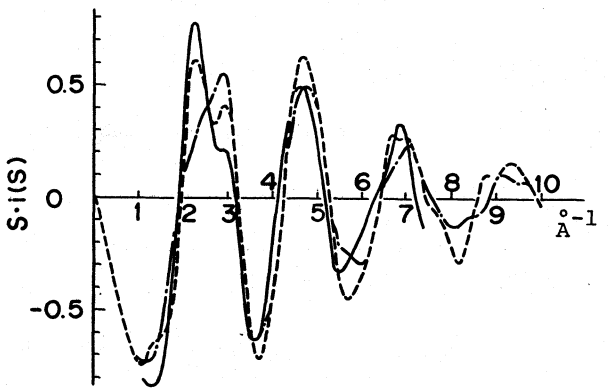

Fig.6 Experimental and computational reduced intensities of molten KCl[8].
(————) x-ray diffraction,
(------) the shell model and
(-·—·-) the rigid ion model.

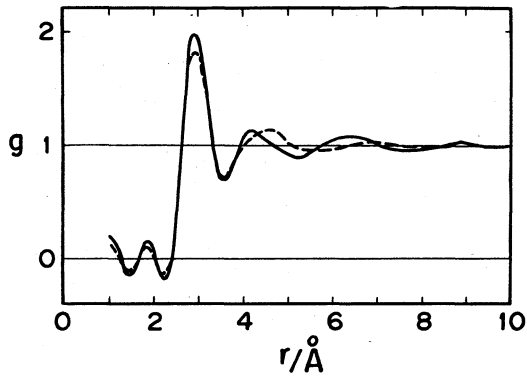

Fig.7 Computational correlation functions of molten KCl[8], the reduced intensities of which are truncated at $S_{max}=7.38Å^{-1}$: (——) the shell model and (---) the rigid ion model.

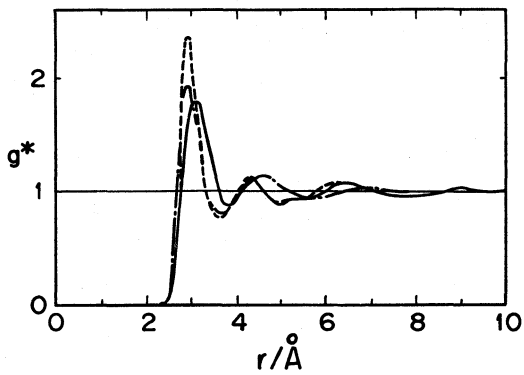

Fig.8 Experimental and computational correlation function of molten KCl[8]:
(———) x-ray diffraction,
(-----) the shell model and
(– – –) the rigid ion model.

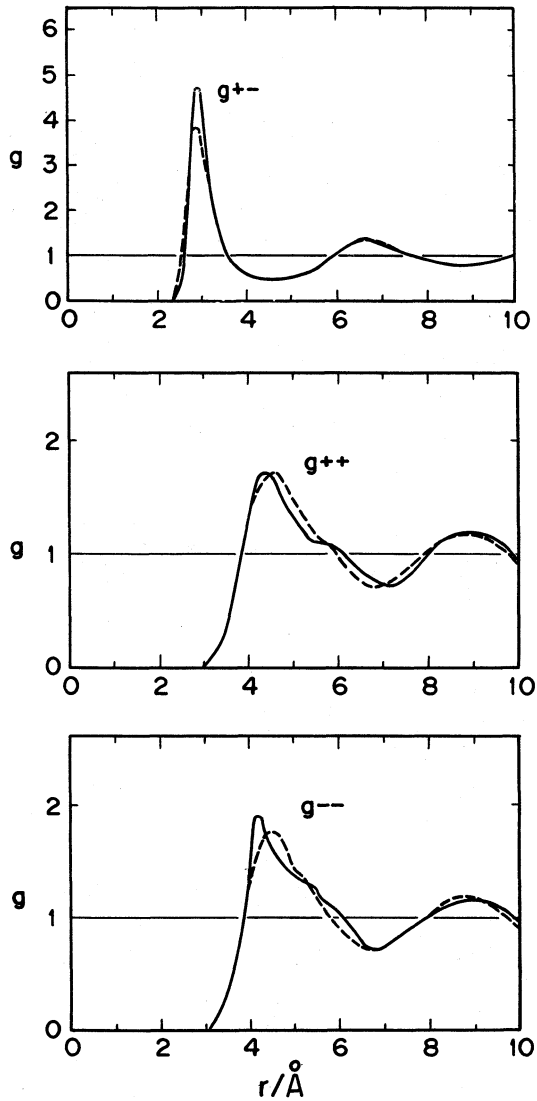

Fig.9 Partial correlation functions of molten KCl[8]: (———)shell model and (----)rigid ion model.

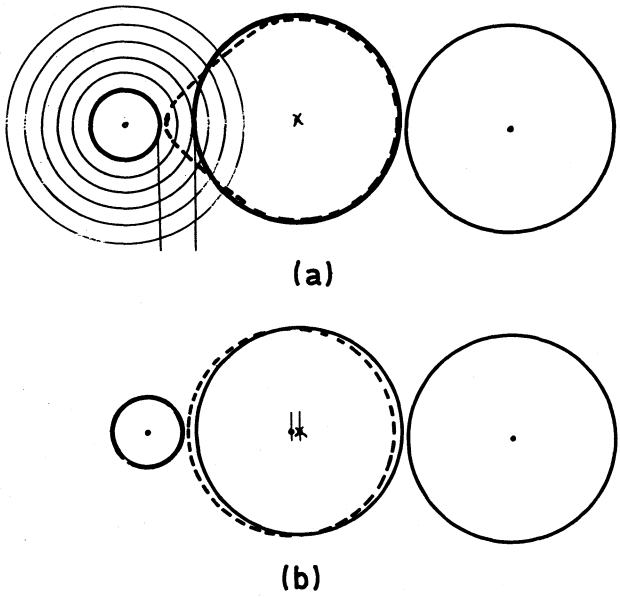

Fig.10 Exagerated presentation of deformable ion model(a) and shell model(b).

DOI: 10.1149/198109.0052PV

THE MOLTEN SALTS STANDARDS PROGRAM AND CALIBRATION-QUALITY MOLTEN SALTS DATA

George J. Janz

Molten Salts Data Center, Cogswell Laboratory
Rensselaer Polytechnic Institute, Troy, N.Y. 12181

ABSTRACT

In the present communication we report the results of a Molten Salts Standards Program initiated in 1973 with participating laboratories in Czechoslovakia, DDR-Germany, Japan, Norway, Poland, Rumania, and USA. Potassium nitrate (m_o 335°C) and sodium chloride (m. 800°C) were selected as standard samples for density, surface tension, viscosity, and electrical conductance measurements. It has been possible to resolve some of the difficulties encountered in accuracy estimates through this "round-robin" series of measurements, and to up-grade some of the data-sets to "calibration-quality" accuracies.

Introduction

The Molten Salts Standards Program was undertaken from two viewpoints:

- to upgrade data to calibration-quality accuracies using selected salts as standard samples

and

- to provide data bases for intercomparisons of measurement techniques re quality judgements.

The former, if achieved, would provide calibration cross-checks on the measurement technique at elevated temperatures. The intercomparisons would assist with accuracy estimates. The latter are based on somewhat subjective quality judgements, and these are hampered through the lack of experimental details in the publications.

The Standards Program was conceived through discussions, principally with Stefania Zuca (Bucharest) and Harald A. Øye (Trondheim)

and was proposed in 1973[1] as part of a cooperative research program coupling our laboratory (RPI) with I. G. Murgulescu's (Bucharest). The program was supported by the National Science Foundation (Office of International Programs) and the Ministry of Science and Technology (Rumania) under the Inter-Academy of Sciences Agreement. The critical data evaluations were part of a project at RPI supported by the Office of Standard Reference Data, National Bureau of Standards.

The objectives, in the first instance, included:

- conductance, density, viscosity, and surface tension

since these are, possibly, the four most widely used data. Two salts, KNO_3 (m. 335°C) and NaCl (m 800°C) were selected as the "round-robin" standard salts. Samples of these were distributed from our data center to participating laboratories for (independent) measurements.

The results, together with experimental details, were received at RPI as input for the evaluations and value judgements.

Participating laboratories were:

- *Czechoslovakia:* Dr. Ing. K. Matiasovsky; CSC; Slovak Academy of Sciences, Institute of Inorganic Chemistry, BRATISLAVA

- *Deutschen Demokratischen Republik-Germany:* Professor Dr. H. H. Emons; Technische Hochschule "Carl Schorlemmer", LEUNA-MERSEBERG, and Bergakademie, FREIBERG

- *Japan:* Professor Tatsuhiko Ejima; Department of Metallurgy, Tohoku University, SENDAI

- *Norway:* Professor Harald A. Øye, Institute of Inorganic Chemistry, Technical University of Norway, TRONDHEIM

- *Poland:* Professor L. Suski; Polish Academy of Sciences, Institute of Physical Chemistry, KRAKOW

- *Rumania:* Dr. Stefania Zuca; Institute of Physical Chemistry, Ministry of Science and Technology, BUCHAREST

- *USA:* Dr. D. A. Nissen; Materials Research Laboratories, Sandia Corporation, ALBUQUERQUE, New Mexico

- *USA:* Professor G. J. Janz; Molten Salts Data Center, Cogswell Laboratory, Rensselaer Polytechnic Institute, TROY, New York

Technical observers included: *France:* Professor M. Chemla, Laboratoire d'Electrochemie, Universite de Paris; *Netherlands:* Professor J. A. A. Ketelaar, Laboratory for Electrochemistry, University of Amsterdam; *USA:* Dr. Jerry Braunstein, Oak Ridge National Laboratory; Dr. L. H. Gevantman, Office of Standard Reference Data, National Bureau of Standards.

Standards Salts

Selection of KNO_3 and NaCl

KNO_3 (m. 335°C ± 2°C) and NaCl (m. 800°C ± 2°C) were selected to meet the need for two salts bracketting the temperature range 350°-1050°C, i.e., for measurements at moderately high and high temperatures, respectively. These are readily dried since they are not strongly hydrated. A further consideration is availability; these salts are commercially available in highest purity.

Purity

Purity specifications for Standards-Quality grades of KNO_3 and NaCl are in Table 1. These are for salts commercially available[2] as "highest purity standards quality or ultra-high purity quality". These grades were used for the "round-robin" samples.

Laboratory Pretreatment

The pretreatments recommended were:

- KNO_3: The samples should be dried under vacuo as the temperature is increased gradually to 120°C and thus maintained for approx. 24 hrs.

- NaCl: The samples should be dried under vacuo as the temperature is gradually increased to 400°-500°C as upper limits; test of small aliquots for neutrality (pH) after drying is also recommended.

The observed mpts. will vary somewhat with the measurement technique (i.e., cryoscopy; DSC; phase-rule); based on comparisons of the input from the participating laboratories, the recommended values for the mpts. are:

KNO_3: 335° ± 2°C; NaCl: 800° ± 2°C

Moisture-content analyses, undertaken at RPI[3] with electrochemically assisted Karl-Fischer type analyses or modifications thereof, confirmed moisture contents as follows:

(50 gm aliquots)	Moisture Content (ppm) KNO_3	NaCl
a) from bottle "as received"	∿ 200	∿ 40
b) 25°C; 24 hrs; 10^{-6} mm Hg	< 26	*
c) 25°C; 48 hrs; 10^{-6} mm Hg	∿ 13	*
d) 500°C, 24 hrs; 10^{-6} mm Hg	*	∿ 20

*: not investigated; [detection limits of technique: ∿ 10 ppm H_2O]

Measurements and Results

The measurement techniques are summarized in Table 2, and it is apparent that, for each property, a variety of approaches has been used.

In the Standards Program, the techniques were:

Density: Archimedean, and an indirect method based on the maximum bubble pressure technique [i.e., Other].

Measurements undertaken at:

BRATISLAVA and SENDAI

Surface Tension: Detachment, and two (2) variations of the maximum bubble pressure technique.

Measurements undertaken at:

ALBUQUERQUE, BUCHAREST, KRAKOW, and SENDAI

Conductance: AC Bridge with various conductance cell designs

Measurements undertaken at:

BUCHAREST, KRAKOW, LEUANA-MERSEBERG, and SENDAI

Viscosity: Capillary (2 variations), and damped oscillation (4 variations)

Measurements undertaken at:

BRATISLAVA, BUCHAREST, KRAKOW, TRONDHEIM, and SENDAI

In Figures 1-8 are shown comparisons of the results relative to the best values recommendations advanced earlier[4-11] under the NSRDS-NBS program. Details on the measurements, techniques, and numerical analyses will be published elsewhere.[12] It is sufficient for the present to note the recommendations from the results of the measurements accomplished through the Molten Salts Standards Program. These are collected in Tables 3 and 4, and the changes relative to the earlier recommendation [see ref. 4,5,6,7, and 8, for example] may be summarized briefly as follows.

Density: The reference data base for KNO_3 is gently shifted to lower values by $\sim$ 0.25%; for NaCl no change is recommended at present.

Surface Tension: For KNO_3, the previously advanced data base receives firm support (within $\sim \pm$ 0.25%); the accuracy limits for the NaCl data base must be set at $\sim \pm$ 1.5% rather than the previously advanced accuracy limits of $\sim \pm$ 0.1%.

Electrical Conductance: Recommendations were first advanced in 1968 for KNO_3; these were upgraded in 1972; the latter data set receives firm support from the Standards Program Measurements (i.e., $\sim \pm$ 0.5%). For NaCl, the previously advanced data base and the Standards results are virtually in exact agreement in the range 800°-850°C; above 850°C the reference data base is now shifted to decreasing values, the departure reaching $\sim$ 3.5% at the upper limit of temperature ($\sim$ 1020°C).

Viscosity: For KNO_3, the reference data base is now shifted to $\sim$ 1% higher values. For NaCl, the results of the Standard Program measurements have shown that previously recommended data base is seriously inaccurate at the lower temperature limit (810°C, $\sim$ 30% too high) and somewhat less at the upper temperature limits (1000°C, $\sim$ 10%) (i.e., outside the accuracy limits of the techniques). The data-set has been upgraded to accuracy limits of $\sim \pm$ 0.2% through the present work. This receives additional support from the damped oscillational techniques (Zuca (1976); Matiasovsky (A: 1979), and capillary measurements (Zuca, 1978).

Additional Measurements

Limited cross-check measurements were undertaken with Reagent Grade Quality chemicals. Such measurements are of interest to sense

out the effects of various additives as trace impurities relative to the thermo-physical properties under consideration in this study.

For KNO_3, with viscosity as "sensor", the results of measurements from three laboratories with the "single" capillary-type viscometers (designed for accurate molten salts measurements) are in Table 5. For NaCl, and with electrical conductivity as "sensor", the results from Bucharest are illustrated as a Percent Departure analysis in Figure 9. The departures, in each instance, fall well within the limits of experimental accuracy (viscosity, ± 1.5%; conductance, ± 0.5%). While Standards-Quality KNO_3 and NaCl were used throughout the Molten Salts Standards Program it appears that Reagent-Grade purities may be used for calibration cross-checks. A cross-check of the damped oscillational technique (immersed sphere) and capillary technique for viscosities was part of this work also. The result is illustrated in Figure 10 (Zuca, 1976). Within the limits of accuracy of the damped oscillational sphere (± 3%) the viscosity data are in exact accord. The accuracy limits can be sharpened considerably if the immersed shape is changed from a sphere to a cylinder. The Trondheim group has shown that the oscillational technique is then capable of accuracies to $\sim$ ± 0.2% for molten salts[13] (and $\sim$ ± 1%, routinely). The Kestin alloy[14,15] (92% platinum, 8% tungsten) has superior qualities (low internal friction and highly stabile elastic constant) and is recommended for the torsion wire of the damped oscillational technique. Adherence of bubbles to the immersed oscillational shape is a possible error source and may be detected through irreproducibilities of results.

A comparison of various capillary viscosity techniques was undertaken as illustrated in Figure 11. For highest accuracy the more conventional designs, as suitably modified at Amsterdam[16], RPI[17], and Bucharest[18,19] appear best. The Cuny-Wolf design[20,21] used at Krakow needs further study. For example, with molten KNO_3, the results are in close accord (see Fig. 7), but at higher temperatures (molten NaCl) the Krakow data fall close to viscosities in which the damped oscillations were perturbed by secondary flow effects (see Fig. 8, Matiasovsky-B, 1976). The resolution of such outstanding questions is difficult without further measurements.

Detailed comparisons of the published literature data for the period 1906 to 1979 will be reported elsewhere.[12]

Acknowledgements

It is a pleasure to acknowledge the participation of the following in the Molten Salts Standards Program: ALBUQUERQUE (Sandia): D. Nissen; BRATISLAVA: K. Matiasovsky, I. Votava; BUCHAREST: S. Zuca, R. Borcan, R. Costin, M. Olteanu, M. Terzi, G. Vasu, M. Muller, S. Wesson; LEUANA-MERSEBERG: H. H. Emons, G. Brautigam; KRAKOW: L. Suski, K. Gadek, J. Galka, L. Stachowicz, P. Tomczyk; SENDAI: T. Ejima, M. Hoshi, Y. Sato, K. Shinakage, T. Yamamura, T. Yoko; TRONDHEIM: H. A. Øye,

K. Tørklep; and at MSDC-RPI, with G. J. Janz: R. P. T. Tomkins S. Wesson, S. Singer, M. Muller, U. Gaur, J. R. Downey, Jr., and E. Boskin.

References

1. Molten Salts Standards Program; G. J. Janz (USA) jointly with S. Zuca (Rumania); part of a 3 year cooperative research program under the Inter-Academy Agreement; proposed to the National Science Foundation (USA) and Ministry of Science and Technology (Rumania).

2. see, for example: J. T. Baker Chemical Co., "Ultrex" high purity products; Spex Industries, Inc. high purity chemicals.

3. Janz, G. J., Muller, M., and Gaur, U., MSDC-RPI Progress Report, (1976).

4. Janz, G. J., Dampier, F. W., Lakshminarayanan, G. R., Lorenz, P. K., and Tomkins, R. P. T., "Molten Salts: Volume 1, Electrical Conductance, Density, and Viscosity Data", Nat. Stand. Ref. Data Ser., NBS (U.S.) 15, 139 pages (Oct. 1968).

5. Janz, G. J., Lakshminarayanan, G. R., Tomkins, R. P. T., and Wong, J., "Molten Salts: Volume 2, Section 2, Surface Tension Data", Nat. Stand. Ref. Data Ser., NBS (U.S.) 28, 62 pages (Aug. 1969).

6. Janz, G. J. , Krebs, U., Siegenthaler, H. F., and Tomkins, R. P. T., "Molten Salts: Volume 3, Nitrates, Nitrites and Mixtures, Electrical Conductance, Density, Viscosity and Surface Tension Data", J. Phys. Chem. Ref. Data, 1, No. 3, 581-746 (1972).

7. Janz, G. J., Gardner, G. L., Krebs, U., and Tomkins, R. P. T., "Molten Salts: Volume 4, Part 1, Fluorides and Mixtures, Electrical Conductance, Density, Viscosity and Surface Tension Data", J. Phys. Chem. Ref. Data, 3, No. 1. 1-116 (1974).

8. Janz, G. J., Tomkins, R. P. T., Allen, C. B., Downey, J. R., Jr., Gardner, G. L., Krebs, U., and Singer, S. K., "Molten Salts: Volume 4, Part 3, Chlorides and Mixtures, Electrical Conductance, Density, Viscosity and Surface Tension Data", J. Phys. Chem. Ref. Data, 4, No. 4, 871-1178 (1975).

9. Janz, G. J., Tomkins, R. P. T., Allen, C. B., Downey, J. R., Jr., and Singer, S. K., "Molten Salts: Volume 4, Part 3, Bromides and Mixtures, Iodides and Mixtures, Electrical Conductance, Density, Viscosity, and Surface Tension Data", J. Phys. Chem. Ref. Data, 6, No. 2, 409-596 (1977).

10. Janz, G. J., Tomkins, R.P. T., and Allen, C. B., "Molten Salts: Volume 4, Part 4, Mixed Halide Melts, Electrical Conductance, Density, Viscosity and Surface Tension Data", J. Phys. Chem. Ref. Data, 8, 125 (1979).

11. Janz, G. J., Tomkins, R. P. T., "Molten Salts: Volume 5, Part 1, Additional Systems with Common Anions; Electrical Conductance, Density, Viscosity, and Surface Tension Data", J. Phys. Chem. Ref. Data, accepted (1980).

12. Janz, G. J., "Molten Salts Reference Data", J. Physical and Chemical Reference Data (submitted, 1980).

13. Tørklep, K., and Øye, H. A., J. Phys. E: Sci. Instrum., 12, 875 (1979).

14. Kestin, J., and Mosynski, J. M., Brown Univ. Report AF 891/11, July (1958), AFOSR 7N-58-752, Astia Doc. No. 201,516.

15. Marvin, R. S., J. Res. Nat. Bur. Stds., 75A, 535 (1971).

16. van Os, N., and Ketelaar, J. A. A., J. Electrochem. Soc., 123, 1359 (1976); van Os, N., Ph.D. Thesis, Amsterdam (1970).

17. Timidei, A., Lederman, G., and Janz, G. J., Chem. Instrum., 2, 309 (1970).

18. Zuca, S. and Costin, R., submitted to Molten Salts Standards Program, MSDC-RPI (1976).

19. Ubbelohde, L., "Zur Viskosimetrie", S. Hirzel Verlag, Stuttgart (1965).

20. Cuny, K. H., and Wolf, K. L., Ann. Phys., 6F, 17, 57 (1956).

21. Suski, L. and Tomczyk, P., J. Chem. Thermodynamics, 7, 823 (1975).

Table 1

Standards Quality Salts: Purity Specifications

KNO_3

- purity assay: 99.999%
- pH (25°C, 5% sol'n): 5.6
- trace impurities: ppm content by spec. analysis

NaCl

- purity assay: 99.999%
- pH (25°C , 5% sol'n): ∿ 7
- trace impurities: ppm content by spec. analysis

Table 2

Molten Salts Measurements Techniques

Electrical Conductance: 750 Studies

AC	Modified AC	DC
93%	6%	1%

Density: 500 Studies

Archimedean	Dilatometric	Pycnometer	Other
87%	7%	3%	3%

Viscosity: 150 studies

Capillary	Damped Oscillation	Rotational	Other
24%	67%	4%	5%

Surface Tension: 200 Studies

Cap. Rise	Max. Bubble P.	Detachment	Other
2%	80%	14%	4%

Table 3. Molten Salts Standards: Recommended Data Bases

	Density	Accuracy
KNO_3	Matiasovsky (1976)	∿ ± 0.25%
NaCl	1968 NSRDS	∿ ± 1%
	Surface Tension	
KNO_3	Nissen (1976)	∿ ± 0.25%
NaCl	1968 NSRDS	∿ ± 1.5%
	Electrical Conductance	
KNO_3	Emons (1976)	∿ ± 0.5%
NaCl	Emons (1976)	∿ ± 1%
	Viscosity	
KNO_3	Zuca (capillary) (1976)	∿ ± 2%
NaCl	Tørklep, Øye (oscillational) (1978)	∿ ± 0.2%

Table 4. Molten Salts Standards: Calibration Data Sets

[T, kelvin temperature scale]

	Density ($g\ cm^{-3}$)
KNO_3	$\rho = 2.3063 - 0.7235 \times 10^{-3}T$
NaCl	$\rho = 2.1389 - 0.5426 \times 10^{-3}T$
	Surface Tension ($mN\ m^{-1}$)
KNO_3	$\gamma = 154.715 - 71.7080 \times 10^{-3}T$
NaCl	$\gamma = 191.1600 - 71.8800 \times 10^{-3}T$
	Electrical Conductance ($\Omega^{-1}\ cm^{-1}$)
KNO_3	$\kappa = -2.1250 + 5.7332 \times 10^{-3}T - 2.0301 \times 10^{-6}T^2$
NaCl	$\kappa = -5.6241 + 13.9640 \times 10^{-3}T - 5.0245 \times 10^{-6}T^2$
	Viscosity ($mN\ s\ m^{-2}$)
KNO_3	$\eta = 29.7085 - 71.1208 \times 10^{-3}T + 44.7023 \times 10^{-6}T^2$
NaCl	$\eta = 89.272 \times 10^{-3} \exp(5248.5/RT)$ $\eta = 3.4877 - 2.6966 \times 10^{-3}T + 0.3819 \times 10^{-6}T^2$

Table 5

Comparison of viscosities of Standards-Quality and Reagent Grade KNO_3

Investigation	Technique	KNO_3	Viscosity (mN s m^{-2})[a]	
			361°C	376°C
Zuca and Costin	capillary	Standards-Quality	2.578	2.379
van Os and Ketelaar	capillary	Reagent Grade	2.585	2.380
Timidei, Lederman, and Janz	capillary	Reagent Grade	2.575	2.376

[a] 1 mN s m^{-2} = 1 cp = 1 mPa s

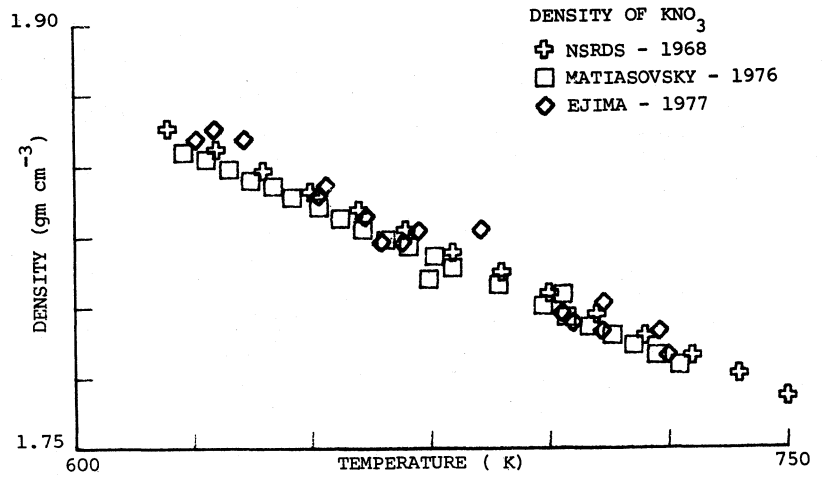

Figure 1 Comparison of KNO_3 density data from the Standards Program with the NSRDS (1968) recommendations

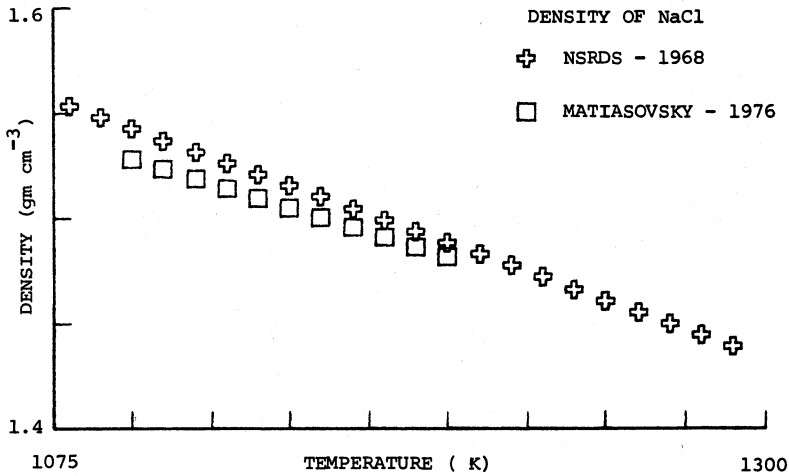

Figure 2 Comparison of NaCl density data from the Standards Program with the NSRDS (1968) recommendation.

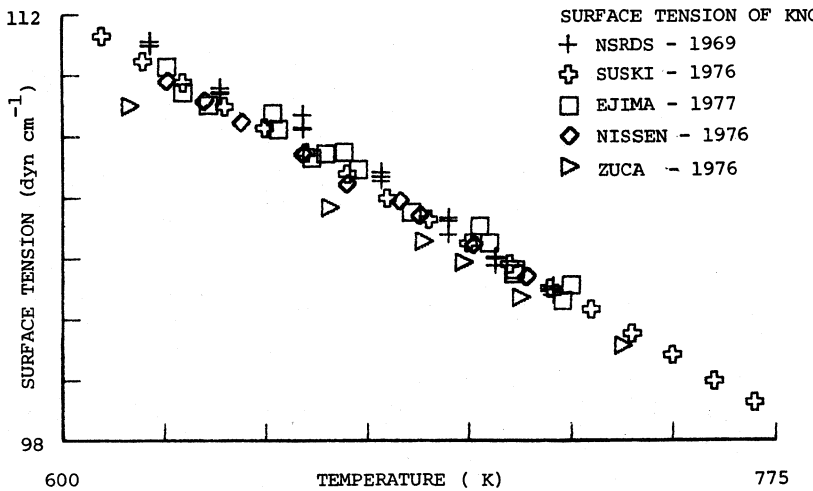

Figure 3 Comparison of KNO_3 surface tension data from the Standards Program with the NSRDS (1969) recommendation.

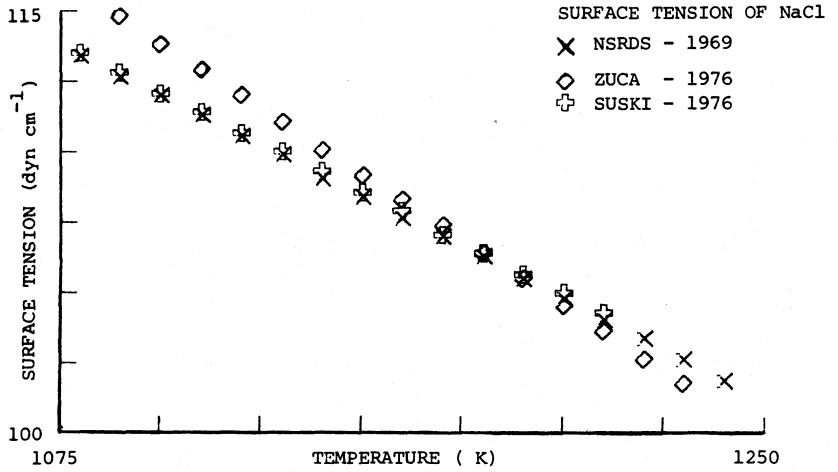

Figure 4 Comparison of NaCl surface tension data from the Standards Program with the NSRDS (1969) recommendation

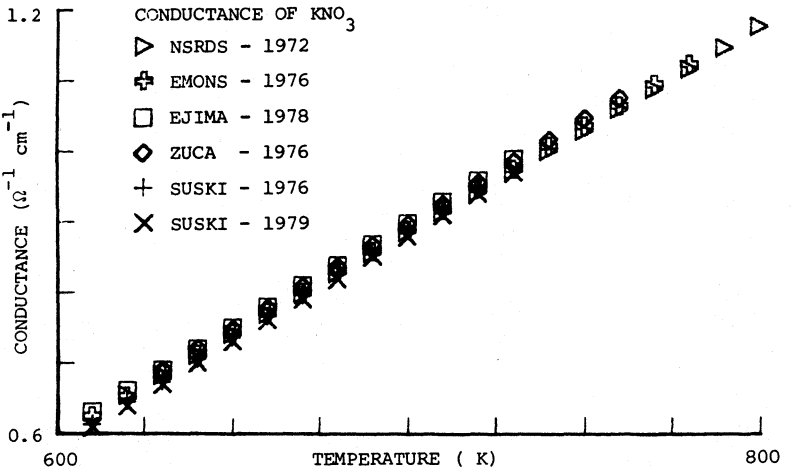

Figure 5 Comparison of KNO_3 specific conductance data from the Standards Program with the NSRDS (1972) recommendation

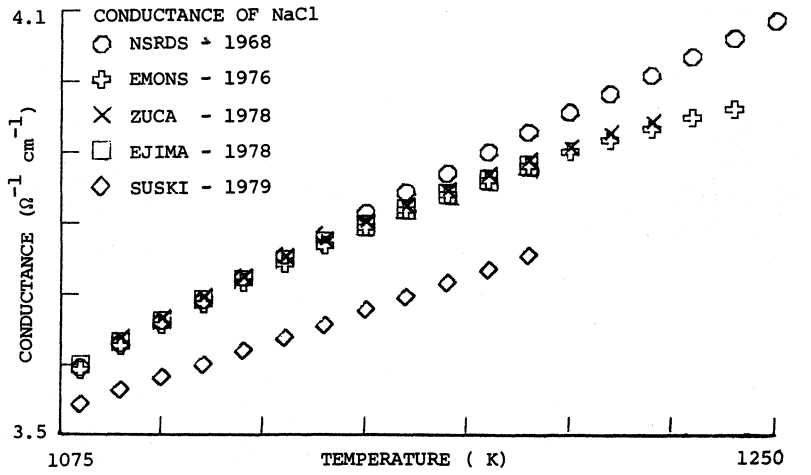

Figure 6 Comparision of NaCl specific conductance data from the Standards Program with the NSRDS (1968) recommendation

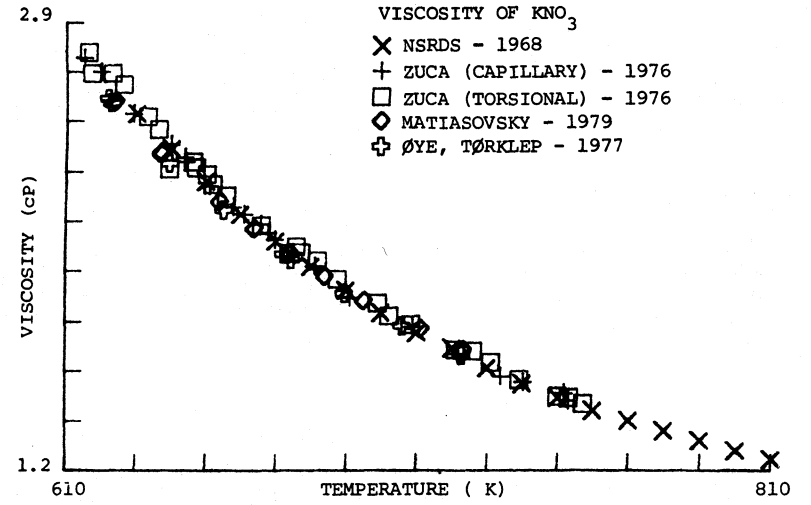

Figure 7 Comparison of KNO_3 viscosity data from the Standards Program with the NSRDS (1968) recommendation

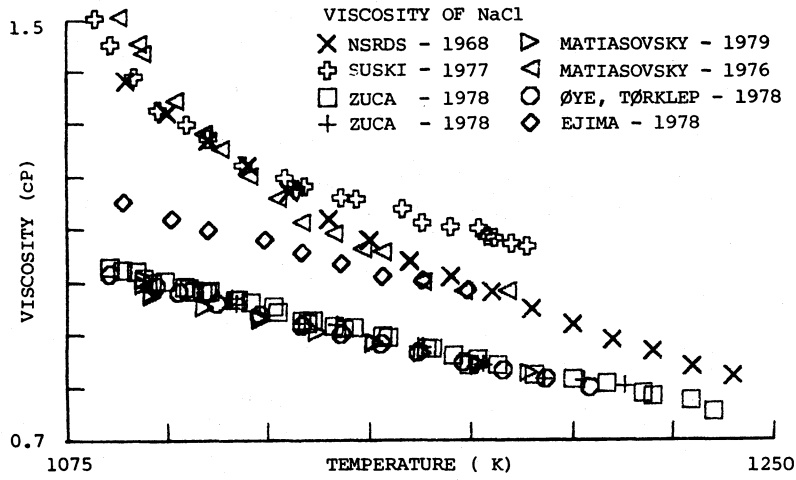

Figure 8 Comparison of NaCl viscosity data from the Standards Program with the NSRDS (1968) recommendation

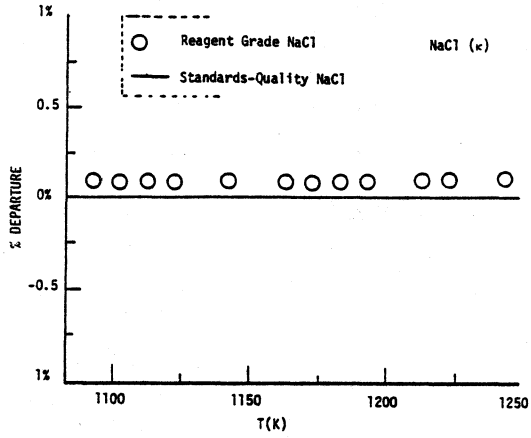

Figure 9 Comparison of the specific conductance of Standards-Quality and Reagent Grade NaCl

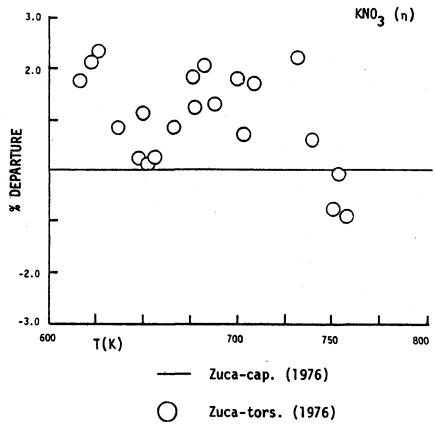

Figure 10 Comparison of the KNO_3 viscosity data from the torsional and capillary techniques

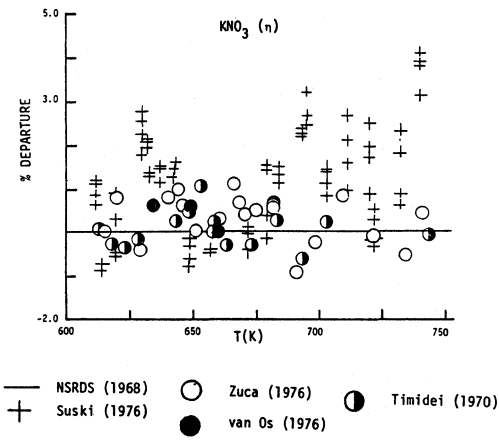

Figure 11 Comparison of KNO_3 viscosity data from capillary techniques

DOI: 10.1149/198109.0068PV

THERMODYNAMIC TREATMENT OF TERNARY AND QUARTERNARY FUSED SALT SYSTEMS

S.N. Flengas[1] and D.R. Sadoway[2]

1. Department of Metallurgy and Materials Science, University of Toronto, Toronto, Ontario, Canada

2. Department of Materials Science and Engineering, Massachusetts Institute of Technology Cambridge, MA 02139 U.S.A.

Equations are developed from which the molar and partial molar excess thermodynamic properties of ternary and quarternary molten salt solutions may be predicted from binary data.

The theory is applicable to molten salt systems which contain one reactive metal chloride such as $MnCl_2$, $CoCl_2$, $NiCl_2$, AgCl, etc. as a ligand acceptor and two or three alkali chlorides as ligand donors.

In ternary systems, where the components 1,2,3 refer respectively to MCl_Z, BCl and ACl, any excess molar or partial molar properties may be calculated from expressions of the type:

$$\Delta Z = (1-t)\ \Delta Z_{1,2} + t\ \Delta Z_{1,3}$$

where, $t = \frac{X_3}{X_2+X_3}$ and X_{MCl_2} is constant.

For a quarternary system where C,A,B,D, represent respectively charge asymmetric components like MCl_2, CsCl, NaCl and KCl, the corresponding expression for any excess molar or partial molar property is written as:

$$\Delta Z = (1-S)\ [(1-t)\ \Delta Z_{CA} + t\ \Delta Z_{CD}] + S\Delta Z_{CB}$$

which is valid at constant MCl_2 content, or constant X_C.

The composition parameters t and S are defined as

$$t = \frac{X_D}{X_A+X_D} \quad \text{and} \quad S = \frac{X_B}{X_A+X_B+X_D}$$

The validity of the theoretical expressions is supported from available experimental data on ternary fused salt solutions.

Introduction

The thermodynamic properties of binary fused salt solutions have been the subject of several systematic investigations, and extensive compilations of data on activities and on enthalpies of mixing are available. However, similar information on ternary fused salt solutions is limited to only a few selected systems, and for quarternary solutions there is hardly any information at all.

Yet, systems of metallurgical importance are usually multi-component and the application of the thermodynamic approach to the evaluation of the high temperature equilibria of interest is restricted by the lack of the necessary data. This situation is not expected to improve significantly because the systematic investigation of a multicomponent system is very time consuming as it requires a large number of experiments.

It is evident that expressions from which the thermodynamic properties of a multicomponent system may be predicted from available information on the related binary systems should be of considerable theoretical and practical interest.

For ternary metallic solutions several such equations have been proposed. These include the analytical expressions by Kohler (1), Bonnier, and Caboz (2), and by Muggianu et al (3), and those derived by Alcock and Richardson (4), and by Toop (5).

The relative merits of each of these expressions have been compared by Spencer et al (6) and by Ansara (7) and by Hillert (8).

In general, these expressions include terms representing the thermodynamic properties of the three binary component systems and differ mainly in the kind of composition parameters used and in the composition path to be followed within the ternary isothermal composition surface.

With the exception of equations derived from the regular solution theory, comparable equations which are applicable to ternary or quarternary fused salt solutions have not yet been proposed.

In a previous publication from this laboratory (9) it has been shown that the thermodynamic properties of dilute ternary fused salt solutions may be predicted from expressions of the type,

$$\Delta Z_{1,2,3} = t\Delta Z_{1,3} + (1-t) \cdot \Delta Z_{1,2} \qquad (1)$$

where ΔZ represents any integral or partial molar excess property.

The ternary solution is denoted by the subscripts 1,2,3, while the two binaries are denoted by the subscripts 1,2 and 1,3. The composition parameter, t, is defined as,

$$t = \frac{X_3}{X_2+X_3} \qquad (2)$$

In this paper it will be shown that expression 1 is generally applicable to ternary charge asymmetric fused salt solutions which consist of reactive metal chlorides like $MnCl_2$ or $CoCl_2$, and two different alkali metal chlorides.

Furthermore, the applicability of this equation is not restricted to only dilute solutions but covers the entire composition range of a ternary.

The theoretical treatment is also extended to quarternary fused salt solutions of the type, MCl_2-ACl-BCl-DCl, where MCl_2 represents the reactive charge asymmetric metal chloride and ACl, BCl, and DCl are three different alkali metals.

Nature of Complex Species Present in Fused Salt Solutions

In charge asymmetric fused salt solutions of the type MCl_Z - ACl the observed deviations from ideality have been attributed to the presence of complex species which are created during mixing (10,11,12).

The concept of complexes in molten ionic salts has been based upon the following postulates (10,11,12); (1) The fused salt is a continuous medium consisting of electrically charged particles and as a result interlocking anionic and cationic quasi-lattices exist to preserve local electrical neutrality. (2) A non-ionic solvent such as water, capable of separating the ionic species, is not present. (3) The difference between a complexed and a non-complexed state involving a cation M^{Z+} and an anion X^- is simply defined by a characteristic average "shorter" bond distance M-X for the complexed state as compared to a longer M-X bond distance for the non-complexed state. (4) Complexed ionic species must still belong to their respective quasi-lattices and not disrupt the continuity of the phase. Hence the ligands X^- in a complex interact with the surrounding A^+ cations in the sequence.

$$--- A^+ --- X \overset{Z+}{---} M \overset{Z+}{---} X --- A^+ ---$$

whereby an anion X^- is always a cation "bridging" species (5). The formation of a complex is initiated by the presence of foreign cations A^+ which compete poorly with the central cations M^{Z+} for the same ligands X^-. Accordingly, the charge density of the cation A^+ is related to its capability of promoting or preventing the formation of complexes.

The spatial arrangement of such complexes within the ionic melt structure is compatible with the requirement of local electrical neutrality and with the concept of interlocked anionic and cationic "quasi-lattices" which has been proposed by Temkin (13).

Although an exact knowledge of the structure of such complexes is not necessary for a thermodynamic treatment there are certain indirect indications regarding their probable configuration. For example, recent structural evidence (14) as well as measurements of electrical conductivities and molar volumes (12,15) suggest that solutions of $MnCl_2$ in alkali chloride melts appear to contain tetrahedrally coordinated complexes of the type $MnCl_4^{2-}$. Similarly, thermodynamic evidence indicates that the solutions of $ZrCl_4$, $HfCl_4$, $NbCl_5$ and $TaCl_5$ (16-19) in alkali chlorides contain octahedrally coordinated complexes of the type MCl_6^{2-} or MCl_6^-. In all these systems, the negative deviations from ideality increase as the size of the alkali metal cation increases as in the sequence, LiCl-NaCl-KCl-RbCl-CsCl.

These trends reflect the effects of competing interactions between the M^{Z+} and A^+ cations for the same Cl^- anions in which the alkali chloride acts as a ligand donor and the reactive metal chloride MCl_Z is the ligand acceptor. Alkali metal cations like Li^+, because of their small size, are strongly attracted to their chloride anions and effectively the LiCl salt is less "dissociated" than other alkali metal chlorides containing larger cations like K^+, Rb^+ or Cs^+. The difference in the strength of the complexes which are formed when a reactive metal chloride MCl_Z is mixed with either of the alkali chlorides ACl or BCl is simply reflected by the difference in the bond distances in configurations of the type M-Cl-A or M-Cl-B.

Ternary Charge Asymmetric Fused Salt Solutions

The composition of a ternary system is usually represented by points within an equilateral triangle in which the points of 100% of each component are situated at the corners.

Any composition P is found by drawing through P lines parallel to each of the three sides. The complement of the distance from each corner to the respective line through P gives the amount of the particular component. If the composition variable is the mole fraction, then the values thus calculated must satisfy the relationship

$$X_1 + X_2 + X_3 = 1 \qquad (3)$$

where 1,2, and 3 are the components MCl_Z, ACl, BCl, respectively.

A tie-line from 1 to the 2, 3 binary represents compositions for which

$$t' = \frac{X_3}{X_2} = \text{constant} \qquad (4)$$

but since t' goes to infinity as X_2 goes to zero, it is more convenient to define

$$t = \frac{X_3}{X_2 + X_3} \qquad (2)$$

which varies from 0 and 1.

When X_1 is constant then $1 - (X_2 + X_3)$ is also constant and the parameter y is defined as $y = X_2 + X_3 = 1 - X_1$. In the binary 1-2, t = 0, and in the binary 1-3, t = 1. For pure component 1, y = 0, and for all values of t in the 2-3 binary y = 1.

Considering the ternary system MCl_2-ACl-BCl in which tetrahedrally corrdinated complexes are formed the following reactions are expected to take place in the respected binaries;

$$2ACl + MCl_2 = A_2MCl_4 \qquad (5)$$

$$2BCl + MCl_2 = B_2MCl_4 \qquad (6)$$

The ternary is divided into two composition regions at y = 0.667, an MCl_2-rich three component subsystem MCl_2-A_2MCl_4-B_2MCl_4 at $1.0 > X_{MCl_2} > 0.667$, and a four component subsystem A_2MCl_4-B_2MCl_4-ACl-BCl for $0.667 > X_{MCl_2} > 0$, as shown in Figure 1.

Figure 1

Along a concentration path representing constant y, the MCl_2 component is distributed between the two complex species A_2MCl_4 and B_2MCl_4 in a ratio equal to the mole ratio of ACl to BCl in the mixture, which is $\frac{1-t}{t}$.

Furthermore, if it is assumed that the partial excess molar properties of MCl_2 in the ternary solution vary linearly with respect to t, then the following relationship is valid:

$$\bar{Z}_{MCl_2} = t(\bar{Z}_{MCl_2})_{1,2} + (1-t)(\bar{Z}_{MCl_2})_{1,3} \qquad (7)$$

where the subscripts 1,2 and 1,3 refer to the binary mixtures 1,2 and 1,3, respectively. $\bar{Z}_{MCl_2}$ is the value of the partial molar property of MCl_2 in the ternary solution.

The mass balance for the ternary composition may be considered for the two regions y > 0.667 and y < 0.667. Table 1 gives the mass balances which are derived on the assumption that equations 5 and 6 proceed to completion.

Table 1

Considering first the region of the ternary for which y < 0.667, any excess molar property Z, such as enthalpy, free energy, or entropy may be expressed as

$$Z = X_{MCl_2}\ \bar{Z}_{MCl_2} + X_{A_2MCl_4}\ \bar{Z}_{A_2MCl_4} + X_{B_2MCl_4}\ \bar{Z}_{B_2MCl_4} \qquad (8)$$

where $\bar{Z}_i$ is a partial excess molar property.

When the X's in this equation are substituted with the equivalent expressions from Table 1, and $\bar{Z}_{MCl_2}$ is expressed as in equation 7, the resulting expression is

$$Z = (1-t)\left(\frac{y}{2}\bar{Z}_{A_2MCl_4} + \frac{2-3y}{2}\bar{Z}_{MCl_2}\right) + t\left(\frac{y}{2}\bar{Z}_{B_2\ MCl_4} + \frac{2-3y}{2}\bar{Z}_{MCl_2}\right) \qquad (9)$$

If it is further assumed that the values of the partial molar properties for each of the complex species considered obey equation (7) for the respective binary systems having the same MCl_2 content, then the quantities in parentheses in equation 9 represent binary systems and it follows that equation 9 may be written as

$$Z = (1-t)\ Z_{1,2} + t\ Z_{1,3} \qquad (10)$$

Following a similar method it may be shown that equation 10 is valid for the composition range for which $y > 0.667$. Equation 10 may also be derived from mass balance calculations corresponding to octahedrally coordinated complexes, like the A_2MCl_6 (16-19), and for that matter any other coordination representing the probable structure of a complex species in solution.

The change in any integral excess property of mixing, ΔZ, representing the reaction:

$$X_1\ MCl_{2\,(liq)} + X_2\ ACl_{(liq)} + X_3\ BCl_{(liq)} \rightarrow [\,(MCl_2)_{X_1} \cdot (ACl)_{X_2} \cdot (BCl)_{X_3}\,]$$

may also be calculated.

In the region $0 < y < 0.667$,

$$\Delta Z = Z - \frac{2-3y}{2}\ Z^o_{MCl_2} - \frac{y(1-t)}{2}\ Z^o_{A_2MCl_4} - \frac{y\ t}{2}\ Z^o_{B_2\ MCl_4} \qquad (11)$$

where the Z^{o} terms represent the molar property for each component in its standard state. The latter is chosen as the pure liquid at the temperature of the experiment.

Substitution of equation 9 into equation 11, followed by multiplication of the second term on the right hand side of equation 11 by the arbitrary term (1-t)+t, yields the expression,

$$\Delta Z = (1-t)\ \Delta Z_{1,2} + t\ \Delta Z_{1,3} \qquad (12)$$

where ΔZ represents any integral excess property in the ternary system. Equation 12 is valid for compositions within the ternary representing constant y, for which the ternary contains the same amounts of MCl_2 as in the two component binaries.

Finally, along a path of constant y, the corresponding expressions for the partial molar excess properties of MCl_2 are readily derived from equation 7 as,

$$\overline{\Delta Z}_{MCl_2} = (1-t)\ \overline{\Delta Z}_{MCl_2(1,2)} + t\ \overline{\Delta Z}_{MCl_2(1,3)} \qquad (13)$$

The expression for the activity of MCl_2 in the ternary is also derived as:

$$a_{MCl_2} = (a_{MCl_2})_{1,2}^{1-t} \cdot (a_{MCl_2})_{1,3}^{t} \qquad (14)$$

which is valid at constant X_{MCl_2}.

Equations 7, 10, 12, 13 and 14 have also been derived previously [9,11] using a quasichemical thermodynamic model which is applicable to charge asymmetric fused salt solutions.

In this model the solution process is taken to consist of two parts. At first, reactions 5 and 6 proceed to completion and then, the reaction products A_2MCl_4 and B_2MCl_4 mix with any unreacted ACl, BCl or MCl_2 to form a solution. For the latter only short range ion-pair type interactions are taken as being significant and the concentration dependence of the solution properties is derived following a regular solution model. The overall expressions include the terms for the reaction and the mixing parts of the solution process.

The validity of equations 10 to 14 is supported by considerable experimental evidence.

Molar volumes in the ternary system $MnCl_2$-NaCl-CsCl have been measured in this laboratory (12) over the entire composition range and

plots of $V_{solution}$ versus the parameter t are given in Figure 2.

Figure 2

The linearity of these curves at constant y-values indicates the validity of equation 10 written as,

$$V_{solution} = (1-t)\ V_{MnCl_2\ -\ NaCl} + t\ V_{MnCl_2\ -CsCl} \qquad (15)$$

Figure 3 shows similar plots for the system $PbCl_2$-LiCl-KCl measured by Gutierrez and Toguri (20).

Figure 3

The integral enthalpies of mixing in the binary systems $MnCl_2$-NaCl and $MnCl_2$-CsCl, as well as those in the ternary system $MnCl_2$-NaCl-CsCl have also been measured in this laboratory (9,11,21). Figure 4 shows the plots of ΔH_m versus t for five y-values ranging from 0.15 to 0.88. The curves are linear as expected from equation 12 written as

$$\Delta H_m = (1-t)\ \Delta H_{m(MnCl_2-NaCl)} + t\ \Delta H_{m(MnCl_2-CsCl)} \qquad (16)$$

Figure 4

Similarly, partial molar enthalpies of mixing for very dilute solutions of $MnCl_2$ in mixtures of NaCl and of CsCl have been calculated from emf measurements and the linear plot of ΔH_{MnCl_2} versus t is shown in Figure 5.

Figure 5

The validity of expression 14 for calculating activities is demonstrated by the linearity of the curves given in Figures 6 and 7.

Figures 6 and 7

The systems shown in these figures include the ternaries of $NiCl_2$-NaCl-KCl and of $CoCl_2$-NaCl-KCl investigated by Hamby and Scott (22), the AgCl-NaCl-RbCl, the $MnCl_2$-NaCl-CsCl systems investigated in this laboratory (11), and the AgCl-LiCl-KCl system reported by Gruner and Thompson (24). At constant y-values, all the plots of log γ_{MnCl_2} versus t in Figures 6 and 7 are linear, as expected from equation 14.

The thermodynamic properties of the ternary systems AgCl-NaCl-KCl and AgCl-NaCl-CsCl have been investigated by Blander et al (25) by emf measurements. Plots of ΔG^E_{AgCl} are almost linear with respect to t along constant y-paths. The ternary systems $PbCl_2$-NaCl-CsCl and $PbCl_2$-NaCl-KCl have been investigated by Hagemark et al (26) and the thermodynamic properties of $PbCl_2$ at 625°C at a mole fraction of $PbCl_2$ equal to 0.3 obey the additivity rule and $\Delta G^E_{PbCl_2}$ varies linearly with t. However, solutions containing 0.5 mole fraction $PbCl_2$ indicated significant deviations from additivity.

It should be noted that systems like the $MnCl_2$-NaCl-CsCl represent a severe test of the validity of equation 14 as the respective binary systems from which the ternary is calculated have pronounced differences in their properties.

Quarternary Charge Asymmetric Fused Salt Solutions

The composition of each of the four components in a quarternary charge asymmetric fused salt system, where A, B, D are three different alkali metal chlorides and C the charge asymmetric compound MCl_Z, is plotted within the volume of an equilateral tetrahedron in which the apexes represent the four pure components A, B, C, and D, the edges represent the six binary systems AB, BD, AD, AC, BC and DC and the triangular faces represent the four ternary systems ABC, ABD, BCD and ACD.

It is a property of the equilateral tetrahedron that lines from any internal point P drawn parallel to the four different faces of the tetrahedron have a total length equal to one edge. Thus, each of these segments defines the mole fraction of a component in the quarternary (27). In view of the complexity of such three dimensional plots, the graphical method cannot be used for plotting compositions for a quarternary system.

Instead, useful composition paths within a quarternary may be defined mathematically using appropriate composition parameters. For the present treatment, the composition parameters are chosen as follows:

$$t = \frac{X_D}{X_A + X_D} \tag{17}$$

$$y = 1 - X_C \tag{18}$$

$$S = \frac{X_B}{X_A + X_B + X_D} \tag{19}$$

Considering Figure 8 in which component C is placed at the apex of the equilateral tetrahedron as shown, constant t represents a pseudoternary composition surface BCE within which the mole ratio of the components A and D is constant.

Figure 8

Compositions having constant y, which is physically the same as a constant mole fraction of component C, are located on the plane ORT which is parallel to the base ABD of the tetrahedron.

For the composition path which is defined by the intersections of planes of constant t and y, i.e., along the line OQ, the parameter S varies between 0 and 1. The limiting values for S are S=0 at Q in the ternary ACD, and S=1 at point O in the binary BC.

If the asymmetric metal chloride is taken to be divalent MCl_2 and the alkali chlorides the salts CsCl, NaCl and KCl, as in Figure 8, then the quarternary system will be taken to contain the complex compounds Na_2MCl_4, K_2MCl_4 and Cs_2MCl_4 which are also present in the corresponding binary systems NaCl-MCl_2, KCl-MCl_2 and CsCl-MCl_2, respectively.

The quarternary may be divided into a MCl_2-rich region where $X_{MCl_2} > 0.333$, which is taken to contain the species MCl_2, Na_2MCl_4, K_2MCl_4 and Cs_2MCl_4, and a MCl_2-lean region at $X_{MCl_2} < 0.333$ which is taken to contain NaCl, KCl, CsCl, Na_2MCl_4, K_2MCl_4 and Cs_2MCl_4.

The composition of the reacted system may be calculated from a mass balance in which all the reactions which produce the complex species are assumed to proceed to completion.

The relationship between the primary mole fractions in the unreacted system and the composition of the reacted system is shown in Table 2.

Table 2

For the composition range at $X_{MCl_2} < 0.333$, the respective amounts of Na_2MCl_4, K_2MCl_4 and Cs_2MCl_4 present are calculated on the assumption that MCl_2 is distributed among these three complex compounds in the same ratio as that of NaCl:KCl:CsCl in the unreacted melt.

The mole numbers of the various components present in the reacted melts are given in Table 2 expressed in terms of the composition parameters t, S and y.

It is readily seen from Table 2 that at constant y and t values, the amount of Na_2MCl_4 increases in proportion to S at the expense of both K_2MCl_4 and Cs_2MCl_4, where the amounts of K_2MCl_4 and Cs_2MCl_4 remaining in the melt are at the constant mole ratio of t/(1-t). Thus, as S changes from 0 to 1 along a y composition plane at constant t-values, the thermodynamic properties of the melts should reflect the predominant influence of the Na_2MCl_4 complex which forms in increasing amounts in proportion to S. The composition parameters S, t and y in this way define composition paths within a quarternary system which are particularly suitable for observing the effects of competing interactions due to the formation of complex species in fused salt systems.

Following the same reasoning as with the ternary charge asymmetric systems, if the partial molar properties of the complex species present in the quarternary system are taken to be the same as in the corresponding binary systems having the same MCl_2 content, then any molar excess property Z may be written as

$$Z = \Sigma \bar{Z}_i \tag{20}$$

where $\bar{Z}_i$ is the relevant partial molar excess property. For example, where $y < 0.667$,

$$Z = \frac{2-3y}{2} \bar{Z}_{MCl_2} + \frac{ys}{2} \bar{Z}_{Na_2MCl_4} + \frac{ty(1-S)}{2} \bar{Z}_{K_2MCl_4} + \frac{y(1-t)(1-S)}{2} \bar{Z}_{Cs_2MCl_4} \tag{21}$$

In Figure 8, considering the path OQ within the quarternary system, the partial molar properties of MCl_2 are also taken to vary linearly with respect to the concentration parameter S, such as

$$\bar{Z}_{MCl_2} = S \bar{Z}_{MCl_{2(at\ Q)}} + (1-S)\bar{Z}_{MCl_{2(at\ 0)}} \tag{22}$$

where, $\bar{Z}_{MCl_{2(at\ Q)}}$ corresponds to the ternary system CAD, and $\bar{Z}_{MCl_{2(at\ 0)}}$

corresponds to the binary system CB.

From equations 7 and 22, it is readily shown that,

$$\bar{Z}_{MCl_2} = (1-S)\ t\ \bar{Z}_{MCl_{2(CD)}} + (1-t)\ \bar{Z}_{MCl_{2(AC)}} + S\ \bar{Z}_{MCl_{2(BC)}} \quad (23)$$

From equations 21 and 23, rearrangement of terms yields,

$$Z = (1-S)\ \{(1-t)\ (\frac{2-3y}{2}\ \bar{Z}_{MCl_2} + \frac{y}{2}\ \bar{Z}_{Cs_2MCl_4}) + t(\frac{2-3y}{2}\ \bar{Z}_{MCl_2} + \frac{y}{2}\ \bar{Z}_{K_2MCl_4})\ \} + S\ \{\frac{2-3y}{2}\ \bar{Z}_{MCl_2} + \frac{y}{2}\ \bar{Z}_{Na_2MCl_4}\} \quad (24)$$

Since the $\bar{Z}_i$ terms for the complex species present are also taken to be linear sums of the values in the binary systems containing the same amount of MCl_2, equation 24 may be written as:

$$Z = (1-S)\ [\ (1-t)\ Z_{AC} + t\ Z_{CD}\ ]\ + S\ Z_{BC} \quad (25)$$

which is valid for any S-path for which the y and t parameters are kept constant.

Following a similar method it may also be shown that equation 25 is also valid for the composition range when y > 0.667.

Any partial molar property of the MCl_2 component in a quarternary melt of this type may be written as

$$\Delta\bar{Z}_{MCl_2} = (1-S)\ [\ (1-t)\ \Delta\bar{Z}_{AC} + t\ \Delta\bar{Z}_{CD}\ ]\ + S\ \Delta\bar{Z}_{BC} \quad (26)$$

From equation 26, the expression for the activity of MCl_2 in the quarternary system is readily derived as:

$$a_{MCl_2} = (a_{MCl_2})^{(1-S)(1-t)}_{AC} \cdot (a_{MCl_2})^{t(1-S)}_{CD} \cdot (a_{MCl_2})^{S}_{BC} \quad (27)$$

where AC, CD and BC are the component binary systems, each containing the same amount of MCl_2 as in the quarternary. Plots of $\overline{\Delta G}^E_{MnCl_2}$ versus S at constant t values have been calculated from data on the binary systems $MnCl_2$-NaCl, $MnCl_2$-KCl and $MnCl_2$-CsCl given in Figure 9 which have been obtained in this laboratory (21). The results of the calculations for the quarternary system are shown in Figure 10.

Figures 9 and 10

It is seen that all compositions along a constant y-plane, which are obtained when t is changed from 0 to 1, are represented by a family of curves which are terminated in the three component binary systems, as shown on the graph.

Thus, the results for the entire composition range for a quarternary system may be represented by groups of curves of this kind, each representing a different constant y-plane. It is also seen in Figure 10 that these plots are useful in defining iso-activity paths within a quarternary system.

In conclusion, it is shown that the thermodynamic properties of ternary and quarternary charge asymmetric fused salt solutions may be calculated from data on component binary systems along composition paths representing a constant content of the charge asymmetric salt component MCl_2. The form of the theoretical expressions are justified if the components of the solutions react internally to form complex species. Although the concept of complex species is extremely useful in understanding the nature and the kinds of interactions present in these melts, the use of equations 10, 12, 13 and 14, 20, 24 and 26 does not depend upon the knowledge of the complex species present, but rather on experimental data in the relevant binary systems.

Regarding quarternary systems, the introduction of the composition parameters S, t and y makes it possible to plot the thermodynamic data along well defined composition paths. This can serve in the planning of experiments to reduce the large number of compositions to be studied in order to characterize the quarternary system adequately. The selection of isoactivity paths has commercial applications when one is trying to minimize the use of certain costly reagents in fixing the activity of the MCl_2 component. Finally, even in systems where the assumption of no interaction between the various alkali chlorides is untenable, plots such as Figure 10 are useful in displaying activity data.

References

1. F. Kohler, Monatsch, Chemie, 91, 738, 1960.
2. E. Bonnier and R. Caboz, C.R. Acad. Sc. 250, 527, 1960.
3. Y.M. Muggianu, M. Gambino and J.P. Bros, J. Chimie Physique, 72, 83, 1975.
4. C.B. Alcock, F.D. Richardson, Acta Met. 6, 305, 1958.
5. G.W. Toop, Trans. TMS -AIME, 233, 850, 1965.
6. P.J. Spencer, F.H. Hayes and O. Kubaschewski, Rev. Chim. Miner. 9, 13, 1972.
7. I. Ansara, Metallurgical Chemistry, Proc. Sympos. Brunel Univ. and NPL, 1971, HMSO, 1972, p. 403.
8. M. Hillert, Calphad, Vol. 4, 1, 1980.
9. D.R. Sadoway, S.N. Flengas, J. Electrochem. Soc. 122, 515, 1975.
10. S.N. Flengas, A.S. Kcuharski, Can. J. Chem. 49, 3971, 1971.
11. S.N. Flengas, J.M. Skeaff, Can. J. Chem. 50, 1345, 1972.
12. N.R. Carmichael, S.N. Flengas, J. Electrochem. Soc. 128, 2098, 1979.
13. M. Temkin, Zhur, Fiz. Khim. 20, 105, 1946.
14. K. Tanemoto, T. Nakamura, Chem. Lett. 351, 356, 1975.
15. N.R. Carmichael and S.N. Flengas, J. Electrochem. Soc. 126, 2104, 1979.
16. R.L. Lister and S.N. Flengas, Can J. Chem. 43, 2947, 1965.
17. J.E. Dutrizac and S.N. Flengas, "Advances in Extractive Metallurgy", The Institution of Mining and Metallurgy, London, England, 1967, pp. 572-599.
18. S.N. Flengas, J.E. Dutrizac, R.L. Lister, Can. J. Chem. 46, 495,1968.
19. D. R. Sadoway, S.N. Flengas, Can. J. Chem. 56, 2538, 1978.
20. A. Gutierrez, J.M. Toguri, Private Communication.
21. A.S. Kucharski, S.N. Flengas, J. Electrochem. Soc. 119, 1170,1972.
22. D.C. Hamby, A.B. Scott, J. Electrochem. Soc. 117, 319, 1970.
23. A.D. Pelton, S.N. Flengas, J. Electrochem. Soc. 118, 1307, 1971.

24. A.C. Gruner, W.T. Thompson, Can. J. Chem. 53, 1084, 1975.

25. J. Guion, M. Blander, D. Hengstenberg, and K. Hagemark, J. Phys. Chem. 72, 2086, 1968.

26. K. Hagemark, D. Hengstenberg, and M. Blander, J. Chem. Eng. Data, 17, 216, 1972.

27. A. Prince, "Alloy Phase Equilibria", Elsevier Publishing Co. N.Y., 1966.

Table 1

TERNARY SYSTEM
MCl_2 - ACl - BCl

	Component	Primary composition	Composition in Reacted System (mole number)	
$y \leq 0.667$	MCl_2	$X_{MCl_2} = 1 - y$	$\frac{2 - 3y}{2}$	MCl_2 rich section of ternary
	ACl	$X_{ACl} = y(1-t)$	0	
	BCl	$X_{BCl} = ty$	0	
	A_2MCl_4	0	$\frac{y(1-t)}{2}$	
	B_2MCl_4	0	$\frac{ty}{2}$	
$y \geq 0.667$	MCl_2	$X_{MCl_2} = 1-y$	0	MCl_2 lean section of ternary.
	ACl	$X_{ACl} = y(1-t)$	$(1-t)(3y-2)$	
	BCl	$X_{BCl} = ty$	$t(3y-2)$	
	A_2MCl_4	0	$2(1-t)(1-y)$	
	B_2MCl_4	0	$2t(1-y)$	

Table 2

QUARTERNARY SYSTEM

PRIMARY SYSTEM			REACTED SYSTEM		
Components		Composition (Mole Fractions)	Composition (Mole Numbers)	$y < 0.667$	$y > 0.667$
CsCl	(A)	$X_A = y(1-t)(1-S)$	η_{MCl_2}	$\frac{2-3y}{2}$	0
NaCl	(B)	$X_B = y\ S$	η_{NaCl}	0	$S(3y-2)$
MCl_2	(C)				
KCl	(D)	$X_C = 1-y$			
		$X_D = ty(1-S)$	η_{KCl}	0	$t(1-S)(3y-2)$
			η_{CsCl}	0	$(1-t)(1-S)(3y-2)$
			$\eta_{Na_2MCl_4}$	$yS/2$	$S(1-y)$
			$\eta_{K_2MCl_4}$	$\frac{ty(1-S)}{2}$	$t(1-S)(1-y)$
			$\eta_{Cs_2MCl_4}$	$y(1-t)(1-S)$	$(1-t)(1-S)(1-y)$

Composition Parameters: $y = 1-X_C$

$$t = \frac{X_D}{X_A+X_D}$$

$$S = \frac{X_B}{X_A+X_B+X_D}$$

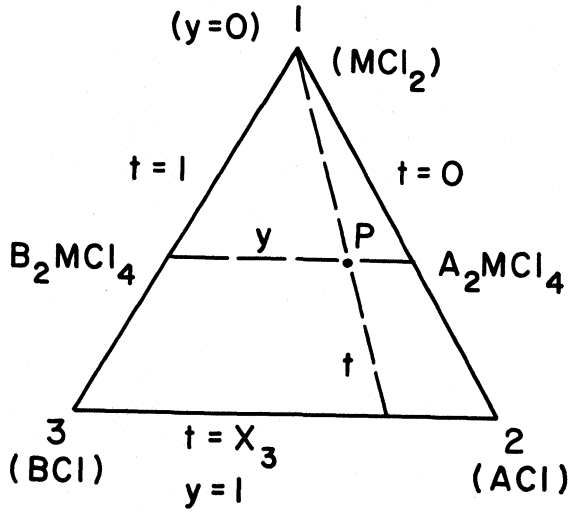

Figure 1: Representation of a composition P in a ternary system MCl_2-ACl-BCl by the intersection of the composition parameters y and t defined as:

$$y = 1 - X_{MCl_2}$$

$$t = \frac{X_{BCl}}{X_{ACl} + X_{BCl}}$$

all compositions are plotted within the surface of the equilateral triangle.

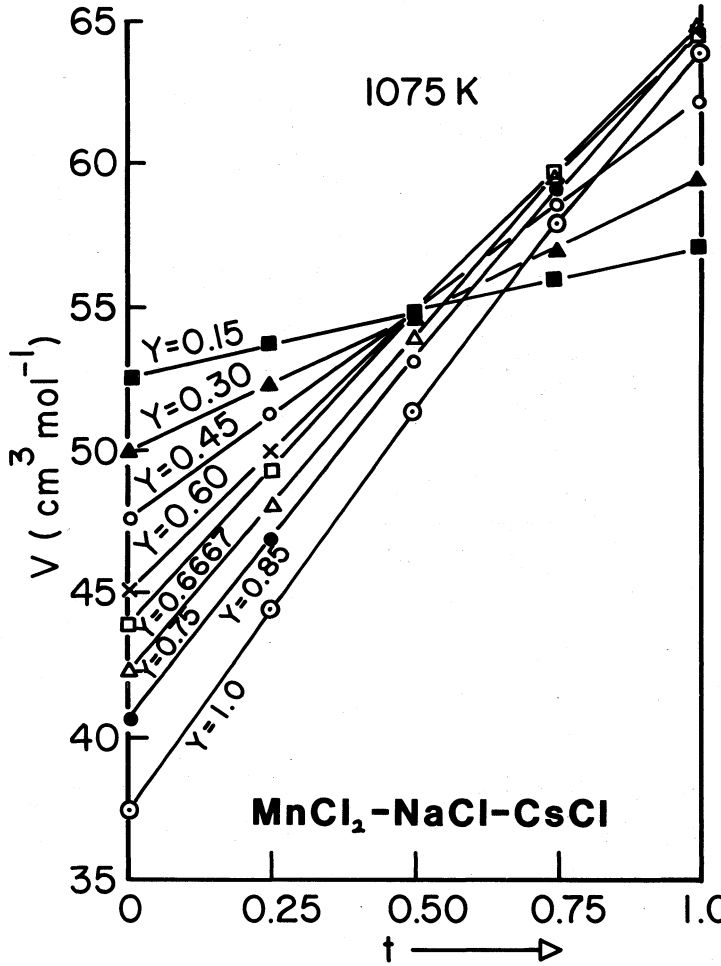

Figure 2: Plots of the molar volumes V versus t, for various y-values in the ternary system $MnCl_2$-NaCl-CsCl.

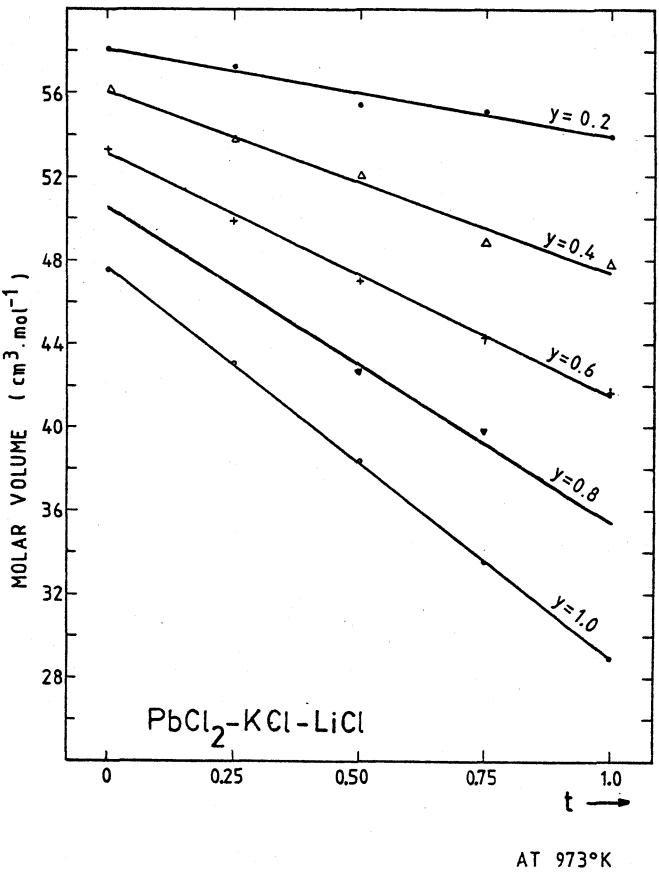

Figure 3: Plots of the molar volumes versus t for various y-values, in the ternary system $PbCl_2$-KCl-LiCl.

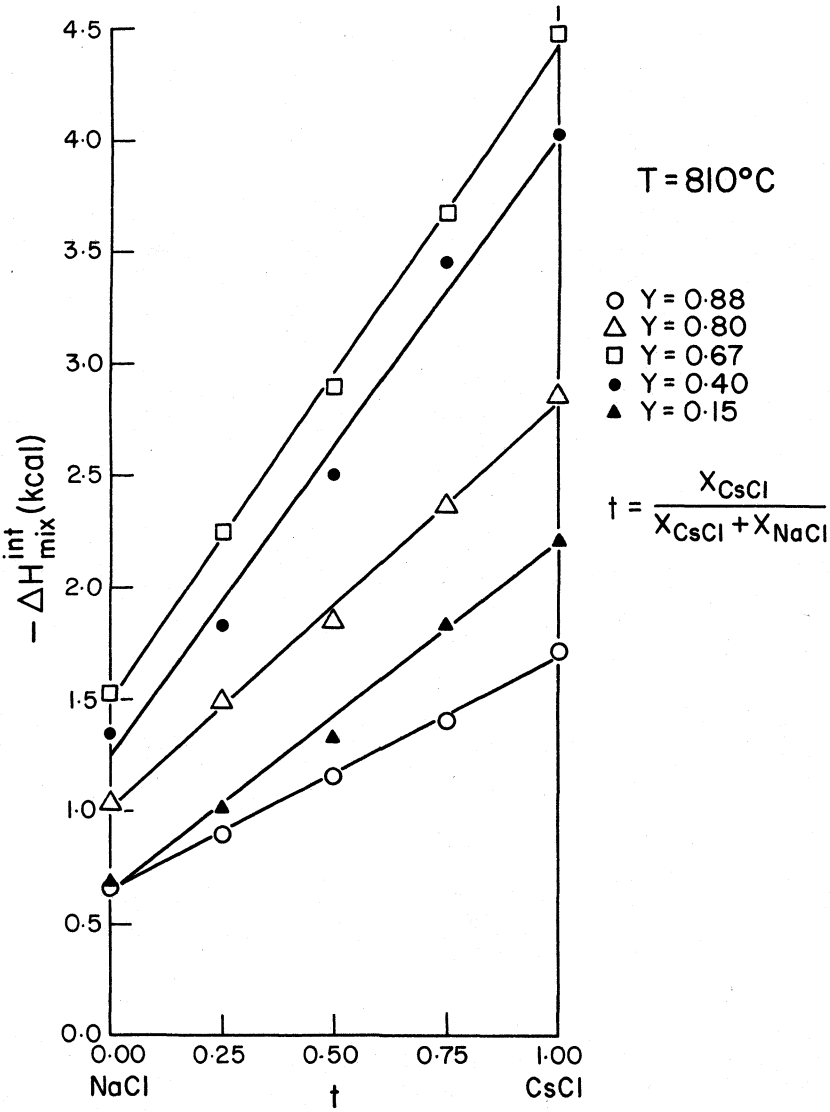

Figure 4: Plots of integral enthalpies of mixing ΔH_{mix} versus t for various y-values in the ternary system $MnCl_2$-NaCl-CsCl.

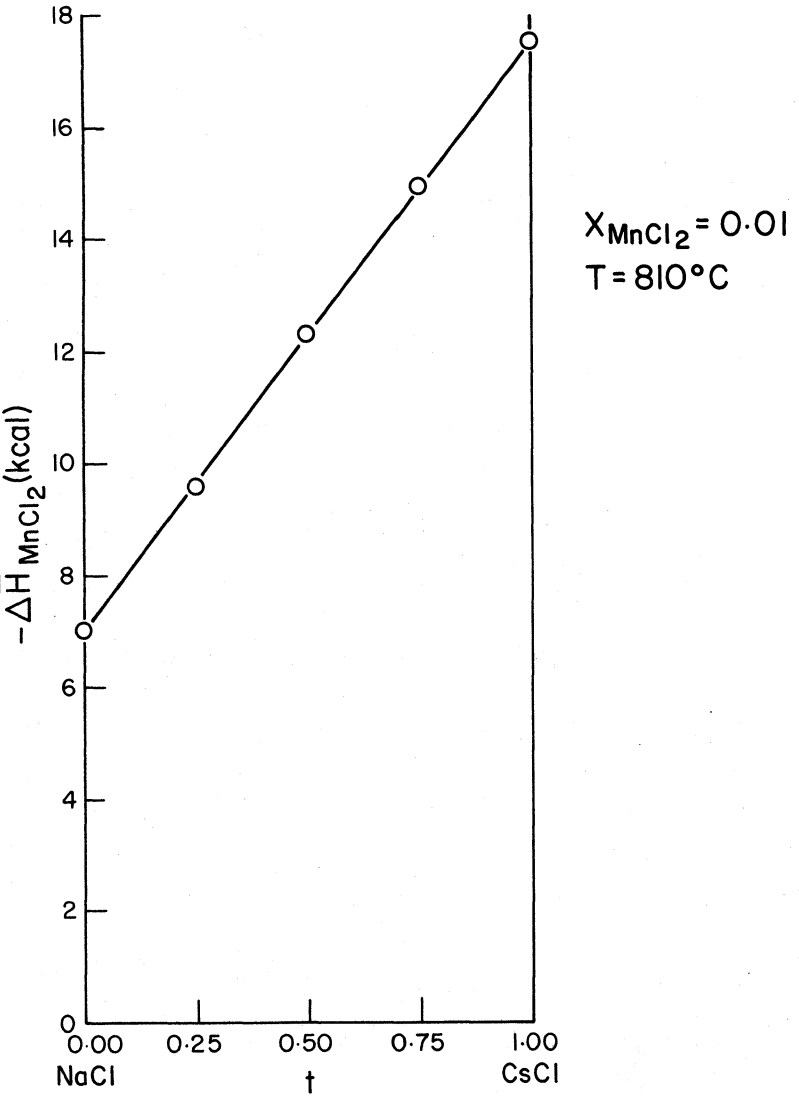

Figure 5: Plots of the partial molar enthalpy of mixing $\overline{\Delta H}_{MnCl_2}$ versus t at $X_{MnCl_2} = 0.01$ in the ternary system $MnCl_2$-NaCl-CsCl.

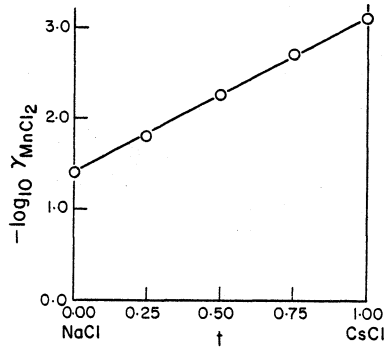

$X_{MnCl_2} = 0{\cdot}01$
$T = 810°C$

6-a

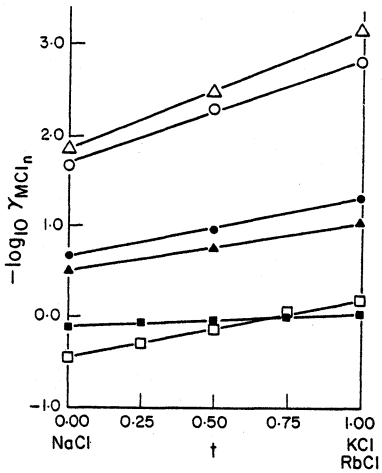

- ○ $CoCl_2$-NaCl-KCl, $X_{CoCl_2} = 0{\cdot}001$ at 800°C
- △ $NiCl_2$-NaCl-KCl, $X_{NiCl_2} = 0{\cdot}001$ at 800°C
- ● $CoCl_2$-NaCl-KCl, $X_{CoCl_2} = 0{\cdot}40$ at 800°C
- ▲ $NiCl_2$-NaCl-KCl, $X_{NiCl_2} = 0{\cdot}40$ at 800°C
- □ AgCl-NaCl-RbCl, $X_{AgCl} = 0{\cdot}03$ at 810°C
- ■ AgCl-NaCl-RbCl, $X_{AgCl} = 0{\cdot}50$ at 810°C

6-b

Figure 6a: Plot of $\log_{10} \gamma_{MnCl_2}$ versus t, at $X_{MnCl_2} = 0.01$ in the ternary system $MnCl_2$-NaCl-CsCl.

6b: Similar plots as above in the ternary systems:
$CoCl_2$-NaCl-KCl (22)
$NiCl_2$-NaCl-KCl (22)
AgCl-NaCl-RbCl (23).

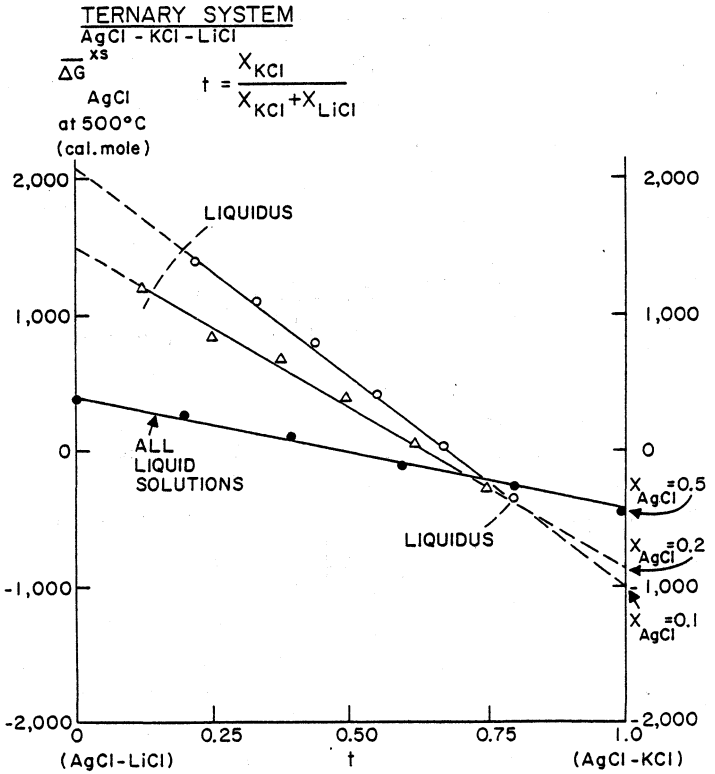

Figure 7: Plots of $\overline{\Delta G}^{XS}_{AgCl}$ versus t at constant X_{AgCl} in the ternary system AgCl-KCl-LiCl (24).

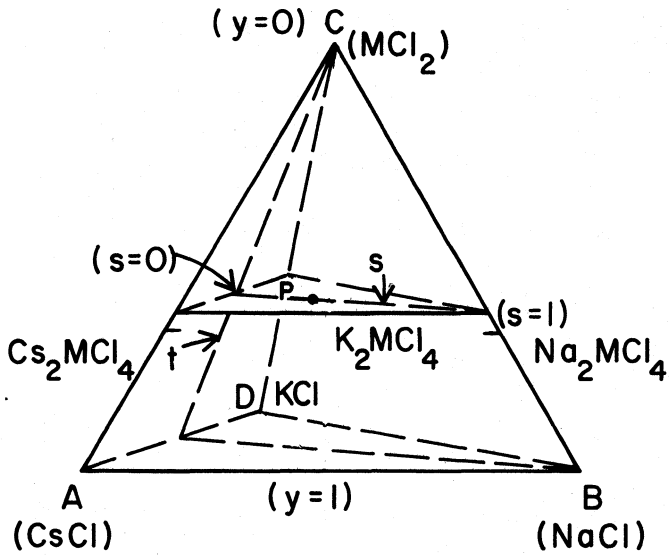

Figure 8: Representation of a composition P within a quarternary system by the intersection of the y and t planes. The position of P is then defined by a third parameter S, which varies from 0 to 1.
The parameters y, t and S are defined as:

$$y = 1 - X_{MCl_2}$$

$$t = \frac{X_{KCl}}{X_{CsCl}+X_{KCl}}$$

$$S = \frac{X_{NaCl}}{X_{NaCl}+X_{KCl}+X_{CsCl}}$$

All compositions are plotted within the volume of the equilateral tetrahedron.

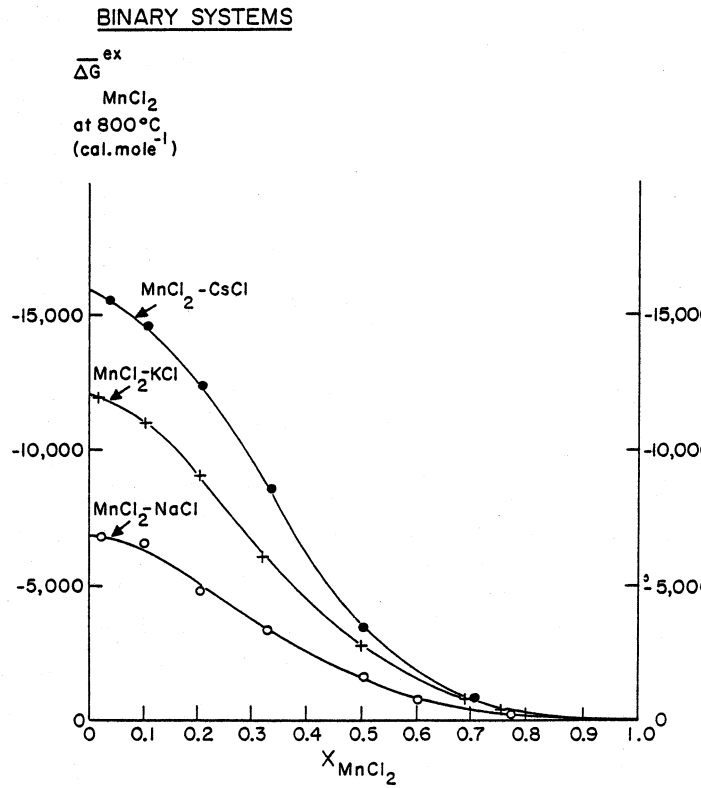

Figure 9: Plots of $\overline{\Delta G}^{XS}_{MnCl_2}$ versus X_{MnCl_2} in the three binary systems: $MnCl_2$-NaCl, $MnCl_2$-KCl, $MnCl_2$-CsCl.

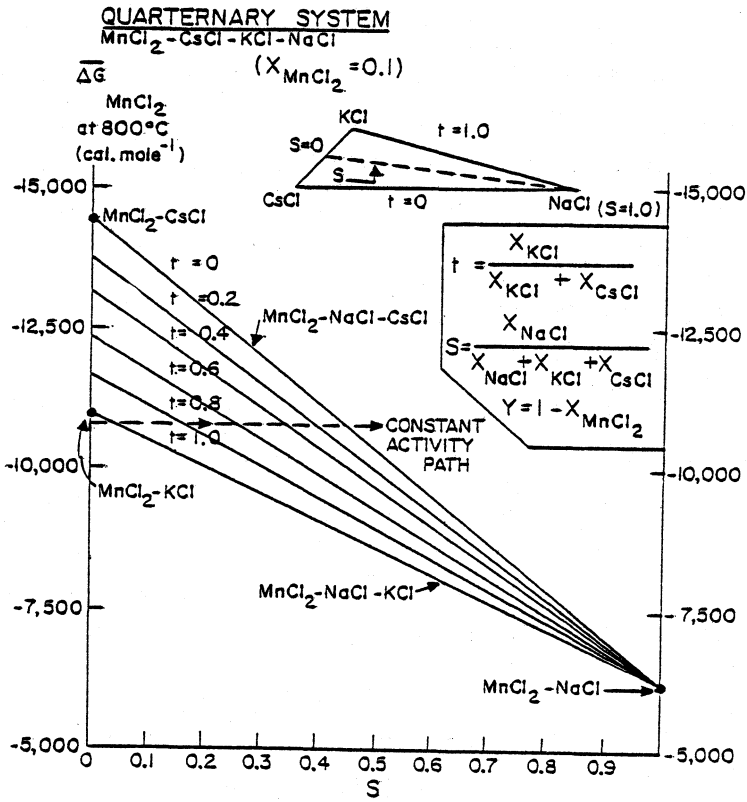

Figure 10: Plots of $\overline{\Delta G}_{MnCl_2}$ versus S at constant y and t values. Solutions having the same $MnCl_2$ content ($X_{MnCl_2} = 0.1$) are located on a y-plane parallel to the base ABD of the tetrahedron, as shown in Figure 9.

DOI: 10.1149/198109.0095PV

NMR STUDIES OF MOLTEN CESIUM-CESIUM HALIDE SOLUTIONS

W. W. Warren, Jr. and S. Sotier*

Bell Laboratories, Inc.
Murray Hill, New Jersey 07974

ABSTRACT

Molten Cs-CsCl and Cs-CsI-I solutions have been investigated by means of ^{133}Cs, ^{35}Cl, and ^{127}I NMR. Resonance shifts and nuclear relaxation rates were measured through the transition from liquid metal to molten salt. Enhanced relaxation rates show that the excess electrons become strongly localized at low concentrations of metal in the salts. From the magnitudes of the local hyperfine fields, we deduce that the distribution of electronic charge in these states is very similar to that of *F*-centers in alkali halide crystals. In contrast, the data do not support models based on single- or multi-site atomic states. Analysis of the relaxation rate data yields the jump time for transport of the localized electrons. The magnitude and concentration dependence of the jump times are consistent with the observed electrical conductivity of CsCl.

I. INTRODUCTION

The study of liquid solutions of the alkali metals with their molten salts has a long history dating from the pioneering work of Bredig and his collaborators in the late 1950's.[1] These solutions are currently attracting renewed attention because of their striking metal-nonmetal transitions and their similarity to so-called ionic alloys such as liquid Cs-Au. The latter exhibit an incompletely understood transition from metallic to salt-like properties around a simple stoichiometric composition (e.g. CsAu).[2]

In this paper we report and discuss NMR results for the liquid systems Cs-CsI-I and Cs-CsCl.[3] In addition to their obvious status as paradigms for Cs-Au and similar alloys, the Cs-CsX solutions have the advantage of complete liquid miscibility over the full range of composition. The metal-nonmetal transition can therefore be followed continuously from pure Cs to pure halide at a temperature close to the melting point of the salt. The nuclear properties of ^{133}Cs are favorable for a relatively strong NMR signal; ^{127}I and ^{35}Cl resonances can also be observed although the latter is considerably weaker than ^{133}Cs and ^{127}I.

In our studies we exploit the high sensitivity of NMR to local magnetic fields produced at the nuclei by the spin paramagnetism of excess electrons in the metal-salt solutions. In interpreting the experimental results we shall be particularly concerned with the following questions. First, as the concentration of metal is reduced toward the dilute limit, do the excess electrons localize or can they be characterized as a low-density gas of nearly-free electrons? Second, if localization occurs, what conclusions can be drawn concerning the structure of these states? Finally, what is the nature of electronic transport in the region of the metal-nonmetal transition and in the range of dilute metal in the molten salt? The experiments show, in fact, that the electrons do become strongly localized and the data reveal some details of the structure and dynamic properties of the localized states.

II. THEORETICAL BACKGROUND: STATIC AND DYNAMIC HYPERFINE FIELDS

The dissolution of an alkali metal M in its halide MX can be represented by the reaction

$$cM + (1-c)MX \rightarrow M^+ + ce^- + (1-c)X^- \quad 0 \leq c \leq 1 \tag{1}$$

Now the magnetic interaction between the nuclei and the excess electrons can be described by

$$H_{hf} = A_{ij}\vec{I}_i \cdot \vec{S}_j \tag{2}$$

where A_{ij} is the hyperfine coupling constant between a nucleus of spin $\vec{I}_i$ and an electron of spin $\vec{S}_j$. The constant A_{ij} is given by

$$A_{ij} = \frac{8\pi}{3}\gamma_n\gamma_e\hbar^2\delta(\vec{r}_j - \vec{R}_i) \tag{3}$$

where γ_e and γ_n are, respectively, the electronic and nuclear gyromagnetic ratios and $\vec{r}_j$ and $\vec{R}_i$ are the respective position coordinates of the j^{th} electron and the i^{th} nucleus. The observable consequences of the magnetic hyperfine interaction are shifts of the frequency (or magnetic field) for NMR absorption and contributions to the line width and spin-lattice relaxation rate. The calculation of these effects using perturbation theory can be found in standard references on NMR[4] and will not be repeated here. In what follows, we merely summarize those results which are important for interpreting our experimental data.

A. Static Effects: NMR Shifts

If the excess electrons indicated on the right-hand-side of reaction (1) are not spin-paired, the hyperfine interaction leads to a time-averaged local field which is proportional to the paramagnetic spin susceptibility. The NMR frequency ω is then shifted by an amount $\gamma_n\Delta H$:

$$\omega = \gamma_n(H_o + \Delta H - \delta H_{chem}) \tag{4}$$

where δH_{chem} is the usual chemical shift due to the orbital magnetism of bound electrons. In most cases we shall consider, $\Delta H \gg \delta H_{chem}$. The relative hyperfine shift is

$$\frac{\Delta H}{H_o} = (\gamma_n \gamma_e \hbar^2 N_o)^{-1} <A> \chi_m^p \tag{5}$$

where N_o is Avogadro's number, χ_m^p is the molar paramagnetic susceptibility, and the average <A> is taken over all unpaired electrons and all resonant nuclei (e.g. ^{133}Cs). Evaluation for a liquid must take into account the fact that structural fluctuations in the liquid state occur on a time scale several orders of magnitude faster than the nuclear Larmor period ($\sim 10^{-8} s$). Thus all nuclei of the same chemical element experience the same average local field even though the instantaneous local fields may differ greatly, for example, according to whether or not a nucleus is near an unpaired electron.

There are three limiting cases which are of great importance for metal-molten salt solutions. The first is the well-known Knight shift in metals:

Case I (metal):
$$\frac{\Delta H}{H_o} = \frac{8\pi}{3} <|\psi(R_n)|^2>_F \chi_n^p \tag{6}$$

where $<|\psi(R_n)|^2>_F$ is the electronic probability amplitude at the resonant nuclear species averaged over all states at the Fermi level and χ_n^p is the Pauli paramagnetic susceptibility. For a molar concentration c_s of non-interacting localized spins ($S = 1/2$) exhibiting a Curie paramagnetic susceptibility we have:

Case II (localized states):
$$\frac{\Delta H}{H_o} = \frac{2\pi}{3} c_s <|\psi(R_n)|^2> \frac{(\gamma_e \hbar)^2}{kT} \tag{7}$$

Finally, a pure salt should exhibit no spin paramagnetism:

Case III (pure salt):
$$\frac{\Delta H}{H_o} = 0 \tag{8}$$

B. Dynamic Effects: Nuclear Relaxation

In general, the hyperfine interaction of Eq. (2) is time dependent because of the relative motions of electrons and nuclei, i.e. $\vec{r}_j(t) - \vec{R}_i(t)$ in Eq. (3), and because of electron spin fluctuations $\vec{S}_j(t)$. The presence in the interaction, Eq. (2) of terms I^+S^- and I^-S^+ means that the time-dependent interaction can induce mutual electron-nuclear spin flips. Thus the hyperfine interaction provides for the flow of energy between the nuclear spin system and the thermal reservoir of the ions ("lattice") by means of the electrons. The stochastic nature of the local field fluctuations leads to their representation in terms of a time correlation function $G(t)$ and correlation time τ_c:

$$G(t) = \frac{1}{4} \sum_{ij} < A_i(t) S_j^+(t) A_i(0) S_j^-(0) > = G(0) e^{-t/\tau_c} \tag{9}$$

The nuclear spin-lattice relaxation time T_1 is then related to the spectral density of $G(t)$ at the nuclear resonant frequency ω_o:

$$\frac{1}{T_1} = \frac{2}{\hbar^2} \int_{-\infty}^{\infty} dt \; e^{-i\omega_o t} G(t) \tag{10}$$

In general for liquids, $\omega_o \tau_c \ll 1$ and the relaxation rate $1/T_1$ is proportional to a mean-square coupling strength, i.e. $G(0)$, and the correlation time τ_c.

We again consider some special examples, analogous to Eqs. (6)-(8). For an itinerant electron system, the coupling strength can be replaced by the Knight shift using Eq. (6) with the result[5]

$$\frac{1}{T_1} \cong \left(\frac{1}{T_1}\right)_{Korr.} \cdot \frac{\tau_c}{\hbar N(E_F)} \tag{11}$$

case I:

$$\left(\frac{1}{T_1}\right)_{Korr.} = \frac{4\pi kT}{\hbar}\left(\frac{\gamma_n}{\gamma_e}\right)^2\left(\frac{\Delta H}{H}\right)^2 \tag{12}$$

where $N(E_F)$ is the density of electronic states per electron at the Fermi level. The factor $\tau_c/\hbar N(E_F)$ is close to 1 in nearly-free-electron metals with the result that the relaxation rate is close to the Korringa rate $(1/T_1)_{Korr}$. The correlation time in this case is roughly the time for an electron to pass through one atomic volume moving at the Fermi velocity ($\tau_c \sim 10^{-15} s$). However, the onset of electronic localization leads to longer values of τ_c as the electron tarries in the vicinity of a particular nucleus. As a consequence, $1/T_1$ becomes enhanced with respect to $(1/T_1)_{Korr}$. Since $(1/T_1)_{Korr.}$ can always be evaluated if the shift is measured, the degree of enhancement $(1/T_1)/(1/T_1)_{Korr.}$ provides a direct experimental measure of electronic localization.

If the electrons are sufficiently well-localized that they can be treated as classical local moments, the relaxation rate for $S = 1/2$ becomes

Case II:
$$\frac{1}{T_1} = \frac{c_s}{2} <(A/\hbar)^2> \tau_c \tag{13}$$

where τ_c is interpreted as the shorter of the on-site spin fluctuation time or the time of association of a particular nucleus-electron pair. In the latter case, and if the electrons are moving more rapidly than the ions, the correlation times in Eqs. (11) and (13) have essentially the same physical meaning.

For the pure salt, the hyperfine contribution to the nuclear relaxation rate vanishes:

Case III:
$$\left(\frac{1}{T_1}\right)_{h.f.} = 0 \tag{14}$$

In this case the experimental rate is determined by other interactions of which the most important is usually nuclear electric quadrupole relaxation associated with ionic and molecular motions.

III. EXPERIMENTAL RESULTS

NMR in Cs-CsCl and Cs-CsI solutions was observed using coherent pulsed NMR techniques at frequencies of 9.7 MHz for ^{133}Cs and ^{127}I and 7.2 MHz for ^{35}Cl. The samples were contained in ceramic (Al_2O_3 or BeO) cells whose open ends were brazed to Nb closure assemblies. The cells were closed with Nb-Nb mechanical seals. The sample cells and molybdenum NMR coil were heated in an argon atmosphere in a cylindrical furnace which fit within the 76 mm gap of the electromagnet.

A. Resonance Shifts

Resonance shifts were measured with respect to the ^{133}Cs, ^{35}Cl, and ^{127}I resonance positions in dilute aqueous solutions of CsCl and KI. The experimental results are summarized in Fig. 1. For ^{133}Cs we observed a dramatic monotonic decrease in $\Delta H/H_o$ from the large Knight shift of pure Cs to the small chemical shifts in pure CsCl and CsI. The halogen shifts are much smaller, showing that the electronic paramagnetism is mainly associated with the Cs^+ ions. The ^{35}Cl shifts in $Cs_{0.20}$ $(CsCl)_{0.80}$ indicate nearly complete exclusion of conduction electron charge from the anion. The charge exclusion is weaker for I^- and the data for $Cs_{0.60}(CsI)_{0.40}$ suggest substantial penetration of the conduction electrons to the I^- nucleus. However, even in this case the anion shift is only 25% of the ^{133}Cs shift value. The ^{133}Cs shift was found to remain unchanged as excess I was added to CsI.

B. Relaxation Rates

The nuclear relaxation rates for ^{133}Cs in Cs-CsCl and Cs-CsI and ^{127}I in Cs-CsI are shown in Fig. 2. Where possible, the spin-lattice relaxation rates $1/T_1$ were measured; in some cases, the free induction decay lifetime $1/T_2^*$ could be measured with more precision than $1/T_1$ because of extremely rapid relaxation. For a liquid in which inhomogeneous broadening is unimportant, as in the present case, so-called "extreme narrowing" conditions lead to $1/T_1 = 1/T_2^*$. This equality was verified experimentally for ^{133}Cs in $Cs_{0.20}(CsI)_{0.80}$.

The essential feature of the relaxation data shown in Fig. 2 is the strong peak in the relaxation rate near 5% excess Cs in the salts. The peak was also observed for ^{127}I, but the smaller magnitude of the relaxation rates indicates, as did the shift values, that the paramagnetism is most closely associated with the Cs^+ ions. The background ^{133}Cs relaxation rates in pure liquid CsCl and CsI are extremely low: $1/T_1 = 0.166 \pm 0.009\ s^{-1}$ for CsCl at 650°C and $1/T_1 = 0.140 \pm 0.005\ s^{-1}$ for CsI at 640°C. The much higher rate observed for ^{127}I in CsI, $1/T_1 = (5.45 \pm 0.10) \times 10^3\ s^{-1}$ at 640°C, is consistent with the much larger electric quadrupole moment of ^{127}I ($^{127}Q/^{133}Q \cong 190$)). In CsI-I solutions, we observed ^{133}Cs relaxation rates in the range 10-100 s^{-1}. While considerably stronger than the rates in pure CsI, these rates are nevertheless some two orders of magnitude smaller than those observed with comparable amounts of excess metal. The observations for solutions containing excess I therefore suggest enhanced electric quadrupolar relaxation due to formation of complexes. A likely candidate for such a complex is the triatomic anion I_3^- formed according to

$$I^- + I_2 \rightarrow I_3^- \tag{15}$$

IV. DISCUSSION

The most important result of our NMR measurements in Cs-CsCl and Cs-CsI is the observation of a strong peak in the nuclear relaxation rates as the concentration of excess metal is reduced toward the pure salts. Since the shift decreases smoothly through this concentration range, it is obvious that the relaxation rate is strongly enhanced relative to the Korringa relation of Eq. (12). Thus interpretation of these solutions as dilute free electron metals[6–8] is untenable and the data can only be understood in terms of dramatically longer correlation times, i.e. electronic localization. In what follows, we assume that for concentrations no higher than a few percent excess metal, the excess electrons can be treated as local moments obeying classical (Boltzmann) statistics and we deduce some properties of these states.

A. Structure of the Localized State

The assumption of classical statistics implies a Curie susceptibility for the localized electrons. In this case the shift is given by Eq. (7). If we identify the concentration c_s of spins with the concentration c of excess metal, we can extract the average hyperfine coupling or, equivalently, $<|\psi(R_n)|^2>$ from the initial rate of increase of $\Delta H/H_o$ with c. This result for ^{133}Cs, normalized to the value $|\psi(\mathrm{Cs})|^2_{atom}$ for the $5s^1$ state of atomic Cs[9] is

$$\frac{<|\psi(\mathrm{Cs})|^2>}{|\psi(\mathrm{Cs})|^2_{atom}} = \begin{cases} 0.26 & \mathrm{Cs-CsCl} \\ 0.22 & \mathrm{Cs-CsI} \end{cases}$$

The average coupling per localized electron is thus much smaller than the atomic value, indicating that the excess metal does not enter the salt as a neutral atom at these concentrations. A similar conclusion may be drawn regarding the multi-site localized states proposed[10] as a consequence of structural disorder. Since such states must have strong $5s$ character near a particular Cs^+ site, it is reasonable to write

$$|\psi(r_i)|^2 = f_i |\psi(\mathrm{Cs})|^2_{atom} \tag{16}$$

for a particular site. Then, if most of the charge is excluded from the anions, in agreement with our halogen shift values, normalization requires $\sum_i f_i \cong 1$. Thus, taking the average over all sites, as appropriate for the NMR shift in a liquid, we should expect

$$<|\psi(\mathrm{Cs})|^2> = \sum_i |\psi(r_i)|^2 \cong |\psi(\mathrm{Cs})|^2_{atom} \tag{17}$$

in contradiction to experiment.

An alternative to single- or multi-site atomic states is the F-center model originally proposed by Pitzer.[11] In this picture the excess electron is localized in a site normally occupied by a negative ion and is surrounded by a number, n_1, of metal ions. In contrast with the crystalline F-center, of course, the value of n_1 in the liquid state can fluctuate around some mean value $\bar{n}_1$. The F-center model has

received considerable support from studies of the optical absorption in dilute solutions[12,13] and, because a substantial amount of charge is localized in the vacancy, the model provides a natural explanation for the small values of the hyperfine coupling obtained from our NMR experiments.

It is instructive to compare the probability amplitude $|\psi_F(R_n)|^2$ on a single neighboring ion in the liquid with corresponding values obtained from electron-nuclear double resonance (ENDOR) studies of F-centers in alkali halide crystals.[14] We note that for the first two neighbor shells,

$$|\psi_F(\mathrm{Cs})|^2 \cong (1/\bar{n}_1)<|\psi(\mathrm{Cs})|^2> \tag{18}$$

$$|\psi_F(\mathrm{X})|^2 \cong (1/\bar{n}_2)<|\psi(\mathrm{X})|^2> \tag{19}$$

where we are neglecting contributions to $<|\psi(R_n)|^2>$ from ions beyond the second neighbors. For a rough estimate we take $\bar{n}_1 = n_{Cs-Cs}$ and $\bar{n}_2 = n_{X-X}$ where n_{Cs-Cs} and n_{X-X} are, respectively, the coordination numbers for Cs-Cs and X-X pair correlations determined by diffraction experiments.[15,16] In comparing values of $|\psi_F(R_n)|^2$, it is useful to remove, in first order, the dependence on the volume of the vacancy. Thus we have plotted, in Fig. 3, values of $|\psi_F(R_n)|^2 d_1^3$ where for crystals, d_1 is the first neighbor metal-halogen ion distance and for liquids, d_1 is the position of the M-X peak in the pair correlation function. It is evident from Fig. 3, that the liquid-state values of $|\psi_F(R_n)|^2 d_1^3$ for Cs-CsCl and Cs-CsI are comparable in magnitude with the crystalline F-center results. This consistency provides direct evidence for the validity of the F-center model of the charge distribution of localized electrons in these solutions.

B. Correlation Times and Electron Transport

The correlation times for fluctuations of the local hyperfine fields can be extracted from the relaxation rate data using Eqs. (11) and (13). Beginning from the metallic limit we have used Eq. (11) and assumed that $N(E_F)$ varies with concentration according to free electron theory. In the localized limit, we use Eq. (13) with $c_s = c$ and $<A^2>^{1/2}$ equal to the value of $<A>$ determined from the composition dependence of the shift. The values of τ_c are found to increase from $\tau_c \sim 10^{-15}s$ for pure liquid Cs to $\tau_c \sim 10^{-12}s$ for roughly 1% Cs in CsCl or CsI. In the composition range near 10% excess Cs, both the enhanced-itinerant- and localized-electron models give comparable values of $\tau_c \sim 3 \times 10^{-13}s$. These results therefore quantify the progressive localization and show that for dilute solutions of metal in the salts, the correlation time becomes comparable with the ionic diffusion time.

The rapidity of the local field fluctuations and the strong concentration dependence of τ_c, even in dilute solutions, imply that τ_c should be interpreted as a characteristic time for translational motion of the electron, rather than a spin-fluctuation time. We test this idea by comparing the magnitude and composition dependence of τ_c with the electronic contribution to the electrical conductivity $\sigma_e = \sigma_{expt} - \sigma_{CsCl}$ for CsCl.[17] We assume a diffusive transport process with jump time τ_c:

$$\sigma_e = n \frac{e^2 <a^2>}{6kT} \frac{1}{\tau_c} \tag{20}$$

where $n = cN_o/\Omega_m$, Ω_m is the molar volume, and $<a^2>$ is the mean square jump distance. Fig. 4 shows a fit of Eq. (20) to the observed conductivity at low concentrations using experimental values of τ_c and $<a^2>^{1/2} = 18$ Å. Although the τ data for CsCl cover only a limited range, this plot shows that the composition dependence is consistent with the observed conductivity. Moreover, the value of the fitting parameter $<a^2>$ is reasonable for jumps between vacancies in the liquid structure. We thus conclude that the hyperfine correlation time measured in these experiments is, in fact, the average jump time for the localized electrons. The results show that the electrons in dilute solutions are localized for times on the order of the ionic diffusion times ($\sim 10^{-12}s$) but that addition of excess metal drastically increases the jump rate and leads to rapid delocalization.

ACKNOWLEDGEMENT

The authors are indebted to G. F. Brennert for technical assistance and to D. W. Murphy for the use of his sample preparation facilities. Discussions of ceramic-Nb seals with W. Freyland were extremely helpful and are gratefully acknowledged.

REFERENCES

* Present address: Fachhochschule München, FB 06 Phys. Technik, and Physik Department, T. U. München, West Germany.

1. M. A. Bredig, in *Molten Salt Chemistry*, ed. M. Blander (Wiley Interscience, New York, 1964), p. 367.
2. See, for example, F. Hensel, Adv. Phys. **28,** 555 (1979).
3. Preliminary reports of our results for Cs-CsI-I are found in W. W. Warren, Jr., and S. Sotier, Bull. Amer. Phys. Soc. **25,** 338 (1980); S. Sotier and W. W. Warren, Jr., Proc. Fourth International Conference on Liquid and Amorphous Metals, Grenoble, 1980.
4. See, for example, A. Abragam, *Principles of Nuclear Magnetism* (Oxford, London, 1961).
5. W. W. Warren, Jr., Phys. Rev. **B3,** 3708 (1971).
6. E. G. Wilson, Phys. Rev. Lett. **10,** 432 (1963).
7. R. H. Arendt and N. H. Nachtrieb, J. Chem. Phys. **53,** 3085 (1970).
8. P. J. Durham and D. A. Greenwood, Phil. Mag. **33,** 427 (1976).
9. P. Kusch and H. Taub, Phys Rev. **75,** 1477 (1949).
10. I. Katz and S. A. Rice, J. Am. Chem. Soc. **94,** 4824 (1972)

11. K. S. Pitzer, J. Am. Chem. Soc. **84,** 2025 (1962).

12. D. M. Gruen, M. Krumpelt, and I. Johnson, in *Molten Salts, Characterization and Analysis,* ed. G. Mamantov (Dekker, New York, 1969), p. 169.

13. W. Schmitt and V. Schindewolf, Ber. Bunsengesell. Phys. Chem. **81,** 584 (1977).

14. H. Seidel and H. C. Wolf, in *Physics of Color Centers,* ed. W. B. Fowler (Academic Press, New York, 1968), p. 538.

15. H. A. Levy and M. D. Danford, in *Molten Salt Chemistry,* ed. M. Blander (Wiley Interscience, New York, 1964), p. 109.

16. Recent isotropic separation neutron diffraction experiments indicate that the coordination numbers are closer to those of the rocksalt crystal structure than reported in Ref. 15 (see, for example, J. E. Enderby, these proceedings). Taking this into account, however, does not alter our conclusions in a significant way.

17. N. H. Nachtrieb, unpublished.

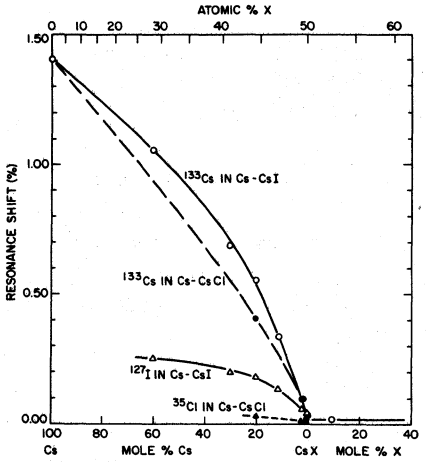

Fig. 1. Resonance shifts versus concentration in Cs-CsI-I and Cs-CsCl solutions.

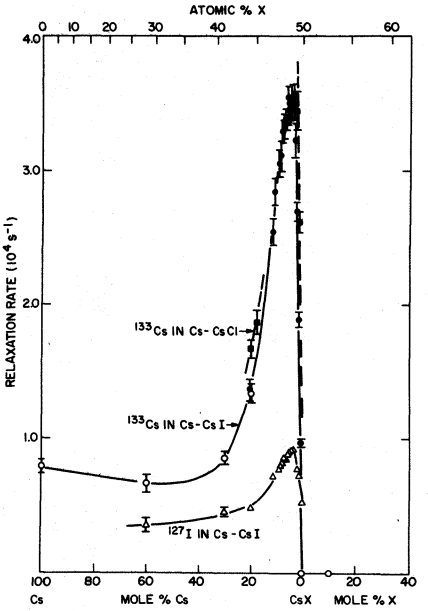

Fig. 2. Nuclear relaxation rates $1/T_1$ (open points) and $1/T_2^*$ (closed points) in Cs-CsI-I and Cs-CsCl solutions.

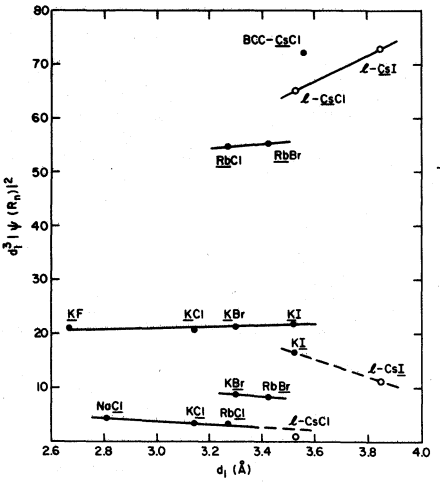

Fig. 3. Volume-corrected F-center probability amplitudes versus metal-halogen distance d_1 in alkali halide crystals (solid points) and Cs-Cs halide liquid solutions (open points).

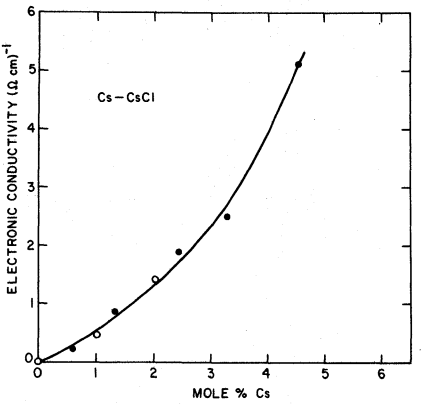

Fig. 4. Electronic contributions to electrical conductivity in Cs-CsCl solutions. Closed points denote observed electronic contribution (Ref. 17), open points denote evaluation of Eq. 20 as described in text.

DOI: 10.1149/198109.0105PV

VAPOR PRESSURE MEASUREMENTS IN K-KBr MIXTURES : METHOD AND PRELIMINARY RESULTS

P. Kozoulia, J.P. Bros, M. Gaune-Escard

Laboratoire de Dynamique et Thermophysique des Fluides
Université de Provence - centre de St Jérôme
13397 Marseille cedex 4 - France.

ABSTRACT

In order to obtain thermodynamic information on mixtures constituted with alkali metals with their halides, we investigated the K-KBr system by vapor pressure measurements.

The method chosen uses the features of both the Rodebush-Dixon and ebullition methods. The apparatus, consistent with the experimental requirements of such a system, allows one to investigate a wide temperature and pressure range.

The determination of the vapor pressure of potassium between 719K and 1045K was a check on the operation of the apparatus.

Vapor pressure measurements above the K-KBr liquid bath between 1000 and 1070K yielded the activity of potassium at X_K=0.2 , X_K=0.5 and X_K=0.8 .

INTRODUCTION

Between liquid alloys and molten salt mixtures, there is an intermediate class of liquids - metal-molten salt systems - which has never been subject to intensive research from both theoretical and practical points of views. These mixtures which show a continuous transition from metallic to non-metallic character and a liquid miscibility gap are of special interest ; therefore, a good knowledge of their thermodynamic properties could afford a better understanding of these phenomena.

We therefore decided to study the solutions of alkali metals in their halides for which some physico-chemical determinations are available (1-4).

The present work deals with the K-KBr system and shows on one hand the feasibility of thermodynamic measurements for such a mixture and provides on the other hand results on the activity of potassium in some K-KBr mixtures.

Many practical reasons explain the few measurements available for such systems. These are :

- the chemical reactivity of these mixtures
- the high vapor pressure of the metal
- the existence of a single-phase liquid only at very high temperature

- the occurence of a wide miscibility gap that does not promote the estimation of the thermodynamic functions.

We choose to measure the vapor pressure of potassium above a K-KBr bath in order to deduce the activities and the Gibbs free energies.

EXPERIMENTAL

The vapor pressure of one component A in equilibrium above a liquid bath AB, when compared with that of the pure component A at the same temperature, yields the activity a_A and the chemical potential μ_A of this component in the mixture.

Principle of measurement

For the present work, the following hypothesis was adopted : the difference between the vapor pressures of the two components is large enough to assume that the vapor above the liquid is only constituted with the more volatile component.

When the total pressure above a liquid bath maintained at constant temperature is decreased, ebullition takes place when pressure becomes equal to the vapor pressure of the liquid ; the total vapor pressure should therefore be measured at the same time as the ebullition process is detected.

This determination can be done :

(i) either by recording the pressure variation against time arising from a microleak in the gas circuit above the liquid bath : when the pressure becomes equal to the vapor pressure, the rate of the pressure variation changes suddenly (point a on the curve figure 1): this is Rodebush-Dixon method (5).

(ii) or by recording the temperature T of the liquid during a variation linear against time of the pressure above the bath.

The ebullition, endothermal process, creates a cooling of the liquid, therefore a break on the curve T = f(t) (point b on the curve, figure 1).

In practice, it is much more interesting to couple these two methods in order to survey a wide investigation range.

The diagram of figure 1 shows the curves obtained with the two detection systems (points a' and b').

Realization

Figure 2 makes it easier to understand the principle of this method and of the working of the apparatus.

The experimental set-up consists of :

- the experimental cell (C) containing the mixture
- a vertical tubular furnace (F) with temperature regulation
- a primary and diffusion pumping group (V)
- a neutral gas tank (G)
- a system for measuring and recording against time the cell temperature (T) and the gas pressure (P)
- a network of pipes with gauges, valves, manometers, connections... :

Each part of the assembly can be insulated and an adjustable micro-leak valve (L) allows one to vary the pressure.

This apparatus, its construction and its setting as well as the several types of experimental cells tested were already described in detail (6).

Only the cell used for the K-KBr mixture will be described here with the experimental care necessary to obtain reliable measurements.

Experimental cell (figure 3)

The part containing the liquid mixture consists of a hollow cylinder 36mm diameter and 107mm high topped by a cylindrical pipe which connects the cell to the rest of apparatus. This connection is made owing to two isolation valves located in (5) and (6).

In the upper end of the pipe, there is a gastight outlet for the protection tube of the temperature thermocouple.

This location of the thermocouple is most suitable :
- the position of the thermocouple junction is height-adjustable, which is necessary for different fillings of the cell.
- a motion to and fro of the protection tube of the thermocouple permits stirring the liquid and therefore an homogenization (this is essential when the liquid mixture exhibits a demixing phenomenon)
- the protection tube of the thermocouple, centered in the connection tube, limits its section which results in a decrease of metallic vapor losses : the concentration of the liquid bath remains therefore quasi-constant.

Experimental care

A large set of trials on many pure substances and mixtures (Cd, Cd-Ga, K, KBr) made it clear that :
- much attention should be paid to the construction of this cell; the metallic weldings and the junction should be gas-tight at every temperature. The pipes must be very *clean* and the welding burrs removed.
- before each experiment, the whole assembly must be perfectly evacuated.

For the investigation of the K-KBr mixture, in the whole concentration and temperature range, a refractory stainless steel type NS 22S was found suitable for the construction of the cells.

It is obvious that the cell must be an isothermal system : accordingly, it is located in the uniform temperature zone of a furnace (200mm high) and surrounded with a refractory felt in order to lessen the convection losses.

Auxiliary equipment

Pressure is measured continuously by means of a piezo-electric detector†, the sensing element of which is a cap of pure single-crystal silicon. The experimental range is between 0 and 1100 mbars. The electric signal of the detector is recorded continuously on a two

†Schlumberger, type CZ 1080

channel potentiometric recorder†.

The neutral gas used is purified argon.

The experimental temperature of the bath is measured by a platinum/platinum-rhodium thermocouple and recorded on the second channel of the previous recorder†.

The furnace is regulated with an electronic system†† driven by a Pt/Pt-Rh 10% thermocouple.

The sensitivities of the systems for pressure and temperature measurements allows one to detect variations of the order of 5.10^{-2} Torr and 0.5 K, respectively.

The sample mass is known with a precision of 10^{-2}g.

Weighings and filling of the cell are made within a glove-box filled with purified argon.

EXPERIMENTAL RESULTS

The relation $a_K = \frac{P_K}{P^o_K}$ shows obviously that the determination of activity at temperature T implies the measurements of the vapor pressures of pure potassium and of potassium above a liquid bath of X_K composition.

Vapor pressure of pure potassium

Measurements were carried out between 719K and 1045K. All the results obtained are reported in figure 4 as the logarithm of the vapor pressure of potassium against reciprocal temperature.

The A and B coefficients of the equation :

$$\log_{10} P = A + B/T \quad (P : \text{torr} , \quad T : \text{Kelvin})$$

were fitted by a least-square method.

From 53 experimental values, the values 7.1510 and 4401.0487 were obtained for A and B respectively.

The mean relative uncertainty of our pressure is about 1.5%.

Our results were compared with those given by Hultgren (7) in his critical compilation. The agreement was found very satisfactory in our experimental temperature range.

From the previous equation, we calculated the enthalpy of vaporization of potassium at 952K (normal ebullition temperature); the value obtained 20.1 kcal.mol^{-1} is to be compared with the mean value 21.33 kcal.mol^{-1} obtained from the many previous works and also with that from Kelley's complation (8) 19.0 kcal.mol^{-1}.

The reliability of the vapor pressures measured for pure potassium points out the validity of the method. These experimental values will be used in the following to evaluate the activity of potassium in K-KBr mixtures.

---

† Sefram, type Servorac BPD

†† Setaram, type PRT 3000

Vapor pressure of potassium above the K-KBr mixture

Figure 5 recalls the equilibrium lines of the phase diagram proposed by Bredig (1). The K-KBr system exhibits a wide miscibility gap in the liquid state and the activity of potassium above a single-phase liquid bath can only be measured in the whole concentration range above 1000K.

All our experiments were therefore carried out between 1000K and 1070K.

We investigated the mixtures with the respective compositions :

$X_K = 0.2$, $X_K = 0.5$, $X_K = 0.8$

The results are reported in figures 6 , 7 and 8. On each diagram $\log_{10} P = f(1/T)$, the straight line corresponds to the equation given previously with coefficients obtained from least-square analysis of data.

The results obtained for the vapor pressure of potassium, pure and above a liquid mixture, were corrected for taking into account the dissociation of K vapor into mono and diatomic molecules (9):

$$2K \rightleftharpoons K_2$$

This method of correction is similar to that used (3) for the similar system Cs-CsCl.

The activities of potassium were then calculated at several temperatures : 1005K, 1035K, 1044K and 1065K and are plotted against the potassium mole fraction X_K in figure 9.

CONCLUSION

In spite of the experimental difficulties encountered in the investigation of metal-molten salt systems and particularly of alkali metal-halide mixtures, the determination of the metal vapor pressure at many temperatures and concentrations seems to be a good approach for determining their thermodynamic properties.

The experimental method chosen was first checked by measuring the vapor pressure of potassium at many temperatures. The activity of potassium was then measured, between 1000K and 1070K, in the mixtures $X_K = 0.2$, $X_K = 0.5$ and $X_K = 0.8$. The departure from ideality is large and the trend of the activity variation against temperature is a precursory sign of the demixing phenomenon.

REFERENCES

(1) M.A. Bredig in *Molten Salt Chemistry*, M. Blander ed., Wiley Interscience, New-York (1964)
(2) N.H. Nachtrieb in *Advances in Chemical Physics*, vol.31, Ed. I. Prigogine (1975)
(3) R.L. McGraw, N.H. Nachtrieb, J. Phys. Chem. (in press)
(4) J.F. Jal, P. Chieux, J. Dupuy, J. Physique 41, 657 (1980)
(5) W.H. Rodebush, A.L. Dixon, Phys. Rev. 26, 851 (1925)
(6) P. Kozoulia, Thèse Doctorat Spécialité, Marseille (1980)

(7) R. Hultgren, P.D. Desai, D.T. Hawkins, M. Gleiser, K.K. Kelley and D.D. Wagman in *Selected values of the thermodynamic properties of the elements*, Am. Soc. Met., Metals Park, Ohio 44073 (1973)
(8) K.K. Kelley, Bull. U.S. Bur. Mines, 383, 985 (1935)
(9) R.J. Thorn, G.H. Winslow, J. Phys. Chem. 65, 1297 (1961)

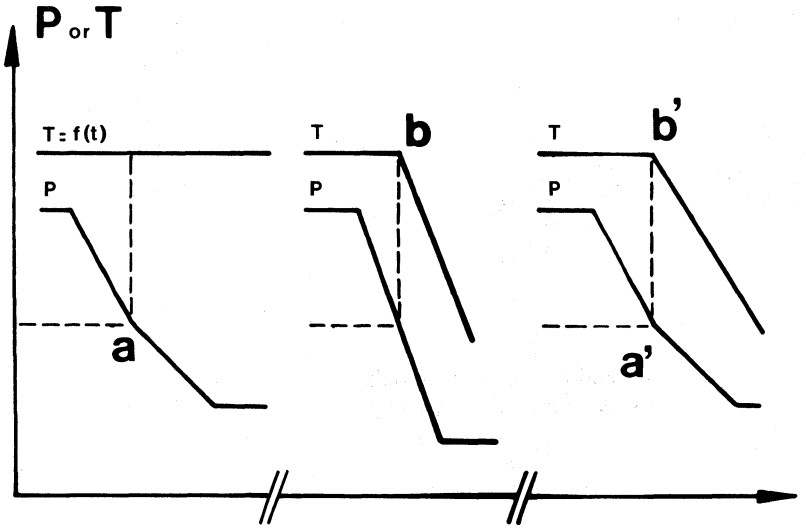

Fig. 1 - Principle diagram of the method.

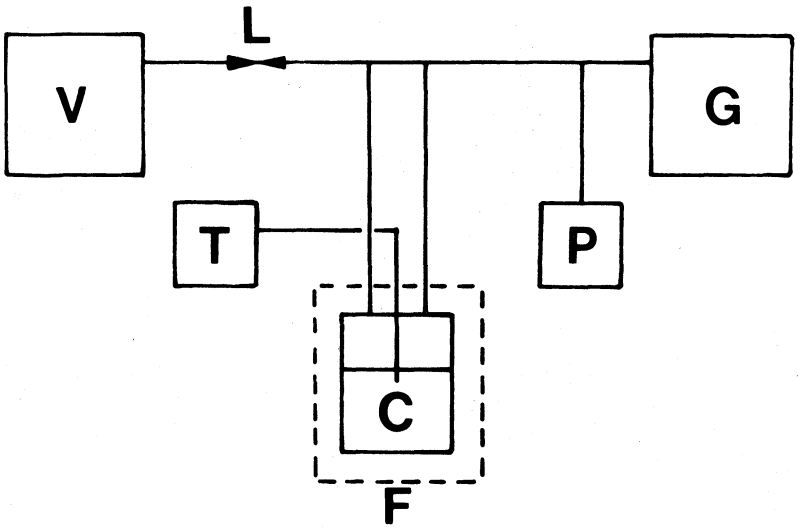

Fig. 2 - Diagram of apparatus

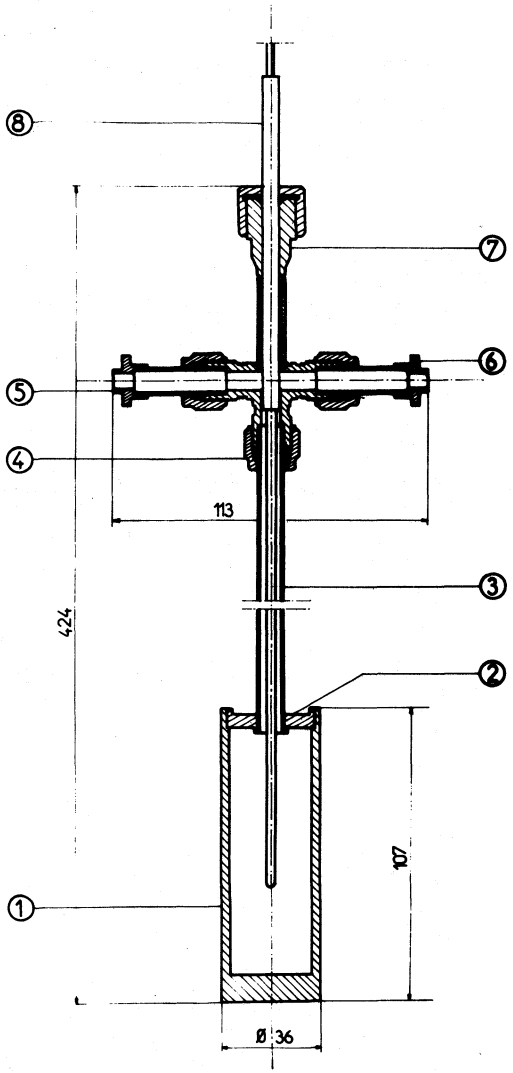

1 : cell
2 : lid
3 : connextion pipe
4 : gastight junction
7 : " "
5 : isolation valve
6 : " "
8 : protection tube of thermocouple

Fig.3 - Experimental cell.

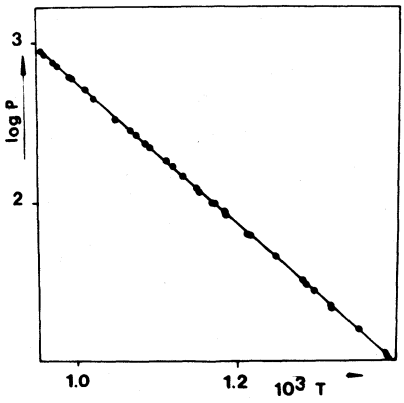

Fig.4 - $\log_{10}P = f(\frac{10^3}{T})$ for pure potassium

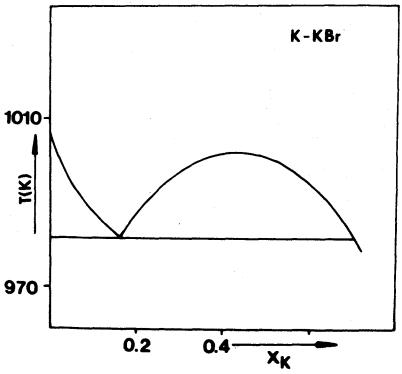

Fig.5 - Equilibrium phase diagram.

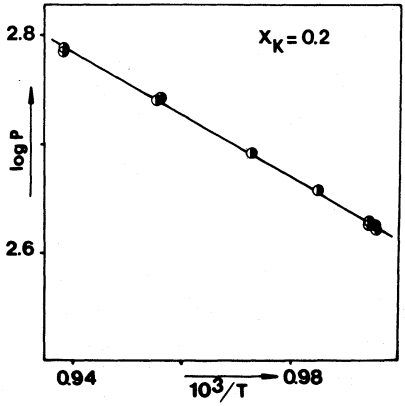

Fig.6 - $\log_{10}P = f(\frac{10^3}{T})$

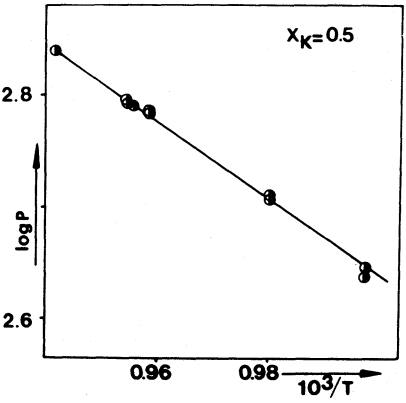

Fig.7 - $\log_{10}P = f(\frac{10^3}{T})$

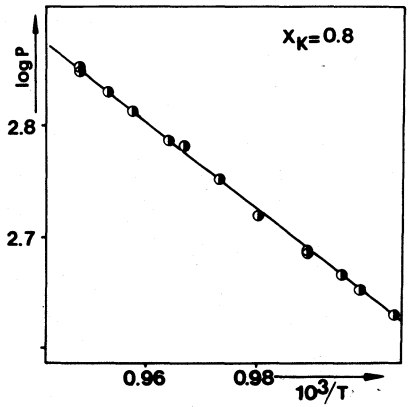

Fig.8 - $\log_{10} P = f(\frac{10^3}{T})$

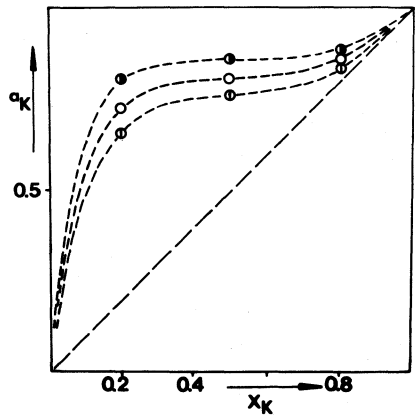

Fig.9 - $a_K = f(X_K)$
●(1005K) ○(1035K) ◐(1065K)

DOI: 10.1149/198109.0115PV

STRUCTURAL ORDER IN METALLIC K-KCl SOLUTIONS

J.F. Jal*, P. Chieux+, J. Dupuy

*Département de Physique des Matériaux, Université Claude Bernard, Lyon Villeurbanne, France

+I.L.L. Grenoble, France

ABSTRACT

The effect of the addition of KCl on the structure of molten potassium at metallic concentrations has been investigated by neutron diffraction. A significant small angle scattering is observed which, after taking into account a concentration dependent contrast effect related to the non ideal behavior of the solutions, is attributed to concentration fluctuations. The ionic KCl distance is detected even at quite low KCl content. An analysis in partial structure factors at the concentration $x_K = 0.80$, shows again the combination of potassium like and KCl like structures. The possible appearance of a short range order peak raises the question of ionic clusters at those concentrations.

The solutions of the alkali metal-molten salt solutions are known (1) for their considerable change in electrical transport properties versus addition of metal. They offer an interesting example of non-metal to metal transition in disordered systems. A detailed study (2) of the concentration fluctuations near the liquid-liquid miscibility gap in the K-KBr system has already been made by small angle neutron scattering (SANS). It provided a quantitative description of the temperature and concentration dependence of the concentration fluctuations while going away from the liquid-liquid critical point (see fig. 1). The critical behavior of these fluctuations is well described by an Ising tridimensional model. The shape of the iso-ξ lines (ξ is the correlation length for the fluctuations) as well as the liquid-liquid miscibility line is in agreement with this model. There are indications that when a liquid-liquid phase separation occurs in the near vicinity of a non-metal to metal transition a special critical behavior might be obtained, as in the metal-ammonia systems (3). In the K-KBr case however, an Ising tridimensional critical behavior is observed as in most systems with liquid-liquid phase separation. This is coherent with the fact that the miscibility gap occurs almost entirely within the metallic concentrations.

Of course it would also be very interesting to know the nature of the short range order in these systems and how it interacts with the

electronic properties. We shall present here a first attempt to elucidate the structure of metallic solutions of potassium in potassium chloride (conductivity greater than $10^3\ \Omega^{-1}cm^{-1}$) where the fluctuations of concentration are definitively small. The gross features of the addition of small amounts of potassium chloride ($0 < x_{KCl} \leq 0.25$) to pure potassium metal at a temperature of about 800 °C will first be presented. We will then focus on a more detailed description of the microscopic order for a particular concentration (0.2 mole fraction of KCl).

The experiments were performed on the D4 machine at the I.L.L. (Grenoble) and the data analyzed as previously (4). The isotopic substitution method has been applied on the chlorine atom at $x_{KCl} = 0.2$.

I. Total Structure Factors as a Function of the Addition of KCl

The structure factors for five solutions of potassium in potassium chloride ($0.95 > x_K > 0.75$) are displayed in Figure 2. Let us comment first on the significant small angle scattering signal observed at all concentrations (although it is weak at $x_K = 0.95$). A high value of the thermodynamic limit S(0) accompanied by a SANS is not uncommon in liquid metallic alloys (5). It has been attributed to concentration fluctuations or to clustering effects. Although the D4 machine is not appropriate for SANS measurements the size of the corresponding fluctuations may be evaluated here to a few Angstroms. It is hard to give a definite physical picture of such short fluctuations but the possible influence of the liquid-liquid phase separation even so far away for the critical point cannot be ruled out. We would like however to comment on the small SANS observed at $x_K = 0.95$ as well as for the Cl^{37} isotopic run at $x_K = 0.80$ (see figure 4).

The anomalies in the thermodynamic limit S(0) of the structure factor of binary systems depend essentially on two terms. Firstly, they depend on the derivative of the chemical potential versus concentration, i.e. on the value of the concentration-concentration partial structure factor

$$S_{cc}(0) = N\, k_B\, T \,/\, \left(\frac{\partial^2 G}{\partial x_2^2}\right)_{T,P,N}$$

Secondly, they depend on a contrast coefficient C, which involves the difference of the neutron scattering length b_i per unit volume between the two components

$$C = \frac{1}{\sum_i x_i b_i^2} \left| \frac{\bar{V}_1 b_2 - \bar{V}_2 b_1}{x_1 \bar{V}_1 + x_2 \bar{V}_2} \right|^2 \qquad (1)$$

where x_i are the mole fractions and $\bar{V}_i$ the partial molar volumes of the two components, K and KCl in our case.

We write

$$S(0) = A + C\, S_{cc}(0) \qquad (2)$$

The A term depends on the isothermal compressibility of the system and is small. The $S_{cc}(0)$ values were obtained with precision as a function of concentration and temperature around the liquid-liquid critical point of K - KBr from SANS measurements. They are developed in reduced coordinates for the other systems of the series. On the K rich side of the critical point we expect, as displayed in Fig. 3 and in agreement with vapor pressure measurements (6), a rapidly and smoothly decreasing signal. If we modulate this signal by the contrast coefficient C computed on a regular solution basis (curve R on fig.3a) we obtain a maximum of S(0) at $x_K = 0.95$, in contradiction with the low SANS signal observed at this concentration. However, on the basis of preliminary density measurements (7) a positive excess volume is observed in both K in KCl and K in KBr systems at metal-rich concentrations (see figure 3b). The maximum in the contrast C is therefore shifted to about $x_K = 0.85$ (curve ΔV_{ex} on figure 3b). The small value of S(0) observed for $x_K = 0.8$ with the isotope ^{37}Cl (see Figure 4) is also explained by a small value for the contrast coefficient C, but due this time to the modification of the neutron scattering lengths. If one solves the equation (2) for the three isotopic substitution measurements performed at the concentration $x_K = 0.8$, one obtains $S_{cc}(0) \simeq 0.35$ which is different from the ideal behavior $S_{cc}(0)=x_1x_2$. And the partial molar volumes obtained (see equation 1,2) for the components are also different from the pure ones.

$$\bar{V}_K = 75\ cm^3mole^{-1} \pm 10 \qquad (V_K^\circ = 58.2\ cm^3mole^{-1})$$

$$\bar{V}_{KCl} = 20\ cm^3mole^{-1} \pm 5 \qquad (\bar{V}_{KCl}^\circ = 49.4\ cm^3mole^{-1})$$

It confirms the positive excess volume on the metal rich side of this system and the ΔV_{ex} curve of Figure 3.

If one considers now the effect of the addition of KCl to the structure factor of the metal, one sees at the same time the decrease of the potassium peak and the appearance at the position $Q_N = 2.33\ Å^{-1}$ of the main characteristic peak of the salt structure (Q_N refers to the main S_{NN} peak in pure molten KCl (4)). This is confirmed by the total distribution functions displayed in figure 5 as a function of concentration, where two characteristic distances occur. Although the experimental accuracy of the S(Q)'S does not allow very accurate Fourier transforms, one believes the results accurate enough to describe unambiguously the concentration trends. At 3.1 Å the ionic KCl distance is quite well detected at $x_K = 0.90$ and possibly as a shoulder already at $x_K = 0.95$. It is noticeable that there is no peak position shift with concentration. The intensity of the 4.5 Å peak characteristic of the K - K distance in the metal, decreases with dilution. The peak split observed at $x_K = 0.90$ has no physical meaning; it is produced by the poor accuracy of the corresponding S(Q). To

summarize, the addition of KCl to pure molten potassium is connected to the appearance of typically salt-like features in the total structure factor. Some kind of ionic cluster should therefore be postulated even at rather low KCl content.

II. Partial Structure Factors at the Concentration $x_K = 0.80$

In order to throw some light on the onset of ionicity in these metallic systems a full development in partial structure factors is necessary. This has been attempted for the concentration $x_K = 0.80$ by isotopic substitution of the chlorine atom. Considering the dilution effect, the data analysis is difficult and the following should only be considered as preliminary results.

A first decomposition of the total structure factors $S_T(Q)$ in partials is made using the relation:

$$S_T(Q) = c_1 b_1^2 S_{11}(Q) + c_2 b_2^2 S_{22}(Q) + 2(c_1 c_2)^{1/2} b_1 b_2 S_{12}(Q) \qquad (3)$$

with $c_1 + c_2 = 1$ and 1, 2 referring to the potassium and chlorine atoms respectively. The results are presented in figure 6. One sees that the predominant effect is the peak observed at 0.7 - 0.8 $Å^{-1}$ corresponding to a distance of about 9 - 10 Å in real space, a little larger than the second neighbor K - K distances (of Figure 5). This effect occurs in both the K - K and the Cl - Cl partials. One must however emphasize that difficulties typical in high temperature experiments such as the aging of the vanadium furnace make the analysis of this rather poor scattering sample quite inaccurate at low momentum transfer and one would like to confirm this finding with better control of the sample environment. The peak near 1.6 $Å^{-1}$ in S_{KK} is as in the metal and corresponds to the packing of the potassium atoms. The large peak in S_{KCl} is located at the same position $Q \simeq 2.33$ $Å^{-1}$ as in the pure KCl salt. Of course, at very low momentum transfer the data are affected by small angle scattering.

Another display of the data can be made by using the Bhatia and Thornton formalism (8). We shall assentially discuss here the S_{NN} partial structure factor and its Fourier Transform $g_{NN}(R)$ which gives the local deviation from the average density. The computation has been made on the basis of the two components K and KCl. In Figure 7 we compare the $g_{NN}(R)$ obtained in the present case ($x_K = 0.80$) at 830 °C to the pure KCl case (we note that $S_{NN}(Q)$ for pure KCl is practically identical to $S_{K^{37}Cl}(Q)$, the total structure factor obtained with ^{37}Cl). We have also displayed the pure potassium metal at 130 °C. One sees that as far as the atomic distributions are concerned, the $x_K = 0.80$ concentration is essentially a combination of the metal and the salt, the KCl interionic distance at 3.1 Å being in first approximation not perturbed. The closest approach distance of K and Cl is however significantly shorter in pure KCl. These are the most accurate partials one may obtain for the time being on this

system since they are extracted from the total structure factors without much loss in accuracy. The S_{CC} and S_{NC} partials will be presented later on.

To conclude, one has several rather contradictory observations to reconcile. Owing to the small angle scattering observation the system has a tendency to fluctuate between ionic rich and metal rich regions. This is confirmed by the $S_{NN}(Q)$ and $g_{NN}(R)$ partials which in a first approximation describe the local order as a combination of pure KCl and potassium. This argues in favor of a non statistical distribution of the chlorine atoms. On the other hand, the still questionable observation of the ordering of the chlorines at distances of 9 - 10 Å, slightly more than twice the spacing of the potassium atoms and its correlated effect due to holes in the potassium distribution, argues in favor of an ordered structure (5,9), where the chlorines keep away from each other. It is still unclear how this ordered structure could coexist with the tendency to segregation. And of course one would like more quantitative information on the local order to look for the possibility of ionic clusters. More has to be done in order to settle these questions.

REFERENCES

(1) see M.A. BREDIG in "Molten salt chemistry", Ed. Blander, M., Wiley, N.Y. (1964)

(2) J.F. JAL, P. CHIEUX, J. DUPUY, J. Physique 41, 657-666 (1980)

(3) P. CHIEUX, P. DAMAY, J. DUPUY, J.F. JAL, J. Phys. Chem. 84 (10) 1211-1215 (1980)

(4) J. DERRIEN, J. DUPUY, J. Physique 36, 191 (1975)
S. EISENBERG, J.F. JAL, W. KNOLL, P. CHIEUX, J. DUPUY, to be published

(5) P. CHIEUX, H. RUPPERSBERG, J. Physique, Colloque C8, 41, C8-145 (1980)

(6) M. GAUNE-ESCARD, J.P. BROS, to be published

(7) J.F. JAL, J. DUPUY, P. CHIEUX, J. Physique, Colloque C8, 41, C8-257 (1980)

(8) A.B. BHATIA, D.E. THORNTON, PhYs. Rev. B2, 3004 (1970)

(9) J. BLETRY, Z. Naturforsch. 33a, 327 (1978)

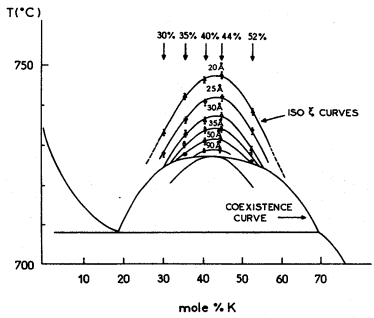

Figure 1. The temperature and concentration dependence of the correlation length ξ for concentration fluctuations in the K-KBr system.

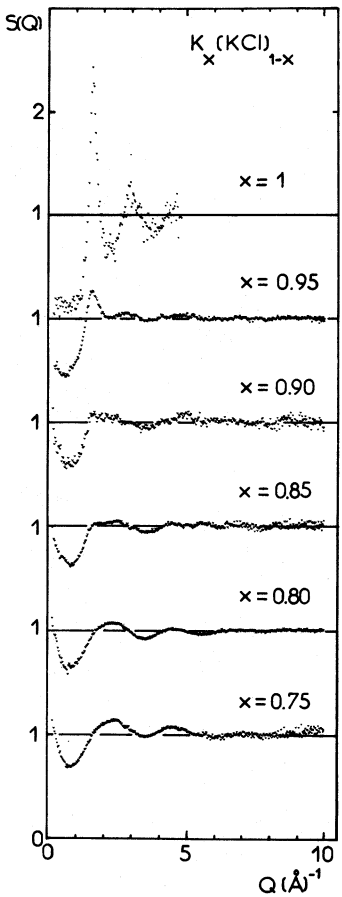

Figure 2. Total structure factors of five solutions of KCl in K. Temperatures 867°, 830°, 800°, 725°, 780° from $x_K = 0.75$ to $x_K = 0.95$. The potassium structure factor is at 130° C.

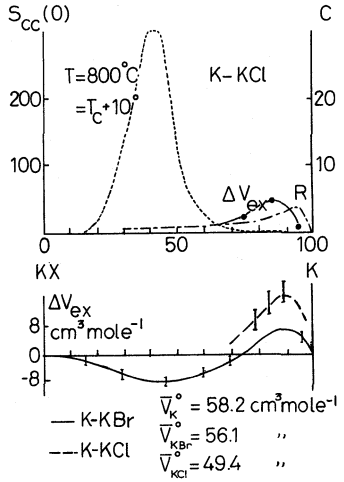

Figure 3. a) $S_{cc}(0)$ and the contrast coefficient C as a function of concentration. The contrast is computed on a regular solution basis (curve R) or on the basis of excess volume data (curve ΔV_{ex}). b) Excess volume as a function of concentration.

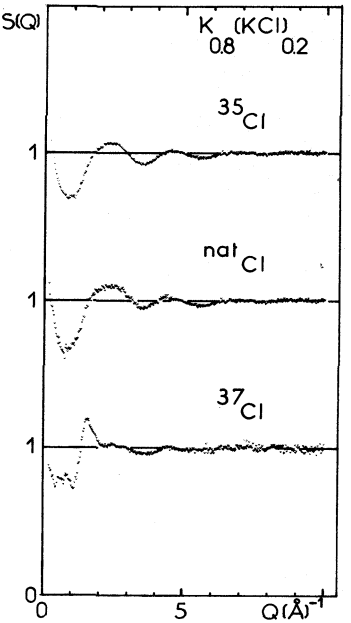

Figure 4. The structure factors of the three isotopic runs for $K_{0.8}$ $(KCl)_{0.20}$.

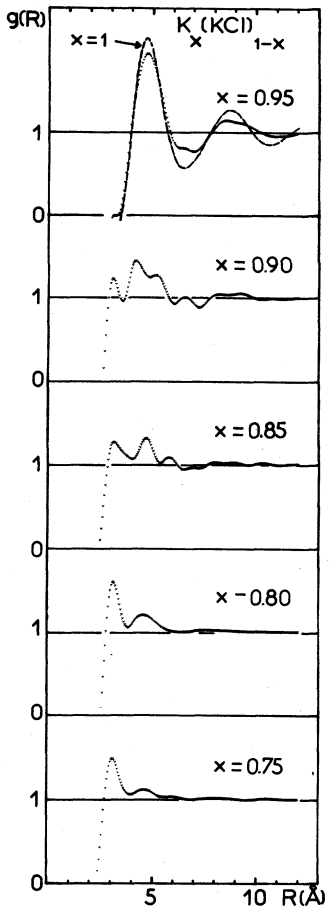

Figure 5. The pair distribution functions as a function of Potassium chloride in Potassium.

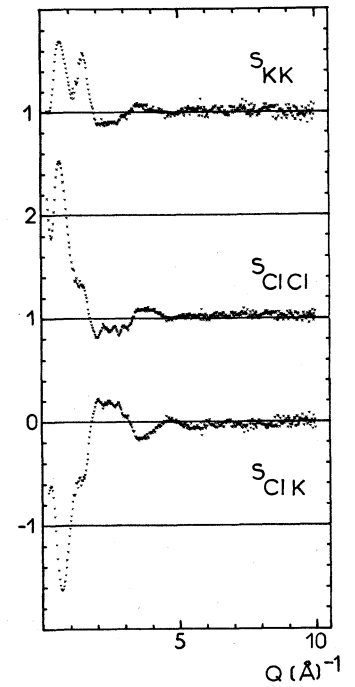

Figure 6. The S_{ij} partial structure factors for $K_{0.8}(KCL)_{0.20}$.

Figure 7. Comparison of the density-density pair distribution function $g_{NN}(R)$ at the concentration x_K = 0.80. and the $g_{NN}(R)$ of pure KCl as well as the g(R) of Potassium.

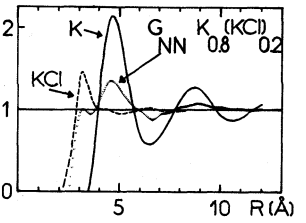

DOI: 10.1149/198109.0123PV

INTERNAL MOBILITIES IN ADDITIVE BINARY MOLTEN HALIDE AND NITRATE MIXTURES. A SURVEY.

A. Klemm
Max-Planck-Institut für Chemie (Otto-Hahn-Institut)
Saarstr. 23, D-6500 Mainz, Germany

Abstract

A rather complete survey is given over the presently known internal mobility isotherms of binary molten salt systems. The methods, by which these have been measured, are indicated and discussed.

A mixture of two salts with one ion in common is called an additive binary mixture. We indicate the two coions with the subscripts 1 and 2, and the counterion with the subscript 3.

If an external electric field E is applied, the ions are transported with the velocities v_1-v_3 and v_2-v_3 relative to each other. The internal mobilities b_{13} and b_{23} are defined as

$$b_{13} = (v_1-v_3)/E, \quad b_{23} = (v_2-v_3)/E.$$

In order to evaluate these and the molar concentrations c_1 and c_2, it is necessary to measure four quantities:

(i) the molar fraction

$$x_1 = c_1/(c_1 + c_2),$$

(ii) the density

$$\rho = M_{13}\, c_1 + M_{23}\, c_2,$$

(iii) the specific conductance

$$\varkappa = F \left| z_1 c_1\, b_{13} + z_2 c_2 b_{23} \right|$$

and

(iiii) the ratio of the internal mobilities

$$\beta_{12} = b_{13}/b_{23}.$$

By means of these four relations, in which the molecular weights (M_{13} and M_{23}), the valencies of the coions (z_1 and z_2) and Faraday's constant (F) are known quantities, c_1, c_2, b_{13} and b_{23} can be evaluated if x_1, ρ, $\varkappa$ and β_{12} have been measured.

x_1 is usually determined in preparing the mixture from weighed quantities of the pure salts, and our knowledge about ρ and $\varkappa$ as functions of x_1 is extensive and has been collected by G.J. Janz and his coworkers in J.Phys.Chem. Ref.Data, Volumes 1 (No.3) 1972, 3 (No.1) 1974, 4 (No.4) 1975, 6 (No.2) 1977 and 8 (No.1) 1979. Far less is known about β_{12}.

The methods of determining β_{12} can be grouped into two classes (I and II):

I. Methods based on the localisation of ions

Fig.1 shows four devices for the localisation of ions in electromigration experiments. They will henceforth be characterized by the words disc, column, layer and boundary.

The disc method is identical with the method usually called Hittorf method. A flow through the disc due to an eventual pressure head between the electrode compartments would falsify the measured ratio of external mobilities but not the measured ratio β_{12}. Exchange of the coions through the disc due to diffusion would, however, affect the obtained value of β_{12}. Therefore the electrotransport experiment must be stopped before the difference in concentrations between the electrode compartments and thus the diffusional transport through the disc becomes substantial.

In the column method a gradient in concentration is built up along a column of grains of alumina by the combined action of electrotransport and diffusion. The experiment is stopped before the gradient reaches the lower end of the column, and thus interference of diffusion in the measurement of β_{12} is avoided even though the difference in concentrations between the electrode compartments may become large.

In the layer method the salt mixture is sucked into a horizontal layer of some porous material connecting the electrode compartments, and radioactive salt is added to a small area of the layer. The displacement of the three radioactive ions during electrotransport is observed by means of counters. This yields, even in the presence of a small flow along the layer due to a pressure head, the correct value of β_{12}. Diffusion is not disturbing in principle, though it broadens the peaks of radioactivity, which renders their localisation more difficult. The overall cross section of the melt must be uniform along the layer.

In the moving boundary method the position of the ions during the electrotransport is visually localized by observing differences in colour or refractivity. Mixtures from the same binary system but of different composition are layered one above the other in such a way that a selfsharpening boundery is maintained during the experiment, the displacement of which during the electrotransport is observed.

II. Methods based on EMF-measurements

These methods are based on a combination of two kinds of measurements:

(i) Determination of the change in chemical potential (μ_{13}) of the salt 13 on a change in its molar fraction (x_1), i.e. determination of $\partial\mu_{13}/\partial x_1$ for the mixture under study.

(ii) Determination of the change in the EMF (ϕ) of a cell containing a liquid junction between two mixtures of the same binary system, one of the two being the mixture under study, on a change of its molar fraction, i.e. determination of $\partial\phi/\partial x_1$.

$\partial\mu_{13}/\partial x_1$ can be determined in different ways, e.g. by calorimetry or EMF measurements on formation cells. This shall not be discussed here. There are cases where errors in these measurements enter strongly into the determination of the internal mobilities.

As for the determination of $\partial\phi/\partial x_1$, two types of cells (A and B) have been used, as symbolized in the following scheme:

Type	Electrode	Mixture I	Mixture II	Electrode
A	3	123	123	3
B	1	123	123	1

The substance indicated under "Electrode" may be a gas, in which case it has to contact inert electron conductors of the same kind on both sides of the cell. The composition of the mixture I is kept constant while that of mixture II is changed continously and $\partial\phi/\partial x_1$ is measured, where ϕ is the difference in electrical potential between the right and left electrode at zero current.

From the knowledge of $\partial \mu_{13}/\partial x_1$ and $\partial \phi/\partial x_1$ the function

$$f_1 = \pm z_1 z_3 F \frac{\partial \phi}{\partial x_1} \Big/ \frac{\partial \mu_{13}}{\partial x_1}$$

is determined, where the upper and lower signs refer to 3 being cationic or anionic, respectively. Depending on the type of cell used, β_{12} results from

$$\beta_{12} = 1 + \frac{1}{y_1} \frac{f_1}{1-f_1} \qquad \text{(Type A)}$$

or

$$\beta_{12} = 1 + \frac{1}{y_1} \frac{(f_1+1)}{1-(f_1+1)} \qquad \text{(Type B)},$$

where $y_1 = z_1 c_1/(z_1 c_1 + z_2 c_2)$,

Measurements with cells of type A have the convenience that $\beta_{12}-1$ and f_1 change sign simultaneously, if at all, on a change of temperature or composition, while in case of type B this happens with $\beta_{12}-1$ if f_1 passes the value minus unity. With both types of cells the accuracy of the measured value of β_{12} becomes lower, the smaller y_1 at constant absolute accuracy of f_1.

The general features of the mobility isotherms observed for additive binary molten salt mixtures are shown in the six diagrams of Fig.2. The heavy points in these diagrams correspond to the conductances of the pure salts. Therefore they are the most reliable points of the experimental curves. For easier comparison they are equally situated in the six diagrams of Fig.2. In the upper row we have the cases that b_{13} and b_{23} are independent of composition, and that they are less different in the mixtures than in the pure salts. The right diagram in the middle row shows the situation where the coion which, if concentrated, is more mobile than the other coion, is less mobile than the other coion if diluted, and in the right diagram of the bottom row the coion which is more mobile in its pure salt, is less mobile at all compositions of the mixtures. The latter two phenomena are sometimes called the Chemla effect. Behaviour as shown in the diagrams on the left side of the middle and bottom rows have also been observed.

Figures 3-10 give a rather complete survey of the systems studied thus far for their internal mobilities. It is seen that the systems are not numerous and that there are discrepancies in cases between the results obtained for the same system by different authors with different methods. The methods used are indicated by the words disc, column, layer,

boundary, emf A and emf B, as explained above. Error margins of the isotherms are not always indicated in the original literature and have been omitted throughout.

REFERENCES

Behl, W.K., J.Electrochem.Soc. 121, 959 (1974)

Behl, W.K. and J.J. Egan, J.Phys.Chem. 71, 1764 (1967)

Chemla, M., F. Lantelme and O.P. Mehta, Electrochim.Acta 14, 505 (1969)

Connan, R., J.Chim.Phys. 70, 888 (1973)

Duke, F.R. and B. Owens, J.Electrochem.Soc. 105, 476 (1958)

Forcheri, S. and V. Wagner, Z.Naturforsch. 22a, 1171 (1967)

Forcheri, S. and V. Wagner, Z.Naturforsch. 24a, 1779 (1969)

Kawamura, K., I. Okada and O. Odawara, Z.Naturforsch. 30a, 69 (1975)

Ketelaar, J.A.A. and J.C.Th. Kwak, Trans.Faraday Soc.65, 139 (1969)

Klemm, A. and E.U. Monse, Z.Naturforsch. 12a, 319 (1957)

Kwak, J.C.Th., J. Ketelaar, P. Maenout and A. Boerboom, J.Phys.Chem. 74, 3449 (1970)

Lantelme, F. and M. Chemla, Bull.Soc.Chim.France 1963, p. 2200

Lantelme, F. and M. Chemla, Electrochimica Acta 10, 663 (1965)

Moynihan, C.T. and R.W. Laity, J.Phys.Chem. 69, 3312 (1964)

Okada, I., R. Takagi and K. Kawamura, Z.Naturforsch. 34a, 498 (1979)

Okada, M. and K. Kawamura, Electrochim.Acta 15, 1 (1970)

Okada, M. and K. Kawamura, Electrochim.Acta 19, 777 (1974)

Poillerat, G. and J. Brenet, J.Chim.Physique 76, 67 (1979)

Richter, J. and E. Amkreuz, Z.Naturforsch. 27a, 280 (1972)

Richter, J., U. Gasseling and R. Conradt, Electrochim.Acta 23, 1165 (1978)

Yang, C., R. Takagi and I. Okada, Z.Naturforsch. 35a, (Nov. 1980)

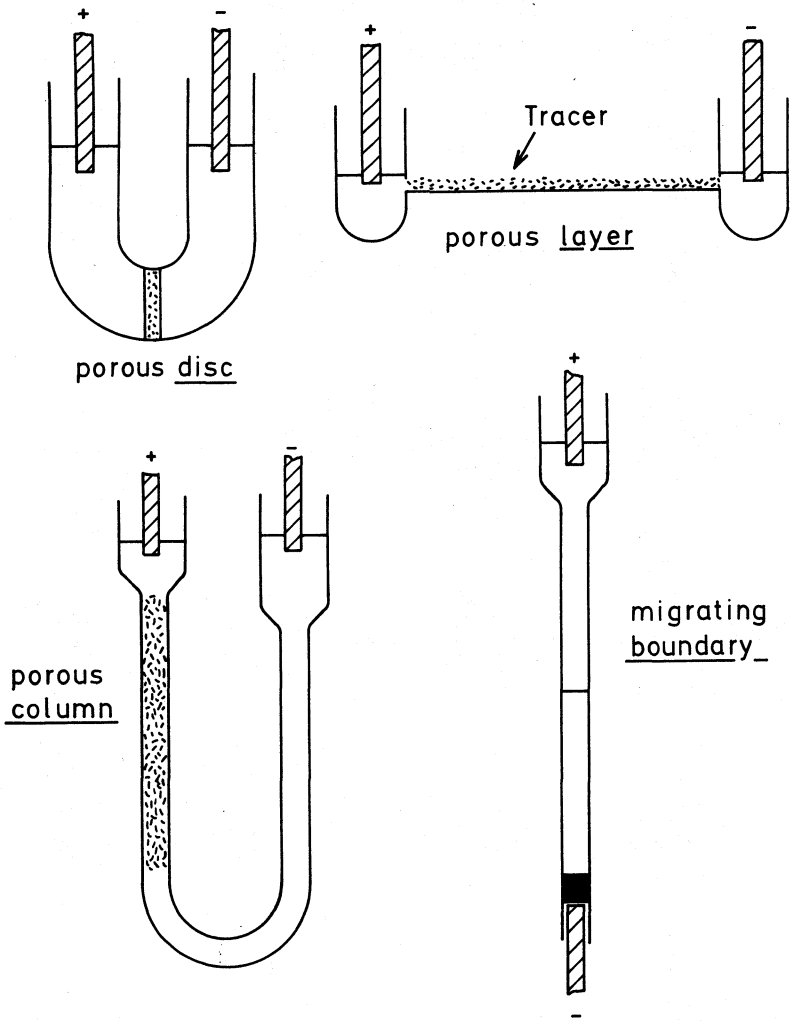
+
-
porous disc
+
-
Tracer
porous layer
+
-
porous column
+
migrating boundary
-

Figure 1

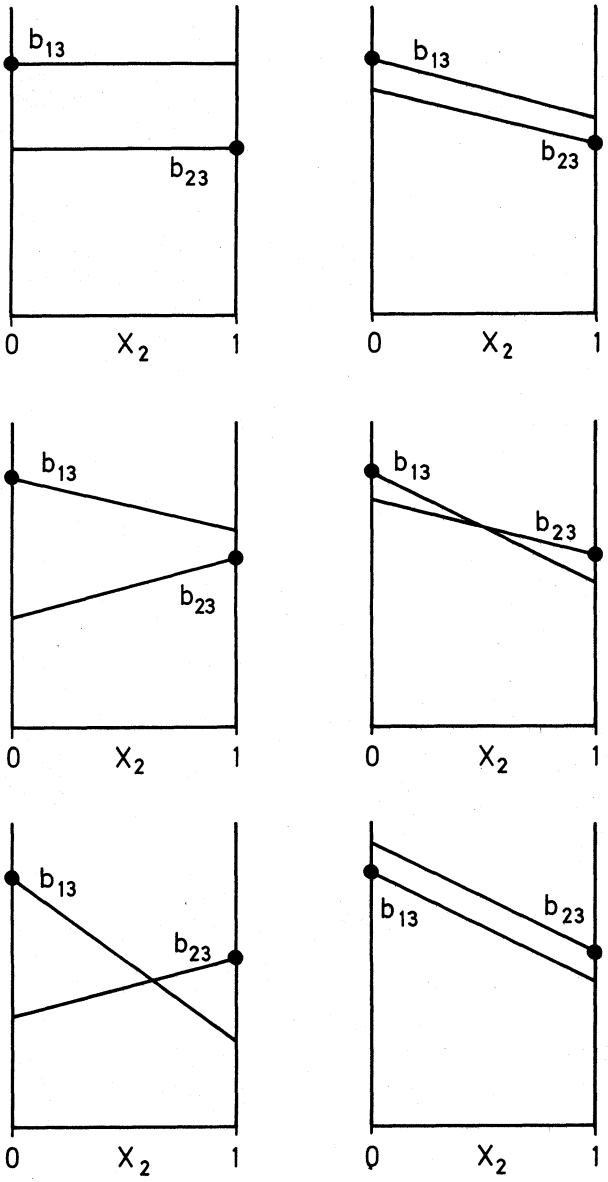
b13
b23
0
X2
1
b13
b23
0
X2
1
b13
b23
0
X2
1
b13
b23
0
X2
1
b13
b23
0
X2
1
b13
b23
0
X2
1

Figure 2

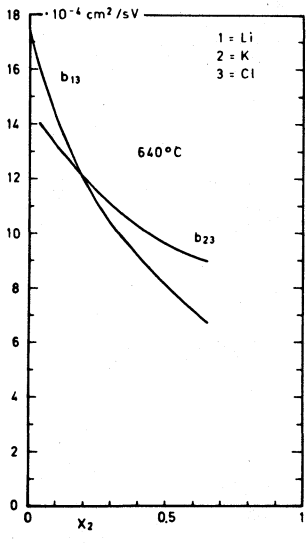

Moynihan, Laity 1964, disc

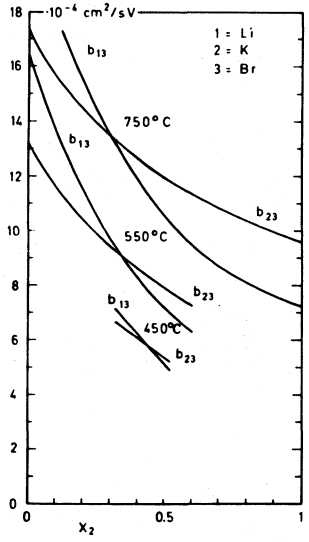

Chemla, Lantelme, Mehta 1969, disc

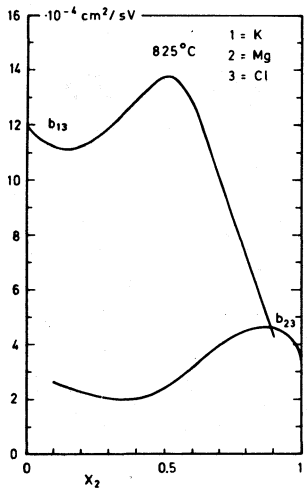

Behl, Egan 1967, emf A

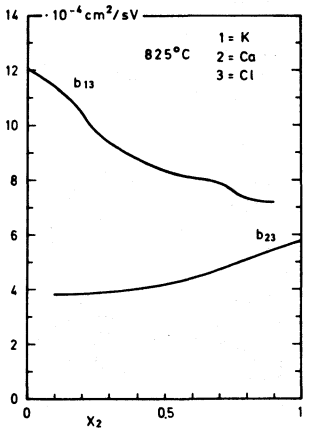

Behl, Egan 1967, emf A

Figure 3

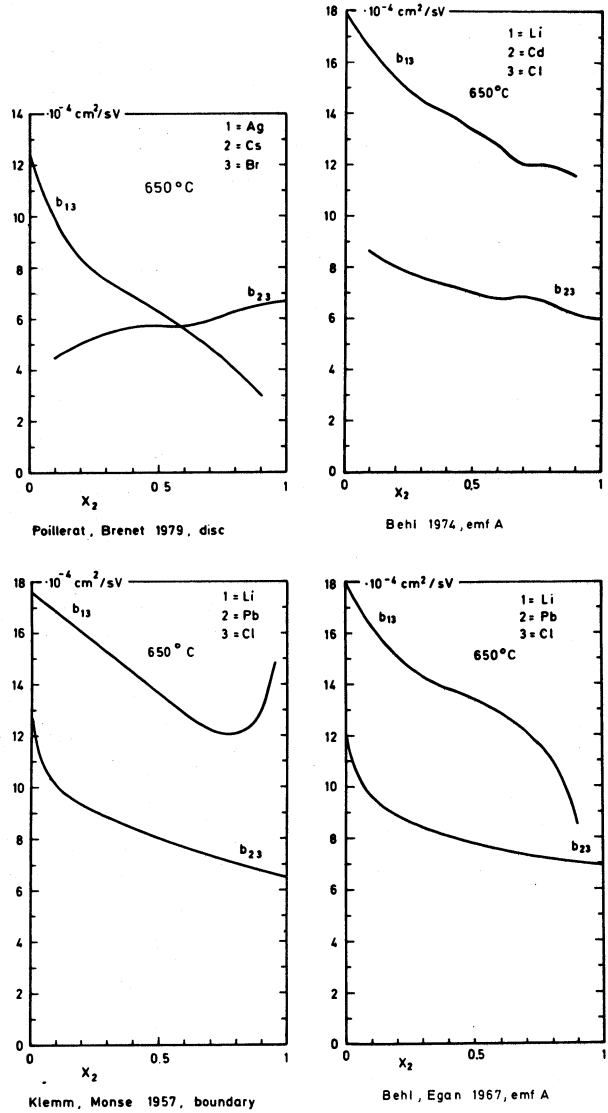
·10⁻⁴ cm²/sV
1 = Ag
2 = Cs
3 = Br
650 °C
b13
b23
X2
Poillerat, Brenet 1979, disc
·10⁻⁴ cm²/sV
1 = Li
2 = Cd
3 = Cl
650°C
b13
b23
X2
Behl 1974, emf A
·10⁻⁴ cm²/sV
1 = Li
2 = Pb
3 = Cl
650 ° C
b13
b23
X2
Klemm, Monse 1957, boundary
·10⁻⁴ cm²/sV
1 = Li
2 = Pb
3 = Cl
650°C
b13
b23
X2
Behl, Egan 1967, emf A

Figure 4

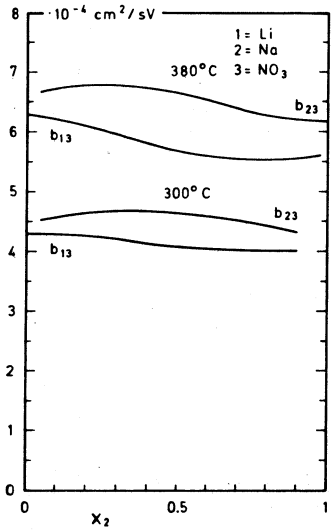

Yang, Takagi, Okada 1980, column

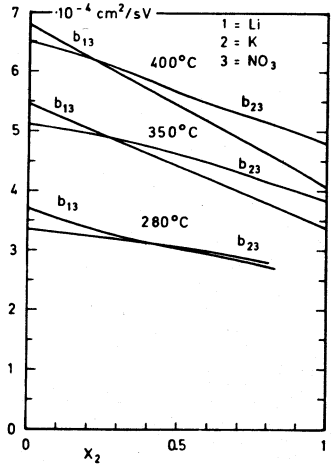

Lantelme, Chemla 1965, disc

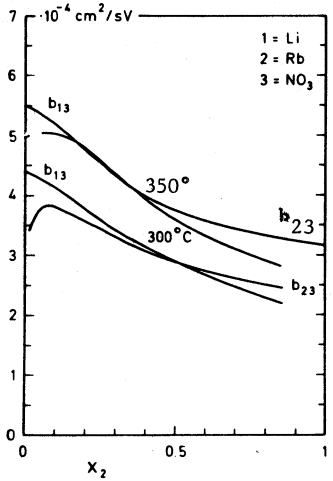

Okada, Takagi, Kawamura 1979, column

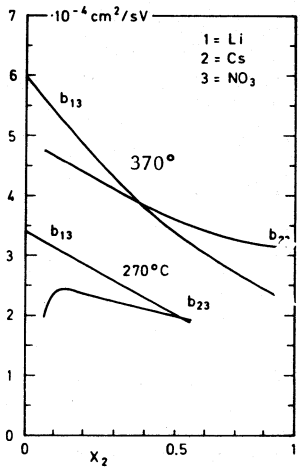

Okada, Takagi, Kawamura 1979, column

Figure 5

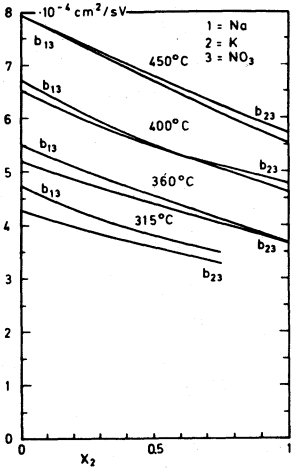

Lantelme, Chemla 1963, disc

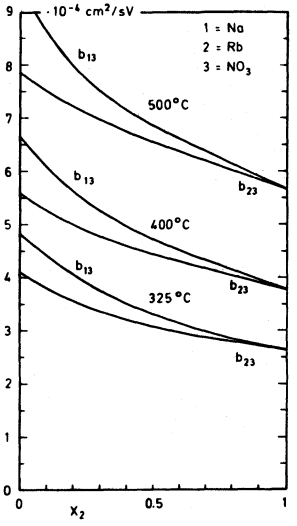

Forcheri, Wagner 1969, layer

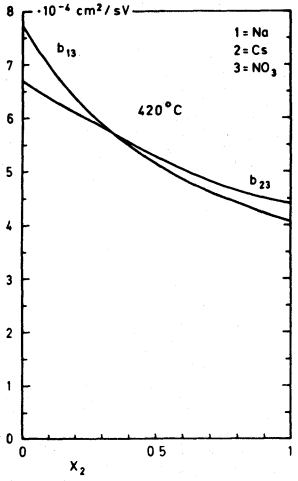

Ketelaar, Kwak 1969, layer

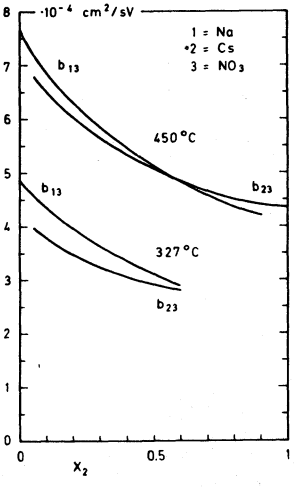

Yang, Takagi, Okada 1980, column

Figure 6

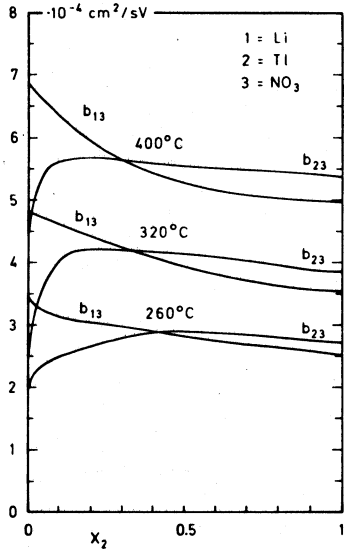

Kawamura, Okada, Odawara 1975, column

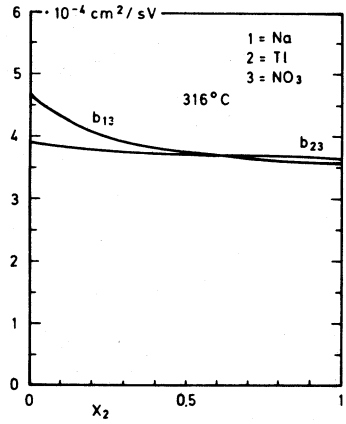

Forcheri, Wagner 1967, layer

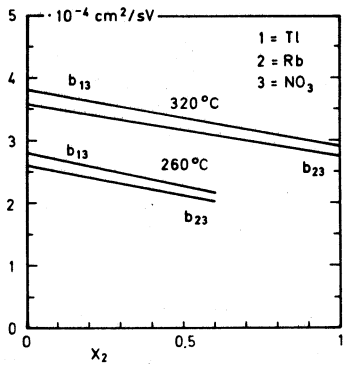

Kawamura, Okada, Odawara 1975, column

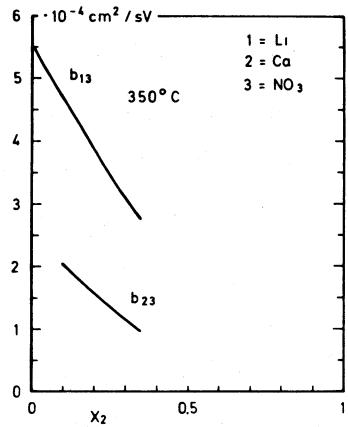

Kwak, Ketelaar et al 1970, layer

Figure 7

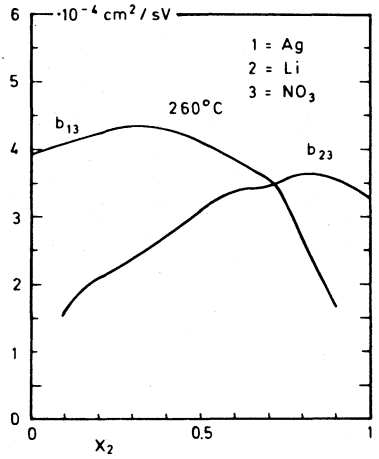

Richter, Amkreuz 1972, emf B

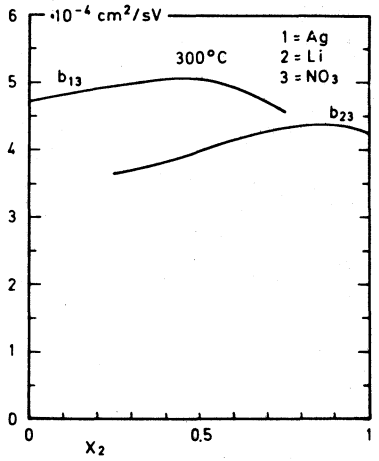

Connan 1973, disc

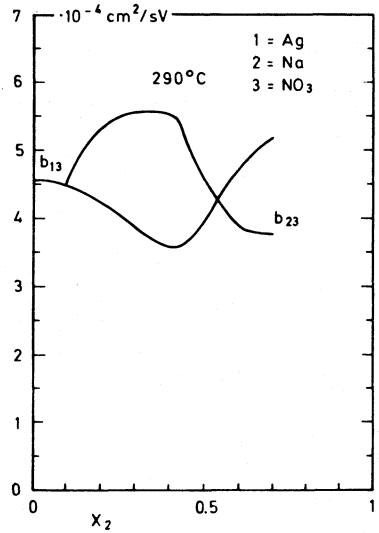

Richter, Amkreuz 1972, emf B

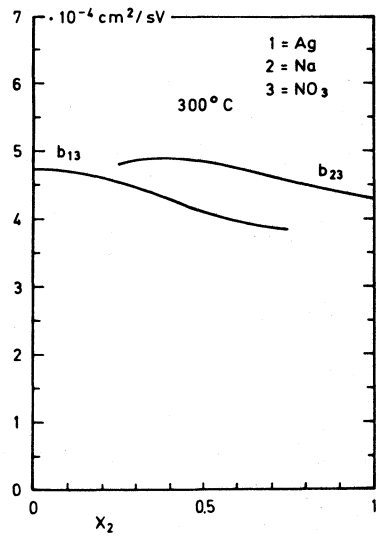

Connan 1973, disc

Figure 8

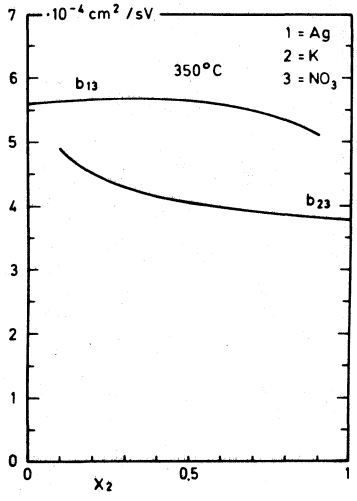

Duke, Owens 1958, disc

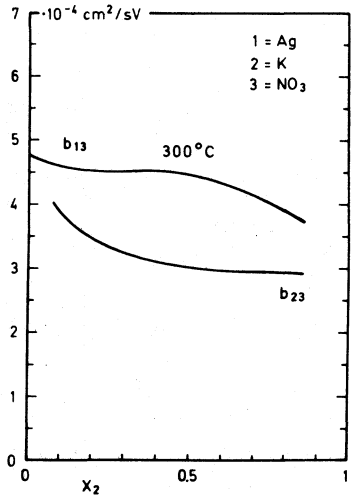

Okada, Kawamura 1970, emf A

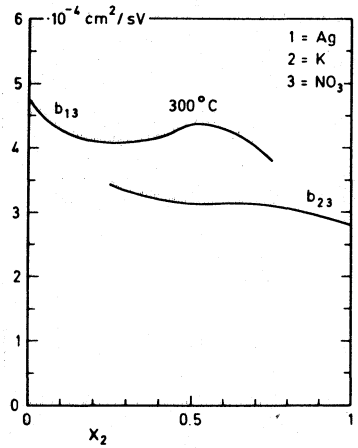

Connan 1973, disc

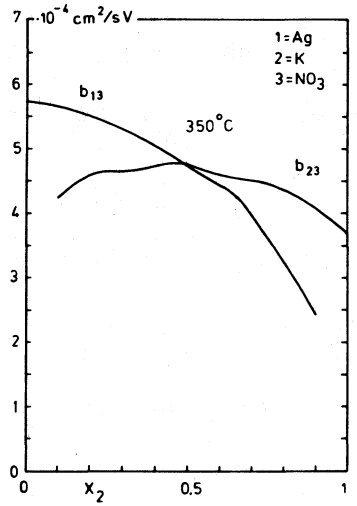

Richter, Gasseling, Conradt 1978, emf B

Figure 9

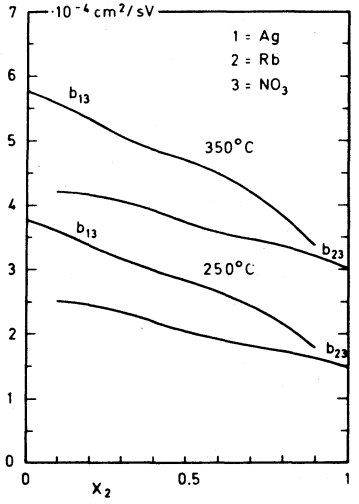

Okada, Kawamura 1974, emf A

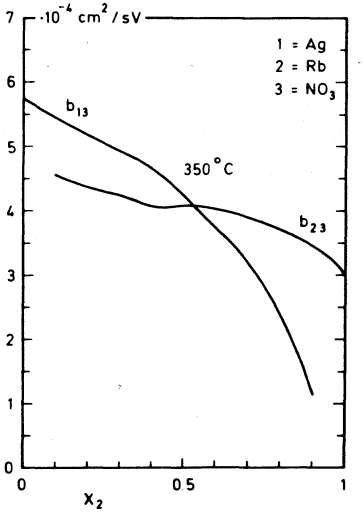

Richter, Gasseling, Conradt 1978, emf B

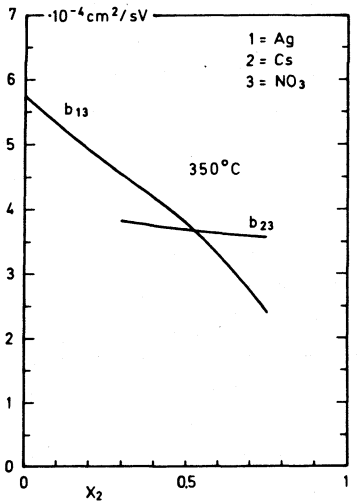

Richter, Gasseling, Conradt 1978, emf B

Figure 10

DOI: 10.1149/198109.0138PV

RECHARGEABLE MOLTEN-SALT CELLS

Elton J. Cairns
Lawrence Berkeley Laboratory, and
University of California
Berkeley, CA 94720

Abstract

Rechargeable molten-salt cells offer the opportunity for achieving higher specific energy than is available from ambient-temperature cells (200 W-h/kg), and a specific power in excess of 100 W/kg. Two main types of rechargeable cells employing molten salts are being developed: those with a molten salt as the sole electrolyte, and those with a combination of a solid electrolyte and a molten salt electrolyte. The status, recent research, and current problems for each of several systems in the above two categories are discussed. The most advanced systems in the first category are LiAl/FeS and Li_4Si/FeS_2; in the second category, $Na/Na_2O{\cdot}xAl_2O_3/S$ is the most advanced system. Interesting new cells continue to be proposed, having special features that may justify development. Overall, rechargeable molten-salt cells are making good progress. The main generic problems requiring additional work include corrosion-resistant current collectors and seals, ceramic electrolytes that resist degradation and thermal cycling, inexpensive corrosion-resistant porous separators, and improved electrode designs.

Introduction

During the last decade, rechargeable molten-salt cells have been the subject of a wide range of investigations, from the most fundamental to highly applied. As time passes, the variety of molten-salt cells increases, resulting in a broader range of choices with regard to operating temperature, reactants, and cell characteristics. On first impression, it would seem that so much research and development activity is perhaps inappropriate, because of the inconvenience of accommodating the elevated-temperature requirement of molten-salt cells. Closer examination reveals that some (but by no means all) molten-salt cells offer the opportunity for the achievement of specific energy and specific power values significantly higher than those available from ambient-temperature rechargeable cells: 200 W-h/kg, and 100+ W/kg. Molten-salt electrolytes allow the use of alkali metal-containing negative electrodes (not possible with aqueous electrolytes), and allow very high concentrations of the alkali metal cation as the charge-carrying species, providing for low mass transport overvoltages. In addition, the elevated temperatures provide for

high exchange-current densities and low charge-transfer overvoltages (compared to the ambient-temperature values).

Two main types of rechargeable cells employing molten salts are being developed: those with a molten salt as the sole electrolyte, and those with a combination of a solid electrolyte (the main electrolyte) and a molten-salt mixture of reactant and subsidiary electrolyte. Examples of cells of each type are given in Table I. The operating temperatures for these cells range from about 450°C for the lithium/iron sulfide cells to about 250°C for the sodium/sulfur tetrachloride cell. In the next section, the status of a number of the cells listed in Table I will be presented and discussed.

Table I. Rechargeable Cells with Molten-Salt Electrolytes

A. Cells with molten salts as the sole electrolyte
   $LiAl/LiCl-KCl/FeS$
   $LiAl/LiCl-KCl/FeS_2$
   $Li_4Si/LiCl-KCl/FeS_2$
   $Ca_2Si/LiCl-NaCl-CaCl_2-BaCl_2/FeS$
   $Ca_2Si/LiCl-NaCl-CaCl_2-BaCl_2/FeS_2$

B. Cells with molten salts as the subsidiary electrolyte
   $Na/Na_2O \cdot xAl_2O_3/Na_2S_n-S$
   $Na/Na\text{-glass}/Na_2S_n-S$
   $Na/Na_2O \cdot xAl_2O_3/SCl_3AlCl_4$ in $NaCl-AlCl_3$
   $Li/Li_2O/LiNO_3-KNO_3/V_2O_5$

Status of Rechargeable Molten-Salt Cells of Current Interest

The LiAl/LiCl-KCl/FeS Cell.

This cell has been undergoing research and development since the early 1970's, as a derivative of the very high specific energy Li/LiCl-KCl/S cell, (1-3) (2600 Wh/kg theoretical) which had liquid electrodes. Difficulties with solubility of polysulfides in the electrolyte, and retention of lithium in its current collector resulted in the use of the solid LiAl and FeS electrodes. There was, of course, a decrease in the theoretical specific energy to 458 Wh/kg, corresponding to the added weights of Al and Fe, and the decreased cell voltage (1.3 vs 2.4 V). This disadvantage is at least partially compensated by the very good stability of performance brought about by the use of solid electrodes of extremely low solubility in the electrolyte.

The overall cell reaction is

$$2LiAl + FeS \rightarrow Li_2S + Fe + 2Al, \qquad [1]$$

which takes place in two stages:.

$$2LiAl + 2FeS \rightarrow Li_2FeS_2 + 2Al + Fe \quad [2]$$

$$2LiAl + Li_2FeS_2 \rightarrow 2Li_2S + 2Al + Fe \quad [3]$$

The cell potentials for Reactions 2 and 3 are essentially the same, 1.3 V at 450°C, so a single-plateau discharge curve is to be expected.

Various designs of LiAl/FeS cells have been operated, one of which is shown in Figure 1. (4) These cells have porous LiAl negative electrodes containing a screen-like current collector, and are in good electrical contact with the steel or stainless steel cell container. The separator, which prevents the electrodes from contacting each other, and must resist attack by the cell reactants and electrolyte, usually has been boron nitride cloth or felt. Recently, progress has been made in the use of relatively inexpensive MgO powder in place of the separator. (5) The positive electrode is a porous composite of FeS particles, graphite powder, and a metallic sheet or screen-like current collector (usually Fe). This porous mass may be molded into a sheet form, or bonded with a carbonaceous cement. Fine-mesh screens or ceramic cloths are used to prevent loss of particles from the positive electrode. Various numbers of positive and negative electrodes can be interleaved to produce "multiplate" cells, with all electrodes of each type connected in parallel, increasing the capacity of the cell (Figure 1 shows 3 negative, 2 positive electrodes). The cell container is welded closed, and has a leak-tight feedthrough to prevent ingress of air and moisture which react with lithium.

Cells of the type described above yield voltage vs capacity curves as shown in Figure 2. (6) The specific energy of such cells falls into the range 60-100 Wh/kg at 30 W/kg, the higher value corresponding to 22% of theoretical, and is for multiplate cells with capacities of about 320 Ah. (7) The specific energy of multiplate cells as a function of the number of complete discharge/recharge cycles is shown in Figure 3. (7) The cells experienced a specific energy decline of about 40% after about 300 cycles. A typical lifetime for the longer-lived cells is 5000 hours.

The specific power achievable with LiAl/FeS cells has been somewhat lower than desired for electric vehicle applications, so attention is being devoted to improved current collectors, especially for the FeS electrode. Also, the specific power can be increased by promoting better, more complete wetting of the BN separator by the electrolyte. This has been accomplished by the use of wetting aids such as $LiAlCl_4$ in small amounts ($\sim$20 mg/cm^2). (7) Other approaches to reducing the cell internal resistance include the use of cobalt sulfides and copper sulfides as additives to the FeS electrode.

In the cycling of cells, it has been found that full recharge is impeded by the formation of djerfischerite ($LiK_6Fe_{24}S_{26}Cl$). (8) The

formation of this material can be reduced or eliminated by operation at higher temperatures and lower potassium ion concentrations in the electrolyte, hence an increased interest in lithium-richer electrolytes (the originally-used electrolyte was the eutectic, 58.8 m/o LiCℓ-41.2 m/o KCℓ, mp = 352°C).

The Li-Aℓ electrode has been found to suffer a loss of capacity and performance as a result of the agglomeration with cycling of the originally finely-structured alloy. This behavior is being investigated in detail, and the possible beneficial effects of alloying agents are being examined. (9)

The most common mode of failure of LiAℓ/FeS cells is shorting, resulting from swelling and extrusion of the FeS electrode. The degree of swelling of the active material is a function of the particle size of the FeS, the electrode composition, the electrolyte composition, and the structural design of the electrode (containment). Optimization of these variables results in cells that can be operated for over 5000 hours and more than 500 cycles.

The progress of the LiAℓ/FeS cell toward the marketplace will be determined to a significant degree by cost. At the present time, the most expensive component of the cell is the BN separator (the woven BN cloth has been $5000/m^2$; the BN felt is less expensive, but still far from a reasonable goal of $10-20/m^2$). An approach to reducing this cost is the use of a powder such as MgO in place of the BN. This is similar to the paste electrolyte used in molten carbonate fuel cells, and in earlier work with lithium/chalcogen cells. (10,11)

Other areas requiring attention in the continuing development of the LiAℓ/FeS cell include the need for an inexpensive leak-free electrical feedthrough, excellent cell capacity matching (or a means of charge balance control), and a good thermal control system. Work in these areas has already begun, and 10-cell batteries of 320 Ah cells have been tested. (7) Even if these issues are successfully addressed, competition from ambient temperature rechargeable cells could have a strong influence on the degree to which the LiAℓ/FeS system finds application. This is true because specific energies above 70 Wh/kg have been reported for some ambient-temperature cells, vs about 100 Wh/kg for LiAℓ/FeS. The status is summarized in Table II.

The $Li_4Si/LiC\ell-KC\ell/FeS_2$ Cell.

This cell is very similar to the one discussed above in many respects, including operating temperature (∿450°C), however an important difference is the significantly higher specific energy of this one (944 Wh/kg vs 458 Wh/kg). The higher specific energy is traceable to the much lower equivalent weights of the reactants, and the higher cell voltage for the first half of the discharge. The overall cell reaction is:

$$Li_4Si + FeS_2 \rightarrow 2Li_2S + Fe + Si \qquad [4]$$

This reaction gives the impression of greater simplicity than is actually the case. Some perspective concerning the reactions of the FeS_2 electrode can be gained by examining Figure 4, which shows the 450°C isothermal section of the Li-Fe-S phase diagram. (8) The path A-Z-X-B is followed by the composition of the FeS_2 electrode during discharge at 450°C, and the steps in the reaction are: (12)

$$2FeS_2 + 3Li \rightarrow Li_3Fe_2S_4 \qquad 2.04 \text{ V (vs Li)} \qquad [5]$$

$$Li_3Fe_2S_4 + Li \rightarrow Fe_{1-X}S + \text{W-phase} \qquad 1.9 \text{ V} \qquad [6]$$

Reaction 6 involves only a few percent of the total charge of Reaction 4 (see Figure 4). Next, the solid-solution W-phase and

Table II

LiAℓ/LiCℓ-KCℓ/FeS
$2LiA\ell + FeS \rightarrow Li_2S + Fe + 2A\ell$
E = 1.33 V; 458 Wh/kg Theoretical
T = 450°C

STATUS

Specific Energy	60-100 Wh/kg @ 30 W/kg
Specific Power	60-100 W/kg, peak
Cycle Life	300+ @ 100% DOD
Lifetime	5000+ h
Cost	>$100/kWh

RECENT WORK

- Multielectrode cells
- LiX-rich electrolyte
- BN felt separators
- Wetting agent for separators
- Powder separators-MgO
- Batteries of 320 Ah cells
- Improved current collectors

PROBLEMS

- Low specific energy
- Low voltage per cell
- Cell shorting major failure mode
- Electrode swelling and extrusion
- Agglomeration of Li-Aℓ with cycling
- Capacity loss
- High separator cost
- Leak-free feedthroughs
- Thermal control

and $Fe_{1-x}S$ are converted to Li_2FeS_2, at which point, half of the overall reaction is completed (2 electrons per FeS_2):

$$Fe_{1-x}S + W + Li \rightarrow Li_2FeS_2 \qquad 1.9\text{-}1.64\ V \qquad [7]$$

This is followed by:

$$2Li_2FeS_2 + 4Li \rightarrow 4Li_2S + 2Fe \qquad 1.64\ V \qquad [8]$$

The lithium-silicon negative electrode also is involved in a number of phase changes as the cell is operated. The phases involved at 450°C are Li_4Si, $Li_{15}Si_4$, $Li_{21}Si_8$, Li_2Si, and Si. (13) These phases provide for a multi-plateau discharge curve. The reversible potentials (measured vs lithium) at 450°C are given in Table III.

Table III. Reversible Potentials for the Li-Si Electrode at 450°C (13)

Phases in Equilibrium	Volts vs Li
$Si\text{-}Li_2Si$	0.326
$Li_2Si\text{-}Li_{21}Si_8$	0.277
$Li_{21}Si_8\text{-}Li_{15}Si_4$	0.149
$Li_{15}Si_4\text{-}Li_{22}Si_5$	0.042
$Li_{22}Si_5$-Li (Sat. with Si)	0.001

This electrode is capable of operating at high current densities ($0.2A/cm^2$) with good utilization (70%+), and apparently does not agglomerate as does the LiAℓ electrode.

Li_4Si/FeS_2 cells comprised of two porous electrodes of Li_4Si powder with reticulated nickel current collectors, and a porous FeS_2 electrode comprised of FeS_2 and graphite powders with graphite cloth and molybdenum expanded mesh current collectors have been operated. (14) These cells contained BN cloth separators and LiCℓ-KCℓ eutectic electrolyte. A capacity of 70-80 Ah was typical, and specific energy values up to 182 Wh/kg (19% of theoretical) were obtained, as shown in Figure 5. Cycle lives of over 700, at 100% depth of discharge were obtained, along with lifetimes of about 11,000 hours. These results are presented in Figure 6.

Detailed post-test examination of Li_4Si/FeS_2 cells revealed some attack of the molybdenum current collector for the FeS_2 electrode, and the cell container (presumably by the Si). A continuing issue of importance is the identification of inexpensive electronically-conductive materials that resist attack in the FeS_2 and Li_4Si electrodes (for current collectors), and inexpensive non-conductive separator materials stable to FeS_2 and Li_4Si. As with the LiAℓ/FeS cell, inexpensive, leak-free feedthroughs are needed.

Recent work has included the operation of small bipolar Li_4Si/FeS_2 cells, and two-cell batteries. (15) This work, if successfully implemented in full-scale systems, could play an important role in decreasing the number of (presumably expensive) feedthroughs needed in a battery system.

Overall, the Li_4Si/FeS_2 is in an earlier stage of development than the LiAℓ/FeS cell, but offers the opportunity for 200 Wh/kg, which is more than double that achieved by any aqueous rechargeable system, and double that for the LiAℓ/FeS cell. This is probably the performance margin appropriate for the inconvenience of operating an elevated-temperature system. A condensed summary of the status of Li_4Si/FeS_2 is presented in Table IV.

Table IV

$Li_4Si/LiCℓ\text{-}KCℓ/FeS_2$

$Li_4Si + FeS_2 \rightarrow 2Li_2S + Fe + Si$

E = 1.8, 1.3 V; 944 Wh/kg Theoretical

Status

Specific Energy	120 Wh/kg @ 30 W/kg
	180 Wh/kg @ 7.5 W/kg
Specific Power	100 W/kg, peak
Cycle Life	700 @ 100% DOD
Lifetime	∿15,000 h
Cost	>$100/kWh

Recent Work

- Bipolar cells
- Li-Si electrodes
- BN felt separators
- 70 Ah cells

Problems

- Materials for FeS_2 current collector
- Leak-free feedthroughs
- High internal resistance
- Low-cost separators needed
- Thermal control

The $Ca_2Si/LiCℓ\text{-}NaCℓ\text{-}CaCℓ_2\text{-}BaCℓ_2/FeS_2$ cell.

This system represents an effort to replace the lithium of the system just discussed by calcium, which is less costly and more abundant. The calcium-silicon alloy can be operated at 460°C over the range Ca_2Si to at least $CaSi_2$ in a Ca-containing electrolyte (the best composition to date is 29% LiCℓ-20% NaCℓ-35% $CaCℓ_2$-16% $BaCℓ_2$). (7) This electrode has supported only relatively low current densities,

and modifications are being sought. One such is $CaAl_{1.2}Si_{0.4}$ (equivalent weight = 83.7 vs 54.1 for Ca_2Si), which yields the voltage-capacity curves shown in Figure 7. (16) The theoretical specific energy for this cell is about 560 Wh/kg (vs 750 Wh/kg for Ca_2Si/FeS_2).

The overall reactions for the Ca_2Si/FeS_2 cell is:

$$Ca_2Si + FeS_2 \rightarrow 2CaS + Fe + Si \qquad [9]$$

This reaction takes place stepwise over the voltage range 2.0 to 1.2 V. Some cells having capacities up to 100 Ah have been operated, but low specific energy values (~40 Wh/kg) and short cycle lives (~60) have been obtained. This system is in too early a stage of investigation to assess whether or not it will compete with the Li_4Si/FeS_2 cell. Considerable improvements in performance and lifetime are necessary before such judgments can be made. The present status of work on this system is summarized in Table V.

Table V

$Ca_2Si/LiCl$-$NaCl$-$CaCl_2$-$BaCl_2/FeS_2$
$Ca_2Si + FeS_2 \rightarrow 2CaS + Fe + Si$
E = 2.0-1.2 V; ~750 Wh/kg Theoretical
T = 480°C

Status		
	Specific Energy	67 Wh/kg @ 13 W/kg
	Specific Power	15 W/kg
	Cycle Life	60
	Cost	too early
Recent Work		
	$BaCl_2$ added to electrolyte	
	Larger cells - 100 Ah	
	Co added to FeS_2	
	Ca-Al-Si electrode	
Problems		
	Low specific power	
	Low current densities	
	BN separator not stable with Ca_2Si	
	Rapid capacity loss	

The $Na/Na_2O \cdot xAl_2O_3/Na_2S_n$-S Cell.

This is the cell most commonly referred to as the sodium/sulfur cell. The sodium polysulfide is included in the designation above to emphasize the fact that Na_2S_n is a molten-salt electrolyte as well as

an electrode reactant. The $Na/Na_2O \cdot xA\ell_2O_3/Na_2S_n$-S cell has been under development for over a decade. (17) It has been the first rechargeable cell of significance to make use of a solid electrolyte ($Na_2O \cdot xA\ell_2O_3$, $5 \leqslant x \leqslant 11$), called beta alumina, and a molten-salt electrolyte (Na_2S_x). The solid electrolyte is used in the form of a closed-end tube, usually with the sodium inside it. The sulfur, with its graphite felt current collector, is kept on the outside of the tubular electrolyte, in the annular space between the solid electrolyte and the metal cell case. One such cell design is shown in Figure 8. (18) The cell must be hermetically sealed to avoid reaction of molten sodium with oxygen or moisture. A typical operating temperature is 350°C.

In the fully-charged condition, essentially all of the sodium is in the sodium compartment of the cell, and the sulfur electrode consists of nearly sodium-free sulfur, which is a poor conductor of electrons and ions. As the cell is discharged, sodium is oxidized to form sodium ions which pass through the electrolyte, and react with sulfur and electrons to form sodium polysulfides, Na_2S_n, which have a low solubility in sulfur. Because of this, the sodium polysulfides form a separate liquid phase, and serve as an electrolyte, transferring sodium ions, and as a reactant ultimately reaching the overall stoichiometry Na_2S_3, at which point Na_2S_2 precipitates. This point is designated the end of discharge, or 100% depth of discharge.

As the cell is charged, the sodium polysulfides are converted to sulfur. Difficulties have been encountered in attempting to obtain full recharge because an insulating layer of sulfur forms on the surface of the beta alumina tube. Various approaches have been taken to ameliorate this problem, including the use of specially shaped graphite current collectors, the addition of C_6N_4 to the sulfur to impart conductivity, and the use of graphite current collectors of graded resistance to appropriately distribute the electrochemical reaction zone.

After small laboratory cells (up to 20 Ah) had achieved acceptable life and performance, scale-up to 100-200 Ah was performed. These cells have demonstrated specific energy values of 85-140 Wh/kg, specific powers of 60-130 W/kg and cycle lives of 200-1500, depending on the cell size and design. Figure 9 shows the capacity of a Na/S cell as a function of the number of cycles. A few batteries of up to 10 kWh have been tested (e.g. reference 19), but the lifetimes of batteries have been relatively short.

The current problems being investigated for the improvement of Na/Na_2S_n-S cells include the search for inexpensive corrosion-resistant metal alloys that can serve as the cell container exposed to sulfur, and corrosion-resistant coatings for use on the sulfur container. Electronically-conductive ceramics such as doped TiO_2 are being evaluated as current collectors in sulfur-core cells. The ceramic electrolyte (β''-$A\ell_2O_3$) remains a very expensive item; work is

being done on the use of lower-cost starting materials and processing. An alternative electrolyte, called Nasicon ($Na_{1+x}Zr_2Si_xP_{3-x}O_{12}$) is being investigated, but cell lifetimes have been shorter than with β''-$A\ell_2O_3$. A problem common to almost all Na/Na_2S_n-S cells is their inability to be cooled down and reheated without damage or performance loss. Frequently, the electrolyte or a ceramic seal is broken. Cracks and breakage of the ceramic electrolyte and its seals are the major cause of cell failure, even without thermal cycling.

The $Na/\beta''A\ell_2O_3/Na_2S_n$-S cell has reached a relatively advanced state of development, and there are several pilot facilities for cell production in operation. Experience with small batteries of cells is beginning to accumulate, and larger batteries will be prepared in test quantities during the next few years. The status of this system is presented in Table VI.

Table VI

Na/Na+ Solid/S

$2Na + 3S \rightarrow Na_2S_3$

$\bar{E}$ = 2.0 V; 758 Wh/kg Theoretical

Status

Specific Energy	85-140 Wh/kg @ 30 W/kg
Specific Power	60-130 W/kg peak
Cycle Life	200-1500
Lifetime	3000-15,000 h
Cost	>$100/kWh

Recent Work

- Batteries, ~10 kWh
- C_6N_4 additive to S
- Ceramic (TiO_2) electronic conductors
- Shaped current collectors
- Tailored resistance current collectors
- Sulfur-core cells
- $Na_{1+x}Zr_2Si_xP_{3-x}O_{12}$
- Thermocompression bonded seals

Problems

- Corrosion-resistant material for contact with S
- Low cost seals
- Low cost electrolyte
- Specific power is low
- Thermal cycling

The Na/Na+ glass/Na_2S_n-S Cell.

This cell operates according to the same principles and phase diagram as the cell discussed just above. The main differences are the substitution of a sodium-ion-conductive borate glass for the ceramic. Because the ionic conductivity of the glass is about a factor of 10^4 lower than that of β''-$A\ell_2O_3$, it is necessary to use very thin electrolyte layers. These take the form of thin, hollow fibers, and are incorporated into a cell structure as shown in Figure 10. (20) This cell design is very interesting because it provides a very large area of glass electrolyte with a very thin wall, allowing practical currents to be obtained at low current densities. Also, mass transport is required only over short distances (perhaps 100 μm).

Implementation of the design shown in Figure 10 requires the development of a highly reliable, durable seal of the thousands of glass fibers to a glass or ceramic tube sheet (glass is currently favored). Current collection is provided in the sulfur electrode by an aluminum foil (with a thin molybdenum or carbon coating to reduce corrosion). Most of the experience with this cell has been obtained with 6 Ah cells, but improvements in lifetime have justified recent work with a 40 Ah cell.

The problems with this version of the Na/Na_2S_n-S cell are similar to those discussed for the ceramic-electrolyte version. Also, there are problems associated with the development of optimum glass compositions for the tube sheet, such that a good seal is achieved, while having sufficient strength to avoid sagging. A status summary for this cell is given in Table VII.

The Na/$Na_2O \cdot xA\ell_2O_3$/$SC\ell_3A\ell C\ell_4$ in $A\ell C\ell_3$-$NaC\ell$ Cell.

One of the more recently-investigated cells makes use of $\beta''A\ell_2O_3$ and a low-melting mixture of $A\ell C\ell_3$ and $NaC\ell$ as electrolytes. (21) The positive-electrode reactant is $SC\ell_3^+$ present as $SC\ell_3A\ell C\ell_4$. This cell is operated at temperatures near 250°C, and offers a relatively high potential of 4.2 V. The overall cell reaction is:

$$4Na + SC\ell_3A\ell C\ell_4 + 3A\ell C\ell_3 \rightarrow S + 4NaA\ell C\ell_4 \qquad [10]$$

Note that sulfur undergoes a valence change of four: from S^{+4} to S^0. The theoretical specific energy for this reaction is 563 Wh/kg. It is also possible to reduce sulfur to S^{-2}, at a somewhat lower voltage.

Simple glass laboratory cells have been operated, with capacities of up to a few ampere hours, yielding voltage charge or capacity curves as shown in Figure 11. (21) It is too early to evaluate specific energy and specific power capabilities for this system; more practical

Table VII

Na/Na^+ glass/S

$2Na + 3S \rightarrow Na_2S_3$

$\bar{E}$ = 2.0 V; 758 Wh/kg Theoretical

Status (6 Ah cells)	
Specific Energy	n.a.
Specific Power	n.a.
Cycle Life	500 (75-100% DOD)
Lifetime	9000h
Cost	>$100/kWh

Recent Work

- Improved tube sheet and seal to tubes
- Mo coating on Aℓ foil
- 40 Ah cells

Problems

- Sagging of tube sheet
- Seal to tubes
- Feedthroughs
- Coating on Aℓ
- Compatibility of tubes and tube sheet

cell designs will be required first. Laboratory cells have operated for about 475 cycles and 7000 hours before failure.

Some of the problems encountered include the corrosiveness of the positive electrode reactant mixture toward metals (tungsten is used as the current collector), the slow wetting of the $\beta''Al_2O_3$ by the sodium, the high vapor pressure of the $AlCl_3$, and cracking of the $\beta''Al_2O_3$. The status of this cell is shown in Table VIII. This system could offer advantages where reduced operating temperatures (below the typical 350-450°C) and higher cell voltage (fewer cells for a given system voltage) are important. Work with more practical cell hardware will be needed for a more complete evaluation.

The $Li/Li_2O/LiNO_3$-KNO_3/V_2O_5 Cell.

A very recent report of a lower-temperature molten salt cell with a lithium electrode (22,23) makes use of a solid lithium or lithium-aluminum electrode with a very thin Li_2O film which acts as a solid lithium-ion conducting electrolyte. The main electrolyte is the $LiNO_3$-KNO_3 eutectic (mp = 135°C), and the positive electrode is V_2O_5 which can intercalate Li. Because of the fact that lithium melts at 180°C, the temperature range for operation is rather narrow: 135-180°C.

Table VIII

$Na/Na_2O \cdot xAl_2O_3/SCl_3AlCl_4$ in $AlCl_3$-NaCl

$4Na + SCl_3AlCl_4 + 3AlCl_3 \rightarrow 4NaCl \cdot AlCl_3 + S$

E = 4.2 V; 563 Wh/kg Theoretical

T = 250°C

Status:	glass lab cells only (4 Ah)
Current Density	20 mA/cm^2 @ 3.5 V
Power Density	150 mW/cm^2 max. @ 2.5 V
Cycle Life	475 @ 100% DOD
Lifetime	7000 h
Cost	too early

Recent Work

- Larger cells - 4 Ah
- Less expensive current collectors

Problems

- Sodium wetting
- Vapor pressure
- Corrosion of metals and some electrolytes
- Electrolyte cracking
- Overcharge?

The overall cell reaction is:

$$xLi + V_2O_5 \rightarrow Li_xV_2O_5 \qquad [11]$$

For x = 1, the theoretical specific energy is 500 W-h/kg, at an average cell voltage of 3.5 V.

This combination of lithium with the nitrate melt imposes certain restrictions: a narrow range of operating temperatures 135-180°C, and a narrow range of potentials for the positive electrode. Above 4.2 V, oxygen and NO_2 are evolved from the positive electrode; below 2.6 V, nitrate is reduced to nitrite plus oxide. Also, there is a small corrosion current at the lithium electrode, corresponding to the dissolution of Li_2O by the nitrate melt.

It is too early to tell if this exploratory work will lead to a lower-temperature lithium cell of practical interest.

Conclusions

Overall, good, solid progress is being made in the research and development of rechargeable molten-salt cells. Full-size cells, and a few full-size batteries have been demonstrated. Cell lifetimes of up to about two years have been achieved for some systems. In

general, specific energy values are lower than desirable, but 180 Wh/kg has been achieved with a Li_4Si/FeS_2 cell.

Materials developments will probably set the pace of progress for the systems discussed above. Inexpensive, corrosion-resistant current collector materials for use with positive electrodes are needed for all of these systems. Corrosion-resistant container materials are also important. All these systems need leak-free feed-throughs that resist alkali metals and highly oxidizing conditions. Inexpensive separators that resist lithium attack are important for all of the lithium-containing systems. The development of a lithium-ion conducting solid electrolyte would add flexibility for many cells, and might make a Li/S cell feasible, offering the possibility of a very high specific energy (perhaps 500 Wh/kg; the theoretical value is 2600 Wh/kg).

REFERENCES

1. E.J. Cairns and H. Shimotake, Science, 164, 1347 (1969).

2. E.J. Cairns, J.P. Ackerman, P.D. Hunt, and B.S. Tani, presented at The Electrochemical Society Meeting, Cleveland, Ohio, October, 1971, Abstract No. 48; see also Extended Abstracts, p. 118.

3. E.J. Cairns, H. Shimotake, E.C. Gay, M.L. Kyle, and R.K. Steunenberg, presented at the International Society of Electrochemistry Meeting, Stockholm, Sweden, August 28-September 2, 1972.

4. P.A. Nelson, D.L. Barney, R.K. Steunenberg, A.A. Chilenskas, E.C. Gay, J.E. Battles, F. Hornstra, W.E. Miller, M.F. Roche, H. Shimotake, R. Hudson, R.J. Rubeschko, and S. Sudar, Progress Report for the Period October 1977-September 1978, Argonne National Lab Report 78-94, November, 1978.

5. T. Olszanski and H. Shimotake, presented at The Electrochemical Society Meeting, Pittsburgh, Pennsylvania, October, 1978, Abstract No. 53; see also Extended Abstracts 78-2 (1978).

6. H. Shimotake, W.J. Walsh, E.S. Carr, and L.G. Bartholme, in Proceedings of the 11th IECEC, Volume 1, American Institute of Chemical Engineers, New York, 1976, p. 473.

7. Argonne National Laboratory, Annual DOE Review of the Lithium/Metal Sulfide Battery Program, June, 1979.

8. M.F. Roche, L.E. Ross, C.C. Sy, S.K. Preto, L.G. Bartholme, and P.F. Eshman, Progress Report for the Period October 1978-March 1979, Argonne National Lab Report No. 70-39, May, 1979, pp. 94-106.

9. A.K. Fischer and D.R. Vissers, presented at The Electrochemical Society Meeting, Hollywood, Florida, October, 1978, Abstract No. 88; see also Extended Abstracts 80-2, 240 (1980).

10. E.J. Cairns and R.K. Steunenberg, in Progress in High-Temperature Physics and Chemistry, Volume 5, C.A. Rouse, ed., Pergamon Press, New York, 1973, p. 63.

11. E.J. Cairns, H. Shimotake, and A.K. Fischer, Argonne Reviews, 5, 87 (1969).

12. Z. Tomczuk and A. Martin, Progress Report for the Period October 1978-September 1979, Argonne National Lab Report No. 79-94, March, 1980, pp. 142-151.

13. R.A. Sharma and R.N. Seefurth, Journal of The Electrochemical Society, 123, 1763 (1976).

14. E.J. Zeitner and J.S. Dunning, in Proceedings of the 13th IECEC, Society of Automotive Engineers, Warrendale, Pennsylvania, 1978, p. 697.

15. T.G. Bradley, in Proceedings of the 15th IECEC, American Institute of Aeronautics and Astronautics, New York, 1980, p. 228.

16. S.K. Preto, L.E. Ross, N.C. Otto, J.F. Lomax, and M.F. Roche, "Calcium/Iron Disulfide Secondary Cells," to be published in Proceedings of the 16th IECEC, Atlanta, Georgia, 1981.

17. N. Weber and J.T. Kummer, in Proceedings of the Annual Power Sources Conference, 21, 37 (1967).

18. General Electric Review of the Advanced Battery Development Program for Electric Utility Application, May 16, 1979.

19. W. Fischer, H.B. Gels, F. Gross, K. Liemert, and H. Meinhold, in Proceedings of the 14th IECEC, American Chemical Society, Washington, D.C., 1979, p. 710.

20. C.A. Levine, in Proceedings of the 10th IECEC, Institute of Electrical and Electronic Engineers, New York, 1975, p. 621.

21. G. Mamantov, R. Marassi, M. Matsunaga, Y. Ogata, J.P. Wiaux, and E.J. Frazer, Journal of The Electrochemical Society, 127, 2319 (1980).

22. J. Poris, I.D. Raistrick, and R.A. Huggins, in Proceedings of the Symposium on Lithium Batteries, The Electrochemical Society, Pennington, New Jersey, 1981.

23. I.D. Raistrick, J. Poris, and R.A. Huggins, in Proceedings of the Symposium on Lithium Batteries, The Electrochemical Society, Pennington, New Jersey, 1981.

24. Ford Aerospace & Communications Corporation, Annual DOE Review of the Sodium-Sulfur Battery Program, April 22, 1980.

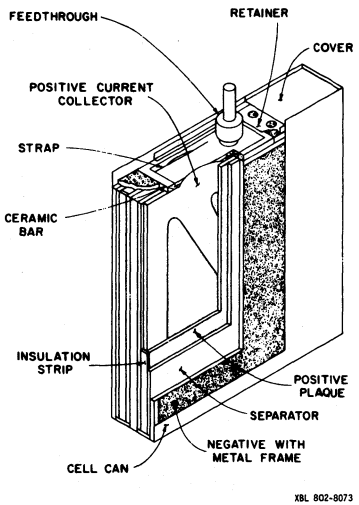

Figure 1. Cutaway view of LiAℓ/FeS cell being developed at Argonne National Lab. (4)

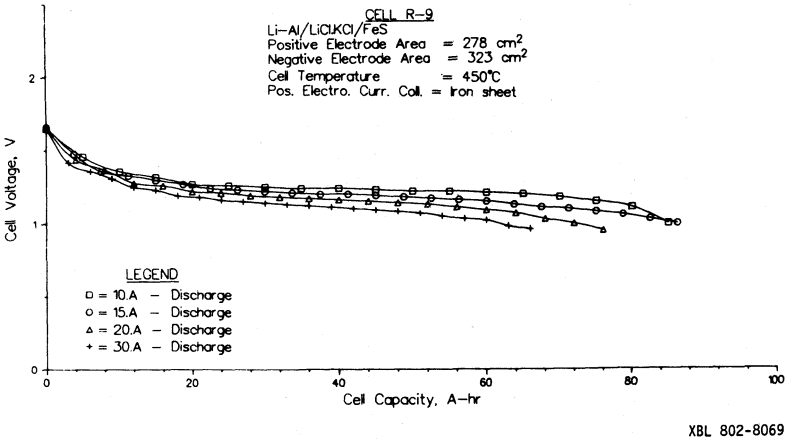

Figure 2. Voltage-capacity curves for a LiAℓ/FeS cell. (6)

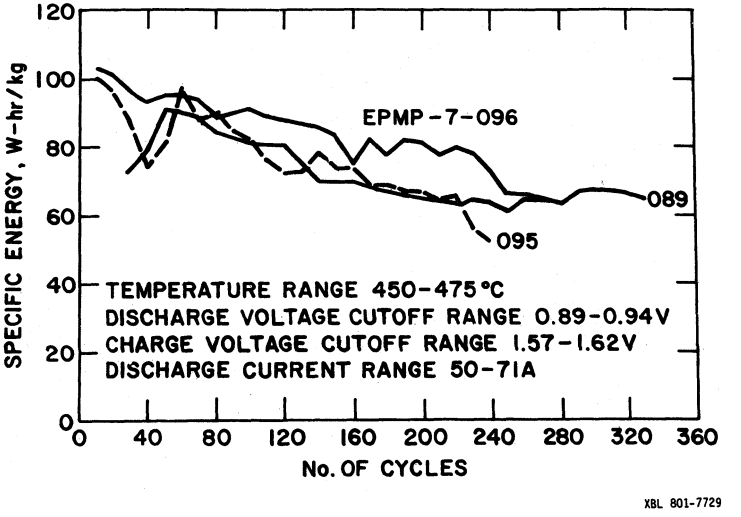

Figure 3. Specific energy vs cycle number of LiAℓ/FeS cells. (7)

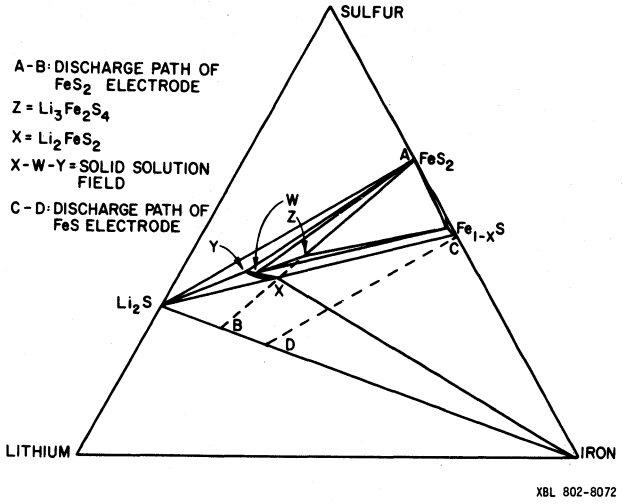

Figure 4. Isothermal section of the lithium-sulfur-iron phase diagram at 450°C. (8)

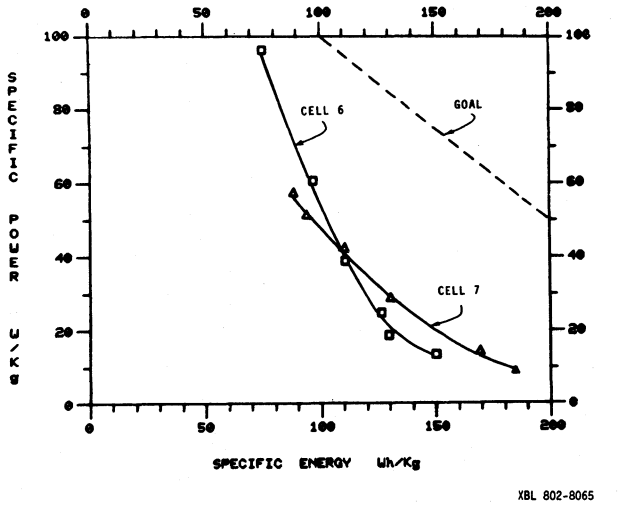

Figure 5. Specific power vs specific energy plot for Li_4Si/FeS_2 cells operating at about 475°C. (14)

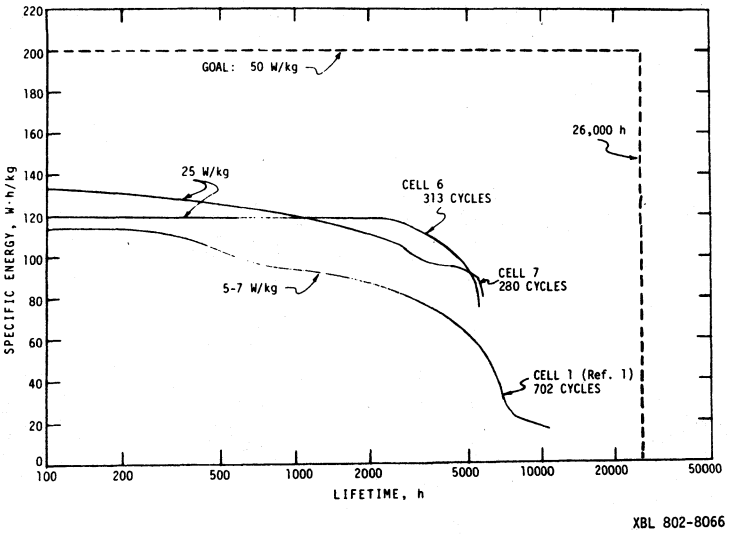

Figure 6. Specific energy vs time for $LiAl/FeS_2$ (Cell 1) and Li_4Si/FeS_2 (Cells 6,7) cells. (14)

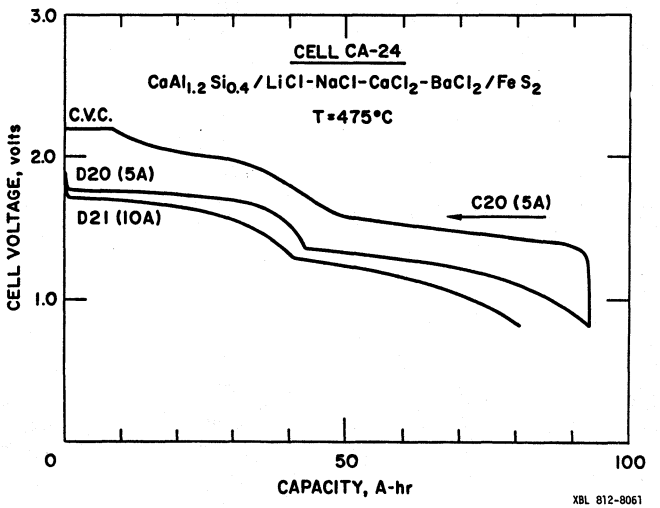

Figure 7. Voltage vs capacity curves for a $CaAl_{1.2}Si_{0.4}/FeS_2$ cell. (16)

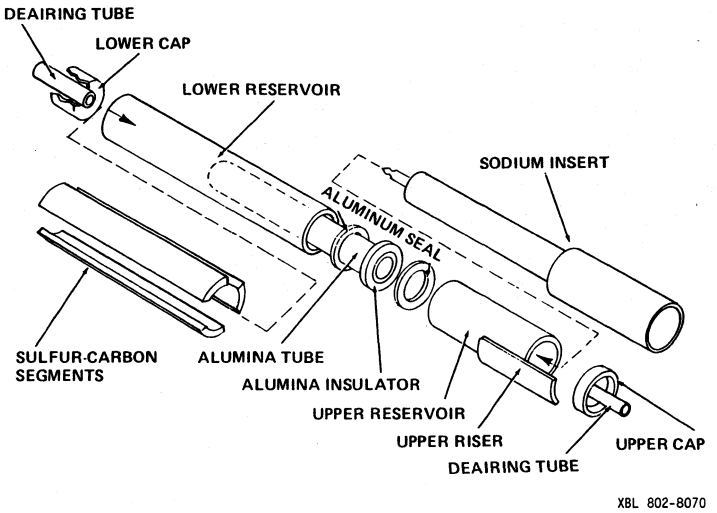

Figure 8. Exploded view of a Na/S cell with a $\beta''A\ell_2O_3$ electrolyte. (18)

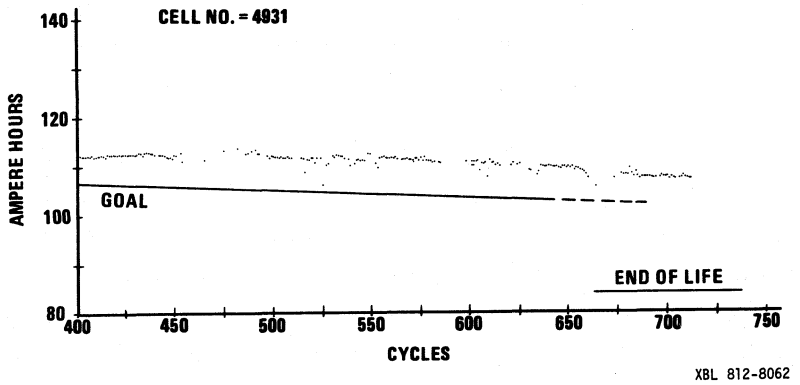

Figure 9. Capacity vs cycle number for a Na/S cell. (24)

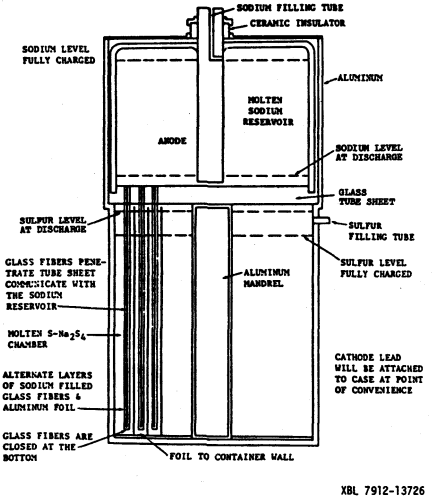

Figure 10. The DOW Sodium/Sulfur Hollow Fiber Cell. (20)

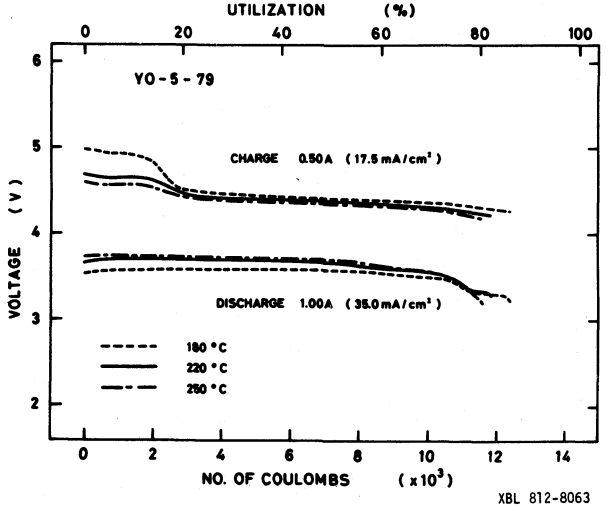

Figure 11. Galvanostatic charge-discharge curves for a $Na/\beta''Al_2O_3/SCl_3AlCl_4$ in $AlCl_3$-NaCl cell at three temperatures. (21)

DOI: 10.1149/198109.0158PV

SPECTROELECTROCHEMICAL AND OTHER STUDIES OF SULFUR AND ITS HALIDES IN CHLOROALUMINATE MELTS: APPLICATION TO A NEW RECHARGEABLE HIGH VOLTAGE LOW TEMPERATURE CELL

G. Mamantov, V. E. Norvell, L. Klatt, K. Tanemoto, R. Marassi, Y. Ogata, M. Matsunaga, J. P. Wiaux, and C. B. Mamantov

Department of Chemistry, The University of Tennessee
Knoxville, Tennessee 37916
and the
Analytical Chemistry Division, Oak Ridge National Laboratory,*
Oak Ridge, TN 37830

ABSTRACT

The electrooxidation of sulfur in molten $AlCl_3$-NaCl has been investigated by means of UV-visible and electron spin resonance spectroelectrochemistry and ring-disk voltammetry. An electrode reaction sequence for the oxidation of S_8 to S(IV) is presented. The use of tetravalent sulfur as a positive electrode material for a rechargeable molten salt cell is briefly discussed.

INTRODUCTION

It has been previously shown (1) that sulfur dissolved in acidic ($AlCl_3$-rich) chloroaluminate melts ($AlCl_3$-NaCl mixtures) can be electrochemically oxidized in three steps to yield tetravalent sulfur. Bulk coulometry (1) and preliminary spectroelectrochemical results (2) indicated that the first oxidation step yields at least two species. Coulometry (1) indicated that the products of the second and third oxidation steps are S(I) and S(IV), respectively.

Based on published electrochemical and spectrophotometric studies, a reaction scheme was proposed for oxidation of sulfur in acidic chloroaluminate melts which involved S_8^+, S_{16}^{2+}, S_8^{2+}, S_2^{2+}, and S(IV) at various stages in the oxidation (1). Previous studies of sulfur cations in oleum and superacid solvents (3-5) and in chloroaluminate melts (6,7) have indicated the existence of several species which were not observed electrochemically. This work has involved ESR spectroelectrochemistry (8), additional UV-visible absorption spectroelectrochemistry (8), and ring-disc voltammetry (9) which have provided a better understanding of the pathways involved in the electrochemical oxidation of sulfur in chloroaluminate melts. The

*Operated by Union Carbide Corporation for the Department of Energy.

experimental details and description of the instrumentation used for the spectroelectrochemical studies are available (2,8).

The feasibility of using tetravalent sulfur as a positive electrode material in rechargeable molten chloroaluminate cells has been demonstrated previously (10-17). Laboratory cells of the type

$$Na/Na^+ \text{ ion conductor}/SCl_3^+ \text{ in molten } AlCl_3\text{-}NaCl$$

have an open circuit voltage of 4.2V and high energy densities; they operate at temperatures in the range of 180-250°C. A brief description of such cells is included in this paper.

RESULTS AND DISCUSSION

Ring-Disc Voltammetry.- Voltammograms obtained at a rotating glassy carbon ring-disc electrode in the $AlCl_3$-NaCl (53-47 mole % ≡ 53/47) melt at 200°C are shown in Fig. 1. The voltammogram obtained at the disc electrode is in good agreement with prior results obtained by other electrochemical methods at stationary electrodes in more acidic melts (63/37) at higher temperatures (1). Such an agreement is reasonable since for chloroaluminate melts an increase in temperature results in a smaller pCl (18). The potential of the ring electrode was kept at a value at which the positive oxidation states of sulfur should be reduced to elemental sulfur. The voltammogram obtained at the ring electrode indicates that the reduction of products is observed as expected.

ESR Studies.- ESR measurements of sulfur oxidized either chemically or electrochemically in chloroaluminate melts indicate the presence of at least three radicals (19). ESR spectroelectrochemical experiments involving oxidation of sulfur at an optically transparent electrode (OTE) at 132-225°C also produced three signals with g-values of 2.0277 (A), 2.0155 (B) and ∿2.013 (C). The potential dependence of these three radicals at 132°, shown in Fig. 2, indicates that signal A reaches its maximum intensity at a less positive potential than does signal C. This suggests that radical A contains sulfur in a lower formal oxidation state than radical C.

This relationship is supported by studies of sulfur radicals with the same g-values which were produced in other solvents (3-5). Hyperfine splitting analysis has determined that radical C is S_5^+ (5). The nature of radical A is uncertain as no hyperfine splitting data are available, however, experimental evidence has shown that this radical is formed under less oxidizing conditions than required for S_5^+ (3,4). The earlier belief that this lower oxidation state radical was S_8^+ (3) has lately been questioned (4), and the matter remains unresolved.

The signal for the third radical observed in the melt, B, is weak in intensity compared to A and C (at 132°), and it appears to

have a different lineshape. The nature of this radical remains to be determined, and it will not be considered further here.

UV-Visible Spectroelectrochemical Studies.- UV-visible spectroelectrochemical measurements on sulfur cations produced in the first oxidation step at 150-250° yield absorption bands with maxima at 600, 730 and 960nm, and a shoulder around 450nm (Fig.3). An additional shoulder, not shown in the Figure, is observed in the 330-350 nm region. The 600nm band has previously been assigned to S_8^{2+}, and the 450, 730 and 960 nm bands have been attributed to S_{16}^{2+}(2,6,7). The absorption in the 330-350 nm region has not been assigned to any specific species in the melt, however, a similar spectral feature observed by Gillespie and coworkers in liquid SO_2 was attributed to a S_{19}^{2+} cation (4).

The observed potential dependence of the 600,730 and 960 nm bands, as illustrated in Fig. 4, is consistent with the relative formal oxidation states of the species assigned to them. A comparison of Figs. 2 and 4 suggests a chemical relationship between the radical A and S_{16}^{2+}, and likewise between C and S_8^{2+}. Such equilibria have been proposed earlier in other solvents (3), however, because of subsequent studies (4), these simple equilibria may no longer be valid.

Further information on the nature of the equilibria in the melt was obtained by studying the effect of sulfur concentration on the absorption bands. These studies indicate that the lower oxidation state products are favored at higher sulfur concentrations. This result is consistent with bulk coulometry measurements(1). Analysis of absorbance *vs.* time curves for the visible absorption bands indicates that S_{16}^{2+} and radical A are formed initially. These products are involved in chemical reactions and equilibria, however, as the electrode potential becomes more positive, they are eventually oxidized further to form S_8^{2+} and S_5^+.

It is clear that an unequivocal reaction sequence for this sulfur oxidation in the melt cannot be formulated due to uncertainties in some of the species involved, particularly radical A. A reaction sequence which supports the experimental data may, however, be suggested if we assume that radical A is S_8^+. This hypothesis is supported by voltammetric data which indicate that a simple one electron transfer is the first step in the oxidation of S_8 in the melt (1). A reaction sequence based on this hypothesis is shown below:

$$S_8 = S_8^+ + e \qquad [1]$$

$$2S_8^+ \rightleftharpoons S_{16}^{2+} \qquad [2]$$

$$S_8^+ = S_8^{2+} + e \qquad [3]$$

$$S_8^{2+} + S_8 \rightleftharpoons S_{16}^{2+} \qquad [4]$$

$$S_{16}^{2+} + S_8^+ \rightleftharpoons S_5^+ + S_{19}^{2+} \qquad [5]$$

$$4S_8^{2+} + S_8 \rightleftharpoons 8S_5^{+} \qquad [6]$$

The second sulfur oxidation step results in the formation of S(I), probably as S_2Cl^+ (1). Fig. 5 illustrates spectra obtained when S(I) is produced at a platinum OTE. The spectrum at 1.85V applied to the OTE is in good agreement with the spectrum obtained when S_2Cl_2 is dissolved in the melt; it is also consistent with the "calculated" spectrum given by Fehrmann et al. (6). Nernst plots were constructed for several reactions proposed for this oxidation step, using the spectroelectrochemical data to calculate the ratio [O]/[R]. The resulting plots suggest that the following reactions are most probable:

$$S_8^{2+} = 4S_2^{2+} + 6e \qquad [7]$$

$$2S_5^{+} = 5S_2^{2+} + 8e \qquad [8]$$

It is possible that these reactions proceed through an S_4^{2+} intermediate, however, the spectroelectrochemical data do not conclusively provide such evidence. S_4^{2+} is known to exist in other solvents (3), and Fehrmann et al. (6) have previously postulated its existence in chloroaluminate melts.

The third oxidation step yields S(IV) which has no absorption maxima in the spectral range studied (6). As S_2^{2+} is oxidized to S(IV), the spectroelectrochemical data indicate the presence of at least two absorbing species. Therefore, this oxidation step may also proceed through an intermediate species, probably involving sulfur in the +2 oxidation state. The overall oxidation step may be described by the following reaction:

$$S_2^{2+} = 2S(IV) + 6e \qquad [9]$$

Application to a Rechargeable Cell.- As mentioned earlier, tetravalent sulfur is being utilized in a new low temperature molten salt rechargeable cell (16,17)

$$Na/\beta''\text{-alumina}/SCl_3^{+} \text{ in molten } AlCl_3\text{-}NaCl.$$

The discharge process involves the reduction of S(IV) to elemental sulfur, which can be reduced further to sulfide.

Typical galvanostatic charge-discharge curves for a cell used to study the discharge of sulfur (IV) to sulfur and the potential of each electrode vs. an aluminum reference electrode are shown in Fig. 6. Most cells had $AlCl_3$/NaCl molar ratios of ~70/30 before discharge and ~50/50 at the end of discharge. High energy density values, large percent utilization of the active positive electrode material and good energy efficiency have been demonstrated. The performance of cells prepared in the discharged and charged states was found to be the

same. One cell was operated continuously for more than 10 months; 476 deep charge-discharge cycles were attained.

ACKNOWLEDGEMENTS

We would like to acknowledge the collaboration of R. Livingston, H. Zeldes, and M. Conradi, Chemistry Division, Oak Ridge National Laboratory, in obtaining preliminary electron spin resonance spectra of sulfur radicals in chloroaluminate melts. We would also like to thank Professor J. Q. Chambers for the use of his ESR spectometer. This work has been supported by the Department of Energy, Contract EY-76-S05-5053, University of California Subcontract 4502810 and the NSF Grant CHE 77-21370. Support by the U. S. Department of Energy, Basic Energy Sciences is also acknowledged. VEN acknowledges receipt of an Oak Ridge Associated Universities Fellowship.

REFERENCES

1. R. Marassi, G. Mamantov, M. Matsunaga, S. E. Springer, and J. P. Wiaux, J. Electrochem. Soc., 126, 231 (1979).
2. G. Mamantov, V. E. Norvell, and L. N. Klatt, J. Electrochem. Soc. 127, 1768 (1980).
3. R. J. Gillespie and J. Passmore, in "Advances in Inorganic Chemistry and Radiochemistry," Vol. 17, H. J. Emeleus and A. G. Sharpe, Editors, pp. 49-89, Academic Press, New York (1975).
4. R. C. Burns, R. J. Gillespie, and J. F. Sawyer, Inorg. Chem., 19, 1423 (1980).
5. H. S. Low and R. A. Beaudet, J. Amer. Chem. Soc., 98, 3849 (1976).
6. R. Fehrmann, N. J. Bjerrum, and F. W. Poulsen, Inorg. Chem., 17, 1195 (1978).
7. N. J. Bjerrum, in "Characterization of Solutes in Non-Aqueous Solvents," G. Mamantov, Editor, pp. 251-271, Plenum Press, New York (1978).
8. V. E. Norvell, K. Tanemoto, G. Mamantov and L. N. Klatt, J. Electrochem. Soc., in press.
9. G. Mamantov and C. B. Mamantov, unpublished work.
10. G. Mamantov, R. Marassi and J. Q. Chambers, "High Energy Cathodes for Fused Salt Batteries," Technical Report ECOM-0060-F, April 1974.
11. G. Mamantov, R. Marassi, and J. Q. Chambers, Abstract 8, p. 24, The Electrochemical Society Extended Abstracts, New York, N. Y., October 13-17, 1974.
12. G. Mamantov, R. Marassi, and J. Q. Chambers, U.S. Pat. 3,966,491 (1976).
13. G. Mamantov, R. Marassi, J. P. Wiaux, S. E. Springer, and E. J. Frazer, Abstract 89, p. 243, The Electrochemical Society Extended Abstracts, Atlanta, Georgia, October 9-14, 1977.
14. G. Mamantov and R. Marassi, U.S. Pat. 4,063,005 (1977).
15. G. Mamantov, R. Marassi, J. P. Wiaux, S. E. Springer and E. J. Frazer, in "Proceedings of the Symposium on Load Leveling," N. P. Yao and J. R. Selman, Editors, pp. 379-383, The Electrochemical

Society Softbound Proceedings Series, Princeton, N.J. (1977).
16. G. Mamantov, R. Marassi, M. Matsunaga, Y. Ogata, J. P. Wiaux and E. J. Frazer, J. Electrochem. Soc., 127, 2319 (1980).
17. G. Mamantov, R. Marassi, Y. Ogata, M. Matsunaga and J. P. Wiaux, in "Proceedings of 15th Intersociety Energy Conversion Engineering Conference," Volume 1, 809107, Seattle, Wash., August 18-22, 1980, American Institute of Aeronautics and Astronautics.
18. G. Torsi and G. Mamantov, Inorg. Chem., 11, 1439 (1972).
19. R. Livingston, G. Mamantov, J. P. Wiaux, H. Zeldes, M. Conradi, and R. Marassi, unpublished work.

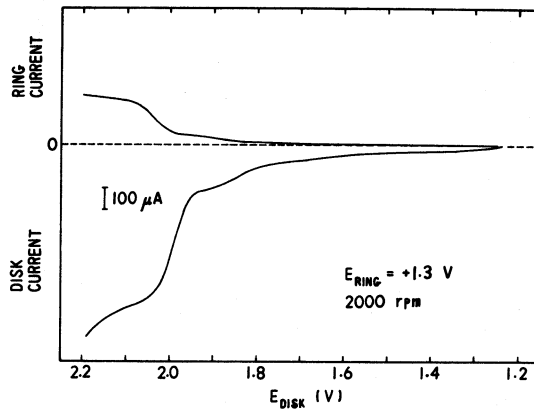

Fig. 1. Current-voltage curve at glassy carbon RRDE in 0.8×10^{-2} M sulfur in 53/47 $AlCl_3$/NaCl melt at 200 °C.

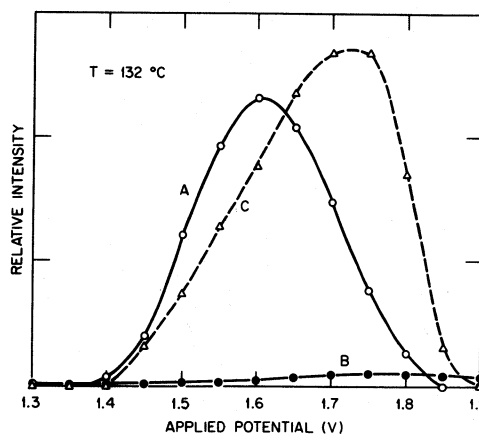

Fig. 2. Potential dependence plot for radicals A, B, and C. Sulfur concentration (as monomer): 8.20×10^{-3} molal.

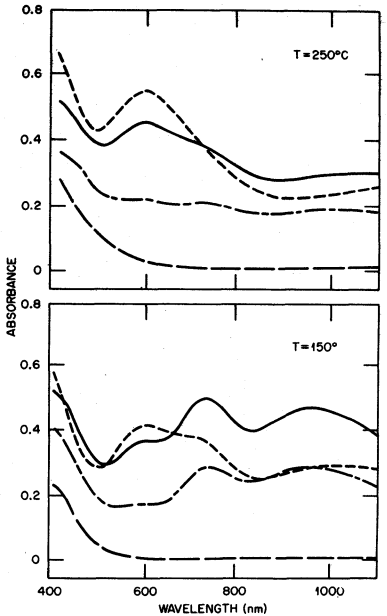

Fig. 3. Absorption spectra of the products of the first sulfur oxidation step for two temperatures. Applied potentials: 1.30V (— — —), 1.50V (— – — –), 1.60V (———), 1.70V (- - - - - -). Sulfur concentration: 1.50 X 10^{-2} molal.

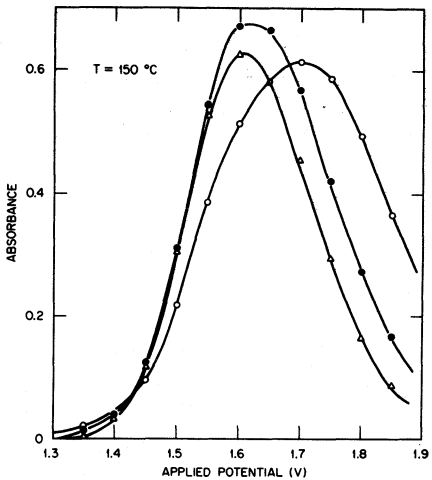

Fig. 4. Potential dependence plot for the absorption bands shown in Fig. 3 at 150°C. o, 600 nm; ●, 730 nm; Δ, 960 nm.

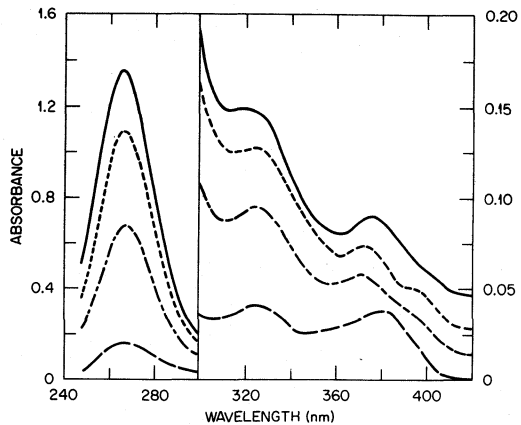

Fig. 5. Absorption spectra of the products of the second sulfur oxidation step at 250°C. Applied potentials: 1.70V (— — —), 1.775V (— - — -), 1.825V (- - - - - -), 1.85V (———). Sulfur concentration: 1.35 X 10^{-2} molal.

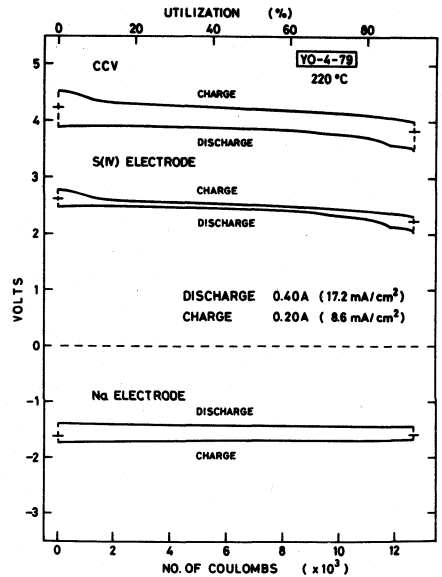

Fig. 6. Galvanostatic charge-discharge curves and potentials of S(IV) and Na electrodes vs. Al(III)/Al (in $NaCl_{sat}$-melt) reference electrode at 220°C. Discharge time 8.8 hr. Percent utilization is calculated for $4e^-$ process.

DOI: 10.1149/198109.0167PV

LINEAR SWEEP VOLTAMMETRIC STUDIES OF THE LITHIUM/ALUMINUM ELECTRODE IN MOLTEN LiCl-KCl

Y.S. Fung*, D. Inman, and S.H. White**

University of Hong Kong, Pokfulam Road, Hong Kong,* Department of Metallurgy, Imperial College, London, England, E.I.C. Laboratories Inc., 55 Chapel Street, Newton, Massachusetts 02158, USA.**

The deposition of lithium on aluminum leads to extensive alloy formation. Several fundamental phenomena, such as monolayer formation and nucleation polarisation, affect the kinetics of the deposition process. In the present investigation these phenomena were studied by (fast) cyclic voltammetry. The latter is a very useful technique for understanding qualitatively the deposition process and in its scanning coulometric modification, which is also utilised in this investigation, it can provide useful semi-quantitative information.

Voltammetric profiles corresponding to the formation of the α-phase (a solid solution of Li and Al), the β-phase (Li-Al) and the γ-phase (Li_3Al) amongst others, were identified and their characteristics investigated. The results are discussed against the background of the possible vitiating effects of impurities in the present paper.

1. Introduction.

The well tested lithium/aluminum electrode has so far proved to be the most promising anode for use in the high-temperature molten salt lithium/iron sulfide battery (1,2). The retention of lithium is good and the potential is stable throughout the α/β phase transformation from 9 a/o to 50 a/o lithium (3). However, only very few fundamental studies of the kinetics of the electrode have been carried out and these have concentrated for the most part on the β-phase (4-7).

The deposition of lithium on aluminum occurs with extensive alloy formation. Several fundamental phenomena seem to affect the kinetics of the deposition process, viz. undervoltage deposition, monolayer formation, nucleation polarisation and the formation of successive alloys with increasing lithium contents.

The present study is concerned with the light that linear sweep voltammetry throws on these phenomena, particularly in the case of the deposition (i.e. charging) process. The aim has been to complement those studies which have already been carried out using different electrochemical as well as structural techniques.
attention has been paid to the processes which occur during overcharge and overdischarge conditions, that is well away from the usual range of operation of the cell but nevertheless conditions which could

(* ** current addresses) The work was conducted at Imperial College.

easily be encountered in the battery (of cells) situation.

Although the rapid linear sweep voltammetric technique, as has been increasingly realised in recent years, is a very powerful one for unravelling the complexities of multistep electrode processes (8-12), it does have some disadvantages in the present case because of the changes of electrode geometry which occur during charging and discharging. Because of this, linear sweep voltammetry can best be regarded as a semi-quantitative tool in the present context. Nevertheless its usefulness lies in its ability to scan the whole potential range and to provide in effect an "electrochemical spectrum". The useful potential range extends from +1.2V to -0.7V vs. a β-phase Li/Al reference electrode (see below). $AlCl_3$ is evolved at the anodic limit and alkali metals are deposited in massive quantities at the cathodic limit. Two types of peak are present in the "electrochemical spectrum": intrinsic peaks which arise from the deposition and stripping of alkali metals from various solid solutions and alloys and extrinsic peaks which, in spite of rigorous purification, can arise from the oxidation and reduction of various oxides, hydroxides and water.

2. Experimental.

The purification of the LiCl-KCl eutectic used as the solvent and the procedure for the assembly of the reaction cells have been described elsewhere (13). In any event, molten salt methodology is now becoming increasingly well known and several general texts describing it are available or will shortly become available (14). Ag/AgCl (0.2 m/o) was used as the reference electrode, along with Li/Al alloyed in the β-phase, particularly in later experiments. The Li/Al electrode potential is -2.27V vs. the Ag/AgCl (0.2 m/o) reference electrode. In early experiments, a graphite electrode was used as the counter electrode but as the chlorine liberated was found to be detrimental to the other cell components, a preformed Li/Al electrode was used as the counter electrode in later experiments. The working electrode was an aluminum wire, diameter 0.74 mm, supplied by BDH. Electrode potentials were controlled using a Wenking Potentiostat Control Amplifier 72L. The current output was recorded using a Bryans 26000 X-Y recorder. In the case of very fast signals, they were recorded by a Datalab DL 501 transient recorder with a Tektronix 564 oscilloscope attachment for temporary viewing. They were later reproduced at a slower rate on the Bryans X-Y recorder. Four methods were used to measure the charge passed to the electrode in the scanning coulometry experiment. The initial two manual methods were quickly superseded by two electronic methods. (a) That in which a Bentham Hi-Tek integrator was used to measure the charge directly. This is a very convenient method to measure the charge passed between the rest potential and the switching potential, as the instrument can be operated either on the total charge passed or on the positive charge alone. However, it cannot be used to measure the charge passed at intermediate potentials. (b) That in which an electronic integrator, built in this laboratory, was used

to measure the charge passed from the rest potential to the switching potential. The integration can be initiated, held or terminated by an external TTL trigger or manually and the initial potential can be set to a potential other than zero. The design is such that if the initial potential is set to a potential other than zero, the charges in the anodic as well as the cathodic sweep can be measured.

3. Results and discussion.

3.1 General aspects.

As a framework for discussing the voltammetric behaviour of the electrode, the plot of electrode potential vs. composition from the paper by Selman, DeNuccio, Sy and Steunenberg, (3), (Figure 1), is very useful. This shows clearly the intervals of stability of the various solid solutions and intermetallic compounds for the Li/Al system at equilibrium. The battery is usually operated in the 9 a/o to 50 a/o Li region. In practice, the aluminum working electrode was always held at a potential of about +0.7v (vs. the LiAl reference electrode) to protect it cathodically before applying the voltammetric sweeps.

3.2 Cathodic to anodic switching potential in the α-phase (solid solution) region.

Figure 2 shows a typical cyclic voltammogram corresponding to the region where the deposited lithium forms a solid solution (the α-phase)(15,16,17) with the substrate aluminum. Lithium begins to deposit in fact at +0.4V vs. the Li-Al reference electrode but it is noteworthy that there is no corresponding anodic stripping peak. (It should be noted of course that there is no cathodic peak anyway.) Coulombic efficiency is low and, especially at the cathodic end, the current is much smaller at the same potential during the reverse scan than during the forward scan. Since the sizes of the lithium and aluminum atoms are similar(1.55Å and 1.38Å respectively) transportation of the lithium within the aluminum will probably be by a vacancy mechanism. The voltammetric behaviour is typical of that for the formation of a solid solution, i.e. the final equilibrium sites of the lithium atoms have a range of energies and therefore the solid solution does not form at a discrete (sharply defined) electrode potential. Also, it is difficult to remove the lithium atoms because of their low rates of diffusion in the solid solution (18,19).

3.3 Switching potential in the β-phase formation region.

Figure 3 shows what happens when the switching potential is shifted in the cathodic direction and beyond what is obviously a critical value. The much larger currents which flow at the cathodic end are marked by sharp anodic stripping peaks. This phenomenon can be related to the formation and stripping of the β-phase (the compound Li-Al) which has a much more open structure than the α-phase (bcc, a = 6.37 Å compared with the fcc structure, a = 4.05 Å of the α-phase, which is in effect an expanded Al lattice) (15,16,17,20), which occurs

over a narrow range of electrode potentials.

3.4 The effect of repetitive cycling.

This is exemplified in figure 4 which shows the increases of current which occur in both the cathodic and anodic modes during repetitive cycling. This phenomenon is known as the development of the electrode and arises from two factors (a) an increase of the surface area of the electrode due to a roughening effect and (b) the creation of new frozen vacancy sites for the accommodation of deposited lithium atoms by the selective dissolution of lithium during the anodic cycles.

3.5 The behavior of newly-immersed aluminum electrodes.

The importance of surface properties is also exemplified by the cyclic voltammetric behavior of a newly-immersed aluminum electrode, shown in figure 5. New, very sharp, cathodic and anodic waves can be seen at +0.63v and +0.75v respectively, vs. the Li/Al reference electrode. The sharpness of the peaks indicates that they may originate from adsorption phenomena. As the charge under one of these peaks is roughly 40 μC and that for the formation of a monolayer (21,22) of lithium about 50 μC, it is tempting to speculate that they arise from the formation and stripping of the latter. However, as indicated by figure 6, the repeated deposition and dissolution of lithium over the α-phase region does not seem to affect these peaks although they do disappear after the electrode is exposed to repeated cycling of the β-phase. There is, of course, the possibility that these peaks may be due to electrode processes involving hydroxides and oxides of aluminum. In this regard it is perhaps worth noting that OH^- ions are cathodically electroactive on platinum at +0.47v vs. the Li/Al reference electrode (23).

Two more pre-peaks, which only appear with newly-immersed aluminum electrodes, are revealed (figure 7) if switching is carried out at more cathodic potentials in the β-phase formation region. These occur at +20 and +100 mv respectively, vs the Li/Al reference electrode and are very sharp. The charge under one of them is about 15 μC. They gradually disappear with cycling in the β-phase region or after the aluminum electrode is immersed in the melt for a few hours. It is tempting to speculate that they are due to the predeposition of lithium atoms (to form the β-phase with the underlying aluminum) on energetically favorable sites and that these sites are annealed out during either operation or prolonged immersion on open-circuit.

3.6 Scanning coulometry.

The phenomena taking place on the aluminum substrate following the predeposition of lithium are further exemplified by the results of scanning coulometry experiments shown in figure (8) and (9). Figure 8 is a plot of total charge vs. electrode potential, whereas figure 9 shows the same data but this time plotted as the average charge

to take account of the variation of time elapsed during a sweep when different switching potentials are utilised. Undervoltage deposition is clearly exemplified as well as the absence of a well defined threshold potential for the formation of the solid solution (α-phase) and the very marked increase of charge passed during the formation of the β-phase.

The ratios of the anodic to the cathodic charges are shown in figures 10 and 11. In the α-phase formation region, the anodic charge is always less than the cathodic charge at the same switching potential. However, as the switching potential moves into the β-phase formation region, the ratio moves closer to unity. The most obvious (and intrinsic) explanation for this reversibility of the charging process is that in this phase the lithium atoms are present in easily accessible sites. An alternative explanation is that the effects of impurities are less marked as the charging and discharging currents increase.

3.7 Dependence of the formation potential of the β-phase on the sweep rate.

Figure 12 shows clearly that the slower the sweep rate, the sharper is the β-phase formation peak because the behavior corresponds more closely to that at equilibrium. At the slowest sweep rate it is noteworthy that the cathodic and anodic peaks are identical. However, the most important factor which emerges from the variation of sweep rate is that the formation potential for the β-phase shifts in the cathodic direction with increase of sweep rate. (In the present study, it is seen that the switching potential has to be shifted in the cathodic direction in order to observe the β-phase formation peak with increasing sweep rate.) On these grounds it is reasonable to speculate that this behavior results from nucleation polarisation which it is necessary to overcome to germinate the β-phase.

3.8 The effects of more cathodic switching.

The effects of sweep rate when the switching potential is made even more cathodic (>0.2v negative to the β-phase potential) are shown in figure 13. Switching is now being carried out after the appearance of a conventional linear sweep voltammetric maximum. This indicates that the current is limited by the rate of diffusion of lithium through the β-phase. The most noteworthy feature is that, for post-peak switching at the same electrode potential, the current during the reverse sweep is smaller than during the forward sweep. The steepness of the slopes of the deposition and stripping waves indicates that the electrode is well poised and that the current is limited mainly by the uncompensated resistance of the cell. Current oscillations appear at low sweep rates, presumably as a result of changes in the (active) surface area of the electrode.

3.9 Effects of holding the electrode potential in the β-phase formation region.

It can be seen (figure 14) that two stripping (anodic) peaks manifest themselves following the 'hold' whereas, if the reverse sweep is carried out immediately following the forward (cathodic) sweep, only one stripping peak appears. The height of the second (more anodic) peak increases with 'hold' time whereas the height of the first peak only increases slightly.

It is probable that this phenomenon arises because the lithium atoms have time (with increasing 'hold' time) to diffuse from their initial sites to more (energetically) stable sites. Needless to say an extrinsic explanation based on impurity effects could also be invoked here.

3.10 Switching at extreme cathodic potentials.

Figure 15 shows that two pairs (anodic/cathodic) of peaks appear in this region. The potentials indicate that the larger pair probably results from the formation (cathodic) and dissolution (anodic) of liquid alloy and that the smaller pair results from the formation and dissolution of the γ-phase. The electrode potentials for both sets however are slightly more cathodic than their equilibrium potentials which perhaps indicates that their formation is attended by nucleation polarisation. Large currents are finally manifested at the most cathodic potentials , the cathodic limit (Fig. 15 C and D). The appearance of current oscillations in the region of the anodic peaks is accompanied by the evolution of gases from the electrode surface and the disappearance of the peaks due to lithium dissolution. Thus the formation of potassium (which is a vapor at 400°C) by the displacement reaction

$$Li + KCl \rightarrow K + LiCl$$

is likely to take place, even though the equilibrium state would be expected to lie to the left, because the reaction is driven by the loss of potassium from the system. To confirm this hypothesis, lithium metal was added to the melt and a voltammogram recorded. The melt turned a reddish-brown and a red deposit appeared on the cool surfaces above the melt. Figure 16 shows that a stripping peak for potassium then appeared.

4. Conclusions.

These are as follows.

1. Undervoltage deposition of lithium on aluminum takes place mainly by the formation of a solid solution (the α- phase) and the β-phase.

2. There is no clear cut threshold potential for the formation of the α-phase.

3. There is a critical potential for the formation of the β-phase which seems to be accompanied by a nucleation polarisation.

4. Once the β-phase is formed, the electrode is well poised (as evidenced by the linear sweep voltammograms) and can sustain a high current with minimum polarisation.

5. The phenomena occuring at the electrode and their kinetics are very much influenced by the surface states of the electrode. Deposited metal monolayers may be involved but oxide/hydroxide arising from impurities can also play a part.

6. Fast cycling of the electrodes leads to their "development", that is both the anodic and cathodic currents flowing increase.

7. If too cathodic potential excursions occur, potassium can form. This would have a deleterious effect by leading to electronic conduction.

ACKNOWLEDGMENTS

We thank the Ministry of Defence for its support of this work and Mr. L. Pearce of the Admiralty Marine Technology Establishment for helpful discussions.

REFERENCES

1. E.G. Gay, D.R. Vissers, F.J. Martino and K.E. Anderson, J. Electrochem. Soc., 123, 1591 (1976).
2. W.J. Walsh and H. Shimotake, Proc. 10th Internat. Power Sources, ed. D.H. Collins, Academic Press, London, 725 (1977).
3. J.R. Selman, D.K. DeNuccio, C.J. Sy and R.K. Steunenberg, J. Electrochem. Soc., 124, 1160 (1977).
4. C.J. Wen, W. Weppner, B.A. Boukamp and R.A. Huggins, J. Electrochem. Soc., 126, 2258 (1979).
5. C.A. Melendres, J. Electrochem. Soc., 124, 650 (1977).
6. A.L. L'vov and A.A. Gnilomedov, Soviet Electrochem. 11, 473 (1975).
7. S.D. James, Electrochim. Acta 21, 157 (1976).
8. J.E.B. Randles, Trans. Faraday Soc. 44, 322, (1948).
9. R.S. Nicholson, Anal. Chem. 37, 667 (1965).
10. R.S. Nicholson, Anal. Chem. 37, 1351 (1965).
11. R.S. Nicholson and I. Shain, Anal. Chem. 37, 190 (1965).
12. R.S. Nicholson, Anal. Chem. 38, 1406 (1966).
13. Fung Ying-Sing, Ph.D. thesis, (London), 1980.
14. D.G. Lovering, (ed.), Molten Salts Techniques, Plenum (New York) to be published.
15. R.P. Elliott, Constitution of Binary Alloys, First Supplement, McGraw-Hill Ltd., New York, N.Y., p. 42 (1965).

16. M. Hansen, Constitution of Binary Alloys, McGraw-Hill Ltd., New York, N.Y., 104-105, (1958).
17. F.A. Shunk, Constitution of Binary Alloys, Second Supplement, McGraw-Hill Ltd., New York, N.Y., 27-28 (1969).
18. S.D. James, Electrochim. Acta 21, 157, (1976).
19. L.P. Costas, U.S. At. Energy Commn. Report, TID-16676, 7pp (1963)
20. L.P. Costas and R.P. Marshall, Trans. AIME 224, 970, (1962).
21. G.J. Hills, D.J. Schiffrin and J. Thompson, J. Electrochem. Soc. 120 (2), 157, (1973).
22. M.M. Nicholson, J. Amer. Chem. Soc. 79, 7, (1957).
23. C.A. Melendres, J.P. Ackerman and R.K. Steunenberg, Proc. Internat. Symp. on Molten Salts - Electrochem. Soc. 575, (1976).

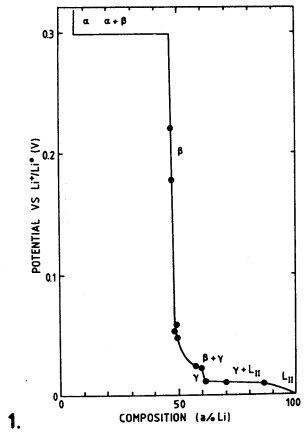

1.

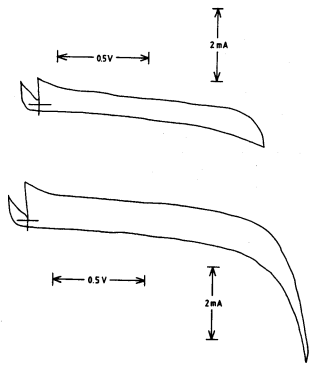

2.

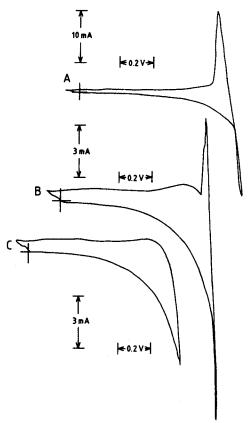

3.

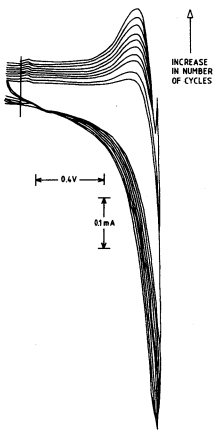

4.

Fig. 1 EMF - Composition diagram of lithium-aluminum alloy at 700 K (3).

Fig. 2 The formation of the α-phase on the aluminum electrode.
Sweep rate: 100 mV/sec.
Rest potential: +1.009 V vs LiAl
Electrode Area: 0.2 cm^2.

Fig. 3. The formation of the β-phase on the aluminum electrode
Switching potential: A -0.96V, B - 0.93V, C -0.90V.
Rest potential: -1.376V vs Ag/AgCl reference electrode (0.2 m/o)
Sweep rate: 100 mV/sec
Electrode area: 0.2 cm^2

Fig. 4 The effect of cycling on the deposition and stripping of lithium from aluminum.
Rest potential: +0.8V vs LiAl
Sweep rate: 100mV/sec
Electrode area: 0.2 cm^2

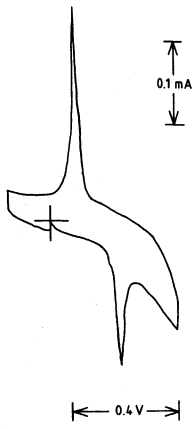

5.

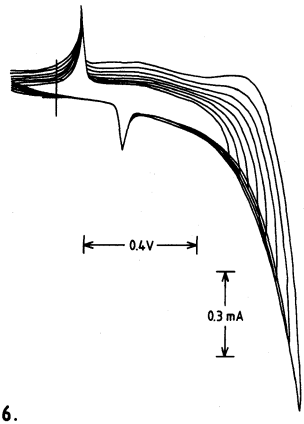

6.

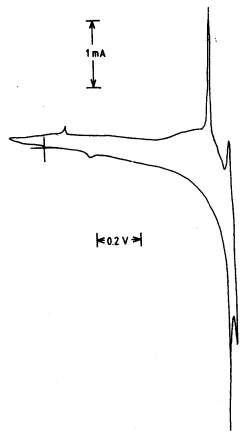

7.

Fig. 5 The voltammetric behavior of a newly immersed aluminum electrode
Sweep rate: 0.1 V/sec
Rest potential: -1.411V vs Ag/AgCl (0.2 m/o)
Electrode area: 0.2 cm^2

Fig. 6 The effects of lithium deposition and dissolution on the behavior of a newly immersed aluminum electrode.
Rest potential: -1.41V vs Ag/AgCl (0.2 m/o)
Sweep rate: 100 mV/sec
Electrode area: 0.2 cm^2

Fig. 7 The behavior of a newly-immersed aluminium electrode in the β-phase formation region.
Sweep rate: 100 mV/sec
Electrode area: 0.2 cm^2
Rest potential: -1.409V vs Ag/AgCl (0.2 m/o)

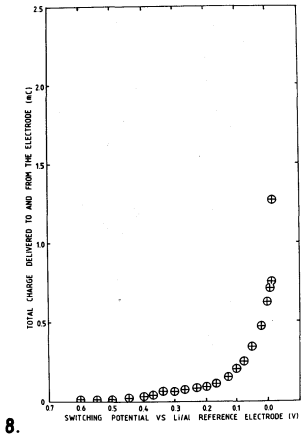

8.

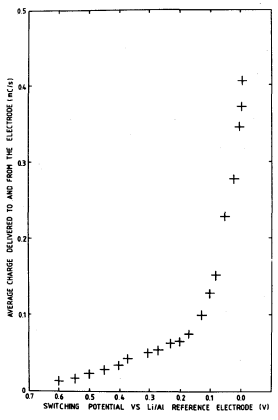

9.

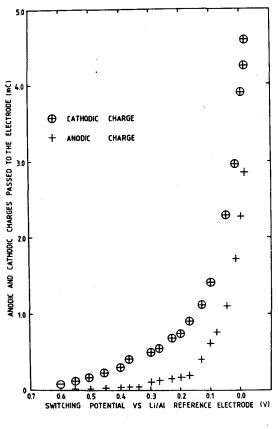

10.

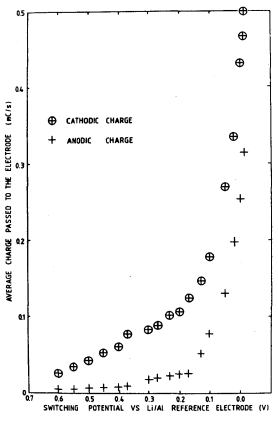

11.

Fig. 8 Switching potential vs total charge delivered to the aluminum electrode

Fig. 9 Switching potential vs average charge delivered to the aluminum electrode.

Fig. 10 Switching potential vs anodic and cathodic charges delivered to the aluminum electrode.

Fig. 11 Switching potential vs average anodic and cathodic charges delivered to the aluminum electrode.

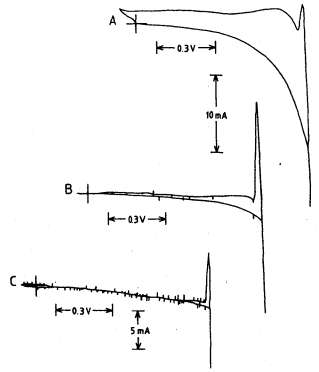

12.

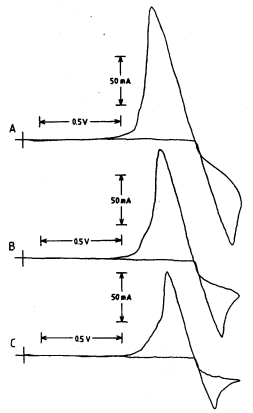

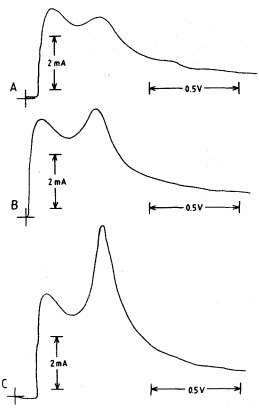

14.

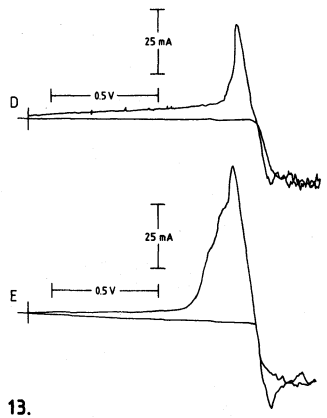

13.

Fig. 12 The effect of the sweep rate on the formation of the β-phase
Sweep rate (mV/sec): A - 100 B - 10 C - 1
Switching potential (V): A -0.9225 B -0.915 C-0.90
Rest potential: -1.375V vs Ag/AgCl reference electrode (0.2 m/o)
Electrode area: 0.2 cm^2

Fig. 13 The effect of scan rate on the deposition of lithium on aluminum.
Sweep rate: A - 100 mV/sec, B - 50 mV/sec, C - 20 mV/sec, D - 2 mV/sec,
E - 5 mV/sec
Rest potential: -1.2V
Switching potential: -2.5V
Electrode area: 0.2 cm^2
All potentials are measured wrt Ag/AgCl (0.2 m/o)

Fig. 14 The effect of different hold times on the stripping voltammogram.
Hold time: A - 5 mins., B - 15 mins., C - 55 mins.
Hold potential: +50 mV vs LiAl reference electrode
Reverse sweep rate: 100 mV/sec
Electrode area: 0.2 cm^2
Rest potential: +0.9V vs LiAl reference electrode.

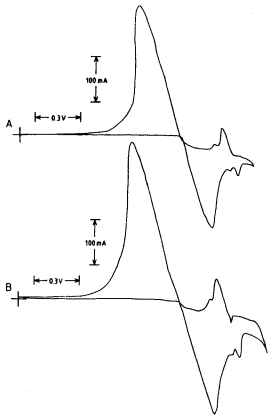

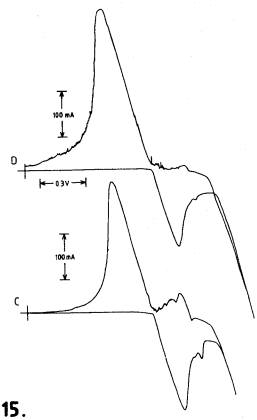

15.

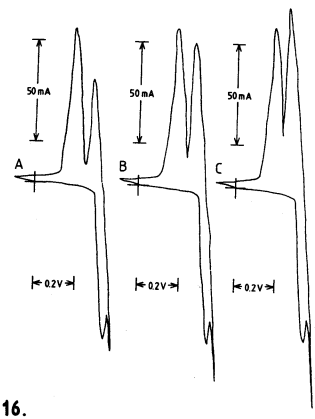

16.

Fig. 15 The effect of switching potential on the deposition of γ-phase and liquid lithium-aluminum alloy
Switching potential: A -2.70V, B -2.80V, C -2.90V, D -3.05V
Rest potential: -1.2V vs Ag/AgCl reference electrode (0.2 m/o)
Sweep rate 100 mV/sec
Electrode area 0.2 cm^2

Fig. 16 The effect of the switching potential on the stripping of lithium and potassium in the presence of dissolved lithium metal.
Switching potential: A -0.40 V, B -0.41V, C -0.42V
Rest potential: +0.6V vs LiAl reference electrode
Sweep rate: 100 mV/sec
Electrode area: 0.2 cm^2

DOI: 10.1149/198109.0180PV

SEM/EDX AND AA MEASUREMENTS OF CURRENT-INDUCED COMPOSITION GRADIENTS IN MOLTEN $NaNO_3$-$AgNO_3$

C. E. Vallet, L. M. Kidd, D. E. Heatherly, R. L. Sherman[†] and J. Braunstein

Chemistry Division
[†]Analytical Chemistry Division
Oak Ridge National Laboratory
Oak Ridge, Tennessee 37830

ABSTRACT

Scanning electron microscopy with energy dispersive x-ray fluorescence, and atomic absorption analysis, are applied to the chemical analysis of composition gradients in quenched binary mixtures of molten salts that have been electrolyzed between silver electrodes. The results demonstrate the merging of the diffusion layers from cathode and from anode, confirming the shapes of the composition profiles predicted from the ion flow analysis based on Faradaic, migrational and diffusional flows. Effective diffusion coefficients for the electrolyte contained in a porous matrix (Y_2O_3) are derived from the ratios of known electrolyte conductance and of measured conductance in the matrix. The methods are shown to be applicable to the analysis of composition gradients in molten salt battery electrolytes.

INTRODUCTION

We have previously demonstrated current-induced composition changes near the electrodes in binary mixtures of molten salts ((K, Ag)NO_3) and ((Na, Ag)NO_3) subjected to electrolysis between silver electrodes (1). In situ measurements were reported of the electrode potential difference, during diffusional relaxation back to the initial composition, after electrolysis. Sections of quenched electrolyte were analyzed by atomic absorption (AA) analysis and by scanning electron microscopy with energy dispersive x-ray fluorescence (SEM/EDX) in order to determine the shapes of the composition profiles; although the directions of the predicted composition changes were confirmed, the electrolysis times were short and the changes at the two electrodes were small and localized relatively near the electrodes (hence independent of one another). The effect of tortuosity resulting from the porous electrolyte matrix (SiO_2 frit) was found significant for

Research sponsored by the Division of Materials Sciences, Office of Basic Energy Sciences, U.S. Department of Energy under contract W-7405-eng-26 with the Union Carbide Corporation.

long time electrolysis, but difficult to correct because of differing porosities from one silica frit to another; an average tortuosity coefficient was therefore used in the calculations. In this paper we present the results of new experiments, with yttria felts, carried out at electrolysis times such that the diffusion layers from the two electrodes are predicted to merge and interact. The more porous yttria felt matrices are better suited to SEM/EDX analysis since they provide more closely spaced salt-filled regions for scanning, and have reproducible porosity from one sample to another. We also present measurements of electrical conductance of electrolyte-filled Y_2O_3 matrices from which, with the measured matrix porosity and literature values of free electrolyte conductance, the effective diffusion coefficient in the matrix is derived.

EXPERIMENTAL

The cell, electrolysis and quenching techniques, cutting of quenched samples for leaching and AA analysis or for SEM/EDX scanning have been described previously (1,2). Porosities of 1 to 6 Y_2O_3 felts placed in an electrolysis cell were determined by weighing in air, again after filling with salt and again by weight loss (of salt) in successive leachings. Electrical conductance of the salt-filled felts was obtained from measurements of the IR drop across the Ag electrodes of the electrolysis cell immediately following imposition of a known constant current. Electrode separations were between 0.1 and 0.6 cm, and the current was between 0.1 and 100 mA cm^{-2}.

RESULTS

Effective Diffusion Coefficient

The conductance results obtained at 300°C are summarized in Fig. 1. The observed IR drop is proportional to current at fixed electrolyte thicknesses as shown by the dotted lines in Fig. 1; the conductivities of 0.2 $AgNO_3$–0.8 $NaNO_3$ contained in yttria felts of differing thickness, κ_f, are shown as the large filled points, whose mean, $0.62_9 \pm 0.039\ \Omega^{-1}\ cm^{-1}$, is the solid horizontal line. The conductivity of the free electrolyte, κ_o, at the same temperature is $0.962_3\ \Omega^{-1}\ cm^{-1}$ (3). The porosity (volume fraction of voids), ε, measured on the seven cells used for conductance measurements is 0.90 ± 0.02. A systematic small increase in the apparent porosity is observed as the number of felt discs increases. The tortuosity coefficient, τ, is esti-

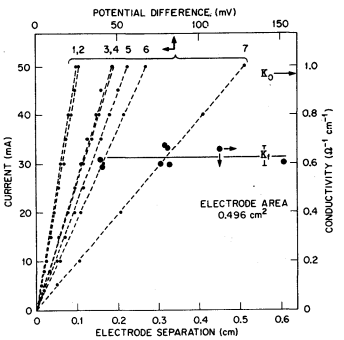

Fig. 1.

Current-Voltage Curves and Conductivity at 300 °C of 0.8 $NaNO_3$ 0.2 $AgNO_3$-Y_2O_3 Felts for Differing Electrode Separations. Separation/cm: 1, 0.157; 2, 0.159; 3, 0.316; 4, 0.322; 5, 0.328; 6, 0.449; 7, 0.610.

mated (4,5) from the measurements of conductivity and of porosity.

$$\tau = \sqrt{\varepsilon \frac{K_o}{K_f}} \quad .$$

The effective diffusion coefficient, D_{eff}, is calculated (5) from the diffusion coefficient in the free electrolyte (6), D.

$$D_{eff} = 0.726\ D$$

In less porous silica frits, with a porosity of 0.4 and a conductivity of the order of 0.2 Ω^{-1} cm^{-1}, the effective diffusion coefficient was estimated (2) to be half the free electrolyte diffusion coefficient. The effect of the correction on the predicted composition profiles in a silica frit is shown in Fig. 2; correspondence of the predicted composition profile to data obtained by SEM/EDX analysis is improved by the correction.

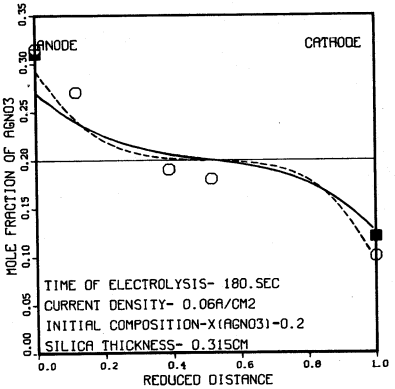

Fig. 2. Experimental and Predicted Profiles: OSEM/EDX; ■ Potentiometry; — calculated with τ=1; --- calculated with τ=1.41.

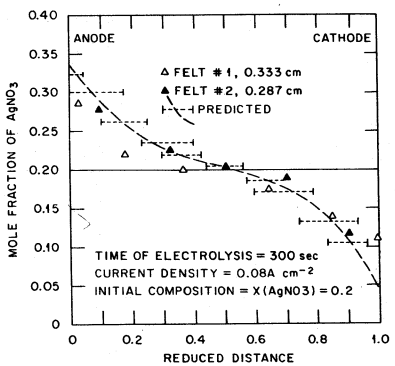

Fig. 3. Composition Profile, A.A analysis in felts #1 and #2; --- calculated with the measured tortuosity.

Atomic Absorption Analysis

Sections of quenched electrolyte with an average thickness of 0.04 cm are analyzed by atomic absorption spectroscopy for sodium and for silver content. Potassium nitrate (2000μg cm^{-3} of potassium) is added to the solution in order to provide enough ions to the flame while silver and sodium stay in an atomic state (7). Figure 3 shows the results of AA analysis of a cut section of quenched electrolyzed samples of two felts, of nearly the same thickness, under identical conditions such that the diffusion layers between the electrodes were predicted to merge and interact. The triangles are the AA results. The dashed line is the predicted composition profile (incorporating the porosity correction), and the horizontal bars indicate the location, thickness and predicted average composition of the analyzed sec-

tions. Results in felt 2 are all within 4% of the predictions. Results in felt 1 appear systematically slightly lower. The other half of these two felts is also analyzed by SEM/EDX. The results clearly indicated the merging of the diffusion layers, but the distance resolution is limited because of the thickness of the saw blade (0.015 cm) and loss of material between cut sections. In order to obtain better resolution, the subsequent effort was devoted to SEM/EDX analysis.

Scanning Electron Microscopy with Energy Dispersive X-ray Fluorescence

The advantage of the SEM/EDX analysis for distance resolution in the composition profiles is indicated in Fig. 4, which shows a section of quenched electrolyzed felt cut perpendicular to the electrodes. Some 70 points are shown over a distance of about 0.3 cm. With 21 keV electrons, the penetration depth is 1-2μm (8) and the overall distance resolution is about 10μm in our measurements made with a magnification factor of 200. The areas scanned are about 3×10^{-6} cm^2. These dimensions permit sampling of regions small enough to give good distance resolution in a diffusion gradient, but large enough to provide local "bulk" compositions averaged over microcrystals of individual salts, and to avoid spurious details of the outermost atom layers and the weighting of pores near the surface from which salt may have been gouged in a nonuniform manner during cutting.

Quantitative measurements require careful calibration with standards of compositions bracketing those in the electrolyzed samples, and prepared in an identical manner. Typical spectra at the cathode and anode surfaces are shown in Fig. 5. The Ag/Na count ratios (integrated peak areas) clearly indicate the expected enrichment in Ag at the anode and depletion at the cathode, but also the much higher sensitivity to silver than to sodium.

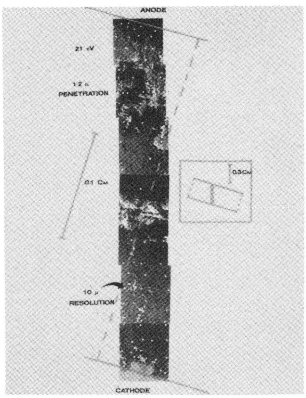

Fig. 4. Electron micrograph of felt #2; magnification, 200.

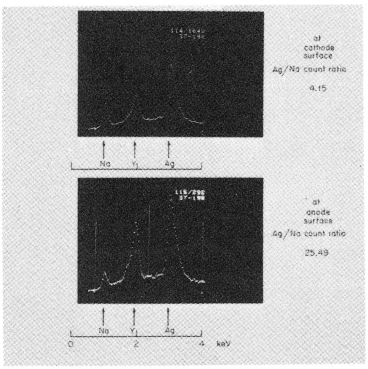

Fig. 5. Energy Dispersive X-Ray Spectra Near Electrode Surfaces in Electrolyzed Felt #2.

Figure 6 shows the measured count ratios for a series of $AgNO_3$-$NaNO_3$ standards contained in yttria felts. The bars show the dispersion in 20-25 determinations. The tilt angle of all standards was 30-32°. The calibration curve shown in solid line includes correction for the variations in depth of penetration of the electron beam into the sample (Z), the absorption of the x-ray by the sample (A) and secondary fluorescence enhancement of lighter elements by heavier ones (F). The three factors, ZAF, are computed from the atomic properties using the FRAME program (9,2). The normalization factor of 3.17 computed to obtain the smallest standard deviation (1.5 Ag/Na count ratio) from the experimental data is consistent with the value of $I°_{Ag}/I°_{Na} = 2.55 \pm 0.3$ measured on pure silver sheet and on NaCl optical grade monocrystal at 32° tilt angle.

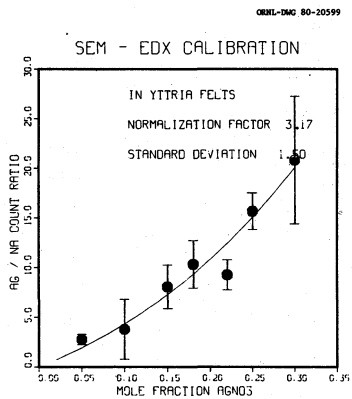

Fig. 6. Calibration Curve, Standards Contained in Y_2O_3 Felts.
Ag/Na Count Ratio with Observed Dispersion.
— Calculated from the ZAF Factors.

Figures 7a and b show the SEM/EDX results of felts #1 and 2, respectively, for which AA results are shown in Fig. 3. The points are the data, with no smoothing, and the dashed predicted curve is superimposed. The same data are shown in solid line as a seven point moving average to smooth out some of the fluctuation. Even with this smoothing, the distance resolution is better than 0.005 cm. In Fig. 7a triangles are results of AA analysis of quenched sections. Results from both analyses on felt #1 are consistent, but deviate systematically from the predictions. The discrepancy between the areas above

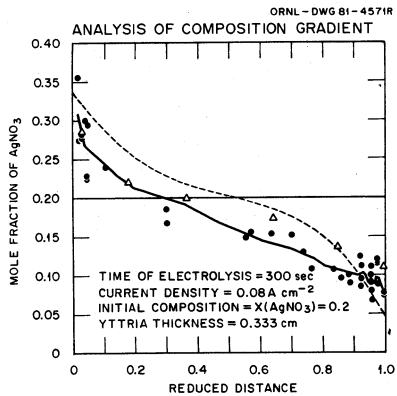

Fig. 7a. Composition Profile in Felt #1. • SEM/EDX; Δ A.A; — smoothing of SEM/EDX data; --- predicted profile.

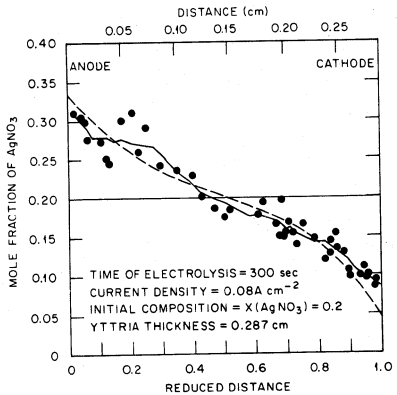

Fig. 7b. Composition Profile in Felt #2. • SEM/EDX; — smoothing of SEM/EDX data; --- predicted profile.

and below the initial (average) composition suggests that an error in the initial composition of the melt might have occurred. SEM/EDX measurements in felt #2, shown in Fig. 7b, confirm the entire predicted composition profile calculated with a correction for porosity of the yttria electrolyte matrix. The standard deviation between measured compositions and predicted is 0.02 mole fraction of $AgNO_3$.

Figure 8 shows the EDX measurements made in felt #3 near anode and near cathode. The conditions of electrolysis lead, in this case, to two nearly independent diffusion layers. The middle part of the felt fragmented during the preparation of the sample for SEM/EDX analysis. Table 1 gives a summary of the AA results for the other half of the same felt.

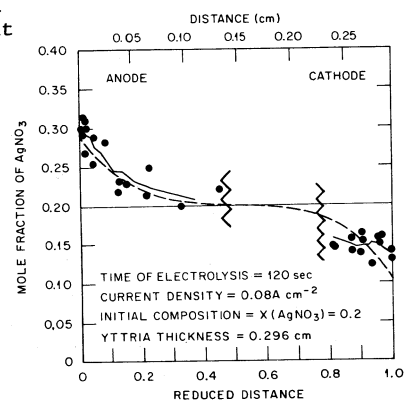

Fig. 8. Composition Profile in Felt #3. • SEM/EDX; — smoothing of SEM/EDX data; --- predicted profile.

Table 1. Concentration of silver nitrate in sections of an electrolyzed felt (#3) from Atomic Absorption Spectroscopy Analysis. Felt thickness: 0.296 cm; $\bar{X}_{AgNO_3}$ = 0.2; time of electrolysis 120 sec; current density = 0.08 A cm^{-2}

Section No.	Thickness (cm)	distance of midpoint from anode (cm)	X_{AgNO_3} From Ag analysis	From Na analysis	From Both	Predicted
1	.013	.0065	.236	.256	.244	.267 (9%)
2	.030	.0430	.224	.232	.227	.234 (3%)
3	.051	.0985	.202	.218	.207	.208 (0.5%)
4	.066	.1720	.194	.181	.190	.197 (3.6%)
5	.048	.2440	.186	.158	.177	.175 (1.1%)
6	.013	.2895	.155	.136	.150	.130 (14.3%)

The comparison of the results obtained by the two methods shows clearly the advantages of using SEM/EDX in analysis of composition gradient in battery electrolytes. Sections 1, 2, and 3 cover the felt thickness near the anode for which 20 determinations are accumulated by the SEM/EDX measurements. Section 6 and part of section 5 are included in the cathodic layer for which 13 SEM/EDX measurements are shown in Fig. 8. In this case, only SEM/EDX measurements can ascertain the shape of composition profile near the electrodes.

Further improvements in reducing the dispersion of the SEM/EDX measurements may be possible. This dispersion may include contributions from incomplete filling of pores, dead end pores and nonuniform current distribution. It is important to ascertain these factors for SEM/EDX analysis of the electrolyte in molten salt batteries, e.g., LiAl/LiCl-KCl/FeS_x (10).

CONCLUSIONS

Electrolyte composition profiles have been measured from anode surface to cathode surface for merged diffusion layers resulting from electrolysis, as well as for independent diffusion layers. Both atomic absorption analysis (AA) of sections of quenched electrolyte, and scanning electron microscopy with energy dispersive x-ray fluores-

cence (SEM/EDX), have been used. The SEM/EDX analysis has been shown to have comparable precision to AA (5-6%) with far better distance resolution for the profile. Measurements of porosity and of electrical conductance of salt filled Y_2O_3 provided porosity corrections to the diffusion coefficients in the predicted composition profiles. The measured profiles confirm the predictions in $NaNO_3$-$AgNO_3$ electrolyzed between Ag electrodes, with no adjustable parameters used in the calculation.

ACKNOWLEDGEMENTS

This work was supported by the Division of Materials Sciences, Office of Basic Energy Sciences, U.S. Department of Energy under contract W-7405-eng-26 with the Union Carbide Corporation.

We are pleased to acknowledge the advice and suggestions of Dr. L. D. Hulett, Analytical Chemistry Division, in the use of SEM/EDX technique for quantitative measurements.

L. M. Kidd was a SCUU student from Centre College, Danville, Kentucky.

REFERENCES

1. C. E. Vallet, D. E. Heatherly and J. Braunstein, J. Electrochem. Soc. 127, 1(1980).

2. C. E. Vallet, D. E. Heatherly, R. L. Sherman and J. Braunstein, (in preparation).

3. J. Byrne, M. Fleming and F. E. W. Wetmore, Can. J. Chem. 30, 922 (1952).

4. J. Newman and T. Tiedeman, "Advances in Electrochemistry and Electrochemical Engineering", Vol. 11, H. Gerisher and C. W. Tobias, editors, Wiley-Interscience, (1977).

5. R. E. Meredith and C. W. Tobias, "Advances in Electrochemistry and Electrochemical Engineering", Vol. 2, C. W. Tobias, editor, Wiley-Interscience (1962).

6. J. Richter, Ber. Bunsenges Physik. Chem. 80, 92(1976).

7. W. P. Kilroy and C. T. Moynihan, Anal. Chim. Acta. 83, 389(1976).

8. L. Curgenven and P. Duncumb, Tube Investments Research Labs Report 303 (1971).

9. H. Yakowitz, R. L. Myklebust, and K. F. J. Heinrich, NBS Technical Note 796, Government Printing Office, Washington, D. C. (1973).

10. J. Braunstein, S. Cantor and C. E. Vallet, "Physical Chemistry of Molten Salt Batteries, Final Report for Period October 1, 1979-September 30, 1980, Current Induced Composition Gradients in Molten LiCl-KCl", ORNL-TM-7639 (1981).

DOI: 10.1149/198109.0188PV

EVALUATION OF THE SINGLE AND DOUBLE PULSE GALVANOSTATIC RELAXATION TECHNIQUES FOR THE MEASUREMENT OF THE KINETICS OF FAST ELECTRODE REACTIONS IN MOLTEN SALTS

Z. Nagy

Argonne National Laboratory
Chemical Engineering Division
Argonne, Illinois 60439

ABSTRACT

It is shown that the maximum measurable standard heterogeneous rate constant is not a sufficient indication of the limitation of a relaxation technique. The errors of the measurement, and consequently the limits of applicability, can only be described generally by certain characteristic times of the electrode system. These are τ_c, the time constant of the double layer capacitance--reaction resistance system and τ_d, the time constant of the diffusion impedance--reaction resistance system. A graphical representation of the field of applicability of a technique is introduced using the log κ *vs* log τ_c diagram, where κ, the rate constant parameter, is equal to $(\pi/4\tau_d)^{1/2}$. Within the field of applicability, the technique can be used to obtain the exchange current density with an error of less than $\pm$20%. Such a representation is completely general and can be useful for a meaningful comparison of all relaxation techniques. Such diagrams are presented for the single and double pulse galvanostatic techniques, with data evaluation by graphical and computer curve-fitting methods. The comparison of the two evaluation methods reveals the general superiority of computer curve-fitting, which extends the field of applicability for both relaxation techniques to about one order of magnitude faster reactions. Comparison of the single and double pulse techniques reveals the superiority of the latter for fast reactions, the improvement being about one order of magnitude in the measurable κ (equivalent to one order of magnitude faster reactions).

The electrochemical reactions that occur in a high-temperature molten salt medium are usually much faster than similar reactions in aqueous solutions. Therefore, special care is needed in the selection of the experimental approach to study the kinetics and mechanism of these reactions. Among the *dc* relaxation techniques, the double pulse galvanostatic technique has usually been considered to be the most useful for the measurement of fast electrode reactions, because it is applicable to reactions having a rate constant about one order of magnitude larger than that measurable by other techniques (1,2). The technique has been used to examine a number of systems, see for example Refs. (3-5). However, Sluyters and coworkers (6-8) recently concluded that, because of experimental difficulties, the double pulse technique is not better for the measurement of fast reactions than the single

pulse technique. The difficulty arises because the original theory of the double pulse technique requires the measurement of the overpotential immediately after the end of the first pulse, but at the end of a fast galvanostatic pulse the potential response is distorted by an inevitable inductive spike and some ringing caused by the impedance mismatch between the cell and the leads. It is therefore of interest to review the literature of the single and double pulse galvanostatic techniques and to compare their field of applicability under conditions as similar as possible.

The theory of the galvanostatic relaxation technique was developed by Berzins and Delahay (9), who derived an exact analytical expression to describe the variation of the electrode potential following the application of an instantaneous constant-current pulse. However, they found the resulting equation too complicated for a straightforward calculation of the exchange current density. Therefore, they simplified the equation to allow a graphical analysis of the data, and estimated that the simplification is acceptable if data taken at long times (t_ℓ > 50 μs) are used. Delahay (2) estimated that, under these conditions, the method will be applicable for reactions with standard heterogeneous rate constants not exceeding 0.2 cm s^{-1}. The conditions and limits of the graphical data-analysis method have been reexamined by several authors (10-12) who have suggested applicability limits in terms of rate constants ranging from 0.015 to 2 cm s^{-1}. The limitations of this evaluation method are caused not only by the restriction of the usable time range but also by the fact that knowledge of the double layer capacitance and the diffusion coefficient of all reactants and products is required for the calculation of the exchange current density. Kooijman and Sluyters (13) suggested a new data-evaluation method based on numerical tables, which eliminates the time restriction of the data. They estimated that their evaluation method will increase the limit of applicability of the single pulse technique by a factor of three. Kooijman extended the idea still further by suggesting the use of nomograms (14) and computer curve-fitting (15) for data evaluation. The last two methods have the additional advantage that the values of the double layer capacitance and the diffusion coefficients are not needed; on the contrary, they, along with the value of the exchange current density, are potentially determinable from the experimental data. Daum (16) also suggested the use of the computer curve-fitting method and compared results obtained from this method with those of the current impulse relaxation technique; however, his comparison was inconclusive. Recently, Nagy (17) carried out a detailed error analysis of the curve-fitting method which he compared to the graphical data-evaluation method and concluded that it extends the field of applicability of the single pulse technique to about one order of magnitude faster reactions.

The galvanostatic double pulse technique was developed by Gerischer and Krause (18) and Matsuda, Oka, and Delahay (19) as an improved galvanostatic relaxation technique. A high-current, short-duration prepulse is applied, before the measuring pulse, to charge the

double layer of the electrode. As a consequence, the technique can be used to make kinetic measurements at times short enough to avoid the disturbing diffusional effects before they become overwhelming. The theory of the original technique required that the prepulse be adjusted to produce a minimum in the overpotential--time curve exactly at the end of the prepulse. Recently, Nagy (20) developed a modified theory of the technique which takes into account the experimental fact that exact potential values can not be measured for a short time immediately after the prepulse. Consequently, he extended the theory of the technique to the case where the minimum in the overpotential curve appears after the prepulse, at a time when exact potential measurements are possible. Two specific cases were investigated: $t_m = t_3 + \Delta t$ and $t_m = qt_3$ where Δt and q are kept constant within a series of measurements. Furthermore, he showed that, for experimental reasons, the ideal case of $t_m = t_3$ can never be achieved and that all previous applications of the technique have probably used the method in which $t_m = t_3 + \Delta t$. This case will henceforth be called the unmodified technique, whereas the case of $t_m = qt_3$ will be called the modified technique. Nagy (20) also demonstrated that, while the unmodified double pulse technique is not better, in general, than the single pulse technique, the modified one is. Recently, he (21) proposed a method for curve-fitting data evaluation of the double pulse technique, which further increases its field of applicability.

In this communication, the error analyses of the most commonly used graphical data-evaluation methods and the most advanced computer curve-fitting methods for the single and double pulse galvanostatic relaxation techniques are reviewed in detail.

THEORY

Basic Equations. The equation describing the relaxation of the electrode potential following the application of a single galvanostatic pulse has been derived by Berzins and Delahay (9), and for the double pulse case by Matsuda, Oka, and Delahay (19), by solving Fick's differential equation for linear diffusion under appropriate initial and boundary conditions. To establish the limitations of the techniques, it is useful to recall all assumptions made in the derivations. It was assumed that the current is *a priori* separable into two independent components, the double layer charging current and the faradaic current; *i.e.*, the double layer capacitance is independent of the electrode potential and the solution composition within limits of the experiment. The solution was assumed to contain a sufficient concentration of supporting electrolyte to allow the faradaic current to be equated with the diffusion rate of the reactant to the surface of the electrode. It was assumed that the applied current pulse is of such magnitude that the current density-overpotential relation can be linearized, thereby limiting the overpotential to a few millivolts. Double layer and adsorption effects were neglected.

Let us consider a generalized redox reaction, O + ne = R, which can take place in any number of chemical and electrochemical elementary steps. Assume that one of the steps is rate determining and that none of the intermediate species is lost by diffusion into the bulk solution. Using the appropriate multi-step Butler-Volmer equation (22-24), the overpotential relaxation for the double pulse technique is given by

$$\eta = \frac{i_1}{c(b-a)}\left[\frac{b}{a^2}G_1(a,t) - \frac{a}{b^2}G_1(b,t)\right] - \frac{i_1 - i_2}{c(b-a)}\left[\frac{b}{a^2}G_1(a,t-t_3) - \frac{a}{b^2}G_1(b,t-t_3)\right] \quad [1]$$

where

$$G_1(x,y) = \exp(x^2y)\,\mathrm{erfc}(xy^{1/2}) + 2x(y/\pi)^{1/2} - 1 \quad [2]$$

$$a = \frac{i_o}{2\nu nF}\left(\frac{1}{D_O^{1/2}C_O} + \frac{1}{D_R^{1/2}C_R}\right) + \left[\frac{i_o^2}{4\nu^2n^2F^2}\left(\frac{1}{D_O^{1/2}C_O} + \frac{1}{D_R^{1/2}C_R}\right)^2 - \frac{nFi_o}{\nu RTc}\right]^{1/2} \quad [3]$$

and "b" is the same as "a" except the expression in brackets is preceded by a minus sign.

For the single pulse technique, the second term in Eq. [1] should be ignored. In this case, when the argument of the exponential error function is large, its value becomes negligibly small and the overpotential can be approximated as:

$$\eta = i\left[\frac{\nu RT}{nFi_o} - \frac{R^2T^2c}{n^4F^4}\left(\frac{1}{D_O^{1/2}C_O} + \frac{1}{D_R^{1/2}C_R}\right)^2 + \frac{2RT}{\pi^{1/2}n^2F^2}\left(\frac{1}{D_O^{1/2}C_O} + \frac{1}{D_R^{1/2}C_R}\right)t^{1/2}\right] \quad [4]$$

This equation forms the basis of the graphical data analysis: i_o is determined from the intercept of an $\eta - \sqrt{t}$ plot.

For the double pulse case, Eq. [1] has to be simplified again to allow a simple graphical evaluation of the data. In this case, a series of experiments is carried out using different prepulse lengths and observing the minimum in the overpotential--time curve with the prepulse current adjusted so as to keep a fixed relation between the

end of the prepulse and the time of the minimum overpotential, as discussed earlier. The overpotential can then be calculated from the intercept of the $\eta_m - \sqrt{t_3}$ plot, using the equation

$$\eta_m = \frac{\nu RT i_2}{nF i_o}\left[1 + A\,\frac{i_o}{\nu nF}\left(\frac{1}{D_O^{1/2}C_O} + \frac{1}{D_R^{1/2}C_R}\right)t_3^{1/2}\right] \qquad [5]$$

Equation [5] results from Eq. [1] using a small- or large-argument expansion of the exponential error function terms. As was shown in Ref. (20), the value of A depends on which approximation is used and whether the unmodified or the modified technique is used.

The above equations assume an ideal pulse shape, which is equivalent to a galvanostat having zero rise-time. In reality, galvanostats have a finite rise-time, and modern instruments can be approximated assuming linear rise-times (constant slew rate), resulting in pulses as shown in Fig. 1. An equation equivalent to Eq. [1] can be derived for this case (24):

$$\eta = \frac{i_1}{ct_1}\left[G_2(t) - G_2(t - t_1)\right] - \frac{i_1 - i_2}{c(t_3 - t_2)}\left[G_2(t - t_2) - G_2(t - t_3)\right] \qquad [6]$$

where

$$G_2(y) = \frac{b}{a^4(b - a)}\,G_1(a,y) - \frac{a}{b^4(b - a)}\,G_1(b,y) + \frac{ab - (a + b)^2}{(ab)^2}\,y + \frac{4(a + b)}{3\sqrt{\pi}\,ab}\,y^{3/2} \qquad [7]$$

Equation [6] is for the double pulse case; for single pulses, the second term of the equation should be ignored.

Error Analysis in Terms of Time Constants. The three quantities that are potentially determinable with these techniques are the ratio of the exchange current density to the stoichiometric number (i_o/ν), the diffusion parameter ($1/D_O^{1/2}C_O + 1/D_R^{1/2}C_R$), and the double layer capacitance. The first one of these is usually the main objective of the measurement, and its determination is emphasized in this communication. It should be noted that, since the technique is limited to the linear current density--overpotential range, the exchange current density cannot be directly determined from a simple measurement, but that the determinable quantity is the ratio of the exchange current density to the stoichiometric number. Hence, for the sake of simplicity, the term "exchange current density" will refer to the i_o/ν ratio in the following discussion, unless it is specifically stated to be i_o.

The errors of the techniques can be conveniently divided into systematic and random errors. The systematic errors are caused by the inadequacy of the mathematical simplifications of Eqs. [4-5]* and the nonideality of the current pulse (finite rise-time of the pulse generator). The random errors include those of the measurement of the current density, potential, and time. In this discussion the errors of the measurement of potential and time are combined, *i.e.*, it is assumed that the error of a potential-time data pair is due to the measurement of the potential only. This error also includes the error of the correction or compensation of the *ir* drop between the working and reference electrodes.

Although it has been customary (1,2,9-12) to express the limitation of the techniques as the largest measurable first-order heterogeneous rate constant, an inspection of the basic equations immediately reveals that the determination of the exchange current density is influenced not only by the magnitude of k_o but also by many other parameters. Kooijman and Sluyters (13) have suggested the rewriting and analysis of the basic equations in terms of two dimensionless parameters involving the quantities "a", "b", and "t_ℓ". While this is a useful approach, it seems more appropriate, from the standpoint of obtaining a clear physical picture, to express the errors as a function of certain characteristic times of the electrode system and the length of the measuring pulse.

The system under consideration can be described by an electrical analog of series-coupled reaction resistance and diffusion impedance, both being shunted by the double layer capacitance. Neglecting one of these components at a time, one can obtain three simple time constants. Only two of these are, of course, independent, and it is convenient to select

$$\tau_c = \frac{\nu RTc}{nFi_o} = \frac{1}{ab} \qquad [8]$$

and

$$\tau_d = \frac{\pi \nu^2 n^2 F^2}{4i_o^2 \left(\frac{1}{D_O^{1/2} C_O} + \frac{1}{D_R^{1/2} C_R} \right)^2} = \frac{\pi}{4(a+b)^2} \qquad [9]$$

Here, τ_c is the well known *rc* time constant of the double layer capacitance--reaction resistance system (neglecting the diffusion impedance) and is defined by

$$\eta = \frac{\nu RTi}{nFi_o} \left[1 - \exp\left(- \frac{t}{\tau_c} \right) \right] \qquad [10]$$

* It is assumed that all assumptions forming the basis of Eq. [1] are strictly fulfilled.

And, τ_d is the time constant of the reaction resistance--diffusion impedance system (neglecting the double layer capacitance) defined by (25)

$$\eta = \frac{\nu RTi}{nFi_o}\left[1 + \left(\frac{t}{\tau_d}\right)^{1/2}\right] \qquad [11]$$

As indicated by Eq. [11], at $t = \tau_d$ the activation and diffusion parts of the total overpotential are equal.

The measurement time is not only important because it affects the validity of the approximate equations. In the analog circuit of the electrode, two of the impedances, (the double layer capacitance and the diffusion impedance) are frequency dependent; hence different impedances may become dominant at different times during a pulse. For the determination of the exchange current density, it is preferable to select measuring times when the reaction resistance is dominant.

Applicability Diagram. The experimenter has full control over the pulse length although the values of τ_c and τ_d can also be varied somewhat through the control of concentrations and temperature. It is therefore practical to describe the limits of a technique as a function of τ_c and τ_d while using reasonable values for the length of the measuring pulse. It is convenient to use the parameter κ, called the rate constant parameter, in place of τ_d. They are simply related:

$$\kappa = \left(\frac{\pi}{4\tau_d}\right)^{1/2} = \frac{i_o}{\nu nF}\left(\frac{1}{D_O^{1/2}C_O} + \frac{1}{D_R^{1/2}C_R}\right) \qquad [12]$$

The advantage of the rate constant parameter is that it can be directly related, under simplified conditions, to the first-order standard heterogeneous rate constant. If one assumes that $D_O = D_R = D$, $C_O = C_R$ and $\nu = 1$, then $\kappa = 2k_o/\sqrt{D}$; and for $D = 10^{-5}cm^{-2}\ s^{-1}$, $\kappa = 632k_o$.

From the results of an error analysis, a diagram of κ *vs* τ_c can be constructed on a log-log scale, and a field of applicability of the technique can be defined such that if an electrode reaction system falls within the limits of this field, its exchange current density is determinable with less than a given error. The error limit was set to $\pm$20% in this work. For example, diagrams of log κ *vs* log τ_c are shown in Fig. 3. A description of some general features of this type of representation is needed. The main scales (log κ and log τ_c) are exact and valid for any combinations of the parameters they contain; under general conditions, only these scales can be used to define the position of an electrode system on the diagram. There are also three approximate, auxiliary scales shown (i_o, k_o, and C). These are convenient because they define a system with familiar parameters, but they are exact only under restricted conditions. The exchange current

density scale assumes that $c = 20\ \mu F\ cm^{-2}$, $T = 298$ K, and $n = \nu = 1$. The concentration scale further assumes that $D_O = D_R = 10^{-5}\ cm^2\ s^{-1}$ and $C_O = C_R = C$. All these restrictions apply to the k_o scale.

ERROR ANALYSIS

The following method was used to determine the errors of the data evaluation methods. "Synthetic" data were generated using Eq. [1] for a large range of values for the parameters. These data were then treated as experimental data and the exchange current density calculated by the different evaluation methods. The "known" and "calculated" exchange current densities were then used to calculate the relative error of the determination. Both the data generation and evaluation were carried out with a digitial computer.

To determine the effect of the accuracy of the overpotential measurements, the synthetic data were rounded off either to the nearest tenth or to the nearest hundredth of a millivolt, thereby creating data sets with $\pm 50\ \mu V$ and $\pm 5\ \mu V$ random errors. A 50 μV accuracy can be achieved by the best analog oscilloscopes, and the 5 μV accuracy is available with some digital oscilloscopes. The error of the measuring current density was determined by offsetting the value of the measuring current density used in the data generation and that used in the data evaluation.

Single Pulse: Graphical Data-Evaluation Method. The basis of the method is Eq. [4]: the exchange current density can be calculated from the intercept of the $\eta - \sqrt{t}$ plot if one knows the values of the double layer capacitance and the diffusion parameter. For these calculations, the known value of the double layer capacitance was used and the diffusion parameter was calculated from the slope of the $\eta - \sqrt{t}$ line. To determine the intercept, fifty data points, uniformly distributed within the measuring time, were generated. The first point was taken at 0.1 μs, and the last ten points were used to define (by a least-squares fit) the $\eta - \sqrt{t}$ line.

By using the time constants, the preferred length of the measuring pulse can immediately be established. For the determination of the exchange current density, it is required that $\tau_c < t_\ell < \tau_d$. At shorter times, most of the current flows through the double layer capacitance, and at longer times, the diffusion overpotential is overwhelmingly larger than the activation overpotential. In either case, the information content of the data, with regard to the exchange current density, (that is, the "kinetic content") is small. Therefore, the requirement $(\tau_d/\tau_c) > 1$ should be fulfilled by the electrode system to permit the meaningful measurement of the exchange current density. This ratio increases as the exchange current density decreases and/or the concentrations increase, other variables remaining constant. It is also obvious that the simultaneous determination of the exchange current density and the double layer capacitance or the diffusion parameter is

not necessarily possible from the same set of data. The determination of the double layer capacitance requires $\tau_c > t_\ell$ whereas determination of the diffusion parameter requires $\tau_d < t_\ell$. It remains to be established how strictly these conditions have to be fulfilled to obtain acceptable results.

A series of calculations was made to determine the effect of the τ_d/τ_c and τ_c/t_ℓ ratios on the error. These ratios were selected on the basis of the criterion that $\tau_c < t_\ell < \tau_d$; furthermore, the systematic error caused by the inadequacies of the mathematical approximations used to derive Eq. [4] is expected to be a function of τ_c/t_ℓ (12). The results are shown in Figs. 2a and 2b for the cases of 50 μV and 5 μV accuracy, respectively. Because of the statistical nature of the extrapolation procedure, there was some spread of the actual data points around the lines shown on the figures. The spread was only a few percent around the solid lines, but in some instances was as large as many tens of percents around the dashed lines.*

It is clear from Figs. 2a and 2b that the useful range of the pulse length (with respect to τ_c) increases as τ_d/τ_c increases. As this ratio becomes small, the useful time range of the experiment decreases to such an extent as to preclude making a practical measurement. The difficulty is enhanced because an estimate of the exchange current density is needed to select the correct length of the pulse. The cut-off point is somewhat subjective; for present purposes it was set to $\tau_d/\tau_c = 100$ for the 50 μV case, and $\tau_d/\tau_c = 10$ for the 5 μV case.

The lower limit of the measuring time is determined by the error resulting from the neglect of the exponential error function terms in Eq. [1]. Although it has been stated earlier that $t_\ell > \tau_c$ is preferred to increase the kinetic content of the transient, this is not a limiting factor since long measuring times are needed anyhow to make Eq. [4] a good approximation. The minimum length of the pulse can be determined from Figs. 2a and 2b (for a maximum error of ±20% for the exchange current density) to be $5\tau_c$ at large τ_d/τ_c ratios, increasing to $50\tau_c$ at $\tau_d/\tau_c = 1$. These results are insensitive to the accuracy of the overpotential measurements.

The upper limit of the measuring time arises from the decrease of the kinetic content at $t_\ell > \tau_d$; this, however, is partially compensated for by the accuracy of the overpotential measurements. The product of τ_d/τ_c and τ_c/t_ℓ is constant at the upper time limit (-20% error); under this condition, at the 50 μV and 5 μV accuracy of potential measurement, the minimum τ_d/t_ℓ values are 4×10^{-2} and 1×10^{-3} and the corresponding maximum length of the pulses are $25\tau_d$ and $1000\tau_d$, respectively.

* It could be readily shown that this fluctuation was due to rounding off the synthetic data: repeating the calculations without rounding off the data produced smooth curves.

This information can now be used to construct the field of applicability of the data-evaluation method on a log κ *vs* log τ_c diagram, as shown in Fig. 3a. The solid line represents the limit for the case of 50 μV accuracy of the overpotential measurement and the dotted line extends the field to the 5 μV case. The limitation of the maximum measurable κ is calculated from the minimum τ_d/t_ℓ ratio with the assumption that the shortest practical transient is 5 μs. The sloping limit line is set by the minimum τ_d/τ_c ratio. The upper limit on the value of τ_c is determined by the onset of convection in the solution layer next to the electrode, which usually occurs at times approaching one minute (26); in Fig. 3a, the limit on τ_c is set equal to 10 s. There is also a lower limit of measurable κ that can be determined from the highest usable concentrations. Solubility limitations and the requirement for a large excess of supporting electrolyte imply that the maximum concentration probably is 10^{-2} mol cm^{-3}. (This limit is only approximate because of the approximate nature of the concentration scale.)

In principle, the highest measurable exchange current density could be limited by the highest usable measuring current density, which is, in turn, limited by the current capacity of available pulse generators and the minimum electrode area compatible with the assumption of linear diffusion. However, this factor is irrelevant, as can be shown by the following, rather conservative considerations. At the 50 μV accuracy level, the highest measurable exchange current density is 5000 A cm^{-2} according to Fig. 3a. If one requires a minimum activation overpotential of 0.5 mV (one tenth of a 5 mV overpotential), the maximum measuring current density would be 100 A cm^{-2}. This is easily achievable since electrodes with diameters as small as 0.01 cm can be used for short pulses without significant edge effects (27), and pulse generators in the few amperes range are readily available. At the 5 μV accurancy level, the measurable exchange current densities are larger, but the overpotential is smaller.

It should be emphasized that, in arriving at the field of applicability shown in Fig. 3a only two types of errors were considered, the errors caused by the inadequacies of the mathematical simplifications and the error of potential measurement. Therefore, the field of applicability is subject to the following caveats.

(i) The value of the double layer capacitance should be known with reasonable accuracy. Its value is needed to calculate the exchange current density from the intercept defined by Eq. [4]. It can be shown that the ratio of the term containing the exchange current density and the correction term containing the double layer capacitance is equal to $4\tau_d/\pi\tau_c$. Therefore, at $\tau_d/\tau_c = 1$, an error of the double layer capacitance causes an approximately equal error in the exchange current density, but at large τ_d/τ_c values this effect is negligible. Since the method is restricted to $\tau_d/\tau_c \gtrsim 10$ by other factors, the determination of the double layer capacitance is not a limiting factor.

(ii) The value of the diffusion parameter $(1/D_O^{1/2}C_O + 1/D_R^{1/2}C_R)$ should be calculated from the slope of the $\eta - \sqrt{t}$ line. It has been determined from a large number of runs that a cancellation of errors occurs in the calculation of the exchange current density. That is, the error of the exchange current density calculated with a diffusion parameter taken from the slope is always less than, or equal to, the error of the exchange current density calculated with an exactly known diffusion parameter. This is the case even when the diffusion parameter taken from the slope is grossly in error.

(iii) The rise time of the galvanostat should be short for the measurement of large exchange current densities. This effect seems independent of τ_c but depends strongly on κ. At low κ values the measurements are rather insensitive to the rise time, and values as large as 0.5 μs hardly affect the error of the exchange current density. However, in the last decade of measurable κ values, the error becomes considerable, and a rise time of 15 ns or less is required to reach the limits shown in Fig. 3a. This is not a limiting factor since instruments with such short rise times are available.

(iv) The error of the measuring current density should be relatively small. An error of the measuring current density causes a nearly equal relative error in the exchange current density, which is approximately additive to the other errors. Figure 3a was calculated for $\pm$1% error of the measuring current density. An increase of this error to $\pm$5% decreases the field of applicability only slightly.

(v) The length of the pulse should fulfill the requirements discussed above. This is relatively easy to achieve at large τ_d/τ_c ratios where the useful range is wide, but becomes increasingly difficult as τ_d/τ_c decreases. This, in effect, was taken into account when determining the minimum τ_d/τ_c ratios.

Single Pulse: Computer Curve-Fitting Data Evaluation. In this method, a multidimensional, nonlinear least-squares curve-fitting is carried out using Eq. [1] to determine the values of i_o/ν, c, and $(1/D_O^{1/2}C_O + 1/D_R^{1/2}C_R)$ which give the best fit between the measured and calculated overpotential--time curves. Similar data-analysis methods are well known for coulostatic transients (28-30). The advantages of this method are (i) that all data points, not only those at long times, are considered (ii) exact values of the double layer capacitance and the diffusion coefficients are not required, and (iii) systematic errors due to mathematical simplifications of the basic equation will obviously not occur. One would expect, therefore, that this method will result in a more exact determination of the exchange current density and extend the field of applicability of the technique.

Synthetic data were generated and analyzed at various κ levels, with varying τ_c values. Subsequently, the error of the exchange current density determination was investigated in terms of the following

variables: the accuracy of the initial guesses, the accuracy of the overpotential measurements, the number of data points used in the calculations, the rise time of the galvanostat, and the error of the measuring current density. The τ_c/t_ℓ and τ_d/t_ℓ ratios also affect the results, but these effects are accounted for by the initial guesses (see discussion below). The details of the curve-fitting calculations are given elsewhere (17,21).

The curve-fitting program requires that starting values of the exchange current density, the diffusion parameter, and the double layer capacitance be estimated by the experimenter. It is desirable that these initial guesses be as close as possible to the actual values of these parameters because large differences increase the chance that the program will find a local, rather than the absolute, minimum and give erroneous results. To simulate the application of the method to actual experimental data, the initial guesses were used not only to start the iteration but also to calculate τ_c and τ_d and to set the value of the pulse length according to fixed rules. As has been discussed before, the ideal conditions for the measurement are $\tau_c < t_\ell < \tau_d$. To satisfy these conditions as closely as possible, the following rules were established: $t_\ell = 10\tau_c$, if $\tau_d > 10\tau_c$; $t_\ell = \tau_d$, if $\tau_c < \tau_d < 10\tau_c$; $(\tau_c+\tau_d)/2$ if $\tau_c > \tau_d$. An incorrect set of initial guesses, therefore, will not only start the iterations at a value very far from the absolute minimum, but also may result in a set of data points having little kinetic content. For the establishment of the field of applicability of the method, all combinations of the possible positive and negative errors were examined, and the combination giving the largest errors was used to establish the maximum allowable error in the initial guesses. The curve-fitting method was found to be very sensitive to the error of the initial guesses. The field of applicability of this method is shown on Fig. 3b for the case where the guesses of the exchange current density, the diffusion coefficients (the concentrations are assumed to be exactly known), and the double layer capacitance were all within a factor of two of their true values. For factor values of 2, 1, 1 (i_o/ν, D, and c, respectively) the field is not considerably larger. For factor values of 10, 10, 3 the field of applicability is somewhat smaller than that shown on Fig. 3a for the graphical data-evaluation method, and for the case of 100, 10, 3 the method is practically useless. The initial guesses can be obtained within the desired limits by using the graphical data-analysis method.

Increasing the accuracy of the overpotential measurements from 50 μV to 5 μV reduces the error of the exchange current density determination and increases the field of applicability by about one unit on the log τ_c scale at all κ values and at all levels of accuracy for the initial guesses (dotted line in Fig. 3b).

Fifty data points, evenly distributed in the time of the measurement, were used in the computer runs defining Fig. 3b. The first point was always taken at 0.1 μs to assure that all initial

distortions of potential are avoided. Fifty is probably the maximum number of points obtainable with an analog oscilloscope, while thousands could be obtained with a digital scope. Increasing the number of points over 50 did have some beneficial effect (decreasing the error sometimes by as much as a factor of two) but at a price of drastically increasing computing times. The time requirements increased from seconds to minutes by going from 50 to 200 points and increased to around an hour at 2000 points.

The curve-fitting method is very sensitive to the rise time of the galvanostat, independent of the κ value. To achieve the field of applicability shown in Fig. 3b, the rise time must not be longer than 15 ns. Increasing the rise time to 0.1 µs decreases the field of applicability by about one unit of log τ_c at all κ values; at a rise time of 0.5 µs, the method is practically useless.

The field of applicability is relatively insensitive to the error of the measuring current density. Figure 3b was calculated for $\pm$1% error of the measuring current density; an increase of the error to $\pm$5% decreases the field of applicability only slightly.

The accuracy of the determination of the exchange current density can be compared for the two methods of data evaluation under the conditions for which Figs. 3a and 3b are valid; that is, for a galvanostat rise time of 15 ns, an error of the measuring current density of $\pm$1%, and pulse length limitations as discussed above. For the graphical method, it is assumed that the double layer capacitance is known exactly, and the diffusion parameter is determined from the slope of the η - $\sqrt{t}$ line; fifty data points are assumed for the curve-fitting method. Under these conditions, the error of the exchange current density for the curve-fitting method is generally smaller or equal to that of the graphical method. At small τ_d/τ_c ratios, it is as much as five times smaller. As the τ_d/τ_c ratio increases, the errors for both methods decrease, and they asymptotically converge to the same limiting value, which is equal to the error of the measuring current density.

With the curve-fitting method, values for the diffusion parameter and the double layer capacitance are also calculated. However, under identical measuring conditions, the fields of applicability for the measurement of these parameters are not identical with that shown on Fig. 3b. Although these aspects of the curve-fitting were not investigated in detail, the following observations were made. Both parameters can be determined in certain areas of the field shown in Fig. 3b, with an accuracy better than $\pm$20%. The diffusion parameter can be determined if log κ is larger than one. Apparently, for smaller values of log κ, the kinetic content of the data is overwhelming. The double layer capacitance can be determined if log τ_c is larger than -8. Apparently, for shorter τ_c values, there is insufficient information in the data regarding the capacitance.

Double Pulse: Graphical Data Evaluation. The following general conditions were used in the calculations for the double pulse technique. It was assumed that the ringing after the prepulse subsided in such a short time that the minimum in the overpotential--time curve was observable between 50 and 100 ns after the prepulse. The minimum prepulse length was set to 100 ns. The shallowness of the minimum in the overpotential--time curve was also considered. The shallowest minimum was required to have a potential change twice that of the uncertainty of the potential measurement in a time duration not longer than two times the prepulse length. The prepulse length and the position of the minimum were then systematically varied, during the data generation, to find a data set with an observable minimum. To minimize the effect of diffusion, the minimum was set close to the end of the prepulse; usually Δt was equal to the shortest t_3 of the series and q was set equal to 1.5. For the graphical data evaluation, a series of four data sets were used with t_3 varying in proportion to 1, 2, 3, 4. (For the curve-fitting, the data set with the shortest t_3 was used with q = 1.5). The error of the exchange current density determination was calculated for a large number of conditions systematically varying τ_c and τ_d.

The applicability diagram constructed for the unmodified technique ($t_m = t_3 + \Delta t$) is shown in Fig. 4a. As before, the solid line demarcates the area within which the exchange current density can be measured with an error of less than $\pm$20% for an overpotential accuracy of $\pm$50 μV; the dotted line extends the field to the case of $\pm$5 μV accuracy. The effects limiting the applicability of the method are different on each section of the diagram. They will be discussed proceeding clockwise from the upper left-hand corner. Here, the applicability is limited by the mathematical approximations used to derive Eq. [5]. At first, the large-argument approximation is applicable, but, proceeding clockwise, the validity range of the small-argument approximation if approached. The measurable κ increases here because the error caused by the inadequacy of the mathematical approximations is larger for the large argument expansion than that for the small-argument expansion of the unmodified technique (20). The following decline of the measurable κ arises from experimental limitations. As the value of τ_c increases, one needs larger t_m values to produce an observable minimum in the overpotential--time curve. Consequently, the kinetic content of the overpotential decreases and this causes an increase in the error of the determination of the exchange current density. All the above limitations can be counteracted by more accurate measurements of the overpotential, as indicated by the dotted line in Fig. 4a. The maximum allowed τ_c was set to 10 s; at larger values, the measuring current density becomes small (less than nA cm^{-2}) and difficult to measure because of the low signal-to-noise ratio. The lower limit is also determined by experimental effects. Below this limit, the pulse lengths required to produce an observable minimum are so long that natural convection of the solution will interfere with the diffusional mass transport. Finally, the highest usable concentration was again set at 10^{-2} mol cm^{-3}.

Figure 4b shows the applicability diagram of the modified technique ($t_m = qt_3$). The main improvement, compared to the unmodified technique, occurs at small τ_c values at the upper left-hand corner of the applicability field. As has been shown before (20), the large- and small-argument approximations give equally good results for the modified technique; therefore, the limitation at small τ_c values is due to the kinetic content of the overpotential, rather than the breakdown of the large-argument approximation. Proceeding clock-wise, the maximum measurable κ decreases to a minimum; this effect is caused by the mathematical approximations of Eq. [5], since in this intermediate range, neither the large- nor small-argument expansions are good approximations. The rest of the limitations are the same as those given for the unmodified technique (Fig. 4a). It is to be noted, however, that the measurable κ levels are somewhat larger for the modified technique at all values of τ_c. The reason for this is the generally smaller errors of the small-argument approximation for the modified technique (20).

The error of the measuring current density does not have much effect on the field of applicability. Figures 4a and 4b are valid for a $\pm$1% error of the measuring current density. An increase of the error to $\pm$5% decreases the fields of applicability only slightly.

The rise time of the galvanostat has only a small effect, as has been shown previously (24). Figures 4a and 4b are valid for a rise time of 15 ns, and increasing the rise time to 50 ns (and even to 0.5 μs, for prepulses of 1 μs or longer) does not significantly alter the fields of applicability.

Double Pulse: Computer Curve-Fitting Data Evaluation. Because it uses the complete overpotential--time Eq. [6], the curve-fitting method is expected to be superior to the graphical data-evaluation method. Indeed, as indicated by Fig. 4c, the field of applicability is improved in the area where the graphical method is limited by the simplified equations (upper left hand corner). No other improvements are produced in the field of applicability shown in Fig. 4c because all other limiting conditions (kinetic content of data, shallowness of minima, *etc.*) are equally applicable to both data-evaluation methods. A further benefit of the curve-fitting evaluation method is the generally higher accuracy of the exchange current density determination. The error of the exchange current density is equal to or less than that resulting from the graphical method everywhere within the field of applicability. The error of the curve-fitting method is as much as one order of magnitude less than that of the graphical method. The field of applicability shown on Fig. 4c is, however, subject to the following caveats.

In the curve-fitting method, there is no need for a fixed relation between t_3 and t_m, since only one measurement is used rather than a series of them. Therefore, one can not distinguish between

the cases of $t_m = t_3 + \Delta t$ and $t_m = qt_3$. However, to assure that the double layer is precharged, it is still required that $t_3 < t_m$ and that the minimum in the overpotential--time curve be observable .

The method is very sensitive to the rise time of the galvanostat when Eq. [1] is used in the curve-fitting program; this effect can be diminished, however, by the use of Eq. [6]. The latter equation was used in the calculations leading to Fig. 4c; in this case, rise times up to 50 ns were examined and were found to have no effect on the results. In these evaluations, the rise and fall of the prepulse (see Fig. 1) were assumed to be linear (24). Any deviation from this assumed linearity will introduce some error in the determination of the exchange current density; this error was not evaluated, but it is expected to be considerably less than the error caused by the complete neglect of the rise time. Figure 4d illustrates the effect of rise time of the galvanostat on the field of applicability. For this graph, the synthetic data were generated with Eq. [6], whereas the data evaluation was carried out with Eq. [1] for rise times of 5, 15, and 50 ns. A comparison of this figure with Fig. 4c reveals that a rise time even as short as 5 ns has a deleterious effect on the accuracy of the determination of the exchange current density and decreases the field of applicability.

The method is also sensitive to errors of the measurement of the overpotential and current density. Similar accuracies were assumed for the two measurements: for the case of the 50 μV potential error, the maximum current density error was set to $\pm 1\%$; and for the 5 μV case, the current density error was limited to $\pm 0.1\%$. The combined effect of these errors is shown in Fig. 4c.

In the calculations leading to Figs. 4c and 4d, the number of data points was always 50, with the points being uniformly spaced during the measuring pulse. The first point was always taken at 0.1 μs after the end of the prepulse to avoid all initial distortions of the potential. Increasing the number of data points can decrease the error of the determination of the exchange current density, at the cost of longer computation times, but will not significantly change the field of applicability. The use of as many as 2000 data points decreases the error by one order of magnitude. The computation time for 50 data points averages about 30 seconds, and it increases approximately in proportion to the number of data points.

To start the calculation, a set of initial guesses is needed for the three parameters to be determined. Figures 4c and 4d are valid for guesses that do not deviate by more than a factor of three from the actual values. A factor of two will produce very similar results. The field of applicability will start to shrink considerably when the factor is four or larger. This is not a problem since the initial guess for the exchange current density can be obtained within the desired limits by the graphical data-evaluation method for the double

pulse technique, and the required values of the diffusion parameter and the double layer capacitance can be obtained within the desired limits from the long-time and short-time slopes of single pulse galvanostatic transients.

The curve-fitting method permits one also to calculate the diffusion parameter, and the double layer capacitance. The fields of applicability for these two parameters, of course, are not necessarily the same as that for the exchange current density, and they were not examined in this work. However, the following observations are relevant. The field of applicability of the diffusion parameter is larger than that of the exchange current density; indeed its field of applicability completely overlaps that of the latter. Within the field of applicability shown on Fig. 4c, the diffusion parameter can be determined with an error that is much less than that of the exchange current density. The fields of applicability for the determination of the double layer capacitance and the exchange current density overlap only partially. The capacitance can be determined with an error less than $\pm 20\%$ on the right-hand side of the field shown in Fig. 4c; but on the left-hand side, the field is limited approximately by the $\tau_c = 10^{-8}$ line. This is probably due to the fact that at such short values of τ_c the usual prepulse length is much longer than τ_c.

DISCUSSION

An examination of the fields of applicability of the galvanostatic techniques suggests that expressing the limitations of the technique in terms of the largest measurable standard heterogeneous rate constant can be rather misleading. The maximum allowable rate constant parameter changes many orders of magnitude as the *rc* time constant of the double layer changes. Furthermore, the relation between the rate constant (k_o) and the rate constant parameter (κ) is unambiguous only under certain restricted conditions. To allow a meaningful comparison of various relaxation techniques, one needs a representation such as the log κ *vs* log τ_c diagrams discussed in this paper. It is to be noted that the construction of applicability diagrams is affected by certain assumptions about and restrictions on quantities such as the length of the measuring pulse, the rise time of the instrumentation, the accuracy of the measurements, *etc*. In order to arrive at reasonable comparison of the different relaxation techniques, these assumptions should be as similar as possible. The limitations for the techniques arise either from theoretical considerations or from equipment limitations. Thus, the best common basis for comparing the various techniques is to assume that each technique is applied using the most correct theoretical basis and the most advanced (presently available) instrumentation under the best (but still practical) laboratory conditions.

A comparison of the two data-evaluation methods of the galvanostatic single pulse technique results in the following conclusions.

The graphical data-analysis method is primarily limited by the error of the mathematical simplifications which form the basis of the graphical method. The computer curve-fitting method is free of this restriction and is limited primarily by the kinetic information of the transient data. This extends the field of applicability of the curve-fitting method to reactions about one order of magnitude faster than those measurable with the graphical method. The initial guesses, needed to start the curve-fitting, can be obtained with sufficient accuracy by a graphical evaluation of single pulse data.

Both the graphical and the computer curve-fitting data-evaluation methods are about equally sensitive to the accuracy of the overpotential measurement and the measuring current density. The curve-fitting method, on the other hand, is much more sensitive to the rise time of the galvanostat (especially at small values of the rate constant parameter) than is the graphical method. This is not a problem since galvanostats with 15 ns rise time are available. Also, one might consider a curve-fitting method based on Eq. [6].

For the double pulse technique, a comparison of the unmodified and modified techniques, coupled with graphical data evaluation, reveals the general superiority of the modified technique. This is caused by the fact that the simplified equation needed for the graphical evaluation is better approximation for the modified case. In general, the field of applicability is enlarged by about one half order of magnitude of κ, and for very fast reactions it is enlarged by about two orders of magnitude.

The computer curve-fitting data-analysis method further extends the field of applicability of the technique by about one order of magnitude of κ at τ_c values around 10^{-8}. At smaller and larger τ_c values, the curve-fitting method is approximately equivalent to the modified graphical method because both methods are limited by the same experimental factors. The initial guesses needed to start the curve-fitting can be obtained with sufficient accuracy from the double pulse technique coupled with graphical data evaluation.

Both data-evaluation methods of the double pulse technique are about equally sensitive to the accuracy of the overpotential measurement, but the curve-fitting method is somewhat more sensitive to the accuracy of the measuring current density. The methods are very different in regard to the effect of the rise time of the galvanostat. The graphical method is unaffected within practical limits while the curve-fitting method is so sensitive that, this effect cannot be neglected even with the best available galvanostats, therefore, the equation taking into consideration the rise time must be used in the computer calculations.

In summary it can be stated that the computer curve-fitting data-evaluation method for the galvanostatic techniques is preferable to

graphical data evaluation because (i) it extends the techniques' fields of applicability to reactions about one order of magnitude faster, (ii) it results in a more accurate determination of the exchange current density, and (iii) potentially it could enable precise determination of the double layer capacitance and the diffusion parameter.

CONCLUSIONS

A comparison of the field of applicability of the galvanostatic single pulse technique with that of the double pulse technique shows that at large κ values (fast reactions) the exchange current density can be measured with smaller error using the double pulse technique, but for slower reactions only the single pulse technique is applicable. Comparing the graphical evaluation methods of both techniques, one can conclude that the modified double pulse technique can be used to measure the exchange current density of reactions that are up to one and a half order of magnitude faster than those measurable with the single pulse technique. The unmodified double pulse technique is applicable to reactions about one order of magnitude faster than the single pulse technique at τ_c values larger than 10^{-6}, but it is worse at smaller τ_c values. Furthermore, using the rather limited criterion of maximum measurable κ at any τ_c, the unmodified double pulse technique is indeed inferior to the single pulse technique, as has been predicted by Sluyters and co-workers (6-8). The application of computer curve-fitting data evaluation increases the fields of applicability of both the single pulse and the double pulse techniques but the double pulse technique remains equal to or better than the single pulse technique, with the improvement being one order of magnitude in measurable κ at some τ_c values.

ACKNOWLEDGEMENT

The author is indebted to Mr. J. E. Harmon for editorial assistance. This work was performed under the auspices of the Division of Materials Sciences, Office of Basic Energy Sciences, U.S. Department of Energy.

LIST OF SYMBOLS

a	Defined by Eq. [3]
b	Defined by Eq. [3]
c	Double layer capacitance (F cm^{-2})
C_j	Concentration of species j in the bulk solution (mol cm^{-3})
D_j	Diffusion coefficient of species j (cm^2 s^{-1})
F	Faraday constant
i_1	Current density (A cm^{-2}), defined by Fig. 1

LIST OF SYMBOLS (Continued)

i_2 Current density (A cm^{-2}), defined by Fig. 1
i_o Apparent exchange current density (A cm^{-2})
k_o Apparent standard heterogeneous rate constant (cm s^{-1}), $k_o = i_o/nFC_O^{\alpha a/n} C_R^{\alpha c/n}$ where α_a and α_c are the anodic and cathodic transfer coefficients
n Total number of electrons transferred in the overall reaction
O (index) Oxidant
R (index) Reductant
R Universal gas constant (J $K^{-1}mol^{-1}$)
q Constant ratio between t_3 and t_m in the modified technique (s)
t Time (s)
t_1 Time (s), defined by Fig. 1
t_2 Time (s), defined by Fig. 1
t_3 End of prepulse (s)
t_ℓ End of the measuring pulse (s)
t_m Time of occurrence of minimum in the overpotential--time curve (s)
Δt Constant difference between t_3 and t_m in the unmodified technique (s)
T Temperature (K)
η Overpotential (V)
η_m Overpotential at the minimum in the overpotential--time curve (V)
κ Rate constant parameter, defined by Eq. [12]
ν Stoichiometric number of the reaction mechanism
τ_c Time constant of the double layer capacitance--reaction resistance system (s)
τ_d Time constant of the diffusion impedance--reaction resistance system (s)

REFERENCES

1. J. Kuta and E. Yeager, in "Techniques of Electrochemistry," Vol. 1, Chap. 3, E. Yeager and A. J. Salkind, Editors, Wiley-Interscience, New York (1972).
2. P. Delahay, "Advances in Electrochemistry and Electrochemical Engineering," Vol. 1, Chap. 5, P. Delahay and C. W. Tobias, Editors, Interscience Publishers, Inc., New York (1961).
3. H. A. Laitinen, R. P. Tischer, and R. K. Roe, J. Electrochem. Soc., 107, 546 (1960).
4. J. Bouteillon, J. DeLepinay, and M. J. Barbier, J. Chim. Phys., 71, 346 (1974).
5. J. Thonstad and S. Rolseth, Electrochim. Acta, 23, 223 (1978).
6. D. J. Kooijman and J. H. Sluyters, J. Electroanal. Chem. Interfacial Electrochem., 13, 152 (1967).
7. H. P. van Leeuwen and J. H. Sluyters, J. Electroanal. Chem. Interfacial Electrochem., 42, 313 (1973).
8. M. Sluyters-Rehbach and J. H. Sluyters, in "Topics in Pure and Applied Electrochemistry," p. 15, S. K. Rangarajan, Editor,

SAEST, Karaikudi (1975).
9. T. Berzins and P. Delahay, J. Am. Chem. Soc., 77, 6448 (1955).
10. D. Inman, J. O'M. Bockris, and E. Blomgren, J. Electroanal. Chem. Interfacial Electrochem., 2, 506 (1961).
11. R. L. Birke and D. K. Roe, Anal. Chem., 37, 450 (1965).
12. D. J. Kooijman and J. H. Sluyters, Electrochim. Acta, 12, 693 (1967).
13. D. J. Kooijman and J. H. Sluyters, Electrochim. Acta, 12, 1579 (1967).
14. D. J. Kooijman, J. Electroanal. Chem. Interfacial Electrochem., 18, 81 (1968).
15. D. J. Kooijman, J. Electroanal. Chem. Interfacial Electrochem., 19, 365 (1968).
16. P. H. Daum, PhD Thesis, Michigan State University, East Lansing, Michigan (1969).
17. Z. Nagy, Electrochim. Acta, accepted for publication.
18. H. Gerischer and M. Krause, Z. phys. Chem. (Frankfurt), 10, 264 (1957).
19. H. Matsuda, S. Oka, and P. Delahay, J. Am. Chem. Soc., 81, 5077 (1959).
20. Z. Nagy, J. Electrochem. Soc., 126, 1148 (1979).
21. Z. Nagy, J. Electrochem. Soc., submitted for publication.
22. J. O'M. Bockris and A. K. N. Reddy, "Modern Electrochemistry," Vol. 2, Chap. 9, Plenum Press, New York (1970).
23. J. O'M. Bockris and Z. Nagy, J. Chem. Ed., 50, 839 (1973) and 51, 803 (1974).
24. Z. Nagy, J. Electrochem. Soc., 125, 1809 (1978).
25. T. Berzins and P. Delahay, J. Chem. Phys., 23, 972 (1955).
26. P. Delahay, "New Instrumental Methods in Electrochemisty," p. 46, Interscience, New York (1954).
27. S. Sarangapani and R. DeLevie, J. Electroanal. Chem. Interfacial Electrochem., 102, 165 (1979).
28. R. F. Martin and D. G. Davies, in "Computers in Chemistry and Instrumentation," Vol. 2, Chap. 4, J. S. Mattson, H. B. Mark, and H. C. MacDonald, Editors, Marcel Dekker, Inc., New York (1972).
29. J. M. Kudirka, P. H. Daum, and C. G. Enke, Anal. Chem., 44, 309 (1972).
30. H. Reller and E. Kirowa-Eisner, J. Electrochem. Soc., 127, 1725 (1980).

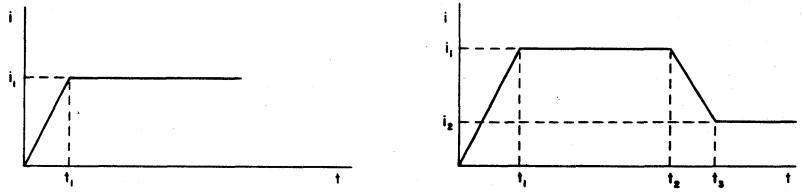

a. Single pulse.

b. Double pulse

Fig. 1. Current pulse shapes.

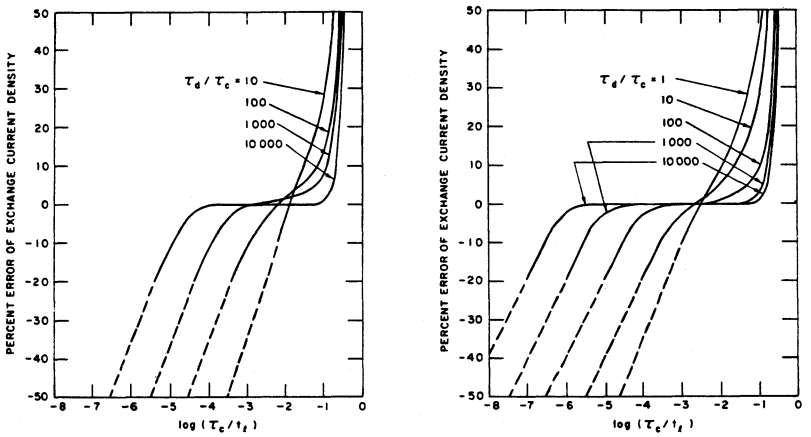

a. Overpotential accuracy: ±50 μV.

b. Overpotential accuracy: ±5 μV.

Fig. 2. Relative error of exchange current density determination for the galvanostatic single pulse technique.

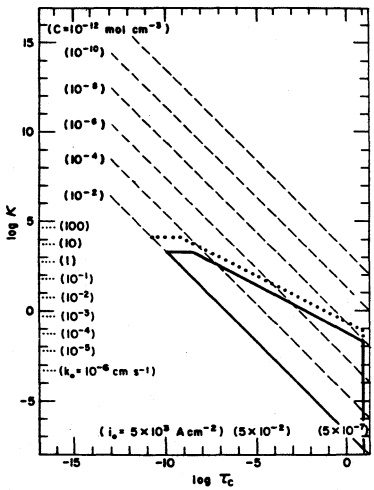

a. Graphical data evaluation.

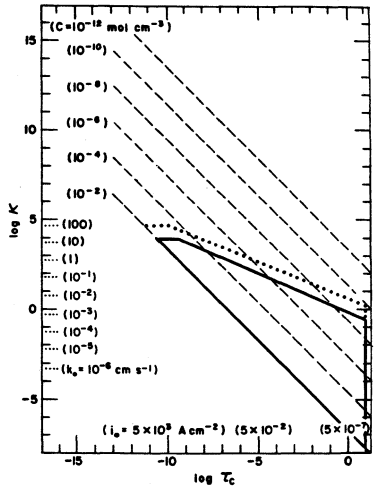

b. Curve-fitting data evaluation.

Fig. 3. Applicability diagrams of the galvanostatic single pulse technique. The solid line marks the field of applicability of the technique for measuring the exchange current density with a maximum error of $\pm 20\%$ and with an accuracy of the overpotential measurement of ± 50 μV. The dotted line extends the field for the ± 5 μV accuracy case.

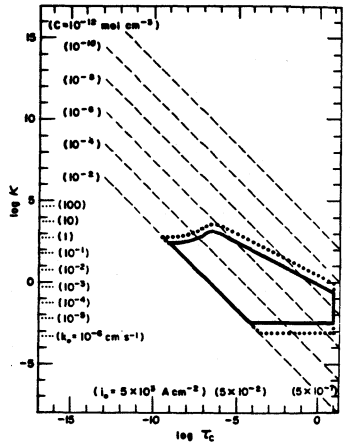

a. Unmodified technique with graphical data evaluation.

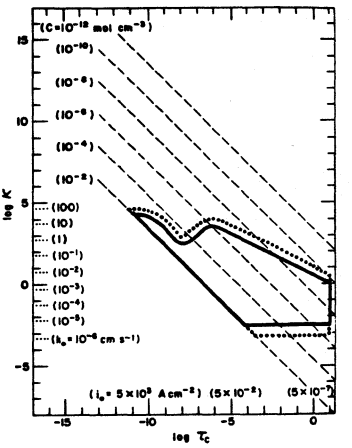

b. Modified technique with graphical data evaluation.

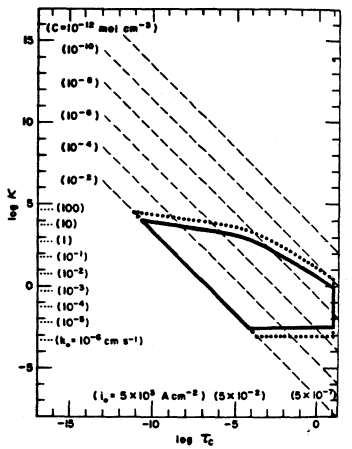

c. Curve-fitting data evalution using equation [6].

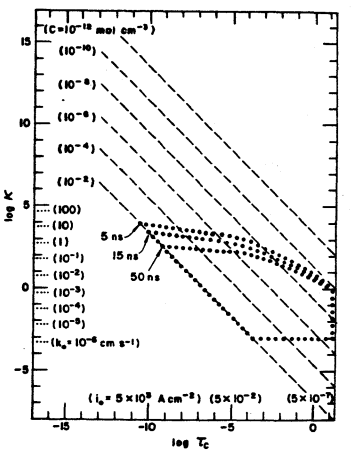

d. Effect of rise time on curve-fitting data evaluation using equation [1].

Fig. 4. Applicability diagrams of the galvanostatic double pulse technique. The solid line marks the field of applicability for measuring the exchange current density with a maximum error of ±20% and with an accuracy of overpotential measurement of ±50 μV. The dotted line extends the field for the ±5 μV accuracy case.

DOI: 10.1149/198109.0212PV

ON THE CONCEPT OF pCl IN CHLOROALUMINATE MELTS

Milton Blander and Marie-Louise Saboungi
Chemical Engineering Division
Argonne National Laboratory
Argonne, Illinois 60439

Abstract

The emf's of the cell

$$Al/AlCl_3\text{-}NaCl(solid)//\ NaCl\text{-}AlCl_3\text{-}MCl_n/M$$

were analyzed assuming that the transference number of Na^+ is unity. When M is Al, values for the activities of NaCl and $AlCl_3$ in NaCl-$AlCl_3$ solutions have been deduced. The results indicate strong structural ordering in the melt. Conditions are defined where values of "pCl" are equal to $-\ln a_{NaCl}$. When M is another metal in dilute solution the emf is given by the equation

$$E = E_o - (RT/nF)\ln(a_{MCl_n}/a^n_{NaCl})$$

Introduction

The acid-base concept is important in inorganic chemistry. However, it is usually qualitative and often difficult to quantify. Emf measurements in chloroaluminate melts such as e.g., NaCl-$AlCl_3$ in a cell schematized as

$$Al/AlCl_3\text{-}NaCl(solid)//NaCl\text{-}AlCl_3/Al \qquad (1)$$

have provided a means for quantifying the basic properties of these melts. The concept of a "chloride ion activity" and pCl has been introduced as a numerical measure of basicity (1,2,3). It is the purpose of this paper to analyze the emf measurements in chloroaluminate melts in order to calculate the thermodynamic properties of NaCl and $AlCl_3$ and precisely define pCl. The activities of NaCl and $AlCl_3$ deduced from our calculations are characteristic of strong structural ordering in these melts. In addition, we will examine the meaning and interpretation of emf measurements of solutes, MCl_n, in chloroaluminate melts in a cell schematized as

$$Al/AlCl_3\text{-}NaCl(solid)//NaCl\text{-}AlCl_3\text{-}MCl_n/M \qquad (2)$$

where the solute MCl_n is in dilute enough solution to obey Henry's law.

Analysis of Emf Cells

The analysis of the cells 1 and 2 requires a knowledge of the transference numbers of the ions of the solvent. For simplicity in the discussion, and because of a lack of data, we assume that the transference number of the Na^+ ion is unity. Although this assumption is reasonable and has been almost universally adopted, no measurements of transference have yet been made in chloroaluminates. Consequently, our conclusions may require modification after such measurements are performed. The total reaction for the passage of one faraday of current (positive) is then

$$\frac{1}{n}\,M + \frac{1}{3}\,AlCl_3(l) + NaCl(r) \rightleftharpoons NaCl(l) + \frac{1}{n}\,MCl_n(r) + \frac{1}{3}\,Al \qquad (3)$$

where (r) and (l) refer to right hand and left hand, respectively, and M can be Al or some other metal. If it is another metal, the concentration of M is usually taken to be small enough to obey Henry's law. The emf's of cells 1 and 2, E, are then given by

$$E = -(RT/F)\ln[a_{MCl_n}^{1/n}(r)\,a_{NaCl}(l)/a_{AlCl_3}^{1/3}(l)\,a_{NaCl}(r)]$$
$$= E_o - (RT/F)\ln[a_{MCl_n}^{1/n}(r)/a_{NaCl}(r)] \qquad (4)$$

where $E_o = -(RT/F)\ln[a_{NaCl}(l)/a_{AlCl_3}^{1/3}(l)]$ and a_i is the activity of the ith component. If MCl_n is $AlCl_3$, then the emf of the cell is a function of the ratio $a_{AlCl_3}^{1/3}/a_{NaCl}$ in the right hand compartment which cannot be directly related to the activity of a component. By definition, the pCl of the electrolyte is (3FE/4RT) which is different from the activity of NaCl according to Eq. 4. In order to directly relate the pCl to a_{NaCl}, a Gibbs-Duhem integration should be performed. If we refer to ($Al_{1/3}Cl$) as component 1 and to NaCl as component 2, then

$$d\ln a_1 = y_2\,d\ln(a_1/a_2) = -(y_2F/RT)\,dE \qquad (5)$$

$$d\ln a_2 = y_1\,d\ln(a_2/a_1) = (y_1F/RT)\,dE \qquad (6)$$

Since one "mole" of these components is also an equivalent, y_1 and y_2 are the equivalent fractions of $AlCl_3$ and NaCl, respectively. These equations have been deduced independently by Øye and King (4). Integration of Eqs. 5 and 6 leads to the results.

$$\ln[a_1(r)/a_1(1)] = -y_2FE/RT + \int_1^r (FE/RT)\,dy_2' \qquad (7)$$

$$\ln[a_2(r)/a_2(1)] = y_1FE/RT - \int_1^r (FE/RT)\,dy_1' \qquad (8)$$

Activities of $AlCl_3$ and NaCl in NaCl-$AlCl_3$ mixtures at 175°C were calculated from the measurements of Boxall, Jones, and Osteryoung (5) which appear to be the most extensive precise measurements available for this system. In Figure 1, we plot (FE/RT) and the logarithms of the activities of $AlCl_3$ and NaCl vs. the composition. The standard states of the plotted activities were chosen as those of the pure solids. The mole (equivalent) fraction of NaCl in a solution of NaCl and $AlCl_3$ saturated with NaCl was taken as 0.5023 (0.2517); for saturation with solid $AlCl_3$, it was taken as 0.3000 (0.1250). Using JANAF values (6) for the free energies of fusion of NaCl and $AlCl_3$, we calculated and plotted in Figure 2 the total excess free energies of mixing of a mole of a solution (components are $AlCl_3$ and NaCl).

Interpretation of the Results

The results for $-\ln a_{NaCl}$ (Fig. 1) differ little from pCl = 3FE/4RT. This stems from the fact that the difference, Δ, between $-\ln a_{NaCl}$ and pCl is given by the expression

$$\Delta = -\int F\ (y_1 - 0.75)\ dE/RT \qquad (9)$$

and that the greatest contribution to the integral of $y_1 dE$ occurs for values of E close to an equivalent (mole) fraction of $AlCl_3$, $y_1 = 0.75$ ($X_1 = 0.50$). Consequently, the values of pCl for this melt are very close to $-\ln a_{NaCl}$ near this composition and exhibit only a small difference of $\sim$0.2 at $y_1 = 0.875$. For melts where measurements of pCl are made over a broader range of compositions such that a larger fraction of the integral occurs at values of y_1 far from 0.75, values of Δ can be much larger. This would be true for NaCl-$AlCl_3$ at much higher temperatures and for other melts where the range of compositions of the liquid is much larger. Of course, all this is predicated on the assumption that the transference number of sodium, $t_{Na^+} = 1$. Deviations from this assumption will lead to even larger differences between pCl and $-\ln a_{NaCl}$. For example, if the average value of t_{Na^+} is 0.9, the difference between pCl and $-\ln a_{NaCl}$ would be greater than unity at $y_1 = 0.875$.

Since each different monovalent cation salt forms a different set of solvents the pCl scale is relative and, at best, only describes the relative basicity of the solutions of a given base with $AlCl_3$. If a NaCl solid saturated melt is defined as having a pCl of zero, the meaning of the scale will shift with temperature. In addition, for different bases at any given temperature, the basicity and its composition dependence will differ in a manner which does not necessarily reflect differences in chemical properties. Even more complications arise when one considers the acidity of the melt, which differs from the basicity by a constant to a good approximation only at compositions close to a mole (equivalent) fraction of 0.5 (0.75).

At compositions very different from this, deviations can be large. For example, in our calculations the sum ($\ln a_{NaCl} + \ln a_{AlCl_3}$) at $X_{AlCl_3} = 0.7$ differs by one unit from that at $X_{AlCl_3} = 0.5$. At yet higher concentrations (e.g., 0.8) of either the acidic or basic compositions (possible at higher temperatures) the differences will increase greatly and the inverse relationship between acidity and basicity breaks down. Of course, for different bases the constants which characterize the sum of the basicity (pCl or -ln activity of the base component) and the acidity ($-\ln a_{AlCl_3}$) parameters will be different. There is an advantage in characterizing an acidity scale rather than a basicity scale since the acidity scale for chloroaluminates can be defined in a manner which reflects a thermodynamically definable chemical characteristic of all melts which is directly comparable and equivalent, i.e., the $AlCl_3$ components in two chloroaluminates having the same acidity are at equilibrium.

Equation 4 is important in another respect. This equation differs from those commonly employed for measurements on solutes in chloroaluminate melts since it includes the term $\ln a_{NaCl}(r)$ on the right hand side. This term has been neglected in prior studies and a reevaluation of the thermodynamic properties of chloride solutes in chloraluminates is required in order to take this into account. Since this term varies from zero to about -12.8 in the NaCl-$AlCl_3$ system at 175°C, the corrections should be large here as well as in other chloraluminate melts.

The pCl dependence of equilibria in chloroaluminate melts has been used in order to deduce the species involved in, for example, oxidation-reduction equilibria with a (right hand compartment) half-cell reaction, which can be written as

$$(MCl_c)^{n-c} + rCl^- + e \longrightarrow (MCl_{c+r})^{n-1-c-r} \qquad (10)$$

which denotes a reduction of the valence, n, of a metal ion M^{+n} coordinated by c chloride ions to a valence (n-1) with a coordination number of c + r where r can be positive or negative. The coordination number (of chloride ions) is usually not determinable from thermodynamic measurements and the cell reaction written thermodynamically for a cell such as cell 2 is

$$1/3Al + NaCl(l) + MCl_n(r) \rightleftharpoons NaCl(r) + 1/3AlCl_3(l) + MCl_{n-1}(r) \qquad (11)$$

$$E = E_o - (RT/F)\ln(a_{MCl_n}/a_{NaCl}a_{MCl_{n-1}}) \qquad (12)$$

where E_o is the same here as in Eq. 4 and the activities are for components in the right hand compartment. If both MCl_n and MCl_{n-1}

are in the Henry's law region, the dependence of E upon pCl stems from the terms $(RT/F)\ln a_{NaCl} \sim -(RT/F)pCl$ and $(RT/F)\ln (\gamma_{MCl_{n-1}}/\gamma_{MCl_n})$ where the ratio of the activity coefficients can be dependent on melt composition. For example, if E varies as -(RT/F)pCl, then the energetics of the two components varies equally with composition; if E is independent of pCl, it means that component MCl_n becomes more stable relative to MCl_{n-1} with an increase in pCl. Can this information be used to deduce the coordination or change of coordination of the metal ion M? This seems unlikely since there is no obvious method of separating the energetic effects from the coordination effects in the solutions of MCl_n and MCl_{n-1}.

Structural Implications

The composition dependence of the excess free energy (Fig. 2) is indicative of strong structural ordering which can be interpreted in a number of ways that can be classified as chemical and structural. For example Øye and coworkers (7) have quantified the consideration of such melts as non-ideal mixtures of $NaCl+NaAlCl_4+NaAl_2Cl_7+Al_2Cl_6$. Such a chemical point of view is valuable and leads to good representations of the thermodynamic data even when the presence of all these constituents may not be proven. We will not discuss this view here since other workers have covered it adequately.

Another point of view is to relate the excess free energies to structural ordering in terms of a model in which particular pairs of cations tend to be or not be next-nearest neighbors. In this particular case the two unlike cations Na^+ and Al^{+3} tend to be next-nearest neighbors and the like pairs $Na^+...Na^+$ and $Al^{+3}...Al^{+3}$ tend to be further apart. The simplest model for expressing this tendency is related to the quasi-chemical theory in which one has a structure with two interlocking sets of cation sites A and B where A sites are next-nearest neighbors of B sites and B sites are next-nearest neighbors of A sites. If, for example, a Na^+ ion resides on an A site, its next-nearest neighbors will tend to be Al^{+3} ions. If there are equal numbers of A and B sites, there will be strong ordering at the 50-50 composition such that most of the Na^+ will, for example, occupy A sites and most of the Al^{+3} will occupy B sites.

The activity coefficients and excess free energies of mixing of such solutions can be calculated from equations deduced from the quasi-chemical theory

$$\ln \gamma_1 = \frac{Z}{2} \ln \left[\frac{\xi - 1 + 2X_1}{X_1(\xi + 1)}\right] \qquad (13)$$

$$\ln \gamma_2 = \frac{Z}{2} \ln \left[\frac{\xi - 1 + 2X_2}{X_2(\xi + 1)}\right] \qquad (14)$$

$$\xi = \left(1 + 4X_1X_2[\exp(2w/ZkT) - 1]\right)^{1/2} \quad (15)$$

and

$$\frac{\Delta G_m^E}{RT} = X_1 \ln\gamma_1 + X_2 \ln\gamma_2 \quad (16)$$

where Z is the coordination number of next-nearest neighbors, w is an energy parameter, and X_1 and X_2 are the mole fractions of $AlCl_3$ and NaCl, respectively. Calculations based on these equations are plotted in Fig. 2 for values of w = -16.479 kcal/mole and for a value of Z = 6*. The calculated curve is in reasonable agreement with the "measured" values for mole fractions of $AlCl_3$ greater than 0.6. The differences at lower concentrations (i.e., X_{AlCl_3} = 0.5-0.6) are consistent with a significantly greater degree of ordering than is implied by the quasi-chemical calculations. By allowing Z to be an arbitrary variable with a value of, for example, 2, the calculations based on Eqs. 13-16 can be made to correspond to the measurements very closely. However, the physical meaning of this procedure is not clear.

More realistically, one should probably consider that the interaction energies of cation next-nearest neighbor pairs is dependent on the local cation environment and is not a constant for a given pair. Thus, for example, if one has a configuration of a Na^+ surrounded by ZAl^{+3} next-nearest neighbors, the energy for the replacement of one Al^{+3} by a Na^+ would be different than if the Na^+ were surrounded by fewer next-nearest neighbor Al^{+3} ions.

The chemical and structural views of these melts can be reconciled. For example, at a 50-50 composition both models consider the melt as consisting of interlocking structures of essentially equal numbers of Na^+ and Al^{+3} cations which are next-nearest neighbors having intervening chloride ions. However, the chemical model specifies the coordination number of Al^{+3} as four to form an $AlCl_4^-$ species. Measured spectra are consistent with the presence of this species. However, unambiguous experimental proof that this is the predominant species has not been presented. In the chemical description, the $NaAlCl_4$ melt dissociates as follows:

$$2\ NaAlCl_4 \rightleftharpoons NaCl + NaAl_2Cl_7 \quad (17)$$

---

* Because the quasi-chemical theory is symmetric and the measurements are asymmetric (e.g., $\ln\gamma_{NaCl} \neq \ln\gamma_{AlCl_3}$ at $X_2 = 0.5$), we have calculated w from values of $\ln\gamma_{AlCl_3}$ and have shifted the standard states for the two components. This discussion is for illustrative purposes only since our choices of parameters are not unique.

with a small dissociation constant. In the structural model, order is not perfect so that one has an equilibrium between ions on the different sites.

$$(Na^+)_A + (Al^{+3})_B \rightleftharpoons (Na^+)_B + (Al^{+3})_A \qquad (18)$$

In a sense, there is some analogy between the two equilibria since $(Na^+)_B$ means that an Na^+ ion has essentially only Na^+ ions on the A structure as next-nearest neighbors, thus resembling NaCl, and $(Al^{+3})_A$ has Al^{+3} ions on the B structure as next-nearest neighbors, thus having some characteristics parallel to but different from $Al_2Cl_7^-$.

Conclusions

1. Activities of NaCl and $AlCl_3$ have been deduced from emf measurements in NaCl-$AlCl_3$ mixtures. The thermodynamic properties are characteristic of highly ordered melts.

2. Conditions have been defined for which the concept of pCl in chloroaluminates can be related to a thermodynamic quantity, i.e., when Δ in Eq. 9 is small, pCl $\sim$ -ln a_{NaCl}.

3. The pCl scale is only relative whereas an acidity scale can be made absolute for chloroaluminate melts.

4. Emf measurements of activities of a dilute solute in a chloroaluminate melt have been analyzed and shown to include an important term for the activity of the basic component (NaCl in the case of NaCl-$AlCl_3$ melts).

Acknowledgment

This work was performed under the Auspices of the Materials Science Office of the Division of Basic Energy Sciences of the U.S. Department of Energy.

References

1. B. Tremillon and G. Letisse, J. Electroanal. Chem., 17, 371 (1968).

2. G. Letisse and B. Tremillon, J. Electroanal. Chem., 17, 387 (1968).

3. G. Torsi and G. Mamantov, Inorg. Chem., 10, 1900 (1971).

References (Cont'd)

4. H. A. Øye and L. A. King, Inorg. Nuclear Chem. Letters, in press.

5. L. G. Boxall, H. L. Jones, and R. A. Osteryoung, J. Electrochem. Soc., 120, 223 (1973).

6. D. R. Stull and H. Prophet, JANAF Thermochemical Tables, NSRDS-NBS37, Supt. of Documents, U.S. Govt. Printing Office, Washington, D.C. (1971).

7. H. Linga, K. Motzfeldt, and H. A. Øye, Ber. Bunsenges. Phys. Chem., 82, 568 (1978).

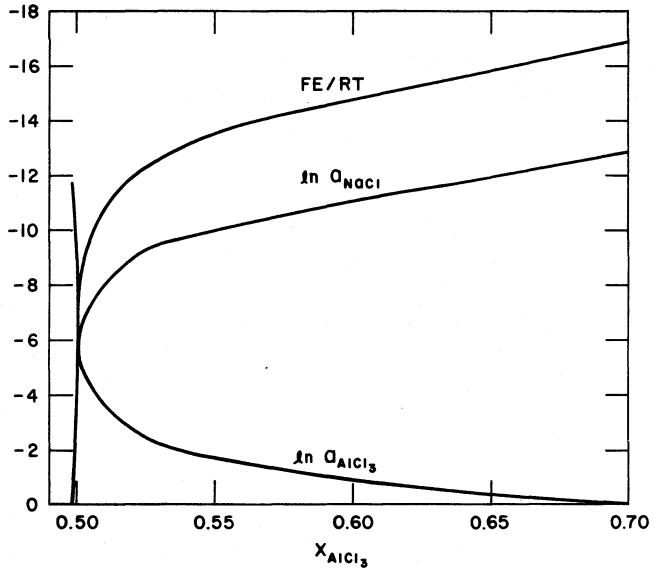

Figure 1. Plots of FE/RT, $\ln a_{NaCl}$ and $\ln a_{AlCl_3}$ versus the mole fraction of $AlCl_3$ in NaCl-$AlCl_3$ melts at 175°C.

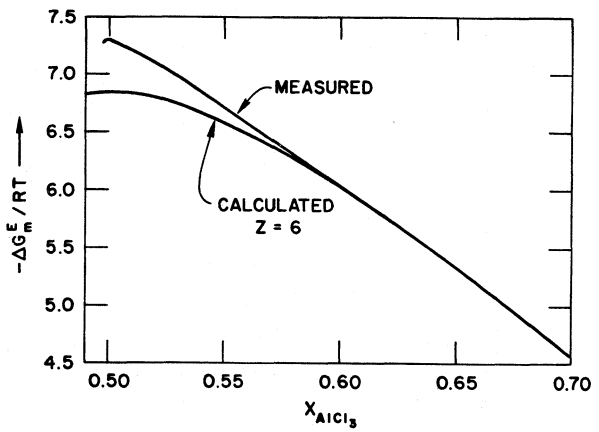

Figure 2. Excess free energies of mixing ($\Delta G_m^E/RT$) versus the mole fraction of $AlCl_3$ in NaCl-$AlCl_3$ melts at 175°C.

DOI: 10.1149/198109.0221PV

STUDIES IN ROOM TEMPERATURE CHLOROALUMINATES

R. A. Osteryoung, G. Cheek and H. Linga
Department of Chemistry
State University of New York at Buffalo
Buffalo, New York 14214

ABSTRACT

Studies on the electrochemistry of anthraquinone have been performed in a room temperature molten salt, N-butylpyridinium chloride:aluminum chloride. Correlation of the electrochemical behavior, which varies markedly with melt acidity, to infra-red spectroscopic observations of the shifts of carbonyl bands in the melt, have been made.

The determination of oxide in these melts has proven to be possible, based on the observation that Ti(IV) forms both a chloro-complex and an oxy-chloro-complex which are in slow equilibrium.

INTRODUCTION

The solvent system N-butylpyridinium chloride (BuPyCl):aluminum chloride was established in our laboratories about three years ago. The new melt has the advantage of being liquid at temperatures in the vicinity of 30°C for mole ratio variations of BuPyCl:$AlCl_3$ from 1:0.6 to 1:2. Raman spectroscopy has established that the 1:1 melt is $BuPy^+AlCl_4^-$, while the 1:2 melt is $BuPy^+Al_2Cl_7^-$ (1). The dominant acid-base equilibrium is similar to that in the NaCl:$AlCl_3$ melt (2), and is:

$$2\ AlCl_4^- \rightleftarrows Al_2Cl_7^- + Cl^- \qquad [1]$$

The equilibrium constant for reaction [1] has been found to be ca. 3.8×10^{-13} at 30°C (3).

We have been interested in the study of a variety of solutes in these melts and here discuss briefly some of the chemistry of an organic solute, anthraquinone and the behavior of an inorganic solute, Ti(IV), which interacts with oxide in the melt. We have also been interested in attempting to correlate infrared spectroscopy of solutes in this melt, which has a reasonable infrared window, with the observed behavior of solutes, and this will be illustrated (4).

A. STUDY OF ANTHRAQUINONE

Aspects of anthraquinone electrochemistry in the $AlCl_3$:BuPyCl melt are illustrated in the series of cyclic voltammograms shown in Figure 1, which portrays the change of electrochemical behavior observed as the melt composition, starting from a 0.8:1 $AlCl_3$:BuPyCl basic melt, was made increasingly acidic by addition of $AlCl_3$. From these voltammograms, it can be seen that the potential which is characteristic of anthraquinone reduction shifts to considerably more positive values as the melt acidity is increased. In addition, there are apparently three different species involved over the range of melt compositions studied: one each in the basic and acidic melts (top and bottom curves in Figure 1, respectively) and another, apparently intermediate species, in the neutral melt. By very careful addition of small amounts of $AlCl_3$ to the melt, a cyclic voltammogram containing all three of these reduction processes could be obtained. Similar behavior can be seen in the return sweep (oxidation scan) of the cyclic voltammograms, there being again three distinct regions of anodic activity.

SPECTROSCOPIC STUDIES

The nature of the various species being reduced in the melt was ascertained primarily by infrared spectroscopy. The favorable absorption window of the butylpyridinium cation in the carbonyl region and the strength of the carbonyl absorption of anthraquinone enabled the effect of increasing melt acidity upon the carbonyl bonds to be investigated (4). Thus, the infrared spectrum of anthraquinone in the acidic melt revealed no absorption at the usual value for the carbonyl stretching frequency (1680 cm^{-1}); however, a new band (not seen in the spectrum of the acidic melt itself) appeared at 1550 cm^{-1} (Figure 2). This is in good agreement with work carried out by Giallanardo in which a yellow bis-$AlCl_3$-AQ complex (structure confirmed by elemental analysis for C, H, and Ag^+ titration for Cl^-), was precipitated from methylene chloride and found to have no absorption at the normal carbonyl frequency but exhibited a shifted band at 1550 cm^{-1} (5). It seems probable that the species present in the acidic melt is the bis-$AlCl_3$-AQ complex, the complexation occurring at the carbonyl functions. Further proof of this characterization was obtained by raising the concentration of AQ in the acidic melt sufficient to cause precipitation of a yellow solid. After centrifuging and both before and after washing with methylene chloride (thus reducing and then entirely eliminating absorption contributions from

butylpyridinium cation), the infrared spectrum of this compound proved to be identical to the entire spectrum published for the isolated bis-$AlCl_3$-AQ complex (5). Furthermore, chemical analysis of the isolated complex indeed showed the existence of two $AlCl_3$ molecules for each AQ molecule.

The infrared spectrum of the neutral melt containing AQ (similar in composition to that corresponding to the fourth scan in Figure 1) revealed bands at both 1680 and 1550 cm^{-1} (Figure 2); this observation is in accordance with the absorption expected of a mono-$AlCl_3$-AQ complex. Finally, the infrared spectrum of AQ in the basic melt has a band at 1680 cm^{-1}, but not at 1550 cm^{-1}, thus indicating that the AQ carbonyl group exists in the uncomplexed form in the basic melt. The visible absorption spectrum of 9,10-anthraquinone in the basic melt revealed one band at 330 nm (ε = 5,210, c.f. γ_{max} = 326 nm, ε = 5,800 in DMF), while the spectrum in the acidic melt showed absorptions at 335 nm (ε = 9,660) and 440 nm (ε = 6,970) (6). It has been previously observed that monoprotonation of 9,10-anthraquinone in sulfuric acid results in a spectrum containing absorbances at 311 nm and 410 nm, again supporting the complexation of anthraquinone by $AlCl_3$ in the acidic melt (7,8). The formation of a bis-$AlCl_3$-AQ complex ($AQ \cdot 2AlCl_3$) accounts for the increased bathochromic shift (to 440 nm), relative to that for monoprotonated AQ above, observed for 9-10-anthraquinone in the acidic melt. It should be noted that the formation of the AQ-$AlCl_3$ complexes is chemically reversible; that is, if an acidic melt containing AQ is made basic, a shift of electrochemical behavior to that characteristic of AQ in the basic melt is observed. The interaction of $AlCl_3$ with AQ appears, then, to account for the observed shifts in the potential of AQ reduction as melt acidity is varied.

ELECTROCHEMISTRY IN BASIC MELTS

The electrochemical behavior of AQ in the basic melt, in which the AQ exists in the uncomplexed form, was further investigated by coulometric reduction at -0.800 V, resulting in an n-value for the reduction of 2.0. Cyclic voltammetry of the reduced species (initial potential -0.300 V, initial cathodic scan) showed that the long-term reduction product (i.e., coulometry product) was identical to that observed in the cyclic voltammetry of AQ, since an anodic peak at 0.00 V was seen in the first positive sweep, the following negative sweep again showing a cathodic reduction peak at -0.55 V due to reduction of AQ. Coulometric oxidation at +0.100 V in the above melt was also found to involve two electrons;

a cyclic voltammogram following oxidation (same conditions as Figure 1) was identical to that in Figure 1 (first scan). A Nernst plot obtained by varying the ratio of AQ to AQ dianion by coulometric reduction and measurement of the corresponding potentials revealed a slope of 31 mV per decade of the above ratio, indicating that AQ and its dianion comprise a potentiometrically reversible two-electron system. Addition of an authentic sample of anthrahydroquinone to a basic melt gave rise to cyclic voltammetric behavior identical to that observed above following coulometric reduction. The anthrahydroquinone, upon addition to the melt, presumably is converted into a complexed dianion by interaction with species in the melt (i.e., $AlCl_4^-$) with the consequent release of two protons, as has been observed upon the addition of tetrachloro-p-benzohydroquinone to the $AlCl_3$:NaCl melt (9). However, in the $AlCl_3$:BuPyCl basic melt, proton reduction is rather ill-defined and occurs near the cathodic limit so that direct observation of proton reduction was not possible. Solutions of both AQ and electrogenerated dianion were found to be stable for several days in the basic melt; thus, the overall aspects of electrochemical reduction of AQ to the dianion and oxidation of this species back to the quinone appear to be quite straightforward. The overall equilibrium between AQ and the AQ dianion in the basic melt can be written, recalling that the evidence indicates that AQ is uncomplexed in the basic melt, as

$$AQ + m\ AlCl_4^- + 2e^- \rightleftarrows AQ\ (AlCl_3)_m^= + m\ Cl^-, \qquad [2]$$

with the corresponding Nernst equation

$$E = E^\circ + \frac{RT}{2F} \ln \frac{[AQ]}{[AQ(AlCl_3)_m^=]} + \frac{mRT}{2F} \ln \frac{[AlCl_4^-]}{[Cl^-]} . \qquad [3]$$

This relationship was examined experimentally by carrying out a coulometric reduction of AQ (passing one equivalent of electricity to produce an equimolar mixture of AQ and AQ dianion) in an initially slightly basic melt (0.95:1) and measuring the equilibrium potential at a glassy carbon electrode after successive additions of BuPyCl. The resulting Nernst plot was linear, with a slope of 80 mV (theoretical slope, 31 mV for m = 1), thereby confirming the involvement of two $AlCl_4^-$ ions with the AQ dianion, with some involvement by a third $AlCl_4^-$. Further evidence for dianion complexation was obtained from the visible absorption spectrum of coulometrically-produced AQ dianion in the basic melt. When compared with literature spectra for reduced AQ species in various solvents, this spectrum, having maxima at 425 nm (ε = 4,970) and 380 nm (ε = 6,570) was found to be most similar to that of anthrahydroquinone (420 nm, 384 nm in DMF), and not that of the free dianion (503 nm, ε = 13,900) (6). Considering that anthrahydroquinone

is actually the AQ dianion complexed by two protons, the similarity of the spectra seen above strongly indicates that the AQ dianion in the basic melt is also complexed by at least two acidic species (i.e., $AlCl_3$).

ELECTROCHEMISTRY IN NEUTRAL MELT

As the melt is made more acidic, another process is observed at +0.00 V, corresponding to reduction of the $AQ \cdot AlCl_3$ complex. As shown in Figure 1 (second scan), if the melt basicity is such that a certain amount of electroactivity due to the uncomplexed AQ is also present (i.e., neutral-basic melt), the reduction of the $AQ \cdot AlCl_3$ complex apparently proceeds in two one-electron steps, since two components, separated by about 100 mV, are visible in the broad reduction peak. With a slight increase in melt acidity or decrease in scan rate, the individual components in the reduction peak merge into a single peak (scans 3 and 4 in Figure 1) and the behavior begins to resemble that of a reversible system (approximately equal reduction and oxidation peak heights, 100 mV peak separation). Since coulometry in the neutral melt is not feasible due to slow equilibration among the quinone complexes, an approximate n-value for $AQ \cdot AlCl_3$ reduction in the neutral melt (as in scan 4, Figure 1) was obtained from normal pulse voltammetric data. This procedure led to an n-value of 2.3 for $AQ \cdot AlCl_3$ reduction which, considering the approximations involved, indicates a two-electron reduction.

The increased degree of reversibility of this system compared to that in the basic melt can probably be ascribed to the prior complexation of the AQ as $AQ \cdot AlCl_3$ in the neutral melt, since reduction of $AQ \cdot AlCl_3$ would yield a complexed anion radical, $AQ \cdot AlCl_3^{\cdot -}$. Thus, the same molecular structure exists before and after electron-transfer to form the complexed anion radical; if the following chemical reactions and electron-transfer are reversible, then, reversible behavior should be observed for the system as a whole. Two effects stemming from the increased acidity of this medium should also be noted: first, the chemical species involved in the equilibria above should also include $Al_2Cl_7^-$ to some extent, since the concentration of this species begins to increase rapidly in the neutral region, and second, the final equilibrium in the series forming $AQ(AlCl_3)_3^{=}$ should be rather complete (as opposed to the partial complexation in the basic melt).

As the melt acidity is increased, the reduction of the $AQ \cdot 2AlCl_3$ complex (2nd and 3rd CV's) at +0.8 V becomes evident.

In addition, the oxidation processes also shift to more positive potentials, suggesting successively higher complexation of the quinone dianion; thus, the species $AQ(AlCl_3)_1^=$, $AQ(AlCl_3)_2^=$, and $AQ(AlCl_3)_3^=$ would account for the oxidation peaks observed. As seen in the third CV in Figure 1, in which $AQ(AlCl_3)$ is the major species, the following chemical reactions become more irreversible as melt acidity increases, thus increasing the amount of dianion oxidized as $AQ(AlCl_3)_2^=$ rather than $AQ(AlCl_3)_1^=$ after $AQ(AlCl_3)$ reduction.

The attainment of equilibrium among the various quinone complexes as reduction proceeds is evidently rather slow, since the relative cyclic voltammetric peak heights for reduction of the three quinone species were found to be essentially constant as a function of scan rate. Normal pulse voltammetry of the complexes in the neutral melt clearly showed the presence of three species over the pulse width range of 20 msec to 750 msec, thus indicating again the slow equilibrium among the species; however, the height of the wave due to $AQ \cdot 2AlCl_3$ reduction (most positive wave) was found to increase relative to those due to reduction of $AQ \cdot AlCl_3$ and AQ as the pulse width was increased. The situation apparently corresponds, then, to the case of an electron transfer preceded by a homogeneous chemical reaction, for which an increase in current, relative to that observed for diffusion only, would be expected (10). The reduction step occurring at the most positive potential, for example, corresponds to the two-electron reduction of $AQ \cdot 2AlCl_3$, the preceding chemical reaction being the complexation of $AQ \cdot AlCl_3$ by $Al_2Cl_7^-$ (i.e., first-order in each species) in response to depletion of $AQ \cdot 2AlCl_3$ by the reduction process; a similar relationship between $AQ \cdot AlCl_3$ and AQ should also hold. The current-time behaviors of the various reduction processes were examined by means of a log i vs. log t (t = pulse width) plot for each process from which slope values $\alpha (i = kt^{\alpha})$ of -0.44, -0.47, and -0.74 for reduction of $AQ \cdot 2AlCl_3$, $AQ \cdot AlCl_3$, and AQ were obtained. When compared to an α value of -0.50 for a purely diffusional process, these values indicate a current decrease less than that expected for diffusion involving reduction of $AQ \cdot 2AlCl_3$ (again indicating a shift in equilibrium toward the $AQ \cdot 2AlCl_3$ complex), while the current-time decrease for uncomplexed AQ is substantially larger than that expected for purely diffusional current-time behavior, reflecting a decrease in AQ concentration as the complexation equilibria shift toward the $AlCl_3$ complexes reduced previously. The α value observed for $AQ \cdot AlCl_3$, being close to 0.50, would seem to affirm

the intermediate nature of this complex; that is, the concentration of $AQ \cdot AlCl_3$ evidently remains relatively constant since it is formed from AQ by $AlCl_3$ complexation but depleted by further complexation to form $AQ \cdot 2AlCl_3$. The slow rate of interconversion among the complexes observed above may be due to the limited availability of $Al_2Cl_7^-$ in the neutral melt (since it is unbuffered with respect to $Al_2Cl_7^-$) and not to unusually low rate constants for the complexation reactions themselves.

ELECTROCHEMISTRY IN ACIDIC MELT

As seen in Figure 1, the electrochemical behavior of AQ in the acidic melt is similar to that observed in the basic melt in that the oxidation and reduction processes are separated by some 500 mV; as mentioned previously, the potential shift of +1.4 V for the system as a whole, with respect to the system in the basic melt, is due to complexation of AQ as $AQ \cdot 2AlCl_3$. The cathodic process again involves the two-electron reduction of the complexed AQ to the quinone dianion, as established by coulometry of AQ in the acidic melt at +0.50 V and comparison of cyclic voltammograms of the final coulometry mixture and of a melt containing authentic anthrahydroquinone (identical oxidation peak potentials). Subsequent coulometric oxidation of the dianion revealed that the anodic process corresponds to two-electron oxidation back to $AQ \cdot 2AlCl_3$, the cyclic voltammetric behavior of the oxidized species in the coulometry melt being identical to that of $AQ \cdot 2AlCl_3$ in the acidic melt. As in the basic melt, a Nernst plot of potential vs. $\log_{10}$ of the ratio of $AQ \cdot 2AlCl_3$ to its coulometrically produced reduction product (slope = 29 mV) indicated a reversible two-electron process. Since charge transfer is apparently rather rapid in the acidic melt, the peak potential separation observed for the cathodic and anodic processes implies that, as in the basic melt, an irreversible chemical reaction following reduction is responsible for the lack of reversibility in the system as a whole. The quinone/quinone dianion redox equilibrium including chemical interaction of $Al_2Cl_7^-$ ions with the dianion (since $Al_2Cl_7^-$ should be more reactive than $AlCl_4^-$ toward oxyanions) can be written as

$$AQ \cdot (AlCl_3)_2 + mAl_2Cl_7^- + 2e^- \rightleftarrows AQ(AlCl_3)_{2+m}^{=} + mAlCl_4^-, \qquad [4]$$

and the corresponding Nernst equation as

$$E = E^\circ + \frac{RT}{2F} \ln \frac{[AQ(AlCl_3)_2]}{[AQ(AlCl_3)_{2+m}^{=}]} + \frac{mRT}{2F} \ln \frac{[Al_2Cl_7^-]}{[AlCl_4^-]} \quad . \qquad [5]$$

A Nernst plot obtained in an acidic melt containing equimolar amounts of $AQ \cdot 2AlCl_3$ and its dianion and varied in $\frac{[Al_2Cl_7^-]}{[AlCl_4^-]}$ by incremental addition of $AlCl_3$ was found to have a slope of 60 mV per decade change in $\frac{[Al_2Cl_7^-]}{[AlCl_4^-]}$, indicating that two $Al_2Cl_7^-$ ions are involved in chemical reactions following $AQ \cdot 2AlCl_3$ reduction. Visible absorption spectroscopy of a solution of coulometrically-produced dianion (absorption maxima at 400, 480, and 360 nm; ε = 8,760; 9,120; 5,470, respectively) showed a blue shift relative to the spectrum obtained in the basic melt. Since previous studies in other systems have indicated that protonation of the AQ dianion to form the hydroquinone (the spectrum of which is very similar to that of the dianion in the basic melt) causes a blue shift in the visible spectra, the further blue shift observed in the present case seems to support the existence of the dianion in the acidic melt as $AQ(AlCl_3)_4^{=}$ (6).

From the cyclic voltammogram in Figure 1, it is apparent that the reduction peak for AQ in the acidic melt is much sharper ($E_{p/2} - E_p$ = 40 mV at 200 mV/sec scan rate; theoretical $E_{p/2} - E_p$ = 31 mV for n = 2 at 40°C) than that in the basic melt ($E_{p/2} - E_p \cong 80$ mV). At lower scan rates (~20 mV/sec), $E_{p/2} - E_p$ values approached the theoretical value, probably indicating the effects of uncompensated cell resistance at higher scan rates. It appears that a two-electron reversible process is involved for AQ reduction in the acidic melt. Normal pulse voltammetric data for $AQ \cdot 2AlCl_3$ reduction (initial potential + 1.20 V) supported this conclusion, the observed slope of an E vs. $\log \frac{i_d - i}{i}$ being 40 mV/log unit; from the i_d value, a diffusion coefficient of $2.6 \pm 0.1 \times 10^{-7}$ cm^2/sec was found for $AQ \cdot 2AlCl_3$ reduction in the 1.2:1.0 melt, compared to a value of $6.2 \pm 0.2 \times 10^{-7}$ cm^2/sec for AQ reduction in the basic (0.8:1.0) melt. The presence of rapid chemical reactions coupled with the charge-transfer process was deduced from the cyclic voltammetric behavior at scan rates higher than 5 V/sec, beyond which an additional cathodic and anodic process (at +0.34V and +0.97V, respectively; 20 V/sec scan rate) began to appear. An i vs. $t^{-1/2}$ plot for chronoamperometric data was found to be linear over a time frame of 10 msec to 5 seconds, again indicating very rapid chemical kinetics.

SUMMARY OF ANTHRAQUINONE ELECTROCHEMISTRY

The electrochemical and spectroscopic behavior of 9,10-anthraquinone in the $AlCl_3$:BuPyCl molten salt system has been found to be profoundly dependent upon the acidity (that is, ratio of $AlCl_3$ to BuPyCl) of the melt, the changes in these properties arising from the complexation of AQ by $Al_2Cl_7^-$ to form successively $AQ \cdot AlCl_3$ and $AQ \cdot 2AlCl_3$ as acidity is increased through the neutral region.

Electrochemical behavior in the basic melt, in which AQ is present in the uncomplexed form, involves an overall two-electron process and, from the appearance of the normal pulse and cyclic voltammograms, slow electron transfer. Since a strong interaction between the reduced AQ and $AlCl_4^-$ is evident both from the separation of potentials observed for reduction of AQ and oxidation of its dianion and from the visible absorption spectrum of the dianion, an ECE mechanism is thought to be involved for AQ reduction in the basic melt.

The effect of $AlCl_3$ in the acidic (1.2:1) melt, forming $AQ \cdot 2AlCl_3$ as established by infrared spectroscopy and chemical analysis, is a marked shift in potential (+1.4V) observed for $AQ \cdot 2AlCl_3$ reduction with respect to that seen for reduction of uncomplexed AQ in the basic melt. The interaction of $AQ \cdot 2AlCl_3$ with the melt upon reduction to form more highly complexed reduction products appears to be more reversible than in the case in the basic melt, since the cyclic voltammetric peak potential separation for the processes corresponding to reduction of $AQ \cdot 2AlCl_3$ and oxidation of the further complexed dianion decreases with an increase in temperature or a decrease in scan rate.

The rapidly changing acidity in the neutral melt gives rise to the interesting electrochemical behavior observed for AQ in this region; that is, as acidity is varied through this region, three distinct reduction processes can be observed corresponding to reduction of uncomplexed AQ, of $AQ \cdot AlCl_3$ (inferred from infrared spectral data), and of $AQ \cdot 2AlCl_3$. It should be noted that the reduction of $AQ \cdot AlCl_3$ cannot be observed separately from the other reduction processes.

In a melt containing all three complexes, it appears that the rate of interconversion among these complexes upon reduction is fairly slow, an observation reflecting the initially low levels of $Al_2Cl_7^-$ present as well as the unbuffered nature of the melt in the neutral region.

B. OXIDE DETERMINATION

The problem of the species of oxide which exists in these chloroaluminate melts has likewise been the subject of controversy, although there appears to be reasonable agreement that the following reactions represent the interaction of oxide with the chloroaluminate melt, depending on the acidity where reaction [6] dominates in acid, and [7]

$$O^{-2} + AlCl_4^- \rightleftarrows AlOCl + 3\ Cl^- \qquad [6]$$

$$O^{-2} + AlCl_4^- \rightleftarrows AlOCl_2^- + 2\ Cl^- \qquad [7]$$

becomes important in the more basic regions (11, 12, 13).

As a portion of studying solute chemistry in the $BuPyCl:AlCl_3$ solvent, we embarked upon a study of the electrochemical behavior of Ti(IV) under conditions where the system was quite basic; i.e., the mole ratio of $BuPyCl:AlCl_3$ was maintained from 1:0.7 to 1:0.95 and when the melt contained added oxide. Under these conditions, Ti(IV) exists as two species in slow equilibrium as a result of the interaction of $TiCl_6^{-2}$ with oxide. Both species are electroactive, with $E_{1/2}$ values, vs an Al reference in a 2:1 $AlCl_3$:BuPyCl melt, of -0.343 V and ca -0.77 V, respectively, in the basic melt. Both Ti(IV) waves were diffusion controlled, and coulometry performed on the diffusion plateau of either wave completely reduced all the Ti(IV) to Ti(III) (14). The slow equilibrium responsible is given as

$$TiCl_6^{-2} + AlOCl_2^- \rightleftarrows TiOCl_4^{-2} + AlCl_4^- \qquad [8]$$

The equilibrium constant of reaction [8] is not very high, approximately 900 or so, and, in a melt where the $AlCl_4^-$ is in great excess, the reaction is not quantitative. In effect, this means that no matter what the concentration of oxide, presumed present as $AlOCl_2^-$ by analogy to the situation in the $NaAlCl_4$ melts, only a fraction of the total Ti(IV) introduced into the melt is converted into the Ti-O-Cl complex by oxide impurity. The

addition of excess oxide, however, added as Li_2CO_3, does shift the reaction [8] to the right. The determination of oxide could be carried out as follows.

The equilibrium constant of reaction [8] has the form

$$K = \frac{C_{TiOCl_4^{-2}} \; C_{AlCl_4^-}}{C_{TiCl_6^{-2}} \; C_{AlOCl_2^-}} \qquad [9]$$

In a basic melt, the concentration of $AlCl_4^-$ is sufficiently great that it will be invarient during a titration. Thus, reaction [9] can be written

$$K' = \frac{K}{C_{AlCl_4^-}} \qquad [10]$$

If oxide is titrated with added $TiCl_4$, assumed to form $TiCl_6^{-2}$ in a "pure" melt, the Ti(IV) will exist either as a single chlorocomplex, $TiCl_6^{-2}$, or as the oxychlorocomplex, $TiOCl_4^{-2}$. Thus,

$$C_{TiCl_6^{-2}} = C_{Ti_{total}} - C_{TiOCl_4^{-2}} \qquad [11]$$

and substituting [11] into [10],

$$K' = \frac{C_{TiOCl_4^{-2}}}{(C_{Ti_{total}} - C_{TiOCl_4^{-2}})\,(C°_{AlOCl_2^-} - C_{TiOCl_4^{-2}})} \qquad [12]$$

where $C_{Ti_{total}}$ denotes the total concentration of Ti(IV) in the melt, and $C°_{AlOCl_2^-}$ the concentration of oxide present, assumed to be $AlOCl_2^-$, either as an initial impurity, or as the total of an initial impurity and a "spiked" sample.

Rearranging this leads to

$$\frac{C_{Ti_{total}}}{C_{TiOCl_4^{-2}}} = \frac{1}{C°_{AlOCL_2^-}} (C_{Ti_{total}} - C_{TiOCl_4^{-2}}) + \frac{K'C°_{ALOCl_2^-} + 1}{K'C°_{AlOCL_2^-}} \qquad [13]$$

From Equation [13] one can see that by plotting $C_{Ti_{total}}/C_{TiOCl_4^{-2}}$ vs $(C_{Ti_{total}} - C_{TiOCl_4^{-2}})$ the slope of the line gives $1/C°_{AlOCl_2^-}$ and the intercept can then be employed to determine K', hence K, since $C_{AlCl_4^-}$ is known. $C_{TiCl_6^{-2}}$ and/or $C_{TiOCl_4^{-2}}$ are determined by a voltammetric experiment.

Titration of oxide in the melt was performed by consecutive addition of several spikes of pure $TiCl_4$ to the melt.

A typical set of normal pulse voltammograms at a glassy carbon electrode during the titration of oxide impurity in the melt is shown in Figure 3. As the amount of Ti(IV) in the melt is increased, both the $TiCl_6^{-2}$ (more positive) wave increase and the $TiOCl_4^{-2}$ (more negative wave) increase. Larger initial concentrations of oxide in the melt yield similar results, except that ratio of the two waves may differ. However, regardless of the oxide concentration, the total height of both waves is linear in $C_{Ti_{total}}$ - i.e., the amount of $TiCl_4$ addded to the melt - and both waves are diffusion controlled, as determined from the time dependence of the normal pulse voltammetric waves for each wave.

Figure 4 shows three titration curves, (a), which is at 60°C with no added oxide impurity, (b), and (c) corresponding to a sample "spiked" with 24 and 35 mM oxide respectively. Data from these determinations are shown in Table 1.

It thus appears that the procedure permits the determination of oxide impurity in these melts at levels of 0.5 to 50mM, and that, at least in our hands, reasonable well prepared and purified melts contain of the order of 1-2 mM oxide impurity.

ACKNOWLEDGEMENTS

This work was supported in part by the Office of Naval Research and the Air Force Office of Scientific Research.

REFERENCES

(1) Gale, R., Gilbert, B. and Osteryoung, R. A., Inorg. Chem., 17, 2728 (1978).

(2) Boxall, L. G., Jones, H. L. and Osteryoung, R. A., J. Electrochem. Soc., 120, 223 (1973).

(3) Gale, R. and Osteryoung, R. A., Inorg. Chem., 18, 1603 (1979).

(4) Gale, R. J. and Osteryoung, R. A., Inorg. Chem., 19, 2240 (1980).

(5) Giallonardo, R. and Susz, B. P., Helv. Chim. Acta, 54, 2402 (1971).

(6) Wightman, R. M. Cockrell, J. R. Murray, R. W., Burnett, J. N. and Jones, S., J. Am. Chem. Soc., 98, 2562 (1976).

(7) Greig, C. C. and Johnson, C. D., J. Am. Chem. Soc., 90, 6453 (1968).

(8) Nepras, M., Titz, M., Snobl, D. and Kratochvil, V., Coll. Czech. Chem. Commun., 38, 2397 (1973).

(9) Bartak, D. E. and Osteryoung, R. A., J. Electroanal. Chem., 74, 68 (1976).

(10) Murray, R. W., in "Techniques of Organic Chemistry," A. Weissberger, Ed.; Vol. I, Part IIA, Chapter VIII, Wiley-Interscience, New York (1971).

(11) Letisse, G. and Tremillon, B., J. Electroanal. Chem., 17, 387 (1968).

(12) Gilbert, B. and Osteryoung, R. A., J. Am. Chem. Soc., 100, 2725 (1978).

(13) Rubinson, J., Gilbert, B. and Osteryoung, R. A., Inorg. Chem., 16, 3040 (1977).

(14) Linga, H. and Osteryoung, R. A., J. Am. Chem. Soc., in press.

Table I

Concentration of oxygen and K' and K values for different melt compositions and temperatures

Melt Composition	Temperature °C	O^{-2},mM added as Li_2CO_3	O^{-2},mM found	$K' \cdot 10^{-3}$ [1/M]	$K \cdot 10^{-3}$	O^{-2} impurity
0.7:1	40	19.8	21.6	0.265	1.0	1.8
0.8:1	40	0	1.9	0.28	.98	1.9
0.8:1	40	11.6	14.0	0.29	1.02	2.4
0.7:1	60	24	25.1	0.20	0.65	1.1
0.8:1	60	0	1.92	0.21	0.75	1.9
0.8:1	60	35	41.4	0.20	0.70	6.4(1)
0.8:1	80	0	2.0	0.175	0.62	2.0
0.8:1	80	0	6.0	0.172	0.61	6.0(1)

(1) Melt pre-electrolyzed between Al electrode prior to titration; apparently introduces added oxide impurity.

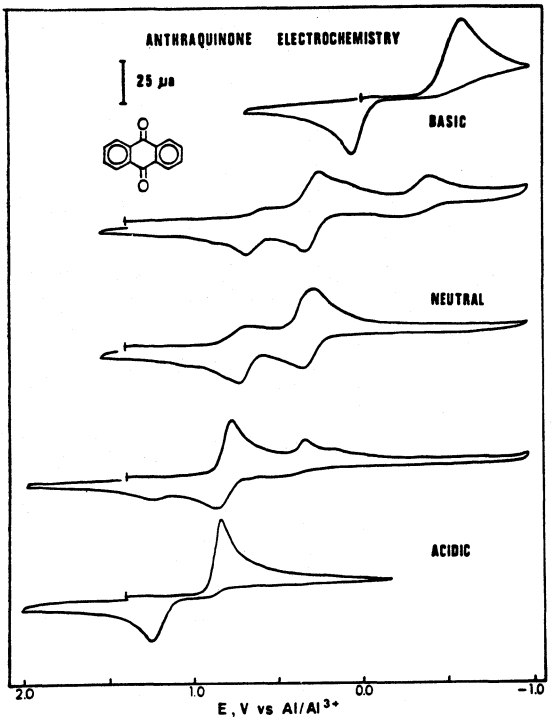

Figure 1: Cyclic voltammograms of 9,10-anthraquinone in 0.8:1.0 basic melt (top scan); in neutral melts (acidity adjusted by small additions of $AlCl_3$ (middle three scans); in 1.2:1.0 acidic melt (bottom scan). Scans recorded at 40°C, 200 mV/sec scan rate; anthraquinone 4 mM.

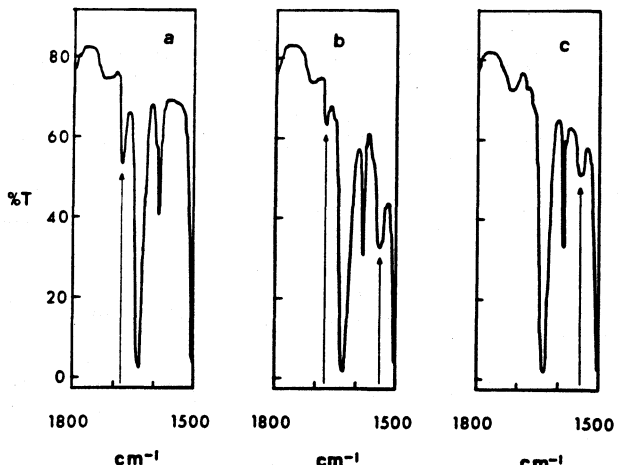

Figure 2: Infrared spectra of anthraquinone (AQ in melts of various acidities: (a) 0.8:1.0 basic melt: $[AQ]_T$ = 34 mM, (b) Neutral melt: $[AQ]_T$ = 49 mM, (c) 1.2:1.0 acidic melt: $[AQ]_T$ = 14 mM. Arrows show band to AQ carbonyl; other bands due to N-butylpyridinium cation. Concentrations estimated by normal pulse voltammetry.

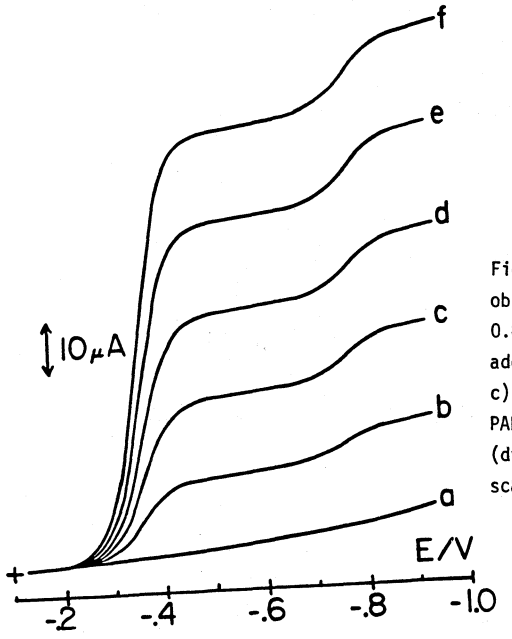

Figure 3: Normal pulse voltammogram obtained during the titration of a 0.8:1 melt at 60°C. Volume of $TiCl_4$ added (microliters) a) 0, b) 5, c) 15, e) 20, f) 25. Instrument: PARC 174; delay between pulses (drop time setting) 2 seconds; scan rate 1 mV s^{-1}.

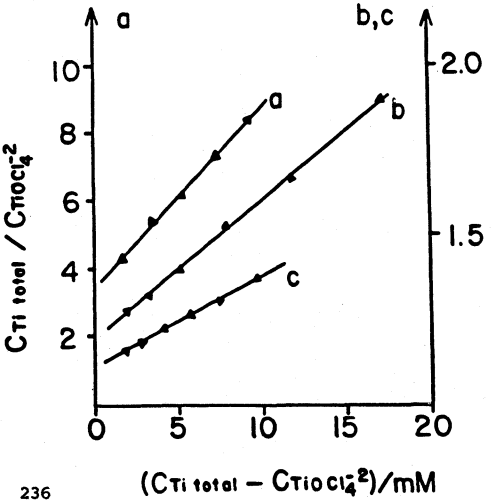

Figure 4: Titration plots of oxide in melts containing oxide added as Li_2CO_3 to form $AlOCl_2^-$. a) 0, b) 25.1 mM, c) 41.4 mM. Data in Table 1.

DOI: 10.1149/198109.0237PV

CORRELATIONS BETWEEN TRANSPORT PROPERTIES, ^{1}HNMR SPECTRA AND STRUCTURE OF MOLTEN METHYLPYRIDINIUM IODIDES

David S. Newman, Rex M. Stevens
Department of Chemistry
Bowling Green State University
Bowling Green, Ohio 43403

Abstract

The equivalent conductance, viscosity and ^{1}HNMR spectra of the molten methylpyridinium iodides were measured as a function of temperature and correlations between structure, spectra, and transport properties were made. In addition, and interesting new compound was found in the 2-methylpyridinium iodide melt.

Introduction

In an earlier study (1), correlations between transport properties, ^{1}HNMR spectra and substituent effects in molten methylpyridinium chlorides and bromides were made. From these correlations, conclusions about the structure of the melts were drawn and it became apparent that hydrogen bonding between the nitrogenic proton and the halide ion, coupled with substituent effects due to the position of the methyl group on the ring, strongly influenced the transport properties as well as the species present. In the methylpyridinium iodides, hydrogen bonding does not occur (2) so by comparing their transport properties and ^{1}HNMR spectra with those of the chlorides and bromides, a more accurate assessment of the influence of hydrogen bonding on the chloride and bromide melts can be made.

The suggestion that molten organic salts have relatively weaker repulsive forces between ions than inorganic salts, and also possess the general property that the ratio of the energy of activation for viscosity, E_η, to the energy of activation for equivalent conductance, E_Λ, is about equal to 1.1, is explored further and the consequences and causes of this ratio are discussed. Finally, the existence of an interesting new species is postulated to be present in the 2-methylpyridinium iodide melt.

Experimental

The methylpyridinium iodide salts were synthesized by methods already described in the literature (3,4), with the exception that the appropriate methylpyridine was mixed with an equal quantity of petroleum ether rather than benzene. Anhydrous HI gas was bubbled through the solution following a ten-minute nitrogen purge that

removed air from the system. White crystals of the methylpyridinium salt began to precipitate after about one minute.

Density measurements were made using the modified Lipkin bicapillary arm pycnometer (5), together with a fiber optic light pipe that greatly facilitated seeing the graduation markings on the pycnometer, which was immersed in a constant temperature oil bath.

Conductivity measurements were made with a Jones bridge at a frequency of 1000 Hz using a capillary cell with platinum electrodes.

Chemical analysis of the salts was done by determining the iodide concentration using a standard KIO_3 solution to titrate the iodide (6).

Viscosities were measured with a Cannon-Fenske viscometer and the ^{1}HNMR spectra were obtained using the variable temperature probe of a Varian CFT 20 NMR machine and external reference standards.

The IR spectra of the four solid methyl salts were obtained using a Perkin-Elmer Model 337 Spectrophotometer.

Results

The densities of the four methylpyridinium iodide isomers are listed as a function of temperature in Table I together with each salt's melting point. It should be noted that the 2-methyl iodide is considerably less dense than the other isomers.

TABLE I - The densities of the four methylpyridinium iodide salts as a function of temperature

$$\rho = A - BT(K)$$

Salt	A	$B(\times 10^4)$	T_m(°C)	Temperature Range
4-mepyr/HI	1.995	8.377	171	171-200
3-mepyr/HI	1.968	7.779	92	93-143
2-mepyr/HI	1.591	7.057	94	94-130
N-mepyr/I*	1.943	6.880	117	117-187

* see ref. 4

The logs of the equivalent conductances as a function of T^{-1} are shown in Fig. 1 while the logs of the viscosities vs T^{-1} are shown in Fig. 2. It should again be noted that the conductance of 2-mepyr/HI does not fall on the same curve as the conductance of the other three isomers.

The ^{1}HNMR spectrum of molten 4-mepyr/HI at 174° is shown in Fig. 3. The reference here is $(CH_3)_2SO_2$. No temperature dependence was observed for any peak over the temperature range studied. Figure 4 shows the ^{1}HNMR spectrum of 3-mepyr/HI are Fig. 5 shows the spectrum of 2-mepyr/HI. DMSO is the reference in both of these melts. Table II lists the chemical shifts, δ, for the three isomers, all corrected to a DMSO reference. The $>N-H^+$ proton in the 3-methyl melt showed a small upfield shift of the $>N-H^+$ peak position as a function of temperature,

TABLE II - Proton chemical shifts for 4,3, and 2-methylpyridinium iodide vs DMSO

Salt	N-H	δ α	β	γ	CH_3	Temperature range(K)
4-mepyr/HI	12.1	7.03	6.08	--	0.64	447
3-mepyr/HI	12.32-12.23	6.93	6.10	6.58	0.50	369-418
2-mepyr/HI	13.10-12.84	6.30	5.22	5.75	0.27	369-400

whereas the ring proton chemical shifts were temperature independent. In the 2-methyl salt, the $>N-H^+$ proton chemical shift showed a rather striking temperature dependence, moving upfield 0.0083 ppm/K. This temperature dependence is larger than any we have yet measured and is in an unexpected direction. Moreover, the integrated area under the $>N-H^+$ peak was approximately 0.5 rather than 1 as it was in each of the other two spectra.

Chemical analysis of six different 2-mepyr/HI salt samples (each analysis in triplicate) indicated a methylpyridine to iodine ratio of 1.99 to 1. In addition, the solid state IR spectrum showed, among other features, a prominent peak at around 400 cm^{-1}.

Discussion

These data are compelling evidence for the existence of a dimeric species in the 2-methylpyridinium iodide melt. The most likely structure of this species is shown in Fig. 6. In the molten state, this 2-methylpyridine hemiperiodide consists of the dimeric cation and an I^- anion. This structure correlates extremely well with the unusual ^{1}HNMR spectrum, density, conductivity, and viscosity of the 2-methyl salt.

To further substantiate the existence of this dimeric species, 3.15g of the salt was dissolved in naphthalene and the solution's freezing point was measured. The solution froze at 65°C whereas a one molal solution of CCl_4 in naphthalene froze at 72°C. The naphthalene/iodide solution was an extremely good ionic conductor whereas the CCl_4/naphthalene did not conduct at all. These data indicate

that approximately 2 moles of particles are present per 1000g naphthalene and since the solution is a highly conducting melt it is reasonable to assume that the freezing point depression is due to the hemiperiodide dissociating into the 2-methylhemipyridinium ion and the iodide ion.

The upfield chemical shift must be due to the $\geq N\text{-}H^+$ becoming more shielded with increasing temperature, rather than less shielded, which means that the $\geq N\text{-}H\text{-}N \leq$ bond is probably asymmetric; the proton lying closer to one nitrogen than the other. As the temperature is raised, the $\geq N\text{-}H\ldots N \leq$ bond is stretched and weakens. This allows the proton to spend more time in the vicinity of the nitrogen it is initially closer to, presumably shielded by the lone pair of electrons in the nitrogen's sp^2 orbital, and consequently it resonates at a higher energy. In other words, as the temperature increases the bond becomes more asymmetric.

The upfield shift of the nitrogenic proton together with the prominent IR peak at 400 cm^{-1} can also be considered evidence for proton tunneling in the melt and is explicable in terms of the Conway, Bockris and Linton model (7,8). If it is assumed the proton tunnels back and forth from one well to another (double minimum), the rate of tunneling will be strongly dependent on the relative orientation of one nitrogen to the other. As the temperature rises and the bond stretches, the molecule also bends so it is quite likely that one N site moves away from the the appropriate position or orientation for maximum tunneling to occur. Therefore, the tunneling rate drops with increasing temperature faster than the rate of hopping over the barrier increases. and the proton resides in a given well for longer and longer periods of time, thus contributing to the upfield shift. The strong absorbance in the low energy region of the spectrum at 400 cm^{-1} may also be due to this tunneling proton according to the several recent calculations (9,10).

Two reasons for the 2-methyl iodide being unique among pyridinium salts studied to date are that the $\geq N\text{-}H^+$ does not hydrogen bond with the I^-, as it does with the Br^- and the Cl^-, so there is no competition between I^- and the basic pair of electrons on the nitrogen, and the methyl groups in the "2" position prevent the I^- from disrupting the $\geq N\text{-}H\text{-}N \leq$ bond once it forms. Precedents for this pyridinium-pyridine type of structure do exist in the literature. X-ray and neutron diffraction studies show $[(C_5H_5)N_2]^+[ZnBr_{3/2}Cl_{3/2}(C_5H_5N)]^-$ to possess an $\geq N\text{-}H\cdot N \leq$ bond (11) and IR together with neutron diffraction indicate 4-aminopyridine hemiperchlorate ($C_5H_6N.1/2HClO_4$) also has a strong $\geq N\text{-}H\text{-}N \leq$ bond (12). More importantly however, this structure correlates very well with both transport properties and the ^{1}HNMR spectrum.

A strong correlation between structure and transport properties exists in the bromide and chloride melts. The equivalent conductance of each of the 4-methyl halides is considerably lower than that of the

corresponding N-methyl melts (1,4) over the entire liquid range of the salts, despite the greater density of the latter liquids and the fact that H^+ ions may contribute to the conductivity the 4-methyl melts, but not to that of the N-methyl melts. The explanation offered was that hydrogen bonding caused this difference in conductance by allowing complexes of the sort

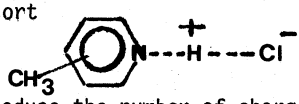

to form and thus reduce the number of charge carriers per unit volume. If this explanation is correct, in the absence of hydrogen bonding a 4-methyl salt should be a better conductor than the corresponding N-methyl isomer. This contention is dramatically borne out by the iodide system where hydrogen bonding does not occur. The 4-methyl iodide is a considerably better conductor than the N-methyl melt, thus clearly reversing the trend observed in the hydrogen bonded systems.

Table III lists the energies of activation of viscosity and equivalent conductance of each of the 4-methyl iodide melts and again

TABLE III - Energies of activation for viscosity and conductance.

Salt	$E_?$ (J/°mole)	E_Λ (J/°mole)	$E_?/E_\Lambda$
N-mepyrI	27.6	26.2	1.05
4-mepyrI	27.6	19.2	1.43
3-mepyrI	30.9	26.7	1.15
2-mepyrI	26.4	18.5	1.42

the ratios are approximately equal to 1.1, except for the 2-methyl iodide and the 4-methyl iodide which are somewhat higher, but still lower than the ratios found for inorganic melts (13). We think the 2-methyl salt is a dimeric species with either a particularly labile proton or a particularly weakly held I^- ion (or both) and would therefore be expected to have a relatively low E_Λ. The reason why the 4-methyl salt's ratio is a bit high is still unclear, but it may be that the proton is again making a substantial contribution to the conductivity. The $E_?$'s for both melts seem normal.

Conclusion

By obtaining correlations between structure, transport properties and ^{1}HNMR spectra of a series of isomeric melts in which no hydrogen bonding occurs, we are better able to assess the contribution of hydrogen bonding to structure and transport properties of those melts in which hydrogen bonding plays an important role. In addition, we have found that by studying a series of compounds in a systematic way, we were able to detect the presence of an interesting new compound

that otherwise might have gone unnoticed. Based on the energies of activation obtained here as well as those measured elsewhere, we suggest classifying those salts whose E_η/E_Λ ratio is between 1 and 1.2 as "soft" salts and those salts whose E_η/E_Λ ratio is between 2 and 5 as "hard" salts. This terminology may even be more apt in molten salt systems than in acid-base theory because those salts whose E_η/E_Λ ratio is 1:1, and therefore would be considered soft, are easily polarizable and have relatively weak repulsive forces. These ideas will be explored at greater length in a subsequent paper.

REFERENCES

1. D. S. Newman, R. R. Rhinebarger, D. Siconolfi, O. A. Banjoko, J. Electrochem Soc. In press.
2. N. Goldstein, J. L. Ragel, J. Chem. Phys. 70 5072 (1979).
3. M. S. Rozhdestvenskii, L. M. Brode, J. Appl. Chem. USSR 10 722 (1973).
4. D. S. Newman, R. T. Tillack, D. P. Morgan, W. C. Wan J. Electrochem. Soc 124 856 (1977).
5. D. S. Nemman, R. T. Tillack, D. P. Morgan, J. Chem. Eng. Data 21 279 (1976).
6. A. I. Vogel, "A Text Book of Quantitative Inorganic Analysis," Longman's Green and Co., London 1951 pp. 360-361.
7. B. E. Conway, J. O'M Bockris, H. Linton, J. Chem. Phys. 24 834 (1956).
8. J. O'M Bockris, S. U. M. Kahn, Quantum Electrochemistry (Plenum Press, New York 1979) Chapt. 9.
9. H. Romanowski and L. Sobczyk, Chem. Phys. 19 361 (1977).
10. E. Grech, Z. Malarski, L. Sobczyk, Spectrosc. Lett. 9 749 (1976).
11. B. E. Villarreal-Salinas, E. O. Schlemper, J. Crystallogr. Mol. Struct. 8 217 (1978).
12. J. Roziere, J. M. Willaims, E. Grech, Z. Malarski, L. Sobcyzk, J. Chem. Phys. 72 6117 (1980).
13. H. Bloom, E. Heymann, Proc. Roy. Soc. London, Ser. A188 392 (1947).

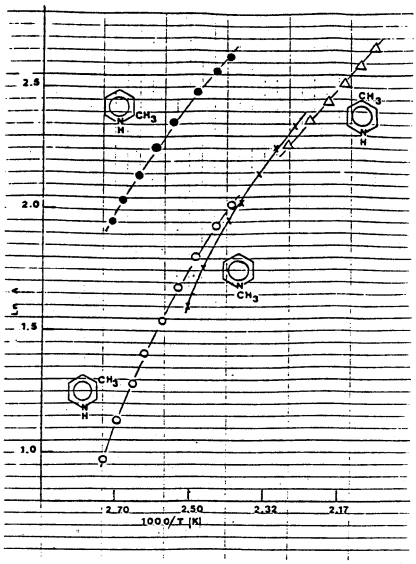

Fig. 1 Ln of Λ vs 1000/T

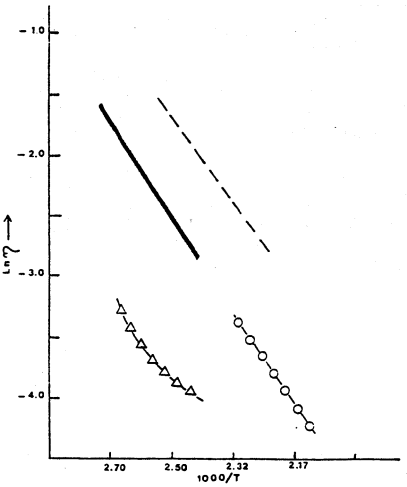

Fig. 2 Ln of ? vs 1000/T.
-△- 2-methylpyridinium iodide;
——— 3-methylpyridinium iodide;
-O-O- 4-methylpyridinium iodide;
– – – N-methylpyridinium iodide

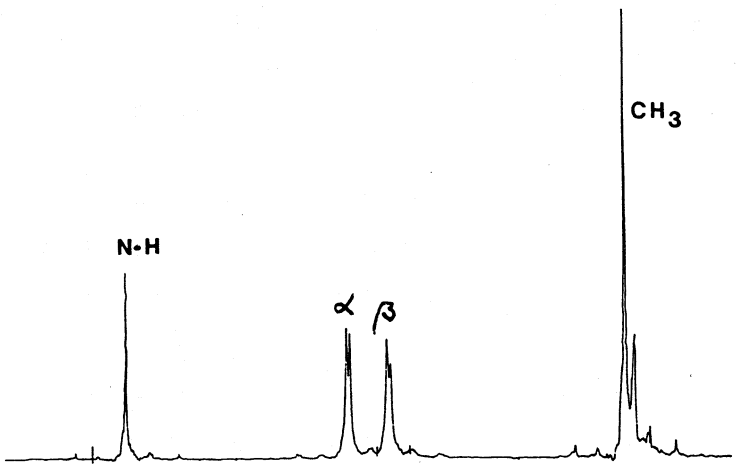

Fig. 3 ^{1}HNMR spectrum of 4-methylpyridinium iodide at 174°C

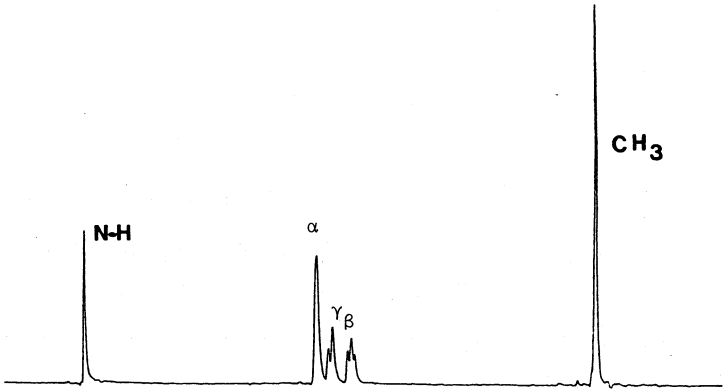

Fig. 4 ^{1}HNMR spectrum of 3-methylpyridinium iodide at 134°C

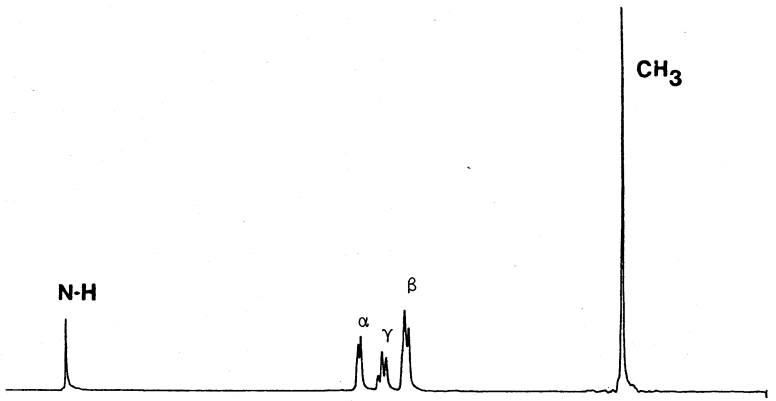

Fig. 5 ^{1}HNMR spectrum of 2-methylpyridinium iodide at 96°C

Fig. 6 Structure of 2-methyl-pyridine hemiperiodide

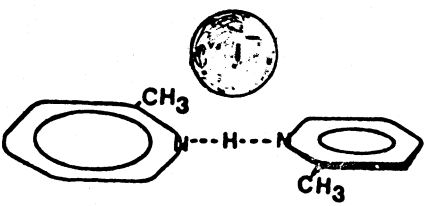

DOI: 10.1149/198109.0245PV

DIALKYLIMIDAZOLIUM CHLOROALUMINATE MOLTEN SALTS

John S. Wilkes, Joseph A. Levisky, and Melvin L. Druelinger

The Frank J. Seiler Research Laboratory
United States Air Force Academy, Colorado 80840

Charles L. Hussey

Department of Chemistry
University of Mississippi
University, MS 38677

ABSTRACT

Earlier work has shown that mixtures of 1-alkylpyridinium chlorides and aluminum chloride form electrolytes that are molten at room temperature. Molecular orbital calculations predicted that 1,3-dialkylimdazolium cations would be more stable cathodically than 1-alkylpyridinium cations. A series of 1-methyl-3-alkylimidazolium chlorides was synthesized and chloroaluminate melts were prepared from them. The imidazolium chlorides themselves have reduction potentials considerbly cathodic of the corresponding pyridinium chlorides in DMF. The new melts have favorable physical properties and wider electrochemical windows than the earlier melts. The Lewis acidity of the melts may be varied over a very broad range.

INTRODUCTION

There has been considerable research in this laboratory in the area of low melting fused salt electrolytes, particularly for use in high density batteries (1). While mixtures of sodium chloride and aluminum chloride were successfully used as the electrolyte in a thermal battery, the minimum temperature for operation was about 175°C. In order to achieve lower operating temperature we investigated mixtures of 1-alkypyridinium chlorides and aluminum chloride, some of which are molten at room temperature. Studies of the physical properties (2) of these melts and the electrochemistry of metal ions dissolved in them (3,4) indicated some promise as battery electrolytes. Osteryoung and coworkers have studied these types of melts extensively and have found them to be easily prepared (5) and have a very wide range of Lewis acidity (6).

One disadvantate of the alkylpyridinium chloroaluminate melts is that aluminum is oxidized in them when the melt is basic (chloride rich). Gale showed that in a melt composed of $AlCl_3$ and 1-butylpyridinium chloride the oxidation of aluminum is accompanied by the reduction of

the 1-butylpyridinium cation (7). We have convincing EPR evidence that in the same melt 1,1'-dibutyl-4,4'-bipyridinium radical cation is formed (8) by reaction with aluminum or by cathodic reduction. The reactivity of these melts towards aluminum is unfortunate, since aluminum would be a useful anode in a battery using the room temperature melt as the electrolyte. We report here our effort to find a room temperature molten salt that would have the favorable physical properties of the melts described above, but would also have a wide enough electrochemical window that aluminum would be stable in them.

EXPERIMENTAL

The MNDO molecular orbital calculations were performed on either a Burroughs 6700 or Digital Equipment Corp. VAX computer using a program provided by Dr. M. J. S. Dewar.

Reduction half-wave potentials were obtained in DMF containing 0.1M tetrabutylammonium perchlorate at a rotating disc electrode (1500 RPM). Potentials were measured at 25°C versus a saturated calomel electrode isolated from the bulk solution via a Vycor tipped bridge tube. The solution was presaturated with and maintained under a blanket of dry nitrogen.

Cyclic voltammetry was performed using a Pt working electrode, a W counter electrode and a reference electrode consisting of an aluminum wire immersed in an $AlCl_3$ rich melt (usually 67 mol% $AlCl_3$) and separated from the cell with a glass frit or glass wool.

Liquidus temperatures were measured using a Perkin-Elmer model DSC-2 differential scanning calorimeter. Specific conductivities were measured using an ac impedance bridge.

All experiments involving moisture sensitive meterials were performed in a Vacuum Atmospheres Corp. glove box containing a dry argon atmosphere. The 1-methylimidazole and 1,2-dimethylimidazole were obtained from the Aldrich Chemical Co. and were distilled before use. The 1-chloropropane and 1-chlorobutane were obtained from the Aldrich Chemical and were used without purification. The chloromethane and chloroethane were obtained from Linde Specialty Gasses. NMR spectra were run on a Varian T-60 spectrometer. IR spectra were run on a Beckman IR-20 spectrophometer. Elemental analyses were performed by Gailbraith Laboratories. Melting points are uncorrected.

1,3-Dimethylimidazolium Chloride: 1-methylimidazole (62.3 g, 0.78 mol) was weighed in a 250 ml glass vessel and chloromethane (100 ml, 1.40 mol) condensed into it using a dry ice condenser. The container was sealed and heated overnight (16 hrs) at 65°C with magnetic stirring. The pressure in the vessel was reduced by cooling in a dry ice/acetone bath and the top was removed. The excess chloromethane was allowed to boil off through a drying tube. The white solid crude product was recrystallized from acetonitrile. Isolated yield was 66.6 g (67%). Melt-

ing point 124.5 - 128°C. Elemental analysis; calculated for $C_5H_9N_2Cl \cdot 0.3H_2O$: 43.23% C, 7.04% H, 20.17% N, 25.53% Cl, 3.17% O. Observed: 42.82% C, 7.32% H, 20.13% N, 26.01% Cl, 3.72% O.

1-Methyl-3-ethylimidazolium Chloride: 1-Methylimidazole (19.3 g, 0.235 mol) was weighed in a 250 ml glass pressure vessel and chloroethane (56.0 g, 0.867 mol) condensed into it using a dry ice condenser. The container was sealed and heated for two days at 75°C with magnetic stirring. The pressure in the vessel was reduced by cooling in a dry ice/acetone bath and the top was removed. The excess chloromethane was allowed to boil off through a drying tube. A slightly off white solid product was obtained that showed no starting material by NMR. Isolated yield was 34.38 g, (99.8%). The product was recrystallized by dissolving in a minimum amount of acetonitrile and dropping it into cold ethyl acetate. Melting point 82-87°C. Elemental analysis calculated for $C_6H_{11}N_2Cl \cdot 0.2H_2O$: 47.97% C, 7.65% H, 18.65% N, 23.60% Cl, 2.13% O. Observed: 48.18% C, 7.80% H, 18.66% N, 23.52% Cl, 1.84% O.

1-Methyl-2-propylimidazolium Chloride: 1-Methylimidazole (10.1 g, 0.123 mol) and 1-chloropropane (12.7 g, 0.161 mol) were mixed in a 250 ml glass pressure vessel. The mixture was heated at 85°C for 20 hours with magnetic stirring. The reaction flask was allowed to cool to room temperature and the excess chloropropane was removed at reduced pressure. The slightly yellow oily product was diluted with about 10 ml of acetonitrile and cooled in the freezer. Crystallization was induced with a seed crystal and took several days. The seed crystals were obtained with much difficulty. Yield was 18.7 g (94.3%). Melting point 58-66°C. Elemental analysis: calculated for $C_7H_{13}N_2Cl \cdot 0.3H_2O$: 50.63% C, 8.26% H, 16.87% N, 21.35% Cl, 2.89% O. Observed: 50.70% C, 8.45% H, 17.08% N, 21.55% Cl, 2.22% O.

1-Methyl-3-butylimidazolium Chloride: 1-Methylimidazole (60 ml, 0.752 mol) and 1-chlorobutane (87 ml, 0.828 mol) were refluxed without additional solvent overnight with stirring. The reaction mixture was cooled to room temperature, the top liquid phase decanted and residual excess chlorobutane removed at reduced pressure. The slightly yellow oil was diluted in about 15 ml acetonitrile and crystallized in the freezer with the aid of a seed crystal. The original seed crystals were obtained with much difficulty. Melting point 65-69°C. Elemental analysis; calculated for $C_8H_{15}N_2Cl \cdot 0.1H_2O$: 54.45% C, 8.68% H, 15.87% N, 20.09% Cl, 0.91% O. Observed: 53.94% C, 8.90% H, 16.03% N, 20.52% Cl, 0.61% O.

1-Methyl-3-benzylimidazolium Chloride: 1-Methylimidazole (5.0 ml, 63.1 mmol) and benzyl chloride (8.0 ml, 69.4 mmol) were stirred together without solvent for 2 hours at room temperature. The reaction mixture set into a hard glass which could not be crystallized despite many attempts.

Chloroaluminate melts were prepared typically as in the following

example: Aluminum chloride (18.28 g, 0.1371 mol) was added in aliquots to 1-methyl-3-ethylimidazolium chloride (10.00 g, 0.0682 mol) with stirring under a dry argon atmosphere. The mixture was then stirred for several hours until dissolution of the aluminum chloride was complete. The material obtained was a clear water-white liquid.

RESULTS AND DISCUSSION

The probable reason for the low liquidus temperatures of the alkylpyridinium chloroaluminate melts is the size of the organic cation. As the size of the alkyl substituent increases, the liquidus temperature decreases. For example 1:1 mixture of the aluminum chloride and 1-methylpyridinium chloride melts at 145°C, while a similar mixture with 1-butylpyridinium chloride melts at 30°C. One might expect that any large organic cation could produce chloroaluminates that are also molten at or near room temperature. The most common source of positive charge in organic compounds is a quaternary nitrogen, as in the alkylpyridinium cations described above. For these reasons we focused our search on large (molecular weight >130) molecules containing quaternary nitrogen. The reason that aluminum is oxidized in the alkylpyridinium chloroaluminate melts and not in the alkali metal chloroaluminate melts is that the alkypridinium cation must be more easily reduced than sodium ion or Al(III). The best candidates should thus have reduction potentials significantly more negative than alkylpyridinium ions.

While one can tell by inspection of the structure of a molecule what its approximate size is and its charge, it is not possible to determine the reduction potential by simple inspection. The reduction potential may be estimated from the structure of the molecule alone using molecular orbital calculations. The newer semi-empirical techniques for performing molecular orbital calculations provide a rapid and relatively easy means for estimating the electron affinities of reasonably large organic molecules. In the MNDO method, developed by Dewar, the electron affinity of a closed shell cation is equal to the negative value of the energy of the lowest unoccupied molecular orbital (LUMO) (9). It is well established that the vacuum electron affinity may be correlated to the solution reduction potential as shown below (10).

$$EA = -LUMO \qquad (1)$$

$$E(red) = EA + \Delta G(solv) + K \qquad (2)$$

Where EA is the electron affinity, LUMO is the energy of the lowest unoccupied molecular orbital, E(red) is the solution reduction potential, $\Delta G(solv)$ is the differential solvation energy, and K is related to the reference electrode. Calculations were performed on a variety of mostly heterocyclic cations chosen as possible cations for chloroaluminate melts. The criteria for the candidates was that the size be about the same as alkylpyridinium and that they be commercially available or readily synthesized. Since the molecules would all be of similar size, the equation (2) could be simplified to:

$$E(red) = EA + C \qquad (3)$$

where the differential solvation energies are combined with the reference potential constant.

The linear relationship implied in equation (3) was tested with a few cations, as shown in Figure 1, where reduction half-wave potentials were used for the observed values. While the data are too few and scattered to make a convincing case for a straight line, it is heartening to note that the least-squares slope is very close to unity. The result in Figure 1 gave us confidence that the MNDO method was useful and reliable for screening candidates for their approximate reduction potentials.

The results of the calculations are tabulated in Table 1 and shown graphically in Figure 2. Tetraalkylammonium is predicted to be the most difficult of the cations to reduce. This is not surprising, since tetraalkylammonium salts are often used as the supporting electrolyte in electrochemical cells. Unfortunately the liquidus temperature for the chloroaluminate melt prepared from one of them(tetraethyl-) was relatively high, so no further consideration was given to that class of cations (11). One might expect that the addition of one or more electron donating substituents to the pyridine ring might lower (make more negative) the reduction potential of the well studied 1-alkylpyridinium system. Molecules with one, two or three methyl groups (ie. the picolines, lutidines and collidine) were actually estimated to have quite similar reduction potentials. In fact the 1-methylcollidinium cation was found to be reduced by aluminum when it was used as the cation in a chloroaluminate melt (12). All of the 6-membered heterocycles containing two nitrogens (the alkylpyridaziniums, -pyrimidiniums and -pyraziniums) have reduction potentials higher than alkypyridinium, so they were removed from consideration. The 5-membered heterocycles containing two nitrogens were more promising. 1,2-Pyrazolium had a significantly lower predicted reduction potential and 1,3-dialkylimidazolium even lower yet. The salts based on imidazole are known compounds and may be prepared simply from commercially available starting materials, so they were chosen for further study.

A homologous series of 1,3-dialkylimidazolium chlorides were prepared (compounds I-V).

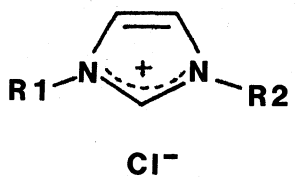

R1	R2	COMPOUND
methyl	methyl	II
methyl	ethyl	II
methyl	propyl	III
methyl	butyl	IV
methyl	benzyl	V

The preparative procedures were similar to those described in the literature for the iodides (13-20), but were modified to accomodate gaseous reagents in the case of some of the chlorides. Briefly, the preparations involve heating 1-methylimidazole with the appropriate chloroalkane, sometimes under pressure. In most cases the products were hygroscopic white solids.

The chloroaluminate melts were prepared by simply mixing aluminum chloride with the imidazolium chloride. The two solids combined to produce a clear, slightly viscous liquid. All operations involving aluminum chloride or chloroaluminate melts were done in a glove box containing a dry argon atmosphere.

The liquidus temperature of the melts was an important physical property. The melting points of the dialkylimidazolium chlorides indicated that larger or more asymmetric cations resulted in lower melting points. This also proved to be true in chloroaluminates having dialkylimidazolium cations, as illustrated in Table 2. The melt having the 1-methyl-3-ethylimidazolium cation (from chloride II) was molten at room temperature over its entire composition range, and its liquidus temperatures were much lower than the closely related melt having the 1,3-dimethylimidazolium cation. Since the molecular weight difference was only 14 daltons, the effect was probably due mostly to the asymmetry of the methyl-ethyl cation rather than the size difference. While the liquidus temperature of the 1-methyl-3-ethylimidazolium melt is quite low, the melt would not be a useful electrolyte at very low temperatures due to the very high viscosity at the low temperatures.

The conductivities of various compositions of the 1-methyl-3-ethylimidazolum melt are tabulated in Table 3. They are not very high by molten salt standards, but this is probably largely due to the temperature at which they were measured. The values are approximately the same as for the 1-alkypyridinium chloroaluminate melts(2).

The new melts would be a major improvement over the 1-alkypyridinium melts only if they had a wider electrochemical window. The test for this would be if aluminum is stable in chloride rich compositions of the melts. If the materials met that test, then the organic cations must reduce cathodic of aluminum in the melt. Cyclic voltammetry is a convenient way of analyzing the anodic and cathodic limits of the melts. Figure 3 is a cyclic voltammogram of an acidic (2:1) melt having the dimethylimidazolium cation. At the anodic limit chloride oxidation was observed, as in all chloroaluminate melts. The wave at the cathodic limit is chacteristic of metal deposition. In a basic melt (0.7:1)Al was unaffected when immersed for several hours at 110°C. The cyclic voltammogram (Figure 4) indicates that the melt decomposition is occuring at the cathodic limit, but that limit is at a high negative potential. The lack of aluminum deposition in the 0.7:1 melt is probably due to the very high chloride concentration at that composition.

In order to prove that aluminum was in fact reduced at the cathodic limit of a slightly acidic melt a deposition/stripping experiment was done, as shown in Figure 5. A constant cathodic current was passed until 0.200 coulombs had acculmulated, then an anodic current was passed until a rapid rise in potential indicated that all of the plated material had been stripped. The 95% overall efficiency is much higher than expected for deposition of an organic species, which would probably be irreversible. In a separate similar experiment the surface of the electrode had metallic gray deposit after deposition, clear evidence that aluminum is reduced and not the organic cation. The experiment also demonstrated the usefulness of the new melt as an aluminum plating medium.

One attractive feature of the 1-alkypyridinium chloroaluminate melts is the wide range of Lewis acidity accessible in them, as expressed by chloride concentration. The chloride concentration in the melts is controlled by the equilibrium:

$$2AlCl_4^- \rightleftarrows Al_2Cl_7^- + Cl^-$$

For the alkylpyridinium chloroaluminate melts the value of the equilibrium constant is 3.83×10^{-13}. (6) The potentiometric titration curve for the 1-methyl-3-ethylimidazolium chloroaluminate melt (Figure 6) provided a value of 2.0×10^{-19} for the same equilibrium. This implies a range of acidity for the new melts at least as broad as the alkypyridinium melts and much broader than the alkali halide chloroaluminate melts.

The use of the new melts in batteries requires that a suitable redox couple be available for the cathode half-reaction. Transition metal ions are commonly used for such purposes. Copper(II) chloride was dissolved in the 1-methyl-3-ethylimidazolium melt and reversible reduction was observed by cyclic voltammetry (Figure 7). Initial results indicate that the copper couple in the new melt is very similar to the same ion in the 1-alkylpyridinium melts (3).

In addition to dissolving inorganic compounds such as $CuCl_2$, the new melts act as solvents for organic compounds. Benzene is miscible in the 1-methyl-3-ethylimidazolium melt to about equal volume. Some other aromatic compounds are also soluble and, as with the alkypridinium melts, some are spontaneously oxidized to the radical cation. For example, thianthrene dissolved in the 1,2-dimethylimidazolium melt immediately turns deep purple and exhibits an EPR spectrum characteristic of thianthrene radical cation.

REFERENCES

1. J. C. Nardi, J. K. Erbacher, C. L. Hussey and L. A. King, J. Power Sources, 3, 81 (1978).
2. R. A. Carpio, L. A. King, R. E. Lindstrom, J. C. Nardi and C. L. Hussey, J. Electrochem. Soc., 126, 1644 (1979).
3. C. L. Hussey, L. A. King and R. A. Carpio, J. Electrochem. Soc., 126, 1029 (1979).
4. C. L. Hussey, L. A. King and J. S. Wilkes, J. Electroanal Chem., 102, 321 (1979).
5. H. L. Chum, V. R. Koch, L. L. Miller and R. A. Osteryoung, J. Am. Chem. Soc., 97, 3264 (1975).
6. R. J. Gale and R. A. Osteryoung, Inorganic Chem., 18, 1603 (1979).
7. R. J. Gale and R. A. Osteryoung, J. Electrochem. Soc., 127, 2167 (1980).
8. J. Wilkes, unpublished results.
9. M. Dewar, H. Kollmar and S. Suck, Theoret. Chim. Acta, 36, 237 (1975).
10. B. Case, N. S. Hush, R. Parsons and M. E. Peover, J. Electroanal. Chem., 10, 360 (1965).
11. C. L. Hussey, unpublished results.
12. R. Gale, personal communication.
13. H. Goldschmidt, Ber, 14, 1845 (1882).
14. O. Wallach and E. Schulze, Ber., 14, 423 (1882).
15. O. Wallach, Ber., 15, 646 (1883).
16. O. Wallach, Ann., 214, 309 (1876).
17. F. Rung and M. Behrand, Ann., 271, 35 (1891).
18. B. Chan, N. Chang and M. Grimmett, Aust. J. Chem., 30, 2005 (1977).
19. O. Wallach, Ber., 16, 535 (1884).
20. K. V. Auwers and W. Maus, Ber., 61, 2418 (1928).

TABLE 1

Calculated Electron Affinities of Some Organic Cations

Cation	Electron Affinity (eV)	$E_{\frac{1}{2}}$ (red) (V)
1-methylpyridinium	5.84	-1.28
1-methyl-2-picolinium	5.74	
1-methyl-2,4-lutidinium	5.71	
1-methyl-2,4,6-collidinium	5.61	
1-methypyridazinium	6.30	
1,2-dimethylpyrazolium	4.86	
1,3-dimethylimidazolium	4.86	-1.981
1-methyl-3-butylimidazolium	4.70	-2.001
tetramethylammonium	4.37	-2.7

TABLE 2

Liquidus Temperatures of Dialkylimidazolium Chloroaluminate Melts

Cation	50 mol% $AlCl_3$	67 mol% $AlCl_3$
1,3-dimethylimidazolium	75° C	15° C
1-methyl-3-ethylimidazolium	8° C	-98° C

TABLE 3

Conductivities of Methylethylimidazolium Chloroaluminate Melts

Composition (mol% $AlCl_3$)	Specific Conductivity $(ohm\text{-}cm)^{-1}$	Temperature (°C)
44	0.0117	29.7
50	0.0227	30.9
67	0.0154	32.2

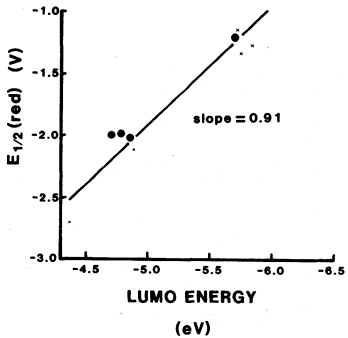

Fig. 1. Correlation of $E_{1/2}$(red) and LUMO energy. $E_{1/2}$ values are from this work (●) or from the literature (x).

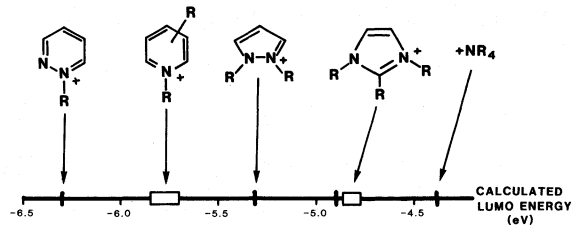

Fig. 2. Types of compounds selected for calculation of LUMO energies.

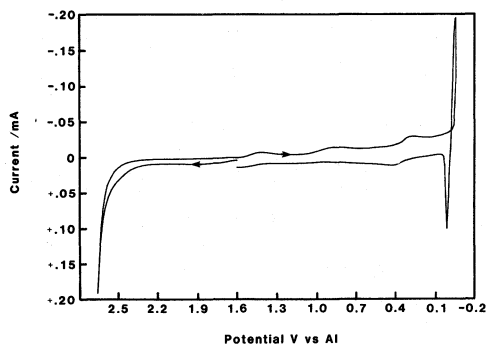

Fig. 3. Electrochemical window of 67 mol% $AlCl_3$/dimethylimidazolium chloride melt.

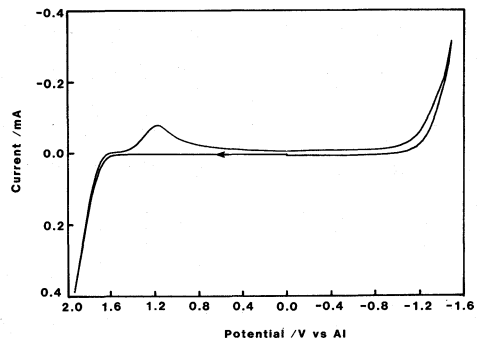

Fig. 4. Electrochemical window of 40 mol% $AlCl_3$/methylethylimidazolium chloride melt.

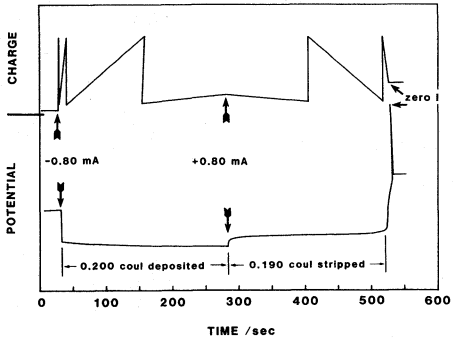

Fig. 5. Galvanostatic aluminum deposition/ stripping on Pt in slightly acidic dimethylimidazolium melt.

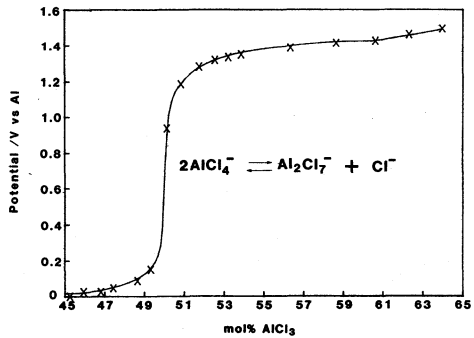

Fig. 6. Potentiometric titration of the methylethylimidazolium chloroaluminate melt.

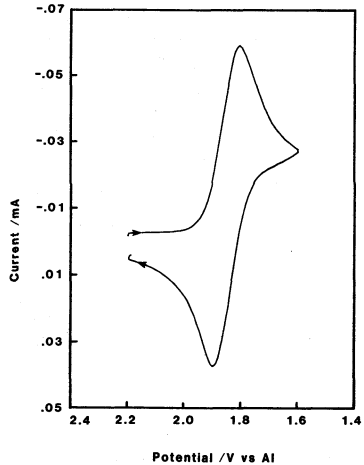

Fig. 7. Cyclic voltammetry of $CuCl_2$ in 67 mol% methylethylimidazolium chloroaluminate melt.

DOI: 10.1149/198109.0256PV

THE ELECTROCHEMISTRY OF COBALT AND MOLYBDENUM SOLUTE SPECIES IN ROOM TEMPERATURE CHLOROALUMINATE MELTS

C. L. Hussey and T. M. Laher
Department of Chemistry
The University of Mississippi
University, MS 38677

ABSTRACT

The electrochemistry and coordination chemistry of cobalt and molybdenum solute species were studied in the room temperature chloroaluminate melt, aluminum chloride-N-(n-butyl)pyridinium chloride ($AlCl_3$-BPC). Cobalt(II) was readily introduced into acidic and basic $AlCl_3$-BPC melts by dissolution of $CoCl_2$. Reduction of Co(II) at a glassy carbon electrode in 2:1 molar ratio melt was accompanied by codeposition of aluminum, but this effect decreased with decreasing acidity of the melt. Evidence was found which indicated that deposition of cobalt metal in 2:1 molar ratio $AlCl_3$-BPC melt is preceded by monolayer formation. The $CoCl_4^{2-}$ species was electroinactive in 0.8:1.0 $AlCl_3$-BPC melt. Potentiometric measurements on the cell $Co|Co(II)_{dil.}$, $AlCl_3$-BPC: fritted disc: 2:1 molar ratio $AlCl_3$-BPC|Al were used to determine formation constants for the reaction $Co^{2+} + 4Cl^- \rightleftharpoons CoCl_4^{2-}$ in BPC rich $AlCl_3$-BPC melt as a function of temperature. Molybdenum(V) was conveniently introduced into 2:1 $AlCl_3$-BPC melt by dissolution of $MoCl_5$; however, $MoCl_5$ and $MoCl_4$ appeared to oxidize BPC rich melt. Four reduction waves with peak potentials of 1.91, 1.10, 0.34, and 0.11 V versus Al were observed during reduction of Mo(V) at a glassy carbon electrode in 2:1 $AlCl_3$-BPC melt. The first reduction wave corresponds to the reversible one-electron reduction of Mo(V) to Mo(IV) and appears to be preceded by a chemical step, possibly dissociation of a dimeric Mo(V) species. The potential of the Mo(V)/Mo(IV) electrode reaction was linearly dependent on the melt pCl, and data for this correlation show that this reaction involves a single chloride ion.

INTRODUCTION

Mixtures of aluminum chloride and N-(n-butyl)pyridinium chloride ($AlCl_3$-BPC) form a molten salt system of adjustable Lewis acidity. One of the most unusual properties of this molten salt system is that it is liquid close to room temperature over the range of compositions from 2:1 to 1:1.33 $AlCl_3$-BPC (1). Recent studies have shown that the distribution of chloroaluminate melt species in the $AlCl_3$-BPC system

is quite different from that of related $AlCl_3$-NaCl melts (2). This species distribution can in fact be represented by a single equilibrium reaction

$$2AlCl_4^- \rightleftharpoons Al_2Cl_7^- + Cl^- \qquad K \qquad (1)$$

with a value of $K \leq 3.8 \times 10^{-13}$ at 30°C (3).

In recent papers we reported the electrochemistry of the Cu(II)/Cu(I) and Cu(I)/Cu (4), and Fe(III)/Fe(II) (5) electrode reactions in $AlCl_3$-BPC and a closely related room temperature chloroaluminate melt, aluminum chloride-N-methylpyridinium chloride. In order to gain further insight into the electrochemical behavior of transition metal ions in $AlCl_3$-BPC melts, cobalt(II) and molybdenum(V) solutes were investigated. The electrochemistry and spectroscopy of Co(II) have been examined in inorganic chloroaluminate melts by several workers (6-13). Thus, data that have been obtained for Co(II) in the $AlCl_3$-BPC molten salt system can be compared to data concerning Co(II) solutes in inorganic chloroaluminates. Molybdenum electrochemistry has also been examined in an inorganic chloroaluminate melt and found to be extremely complex (14). Results are presented in this paper which show that the chemistry and electrochemistry of Mo(V) in $AlCl_3$-BPC melt vary substantially from that reported in inorganic chloroaluminate melts (14).

EXPERIMENTAL SECTION

The preparation and purification of the $AlCl_3$-BPC melt are detailed in a previous publication (15). Anhydrous $CoCl_2$, 99.9%, was obtained from CERAC, Inc. Samples of anhydrous $CoCl_2$ were also obtained from Alfa Products and used in some experiments. Anhydrous $MoCl_5$ was purchased from Alfa Products, and anhydrous $MoCl_4$, 99.5% was acquired from CERAC, Inc.

All experiments were conducted in a dry nitrogen atmosphere inside a Kewaunee Scientific Equipment Corp. drybox equipped with a 3 cfm inert gas purifier for removing moisture and oxygen. Cyclic voltammetry was performed using an AMEL model 551 potentiostat/galvanostat equipped with an AMEL model 566 function generator. Cyclic voltammograms were recorded using a Houston model 100 X-Y recorder. Resistance compensation was applied during cyclic voltammetric measurements. The potentiostat was equipped with an AMEL model 731 digital integrator during coulometric generation of Co(II).

The electrochemical cell and glassy carbon working electrode, geometric area = 0.07 cm^2, were similar to those used in previous studies (4, 5). A glassy carbon crucible (Tokai) was used as the working electrode during controlled potential electrolysis experiments. A spiral wire cobalt metal working electrode was fashioned from 0.25 mm cobalt wire (Alfa Products, m2N7). The electrode was dipped briefly into concentrated HNO_3 followed by similar treatment with concentrated HCl. The electrode was rinsed thoroughly with distilled H_2O

and dried in an oven prior to use. All potentials were referenced to an aluminum wire immersed in 2:1 $AlCl_3$-BPC melt, separated from the bulk melt compartment by a fine porosity frit.

The electrochemical cell temperature was maintained to within ±0.2°C of the desired temperature with a thermistor-controlled furnace. The furnace consisted of an insulated aluminum block containing a Vulcan Electric 150 watt cartridge heater. Regulated current to power the furnace was provided by an Ace Glass temperature controller.

RESULTS AND DISCUSSION

Voltammetry of cobalt(II) in $AlCl_3$-BPC melt.- Anhydrous $CoCl_2$ was readily soluble in the acidic ($AlCl_3$ rich) and basic (BPC rich) $AlCl_3$-BPC melt. Solutions of $CoCl_2$ in basic melt were aquamarine while acidic solutions were deep blue in color. A cyclic voltammogram for the reduction of Co(II) in 2:1 $AlCl_3$-BPC melt at a glassy carbon electrode is shown in Fig. 1a. The reduction peak potential for deposition of cobalt metal from the 2:1 $AlCl_3$-BPC melt shifts negatively by about 160 mV for each order of magnitude increase in scan rate. In addition, the reverse scan in Fig. 1a exhibits a hysteresis-like effect. Chronoamperometric current-time curves for Co(II) reduction in 2:1 $AlCl_3$-BPC exhibit maxima with induction times dependent on the applied potential, as depicted in Fig. 2. These electrochemical data suggest that deposition of cobalt metal on glassy carbon from 2:1 $AlCl_3$-BPC melt is controlled by the rate of nucleation during the initial phases of deposit formation (16). Similar behavior has been reported for deposition of copper (4) and aluminum (17) at glassy carbon in room temperature chloroaluminate melts.

Two stripping peaks, located at ca. 0.8 and 0.5 V, which correspond to reoxidation of material deposited on the electrode surface are also evident in Fig. 1a. The peak at 0.5 V may be due to reoxidation of aluminum codeposited with cobalt, since the Co(II) reduction process at 0.1 V is very close to the potential for reduction of $Al_2Cl_7^-$ at glassy carbon at ca. -0.15 V (17). As the melt is made less acidic by successive additions of BPC and the $Al_2Cl_7^-$ ion concentration is reduced, the peak attributed to reoxidation of deposited aluminum at 0.5 V begins to decrease (Fig 1b), and the large featureless reduction wave observed at 0.13 V in Fig. 1a begins to broaden and split into a well-defined reduction wave at 0.25 V and a broad indistinct wave at 0.13 V. Reversal of the scan after the first reduction wave considerably diminishes the oxidation wave at 0.5 V. After further decrease in the $Al_2Cl_7^-$ concentration it is possible to obtain a deposition-stripping voltammogram that can be attributed solely to deposition and reoxidation of cobalt metal (Fig. 1c).

If the acidity of the melt is further decreased to the 1:1 $AlCl_3$-BPC composition, the melt becomes cloudy and some of the Co(II) precipitates from the melt, presumably as $CoCl_2$. Similar behavior for Co(II) has been reported in inorganic chloroaluminate melts (10).

No reduction or reoxidation wave was observed for Co(II) in basic $AlCl_3$-BPC mixtures over the available potential range. Thus, Co(II) may be electroinactive at the glassy carbon electrode when complexed as $CoCl_4^{2-}$, or it may be reduced at potentials negative of the electrochemical window of the melt.

Predeposition of cobalt metal on glassy carbon.- An additional feature present in the voltammogram shown in Fig. 1a is a small wave at about 0.35 V. The presence of this peak was independent of the source of Co(II), i.e., the peak was present after the addition of anhydrous $CoCl_2$ from two different commercial sources or generation of Co(II) from a cobalt wire electrode by controlled potential electrolysis. This peak was not present in pure $AlCl_3$-BPC melt prior to addition of Co(II). An expanded scale, multiple scan cyclic voltammogram which encompasses this reduction peak but avoids the main deposition process is shown in Fig. 3. Cyclic scans which include this reduction wave reveal an associated stripping process at about 0.8 V. Several cycles are necessary before the area of this stripping peak begins to approximate that of the original reduction process. The potential at which the stripping peak is observed is proximate to the peak for stripping of cobalt metal as shown by comparison of Figs. 1a and 3.

Similar deposition and stripping of a monolayer or less of aluminum metal positive of the main deposition-stripping process in acidic $AlCl_3$-BPC melt was observed in previous studies and attributed to an underpotential deposition process (17). Integration of the area under the voltammetric predeposition peak (first scan) shown in Fig. 3 with respect to charge was undertaken at several concentrations of Co(II). These results are presented in Table I and indicate that the charge under this peak may correspond to as much as one monolayer of deposited cobalt metal. Thus, deposition of cobalt metal on glassy carbon would seem to be preceded by predeposition of a monolayer of the metal. The amount of predeposited cobalt appears to recede at high concentrations of Co(II). Formation of a complete monolayer is most favorable at low Co(II) concentrations. This observation contrasts with results reported by Hills et al (18) for monolayer formation during the reduction of Ni(II) and Ag(I) in LiCl-KCl eutectic. These workers reported that monolayer formation was relatively independent of the substrate ion concentration.

In the present case this process could hardly be described as underpotential deposition in the thermodynamic sense, because E_M° for the Co(II)/Co couple (Table II) is positive of the predeposition wave by about 0.5 V. In addition, the reported $E_{1/2}$ value for Co(II) reduction in an inorganic chloroaluminate melt (8) is also significantly positive of the potential reported for this predeposition wave. A complete explanation of this phenomenon awaits further studies.

Table I. Effect of Concentration on the Predeposition of Cobalt Metal at Glassy Carbon

Co(II) Concentration (M)	Cobalt Metal (moles)	% Monolayer Coverage[a]
12.6×10^{-3}	2.72×10^{-10}	92
21.1×10^{-3}	2.46×10^{-10}	83
30.1×10^{-3}	2.33×10^{-10}	79
51.7×10^{-3}	1.88×10^{-10}	63

[a]Assuming that the geometrical area of the electrode represents its true area, 2.96×10^{-10} moles of cobalt metal are required per monolayer.

Table II. Standard Potential Data for the Co(II)/Co Couple in 2:1 $AlCl_3$-BPC Melt

E°(V)		Slope of Nernst Plot	t(°C)
Molar	Mole Fraction		
0.935±0.002	0.960±0.002	0.032±0.001	40.0
0.886±0.002	0.914±0.002	0.036±0.001	100.0

Potentiometric titration studies.- The nature and strength of the coordination of Co(II) was further probed in the acidic and basic $AlCl_3$-BPC melts using a potentiometric titration procedure. Potential measurements were made on the cell

$$Co|Co(II)_{dil.}, AlCl_3\text{-BPC}:\text{fritted disk}:\text{2:1 molar ratio } AlCl_3\text{-BPC}|Al \quad (2)$$

as a function of the ratio of $AlCl_3$ to BPC in the left-hand compartment. There is at present no information about the external transport numbers of the various ionic species in room temperature chloroaluminate melts with which to estimate the magnitude of the liquid junction potential for this cell. However, very little shift in the cyclic voltammetric half-peak potential for the ferrocenium/ferrocene couple was observed in a similar cell with wide variation in the $AlCl_3$-BPC melt composition (1). Based on this indirect evidence, corrections for the liquid junction were assumed small and ignored in all calculations.

Figure 4 shows a plot of the cell potential for the cell depicted in Eq. 2 as a function of the apparent mole fraction of $AlCl_3$, X_{AlCl_3}, in the left-hand cell compartment. The cell potential is relatively independent of X_{AlCl_3} in the acidic melt composition region despite variation of X_{AlCl_3} from 0.66 to approximately 0.55. Substantial changes in the ion mole fractions for the ionic melt constituents $Al_2Cl_7^-$, $AlCl_4^-$, and Cl^- take place over this composition interval. Subsequent analysis of the cell potential data with variation of the logarithm of the ion mole fractions of $Al_2Cl_7^-$, $AlCl_4^-$, and Co^{2+}

revealed a linear correlation only for the plot involving the ion mole fraction of Co^{2+}.

Further decrease in X_{AlCl_3} to about 0.51 results in precipitation of $CoCl_2$ as previously described. When X_{AlCl_3} is decreased to approximately 0.49 the $CoCl_2$ precipitate redissolves. Plots of the cell potential as a function of the negative logarithm of the chloride ion mole fraction, X_{Cl^-}, (Fig. 5) obtained by variation of X_{AlCl_3} from 0.49 to 0.44 are linear and exhibit slopes of 127±4 and 154±2 mV at 40.0 and 100.0°C. These slopes are consistent with theoretical slopes of 124 and 148 mV for fourth-power dependence of the cell potential on X_{Cl^-}.

These potentiometric studies indicate that the predominant Co(II) ion equilibrium reaction in chloride rich $AlCl_3$-BPC melt may be represented by the expression given in Eq. 3.

$$Co^{2+} + 4Cl^- \rightleftharpoons CoCl_4^{2-} \qquad K_f \qquad (3)$$

The relationship between the potential of the cell depicted in Eq. 2 and X_{Cl^-} in the left-hand compartment of the cell is given by the Nernst equation represented by Eq. 4.

$$E = E_x^\circ + \frac{RT}{2F} \ln X_{CoCl_4^{2-}} - \frac{RT}{2F} \ln K_f - \frac{RT}{2F} \ln X_{Cl^-}^4 \qquad (4)$$

In deriving this expression, the activities of the various species have been replaced by their mole fractions, E_x° is the standard potential of the Co(II)/Co couple on the mole fraction scale in 2:1 $AlCl_3$-BPC melt, and K_f is the formation constant for the cobalt chlorocomplex.

Values of K_f for the process represented by Eq. 3 may be calculated at each value of E and X_{Cl^-} shown in Fig. 5 using Eq. 4 if E_x° is known and $X_{CoCl_4^{2-}}$ can be estimated. Estimates of E_x° for the Co(II)/Co couple at 40.0 and 100.0°C were obtained from the intercepts of Nernst plots. Data with which to construct these plots were acquired by anodizing a cobalt electrode and coulometrically monitoring the Co(II) concentration. Values of E_x° are summarized in Table II. The observed potentials, various ion mole fractions, and calculated K_f values for a representative calculation at 40.0°C are listed in Table III. Table IV contains the results of an additional determination of K_f at 100.0°C. Values of K_f for cobalt chlorocomplex formation in inorganic chloroaluminate melts are also included in this table for comparison.

The values of K_f observed in $AlCl_3$-BPC melt are larger by many orders of magnitude than those observed in inorganic chloroaluminate melts, and they show a very slight reduction in magnitude with increased temperature. These results are consistent with the decreased ionic field strength of the N-(n-butyl)pyridinium cation resulting from its larger ionic radius relative to that of alkali metal cations. The reaction depicted in Eq. 3 is much more favorable from an electrostatic

point of view since the N-(n-butyl)pyridinium cation can exert only weak electrostatic attraction for melt chloride ion. The effect observed is quite similar to that proposed to account for the increased extent of $Al_2Cl_7^-$ ion formation in molten chloroaluminates when the cation ionic field strength is decreased (3, 19).

Table III. Potentials, Species Mole Fractions, and Calculated Formation Constants for Titration of 3.71×10^{-3} M $CoCl_2$ in 0.8:1 $AlCl_3$-BPC Melt at 40.0°C

E (V)	X_{Cl^-} [a]	$X_{CoCl_4^{2-}}$	X_{Cl^-} [b]	K_f
-0.338	1.01×10^{-1}	3.87×10^{-4}	9.98×10^{-2}	2.27×10^{42}
-0.324	8.63×10^{-2}	3.87×10^{-4}	8.55×10^{-2}	1.60×10^{42}
-0.318	7.34×10^{-2}	3.87×10^{-4}	7.26×10^{-2}	1.90×10^{42}
-0.306	6.11×10^{-2}	3.87×10^{-4}	6.04×10^{-2}	1.69×10^{42}
-0.295	4.98×10^{-2}	3.87×10^{-4}	4.90×10^{-2}	1.72×10^{42}
-0.278	3.96×10^{-2}	3.87×10^{-4}	3.61×10^{-2}	1.63×10^{42}
-0.257	2.34×10^{-2}	3.87×10^{-4}	2.27×10^{-2}	2.14×10^{42}

[a] Chloride ion mole fraction in excess of the 1:1 $AlCl_3$-BPC melt composition

[b] Excess chloride ion minus amount complexed with $CoCl_2$

Table IV. Cobalt Chlorocomplex Formation Constants in Chloroaluminate Melts

Melt System	t (°C)	log K_f	Ref.
$AlCl_3$-LiCl	300	6.5	13
$AlCl_3$-NaCl	300	11.2	13
$AlCl_3$-CsCl	400	19.7	13
$AlCl_3$-BPC	40	42.3±0.1	this work
$AlCl_3$-BPC	100	41.3±0.1	this work

Voltammetry of Mo(V) in $AlCl_3$-BPC melt.- Molybdenum(V) chloride dissolved readily in acidic AlCl-BPC melt to give a reddish-purple solution. It was possible to dissolve considerable amounts of $MoCl_5$ in the melt, and solutions with concentrations exceeding 100 mM could be readily obtained.

Figure 6 shows a cyclic voltammogram for the reduction of $MoCl_5$ at a glassy carbon electrode in 2:1 $AlCl_3$-BPC melt. Four reduction waves with peak potentials of 1.91, 1.10, 0.34, and 0.11 V are evident. Reversal of the voltammetric scan immediately after the first reduction wave at 1.91 V results in an oxidation wave at 1.97 V. The shape of this cyclic voltammogram suggests that it may arise from a reversible or quasireversible redox process. If the voltammetric scan is reversed at 0.4 V a small oxidation wave at 1.78 V can be observed

prior to the oxidation wave at 1.97 V. Reversal of the voltammetric scan at 0.0 V results in the appearance of an additional ill-defined oxidation wave slightly negative of the wave at 1.78 V. The reduction waves at 1.10, 0.34, and 0.11 V and associated oxidation waves were not subjected to additional study during this investigation.

Cyclic voltammetric data for the first redox process depicted in Fig. 6 are summarized in Table V. The average value of $E_p^a - E_p^c$ presented in this table for scan rates less than 0.5 V/sec is about 63 mV. This value compares favorably with the theoretically predicted value of 62 mV for a one-electron reversible electrode reaction at 40.0°C. Values for $E_p^c - E_{1/2}$ average about 31 mV and likewise compare well with the theoretical value expected for this parameter under the same conditions, 30 mV. However, a quasireversible, multielectron charge transfer process can not be ruled out based on this data alone.

Table V. Cyclic Voltammetric Data for the Reduction of 12.9 mM $MoCl_5$ in 2:1 $AlCl_3$-BPC Melt at 40.0°C

ν (V/sec)	E_p^c (V)	$E_p^a - E_p^c$ (V)	$E_p^c - E_{1/2}$ (V)	$i_p^c/\nu^{1/2}$ (A $sec^{1/2}/V^{1/2}$)	i_p^a/i_p^c
0.01	1.910	0.060	-0.030	2.2×10^{-4}	1.00
0.05	1.906	0.064	-0.031	2.2×10^{-4}	1.07
0.20	1.908	0.066	-0.032	2.2×10^{-4}	1.13
0.50	1.910	0.063	-0.030	2.3×10^{-4}	1.20
2.00	1.912	0.069	-0.028	2.3×10^{-4}	1.24
5.00	1.908	0.082	-0.032	2.3×10^{-4}	1.28

A convenient method for determining the number of electrons involved in the charge transfer process, n, involves comparison of the voltammetric current function, $i_p^c/\nu^{1/2}$, with chronoamperometric values of $it^{1/2}$ according to Eq. 5 (20).

$$i_p^c/\nu^{1/2}/it^{1/2} = 86.31(n/T)^{1/2} \qquad (5)$$

Calculations based on this equation yielded a value of 0.9 for n, confirming that the first redox process depicted in Fig. 6 corresponds to a one electron charge transfer reaction. In addition the voltammetric peak current at a fixed scan rate of 50 mV/sec was linearly dependent on the molar concentration of $MoCl_5$ (Fig. 7). Combined together, this data suggests that Mo(V), introduced into the melt by addition of $MoCl_5$, undergoes a one-electron reduction to Mo(IV).

Values of $i_p^c/\nu^{1/2}$ shown in Table V are relatively constant with scan rate; but the peak current ratio, i_p^a/i_p^c, calculated using Nicholson's empirical method (21), increases with increasing scan rate. This behavior is usually associated with a chemical step which precedes the charge transfer reaction (22). An equilibrium process that can be proposed for this chemical step is the dissociation

equilibrium between electroinactive Mo(V) dimer and electroactive Mo(V) monomer. Dimeric Mo(V) species are well known (23).

Similar cyclic voltammetric experiments were undertaken after additions of $MoCl_5$ or $MoCl_4$ to 0.8:1 $AlCl_3$-BPC melt. However, a very large reduction wave was observed at ca. 0.7 V (vs. Al in the 2:1 $AlCl_3$-BPC melt) after these additions. A similar voltammetric wave was obtained after pure melt was saturated with chlorine gas. From these results, it was concluded that both $MoCl_5$ and $MoCl_4$ oxidize BPC rich $AlCl_3$-BPC melt, and that the molybdenum species which remained in the melt after these additions possessed an oxidation state less than four. The instability of Mo(V) in BPC rich $AlCl_3$-BPC melt contrasts sharply with its stability in NaCl saturated $AlCl_3$-NaCl melt at 175°C (14).

Variation of the average of the anodic and cathodic peak potentials for the Mo(V)/Mo(IV) electrode process, $(E_p^a+E_p^c)/2$, was studied using cyclic voltammetry as X_{AlCl_3} was varied from 0.664 to 0.516. A linear plot was obtained for $(E_p^a+E_p^c)/2$ as a function of the negative logarithm of the chloride concentration or pCl^- (Fig. 8). The slope of this plot was 59±6 mV and was in excellent agreement with the 62 mV theoretical slope expected for an electrode reaction involving a single chloride ion. The overall sequence for the one-electron reduction of Mo(V) in $AlCl_3$ rich $AlCl_3$-BPC melt can therefore be summarized by the reactions depicted in Eqs. 6 and 7.

$$Mo(V)_2 \rightleftharpoons 2Mo(V) \tag{6}$$

$$Mo(V) + e^- \rightleftharpoons Mo(IV) + Cl^- \tag{7}$$

ACKNOWLEDGMENT

Support of this work by a Hooker Chemical Corporation Grant of the Research Corporation and by a University of Mississippi Faculty Research Grant is gratefully acknowledged.

LIST OF SYMBOLS

E	potential (V)
$E_{1/2}$	polarographic half-wave potential (V)
E_M°	standard electrode potential, molar scale (V)
E_X°	standard electrode potential, mole fraction scale (V)
E_p^a, E_p^c	anodic and cathodic voltammetric peak potentials (V)
F	faraday (C)
i	current (A)
i_p^a, i_p^c	anodic and cathodic voltammetric peak currents (A)
K	equilibrium constant
K_f	formation constant

M	molarity (moles/liter)
n	number of electrons in charge transfer step
R	gas constant (joules/mole K)
t	time (sec) or temperature (°C)
T	temperature (K)
X_{AlCl_3}	apparent mole fraction of $AlCl_3$
$X_{Al_2Cl_7^-}$, $X_{AlCl_4^-}$	ion mole fractions of $Al_2Cl_7^-$ and $AlCl_4^-$
$X_{Co^{2+}}$, X_{Cl^-}	ion mole fractions of Co^{2+} and Cl^-
ν	voltammetric sweep rate (V/sec)

REFERENCES

1. J. Robinson and R. A. Osteryoung, J. Amer. Chem. Soc., 101, 323 (1979).
2. R. J. Gale, B. Gilbert, and R. A. Osteryoung, Inorg. Chem., 17, 2728 (1978).
3. R. J. Gale and R. A. Osteryoung, ibid., 18, 1603 (1979).
4. C. L. Hussey, L. A. King, and R. A. Carpio, J. Electrochem. Soc., 126, 1029 (1979).
5. C. L. Hussey, L. A. King, and J. S. Wilkes, J. Electroanal. Chem., 102, 321 (1979).
6. R. G. Verdieck and L. F. Yntema, J. Phys. Chem., 46, 344 (1942).
7. Yu. K. Delimarskii, E. M. Skobets, and L. S. Berenblyum, Zhur. Fiz. Khim., 22, 1108 (1948).
8. R. M. de Fremont, R. Rosset, and M. Leroy, Bull. Soc. Chem. Fr., 706, (1964).
9. H. A. Øye and D. M. Gruen, Inorg. Chem., 3, 836 (1964).
10. H. A. Øye and D. M. Gruen, ibid., 4, 1173 (1965).
11. C. A. Angell and D. M. Gruen, J. Inorg. Nucl. Chem., 29, 2243 (1967).
12. R. Nikolic and H. A. Øye, Z. Phys. Chemie, Leipzig, 260, 841 (1979).
13. T. Kvaal and H. A. Øye, Acta Chem. Scand., 26, 1647 (1972).
14. J. Phillips and R. A. Osteryoung, J. Electrochem. Soc., 124, 1465 (1977).
15. R. A. Carpio, L. A. King, R. E. Lindstrom, J. C. Nardi, and C. L. Hussey, J. Electrochem. Soc., 126, 1644 (1979).
16. G. J. Hills, D. J. Schiffrin, and J. Thompson, Electrochim. Acta, 19, 657 (1974).
17. J. Robinson and R. A. Osteryoung, J. Electrochem. Soc., 127, 122 (1980).
18. G. J. Hills, D. J. Schiffrin, and J. Thompson, ibid., 120, 157 (1973).
19. G. Torsi and G. Mamantov, Inorg. Chem., 11, 1439 (1972).
20. G. Ting, K. W. Fung, and G. Mamantov, J. Electrochem. Soc., 123, 624 (1976).
21. R. S. Nicholson, Anal. Chem., 38, 1406 (1966).
22. R. S. Nicholson and I. Shain, Ibid., 36, 706 (1964).
23. F. A. Cotton and G. Wilkinson, "Advanced Inorganic Chemistry", 3rd ed, John Wiley and Sons, New York, N.Y., 1972, chap. 26.

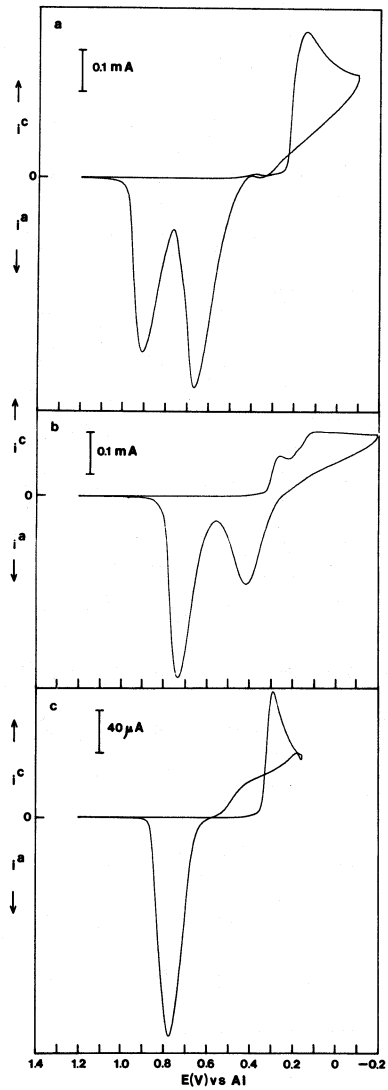

Figure 1. Cyclic voltammograms for 5 mM Co(II) at a glassy carbon electrode at 40.0°C; sweep rates are 0.020 V/sec. (a) 2:1 $AlCl_3$-BPC melt (b) 1.33:1 $AlCl_3$-BPC melt (c) 1.14:1 $AlCl_3$-BPC melt.

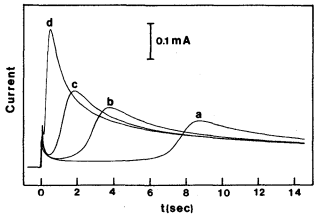

Figure 2. Current-time transients for Co(II) reduction at a glassy carbon electrode (area = 0.071 cm^2) at 40.0°C; Co(II) concentration was 1.26 x 10^{-2} M. (a) 0.050 V (b) 0.025 V (c) 0.0 V (d) -0.050 V.

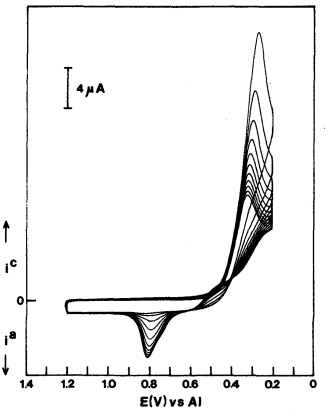

Figure 3. Multiple cyclic voltammograms of the Co(II) predeposition-stripping process at a glassy carbon electrode (area = 0.071 cm^2) in 2:1 $AlCl_3$-BPC melt at 40.0°C; Co(II) concentration was 5.17 x 10^{-2} M; sweep rate was 0.200 V/sec.

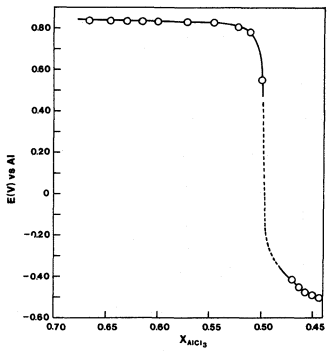

Figure 4. Dependence of the potential of the cell depicted in Eq. 2 on the apparent mole fraction of $AlCl_3$.

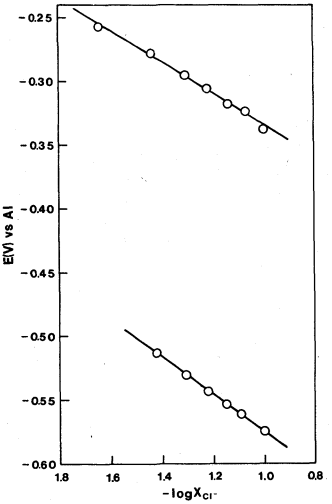

Figure 5. Dependence of the potential of the cell depicted in Eq. 2 on the Cl^- ion mole fraction. The apparent mole fraction of $AlCl_3$ in the left-hand cell compartment was varied from 0.49 to 0.44; 100.0°C (upper line) and 40.0°C (lower line).

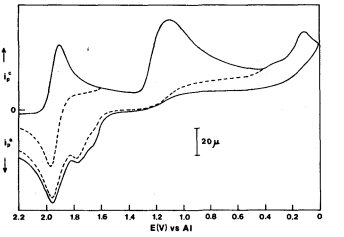

Figure 6. Cyclic voltammogram for the reduction of Mo(V) at a glassy carbon electrode in 2:1 $AlCl_3$-BPC melt. Sweep rate was 50 mV/sec; Mo(V) concentration was 12.9 mM; and temperature was 40.0°C.

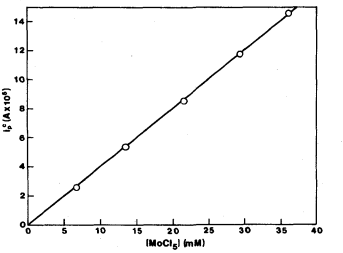

Figure 7. Variation of the voltammetric peak current for reduction of Mo(V) at a glassy carbon electrode in 2:1 $AlCl_3$-BPC melt with the concentration of Mo(V). Sweep rate was 50 mV/sec; temperature was 40.0°C.

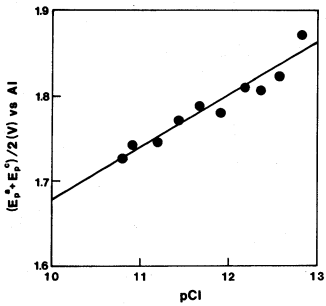

Figure 8. Plot of the average of the anodic and cathodic voltammetric peak potentials for the Mo(V)/Mo(IV) electrode process versus the melt pCl. Sweep rate was 50 mV/sec; temperature was 40.0°C.

DOI: 10.1149/198109.0270PV

SOLUBILITY AND ELECTROANALYTICAL BEHAVIOR OF AMMONIA IN IONIC SOLVENTS. A BRIEF REVIEW.

P.G.Zambonin, E.Desimoni, F.Palmisano, L.Sabbatini
Istituto di Chimica Analitica, Università, Via Amendola 173
70126 Bari Italy

ABSTRACT

The literature information concerning the chemical and electrochemical behavior of ammonia in molten salts is briefly reviewed and complemented by preliminary data obtained in the course of the work in progress in nitrate melts.

Anomalous dissolution kinetics observed for ammonia in molten nitrates are described and discussed on the basis of the platinum-catalyzed chemical decomposition of ammonia. The hydrogen produced in the first decomposition step can be detected on using the platinum itself as hydrogen sensitive electrode. The hydrogen electrooxidation current obtained in hydroxide-containing melts saturated with ammonia is more than two orders of magnitude higher than the corresponding one relevant to a melt directly saturated with hydrogen at the same working pressure.

Preliminary results relevant to the electroanalytical behavior of ammonia in anhydrous or slightly wet (Na-K)NO_3 equimolar melt are also reported.

INTRODUCTION

Ammonia is a hydrogen-derived fuel which can play a significant role in the "Hydrogen Economy" context (1-3). As a matter of fact investigations on direct ammonia fuel cells showed promising results even if to date no technologically viable prototype was developed (4-8). Exhaustive literature data can be found on the electrooxidation of ammonia in alkali aqueous electrolytes (9-15) while a quite complete lack of information exhists about ammonia-fused salt systems. This is still more surprising on considering that these solvents are widely used for fuel cell applications (16). As far as we know,the only papers quoted in the literature are a qualitative investigation on the behavior of some ammonia systems in fused hydroxides (17) and two manometric studies on its solubility in perchlorate (18) and in several nitrate melts (18, 19).

In the course of a systematic investigation on the interaction of

gases with ionic melts (19-23) anomalous dissolution kinetics were observed (24) when platinum beakers were used to contain the ammonia saturated nitrate melt. The phenomenon was easily related to the platinum catalyzed chemical decomposition of ammonia and to the consequent production (25) of hydrogen.

The deep knowledge of the electroanalytical behavior of hydrogen systems in nitrate melts (26-32) enabled this research group to undertake,with a reasonable possibility of success,the study of the complex behavior of ammonia and its decomposition products. In this paper, after a survey on previous literature data on ammonia-fused salt systems, preliminary information is given on work in progress about the chemical stability and electroactivity of ammonia in nitrate melts.

SURVEY OF LITERATURE INFORMATION ABOUT NH_3-MOLTEN SALT SYSTEMS

Ammonia systems in hydroxide melts

Ammonia solubility data (see Table I) and qualitative information on the chemical and electrochemical behavior of different ammonia systems in the (Na-K)OH eutectic melt are given by Goret (17). Preliminary platinum rotating wire electrode voltammetric experiments permitted the identification of the wave due to the ammonia reduction according to the overall equation

$$NH_3 + e = \tfrac{1}{2} H_2 + NH_2^- \qquad 1$$

whose half-wave potential is found to be 0.45 V vs.a "standard sodium" reference electrode. In acidic melts this wave and the water electroreduction wave ($E_{\frac{1}{2}} \simeq 0.7$ V vs.the same reference) partially merge.

The author could not evidence the hydrogen electrooxidation wave in amide-containing melts (expected to be)

$$NH_2^- + \tfrac{1}{2} H_2 = NH_3 + e \qquad 2$$

because of the presence of the following chemical equilibrium

$$H_2 + NH_2^- = NH_3 + H^- \qquad 3$$

which lies to the right. In effect it may be used for the production of sodium hydride (33).

Both ammonia and amide ions can be electrooxidized to nitrogen in acidic melts and to nitrite and/or nitrate in basic melts but the author did not report any electrodic process for the observed electrooxidation waves (17). However, on the basis of literature information (9-15) the following overall processes

$$NH_3 + 3\ OH^- = \tfrac{1}{2} N_2 + 3\ H_2O + 3\ e \qquad 4$$

$$NH_2^- + 2\ OH^- = \tfrac{1}{2}\ N_2 + 2\ H_2O + 3\ e \qquad 5$$

appear acceptable for the given electrode reactions.

The acid-base properties of the NH_3/NH_2^- couple were also evaluated. From voltammetric data the following constant

$$K_A = \frac{|NH_2^-||H_2O|}{|NH_3|} \qquad 6$$

was estimated to be $(1.76 \pm 1.44).10^{-3}$ at 513 K (17).

Solubility measurements of ammonia in perchlorate and nitrate melts

Allulli measured the solubility of ammonia in (Li-K)ClO_4 and in lithium containing nitrate melts (18) on using a manometric technique. Later Paniccia and Zambonin measured the solubility of ammonia (and carbon dioxide) in pure $LiNO_3$, $NaNO_3$ and KNO_3 and in different binary nitrate melts (19). A detailed description of the apparatus and methodology used in this laboratory can be found in references 27 and 32.

The Henry's constants and the relevant thermodynamic parameters for the dissolution of ammonia are summarized in Table I (to simplify the comparison between data from different laboratories unified units are used). In particular, according to Grimes et al.(34,35) the different entrophy variations are defined as follows

$$\Delta S_1 = \Delta H / T \qquad 7$$

$$\Delta S_2 = R \ln C_d / C_g \qquad 8$$

$$\Delta S^\circ = \Delta S_1 + \Delta S_2 \qquad 9$$

where C_d represents the concentration of dissolved ammonia in equilibrium with gaseous ammonia at the concentration C_g and the other parameters have their usual meaning in thermodynamics.

For discussion about the solute-solvent interaction effects on the dissolution process the reader is referred to the original papers.

REPORT ON PREVIOUS RESULTS AND WORK IN PROGRESS ON AMMONIA-NITRATE MELT SYSTEM

Experimental system and chemicals

The cell, the thermostatic system and the voltammetric set-up used in the course of electroanalytical investigations in nitrate melts are described elsewhere (27,32).

Care was taken to ensure that the only platinum surface in contact

with the ammonia-containing melt was the rotating disk electrode surface ($7.85.10^{-3}$ cm^2). For this purpose teflon containers and a teflon-shielded counter-electrode were used.

The solvent was the (Na-K)NO_3 equimolar mixture, purified by direct injection of concentrated aqueous nitric acid (31). It was usually maintained under bubbling of nitrogen (UPP grade, SIO, Milan) or ammonia (anhydrous grade, Matheson). The gases were further dried using traps of Molecular Sieves 5A (Carlo Erba, Milan) at -80°C and sodium amide (97%, Alfa) respectively.

When necessary a 10% ammonia: nitrogen mixture was prepared by using a Matheson 7400 Rotameter.

Influence of noble metals on the ammonia dissolution kinetics

When lithium was involved in the course of the previously mentioned experiments on the solubility of ammonia (24) teflon or platinum vessels were used since lithium ions attack the glass containers. Two examples of pressure variation (ΔP) vs. time plots obtained at 550 K on using, ceteris paribus, teflon or platinum beakers are compared in figure 1: see curves a and b respectively. The reported K_H value was calculated from the data of reference 19 (see Table I) on using the equation

$$\log K_H \ (torr^{-1}) = - 8.675 + 2415.2/T \qquad 10$$

As it can be seen in curve a the pressure variation increases rapidly up to a maximum constant value which corresponds to the attainment of equilibrium. When platinum vessels are used the ΔP reaches an initial maximum and then decreases to a nearly constant value lower than in curve a. This result seems to indicate that gaseous products are formed, likely via a chemical decomposition of ammonia, when a platinum surface is in contact with the ammonia-containing melt.

Preliminary ex situ gas-cromatographic analysis of the gaseous atmosphere (36) indicated the presence of NO, NO_2 and H_2O,which can be likely produced by different rection pathways, such as for example

$$3\ NO_3^- + 2\ NH_3 = 3\ NO_2^- + N_2 + 3\ H_2O \qquad 11$$

$$2\ NO_3^- + NH_3 = 2\ NO_2^- + NO_2 + 3/2\ H_2 \qquad 12$$

which can involve additional steps such as the known (28,37)

$$NO_2^- + NO_2 = NO_3^- + NO \qquad 13$$

$$NO_3^- + H_2 = NO_2^- + H_2O \qquad 14$$

On-line gas-cromatographic experiments are in progress for a deeper understanding of the ammonia decomposition kinetics.

Rotating disk electrode voltammetric detection of hydrogen generated by ammonia decomposition

The hydrogen produced by the platinum-catalyzed decomposition of ammonia was electroanalitically detected by substituting the platinum beaker with an inert one (in order to avoid a massive production of NO, NO_2 and H_2O in the bulk solution) and by using (36) a platinum rotating disk electrode (RDE) both as catalyst and hydrogen-sensitive probe. Since proton acceptor species are necessary for the hydrogen electrooxidation in nitrate melts (27,29-32) preliminary voltammetric experiments were performed in hydroxide-containing melts maintained under anhydrous ammonia atmosphere (36,38). Typical current-potential profiles are shown in figure 2 and compared with voltammograms recorded under comparable experimental conditions in hydrogen atmosphere: see figure 3 which shows the peculiar voltammetric behavior of the $(Pt)H_2O/H_2,OH^-$ system in molten alkali nitrates (29,30,32). In particular curves a, b and c in figure 3 can be obtained when hydrogen is present in excess, in stoichiometric ratio (1:2) and respectively in defect with respect to hydroxide ions,within the diffusion layer. As it can be seen the ammonia-hydroxide system behaves, from a qualitative point of view, as the hydrogen-hydroxide one in comparable experimental conditions. The same characteristic minimum of the anodic current can be obtained on working in the presence of an electrodic excess of hydroxide ions on ammonia (compare curves 2c and 3c) and perfectly similar current-potential profiles are obtained when the stoichiometric ratio is realized between hydrogen or ammonia and hydroxide (compare curves 2b and 3b). When ammonia is present in electrodic excess curve 2a is obtained which seems different from curve 3a. However this difference can be easily interpreted on considering the electroactivity properties of ammonia and hydrogen. Since ammonia can be electrooxidized even in the absence of hydroxide ions (see the next paragraph) its excess gives rise to the second anodic wave ($E_{\frac{1}{2}} \simeq -0.15$ V)of curve 2a. The same behavior cannot be observed with the unreactive hydrogen species.

These results seem to confirm that hydrogen is produced in the first decomposition step of ammonia in nitrate melts. Owing to the large solubility difference between ammonia and hydrogen (19,23) the hydrogen electrooxidation current obtained in hydroxide-containing melts saturated with ammonia is more than two orders of magnitude higher than the corresponding one relevant to hydroxide-containing melts directly saturated with hydrogen at the same working pressure.

The electroanalytical behavior of the ammonia-hydroxide system is still under study in this laboratory.

Electroanalytical behavior of ammonia in anhydrous or slightly wet melts

Preliminary voltammetric experiments were performed in a purified (Na-K)NO_3 equimolar melt at 513 K. Curve a in figure 4 is the base cathodic voltammogram obtained under flux of anhydrous nitrogen. The sharp current raise after about -1.5 V is relevant to the nitrate ions electroreduction (39-41). Curves such as b can be obtained when 10% anhydrous ammonia is fluxed through the melt (diluted ammonia was used to lower the rather evident current noise mainly related to hydrodynamic turbulences by chemically or electrochemically produced gaseous products: see for example figure 2). The new cathodic wave in curve b can be likely attributed to the ammonia electroreduction. Sometimes, however, curve b is splitted into two consecutive waves. When 10% ammonia is fluxed in slightly wet melts curve c in figure 4 can be obtained as results from the consecutive electroreduction of water (20,42-44) and ammonia.

Curve a in figure 5 is the base anodic voltammogram obtained under anhydrous nitrogen atmosphere. The nitrite electrooxidation wave (45,46) is absent because the residual nitrite concentration is lower than the Pt-RDE detection limit (i.e. $|NO_2^-| < 1.10^{-5}$ mol Kg^{-1}). An example of voltammogram recorded when 10% ammonia is fluxed through the melt is curve b in figure 5: the new anodic wave can be likely attributed to the ammonia electrooxidation. Its half-wave potential is about -0.15 V. Irreproducible results were obtained if the voltammogram, on the contrary of curve b, was scanned from positive towards negative potential values.

As a matter of fact the experimental ratio between the cathodic and anodic diffusion currents of ammonia in anhydrous melts ranges between 2.4 and 3.0.

At the present time the formulation of detailed electrode mechanisms is not possible. Overall reactions such as

$$4\ NH_3 = 3\ NH_4^+ + \tfrac{1}{2}\ N_2 + 3\ e \qquad 15$$

for the ammonia electrooxidation and

$$NH_3 + e = NH_2^- + \tfrac{1}{2}\ H_2 \qquad 1$$

for the ammonia electroreduction were proposed in liquid ammonia (47) and in fused hydroxides (19). Reactions 15+1 are not consistent with the experimental value of the cathodic/anodic diffusion currents ratio ($\sim$ 2.7) observed for ammonia thus indicating that, in molten nitrates, the solvent anions likely play a role in the discharge mechanisms. In effect preliminary results seem to indicate that NO_3^- ions are involved in the electroreduction of ammonia while its electrooxidation likely occurs according to reaction 15.

Work is in progress to elucidate the actual electrode mechanisms as well as to characterize the electroanalytical behavior of ammonium and amide ions and their chemical stability.

ACKNOWLEDGEMENTS

Work carried out with the financial assistance of the Italian National Research Council (C.N.R. Rome).

REFERENCES

1) C.Marchetti, Euro Spectra, 10, 117 (1971)
2) D.P.Gregory, Sci.Am., 228, 13 (1973)
3) D.P.Gregory, 13rd World Gas Conference, London (1976)
4) E.J.Cairns, E.L.Simons, A.D.Tavebaugh, Nature, 217, 780 (1968)
5) E.L.Simons, E.J.Cairns, D.J.Surd, J.Electrochem.Soc., 116, 556 (1969)
6) D.W.McKee, A.J.Scarpellino, I.F.Danzig, M.S.Pak, ibid, 116, 562 (1969)
7) D.W.McKee, A.J.Scarpellino, Fr.I,571,482(Cl;HOIm)20 Jun 1969, US Appl. 01 Jun 1967
8) J.D.Giner, J.R.Moser, US. 3,650,838 (Cl 136/86;HOIm) 21 Mar 1972, Appl. 491,759, 30 Sep 1965
9) H.G.Oswin, M.Salomon, Can.J.Chem., 41, 1686 (1963)
10) T.Katan, R.J.Galiotto, J.Electrochem.Soc., 110, 1022 (1963)
11) D.Spahrbier, G.Wolf, Z.Naturforsch., 19a, 614 (1964)
12) A.R.Despic, D.M.Drazic, P.M.Rakin, Electrochim.Acta, 11, 997 (1966)
13) K.Sasaki, Y.Hisatomi, J.Electrochem.Soc., 117, 758 (1970)
14) W.Vielstich, U.Vogel, M.Kamat, J.Mrha, Entropie, 32, 31 (1970)
15) W.Vielstich, U.Vogel, Chem.Ing.Tech., 4, 195 (1971)
16) K.V.Kordesch, J.Electrochem.Soc., 125, 77C (1978)
17) J.Goret, Thesis, Université de Paris (1966)
18) S.Allulli, J.Phys.Chem., 73, 1084 (1969)
19) F.Paniccia, P.G.Zambonin, JCS Faraday I, 69, 2019 (1970)
20) P.G.Zambonin, V.L.Cardetta, G.Signorile, J.Electroanal.Chem., 28, 237 (1970)
21) F.Paniccia, P.G.Zambonin, JCS Faraday I, 68, 2083 (1972)
22) E.Desimoni, F.Paniccia, P.G.Zambonin, J.Electroanal.Chem., 38, 373 (1972)
23) E.Desimoni, F.Paniccia, P.G.Zambonin, JCS Faraday I, 69, 2014 (1973)
24) P.G.Zambonin, unpublished data
25) D.G.Löffler, L.D.Schmidt, J.Catalysis, 41, 440 (1976)
26) E.Desimoni, F.Paniccia, L.Sabbatini, P.G.Zambonin, J.Appl.Electrochem., 6, 445 (1976)
27) E.Desimoni, F.Paniccia, L.Sabbatini, P.G.Zambonin, "Proceedings of the International Symposium on Molten Salts", J.P.Pemsler et al. Eds. The Electrochemical Soc., Inc. 584 (1976)

28) E.Desimoni, F.Paniccia, P.G.Zambonin, J.Phys.Chem., 81, 1985 (1977)
29) E.Desimoni, F.Palmisano, P.G.Zambonin, J.Electroanal.Chem., 84, 323 (1977)
30) E.Desimoni, B.Morelli, F.Palmisano, P.G.Zambonin, Annali Chim.(Rome) 67, 451 (1977)
31) E.Desimoni, F.Palmisano, L.Sabbatini, P.G.Zambonin, Anal.Chem., 50, 1895 (1978)
32) P.G.Zambonin, E.Desimoni, F.Palmisano, L.Sabbatini, "Ionic Liquids", D.Lovering and D.Inman Eds., Plenum Publishing Company Ltd, London, 249 (1980)
33) Russian Patent 43.634; 31.7.1935
34) W.R.Grimes, N.V.Smith, G.M.Watson, J.Phys.Chem., 62, 862 (1958)
35) M.Blander, W.R.Grimes, N.V.Smith, G.M.Watson, ibid, 63, 1164 (1959)
36) E.Desimoni, F.Paniccia, P.G.Zambonin, Annali Chim.(Rome)351 (1980)
37) P.G.McCormick, H.S.Swofford, Anal.Chem., 41, 146 (1969)
38) E.Desimoni, F.Palmisano, L.Sabbatini, P.G.Zambonin, 31st ISE Meeting, Venice (1980), Extended Abstracts Volume p.769
39) H.S.Swofford, H.A.Laitinen, J.Electrochem.Soc., 110 (1963)814
40) L.B.Topol, R.A.Osteryoung, J.M.Christie, J.Phys.Chem., 70, 2857 (1966)
41) P.G.Zambonin, J.Electroanal.Chem., 24, 365 (1970)
42) M.Peleg, J.Phys.Chem., 71, 4553 (1967)
43) D.G.Lovering, R.M.Oblath, A.K.Turner, JCS Chem.Comm., 673 (1976)
44) A.Espinola, J.Jordan, "Characterization of Solutes in Non Aqueous Solvents", G.Mamantov Ed., Plenum Publishing Corp., New York,N.Y., 311 (1978)
45) E.Desimoni, F.Palmisano, P.G.Zambonin, J.Electroanal.Chem., 84, 315 (1977)
46) F.Palmisano, L.Sabbatini, E.Desimoni, P.G.Zambonin, ibid, 89, 311 (1978)
47) J.J.Lagowski, International Symposium on Non Aqueous Electrochemistry, London, Butterworths, 441 (1970)

TABLE I

Thermodynamic parameters for the dissolution of ammonia in some fused salts

SOLVENT	MOLE RATIO	$K_H.10^5$ $torr^{-1}$	T K	ΔH Kcal/mol	ΔS_1 cal/mol K	ΔS_2 cal/mol K	$\Delta S°$ cal/mol K	REF
(Na-K)OH	1:0.96	∿0.0033						17
$LiNO_3$		8.8	523	-13.1	-25.1	8.6	-16.5	19
		1.6	623		-21.0	5.5	-15.5	19
		12.5	533	-16.5	-30.4	8.7	-21.7	18
		7.05	556					18
		4.1	576					18
		3.1	588					18
$NaNO_3$		0.32	523	-5.5	-10.3	1.8	-8.6	19
		0.15	623		-8.6	0.41	-8.1	19
KNO_3		0.11	523	-2.6	-5.0	-0.67	-5.7	19
		0.077	623		-4.3	-1.1	-5.5	19
(Li-K)NO_3	1:1.33	4.1	433	-7.0	-13.4	3.9	-9.5	18
		2.45	463					18
		1.7	483					18
		1.05	523					18
	1:1	1.2	523	-7.6	-14.8	4.3	-10.5	19
		0.36	623		-12.4	2.1	-10.3	19
	2:1	2.3	523	-8.8	-17.2	5.5	-11.7	19
		0.56	623		-14.3	3.1	-11.2	19

TABLE I (cont.)

SOLVENT	MOLE RATIO	$K_H \cdot 10^5$ $torr^{-1}$	T K	ΔH $\frac{Kcal}{mol}$	ΔS_1 $\frac{cal}{mol\ K}$	ΔS_2 $\frac{cal}{mol\ K}$	$\Delta S°$ $\frac{cal}{mol\ K}$	REF
$(Li\text{-}K)NO_3$	3:1	4.2	515	-11.8	-22.8	6.6	-16.2	18
		2.05	548					18
		1.5	565					18
		0.85	598					18
	5.7:1	3.6	523	-10.5	-20.3	6.7	-13.6	19
		0.97	623		-17.0	4.3	-12.7	19
$(Na\text{-}K)NO_3$	1:1	0.21	523	-4.3	-8.1	0.67	-7.4	19
		0.11	623		-6.9	-0.36	-7.2	19
$(Li\text{-}Na\text{-}K)NO_3$	1.5:1:3	2.1	433	-5.8	-11.1	3.1	-8.0	18
		1.5	458					18
		1.15	475					18
		0.7	523					18
$(Li\text{-}K)ClO_4$	3.2:1	128	507	-13.8	-26.4	12.4	-14.4	18
		84	524					18
		61.5	539					18
		37	561					18
		23	584					18

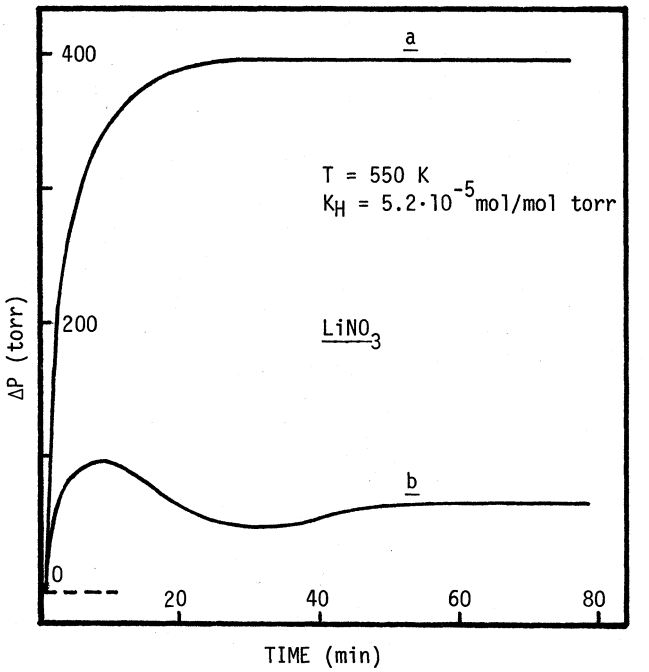

Figure 1: Typical pressure variation (ΔP) vs. time plots for the ammonia dissolution in fused $LiNO_3$ at 550 K obtained on using teflon (curve a) or platinum (curve b) containers. Initial pressure: 510 torr; solvent weight: 90 g.

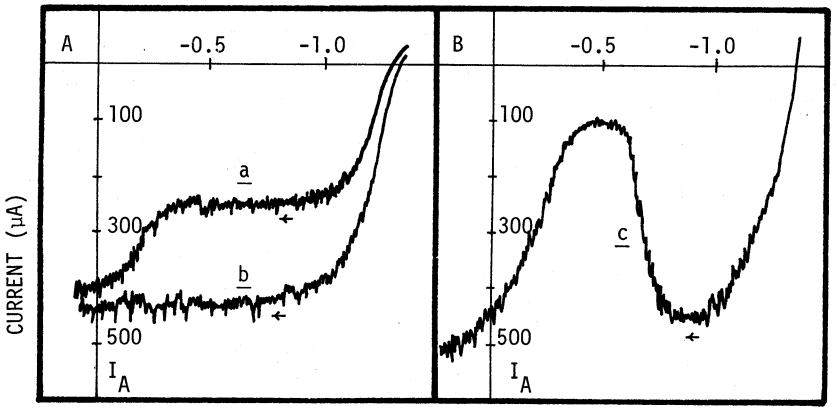

Figure 2: Platinum-rotating disk electrode voltammetric profiles obtained in hydroxide-containing $(Na\text{-}K)NO_3$ equimolar melts maintained under 1 atm of ammonia. T: 518 K. Curve a: $|OH^-| \simeq 8.10^{-2}$ mol Kg^{-1}; curve b: $|OH^-| \simeq 0.16$ mol Kg^{-1}; curve c: $|OH^-| \simeq 0.19$ mol Kg^{-1}.

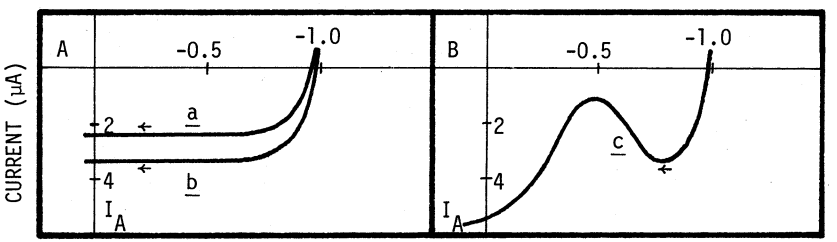

Figure 3: Platinum-rotating disk electrode voltammetric profiles obtained in hydroxide-containing $(Na\text{-}K)NO_3$ equimolar melts maintained under 1 atm of hydrogen. T: 513 K. Curve a: $|OH^-| \simeq 7.5 \cdot 10^{-4}$ mol Kg^{-1}; curve b: $|OH^-| \simeq 1.10^{-3}$ mol Kg^{-1}; curve c: $|OH^-| \simeq 1.8 \cdot 10^{-3}$ mol Kg^{-1}.

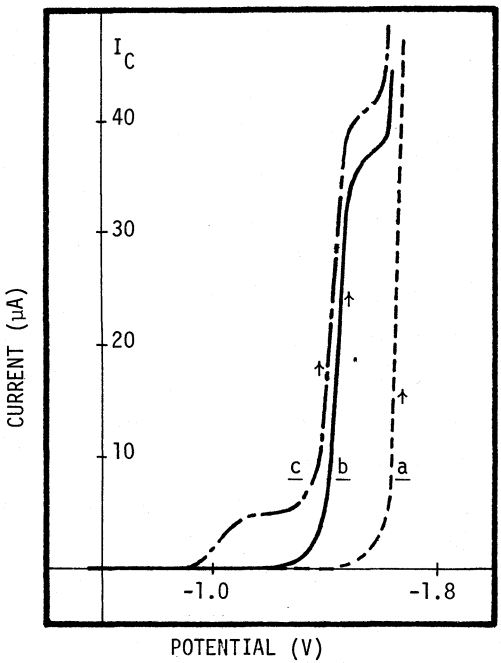

Figure 4: Platinum-rotating disk electrode voltammetric profiles obtained in a purified (Na-K)NO_3 equimolar melt at 518 K. Curve a: base voltammogram obtained in anhydrous nitrogen atmosphere; curve b: current-potential profile obtained when anhydrous ammonia (partial pressure of ammonia:0.1 atm; partial pressure of nitrogen: 0.9 atm) is fluxed through the melt; curve c: current-potential profile obtained in a slightly wet melt ($|\overline{H_2O}| = 2.4 \cdot 10^{-4}$ mol Kg^{-1}) under ammonia atmosphere (partial pressure of ammonia: 0.1 atm; partial pressure of nitrogen about 0.9 atm).

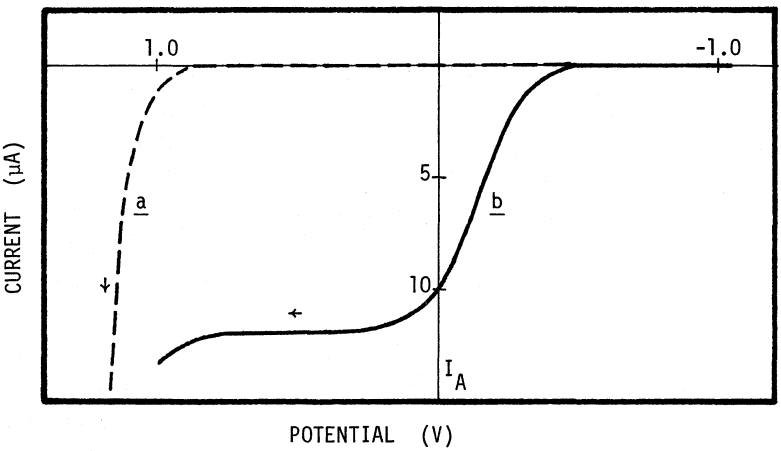

Figure 5: Platinum-rotating disk electrode voltammetric profiles obtained in a purified (Na-K)NO_3 equimolar melt at 518 K. Curve a: base voltammogram obtained under anhydrous nitrogen atmosphere; curve b: current-potential profile obtained when anhydrous ammonia (partial pressure of ammonia: 0.1 atm; partial pressure of nitrogen: 0.9 atm) is fluxed through the melt.

DOI: 10.1149/198109.0284PV

IN-SITU ELECTROCHEMICAL STUDIES TO INVESTIGATE INTERACTIONS OF ATMOSPHERIC COMPONENTS WITH ALKALI METAL NITRATE SOLVENTS

S. H. White and U. M. Twardoch
EIC Laboratories, Inc., 55 Chapel Street, Newton, MA 02158

ABSTRACT

The diffusion coefficient of nitrite ions was determined in 50 mol% $NaNO_3$-KNO_3 from cyclic voltammetric and chronopotentiometric measurements using gold electrodes over the temperature range 250-400°C. The solubility of water was determined indirectly using cyclic voltammetry over a similar range of temperature.

INTRODUCTION

Recently the molten nitrates of sodium and potassium have been selected as potential candidates for thermal storage media in solar-thermal applications (1). This use would involve handling many thousands of tons of salt in the liquid phase at temperatures between 300-600°C. The handling, containing, and chemical reactivity of such solvents are of paramount importance in such an undertaking, particularly since these liquids would be exposed to variable atmospheric conditions. Interactions with atmospheric components are important, particularly with respect to the oxygen, water and carbon dioxide content of the atmosphere. The likelihood of interaction between these atmosphere components and the liquid nitrates is small at lower temperatures (<300°C for the binary $NaNO_3$-KNO_3 mixture). However, the high temperatures and the use of metallic containers will most certainly lead to decomposition of the nitrate. The presence of oxygen, carbon dioxide and water may moderate the reaction pathways available (2,3). The characterization of the reactions involving water and carbon dioxide with these nitrate melts under aerial conditions is therefore of prime importance.

Thermal decomposition of these nitrate melts is referred to in the literature (4). Nitrite (5,6) is a commonly observed product of this degradation and is often reported even when the salts have been carefully treated under inert atmosphere. The presence of oxygen in the atmosphere in contact with these salts can result in further reactions. Some studies have reportedly prepared nitrite free melts ($<10^{-4}$M NO_2^-) at low temperature (<280°C) and in such cases Zambonin and co-workers (3,7) have studied manometrically the solubility of gases such as O_2, CO_2, H_2, and water vapor in the binary melt over the temperature range 225-270°C. Jordan and Zambonin (8,9) reported that the chemistry of oxide ion in nitrate melts was affected not only by the presence of oxygen but also by the container material such as Pyrex glass which tended to buffer the oxide content of the melt as well as introduce

silicate moieties into the system (10). Because of this and the need to work up to 600°C, we have selected alumina ware for containment of the melt and structural material for the electrodes. This will ensure inertness of the working materials. Platinum was discounted because of a suspicion of catalytic interactions with the nitrate at the higher temperature (11).

In this paper some preliminary data are reported for the nitrite solute and for water, a major component in the atmosphere. Table 1 illustrates the variations reported by previous workers for the diffusional characteristics of the nitrite ions in the binary mixture. To monitor nitrite ion changes in the melt in thermal decomposition/atmospheric reactions, it is necessary to have more precise data for this solute over a wide temperature interval.

The behavior of water in molten nitrates has been studied by numerous workers and has generated some controversy. Zambonin has investigated the solubility of this solute over a limited temperature range in $NaNO_3$-KNO_3 using a manometric method (14). From these results and RDE experiments he reported Henrian constants, a heat of solution, and a diffusion coefficient for water at 603°K. Table 1 summarizes these previous results. The results reported here extend these data to higher temperatures.

EXPERIMENTAL

The experimental cell is shown in Figure 1. Figure 2 shows detail of the individual electrodes. The reference electrode was

$$Ag|AgNO_3\ 0.07m,\ KNO_3\text{-}NaNO_3 \,\|\, \text{glass membrane}$$

which was enclosed in a sodium-β alumina tube containing the binary mixture. This ensured that the melt in the main compartment did not come into contact with Pyrex glass. The gold counter electrode was contained in a separate alumina tube. The working electrode was a gold flag mounted on a gold wire sealed into alumina. The surface areas of the working electrodes were measured by the method of Wolfe and Caton (15). The agreement between the measured and geometric areas was better than 10%.

The melts were prepared either by vacuum fusion of the ultrapure salts or from P_2O_5 dried ACS grade salts which were then dried up to 200°C under vacuum, melted under pure oxygen, evacuated, and subsequently filtered. The latter material was almost transparent.

Water was added in the form of $LiNO_3 3H_2O$ or by saturating argon gas at a known partial pressure. ACS grade sodium nitrite, dried over P_2O_5 under vacuum,was added in the pilot ion studies.

Cyclic voltammetry and chronopotentiometry were made using a PAR 175 universal generator, a PAR 174A polarographic unit, a 373

potentiostat, and either a Plotamatic X-Y recorder or a Bascom-Turner microprocessor controlled data logger.

RESULTS

Melt Purity. The initial state of the solvents used in these experiments was examined voltammetrically. The measurements showed the initial nitrite ion content to be about $\sim 2 \times 10^{-3}$ molal when the vacuum melting procedure was used. Melting under oxygen reduced this nitrite ion content to approximately $0.3\text{-}0.7 \times 10^{-3}$ molal. Figure 3 shows a typical background for the oxygen treated melt. The effect of oxygen is probably to oxidize organic residues which otherwise reduce nitrate to nitrite. These results are higher than those reported by Goeting and Ketelaar (5), but the temperature (which is thought to play a significant role) was somewhat higher (250-350°C) in our case. The remaining background between $\sim +0.400$V to -1.00V Ag/AgI (0.07m) showed current densities less than 150 $\mu A\text{-}cm^{-2}$ at a scan rate of 100 $mV\text{-}sec^{-1}$.

Nitrite Ion as Solute. The assessment of the nitrite ion content of the melts required a knowledge of the diffusion characteristics of nitrite ions. The data in the literature are inconsistent. Pilot ion additions of nitrite were made at each temperature to enable suitable background corrections to be made. The measurements were made in decreasing order of temperature followed by reheating to 375°C and then cooling to the lowest temperature in the initial cycle (275°C). Cyclic voltammetric measurements (Figure 4) at several differing scan rates and chronopotentiometric measurements (Figure 5) at several current densities were made at each temperature plateau.

The results were analyzed assuming the nitrite ion oxidation to be reversible (12), viz.,

$$NO_2^- \rightleftarrows NO_2(g) + e.$$

The number of electrons involved in this process was confirmed from the ratio of $i_p/\omega^{\frac{1}{2}}/i\tau^{\frac{1}{2}}$ at each temperature. The cyclic voltammetric and chronopotentiometric data which was obtained were found to agree with the Randles-Sevcik and Sand equations, respectively, for each concentration and temperature employed. The mean values of $i_p/\omega^{\frac{1}{2}}C$ and $i\tau^{\frac{1}{2}}/C$ and their standard deviations were used to evaluate the diffusion coefficient at each temperature. These results are combined in the form of an Arrhenius plot given in Figure 6. Using a least square procedure these data were fitted to a straight line expressed by

$$\ln D = -6.427 - 2.921T^{-1} \qquad (1)$$

from which the activation energy for diffusion of the nitrite ion was found to be 5.8 $kcal\text{-}mol^{-1}$. This value is typical for diffusional processes in molten nitrates (16). Table 2 shows typical diffusion coefficients calculated from the above equation (1) and compares these

values with those reported in the literature. Our results are consistent with those of Zambonin (9) and have been confirmed by recent pulse polarographic measurement at a gold electrode (17). The inconsistency of the literature data calculated from chronopotentiometric measurements may arise from the serial oxidation of the platinum electrodes and nitrite ions (7).

The maximum nitrite content which was reached after several additions (1.07×10^{-2} molal) was readily reduced to the original background concentration at 300°C in our experimental cell by NO_2 gas purging (5).

Water Solute. Two kinds of experiments have been carried out for water:

(1) Use of argon saturated with known water vapor pressures, as the water source.

(2) Use of lithium nitrate trihydrate as the source of water.

The rapid quantitative uptake and removal of water from this melt has been demonstrated by following the cathodic reduction peak associated with water.

Zambonin (14) reported a single datum for the diffusion coefficient of water based upon RDE measurements. By observing the cyclic voltammograms (Figure 7) at different temperatures for a constant water partial pressure, an activation energy was obtained (Figure 8) which is made up of a contribution from the heat of solution and an activation energy for diffusion of water. Using a heat of solution determined from manometric data by Zambonin and co-workers (14), the diffusional contribution to this total activation energy has been calculated. A value of 4.4 kcal mol^{-1} was obtained. From this result and the single diffusion coefficient given by Zambonin (14), Henry's law constants for water solubility up to 350°C were calculated. Table 3 compares solubility data derived from cyclic voltammetric results with those reported by Zambonin. The agreement is satisfactory, considering the different techniques employed.

In an attempt to substantiate the diffusion coefficient for water reported by Zambonin, additions of $LiNO_3$ trihydrate were made to both open and closed experimental cells, measuring the cathodic peak at a function of time after each addition. Figure 9 shows two typical results. From an extrapolation of the line to t=0, a value of i_p was found, from which the diffusion coefficient for water was calculated (18). Table 4 shows the results and compares them with those calculated by the previous method. The reasonable agreement between the results lends confidence to the procedures and the data so obtained. It is intended to measure these properties more precisely using a combination of rotating disc and stationary electrode measurements to resolve, simultaneously, the concentration and diffusion coefficient of these species.

ACKNOWLEDGMENT

This work was supported by the Sandia Laboratories, Livermore, California. The authors thank Mr. Michael Bower for technical assistance.

REFERENCES

1. For example, Energy Technology, Third Annual Proceedings of Thermal Storage Information Exchange Meeting, SLL/DOE, Virginia (1978).

2. D. Desimoni, F. Panaccia and P. G. Zambonin, J. Electroanal. Chem., 38, 373 (1972).

3. P. G. Zambonin, J. Electroanal. Chem., 33, 243 (1971).

4. D. Inman and J. Braunstein, Chem. Comm., 148 (1966).

5. A. F. J. Goeting and J. A. A. Ketelaar, Electrochim. Acta, 19, 267 (1974).

6. P. G. McCormick and H. S. Swofford, Anal. Chem., 41, 146 (1969).

7. S. H. White, "Role of Water during the Purification of High Temperature Ionic Liquids," Proc. Conf., St. Johns, Oxford Plenum, Feb. 1981.

8. J. Jordan, J. Electroanal. Chem., 29, 127 (1971).

9. P. G. Zambonin, Anal. Chem., 41, 868 (1969).

10. J. D. Burke and D. H. Kerridge, Electrochim. Acta, 19, 251 (1974).

11. Private Communication, R. Carling, Sandia, July 1980.

12. L. E. Topol, R. A. Osteryoung and J. H. Christie, J. Phys. Chem., 70, 2857 (1966).

13. D. Inman, R. Spencer and S. H. White, unpublished work, see R. Spencer B.Sc. Thesis, City University, London, 1967.

14. P. G. Zambonin, V. L. Cardetta and G. Signorile, J. Electroanal. Chem., 28, 237 (1970).

15. C. R. Wolfe and R. D. Caton, Jr., Anal. Chem., 43, 663 (1971).

16. G. J. Janz, Molten Salts Handbook, Academic Press, 1967.

17. S. H. White, U. M. Twardoch, unpublished work, 1980.

18. S. B. Aganesova, P. Ladari, V. P. Yurkinskii and A. G. Morachevskii, Zhur. Prik Khim., 48(5), 1164 (1975).

TABLE 1. DATA RELATING TO NITRITE AND WATER IN BINARY $NaNO_3$-KNO_3

Species	E(V)	Diffusional Characteristics 10^5D cm^2sec^{-1}	Temp. °K	Method	Ref.
NO_2^-	$E_{\tau/4}^{NO_2/NO_2^-} = -0.44$	5.2	571	Chronopotentiometry	12
	$E_{1/2} = -0.44$	0.525	502	Rotating Disc Electrode	19
		2.4 ± 0.7	523	Chronopotentiometry	13
H_2O	$E_{1/2} = -1.19$	1.9	502	Rotating Disc Electrode	14

H_2O Solubility in Molten Nitrates

Solvent	Temp. °C	Henry's Constant mol $mol^{-1}mm^{-1}$	Range of HL	ΔH_{soln} kcal mol^{-1}	10^5D cm^2sec^{-1}	Ref.
$NaNO_3$-KNO_3	227	176	20 mm	-8.4	1.94	14
50:50 mol%	294	63	20 mm			3

TABLE 2. COMPARISON OF EXPERIMENTAL AND LITERATURE DATA FOR NITRITE ION DIFFUSION COEFFICIENTS

Temp. °K	Diffusion Coefficient This Paper	Diffusion Coefficient Literature Data	Ref.	Method
	$D \times 10^6$ cm^2-sec^{-1}	$D \times 10^6$ cm^2-sec^{-1}		
573	9.9 ± 0.5	9.3 ± 0.5	17	Pulse Polarography
571	9.7 ± 0.5	5.2 ± 2	12	Chronopotentiometry
523	6.0 ± 0.3	24.8 ± 7	13	Chronopotentiometry
523	6.0 ± 0.3	27.5	6	Chronopotentiometry
510	5.3 ± 0.3	5.25 ± 0.1	9	Rotating Disc Electrode

$$\ln D = -6.427 - 2.921 \times 10^3 T^{-1}(°K)$$

TABLE 3. EXPERIMENTAL AND DERIVED RESULTS FOR WATER IN MOLTEN SODIUM POTASSIUM NITRATE MIXTURE (50 mol%)

Temp. °K	P mm Hg	$i_p/v^{\frac{1}{2}}A$ A $cm^{-2}v^{-\frac{1}{2}}s^{\frac{1}{2}}$	D x 10^6 cm^2s^{-1}	C x 10^3 mol kg^{-1}	K_H x 10^4 mol $kg^{-1}mm^{-1}$	K_H x 10^4 Literature[12] mol $kg^{-1}mm^{-1}$
523	20.94	50.98	22	9.82	4.6	6.0
573	9.21	18.85	32	3.20	3.4	-
573	19.35	36.06	32	6.15	3.1	-
573	20.82	33.77	32	5.26	2.5	3.3
573	31.82	45.24	32	7.68	2.4	-
598	8.04	5.76	37	0.94	1.1	-
598	20.94	25.57	37	4.19	2.0	-
623	20.94	19.34	44	2.96	1.4	-

Note: Calculation based upon D_{H_2O} = 19 x 10^6 cm^2sec^{-1} at 503°K and an activation energy for diffusion of 4.4 kcal mol^{-1}.

TABLE 4. DIFFUSION COEFFICIENT FOR WATER AT 300°C

	D_{H_2O} cm^2sec^{-1}	Conc. $LiNO_3 3H_2O$ Added
Open (Argon Flowing)	13 x 10^{-6}	4.08 x 10^{-3} knol kg^{-1}
Closed (Argon Stationary)	21 x 10^{-6}	6.65 x 10^{-3} mol kg^{-1}
Calculated	32 x 10^{-6}	From Zambonin's value of 19 x 10^{-6} at 230°C (14) and our activation energy for diffusion of 4.4 kcal mol^{-1}.

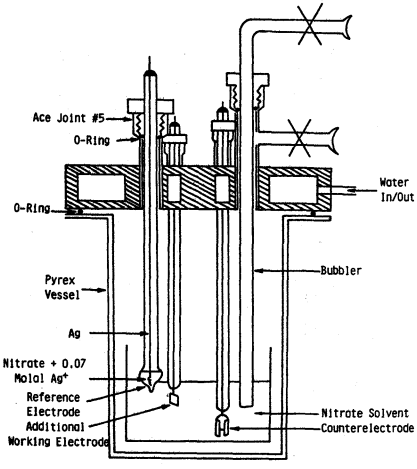

Fig. 1. Electrochemical cell.

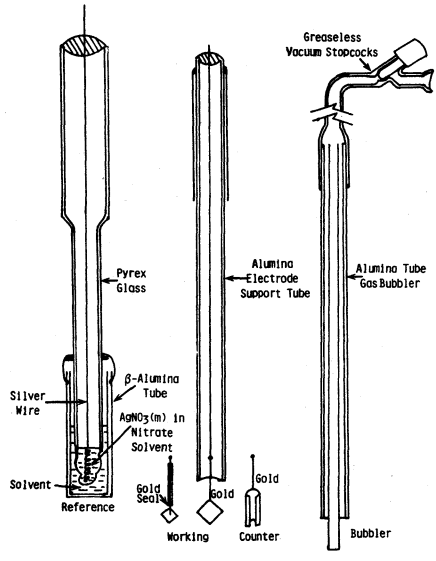

Fig. 2. Individual cell components.

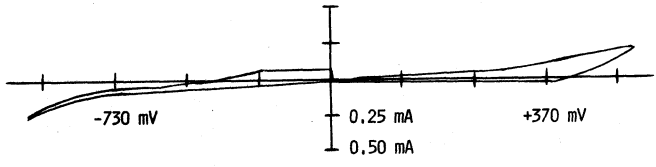

Fig. 3. Binary nitrate, background cycle oxygen treatment.

Area = 0.365 cm2
Scan Rate = 100 mV sec^{-1}
Temperature = 350°C

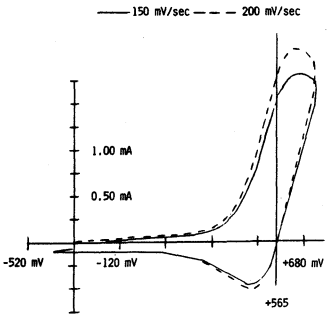

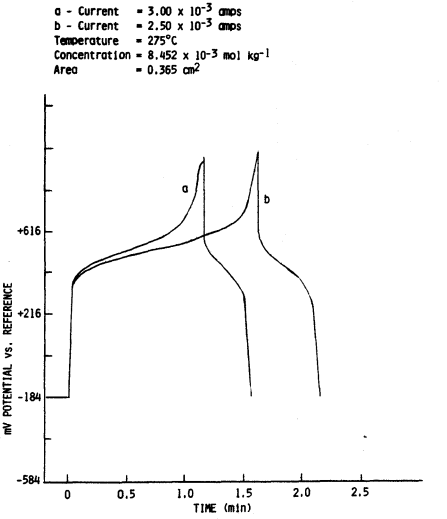

Fig. 4. Typical cyclic voltammogram for nitrite ion oxidation.

Conc. NO_2^- = 1.044 x 10^{-2}mol kg^{-1}
Area = 0.365 cm^2
Temperature = 375°C

Fig. 5. Typical chronopotentiogram for nitrite ion oxidation.

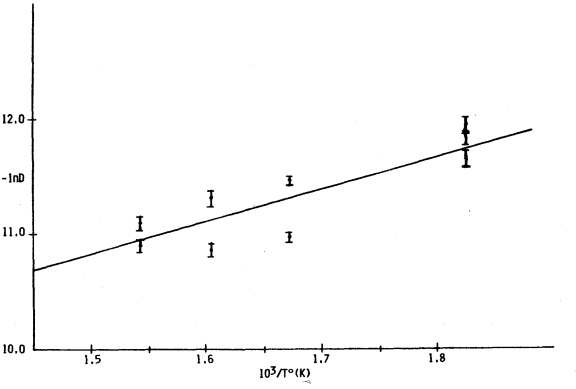

Fig. 6. Arrhenius plot for nitrite ion diffusion.

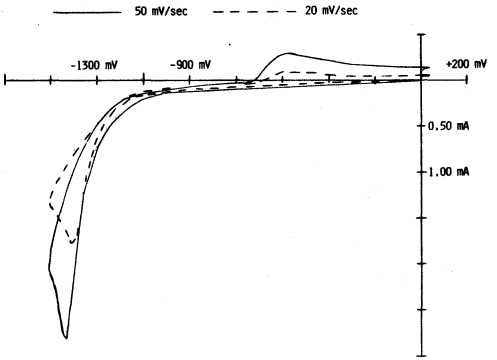

Fig. 7. Cyclic voltammograms for cathodic process involving water.

Temperature = 305°C; P_{H_2O} = 20.5 mm; Area = 0.365.

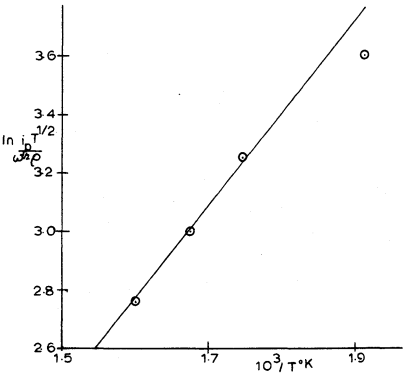

Fig. 8. Arrhenius plot for water from cyclic voltammetric data.

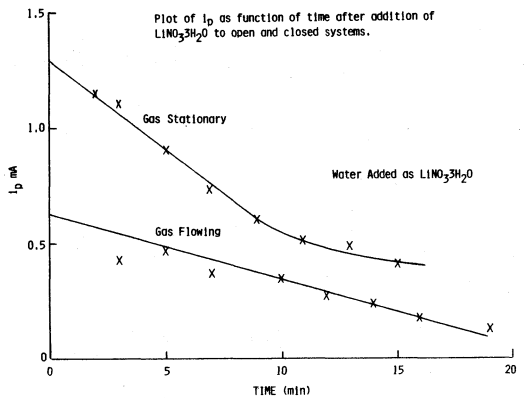

Fig. 9. Plot of i_p as function of time after addition of $LiNO_3 3H_2O$ to open and closed systems.

DOI: 10.1149/198109.0295PV

ROOM-TEMPERATURE MOLTEN SALT ELECTROLYTES FOR PHOTOELECTROCHEMICAL APPLICATIONS

Krishnan Rajeshwar
Paramjit Singh
and Joel DuBow

Department of Electrical Engineering
Colorado State University
Fort Collins, Colorado 80523

ABSTRACT

Mixtures of aluminum chloride ($AlCl_3$) with triethylammonium chloride (Et_3NHCl), 1,6-ethyl lutidinium bromide (EtluBr), tert-butyl pyridinium bromide (BPBr) and dialkyl imidazolium chloride (R_2ImCl), in certain molar ratios yielded ionic liquids at room temperature which were characterized with a view to test their applicability as electrolytes in photoelectrochemical (PEC) cells. Background voltammograms were obtained for these electrolytes on carbon and n-GaAs electrodes. The anodic stability limit was found to be enhanced on n-GaAs relative to carbon in all cases. The cathodic decomposition potential of the electrolyte showed a smaller positive shift on n-GaAs with the exception of the 3:1 $AlCl_3$-BPBr electrolyte. The difference in electrolyte stability behavior on carbon and n-GaAs is interpreted in terms of carrier density effects. Cyclic voltammograms were compared on carbon in the various electrolytes for a model redox system comprising the ferrocene/ferricenium couple. The separation of the cathodic and anodic waves in all the cases was consistent with a quasi-reversible redox behavior--the most sluggish electron transfer being observed in the case of the 3:1 $AlCl_3$-BPBr electrolyte. These results are compared with

those obtained previously on the $AlCl_3$-butyl pyridinium chloride (BPC) system. Capacitance-voltage measurements were made on n-GaAs electrodes in contact with the various electrolytes. Flatband-potentials (V_{fb}) were deduced from these data using Mott-Schottky plots. The relative positions of the n-GaAs band-edges and the redox levels were mapped on a common potential scale utilizing these data. The ferrocene/ferricenium redox level was placed negative of the conduction band-edge in n-GaAs in all the cases. The implications of this result for PEC applications and the role of specific ion adsorption of electrolyte species on the electrostatic aspects of the n-GaAs/molten salt electrolyte interface are discussed with the aid of energy band diagrams.

INTRODUCTION

There has been much discussion in recent years on photoelectrochemical (PEC) methods of solar energy conversion and storage (1,2). A major obstacle to practical applications of PEC devices is the photodissolution undergone by the semiconductor electrode. Most small-band gap n-type semiconductors are prone to photodissolution in contact with aqueous electrolytes (3). Attempts have been made therefore in recent years to construct PEC devices based on non-aqueous electrolytes (4-6). A promising class of solvents in this regard are the room-temperature molten salts; these electrolytes offer the combined advantage of good electrical conductivity coupled with aprotic chemical characteristics (7). The feasibility of solar energy conversion in PEC devices based on molten salt electrolytes was demonstrated in this laboratory using a model system comprising the n-GaAs/$AlCl_3$-n-Butyl Pyridinium Chloride (BPC) interface (8). In this paper, we present preliminary results of an evaluation of alternative molten salt electrolyte systems for PEC applications. Among the systems examined were those based on mixtures of $AlCl_3$ with triethylammonium chloride (c.f. Refs. 9,10) and dialkylimidazolium chloride (11). The dark electrochemical behavior of carbon and the PEC behavior of n-GaAs electrodes in contact with these and other electrolytes, were probed with the aid of potentiostated current-voltage and capacitance-voltage measurements.

CRITERIA UNDERLYING CHOICE OF ELECTROLYTES FOR PEC APPLICATIONS

Outlined below are the main factors to be taken into consideration for design and choice of electrolytes for PEC devices for solar applications. A more detailed review of these aspects is presented elsewhere (12).

(a) Electrical Conductivity: Should be as high as possible to avoid problems associated with polarization and iR voltage drops across the electrolyte layer in the PEC cell. Non-aqueous electrolytes are usually handicapped in this regard relative to aqueous systems although molten-salt electrolytes offer potentially higher conductivity characteristics.

(b) Viscosity: Should be low to facilitate mass transfer in the electrolyte. This is a common problem with concentrated electrolytes such as molten salts. Admixture with organic solvents (e.g., benzene) is one method of countering this difficulty (13,14). Viscosity data on some binary molten salt electrolytes are available in the literature (7,10).

(c) Redox Solubility: Should be high to sustain high current densities in the PEC electrolyte. This factor is related in this regard to (a) above. Non-aqueous electrolytes in general, are handicapped by poor redox solubility, although molten salts such as $AlCl_3$-BPC mixtures offer some possibilities for improvement (c.f. Ref. 12). Solubility limitations in aqueous electrolytes, on the other hand, are relatively less severe.

(d) Redox Reversibility: The reversibility of the electron-transfer reaction at the counterelectrode is a critical factor in PEC cell operation. Any irreversibility in charge transfer characteristics at this electrode will manifest as overpotential losses and consequent degradation of the cell efficiency.

(e) Electrolyte Stability: The potential window over which the electrolyte is electrochemically stable should be as wide as possible and should at least span the band-gap of the semiconductor electrode. Non-aqueous electrolytes including molten salts offer an important advantage relative to aqueous systems in this regard (8). All the electrolytes included in this study as well as $AlCl_3$-BPC mixtures have wider stability windows compared to the 1.23 V range available with aqueous systems.

(f) Substrate/Electrolyte Compatibility: Perhaps the most important factor in the efficient performance of PEC devices for solar applications concerns the relative positions of the energy band edges of semiconductor electrode in the particular electrolyte and the redox energy level. Ideally the flat-band potential (V_{fb}) (15) should be as negative and the redox potential should be as positive as possible so that the difference between the two levels, which determines

the voltage output of the device, is maximized. The factors limiting choice of redox couples with very positive potentials are the electrode decomposition potential (V_d) and the electrode valence band edge as discussed elsewhere (16). Non-aqueous electrolytes (including molten salts) offer an important advantage over aqueous systems in that V_d values are generally positive of corresponding levels in aqueous electrolytes (8,13).

The results to be discussed in this paper pertain to items (d)-(f) above. The characteristics of each individual molten salt electrolyte with reference to factors (d) and (e) above were established by cyclic voltammetry on carbon and n-GaAs electrodes. The extent of substrate (n-GaAs)/electrolyte compatibility in the various electrolytes was evaluated using capacitance-voltage and current-voltage measurements in the dark and under illumination with simulated solar insolation (17). The ferrocene/ferricenium ion couple ($Fe(Cp)_2$/ $Fe(Cp)_2^+$) was used as a model redox system for these studies.

EXPERIMENTAL

Electrodes were fabricated from n-GaAs wafers (Te doped, <111> orientation, donor density: 2.17×10^{17} cm^{-3}) as described elsewhere(18). Etching and prior treatment procedures for these photoelectrodes followed those outlined previously (8,12,18). A vitreous carbon plate (nominal dimensions: 1.5x15x30 mm) was used as the counterelectrode in the PEC devices.

Aluminium chloride, obtained from commercial sources, was purified by procedures described elsewhere (19). Ethyl lutidinium bromide (EtLuBr) was prepared by refluxing stoichiometric mixtures of ethyl bromide and 2,6 lutidine for 48 hours. The product was dissolved in acetonitrile and precipitated from ethyl acetate as described elsewhere (20). t-Butyl pyridinium bromide (t-BPBr) was prepared in a similar fashion from reactants comprising mixtures of pyridine and t-butyl bromide. Triethylammonium chloride (Et_3NHCl) was prepared according to a procedure described by previous authors (10). A sample of methyl ethyl imidazolium chloride (MeEtImCl) was kindly donated by Dr. John Wilkes of the USAF Academy, Colorado Springs.

Molten salt electrolytes were prepared by simple mixing of $AlCl_3$ and EtLuBr, BPBr or Et_3NHCl in various proportions. Mixtures of $AlCl_3$ and EtLuBr (2:1 molar ratio), $AlCl_3$ and BPBr (3:1 molar ratio) and $AlCl_3$ and Et_3NHCl (2:1 molar ratio) were found to be molten at room

temperature. Similarly a mixture of $AlCl_3$ and MeEtImCl in the 2:1 molar ratio was found to be molten at room temperature. Similar results were obtained on this system by previous authors (11).

Ferrocene and ferricenium chloride ($Fe(Cp)_2Cl$) were obtained from commercial sources. They were purified as described elsewhere (8). Nominal concentrations of the $Fe(Cp)_2/Fe(Cp)_2^+$ couple in the various electrolytes were 0.1 M.

All manipulations with redox chemicals and the molten salt electrolytes were carried out in a dry box under argon atmosphere.

A 300 W tungsten halogen lamp was used to illuminate the n-GaAs electrodes. The intensity of the light source was calibrated using a radiometer/photometer. The light intensities reported below are not corrected for reflection and absorption losses in the cell and in the electrolyte.

Current-voltage measurements were performed on a Princeton Applied Research (PAR) Model 173 potentiostat equipped with a PAR coulometer accessory. Capacitance-voltage measurements followed procedures previously described (8). Three electrode cell geometries were employed for these experiments. The quasi-reference electrode consisted of an Al wire immersed in the 2:1 $AlCl_3$-BPC electrolyte and separated from the main compartment by a fine-porosity glass frit. All potentials below are referred to this electrode.

RESULTS AND DISCUSSION

Stability Limits

Figures 1a-d illustrate background voltammograms for $AlCl_3$-Et_3NHCl (2:1 molar ratio), $AlCl_3$-EtLuBr (2:1 molar ratio), $AlCl_3$-BPBr (3:1 molar ratio) and $AlCl_3$-MeEtImCl (2:1 molar ratio) electrolytes, respectively. Data are compared for carbon and n-GaAs electrodes. The stability limits for these electrolytes on the two electrodes (as determined from the onset potential for anodic and cathodic current flow) are listed in Table 1. One trend that is apparent from these data is that the stability limit on the anodic side is considerably more extended on n-GaAs electrodes relative to carbon (i.e., the potential for anodic current flow is more positive on n-GaAs than on carbon). On the other hand, the potential for cathodic current flow also shows a positive shift on n-GaAs relative to carbon. This shift, however, is much smaller than for the anodic case. The net result is that the stability window for each electrolyte on n-GaAs is significantly wider than on carbon. A similar behavior was observed in a

previous study for the $AlCl_3$-BPC electrolyte (8). The above difference in behavior between carbon (or metal) and n-GaAs (semiconductor) electrodes may be rationalized by the difference in carrier densities in the two cases. The important consequences of this difference on the potential and charge distribution at the electrode/electrolyte difference have been noted by previous authors (15). It suffices here to note that the non-availability of minority carriers (holes in this case) in the dark on n-GaAs and the potential barrier for transport for holes to the electrolyte (vide infra) results in suppression of electrolyte oxidation and a consequent overpotential for anodic current flow relative to carbon. On the other hand, the electrolyte reduction reaction is facilitated to a greater degree on n-GaAs relative to carbon (Table 1). The lone exception to this trend is the 3:1 $AlCl_3$-BPBr case. The anodic shift in the onset potential for the reduction reaction on n-GaAs relative to carbon is attributed to electrostatic effects across the semiconductor/electrolyte interface. The capacitance-voltage data to be described below, are consistent with the presence of an accumulation layer (15) on the n-GaAs surface. The consequent potential gradient assists electron transfer from the n-GaAs electrode to the electrolyte in all cases except the $AlCl_3$-BPBr electrolyte where a weak depletion layer seems to exist on the electrode surface (vide infra). It is also conceivable that surface states on n-GaAs mediate in the reduction reactions (c.f. n-GaAs/$AlCl_3$-BPC system, Refs. 8,18).

It is pertinent to note that the stability windows on n-GaAs for all the electrolytes examined in the present study are wider than the energy band-gap of n-GaAs (1.43 eV). This result has important consequences for PEC applications in that the available range of potentials is wide enough to probe the entire band gap region. The stability windows in n-GaAs are also wider than the 1.23 eV available for aqueous systems for all the electrolytes in the present study and illustrate an important advantage in the use of non-aqueous electrolytes for PEC applications. The $AlCl_3$-MeEtImCl electrolyte, in particular, offers a significantly wide range of potentials spanning ~3 V. A similar behavior was noted by previous authors (11) for this electrolyte on carbon.

Redox Behavior

Figure 2 illustrates typical cyclic voltammograms on carbon for the $Fe(Cp)_2/Fe(Cp)_2^+$ couple in the 2:1 $AlCl_3$-Et_3NHCl (Figure 2a), 2:1 $AlCl_3$-EtLuBr (Figure 2b), 3:1 $AlCl_3$-BPBr (Figure 2c) and 2:1 $AlCl_3$-MeEtImCl (Figure 2d) electrolytes. The peak potentials for the cathodic and anodic waves for the various electrolytes are assembled

in Table 2 along with the equilibrium potential ($V^o = (V_{pa} + V_{pc})/2$) The data in Table 2 pertain to a scan rate of 20 mV/sec. The variation of currents with scan rate was consistent with a diffusion-controlled reaction. The separation between the anodic and cathodic peaks was somewhat larger than the theoretically predicted value (59 mV) for a one-electron reversible redox process--the departure from ideal behavior being most severe for the $AlCl_3$-BPBr case. The results in Table 2 and Figure 2 indicate quasi-reversible redox behavior for the $Fe(Cp)_2/Fe(Cp)_2^+$ couple in all the four electrolytes investigated. In this regard, the redox reaction appears to be inherently more sluggish than in the $AlCl_3$-BPC case previously studied (c.f. Table 2, Ref. 8).

Location of n-GaAs Band-edges in the Electrolytes

A comparison of the relative disposition of the energy levels in the semiconductor electrode and in the electrolyte (redox level) is useful in evaluating the efficacy of a particular electrode/redox electrolyte combination for PEC applications. The most common technique for locating the band-edge positions of the semiconductor involves capacitance-voltage measurements (21). Under favorable conditions, the Mott-Schottky relation (15) will hold and a plot of $1/C_{sc}^2$ (where C_{sc} = space-charge capacitance) versus electrode potential will yield straight lines whose intercept yields a value for V_{fb} (after applying a small correction for the thermal voltage term, c.f. Ref. 15). Such plots are shown in Figure 3 for the n-GaAs electrode in contact with the $AlCl_3$-Et_3NHCl (Figure 3a), $AlCl_3$-EtLuBr (Figure 3b), $AlCl_3$-BPBr (Figure 3c) and $AlCl_3$-MeEtImCl (Figure 3d) electrolytes. The V_{fb} values deduced from these plots are assembled in Table 3 for the various electrolytes.

For heavily-doped semiconductors such as the samples employed in the present study, the difference between the Fermi level and the conduction band-edge (E_{CB}) may be neglected so that $qV_{fb} \simeq E_{CB}$. Once E_{CB} is located, the valence-band edge (E_{VB}) is immediately determined from the band-gap of the semiconductor (1.43 eV in this case). The relative positions of $E_{CB/q}$, $E_{VB/q}$ and V^o are compared on a common potential scale for the four electrolytes in Figure 4. In each case, the redox couple is seen to be placed more negative relative to the conduction band-edge in n-GaAs. The positions of the band-edges are comparable in the two chloride-based electrolyte systems, namely

$AlCl_3$-Et_3NHCl and $AlCl_3$-MeEtImCl whereas they are more negative in the bromide salts. The redox potentials follow essentially the same trend, the V_o value being most negative in the $AlCl_3$-BPBr electrolyte (Table 2).

GENERAL DISCUSSION

All the electrolytes examined in this study have appropriate stability windows for construction of PEC devices based on n-GaAs electrodes. As mentioned in the preceding section, the $AlCl_3$-MeEtImCl system has an exceptionally wide stability range in this regard. The $Fe(Cp)_2/Fe(Cp)_2^+$ couple, however, seems to be nonoptimally placed relative to the n-GaAs band-edges in these electrolytes (Figure 4). For PEC devices based on n-type semiconductors, V^o has to lie significantly positive of E_{CB} in order to yield any significant photovoltage (or band-bending at the semiconductor/electrolyte interface). The importance of the chemistry in the interfacial layer in shifting the relative positions of E_{CB} (and V_{fb}) and V^o has been emphasized in previous studies (16,18). Specific adsorption of electronegative ionic species on the semiconductor surface can shift the V_{fb} to negative potentials in such a manner that E_{CB} would move significantly negative of V^o relative to the situation in the absence of such adsorption effects. This favorable situation is obtained in basic $AlCl_3$-BPC electrolytes containing a significant concentration of free Cl^- ions (18). The relatively positive V_{fb} values observed for the chloride electrolytes in the present study (Table 3) seems to imply that the equilibrium:

$$2AlCl_4^- \rightleftharpoons Al_2Cl_7^- + Cl^- \qquad (1)$$

is shifted far to the left with a consequent reduction in the concentration of free Cl^- species. In this regard, these salts approximate the behavior for the acidic $AlCl_3$-BPC systems (8,18). The strategy of decreasing the molar concentration of $AlCl_3$ in the $AlCl_3$-Et_3NHCl and $AlCl_3$-MeEtImCl mixtures (and thereby increasing the free Cl^- concentration in the melt) seems to be hampered by the relatively high melting point of basic electrolytes (e.g., 1:1 $AlCl_3$-Me_2 ImCl has a melting point of 75°C compared to a value of 15°C for the 2:1 molar ratio mixture, Ref. 11). The bromide-based salts show better promise in that the n-GaAs band-edges are placed at more negative potentials

although unfortunately, the interaction between the $Fe(Cp)_2/Fe(Cp)_2^+$ couple and the melt results in a concomitant negative shift in V^o (Figure 4). An unfavorable side effect of specific ion adsorption of electrolyte species in these systems is charge transfer limitations imposed by steric effects, i.e., the adsorbed Cl^- ions, while aiding in the desired negative potential shift in V_{fb} (and qE_{CB}), also seem to block close approach of $Fe(Cp)_2$ molecules to the electrode surface (18). An optimum situation would be to have the reduced redox species themselves adsorb specifically on the semiconductor surface. This seems to be the case for PEC systems based on aqueous electrolytes containing the polychalcogenide and iodine/iodide redox species (16). Work on the design of molten salt electrolytes based on PEC cells, taking the above considerations into account, is currently in progress in this laboratory.

Considering the importance of the interfacial layer in modifying PEC performance, it seems relevant at this point to examine the present data in the light of the electrostatic aspects at the electrode/electrolyte interface. Depending on the degree and nature of interaction of the electrolyte species (either constituent ions or redox species) with the electrode surface, four situations are envisaged as schematized in Figure 5. In Figure 5a, the coupling between the highly electronegative electrolyte species and the electrode surface is such that an inversion layer is induced at the interface. Figures 5b-d represent progressively weaker interaction between the electrolyte and the interface resulting in strong depletion (Figure 5b), weak depletion (Figure 5c) and, in the extreme case, an accumulation layer at the interface resulting in unfavorable band bending in the semiconductor (Figure 5d). The situation as shown in Figure 5 pertains to an n-type semiconductor although analogous considerations apply in the p-type case. The situation shown in Figure 5d seems to apply in the case of n-GaAs electrodes in contact with the $AlCl_3$-Et_3NHCl, $AlCl_3$-EtLuBr and $AlCl_3$-MeEtImCl electrolytes for reasons noted in the preceding paragraph. In the case of the $AlCl_3$-BPBr electrolyte, a weak depletion layer seems to exist on the n-GaAs surface. For PEC applications, the ideal situation is that shown in Figure 5a for reasons noted elsewhere (13).

Figures 6-8 represent current-voltage curves in the dark and under illumination for n-GaAs electrodes in contact with the 2:1 $AlCl_3$-Et_3NHCl, 2:1 $AlCl_3$-EtLuBr and 3:1 $AlCl_3$-BPBr electrolytes, respectively. The electrolytes in all cases contained the $Fe(Cp)_2/Fe(Cp)_2^+$ redox couple. The data in these figures are consistent with the picture described above (c.f. Figure 4). While reduction currents are readily sustained on the n-GaAs electrode, considerable

suppression is observed for the photocurrents. The situation is particularly well illustrated for the $AlCl_3$-EtLuBr case (Figure 7) where potentials ~0.5 V positive of V_{fb} have to be applied before appreciable photocurrents start to flow. On the other hand, less severe conditions are required in the $AlCl_3$-BPBr case and photocurrents are observed at potentials close to V_{fb}. These trends are consistent with the V_{fb} data and the energy band diagrams (c.f. Table 3, Figure 5). Obvious from these data is the need to explore other redox couples more favorably located with respect to the band-edges in these electrolytes. Such studies are presently in progress.

ACKNOWLEDGMENT

The authors thank the Solar Energy Research Institute for financial support of this research program (Grant XS-0-9272-1) and C. Wade for help in the various experiments reported here. They also appreciate the generous donation of a sample of MeEtImCl by John Wilkes of the USAF Academy, Colorado.

REFERENCES

1. K. Rajeshwar, P. Singh and J. DuBow, Electrochim. Acta 23, 117 (1978).

2. S. Kar, K. Rajeshwar, P. Singh and J. DuBow, Solar Energy 23, 129 (1979).

3. H. Gerischer, J. Electroanal. Chem. 82, 133 (1977).

4. P. A. Kohl and A. J. Bard, J. Electrochem. Soc. 126, 598 (1979); see also references cited therein.

5. H. Tsubomura, M. Matsumura, K. Nakatani, K. Yamamoto and K. Maeda, Sol. Energy 21, 93 (1978).

6. K. D. Legg, A. B. Ellis, J. M. Bolts and M. S. Wrighton, Proc. Natl. Acad. Sci. U.S.A. 79, 4116 (1977).

7. R. A. Carpio, L. A. King, R. E. Lindstrom, T. C. Nardi and C. L. Hussey, J. Electrochem. Soc. 126, 1644 (1979).

8. P. Singh, K. Rajeshwar, J. DuBow and R. Job, J. Am. Chem. Soc. 102, 4676 (1980).

9. W. W. Porterfield and J. T. Yoke, Adv. Chem. Ser. 150, 104 (1976).

10. J. R. Silkey and J. T. Yoke, J. Electrochem. Soc. 127, 1091, (1980).

11. J. S. Wilkes, personal communication; J. S. Wilkes, J. A. Levisky, C. O. Hussey and M. L. Druelinger, Abstract No. 648, Electrochemical Society Meeting, Hollywood, Florida, October (1980).

12. R. Gale and J. DuBow, Solar Energy Materials, in press.

13. P. Singh, R. Singh, K. Rajeshwar and J. DuBow, J. Electrochem. Soc., in press.

14. J. Robinson, R. C. Bugle, H. L. Chum, D. Koran, and R. A. Osteryoung, J. Am. Chem. Soc. 101, 3776 (1979).

15. H. Gerisher, in "Physical Chemistry--An Advanced Treatise," (edited by H. Eyring), Vol. 1XA, Chapter 5, Academic Press, New York (1970).

16. P. Singh, R. Singh, R. Gale, K. Rajeshwar and J. DuBow, J. Appl. Phys. January (1981) in press.

17. M. D. Archer, J. Appl. Electrochem. 5, 17 (1975).

18. P. Singh and K. Rajeshwar, J. Electrochem. Soc., in press.

19. R. J. Gale, B. Gilbert and R. A. Osteryoung, Inorg. Chem. 17, 2728 (1978).

20. P. Singh, Ph.D. Thesis, Colorado State University, Fort Collins, Colorado (1980), unpublished.

21. S. R. Morrison, "The Chemical Physics of Surfaces," Plenum Press, New York (1977).

Table 1. Stability limits for the various molten-salt electrolytes as defined by the onset potential for anodic and cathodic current flow on carbon and n-GaAs electrodes[a)]

Electrolyte	Carbon			n-GaAs		
	V_a	V vs. $Al^{0/3+}$	V_c	V_a	V vs. $Al^{0/3+}$	V_c
2:1 $AlCl_3$-Et_3NHCl	1.6		0.6	>2.8		1.0
2:1 $AlCl_3$-EtLuBr	1.5		0.0	>2.8		0.4
3:1 $AlCl_3$-BPBr	1.0		-0.3	>2.1		-0.3
2:1 $AlCl_3$-MeEtImCl	2.3		0.1	4.4		1.2

a)The electrolytes contained no deliberately added electroactive species (c.f. Figure 1).

Table 2. Cyclic voltammetric data for the $Fe(Cp)_2/Fe(Cp)_2^+$ couple on carbon electrodes in the various electrolytes.

Electrolyte	V_{pa} V vs. $Al^{0/3+}$	V_{pc} V vs. $Al^{0/3+}$	$V_{pa} - V_{pc}$ V vs. $Al^{0/3+}$	$V_{1/2} = (V_{pa} + V_{pc})/2$ V vs. $Al^{0/3+}$
2:1 $AlCl_3$-Et_3NHCl	0.45	0.53	0.08	0.49
2:1 $AlCl_3$-EtLuBr	0.10	0.0	0.10	0.05
3:1 $AlCl_3$-BPBr	-0.36	-0.63	0.27	-0.50
2:1 $AlCl_3$-MeEtImCl	0.55	0.47	0.08	0.51
2:1 $AlCl_3$-BPC[a)]	0.27	0.21	0.06	0.24

[a)] Data from Ref. 8.

Table 3. Flat-band potential of n-GaAs electrodes in the various electrolytes[a)]

Electrolyte	V_{fb}[b)] V vs. $Al^{0/3+}$
2:1 $AlCl_3$-Et_3NHCl	0.70
2:1 $AlCl_3$-EtLuBr	0.10
3:1 $AlCl_3$-BPBr	-0.15
3:1 $AlCl_3$-MeEtImCl	0.60

a)Addition of $Fe(Cp)_2$ and $Fe(Cp)_2Cl$ to be electrolyte did not significantly affect the V_{fb} values indicating absence of specific adsorption.

b)Nominal error in values: ±0.05 V.

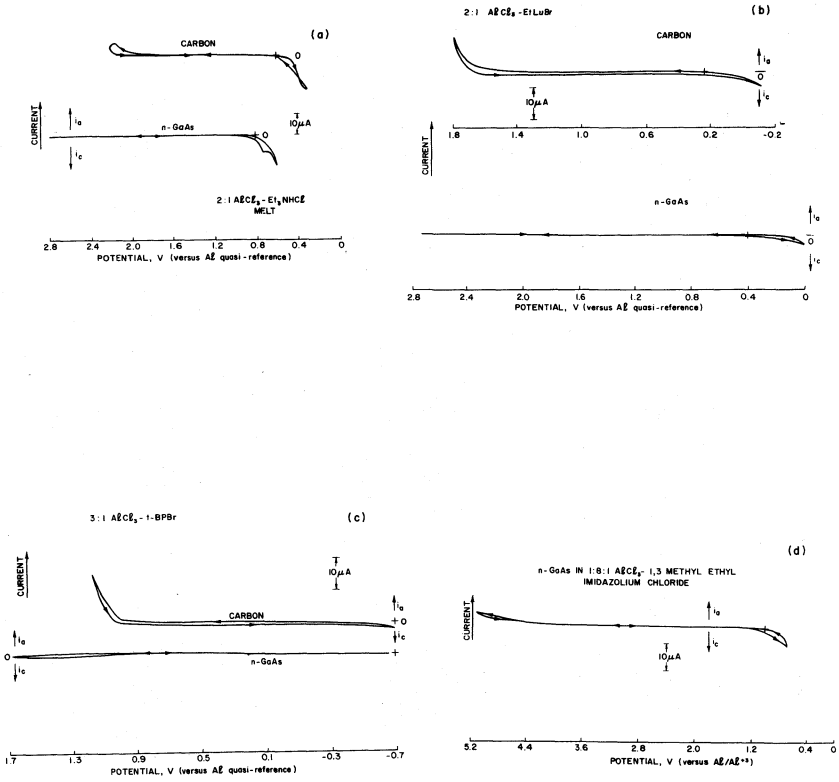

Figure 1: Background voltammograms for (a) 2:1 $AlCl_3$-Et_3NHCl, (b) 2:1 $AlCl_3$-EtLuBr, (c) 3:1 $AlCl_3$-BPBr, and (d) 2:1 $AlCl_3$-MeEtImCl electrolytes. Scan rate: 20 mV/sec. The electrolytes contained no deliberately added electroactive species.

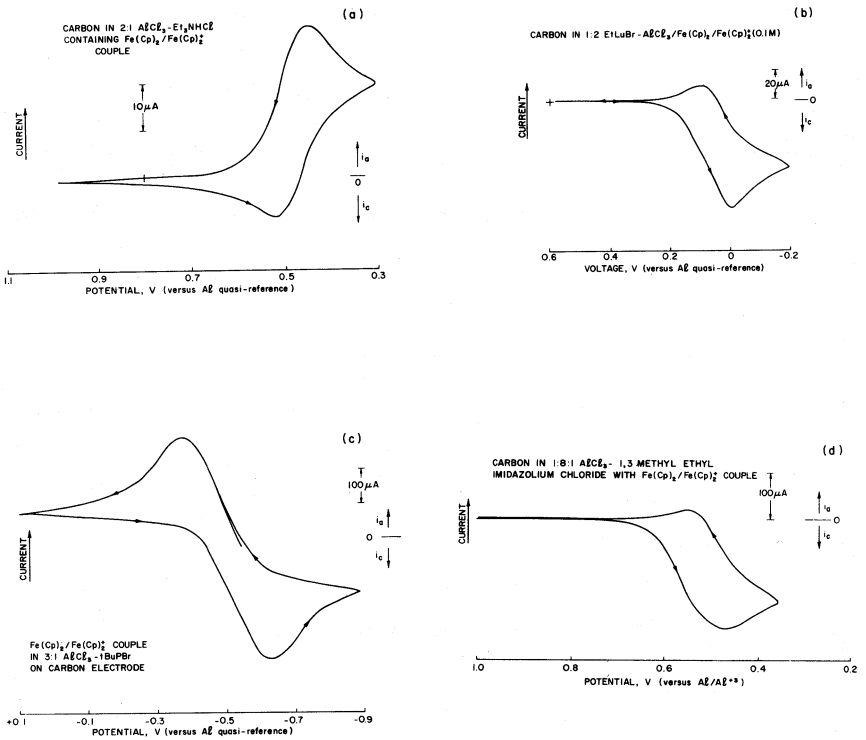

Figure 2: Cyclic voltammograms (scan rate: 20 mV/sec) on vitreous carbon electrodes in (a) 2:1 $AlCl_3$-Et_3NHCl, (b) 2:1 $AlCl_3$-EtLuBr, (c) 3:1 $AlCl_3$-BPBr, and (d) 2:1 $AlCl_3$-MeEtImCl electrolytes. The electrolytes contained 0.1 M $Fe(Cp)_2$ and $Fe(Cp)_2Cl$.

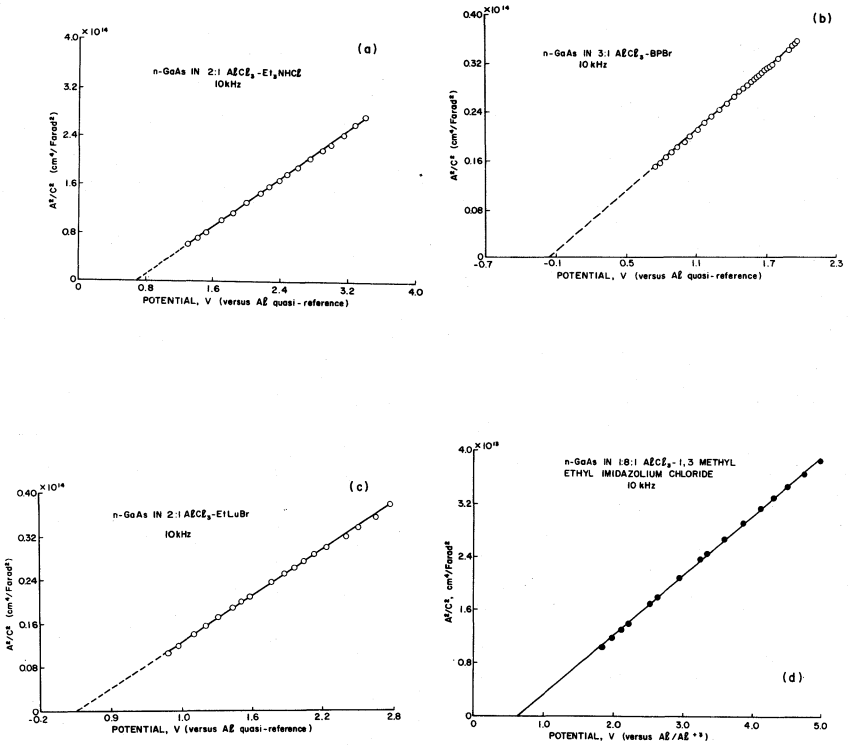

Figure 3. Mott-Schottky plots for n-GaAs electrodes in (a) 2:1 $AlCl_3$-Et_3NHCl, (b) 2:1 $AlCl_3$-EtLuBr, (c) 3:1 $AlCl_3$-BPBr, and (d) 2:1 $AlCl_3$-MeEtImCl electrolytes. The ac signal frequency was 10 kHz for these measurements.

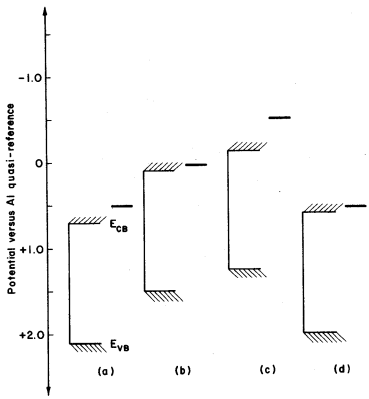

Figure 4: Relative positions of n-GaAs band-edges and the $Fe(Cp)_2/Fe(Cp)_2^+$ redox cople (denoted by bars) on a common potential scale in the various electrolytes. Symbols (a)-(d) correspond to those in previous figures.

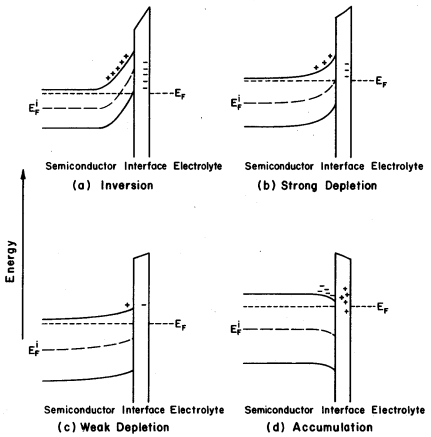

Figure 5: Energy band diagrams under equilibrium) for an n-type semiconductor in contact with an electrolyte. See text for details. E_F^i = intrinsic Fermi level, E_F = Fermi level for doped semiconductor.

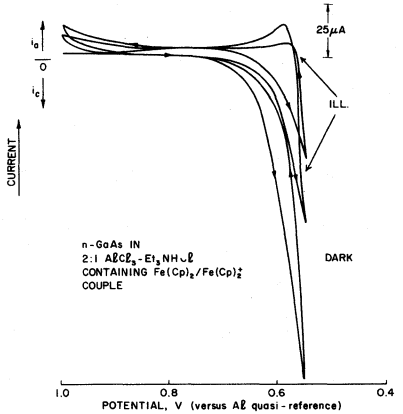

Figure 6: Current-voltage curves in the dark and under illumination for n-GaAs in the 2:1 $AlCl_3$-Et_3NHCl electrolyte containing the $Fe(Cp)_2/Fe(Cp)_2^+$ couple. the curves marked "ILL" denote data at two different light intensities (70 and 100 mW/cm^2).

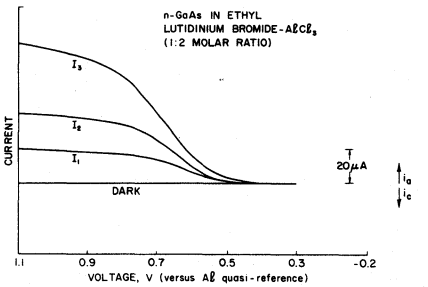

Figure 7: Current-voltage curves in the dark and under illumination for n-GaAs in 2:1 $AlCl_3$-EtLuBr electrolyte. Data are shown for three different light intensities ($I_3 > I_2 > I_1$).

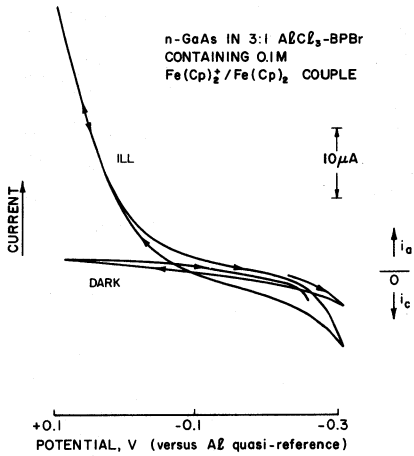

Figure 8: Current-voltage curves in the dark and under illumination ($\sim$ 70 mW/cm^2) for n-GaAs electrode in the 3:1 $AlCl_3$-BPBr electrolyte containing the $Fe(Cp)_2/Fe(Cp)_2^+$ couple.

DOI: 10.1149/198109.0316PV

ELECTROCHEMICAL OXIDATION OF CARBON IN A MOLTEN CARBONATE COAL-AIR FUEL CELL

Robert D. Weaver and Leonard Nanis

Electrochemistry Program
SRI International
Menlo Park, California 94025

ABSTRACT

Carbon anodes are oxidized in a Li-Na-K carbonate eutectic melt according to

$$C + 2CO_3^{=} \rightarrow 3CO_2 + 4e^- \quad (1)$$

When combined with a cathode reaction involving CO_2 and O_2 (air)

$$2CO_2 + O_2 + 4e^- \rightarrow 2CO_3^{=} \quad (2)$$

a fuel cell may be successfully operated with the overall reaction

$$C + O_2 \rightarrow CO_2 \quad (3)$$

The oxidation shown in Equation 1 can be accomplished with carbon derived from coal by a pyrolysis process, as well as with a wide variety of carbons. The reaction in Equation 1 has been established by gravimetry, analysis of gas evolved at the anode, and by the rate of gas evolution over a wide range of current densities. The overall coal/air electrochemical system affords a path to electrical power generation which is economical, non-polluting and efficient.

INTRODUCTION

The electrochemical oxidation of carbon derived from coal was explored early in this century as a means to increase the efficiency of electrical generation as compared with heat-engines. These electrochemical studies ceased when it was learned both that the principal

product of oxidation of hydroxide/carbonate melts was carbon monoxide rather than carbon dioxide and when the efficiency of thermal conversion in heat engines increased from less than 5% in 1900 to values in excess of 30% by 1930. The history of this period is concisely reviewed by Liebhafsky and Cairns.[1]

Coal has been increasingly considered as a source of energy in recent years and, because the molten carbonates are known to be efficient in the entrapment of pollutants derived from the combustion of coal, a project was undertaken at SRI International to investigate the clean electrochemical oxidation of carbon in a carbonate electrolyte. During the course of that study, it was found that the principal anode product was carbon dioxide, thus overcoming previous energy limitations associated with partial oxidation to carbon monoxide.

EXPERIMENTAL PROCEDURES

Reagents: All chemicals employed were of reagent grade quality. The electrolyte mixture used was the ternary eutectic of Li_2CO_3, Na_2CO_3, and K_2CO_3 in a 43, 32, 25 M/o (mole percent). Samples of coal were obtained from the Commercial Testing and Engineering Company, Chicago, Illinois and were identified as: Illinois No. 6 Seam, Decker Mine, Pocahontas, and Kentucky No. 9. Proximate analyses of the coals indicated carbon contents in the range 55 to 75 weight percent and sulfur contents ranging from 0.4 to 2 weight percent. Control experiments were made with spectroscopic carbon rods (National Carbon Company) which served as a convenient source of pure graphite.

Analytical Equipment: Gas chromatography was used to analyze the gaseous products of oxidation. A 150 cm long, 0.64 cm ID copper tube packed with Linde No. 5 molecular sieve and a 300 cm, 0.64 cm ID copper

tube packed with POROPAC Q ® were used for chromatographic separation of the product gases. The columns were operated 130°C with helium as the carrier gas. Coulometric efficiency was determined gravimetrically from the weight of anodes before and after electrolysis. The anodes were Soxhlet extracted with $H_2O \cdot HCl$ azeotrope and were vacuum dried at 80°C prior to all weighings. Gases used for the electrochemical cell were obtained from commercial grade cylinder gases and were dried by passing through molecular sieve columns.

Typical Procedure: The cell anode compartment (Figure 1) was flushed with helium carrier gas until all other gases in the effluent carrier stream, including water, had been reduced to background level, typically less that 5 v/o (volume percent) total for all gases, as determined by chromatography. Constant current, using a PAR Model 173 potentiostat in galvanostatic mode, was passed through the cell and analyses were performed on the exhaust gases until steady-state values were obtained. The anode was then removed for weighing. Cell and anode-reference voltages were recorded continuously. For electrode kinetic studies, the carrier gas was changed to carbon dioxide so as to provide a poised environment for the electrode.

Anode Preparation: Anodes were fabricated by heating crushed coal under pressures in the range 200 to 1000 lbs/in^2. During heating, the coal underwent destructive distillation and coalesced into a porous mass suitable for use as an electrode. The coalescence was generally complete in the time interval required for the temperature to reach 500°C. In a final step, the formed carbon was heated to 1000°C to render the charred coal electrically conductive.

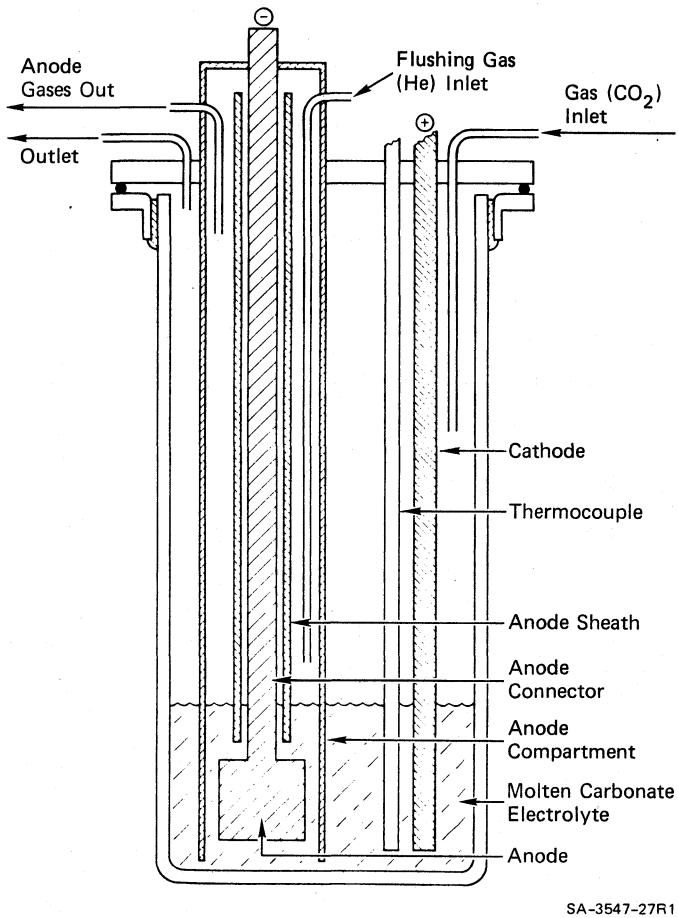

Figure 1. Illustration of Cell Used for Carbon Anode Studies Direct Coal/Air Power Generation

RESULTS

Coal Derived Anodes: For the purpose of this study it was essential that carbon obtained from coal be electrically conductive and sufficiently strong to permit anode fabrication. The properties of the anodes prepared from the coal samples are shown in Table 1.

Coulombic Efficiency: The course of oxidation was correlated with kind and evolution rate of gaseous product. Typical results are presented in Figure 2.

For a minimum of two hours before electrolysis was started, the flow rate of the gas exiting from the anode compartment was monitored. Chromatographic analysis was used to determine CO and CO_2 composition. As shown in Figure 2, these measured values were essentially constant before electrolysis was begun. After electrolysis was started, the flow rate of the gases emerging from the anode, and the percentage of CO_2 both increased significantly. After reasonably steady-state values had been observed, the electrolysis current was galvanostatically increased, typically by a factor of three, as shown in Figure 2. The CO_2 concentration and flow rate increased proportionally with the current.

Results were correlated in the manner presented in Table 2. The percentage of carbon dioxide formed compared with the total of carbon dioxide and carbon monoxide, as determined by gas chromatography, is presented in the second column of Table 2. The % FRA (percent flow rate agreement) is an index that allowed comparison of flow rate of helium carrier gas into the anode compartment as compared with the total flow rate of all combined gases which exited from the cell. The % FRA values are presented in the third column. The % FRA index served as a measure of leaks or presence of gases which were undetected by

Table 1

COAL-DERIVED
ANODE CARBON CHARACTERISTICS

Test	Nominal Value	Range
Density, g/cm^3	1.0	0.8-1.2
Specific volume resistivity, ohm-cm	0.01	0.008-0.02
Modulus of rupture, psi	2700	1600-3200
Porosity	50%	40%-65%
Pore Size	50 μm	1-100 μm

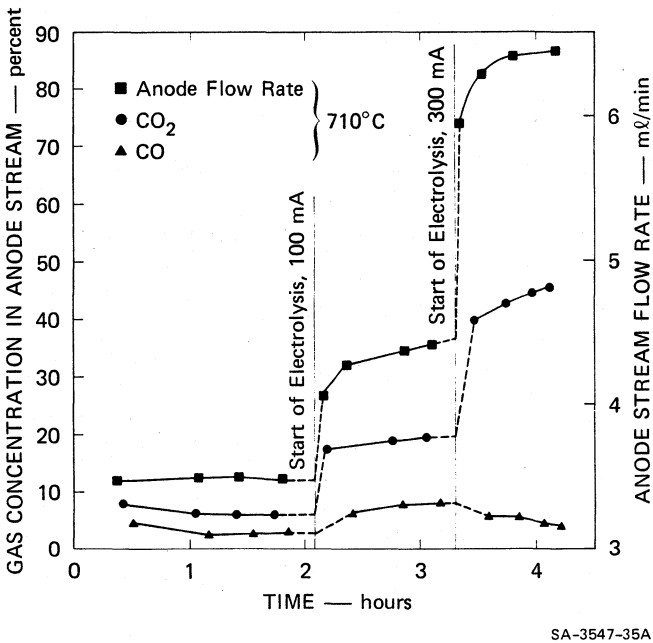

Figure 2. Gas Composition with Time Behavior for Pocahontas Coal

Table 2

GRAPHITE STOICHIOMETRIC
AND COULOMETRIC CORRELATIONS

n-Run	% CO_2	% FRA	% CA	n
I	99.1	100	95	3.8
II	99.7	95	100	4.4
III	99.5	-	100	2.5
IV	100.0	100	100	2.3
V	99.7	100	95	2.6
VI	99.3	105	95	2.3
VII	99.6	100	95	3.6
VIII	99.6	100	95	3.8

chromatography. Percent current agreement (% CA) is listed in column four of Table 2 and is based on the four electron change in Reaction 1. This coulometric test of Reaction 1 is in complete agreement when % CA = 100, which indicates 1.141 x 10^{-2} ml CO_2 evolved (STP) for each mA-min. The final column in Table 2 lists the $\underline{n}$ value (number of electrons) directly determined by comparison of the loss of weight of the carbon anode due to electrolysis and the known total coulombs passed through the cell. Comparison of these correlations is shown in Table 2 for a series of experiments with pure graphite used as a control anode.

A blank run in which an anode was subjected to all procedures except electrolysis was also made. The carbon weight loss was less than 2 mg. By comparison, most runs involved weight losses due to electrolysis ranging from 30 to 300 mg depending on the number of coulombs passed.

Stoichiometric studies with coal-derived carbon anodes (Pocahontas coal) were performed with pure CO_2 as the carrier stream. The observed increase in flow rate of CO_2 was correlated with the current. The agreement, %CA, was always 95 to 100% throughout the polarization range studied (0 to 400 mV).

Voltage Behavior: The voltage behavior of carbon derived from coal was studied as a function of temperature and current density. Typical open-circuit values of various carbon electrodes are shown in Table 3 and in Figure 3. The voltages were measured with respect to the Au, O_2 (1/3), CO_2 (2/3)//$CO_3^=$ reference electrode. For comparison purposes, the open-circuit cell voltages calculated from thermodynamic data (Reference 4) for various cathode gas mixtures are shown in Figure 4.

The variation in electrode behavior with current density was studied for various carbons as a function of temperature. Voltammograms for carbon derived for coal (28 to 40% porosity) are shown in Figure 5.

Table 3

OPEN-CIRCUIT POTENTIALS FOR VARIOUS CARBONS AT 700°C*

Anode	Open Circuit Voltage
Kentucky No. 9	1.1
Pocahontas	1.1
Illinois No. 6 Seam	1.1
Graphite	0.7 - 1.1

*Referenced to Au, O_2, $CO_2/CO_3^=$ electrode and taken in ternary eutectic electrolyte containing 10 weight percent of fly ash.

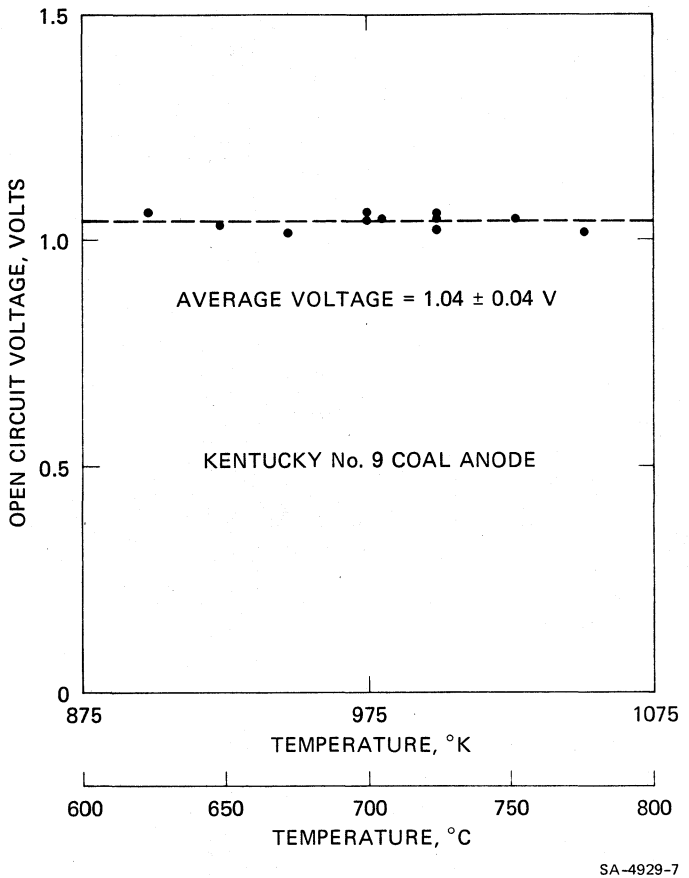

Figure 3. Open-Circuit Voltages of a Coal Electrode as a Function of Temperature

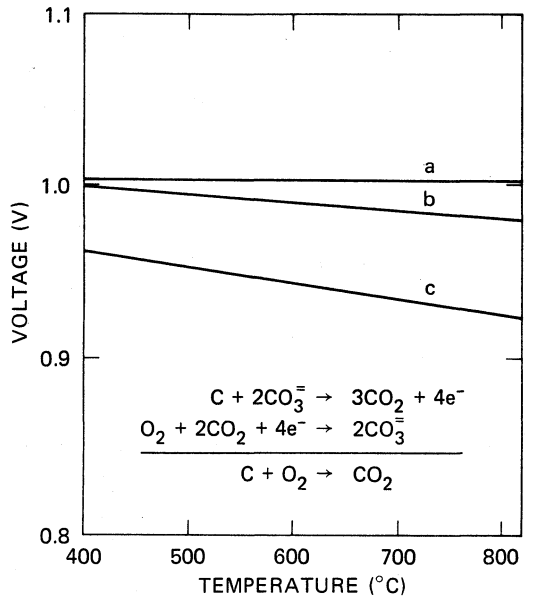

Case	Anode	Cathode
a	pCO_2 = 1*; pure carbon	pO_2 = 1 pCO_2 = 1
b	pCO_2 = 1 ; pure carbon	pO_2 = 1/3 pCO_2 = 2/3
c	pCO_2 = 1 ; pure carbon	pO_2 = 1/7 pCO_2 = 2/7 pN_2 = 4/7

*p = Pressure in atmospheres

SA-4929-16

Figure 4. Cell Voltage Calculated from Thermodynamic Data

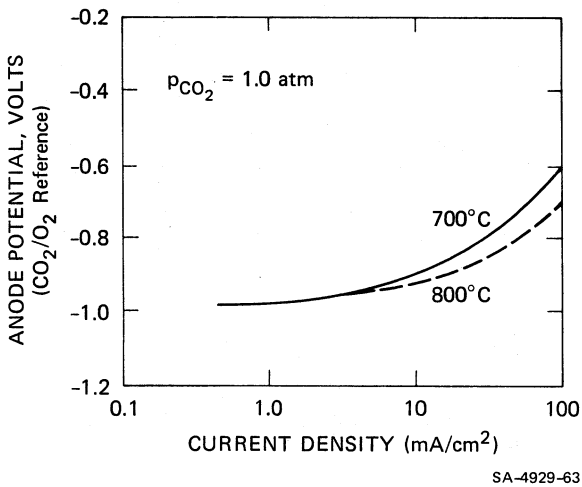

Figure 5. Current-Voltage Behavior of Pocahontas Char

DISCUSSION AND CONCLUSIONS

A practical coal/air fuel cell may be designed to operate with solid charred-coal slab anodes, with large pieces the size of conventional charcoal briquettes, or with a slurry of carbon particles dispersed in the electrolyte. For the present studies, the charring process provided rigid material of suitable strength. The electrical resistivity of the anode material is only 10 times greater than that of graphite[2], in agreement with the work of Waters[3].

The composition of gas evolved, its rate of evolution (Figure 2), and gravimetric determination of carbon consumption were correlated with coulombs passed for each coal derived carbon anode and also for a control spectrographic carbon. Typical correlations are summarized in Table 2 and yield the following conclusions. The major constituent of the anode product gas was CO_2 (second column, Table 2). The comparison of observed to calculated flow rates, the % FRA column, served as a sensitive test both for the presence of leaks in the system and for the possible presence of gases that might not have been detected by the gas chromatograph. From this test it is concluded that no gaseous product other than CO or CO_2 was formed at any significant rate. The agreement between Faraday's law, for an assumed $\underline{n}$ value of 4, and the rate of CO_2 evolution compared with the current, shown in the % CA column, provides the basis for the conclusion that the overall reaction proceeds according to the 4 electron oxidation of carbon to carbon dioxide, as shown in Equation 1.

The analytical result indicating carbon dioxide as the principal product of electrochemical oxidation was necessary to support the conclusion that the oxidation proceeded to carbon dioxide. The responses

shown in Table 2 are characteristic of those observed for all experiments. Although a necessary condition, the presence of carbon dioxide alone is not sufficient because the first stage of oxidation could hypothetically proceed by evolving CO (Equation 4)

$$2C + CO_3^{=} \rightarrow 3CO + 2e \qquad (4)$$

followed by the Boudouard reaction

$$2CO \rightleftarrows C + CO_2 \qquad (5)$$

If the carbon from the Boudouard Reaction (Equation 5) were deposited in cold regions remote from the anode, thus becoming electrochemically inactive, the overall anode reaction would be

$$2C + CO_3^{=} \rightarrow 3/2\ C\ (\text{inactive}) + 3/2\ CO_2 + 2e \qquad (6)$$

In such a case, the $\underline{n}$ value based on carbon is $\underline{n} = 1$ (also for Equation 4) rather than $\underline{n} = 4$; however, Equation 6 indicates three moles of CO_2 are released per four Faradays, as in the direct oxidation to carbon dioxide,

$$C + 2CO_3^{=} \rightarrow 3CO_2 + 4e^{-} \qquad (1)$$

In Reaction 1, $\underline{n} = 4$ for carbon, but as in Reaction 6, three moles of CO_2 are released with the passage of the four Faradays of charge. Thus, to supplement the consistent results obtained from gas analysis and flow measurements shown in the first three columns of Table 2, anode weight change was determined to assay for $\underline{n}$. The results, (fourth column, Table 2) show clearly $\underline{n} > 2$, and trend toward $\underline{n} = 4$. Values of $\underline{n} < 4$ were obtained when carbon was lost during leaching of solidified carbonate from the porous anode. These results, both the gas-phase analyses and the gravimetric determination, are taken as necessary and sufficient proof that the electrochemical oxidation of carbon proceeds to carbon dioxide in the ternary carbonate electrolyte at 700°C.

The open-circuit voltage of the anode against the 1/3 O_2, 2/3 CO_2 reference electrode is nearly the same as would be observed from an actual cell with an air cathode. Cell voltage is particularly unsuited for selecting between oxidation to carbon monoxide or to carbon dioxide at 700°C because both reactions have essentially the same cell potential at this temperature. However, the calculated voltage of the system should increase with increasing temperature if the products are governed by the Boudouard reaction (Equation 5), which predicts significant shifts to CO at temperatures in excess of 400°C. Thus, under equilibrium conditions, the calculated CO concentration rises from 60% at 700°C to 90% at 800°C [4,5]. However, as shown in Figure 2 and Table 2, the concentration of CO_2 was found to be much larger than the value expected from thermodynamic equilibrium considerations. Also, the voltages observed remained constant with temperature, as shown in Figure 3. If the Boudouard reaction (5) is assumed to be kinetically inhibited and the anode reaction is assumed to proceed directly to CO_2 as written in Equation 1, calculated cell potentials are not very dependent on temperature, as indicated in Figure 4 for different cathode gas mixtures. The temperature trend predicted in Figure 4 is in close agreement with observation, as shown for a typical coal derived anode in Figure 3.

The dynamic behavior of coal-derived carbons was found to fall in the range of practical levels. As shown in Figure 5, the polarization observed would allow operation of a cell at acceptable levels of polarization up to 100 mA/cm^2. Based on these results, operation at near one-atmosphere pressure might yield powers of 50-100 watts per ft^2 at cell electrical efficiencies in excess of 60%.

From these results it is possible to conceive of a carbon/air fuel cell, using carbon anodes directly obtained from coal, that would operate according to the reactions:

Anode	$C + 2CO_3^{=} \rightarrow 3CO_2 + 4e^-$	(1)
Cathode	$O_2 + 2CO_2 + 4e^- \rightarrow 2CO_3^{=}$	(2)
Cell	$C + O_2 \rightarrow CO_2$	(3)

The cell would be of the invariant electrolyte type, as indicated in the above equations, and would retain the known pollution scavenging properties of the carbonates. The fact that the potential of the anode was unaffected by the presence of 10 weight percent fly ash (Table 3) is encouraging. Additional work is needed to verify that ash buildup in the electrolyte does not adversely affect dynamic electrode performance.

Using the stoichiometry of Equations 1, 2, and 3, capital costs of various coal-fueled power plant designs were estimated[6]. The results of these initial estimates indicate that an efficient, non-polluting, direct approach to the use of coal to produce electricity may be cost competitive with exisiting and planned approaches. The estimates ranged from $1500 to $750 per kilowatt of plant capacity and showed thermal efficiencies, ranging from 45 to 60% based on bottoming cycle turbine approaches. These results may be favorably compared with present day steam turbine power plant costs of about $1000 per kilowatt and efficiencies of about 40% and also with predictions for indirect conversion natural gas carbonate fuel cell systems which indicate somewhat lower efficiencies and similar costs[8].

ACKNOWLEDGMENT

The authors express their gratitude to colleagues who have contributed to this work as indicated in References 5-7. They are: Mr. Arthur Bayce, E. Capener, Dr. Daniel Cubicciotti, Pat Martin, C. Marynowski, Laura Tietz, and Dr. Masaki Yasuda. We also express our thanks for the support of the U.S. Environmental Protection Agency and the U.S. Department of Energy.

REFERENCES

1. H. A. Liebhafsky and E. V. Cairns, Fuel Cells and Fuel Batteries, John Wiley and Sons, Inc., New York 1968, Chapter 2.

2. Handbook of Chemistry and Physics, 55th Ed., page F-159, CRC Press, Cleveland, Ohio, 1974.

3. P. L. Waters, "Semiconducting Properties of Carbonized Coal," proceedings of the Fifth Converence on Carbon, Volume 2, Page 131-148, MacMillan Company, New York, (1963).

4. JANAF Thermochemical Tables, Second Edition, Superintendent of Documents, U.S. Government Printing Office, Washington, D.C. 20402, Cat. No. C13.48:37 (1971).

5. "Direct Electrochemical Generation of Electricity from Coal," Robert D. Weaver, Masaki Yasuda, Arthur E. Bayce, and Leonard Nanis, ERDA Annual Report 1976-1977.

6. "Direct Electrochemical Generation of Electricity from Coal," Robert D. Weaver, Steven C. Leach, Arthur E. Bayce, and Leonard Nanis, Department of Energy, Contract EY-76-C-03-0115, Report for 1977-1979.

7. "Direct Use of Coal in a Fuel Cell: Feasibility Investigation," Robert D. Weaver, Laura Tietz, and Daniel Cubicciotti, Environmental Protection Agency, June 1975, Contract No. 68-02-1808.

8. "Evaluation of Natural Gas Carbonate Power Plants," Gas Research Institute, GRI Contract No. 5014-344-0293, March 1980-May 1980.

DOI: 10.1149/198109.0334PV

THE ELECTROCHEMISTRY OF OXYGEN AND CARBON DIOXIDE AT GOLD ELECTRODES IN MOLTEN Li_2CO_3-Na_2CO_3-K_2CO_3 EUTECTIC

S. H. White and M. M. Bower
EIC Laboratories, Inc., 55 Chapel Street, Newton, MA 02158

ABSTRACT

Molten alkali carbonate mixtures are of interest for fuel cell electrolytes. Their solution chemistry in contact with both fuel and oxidant gases is complex and is of significance to the electrode reactions taking place. Preliminary results obtained for ternary Li_2-Na_2-K_2CO_3 eutectic at 660°C under oxygen/nitrogen atmospheres, carbon dioxide and argon are discussed. The diffusion coefficient for carbon dioxide is $9 \pm 2 \times 10^{-6} cm^2 sec^{-1}$. The solution under oxygen-nitrogen probably involves the equilibrium

$$O_2 + O_2^{2-} \rightleftarrows 2O_2^-$$

and the $E_{\frac{1}{4}}$ for peroxide and superoxide ion reduction are close.

INTRODUCTION

The molten alkali metal carbonates are components of the electrolytes employed in the high temperature fuel cell under development at the present time. The early work on molten carbonate fuel cells stalled on the technology associated with electrode composition and electrolyte immobilization (1). Recent developments have shown that nickel/nickel oxide is a suitable porous electrode material and the development of lithium aluminate tile structures has led to active development of a molten carbonate fuel cell prototype. The current fuel cell technology may be compared to that which existed for many years during the development of the Hall-Heroult process, i.e., a commercially viable technology supported by little in depth understanding of the chemistry and electrochemistry involved.

During the sixties Janz and co-workers and others developed a sound basis for the physicochemical properties of molten carbonates (2). These data were recently drawn together and reviewed by workers at IGT (3). This emphasized the areas in which further contributions to the chemistry and electrochemistry of the molten carbonate fuel cell system were needed.

In particular, the chemistry of the complex interactions between fuel gases, oxidant gases, and the electrolyte is still uncertain although the pioneering work of Appleby (4) has highlighted the importance

of species such as peroxide and superoxide in these systems. On the other hand, the details of the electrode reactions are barely understood, in spite of a number of attempts to measure exchange current densities and identify mechanisms (5,6). The limited success of these studies arises partly from the complexity of the systems and partly because of the level of understanding of the electrochemical problem. The use of relaxation techniques is notoriously difficult (7,8), and much of the work suffers from a lack of an appreciation of this fact.

In any kinetic study, the nature of the reactants and products should be identified prior to detailed mechanism studies. It has been our purpose to secure an understanding of this aspect of the oxygen electrode in molten carbonates before proceeding to a detailed kinetic study, initially employing gold planar electrodes. The treatment of three-dimensional porous electrode made of nickel oxide is a formidable problem, and a data base for smooth gold electrodes has been our goal.

The chemistry of molten carbonates is characterized by acid-base behavior of the carbonate ion modified by the alkali metal cation

$$\underset{}{CO_3^{2-}} \rightleftarrows \underset{\text{acid}}{CO_2} + \underset{\text{base}}{O^{2-}} \qquad (1)$$

Thermodynamic calculations (9) indeed show that the reductive processes vary from carbon deposition in the case of Li_2CO_3 to alkali metal formation in the case of K_2CO_3 reflecting in these melts the differing basicity defined as $P_O^{2-} = -\log[O^{2-}]$. Such behavior has been confirmed experimentally and discussed in more detail (10,11).

On the other hand, the interactive behavior of the molten carbonate with gases such as CO (12), CO_2, and O_2 is little understood. It is likely that in these systems oxygen behaves as an oxidizing acid competing with CO_2 for oxide ion, which results in the formation of peroxide or superoxide ions viz.

$$2CO_3^{2-} + O_2 \rightleftarrows 2CO_2 + 2O_2^{2-} \qquad (2)$$

$$2CO_3^{2-} + 3O_2 \rightleftarrows 2CO_2 + 4O_2^{-} \qquad (3)$$

These equilibria also involve the oxygen/carbon dioxide partial pressure ratio, a quantity of some importance in fuel cell operations. Appleby and Nicholson have interpreted their electrochemical studies in Li_2CO_3 (13), Li_2CO_3-K_2CO_3 and Na_2CO_3-K_2CO_3 (14) in terms of reduction of peroxide (Li_2CO_3) and peroxide and superoxide mixture for various O_2/CO_2 ratios equilibrated with the melts. Thermodynamic data to some extent support these findings (15). The influence of basicity has been inferred also from these results (11).

The electrochemical studies reported here are for the ternary (43.5 mol%), Li_2CO_3 (31.5 mol%), Na_2CO_3 (25 mol%) K_2CO_3 system which is a candidate for fuel cell applications and which enables measurements

to be obtained over a much wider range of temperatures (400-900°C) than is possible with Li_2CO_3 or the binary mixtures. The reported data are obtained close to the fuel cell operational temperature of 680°C and supplemented where necessary with results at other temperatures.

EXPERIMENTAL

The ternary carbonate mixture 43.5 mol% Li_2CO_3, 31.5 mol% Na_2CO_3, 25 mol% K_2CO_3 was made up from ACS Fisher chemicals which were further dried over P_2O_5 in a vacuum desiccator. The mixture, contained in an alumina crucible, was slowly evacuated while heating to just above the melting point (397°C). Surface carbon was removed by treatment with oxygen which was followed by carbon dioxide to convert any base to carbonate. The melt was cooled and subsequently handled in the dry box. The cell consisted of a closed end silica tube capped with a water-cooled brass head through which various working electrodes were introduced using "Ace" threaded joints (Figure 1). The electrodes were gold flags of varying sizes supported on gold wires sealed in alumina capillary tubes. The working electrode areas were measured in the later work by an electrochemical method described by Wolfe and Caton (16). The reference electrode was similar to that described by Danner and Rey (17). The silver concentration was 0.25M Ag_2SO_4 in Li_2SO_4-Na_2SO_4-K_2SO_4 eutectic. The aluminous porcelain tube was separated from the main compartment via a high purity alumina tube with a pinhole in the closed end. Cyclic voltammetric and chronopotentiometric measurements were made using either an AMEL 551 or a PAR 373 potentiostat and a PAR 175 signal generator. The resultant transients were recorded on an X-Y recorder or at high frequencies on a Bascom-Turner microprocessor-controlled data recorder and stored on floppy disc for subsequent analysis.

RESULTS AND DISCUSSION

Argon. Initially, the ternary electrolyte was examined under argon at lower temperatures to assess the purity of the melt. Figure 2 shows a low sensitivity cyclic voltammogram indicating the accessible range of this melt at 430°C. The cathodic peak arises from the reduction of carbonate to carbon as demonstrated by potential-controlled electrolysis at these potentials on the substrates. These observations are in agreement with the earlier results of Ingram, Baron and Janz (18) at 600°C. The sharp stripping peak confirms the presence of an insoluble reduction product.

High sensitivity (100X more sensitive) cyclic voltammograms are shown in Figure 3 for several different cell atmospheres at 680°C.

Under argon at the higher sensitivity, an anodic rising current is seen which, under closer inspection, shows the presence of a shoulder. The $E_{\frac{1}{2}}$ is similar to peaks observed in the presence of added oxide (19). Thus, even at 680°C some decomposition of the carbonate ion takes place viz.,

$$CO_3^{2-}(\ell) \rightleftharpoons CO_2(g) + O^{2-} \text{ (soln)} \qquad (4)$$

for which

$$P_{CO_2} = \frac{K}{a_{O^{2-}}}$$

Now since the oxide activity is inversely proportional to the CO_2 pressure, as the oxide ion activity rises, P_{CO_2} falls and eventually a steady state is reached in which CO_2 loss becomes negligibly slow. The observed residual oxide peaks reflect this situation. Preliminary measurements suggest the oxide ion concentration in this case to be 0.8×10^{-6} mol-cm^{-3}. The oxide ion concentration calculated using the data given by Janz (20) at the dissociation pressure of the carbonate is 0.6×10^{-6} mol-cm^{-3}. The latter figure represents a lower estimate and our value is therefore reasonable. Further, at the dissociation pressure of CO_2 the solubility of CO_2 will be small and the cyclic voltammetry will not detect such a low concentration. This is supported by the scan shown in Figure 3. No further peaks are detected in the potential region 0 to -1.506V with respect to CO_2/O_2(2:1) reference electrode.

Carbon Dioxide. Changing from argon to carbon dioxide atmosphere above the melt resulted in the development of a reduction peak at $E_{\frac{1}{2}} \sim$-1100 with respect to the CO_2/O_2(2:1) reference. The reduction peak showed a reverse anodic peak, much less than expected for a reversible system. There was a slight dependence of peak potential on scan rate for the limited range of scan rates. Using the solubility data reported by Appleby and Van Drunen (21) at 700°C, and assuming no temperature dependence between their working temperature and our temperature of 660°C, (for n = 1 from $\Delta E_{p/2}$) the diffusion coefficient for carbon dioxide is $9 \pm 2 \times 10^{-6}$ cm^{2}sec^{-1}.

According to Andersen (15),

$$K_D = \frac{P_{CO_2} N_{O^{2-}}}{N_{CO_3}} = 1.77 \times 10^{-8} \text{ atm}$$

Thus, at 1 atmosphere CO_2, the concentration of oxide ions will be $\sim 10^{-10}$ mol-cm^{-3}, well below the detection limit of cyclic voltammetry. This is then consistent with the disappearance of the oxide wave under a carbon dioxide atmosphere.

Oxygen-Carbon Dioxide 3:1 Mixture. The cyclic voltammograms under this mixture at comparable sensitivities to those used for CO_2 and argon are rather featureless (Fig. 3). The carbon dioxide solubility was not detected. New equilibria (2)and (3) may now control the solution chemistry and suppress lower oxidation states of oxygen.

Oxygen-Nitrogen Mixtures. The introduction of differing oxygen-nitrogen mixtures has a dramatic effect on the solution chemistry which is highlighted both in the cyclic voltammetric and chronopotentiometric responses at gold electrodes. Figures 3, 4 and 5 illustrates typical cathodic and anodic scans from the open circuit potential of the gold electrode. Figure 6 shows the variation of peak current with gas composition at scan rates up to 250 mV-sec^{-1} and Figure 7 shows the variation of $\tau^{\frac{1}{2}}$ (τ = transition time) as a function of applied current i and gas atmosphere. The Sand equation is clearly verified and $E_{\tau/4}$ was apparently independent of applied current density indicating the presence of a diffusion-controlled reaction.

The observation that the rest potential lies within the cyclic voltammetric envelope is interesting because it indicates the presence of more than one redox species at equilibrium. An attempt to resolve these species can be made by recognizing the relationship between the concentration of the solution species undergoing reduction, the Sand constant, and the oxygen partial pressure. Again, it is anticipated that reactions such as (2) and (3) will reach a steady state since it is actually the $P^2_{CO_2}/P_{O_2}$ ratio that ultimately fixes the equilibrium. The coexistence of peroxide ions and superoxide ions under varying oxygen partial pressure must also be considered in addition to the reactions in reactions (2) and (3). This is expressed by

$$O_2^{2-} + O_2 \rightleftarrows 2O_2^- \qquad (5)$$

The various relationships derived between the Sand constant $i\tau^{\frac{1}{2}}$ and the oxygen partial pressure are given in Table 1. The cyclic voltammetric data are not subject to this analysis because (a) the Randles Sevcik equation is dependent on the model, i.e., $\chi(i)_{max}$ is a variable function which depends on whether the product of reaction is soluble, insoluble, and coupled to subsequent chemical reactions or whether the electrochemical reaction is reversible or irreversible under the experimental conditions, and (b) the value of "n" the number of electrons in the overall reaction (diffusion control) or the number of electrons in the rate determining step times α the transfer coefficient (kinetic control) appear in the slope.

From the limited data so far available, the slope observed is close to the theoretical (Fig. 8) 0.5. This implies that either peroxide ions are the solution species if a single moiety is present or more reasonably that the equilibrium (5) controls the solution chemistry and superoxide ions are the electroactive species. This latter choice is supported by the cyclic voltammetric data. Diagnostic potential analysis of the cyclic voltammograms using $\Delta E_{p/2} = E_p - E_{p/2}$ in particular, shows the initial cathodic cycle to involve 3 electrons in a diffusion controlled process consistent only with superoxide ion being reduced.

Subsequent reversal of the cathodic sweep produced an anodic peak (Fig. 4) whose $\Delta E_{p/2}$ is consistent with n = 2, implying

$$2O^{2-} \rightleftarrows O_2^{2-} + 2e \quad (6)$$

The second cycle of the voltammogram (cathodic) produced a peak whose $\Delta E_{p/2}$ are now consistent with n = 2, i.e.,

$$O_2^{2-} + 2e \rightleftarrows 2O^{2-} \quad (7)$$

Table 2 illustrates this potential data. The involvement of oxide ions as the final reduction product is supported by the observation that no further reduction peaks are observed beyond about -350 mV vs. CO_2/O_2(2:1) reference electrode.

The results imply that the reduction potentials of superoxide ion and peroxide ions may be very close in this melt. Appleby has reported such overlap for the reduction of these ions in Li_2CO_3/K_2CO_3. Further work is underway to confirm this identification of the solution species and to investigate the influence of small controlled amounts of CO_2 in the gas streams. The kinetics of these processes will then be open to direct measurement.

ACKNOWLEDGMENT

This work was supported by the Department of Energy under Contract No. DE-AC05-79ET15403. The authors would like to thank Dr. Urszula Twardoch for valuable discussions.

REFERENCES

1. See, for example, I Trachtenberg and C. F. Cole, "Electrolyte Studies on Molten Carbonate Fuel Cells," in Fuel Cell Systems II, ed. by B. S. Baker, Advances in Chemistry Series 90, 268, ACS, 1969.

2. See, for example, G. J. Janz and M. R. Lorenz, J. Electrochem. Soc., 108, 1052 (1961; G. J. Janz and F. Saegusa, ibid., 110, 452 (1963); A. T. Ward and G. J. Janz, Electrochim. Acta, 10, 849 (1965).

3. H. C. Maru et al., "Characteristics of Carbonate Melts," Vol II, IGT report under Contract 31-109-38-3552, Argonne National Laboratory, 1976.

4. A. J. Appleby and S. Nicholson, J. Electroanal. Chem., 38, 1972, App B.

5. M. V. Smirnov, I. Ya Lynbimtseva and L. A. Tsiovkina, Elektrokhimiya, 7(4), 135,566 (1971).

6. A. Borucka and C. M. Sugiyama, Electrochim. Acta, 14, 871 (1969).

7. P. Delahay, in Advances in Electrochemistry and Electrochemical Engineering, ed. by P. Delahay and C. W. Tobias, Vol. 1, Chapter 5 (Interscience, 1963).

8. A. D. Graves, G. J. Hills and D. Inman, in Advances in Electrochemistry and Electrochemical Engineering, ed. by P. Delahay and C. W. Tobias, Vol. 4, Chapter 3 (Interscience, 1966).

9. H. E. Bartlett and K. E. Johnson, Canadian J. Chem., 44, 2119 (1966).

10. N. Busson, S. Palous, J. Millet and R. Buvet, Electrochim. Acta, 12, 1609 (1967).

11. A. J. Appleby and S. B. Nicholson, J. Electroanal. Chem., 112, 71 (1980).

12. A. Borucka and A. J. Appleby, J. Chem. Soc. Faraday Trans I, 73, 1420 (1977).

13. A. J. Appleby and S. Nicholson, J. Electroanal. Chem., 53, 105 (1974).

14. A. J. Appleby and S. Nicholson, J. Electroanal. Chem., 83, 309 (1977).

15. B. K. Andersen, Ph.D. Thesis, The Technical University of Denmark, 1975.

16. C. R. Wolfe and R. D. Caton, Jr., Anal. Chem., 43, 663 (1971).

17. G. Danner and M. Rey, Electrochim. Acta, 4, 274 (1961).

18. M. D. Ingram, B. Baron and G. J. Janz, Electrochim. Acta, 11, 1629 (1966).

19. S. H. White, unpublished work, 1980.

20. G. J. Janz, Molten Salts Handbook (Academic Press, 1967).

21. A. J. Appleby and C. Van Drunen, J. Electrochem. Soc., 127, 1655 (1980).

22. M. S. Shuman, Anal. Chem., 41, 142 (1969).

TABLE 1. RELATIONSHIPS BETWEEN SAND'S CONSTANT AND OXYGEN PARTIAL PRESSURE

No.	Solution Reaction	Equation	Chronopotentiometric/O_2 Partial Pressure Dependence	Slope
2	Peroxide Formation	$2CO_3^{=} + O_2 \rightleftarrows 2CO_2 + O_2^{2-}$	$\log \frac{i\tau^{\frac{1}{2}}}{\pi^{\frac{1}{2}}FA} = 0.51 \log P_{O_2} - \log \frac{K'}{nD^{\frac{1}{2}}}$	0.5
3	Superoxide Formation	$2CO_3 + 3O_2 \rightleftarrows 2CO_2 + 4O_2^{-}$	$\log \frac{i\tau^{\frac{1}{2}}}{\pi^{\frac{1}{2}}FA} = 0.75 \log P_{O_2} - \log \frac{K''}{nD^{\frac{1}{2}}}$	0.75
5	Equilibrium	Superoxide Reduced $O_2^{2-} + O_2 \rightleftarrows 2O_2^{-}$	$\log \frac{i\tau^{\frac{1}{2}}}{\pi^{\frac{1}{2}}FA} = 0.5 \log P_{O_2} - \log \frac{K'''}{nD^{\frac{1}{2}}}$	0.5
		Peroxide Reduced $O_2^{2-} + O_2 \rightleftarrows 2O_2^{-}$	$\log \frac{i\tau^{\frac{1}{2}}}{\pi^{\frac{1}{2}}FA} = - \log P_{O_2} - \log \frac{K'''}{nD^{\frac{1}{2}}}$	-1.0

TABLE 2. DIAGNOSTIC POTENTIAL ANALYSIS OF CYCLIC VOLTAMMETRIC RESULTS

Atmosphere	First Cathodic Cycle $\Delta E_{p/2}$ mV	Second Cathodic Cycle $\Delta E_{p/2}$ mV	Anodic Cycle $\Delta E_{p/2}$ mV
100% O_2	86 ± 3	95 ± 3	101 ± 2
22% O_2/78% N_2	66 ± 1	84 ± 2	102 ± 5
10% O_2/90% N_2	67 ± 4	87 ± 4	115 ± 6
	n = 3	n = 2	n = 2

$ox = ne \rightleftarrows Red$ $\quad \Delta E_{p/2} = \frac{176}{n}$ at 660°C

$2ox \rightleftarrows Red + ne$ (22) $\quad \Delta E_{p/2} = \frac{243}{n}$ at 660°C

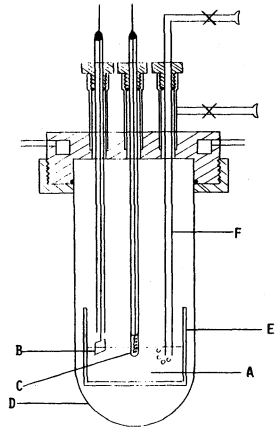

Fig. 1. Cell for electrochemical measurements in carbonate melts.

A - Carbonate Melt
B - Gold Flag Electrode
C - Ag/Ag_2SO_4 in $(LiNaK)_2SO_4$
D - Silica or Pyrex
E - Alumina Crucible
F - Gas Bubbler

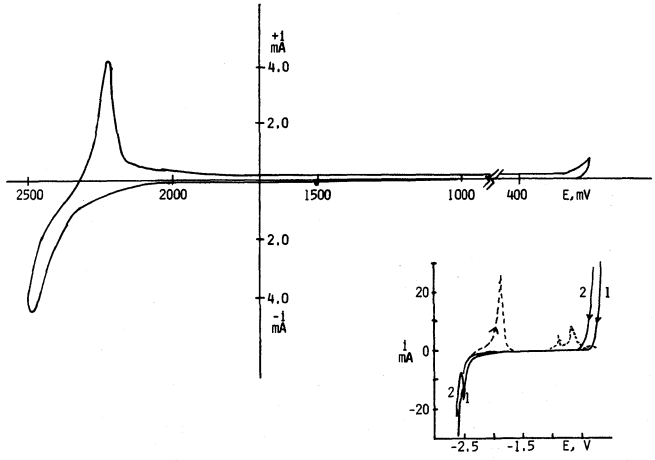

Fig. 2. Low sensitivity cyclic voltammogram, ternary carbonate melt, T = 430°C. Atmosphere argon, 200 mV-sec^{-1}, Au sphere area 0.08 cm^2. Insert (Ref. 18) - (1) CO_2, (2) argon atmosphere, T = 600°C.

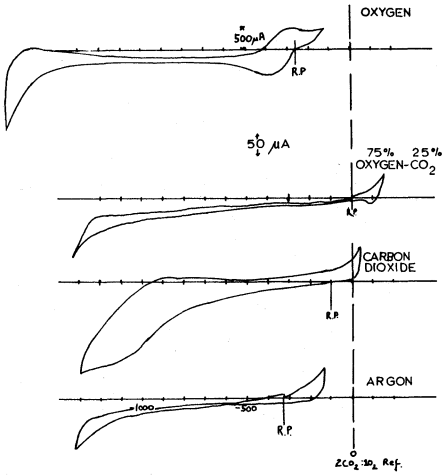

Fig. 3. Cyclic voltammetry in carbonate melt under different atmospheres. Sweep rate = 100 mV-sec^{-1}, area = 0.367 cm^2, T = 680°C.

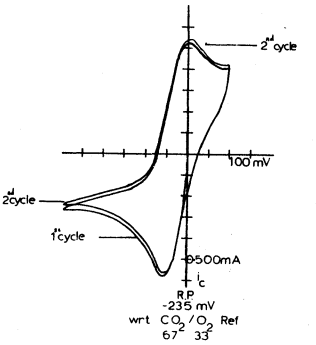

Fig. 4. Cyclic voltammogram under pure oxygen; 100% O_2 atmosphere, Au electrode, area = 0.367 cm^2, sweep rate = 125 mV-sec^{-1}.

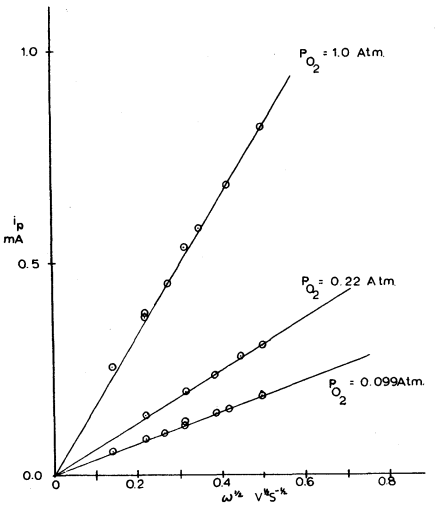

Fig. 5. Variation of peak current as a function of scan rate and oxygen partial pressure. T = 660°C.

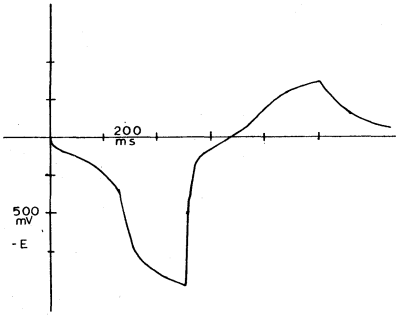

Fig. 6. Chronopotentiogram at gold electrode under pure oxygen. Applied current density = 3.27 mA/cm^{-2}, rest potential = -226 mV vs. CO_2 67%/O_3 33%, reference electrode.

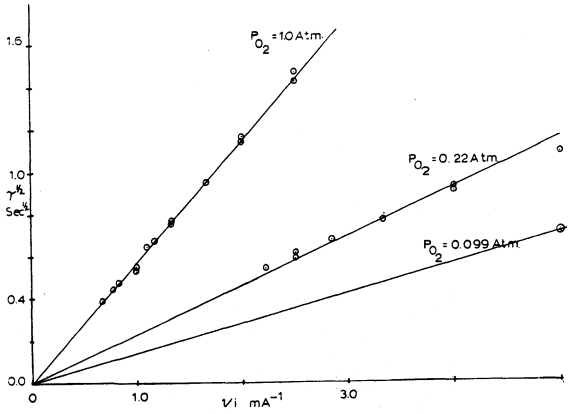

Fig. 7. Variation of $\tau^{\frac{1}{2}}$ with reciprocal current and oxygen partial pressure. T = 660°C.

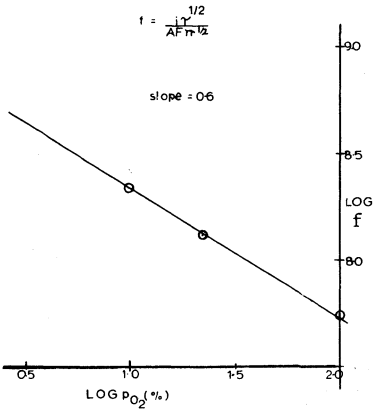

Fig. 8. Chronopotentiometric function plotted vs. oxygen partial pressure.

DOI: 10.1149/198109.0346PV

THE DETERMINATION OF THE CORROSION RATES OF NICKEL, CHROMIUM AND IRON IN MOLTEN SULFATES BY A NEW SPECTROSCOPIC TECHNIQUE

Trevor R. Griffiths and Keith King*

Department of Inorganic and Structural Chemistry,
The University, Leeds LS2 9JT, England.

*Present Address: Shell Research Limited,
Thornton Research Centre, P.O. Box 1,
Chester CH1 3SH, England.

ABSTRACT

Uv-visible absorption spectral measurements have been applied, for the first time, to the corrosion by molten salt deposits of superheater tubes in coal-fired power stations. Metal corrosion rates in sulfate melts, experiencing a heat flux, have been determined for nickel, chromium and iron, using a novel application of the spectroscopic technique. Several new observations have been made, and an important feature of current theories of the corrosion process across molten salt layers is now experimentally confirmed. Using this technique it is now essentially possible to determine accurately corrosion rates for any alloy, or coated-alloy, under almost any conditions a manufacturer or user might specify, including the magnitude of the thermal gradient, the temperature of the alloy, the composition of the aggressive salt layer and the composition of the flue gas.

INTRODUCTION

High temperature corrosion is of major interest and concern in a wide range of essential power generation and chemical plant. For example, the maximum steam temperatures in coal and oil-fired generating plant are restricted to 568° and 540°C respectively, largely because of corrosion limitations, even though, on thermodynamic grounds, higher temperatures would lead to significantly higher efficiency. A similar situation arises in gas turbine plant, for aviation and marine applications, where temperatures in the range 900-1100°C can be achieved, albeit for short component lives and by using highly refined fuel. Comparable cases of hot corrosion can be

found in chemical plant, and this is expected to become an important future consideration, particularly in novel methods for utilizing lower grade fuels and in coal conversion plant.

Combustion gases invariably include nitrogen, water vapour, nitrogen oxides, sulfur oxides (or hydrogen sulfide), carbon dioxide, and possibly carbon monoxide, or excess oxygen, and in them corrosion may occur over a wide temperature range (350-1200°C). (At lower temperatures materials may suffer attack by H_2SO_4 mists: 1200°C is about the practical limit for commercial materials.) A heat flux or temperature gradient is usually found on the components of the furnace, and oxide and sulfide scales form on metal surfaces. In addition, and in almost all cases, molten slags form at various locations on the furnace component alloys, derived from the common fuel impurities such as alkali metals, chlorine and vanadium. These molten deposits are aggresive, and can dissolve and disrupt the scale, accelerating corrosion at these points, occasionally even to disasterous levels.

Before describing the new technique we review briefly the information currently available from existing techniques used in the study of hot corrosion.

CONVENTIONAL TECHNIQUES

These techniques are:

A. Examination of ex-plant components;

B. Small scale laboratory test rigs attempting to simulate plant environments;

C. Electrochemical studies; and

D. Thermogravimetry in simplified conditions.

Information from method (A) is limited because observations are made on cold samples after exposure to conditions not usually controlled in a scientific way, i.e. only an average of plant conditions is experienced.

Method (B) frequently omits important aspects such as heat flux, and the data arising can be obtained only by interrupting the experiment, and not by continuous measurements on hot samples. Realistic simulation of plant conditions is also very costly.

Method (C) does yield data during the experiment, but this can be difficult to interpret, particularly regarding the nature and geometry of the complex ions which constitute the corrosion products; melts which reflect the composition of deposits found on superheater tubes tend not to have been used; and heat fluxes cannot be employed.

Method (D) is not very suitable for studying molten salt corrosion, unless very rapid corrosion rates are involved.

The consequence of the limitations of these methods is that whilst models have been advanced for corrosion mechanisms in many of the existing complex environments, they are either not proven or are not quantitative, i.e. a reliable prediction of corrosion rate or component life cannot always be made. Reliable predictions are certainly not at present possible for new environments and materials.

A NEW APPROACH

Over the past four years, in the Department of Inorganic and Structural Chemistry, at the University of Leeds we have developed and proved a new technique which essentially overcomes all of the above difficulties. It provides accurate corrosion data, and has the potential for excellent predictions of corrosion rates. The conditions, including thermal gradients, of almost any example of high temperature corrosion involving an aggressive salt layer can be reproduced, and corrosion rates obtained, together with much additional valuable information not previously attainable.

It is necessary first to understand the industrial situation. Figure 1 shows a schematic diagram of a front-fired boiler some 300 ft high. The regions most susceptible to hot corrosion (in this situation often termed fire-side corrosion) by the combustion gases and ash particles are indicated. The coal or oil fuel is fed, together with the combustion air, to burners in the furnace section. The furnace walls consist of mild-steel evaporator tubes in which the feed water is converted into steam. The temperature of the combustion gases falls as they pass through the pendant superheater and secondary reheater tube banks, then down through the primary reheater and economiser tubing, which is not shown. Figure 2 shows a cross-section of a leading superheater or reheater tube. A nose-cone of ash builds up at the leading face (at 'twelve-o'clock'), providing sufficient insulation at this position to keep the metal surface temperature quite low.

However the ash is much thinner at the 'two-o'clock' and 'ten-o'clock' positions around the side of the tube, and the high heat flux results in the sulfate deposited at these points becoming molten, and this molten sulfate layer is aggressive and leads to severe wastage. The estimated thermal profile of the heat flux across the tube in this wastage region is shown in Figure 3. The overall mechanism of superheater tube corrosion is currently viewed as a continuous process of metal oxidation at the tube surface, dissolution of this oxide in the molten sulfate, diffusion across this layer, and precipitation as porous haematite (Fe_2O_3) beneath the outer covering layer of ash. The thickness of the protective oxide layer on the surface of the metal is thus reduced and the oxidation of the metal can proceed more rapidly.

To replicate these conditions, and determine the identities and concentrations of the corrosion products at any point within the molten sulfate layer we have modified an absorption spectrophotometer so that the concentrations of dissolved transition metal complexes, the corrosion products, and their d-d absorption spectra can be measured.

Basically the method is very simple. An Applied Physics Cary 14H spectrophotometer was employed, a model which was specially designed for recording molten salt spectra and which has reversed-beam optics, so that any light emitted from the hot sample is eliminated. The optical path was modified so that a fixed thin (1 mm) horizontal slot of light passed through the sample. The sample was a molten salt, in a 10 mm silica cuvette, heated from above to avoid convection currents and to generate a thermal gradient down the cell. A coupon of metal was placed at the bottom, the low temperature region, of the cell, and a synthetic flue gas was passed over the upper surface of the melt. The furnace employed could be raised or lowered relative to the slot. Kaowool catalyst was placed in the gas stream, just above the melt surface, to convert some of the SO_2 to SO_3, which reaction is normally effected by the porous ash deposit. The extension of the normal melt layer of around 1 mm thick to around 45 mm does not affect the situation, and does permit the spectra, and hence the concentration of dissolved species to be recorded as a function of time and distance from the coupon in the melt experiencing the thermal gradient. Plots of concentration against time at various depths admit the calculation of the rate of dissolution of the metal. Because the spectra are digitized some 400 separate determinations of each corrosion rate are in principle available, but this requires interactive VDU facilities to be effective. The surface of corroded specimens are also

examined by scanning electron microscopy, electron microprobe analysis and by X-ray studies, to provide as complete a picture as possible of high temperature corrosion. And once the corrosion behaviour has been established for our experimental set-up, the behaviour predominating at any film thickness can readily be deduced. Thus this new technique gives corrosion data under conditions which reproduce the industrial environment much more precisely than any previous technique.

ADVANTAGES AND CAPABILITIES

The value of this new approach may be summarised under ten headings.

1. Thermal gradients are employed across the melt layer, and these may be varied as required.

2. Corrosion rates occurring under the conditions of the applied thermal gradient are determined, and this is the first time this has been achieved.

3. As a metal is corroded the concentration of dissolved metal at any point within the molten salt layer experiencing the thermal gradient may be determined.

4. The conditions of the experiment may be changed and the effects produced monitored. Cycling effects and step changes are common in power generation plant, and stress corrosion has been so studied, but the results of these changes on hot corrosion has not been previously investigated, because of the limitations of previous techniques.

5. Since the electronic (charge transfer and ligand field) absorption spectra of the melts are recorded the nature, identities and even the geometries in solution of the dissolved metal complex ions, the corrosion products, may be determined. (This is the subject of our second contribution to this Symposium.)

6. The nature and geometry of some of these species are at times dependent upon temperature, particularly in melts containing more than one anion, e.g. sulfate and chloride, and thus how they change and the reactions involved on traversing the thermal gradient can be followed.

7. The initial evolution of gas as a melt first attacks the scale may be monitored: this phenomenon was an

entirely new observation.

8. To obtain accurate corrosion rates an accurate knowledge of both diffusion and Soret coefficients is required. These data are limited for molten salts, and have not been measured for representative melts that form in hot corrosion conditions. Our technique is also capable of good determinations of these coefficients under the exact conditions for which they are required, and the procedure is a new one.

9. The data obtained can be treated in two independent ways to yield corrosion rates, and this should provide an independent check on our measured diffusion and Soret coefficients. At the present time the data available has not all been examined: the indications are that if the coefficients are not confirmed by the alternative calculations then this will assist in a better understanding of the process of formation and dissolution of the metal oxide scale in contact with the molten sulfate.

10. Each rate determined can be the mean of some 400 separate determinations and almost all the parameters that one might want to vary or investigate can be examined. These include, in addition to those mentioned above, melt composition, the composition (and temperature) of the flue gas flowing over the melt, the temperature of the specimen, and the specimen itself.

REPRESENTATIVE SULFATE MELTS

Previous studies of corrosion by fused salt deposits in coal-fired boilers have employed crucible and electrochemical investigations involving generally the eutectic mixture of lithium, sodium, potassium sulfate $(Li,Na,K)SO_4$. Boiler deposits, however, contain no lithium: it has been customary to add it to produce a mixed sulfate which is molten at the superheater tube metal temperature of around 550-650^{o}C, since although sodium and potassium are the most abundant cations in the deposit, the sodium-potassium sulfate eutectic melts at 823^{o}C. Other workers (1) have used $(Na,K,Fe)SO_4$ melts, but whilst these do not contain lithium they suffer from a higher than normal amount of iron. We have examined the reported analyses of superheater deposits, and concluded that the next most abundant cation was aluminum, and have established that additions of relatively small amounts of aluminum lowered the melting point of $(Na,K)SO_4$ eutectic sufficiently (2).

The melt composition chosen for this study as a good representative melt had the composition in mol cation %, Na, 42.5; K, 42.5; Al, 15. This should be compared with the eutectic composition of $(Li,Na,K)SO_4$ of Li, 78; Na, 13.5; K, 8.5. Preliminary tests have shown that the aluminum-containing melt is almost twice as aggressive to 316 stainless steel as the lithium-containing melt, and it is recommended (2) that future studies should employ aluminum-containing melts.

EXPERIMENTAL PROCEDURE

The details of the thermal gradient furnace mentioned above will be published elsewhere. Corrosion experiments were performed at four metal temperatures in the range 580-640°C for samples of nickel, chromium and iron. The thermal gradient in the fused silica optical cuvette containing the molten $(Na,K,Al)SO_4$ was 35 K cm^{-1} in the nickel experiments and 24 K cm^{-1} for chromium and iron. (This difference was due to rewinding following failure of the heating element at the end of the nickel experiments.) Assuming a value of approximately 0.4 W m^{-1} K^{-1} for the thermal conductivity of the melt (3), the corresponding heat fluxes were 1.4 kW m^{-2} for nickel, and 0.96 kW m^{-2} for chromium and iron.

The metal coupons were pre-oxidized, and the dimensions determined with a micrometer, before being placed at the bottom of the cuvette.

During the experiments the flow of synthetic flue gas over the melt was approximately 0.1 cm^3 s^{-1}. The composition of the gas, before its passage over the platinised Kaowool catalyst was, by volume, 16% CO_2, 3% O_2, 4000 ppm SO_2, balance N_2. This corresponds to a typical boiler flue gas composition, apart from the exclusion of water vapour, which normally comprises 8-10% of the gas. Water was omitted from our flue gas partly because the extent of its penetration of the ash deposit above the molten salt layer was not known, and partly because it was then feared that the presence of water in the melt might cause it to attack the silica cuvette. We now consider that this is unlikely, because acidic melts are much less aggressive towards silica than melts containing oxide ions, and plan to include water vapour in the gas stream in future experiments. However, since, as we shall show, our present results are consistent with current knowledge and expectations of hot corrosion we do not expect any dramatic effects when water is added to the flue gas.

Concentration gradients for dissolved metal ions were

obtained by recording spectra at different distances above the coupon. The horizontal sections of the melt being examined in the case of chromium and iron were 5, 18, 28 and 38 mm above the coupon surface. For nickel, which had a more rapid dissolution rate, and a larger wavelength range needed to be scanned, only three points could be examined, at 4, 21 and 31 mm above the coupon.

At the end of each experiment the cuvette was removed from the furnace and the melt poured off. After cooling the corroded coupon was retrieved from the cuvette and examined by scanning electron microscopy, electron microprobe analysis, and the adhering solidified melt sometimes analysed using X-rays.

CALCULATION OF DISSOLUTION RATE

In order to calculate the rate of dissolution of metal ions into the sulfate melt it is necessary first to determine the flux of dissolved metal ions away from the metal surface. This flux, J, in moles cm^{-2} s^{-1}, is given (4) by

$$J = -Dm(dN/dx + SN(1 - N)dT/dx)$$

where D is the chemical diffusion coefficient of the metal complex in the melt (cm^2 s^{-1}); m is the total number of moles in a unit volume of the molten deposit (moles cm^{-3}); N is the mol fraction of dissolved corrosion product; x is the distance it has travelled through the melt (cm); S is the Soret coefficient of thermal diffusion; and T is the temperature (K).

The diffusion coefficients for nickel(II) and iron(III) ions in the $(Li,K)SO_4$ eutectic melt at 600°C have been reported by Inman et al. (5), and these values have been used as none have been reported for aluminum-containing melts. No value for chromium(III) in a sulfate melt is available, and in view of the similarity of size and charge between iron(III) and chromium(III), it was decided to use the value for iron. However, since in our second paper in this Symposium we concluded that in our aluminum-containing melts the sulfato-chromium(III) complex is octahedral, and the sulfato-iron(III) complex tetrahedral the validity of the value used for chromium(III) may be questioned, and we hope shortly to determine all three diffusion coefficients in $(Na,K,Al)SO_4$.

The temperature dependence of D, as expressed by the Stokes-Einstein equation (4), gives $D \propto T/\eta$, where T is

the temperature (K) and η the melt viscosity. Calculations based on data given by Janz (6) indicated that η decreases by less than 10% on going from 580 to 770°C. It was thus decided to ignore the contribution of viscosity and assume a direct temperature dependence for D.

For the Soret coefficient it was necessary to use an approximation. Backlund *et al.* (7) obtained values of the order 10^{-3} K^{-1} for a number of species in nitrate melts, and similar values are reported for solutes in aqueous solutions: a value of $S = 1 \times 10^{-3}$ K^{-1} has thus been used.

The flux J is converted into the metal loss rate, r (nm h^{-1}), according to (8) by $r = J(nA/\rho)\ 3.6 \times 10^{10}$, where n is the number of metal atoms in the solvated complex (here in each case unity); A is the atomic weight of the metal; and ρ the density of the metal at the given temperature.

RESULTS: NICKEL

The four metal temperatures and the corresponding temperatures at the sampling points and the melt surface are given in Table 1.

Table 1

Temperatures (°C) at Various Points in the (Na,K,Al)SO_4 Melt

Coupon/Melt Interface	Distance from Nickel Coupon 4 mm	21 mm	36 mm	Melt/Gas Interface
587	595	638	699	731
606	611	650	711	742
616	621	663	728	756
632	640	681	742	771

	Distance from Chromium and Iron Coupons 5 mm	18 mm	28 mm	38 mm	
590	595	608	629	660	700
605	610	623	644	674	714
620	625	637	656	687	727
635	639	650	669	700	740

Spectra were recorded in the range 300-900 nm and the dissolved nickel concentration calculated from the absorbance of the peak at around 21,000 cm^{-1}, using molar absorbance values determined by calibration experiments.

The duration of the experiments was limited to a maximum of 13 h by the progressive formation of a precipi-

tate. The initial, precipitate-free period was sensitive to temperature, and decreased on going from the experiment with metal temperature 587°C to that at 632°C. The precipitate adhered to the cuvette walls, and to the faces of the solid, optically-flat silica insert used to reduce the optical path length so that spectra could be recorded.

At each sampling point, and for all four metal temperatures, the dissolved nickel concentration, c, increased parabolically with time, t. This was established by plotting c^2 versus t, Figure 4. The straight line shown is a least square fit to the data. Good linear plots were obtained at all temperatures and at all points within the thermal gradient: the results for the nickel coupon temperature of 606°C are shown in Figure 5. The parabolic curves drawn were obtained from the least squares fits. The dissolution rates, expressed as metal loss rates, for the four metal temperatures are shown in Figure 6.

Evolution of a gas from the metal/melt interface was observed during the corrosion experiment. It was initially fairly vigorous and was estimated as around 1 cm^{-3} min^{-1}, but decreased with time. The passage of bubbles through the horizontal light slot produced spikes on the recorded spectra. Recording was generally stopped until the bubble had moved out of the light beam. This feature contributed greatly to the scatter of points seen, for example, in Figure 5.

Examination of Corroded Coupons

The pre-oxidation of the nickel coupons gave an oxide layer 1-2 μm thick. Subsequent examination showed no significant differences between coupons corroded at different temperatures and the micrographs for the experiment at 616°C metal temperature are typical (Figures 7 and 8). The coupon shown was ground to 600 grit silicon carbide paper along one edge to expose the bare metal, and is thus viewed with adhering solidified melt on both faces. Further polishing to 1 μm diamond paste was employed to obtain the higher magnification micrographs in Figure 8.

Figure 7 shows an electron microprobe analysis, magnified 25 times, of the nickel coupon for the elements nickel, aluminum, sodium, potassium and sulfur. These were determined on a Cambridge Stereoscan 600 electron microscope at the Scientific Services Division Laboratories of the Central Electricity Generating Board at Harrogate. Figure 8 is a scanning electron micrograph, obtained using the above instrument, of the corrosion scale attached to the surface of the nickel coupon.

There is a pronounced layered structure to the melt, in which the inner band, approximately 0.2 mm thick, is rich in nickel and aluminum, but deficient in sodium and potassium, relative to the outer layer, presumed to be representative of the bulk melt.

The corrosion scale immediately adjacent to the metal has a much finer layered structure of predominantly NiS and predominantly NiO bands, as shown in Figure 8.

It is difficult to estimate the metal loss rate from the final thickness of the coupon, because of the uneven nature of the attack, with pits up to 150 μm deep. However a value of approximately 7000 nm h^{-1} may be taken as representative.

Nature of the Precipitate

It should first be noted that the $(Na,K,Al)SO_4$ mixture we have employed is stable in the molten state: a white precipitate appeared after several hours only when nickel coupons were in the melt. A white precipitate of alumina was however immediately obtained on adding small amounts of Na_2O to the molten sulfate. The white insoluble residue obtained at the end of the nickel corrosion experiments was examined by X-ray diffraction. The patterns produced were extremely complex, and no clear identification was possible.

It had been expected that the precipitate would be largely alumina. In each sample α-Al_2O_3 was found, but only as a minor constituent. The remaining patterns were either unidentified or tentatively assigned by the analyst to mixed sulfates, such as $NaAl(SO_4)_2$ and $KNaSO_4$. However the presence of these water soluble sulfates may be doubtful, since the residues had been subjected to combined heating and ultrasonic agitation in large volumes of distilled water before analysis, to leach out all water soluble species. It should be noted that no nickel compounds were found in the precipitates.

RESULTS: CHROMIUM

The four metal temperatures, and the corresponding temperatures at the sampling points and melt surface, are given in Table 1. The spectrum was scanned in the range 300-1000 nm, and the chromium concentrations determined from the absorbance coefficient obtained from calibration experiments. This band, rather than the main peak at 21,000 cm^{-1}, was used since the latter is susceptible to interference from the charge transfer edge, particularly

when decomposition of the chromium species occurs after some hours.

No precipiptate was formed during the experiments, and thus each one was continued for a fixed time of 80 h. The dissolution rate was very slow compared with that of nickel. The initial evolution of gas from the coupon was very slow, being at least two orders of magnitude less than that for nickel. Evolution ceased completely after approximately four hours.

A parabolic relationship between concentration of dissolved chromium and time was not found at any of the sampling points; c versus t plots were not linear. Typical results, at 620°C, are shown in Figure 9, where the concentrations are seen to tend to a limiting value at all points within the thermal gradient. Only the results at the lowest temperature of 590°C did not follow this pattern. Here the chromium concentrations are still rising after 80 h.

Consistent with this is the observation that the spectra recorded for metal temperatures other than 590°C all indicated chromium oxide precipitation from the melt, whereas no precipitation was observed with the metal temperature at 590°C. Insoluble residues isolated from melt samples were too small for analysis, which is not surprising in view of the low levels of dissolved chromium.

The dissolution rates, in terms of metal loss, calculated from the concentration curves (Figure 11) are low, around 1 nm h^{-1}, and the exception, at 590°C, is not significantly different at 2 nm h^{-1}.

Examination of Corroded Coupons

The pre-oxidation process formed a very thin oxide layer on the coupons, estimated at 200 nm thick. In the subsequent examination of corroded specimens, this oxide layer was not detected. This does not imply that it was no longer present: great difficulty had been experienced in identifying it on the non-corroded coupons. However, it may be concluded that, in contradistinction to nickel, no gross scale formation or sulphidation occurred. Similarly, there was no aluminum-rich layer adjacent to the metal, in the adhering melt.

IRON: RESULTS

The metal temperatures were the same as those for

chromium (Table 1). The dissolved iron concentration was obtained from the absorbance at two points, 500 and 550 nm, on the charge transfer absorption edges, the linear dependence of absorbance on concentration at these points having been previously verified. The molar extinction coefficients had been established independently. The spectra were recorded from 800 nm down to the point at which the pen went off-scale.

The experiments were again not limited by precipitate formation, and were therefore continued for a standard time of 50 h. For metal temperatures of 620 and 635°C, a ring of red-brown solid was observed on the melt surface at the end of the experiment. Again, although it was not possible to isolate sufficient for analysis, its colour suggested strongly that it was haematite, Fe_2O_3.

Gas was evolved from the coupon/melt interface at an initial rate somewhat less than that during the nickel experiments, at around 0.5 cm^{-3} min^{-1}, and again the rate of evolution decreased with time.

At 590°C metal temperature, the dependence of dissolved iron concentration on time was parabolic (Figure 12). The results at 605°C gave poor agreement for a parabolic relationship, while those for metal temperatures of 620 and 635°C clearly tended to limiting concentrations (Figure 13). The metal loss rates corresponding to the dissolution rates are shown in Figure 14.

Examination of Corroded Coupons

As a result of pre-oxidation, the oxide thickness on the specimens was 6-7 μm, comprising equally thick layers of Fe_3O_4 (inner) and Fe_2O_3 (outer). Corroded coupons had an uneven oxide layer, approximately 50 μm thick. Consequently it was not possible to discern any dependence of thickness on metal temperature. Typical values for the inner and outer layers were: Fe_3O_4, 15 μm; Fe_2O_3, 35 μm. An overall increase in oxide thickness of approximately 45 μm may be taken as a metal loss of around 20 μm. This is equivalent to a metal loss rate of 400 nm h^{-1} over the 50 h corrosion.

As in the case of chromium, no sulfides were detected in the corrosion scale, and the adhering melt exhibited no layered structure.

DISCUSSION

We have shown that our new spectroscopic techique is capable of determining dissolution rates for nickel, chromium and iron in molten $(Na,K,Al)SO_4$. These rates are also very much less than the rate of scale formation for nickel and iron. However, at this time we would point out that while these rates are accurate they are not yet absolute: they will be when diffusion and Soret coefficients have been determined for the experimental conditions actually used. Figure 15 shows the separate contributions of the diffusion and Soret components to the overall measured dissolution rate for nickel, at a metal temperature of 587°C, determined using best estimates from current literature values. Among our immediate future projects is the determination of these coefficients under the conditions of corrosion experiments, by a simple modification of the current experimental set-up. The relative contributions of the diffusion and Soret components in say, Figure 15, will thus soon be established, together with the absolute dissolution rate.

The results here presented are, while of the right order of magnitude, preliminary. We have, for example, earlier remarked that the spectroscopic data may be treated by another, independent, procedure to determine dissolution rates. Initial results suggest that the dissolution rates are greater than those here reported. This second approach does not include the diffusion and Soret coefficients and thus it is of prime importance that they be determined soon and accurately. However we can say that the evidence gleaned so far is likely to provide useful information concerning the role of the scale formed on the metal surface upon the dissolution rate, assuming the two approaches yield different dissolution rates, and that in future measurements will be taken, and the experiments conducted, so that there is sufficient data for both methods to determine accurately dissolution, and hence corrosion rates.

We must also record that, once this data has been determined for our extended melt layers of around 45 mm thick, it will then be possible to ascertain what is happening, and which processes predominate for thin films of 1 mm thick or less.

Comparison of Nickel, Chromium and Iron

We can, however, at this time, make a number of valid points concerning the data here presented, which are not affected by the above cautions, particularly certain

comparisons. A direct comparison of the various dissolution rates is not strictly correct, since the heat flux was some 40% greater for the nickel experiments, but the patterns of behaviour of the three metals are of interest.

For nickel, the dissolved ion concentration was related parabolically to time at all temperatures. This indicates that the concentration at each point in the melt layer experiencing the thermal gradient was diffusion controlled. This would be expected, in view of the known stability of nickel species in molten salts beyond the highest temperature experienced in the thermal gradient. The dissolution rates, expressed as metal loss rates, also increased steadily with increase in the metal temperature, the thermal gradient being kept constant at close to 100°C. The rates were also increasing with time, but since the experiments had to be terminated after 12 h it is expected that over a longer time period the rates would level off and decrease, ultimately to zero, as the melt became saturated with nickel.

In the case of chromium, where the experiments were continued for 80 h, the concentration of dissolved chromium at each point in the melt tended to a limiting value, for metal temperatures of 605°C and above. The behaviour for a metal temperature of 590°C was anomalous in that the concentration neither tended to a limiting value, nor was parabolically related to time (Figures 10 and 11). For 605-635°C, the dissolution rates were constant and virtually temperature independent, and were equivalent to a metal loss rate of 1 nm h^{-1} : at 590°C, the rate was increasing with time, reaching a value of 2.2 nm h^{-1} after 80 h. (These rates are relative, the above proviso on diffusion and Soret coefficients holds.) Two points arise.

First, there was spectral evidence for the decomposition of dissolved chromium at the high temperature end of the thermal gradient for metal temperatures of 605-635°C, but not for 590°C. Thus limiting values for the higher metal temperatures are not unexpected, since this can be related to a mechanism whereby chromium is removed from solution as the oxide at the high temperature side of the thermal gradient at approximately the same rate as it enters solution from the metal or metal scale. The results of the 590°C experiment imply that the dissolution rate continues to increase because no chromium is lost from solution at temperatures below 700°C, and the melt has not yet become saturated in chromium.

Second, the rate of diffusion of dissolved chromium species across the 45 mm molten salt layer would appear to

be quite fast since the 590°C metal temperature dissolution rate plot has not reversed direction by 80 h, which if it did, would indicate approaching saturation. (The saturation datum also needs determining for each corrosion system.) Inspection showed that the melt soon became coloured at the high temperature end. Because the 590°C experiment did not follow the parabolic rate law it is possible that it represented a transition between a diffusion controlled and a decomposition mechanism.

The results for iron demonstrate more clearly such a transition. At 590°C, the concentration increase was parabolic (Figure 12), and thus diffusion controlled. At 605°C, the behaviour was similar to that for chromium at 590°C, with concentration increase neither precisely parabolic nor tending to a limit. With metal temperatures of 620 and 635°C, the curves tended to a limiting value (Figure 13).

The dissolution rates for iron, expressed as metal loss, again showed this distinction (Figure 14). As with chromium, for metal temperatures of 605-635°C, dissolution rates were constant and essentially temperature independent, being 2.4 nm h^{-1} (cp. 1 nm h^{-1} for Cr). For iron, the rate at 590°C was less, but was steadily increasing with time from 1.8 to 2 nm h^{-1}. Thus, again, there is a rapid diffusion of iron to the melt/gas interface, but the 590°C data shows that saturation has not been reached, and if the experiment was continued for longer the rate would be expected to exceed 2.4 nm h^{-1} before beginning to decrease.

The appearance of Fe_2O_3 at the melt/gas interface in the higher temperature experiments was anticipated since the current approach to hot corrosion in steam-generating boilers postulates the dissolution of iron into the molten sulfate at the low temperature side of the thermal gradient, its transport across the gradient, and its precipitation as haematite as a consequence of decomposition at the high temperature side. This is therefore the first time that this postulate has been demonstrated.

It has been calculated (9) that the decomposition temperature for iron(III) in a sulfate melt with a flue gas containing 1% O_2 and 0.3% SO_2 is 720°C. The minimum temperature of the melt surface where decomposition was observed was around 715°C. In preparation for this result we had maintained a solution of iron(III) in molten $(Na,K,Al)SO_4$ at 805°C for six hours, but no precipitation of iron oxide was observed. However, as the brown ring was not observed in the corrosion experiment, which was continued for 50 h, until towards the end of the experiment

we conclude that the rate of decomposition is slow. We also note that the concentration of iron in the melt approaches a limiting value after about 20 h (Figure 13).

The contribution of dissolution to overall corrosion rate varied considerably between metals. For nickel, metal loss by scale formation was several orders of magnitude greater than that by dissolution, 7000 compared with 15 nm h^{-1} respectively. Nickel was unique in that the corrosion scale contained sulfide as well as oxide. In the case of chromium, with a very thin initial oxide layer, and no subsequently detectable scale formation the dissolution rate can be taken as the total corrosion rate. For iron, oxide scale formation contributed the major portion of the total metal loss, typical values of metal loss from scale formation being 400 nm h^{-1} and 2.5 nm h^{-1} for dissolution.

The measurement of corrosion rates for the pure metals, nickel, chromium and iron, by electrochemical methods have not been reported. A comparison is therefore made with rates obtained for a number of alloys used in superheater and turbine blade construction.

The corrosion of the nickel-based alloy Nimonic 105 in the $(Li,Na,K)SO_4$ eutectic has been observed (10,11) in the temperature range 700-900°C, and corrosion rates between 10 and 100 nm h^{-1} were obtained over periods up to 100 h. Another nickel-based alloy, IN738, in the same melt at 820°C gave corrosion rates of approximately 10 nm h^{-1} after 100 h.

An austenitic stainless steel, containing 18% Cr and 8% Ni has been investigated by a number of workers (10,12-14). Again, using the $(Li,Na,K)SO_4$ rates varying between 100 and 1000 nm h^{-1} have been reported for tests of up to 1000 h.

The overall corrosion rate of 400 nm h^{-1} obtained for iron in this study is in reasonably good agreement with those rates for 18Cr-8Ni steel, measured by electrochemical methods. No comparison can be drawn for the chromium values here reported, since no other data for chromium-based alloys are available. The scaling rate of 7000 nm h^{-1} for nickel is an order of magnitude greater than the corrosion rates reported for the nickel-based alloys. This disparity may be attributed to the passivating effect of the other constituents, especially chromium, of the alloys.

We now have a data bank of the individual spectra of the various transition metal species in $(Na,K,Al)SO_4$ over a

representative range of conditions. Our next stage is therefore to examine the corrosion of various stainless steels in this melt and, using a computer program, deconvolute the spectra into those of the component species, and hence obtain their relative and absolute concentrations. Comparisons with the alloy composition will yield important information on the nature of corrosion attack.

Precipitate Formation During Nickel Dissolution

The behavior of nickel was anomalous in two ways. First, a precipitate was formed in the bulk melt during the experiments, and second, an aluminum-rich layer was present in the melt adjacent to the oxide-sulfide scale. Neither of these features was exhibited by chromium or iron.

The failure of X-ray diffraction to identify the insoluble white residue does not preclude the possibility of it being Al_2O_3. Fourteen different Al_2O_3 structures are listed in the search-file used for the analysis, and it may be that Al_2O_3 adopts an unlisted structure when formed under these conditions, or that it has a complex combination of modifications which make identification impossible. The presence of patterns similar to those for mixed sulfates may imply incorporation or occlusion of such species, which subsequently cannot be leached out, during the precipitate formation in the melt. Alternatively, the precipitate may be an insoluble aluminum sulfate mineral, of which a number exist. Efforts to identify definitively the residue are proceeding.

When considering the aluminum-rich layer in the melt adjacent to the corrosion scale, it should be stressed that the layer is on both the upper and under surfaces of the coupon (Figure 7), and is therefore not a result of settlement by the precipitate from the bulk melt. Assuming that the precipitate in the bulk melt, and the aluminum component of the 0.2 mm thick layer adjacent to the corrosion scale are both Al_2O_3, then two possible mechanisms may be proposed to explain their formation.

The first of these suggests that the decomposition of the melt is catalysed by the dissolved nickel ions, since similar behaviour is not observed for chromium and iron. If this is so, then the high, local dissolved nickel concentration at the scale/melt interface would give rise to the aluminum-rich layer observed. The lower nickel concentration in the bulk melt would also result in precipitate formation, but to a lesser extent than at the surface. This cannot be the complete story, since solutions of Ni(II) in fused $(Na,K,Al)SO_4$ were stable for

hours.

A second view is that the greater solubility of nickel oxide in this melt, as compared with chromium and iron oxides, gives sufficient oxide ion concentrations to precipitate Al_2O_3. Again, high local oxide activities explain the aluminum-rich layer at the scale/melt interface. Experiments in which oxide ions (as Na_2O) were added to $(Na,K,Al)SO_4$ resulted in the immediate formation of a precipitate, which was identified successfully as Al_2O_3 by elemental analysis.

These mechanisms are not mutually exclusive, and on the contrary, dissolution of the oxide scale would lead to increases in both dissolved nickel and oxide activities. Thus both processes may be taking place.

However, these are more likely additions to the main corrosion mechanism which offer an explanation for the nickel- and aluminum-rich layer. When corrosion is considered in terms of the electrode processes taking place the anodic oxidation of the metal, M, is represented as:

$$M \longrightarrow M^{2+} + 2e^- \qquad \text{(eqn. 1)}$$

(the metal is assumed for simplicity to be divalent). The corresponding cathodic reductions of SO_4^{2-} and SO_3 are:

$$SO_4^{2-} + 8e^- \longrightarrow S^{2-} + 4O^{2-} \qquad \text{(eqn. 2)}$$

and $$SO_3 + 8e^- \longrightarrow S^{2-} + 3O^{2-} \qquad \text{(eqn. 3)}$$

the reduction of SO_3 occurring at smaller negative potentials than that of SO_4^{2-}. SO_3 is present in the melt from the acid-base equilibrium

$$SO_4^{2-} \rightleftharpoons SO_3 + O^{2-} \qquad \text{(eqn. 4)}$$

which is thus a source of oxide ions, and from the flue gas, as it is very soluble in sulfate melts, forming pyrosulfates,

$$SO_4^{2-} + SO_3 \rightleftharpoons S_2O_7^{2-} \qquad \text{(eqn. 5)}$$

It is also rapidly transported through the melt via bond rearrangement, a mechanism analogous to the Grotthus mechanism for the transport of protons in water.

Thus in view of the extensive corrosion of nickel, and the appearance of oxide and sulfide layers of approximately equal thickness (Figure 8), while the the reduction of SO_4^{2-} and SO_3 (eqns. 2 and 3) yield four and three times,

respectively, the number of oxide ions as sulfide ions, there is thus an adequate source of sufficient oxide ions to cause the precipitation of Al_2O_3 from the bulk melt.

Sulfidation of Nickel

The sulfidation process has been discussed (10) in terms of the equilibria

$$SO_3 \rightleftharpoons SO_2 + \tfrac{1}{2}O_2 \qquad \text{(eqn. 6)}$$

and

$$SO_2 \rightleftharpoons \tfrac{1}{2}S_2 + O_2 \qquad \text{(eqn. 7)}$$

at the oxide/melt interface, which give rise to fluxes of oxygen and sulfur into the scale. Corresponding fluxes of metal cations from the metal/oxide interface result in the formation of a mixed oxide and sulfide scale.

In this study, alternate layers of oxide and sulfide were observed. Additionally, the rate of scale formation was too great to be sustained by ion transport across the scale. It is proposed, therefore, that the mechanism in this case involves the vapour phase penetration of the porous, initial oxide layer, so that the equilibria in eqns. 6 and 7 may take place, initially, beneath the oxide layer. Assuming that further oxide formation takes place at this interface, a high local sulfur activity will be generated (eqn. 7). The newly formed oxide layer is then penetrated by the sulfur, to form a sulfide layer between the metal and the oxide. This in turn increases the oxygen partial pressure, and thus a new oxide layer is formed beneath the sulfide. The mechanism for the formation of alternating oxide and sulfide layers thus proceeds, and the rate of scale formation at any instant depends only on diffusion across the most recently formed layer.

Nature of Evolved Gas

The observation of gas evolution from the oxide/melt interface almost as soon as the metal coupon was introduced into the molten sulfate is, as far as we are aware, new. The synthetic flue gas had been passed over the melt surface for some before the introduction, and thus there would be some pyrosulfate (eqn. 5) in the melt. The most likely candidates for the gas are sulfur dioxide and oxygen, since both have very low solubilities in molten salts (reported (10) as approximately 10^{-7} mol cm^{-3} atm^{-1}). The former probably predominates, since it can be formed from reduction of SO_3. Although difficult to reconcile with an 'oxidation' process, the evolution of oxygen cannot be ruled out: it may arise from the cathodic process

$$SO_4^{2-} \longrightarrow SO_3 + \tfrac{1}{2}O_2 + 2e^- \qquad \text{(eqn. 8)}$$

The reaction $O^{2-} \rightarrow \tfrac{1}{2}O_2 + 2e^-$ seems unlikely in view of the formation of stable alumina.

Radio-chemical experiments are currently under consideration as a means of identifying the components of the gas.

CONCLUSIONS

We have successfully tested and proved a new spectroscopic technique which can determine accurately the rate of hot corrosion of a metal under an applied thermal gradient, and other conditions which replicate more closely the industrial situation than any previous technique.

We would, however, stress that the dissolution rates here reported, which at times appear to be increasing with time, particularly in the case of nickel, are a consequence of the application of the Tyrrell (4) flux equation we have employed. A parabolic decrease with time is the normal expectation and there is evidence that this applies in these experiments excepting those in which precipitation of corrosion products took place at the melt/gas interface.

Thus we are now essentially at the stage where we can say to a manufacturer or user of alloys subject to hot corrosion: tell us the temperature of the alloy at which you want its hot corrosion studied, the composition (or range of compositions) of the aggressive molten salt, the probable thermal gradient and approximate composition of the flux gas - and we will tell you the corrosion rate, plus a lot more information concerning the nature of the corrosion products (this latter is the subject of our second paper).

ACKNOWLEDGEMENTS

We thank Dr. D. Mortimer, Head of the Combustion and Corrosion Division, Scientific Services Division, Central Electricity Generating Board, Harrogate, North Yorkshire, and his colleagues, for valued discussions, and C. Plowman for the X-ray diffraction studies. We also thank the Board for SEM and EMPA facilities and K.K. acknowledges a CASE Research Studentship with the Board and the Science Research Council.

REFERENCES

1. A. Hendry and D.J. Lees, Corrosion Science, 20, 383 (1980).
2. T.R. Griffiths and K. King, submitted to J.C.S. Faraday I.
3. A.G. Turnbull, Aust. J. Appl. Sci., 12, 324 (1961).
4. H.J.V. Tyrrell, 'Diffusion and Heat Flow in Liquids', Butterworths, London (1961).
5. D. Inman, D. Jovanovic and S.H. White, Electroanal. Chem. Interfacial Electrochem., 43, 37 (1973).
6. G.J. Janz, 'Molten Salts Handbook', Academic Press (1967).
7. V. Backlund, J. Dupuy, S. Gustafsson and A. Luden, Z. Naturforsch., A22, 471 (1967).
8. A.J.B. Cutler, J. Appl. Electrochem., 1, 19 (1971).
9. A. Hendry and D.J. Lees, Corrosion Science, 20, 383 (1980).
10. A.J.B. Cutler and C.J. Grant, in 'Metal-Slag-Gas Reactions and Processes', Eds. Z.A. Foroulis and W.W. Smeltzer, The Electrochemical Soc., Princeton, N.J. (1975).
11. C.J. Grant, private communication.
12. A.J.B. Cutler and C.J. Grant, 'Metal-Slag-Gas Reactions and Processes', Eds. Z.A. Foroulis and W.W. Smeltzer, The Electrochemical Soc., Princeton, N.J. (1975).
13. A.J.B. Cutler, J. Appl. Electrochem., 1, 19 (1971).
14. A.J.B. Cutler and C.J. Grant, private communication.

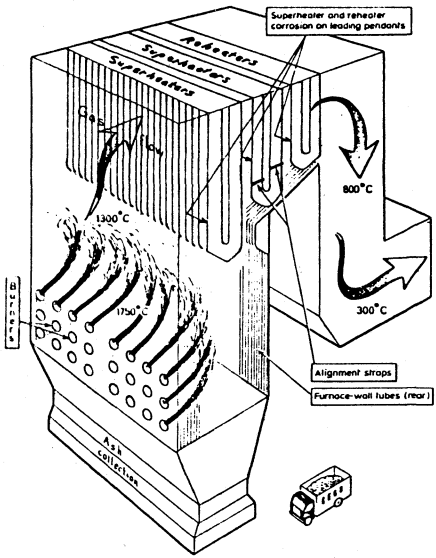

Figure 1: Schematic diagram of a front-fired boiler. The regions most susceptible to hot corrosion are the leading pendants of the superheater and reheater tubes.

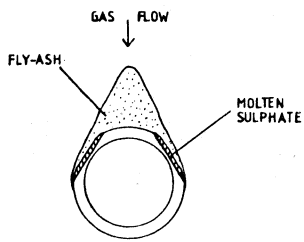

Figure 2: Superheater and reheater corrosion profile.

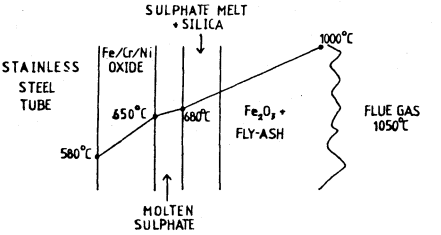

Figure 3: The structure of scale and deposits on superheater tubing and the temperature gradients within them.

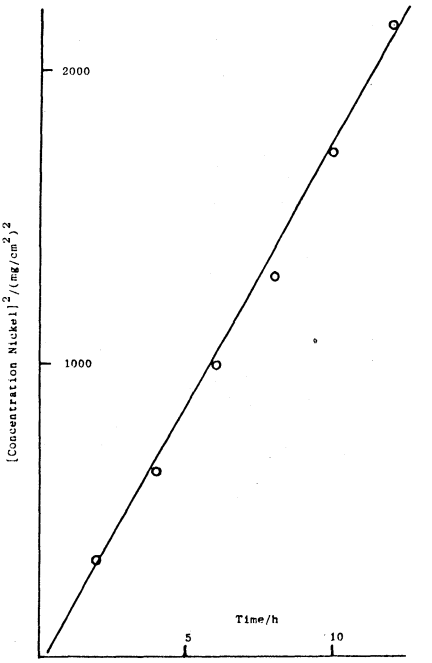

Figure 4: Plot showing concentration of nickel dissolved increases parabolically with time.

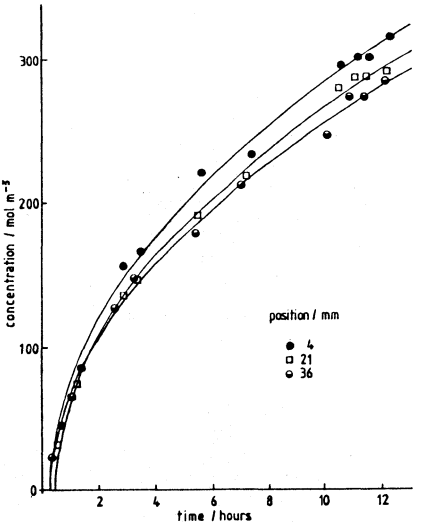

Figure 5: Time dependence of dissolved nickel at different positions above nickel coupon in $(Na,K,Al)SO_4$. Metal temperature 606°C; thermal gradient 35 K cm^{-1}; curves are least-squares parabolic fits.

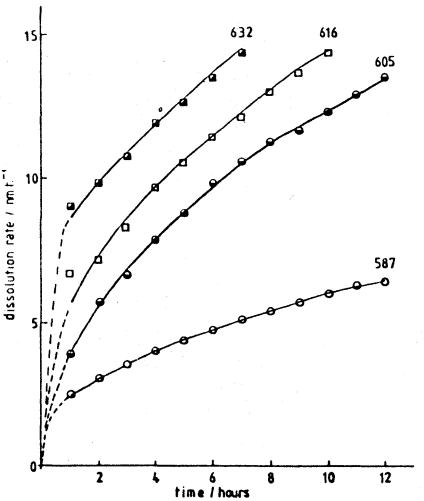

Figure 6: Dissolution rates for nickel at the four metal temperatures (°C) examined.

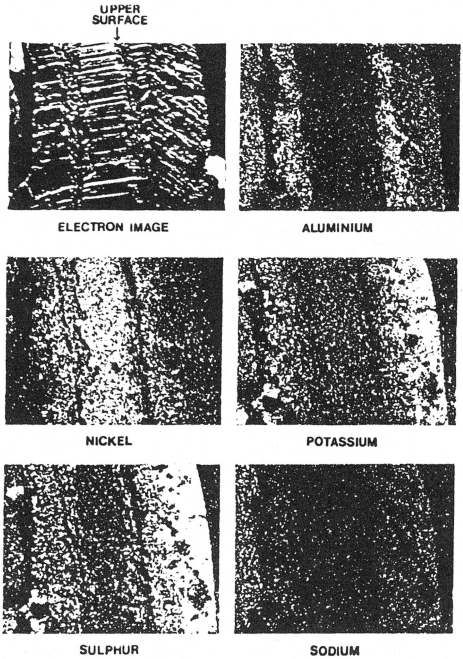

Figure 7: Electron microprobe analysis of corroded nickel coupon and adhering melt, from experiment at 616°C. Magnification x25.

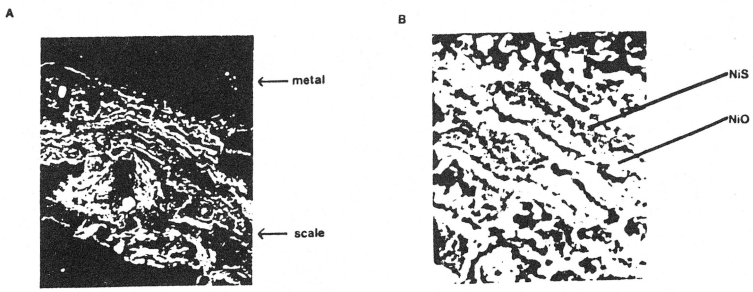

Figure 8: Magnified SEM images of scale adjacent to metal surface for nickel coupon in Figure 7. A, magnification x860; B, magnification x3600.

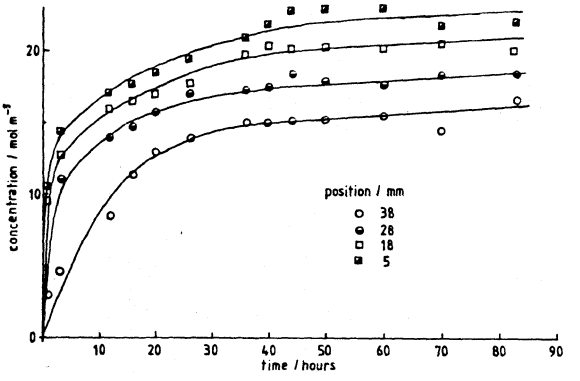

Figure 9: Change of dissolved chromium concentration with time at different positions above chromium coupon in $(Na,K,Al)SO_4$. Metal temperature 620°C; thermal gradient 24 K cm^{-1}

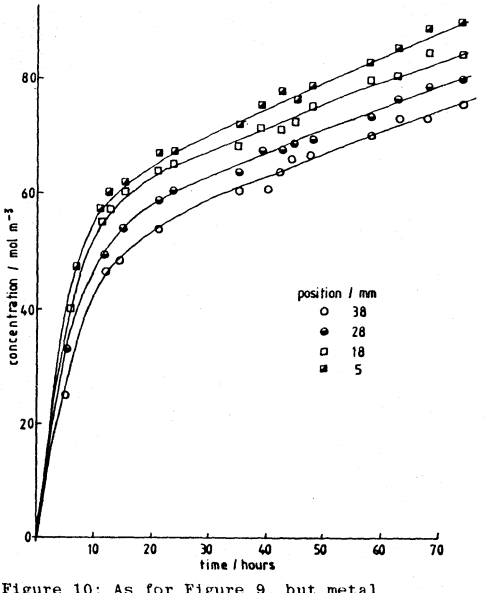

Figure 10: As for Figure 9, but metal temperature 590°C.

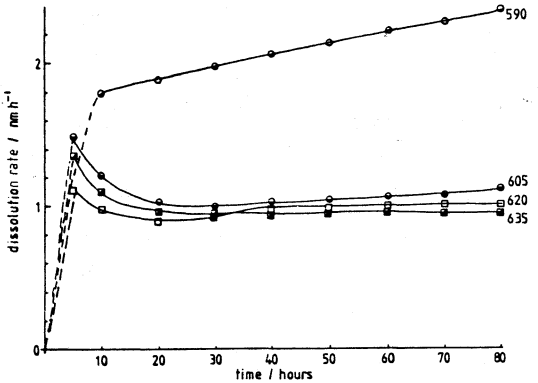

Figure 11: Dissolution rates for chromium at the four metal temperatures (°C) examined.

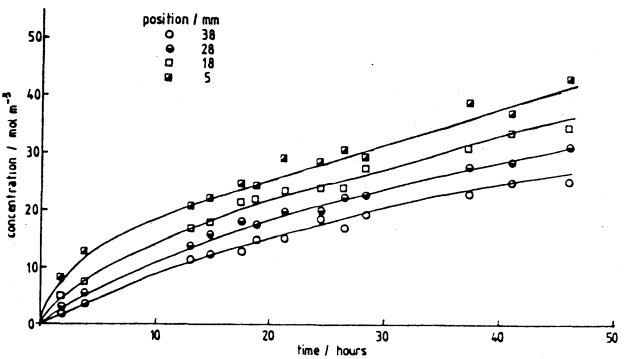

Figure 12: Change of dissolved iron concentration with time at different positions above iron coupon in $(Na,K,Al)SO_4$. Metal temperature 590°C thermal gradient 24 K cm^{-1}.

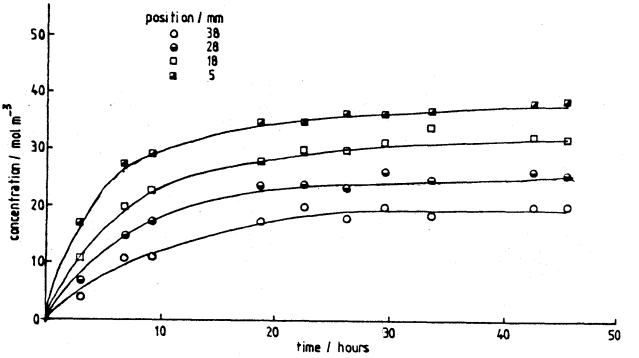

Figure 13: As for Figure 12, but metal temperature 635°C.

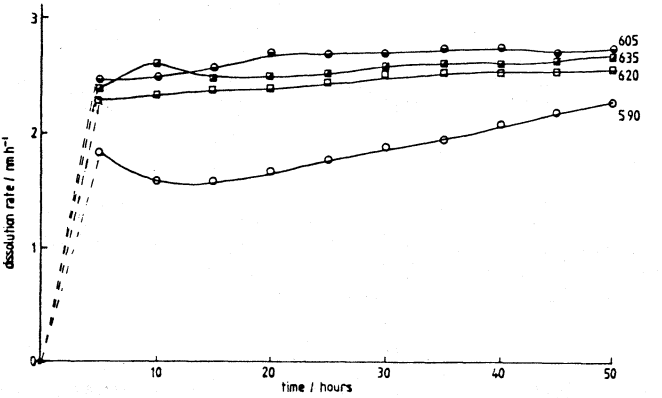

Figure 14: Dissolution rates for iron at the four metal temperatures (°C) examined.

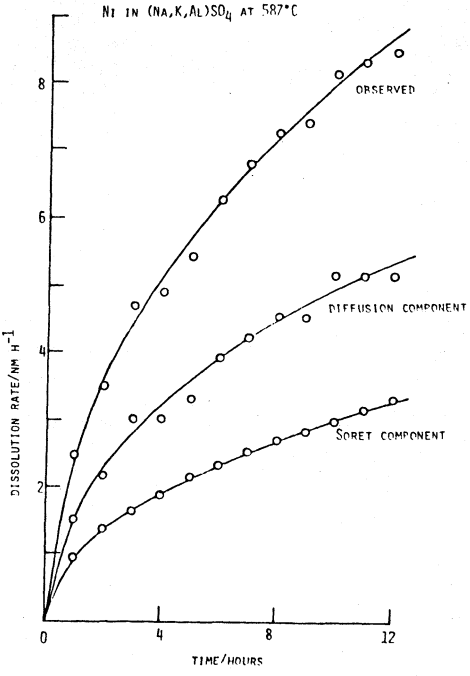

Figure 15: Diffusion and Soret components of nickel dissolution.

DOI: 10.1149/198109.0376PV

SOLUBILITY PRODUCTS OF NICKEL AND COBALT OXIDES IN MOLTEN NaCl AND Na_2SO_4 BY COULOMETRIC TITRATION OF OXIDE ION THROUGH ZIRCONIA ELECTRODES

M. L. Deanhardt and K. H. Stern
Chemistry Department, George Mason University, Fairfax, VA., 22030, and Chemistry Division, Naval Research Laboratory, Washington, D.C. 20375

ABSTRACT

Solubility products of nickel and cobalt oxides in molten NaCl (1100 K) and Na_2SO_4 (1200 K) have been measured by coulometric titration of the respective chlorides ($NiCl_2$, $CoCl_2$) and sulfates ($NiSO_4$, $CoSO_4$) with electrochemically generated oxide ion, using a stabilized zirconia electrode as an oxide pump. Values obtained are compared with those derived from thermodynamic calculations. The metal oxide equilibria were complicated by competitive paths leading to Na_2O_2, $NaNiO_2$ and $NaCoO_2$ formation.

A knowledge of the behavior of metal oxides in molten salts is important in understanding corrosion processes in marine-operated gas turbines, molten salt fuel cells and batteries, salt processing baths, and solar energy storage by molten salts. Measurement of the solubility of metal oxides used as protective coatings in such systems is needed. This information should aid in the development of new materials and in the prevention of hot corrosion.

Recent studies (1,2) have shown that stabilized zirconia (SZ), an oxide-conducting solid electrolyte, can function as an O^{2-} ion pump in molten NaCl at 1100 K and Na_2SO_4 at 1200 K. By applying a voltage to the cell

$$\text{Pt} \mid \text{Melt} \mid \underset{(Na^+)}{\text{Mullite}} \mid \underset{+\ Na_2O}{\text{Melt}} \mid \text{SZ} \mid O_2(\text{Pt}), \qquad [1]$$

the O^{2-} ion concentration of the melt under study may be increased or decreased by driving the reaction at the O_2 electrode,

$$1/2\ O_2 + 2e^- \rightleftarrows O^{2-}\ (\text{in melt}) \qquad [2]$$

left or right. The O^{2-} activity in the melt is measured potentiometrically with another SZ electrode using the cell

$$Ag \left| \begin{matrix} \text{Melt} + \\ AgCl \text{ or } Ag_2SO_4(10 \text{ m/o}) \end{matrix} \right| \begin{matrix} \text{Mullite} \\ (Na^+) \end{matrix} \left| \begin{matrix} \text{Melt} + \\ Na_2O \end{matrix} \right| SZ \left| O_2(Pt) \right. . \quad [3]$$

The reaction and emf of cell 3 in molten NaCl are

$$2\ Ag(s) + 1/2\ O_2(g) + 2\ NaCl(\ell) \rightleftarrows 2\ AgCl(\ell) + Na_2O(\ell) \quad [4]$$

$$E_{cell} = E^\circ - \frac{RT}{2F} \ell n \left(\frac{a^2_{AgCl} a_{Na_2O}}{p^{1/2}_{O_2} a^2_{NaCl}} \right) \quad [5]$$

Similarly, the reaction and emf of cell 3 in molten Na_2SO_4 are

$$2\ Ag(s) + 1/2\ O_2(g) + Na_2SO_4(\ell) = Ag_2SO_4(\ell) + Na_2O(\ell) \quad [6]$$

$$E_{cell} = E^\circ - \frac{RT}{2F} \ell n \left(\frac{a_{Ag_2SO_4} a_{Na_2O}}{p^{1/2}_{O_2} a_{Na_2SO_4}} \right) . \quad [7]$$

The SZ electrode in cell 1 (referred to as the generating electrode) serves as an O^{2-} ion source, while the SZ electrode in cell 3 (referred to as the indicating electrode) serves as an O^{2-} ion monitor.

It is known (3-5) that in Na_2O-NaCl and Na_2O-Na_2SO_4 melts, oxide is partially converted to peroxide according to the following reaction:

$$Na_2O + 1/2\ O_2 \rightleftarrows Na_2O_2. \quad [8]$$

At constant O_2 pressure,

$$[Na_2O_2] / [Na_2O] = K_{e_1} p^{1/2}_{O_2} = K'_{e_1} \quad [9]$$

where the brackets denote mole fractions. Cell 3 responds only to changes in the activity of Na_2O in the melt. The following relationships between the measured emf in equations 5 and 7 and equivalents of charge Q passed through cell 1 have been derived and verified (2):

1. Electrolysis of Na_2O into the Melt

$$E_{cell} = E^{\circ\prime} - \frac{RT}{2F} \ell n \left([Na_2O]_o + \frac{Q}{2n(K'_{e_1}+1)} \right) \qquad [10]$$

2. Electrolysis of Na_2O out of the Melt

$$E_{cell} = E^{\circ\prime} - \frac{RT}{2F} \ell n \left[([Na_2O]_a - \frac{Q}{2n})/(K'_{e_1} + 1) \right] \qquad [11]$$

where $E^{\circ\prime} = E^{\circ} - \frac{RT}{2F} \ell n \left(\frac{\gamma_{Na_2O} a^2_{AgCl}}{p^{1/2}_{O_2} a^2_{NaCl}} \right)$ for NaCl,

$$E^{\circ\prime} = E^{\circ} - \frac{RT}{2F} \ell n \left(\frac{\gamma_{Na_2O} a_{Ag_2SO_4}}{p^{1/2}_{O_2} a_{Na_2SO_4}} \right)$$ for Na_2SO_4,

where

n = total number of moles,

γ_{Na_2O} = activity coefficient of Na_2O,

$[Na_2O]_o$ = initial (impurity) concentration of Na_2O,

$[Na_2O]_a$ = added concentration of Na_2O.

It is assumed that the electrolysis is slow enough that the oxide/peroxide equilibrium (equation 8) is maintained at all times.

In the present work, this technique has been applied to the measurement of the solubility products of NiO and Co_3O_4 in NaCl at 1100 K, and NiO and CoO in Na_2SO_4 at 1200 K. Solubility products were determined via coulometric titration curves in which the charge passed through the generating SZ electrode was measured as a function of the emf of the indicating cell 3. Oxygen pressure above the melts was ~0.2 atm. Gupta and Rapp (6) recently measured the solubility of nickel and cobalt oxide in molten Na_2SO_4 as a function of salt basicity (log a_{Na_2O}).

Results from their work as well as results from thermodynamic data are compared with the results in this study.

Experimental

Experiments were carried out in a helium-oxygen-filled (20% O_2) dry box (Vacuum/Atmospheres Corp.) with recirculating dry train in which moisture and CO_2 were generally kept below 1 ppm. The electrodes, cell design, and experimental techniques have been described elsewhere (1,2). High purity (99.8%) alumina crucibles were used in all experiments.

Reagents - Reagent grade NaCl and Na_2SO_4 were vacuum-dried at 500°C before use. Anhydrous $NiCl_2$, $CoCl_2$, and reagent grade Na_2O (Alfa Inorganics) were used without pretreatment. Anhydrous $NiSO_4$ and $CoSO_4$ were prepared from reagent grade hydrate salts using a procedure described by Sanderson (7). The prepared salts were analyzed for purity by atomic absorption analysis of Ni and Co. All weighings and transfer operations were carried out in the dry box in which the experiments were done.

Procedures - The emf of cell 3 was measured with a high impedance electrometer (Keithley model 616). Cathodic potentials were applied to the generating SZ electrode using a PAR 173 potentiostat/galvanostat. Charge passed through cell 1 was measured with a PAR 179 digital coulometer. Since the coulometric titrations were generally run overnight, charge passed and emfs measured were recorded automatically on a Fluke 2200B datalogger.

Least squares fits of the experimental data were calculated using a Hewlett Packard model 9815S computer and its associated software. The titration curves were plotted with a Hewlett Packard model 9865A digital plotter interfaced to the 9815S computer.

The melts were analyzed for their Co and Ni content before each titration. Samples were taken by dipping cold ceramic rods into the melt. The quenched-melt samples were analyzed by atomic absorption using a Perkin Elmer model 360 spectrophotometer.

Results

The total number of moles of Na_2O added to a NaCl or Na_2SO_4 melt was determined by measuring the charge passed

through the generating SZ electrode. The indicating SZ electrode, which monitors the unreacted oxide ion in the melt, responds only to the activity of sodium oxide. In order to measure the solubility products of nickel and cobalt oxides in terms of mole fractions, it is necessary to know the activity coefficient of Na_2O in these systems. These are taken from reference 8.

Solubility products of nickel and cobalt oxides - The metal ion was added to the melt as $NiCl_2$ and $CoCl_2$, respectively, in NaCl, and as $NiSO_4$ and $CoSO_4$ in Na_2SO_4. As O^{2-} is coulometrically added to the melt, the insoluble metal oxide precipitates. A plot of emf vs. Q results in a typical titration curve as shown in Figures 1-4. The reduction of oxygen to oxide could be carried out by either controlled potential electrolysis or controlled current electrolysis. In either case, care was taken not to exceed the electrolysis potential at which zirconia is reduced to substiochiometric ZrO_2 (2). A typical titration took ~24 hours at an electrolysis current of ~2.5 ma and a total Q of ~2000 μeq.

Two stable forms of nickel oxide exist in both molten NaCl and Na_2SO_4. In acidic melts (low oxide activity), the predominant form of nickel is NiO. Before the endpoint of each titration, the oxide activity remains low due to the following reactions:

$$NiCl_2 + Na_2O \rightleftarrows 2\ NaCl + NiO \qquad [12]$$

$$NiSO_4 + Na_2O \rightleftarrows NiO + Na_2SO_4 \qquad [13]$$

After all of the nickel precipitates as NiO, the melt becomes basic (high oxide activity). In basic melts, NiO reacts with Na_2O and O_2 to form $NaNiO_2$ (6):

$$Na_2O + 2\ NiO + 1/2\ O_2 \rightleftarrows 2\ NaNiO_2 \qquad [14]$$

(The presence of Na_2NiO_2 in the melt is unlikely, especially in the presence of oxygen. Using thermodynamic data in Table II, the equilibrium constant for the reaction,

$$Na_2NiO_2 + 1/4\ O_2 \rightleftarrows NaNiO_2 + 1/2\ Na_2O, \qquad [15]$$

is 4.4×10^2 at 1100 K and 1.6×10^2 at 1200 K. At the oxygen pressures and Na_2O activities encountered during the titrations, the activity ratio of $NaNiO_2$ to Na_2NiO_2 would be greater than 10^5.)

The form of cobalt in acidic melts depends on the temperature and oxygen pressure according to the following equilibrium:

$$3\ CoO + 1/2\ O_2 \rightleftarrows Co_3O_4. \qquad [16]$$

Using thermodynamic data in Table I, the equilibrium pressures of oxygen, p_{O_2}, at 1100 and 1200 K are 0.015 and 0.55 atm, respectively. At 1100 K and 0.2 atm O_2, the stable form of cobalt oxide is Co_3O_4:

$$CoCl_2 + Na_2O + 1/6\ O_2 \rightleftarrows 1/3\ Co_3O_5 + 2\ NaCl. \qquad [17]$$

At 1200 K and 0.2 atm O_2, the stable form of cobalt oxide is CoO:

$$CoSO_4 + Na_2O \rightleftarrows CoO + Na_2SO_4. \qquad [18]$$

In basic melts (past the endpoint), cobalt oxide reacts with Na_2O and O_2 to form sodium cobaltate, $NaCoO_2$, as indicated in the following equations:

$$Na_2O + 2/3\ Co_3O_4 + 1/6\ O_2 \rightleftarrows 2\ NaCoO_2, \qquad [19]$$

$$Na_2O + 2\ CoO + 1/2\ O_2 \rightleftarrows 2\ NaCoO_2. \qquad [20]$$

As sodium oxide is added coulometrically to each melt, three equilibria are established. For example, in the case of molten NaCl, the equilibria are represented by equations 8, 12, and 14. Each titration curve can be derived theoretically by considering all three equilibria simultaneously. For brevity, theoretical calculations will be discussed below only for the case of nickel in molten NaCl.

The K_{sp} is defined in terms of the equilibrium constant for reaction 12, viz.

$$K_{sp} = 1/K_{12} = [Na_2O]\,[NiCl_2] \qquad [21]$$

and the equilibrium constant for reaction 14 is

$$K'_{e_2} = K_{e_2}\, p_{O_2}^{1/2} = [NaNiO_2]^2 / [Na_2O]. \qquad [22]$$

The equilibrium constant for reaction 8 is defined in equation 9. Letting Q equal the number of equivalents of charge passed through cell 1, the amount of oxide that reacts to form NiO, Na_2O_2, and $NaNiO_2$ at equilibrium is $Q/2n - [Na_2O]$. It is assumed that the initial Na_2O

concentration in the melt is negligible. The amount of NiO formed is $[NiCl_2]_o - [NiCl_2]$, where $[NiCl_2]_o$ is the initial concentration of $NiCl_2$. Combining these two relationships results in the following equation:

$$Q/2n - [Na_2O] = [NiCl_2]_o - [NiCl_2] + [Na_2O_2] + 1/2\ [NaNiO_2]. \quad [23]$$

Substitution of equations 8, 21, and 22 into equation 23 yields

$$Q/2n - [NiCl_2]_o = -K_{sp}(1/[Na_2O]) + (K'_{e_1} + 1)([Na_2O]) + K'^{1/2}_{e_2} ([Na_2O]^{1/2}/2). \quad [24]$$

The relationship between $[Na_2O]$ and the emf of cell 3 can be calculated from equation 5 and the activity coefficient of Na_2O:

$$[Na_2O] = \exp\left\{\frac{2F}{RT}(E^{o'} - E_{cell})\right\}. \quad [25]$$

Substitution of equation 25 into equation 24 gives the E_{cell} - Q relationship for the titration of $NiCl_2$ with Na_2O in molten NaCl:

$$Q/2n - [NiCl_2]_o = -K_{sp}\left[\exp\left\{\frac{2F}{RT}(E^{o'} - E_{cell})\right\}\right]^{-1} + (K'_{e_1} + 1)\left[\exp\left\{\frac{2F}{RT}(E^{o'} - E_{cell})\right\}\right] + K'^{1/2}_{e_2}\left[\exp\left\{\frac{F}{RT}(E^{o'} - E_{cell})\right\} / 2\right]. \quad [26]$$

The three equilibrium constants in equation 26 were calculated for each titration by multiple regression analysis (14) of the E_{cell} - Q data. Results are listed in Table II. Equilibrium constants are defined in terms of mole fractions. The numbers in parentheses indicate the range of the data from a total of 16 titrations. Equilibrium constants calculated in this manner were used to plot the titration curves labeled A in Figures 1-4. In addition, multiple regression analyses were used to determine K_{sp} values assuming no peroxide, nickelate, or cobaltate formation (i.e., $K_{e_1} = K_{e_2} = 0$). Curves labeled B in Figures 1-4 were calculated from these data.

Also included in Table II are equilibrium constants calculated from thermodynamic data in Table I. There are no data reported in the literature for $(\Delta G°_f)_{NaCoO_2}$. In order to carry out the calculations, we have assumed that $(\Delta G°_f)_{NaCoO_2} = (\Delta G°_f)_{NaNiO_2}$.

Activity coefficients of soluble salts of nickel and cobalt - The data in Table III were used to calculate the activity coefficients of the soluble salts of nickel and cobalt in the two melts. The calculated values along with literature values are given in Table III. The standard states for the salts are the pure solids (pure liquid for $CoCl_2$) and therefore the activity coefficients measure deviations from Raoult's law. The activity coefficient for $NaCoO_2$ in both NaCl and Na_2SO_4 is based on the assumption that $(\Delta G°_f)_{NaCoO_2} = (\Delta G°_f)_{NaNiO_2}$.

Discussion

The data in Table II indicates that the major reaction of Na_2O in the melts is formation of the insoluble metal oxides: NiO, Co_3O_4, and CoO. The competing equilibria (i.e., peroxide, nickelate or cobaltate formation) are not significant before the endpoints of the titrations. This is borne out by curves A and B in Figures 1-4. Curve A (competing equilibria assumed) and B (competing equilibria ignored) are identical before the endpoint of a titration.

The titration curves in Figures 1-4 strongly suggest that competing equilibria exist in these systems. The Na_2O activities after the endpoints are considerably lower than one would expect based only on metal oxide formation. Formation of peroxide and nickelate or cobaltate would indeed lower the activity of Na_2O after the titration endpoint. Confirmation of Na_2O_2 in NaCl and Na_2SO_4 and $NaNiO_2$ in Na_2SO_4 have been reported in the literature (3,4,6).

The measured activity coefficients for $NiCl_2$ and $CoCl_2$ in molten NaCl (Table III) agree very well with values reported by Hamby and Scott (15,16). Comparable values of the activity coefficients of $NaNiO_2$ and $NaCoO_2$ in molten NaCl were not available in the literature. The measured activity coefficients of soluble salts of nickel and cobalt in molten Na_2SO_4 were compared with data of Gupta

and Rapp (6). In order to compare the activity coefficients for $NaNiO_2$ with the value obtained by Gupta and Rapp, their value of $\Delta G°_f$ was changed to that used in this work. Good agreement occurs for the activity coefficients of $NaNiO_2$ and $NaCoO_2$; however, our activity coefficients for $NiSO_4$ and $CoSO_4$ were at least a factor of ten lower than those reported by Gupta and Rapp.

Conclusions

The results of this study clearly show that the SZ electrode can be used to determine the solubility products of metal oxides in molten salts. Solubility products of NiO and CoO (Co_3O_4 in molten NaCl) have been determined in molten NaCl and Na_2SO_4 as have equilibrium constants of competing equilibria leading to the formation of Na_2O_2, $NaNiO_2$, and $NaCoO_2$. Activity coefficients of soluble salts of nickel and cobalt were also calculated and compared with literature values.

References

1. K. H. Stern, J. Electrochem. Soc. 127, 2375 (1980).
2. M. L. Deanhardt and K. H. Stern, J. Phys. Chem. 84, 2831 (1980).
3. K. H. Stern, Rm. Panayappan, and D. R. Flinn, J. Electrochem. Soc., 124, 641 (1977).
4. K. H. Stern, M. L. Deanhardt, and Rm. Panayappan, J. Phys. Chem., 83, 2848 (1979).
5. M. L. Deanhardt and K. H. Stern, J. Electrochem. Soc. (Dec. 1980).
6. D. K. Gupta and R. A. Rapp, J. Electrochem. Soc., 127, 2194 (1980).
7. R. T. Sanderson, J. Chem. Ed., 29, 539 (1952).
8. K. H. Stern, Electrochim. Acta, 24, 509 (1979).
9. G. J. Janz and Chr. G. M. Dijkhuis, Molten Salts: Vol. 2, Nat. Stand. Ref. Data Ser., Nat. Bur. Stand., 28 (1969).

10. K. K. Kelley, Contributions to the Data on Theoretical Metallurgy, U.S. Dept. of the Interior, Bureau of Mines, Bulletin 406 (1937).

11. JANAF Thermochemical Tables, 2nd Ed., Nat. Stand. Ref. Data Serv., Nat. Bur. Stand., 37 (1971) and 1974, 1975, 1978 Supplements.

12. B. J. Shaiu, P. C. S. Wu, and P. Chiotti, J. of Nucl. Mat., 67, 13 (1977).

13. A. D. Mah and L. B. Pankratz, Contributions to the Data on Theoretical Metallurgy, U.S. Dept. of the Interior, Bureau of Mines, Bulletin 668 (1976).

14. W. J. Dixon and F. J. Massey, Jr., "Introduction to Statistical Analysis," McGraw-Hill, N.Y., 212 (1969).

15. D. C. Hamby and A. B. Scott, J. Electrochem. Soc., 115, 704 (1968).

16. D. C. Hamby and A. B. Scott, J. Electrochem. Soc., 117, 319 (1970).

TABLE I. THERMODYNAMIC DATA

Compound	ΔG_f° (1100 K) kJ/mole	ΔG_f° (1200 K) kJ/mole	Reference
AgCl (ℓ)	-7.33×10^1		9
Ag_3SO_4 (ℓ)		-3.33×10^2	10
$CoCl_2$ (ℓ)	-1.70×10^2		11
CoO (s)	-1.56×10^2	-1.50×10^2	11
Co_3O_4 (s)	-4.89×10^2	-4.51×10^2	11
$CoSO_4$ (s)		-4.45×10^2	11
NaCl (ℓ)	-3.11×10^2		11
$NaNiO_2$ (s)	-3.19×10^2	-3.00×10^2	12
Na_2NiO_2 (s)	-3.97×10^2	-3.74×10^2	12
Na_2O (s)	-2.67×10^2	-2.50×10^2	11
Na_2O_2 (s)	-2.78×10^2	-2.54×10^2	11
Na_2SO_4 (ℓ)		-8.94×10^2	11
$NiCl_2$ (s)	-1.43×10^2		13
NiO (s)	-1.41×10^2	-1.32×10^2	13
$NiSO_4$ (s)		-4.05×10^2	13
SO_3 (g)		-2.61×10^2	11

TABLE II. EQUILIBRIUM CONSTANTS DERIVED FROM TITRATION AND THERMODYNAMIC DATA

Solvent	Sample Titrated	Reaction	Equilibrium Constant[a] (Titration Data)	Equilibrium Constant[b] (Thermodynamic Data)
NaCl	$NiCl_2$	$NiO + 2NaCl \rightleftarrows NiCl_2 + Na_2O$	$(2.9\text{-}6.7)\times10^{-12}$	1.82×10^{-17}
(1100 K)		$Na_2O + 1/2\ O_2 \rightleftarrows Na_2O_2$	0.5-3.1	3.11
		$Na_2O + 2NiO + 1/2\ O_2 \rightleftarrows 2NaNiO_2$	$(0.2\text{-}2.0)\times10^{-4}$	1.57×10^{4}
	$CoCl_2$	$1/3\ Co_3O_4 + 2NaCl \rightleftarrows CoCl_2 + Na_2O + 1/6\ O_2$	$(1.4\text{-}5.2)\times10^{-11}$	3.34×10^{-17}
		$Na_2O + 1/2\ O_2 \rightleftarrows Na_2O_2$	1-10	3.11
		$Na_2O + 2/3\ Co_3O_4 + 1/6\ O_2 \rightleftarrows 2NaCoO_2$	$(0.4\text{-}1.2)\times10^{-5}$	1.25×10^{2} [c]
Na_2SO_4	$NiSO_4$	$NiO + Na_2SO_4 \rightleftarrows NiSO_4 + Na_2O$	$(2.1\text{-}9.9)\times10^{-11}$	7.02×10^{-17}
(1200 K)		$Na_2O + 1/2\ O_2 \rightleftarrows Na_2O_2$	6-56	1.40
		$Na_2O + 2NiO + 1/2\ O_2 \rightleftarrows 2NaNiO_2$	$(4.0\text{-}6.4)\times10^{-2}$	4.79×10^{3}
	$CoSO_4$	$CoO + Na_2SO_4 \rightleftarrows CoSO_4 + Na_2O$	$(1.0\text{-}2.8)\times10^{-10}$	7.30×10^{-16}
		$Na_2O + 1/2\ O_2 \rightleftarrows Na_2O_2$	1.7-9.3	1.40
		$Na_2O + 2CoO + 1/2\ O_2 \rightleftarrows 2NaCoO_2$	$(0.4\text{-}3.2)\times10^{-2}$	1.54×10^{2} [c]

a - Defined in terms of mole fractions using γ_{Na_2O} in Reference 8.

b - Defined in terms of activities.

c - Assuming $(\Delta G°f)_{NaCoO_2} = (\Delta G°f)_{NaNiO_2}$.

TABLE III. ACTIVITY COEFFICIENTS OF SOLUBLE SALTS OF NICKEL AND COBALT

Melt	Salt	γ (This work)[c]	γ (Literature)	Reference
NaCl	$NiCl_2$	$(2.2\text{-}5.8)\times10^{-2}$	2.36×10^{-2}	(15)
(1100K)	$NaNiO_2$	$(0.3\text{-}1.2)\times10^{2}$		
	$CoCl_2$	$(0.6\text{-}2.2)\times10^{-2}$	1.57×10^{-2}	(16)
	$NaCoO_2$	34-56[a]		
Na_2SO_4	$NiSO_4$	$(2.0\text{-}9.6)\times10^{-3}$	0.11 - 0.24	(6)
(1200K)	$NaNiO_2$	5.2-6.6	2.8 - 84	(6)
	$CoSO_4$	$(0.7\text{-}1.9)\times10^{-2}$	0.60 - 3.0	(6)
	$NaCoO_2$	1.3-4.1[a]	2.8 - 84[b]	(6)

[a] Assuming $(\Delta G^\circ_f)_{NaCoO_2} = (\Delta G^\circ_f)_{NaNiO_2}$.

[b] Assuming $\gamma_{NaCoO_2} = \gamma_{NaNiO_2}$.

[c] Range for a total of 16 titrations.

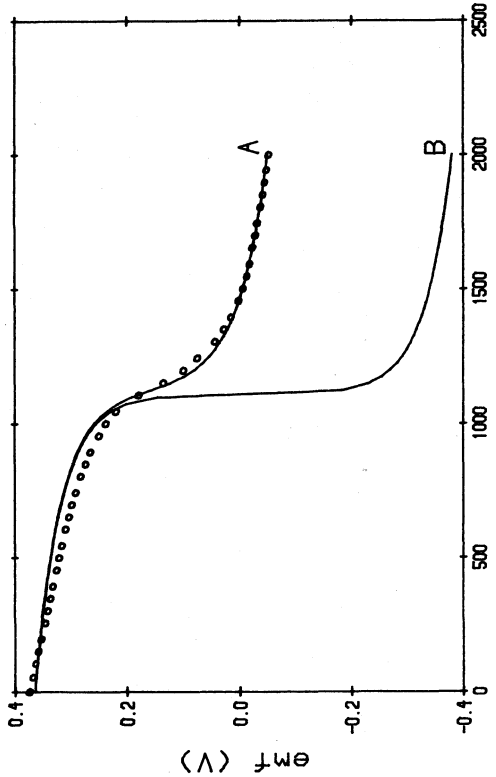

Fig. 1. Titration of $NiCl_2$ with Na_2O in molten NaCl. (o) experimental points; (——) least squares fit using equation 24; A. K_{sp} = 1.30×10^{-14}, $K_{e_1} = 1.76 \times 10^{3}$, $K_{e_2} = 9.55 \times 10^{-2}$; B. K_{sp} = 1.29×10^{-14}, $K_{e_1} = K_{e_2} = 0$.

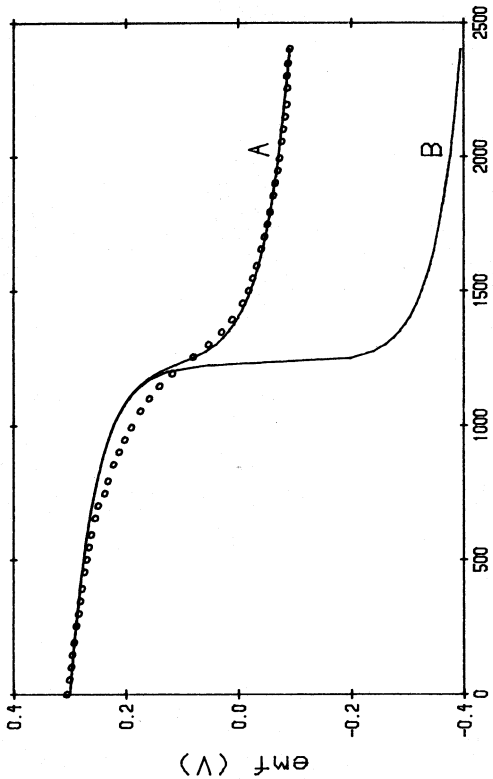

Fig. 2. Titration of $CoCl_2$ with Na_2O in molten NaCl. A. $K_{sp} = 4.14 \times 10^{-14}$, $K_{e_1} = 1.33 \times 10^{3}$, $K_{e_2} = 3.97 \times 10^{-3}$; B. $K_{sp} = 4.13 \times 10^{-14}$, $K_{e_1} = K_{e_2} = 0$.

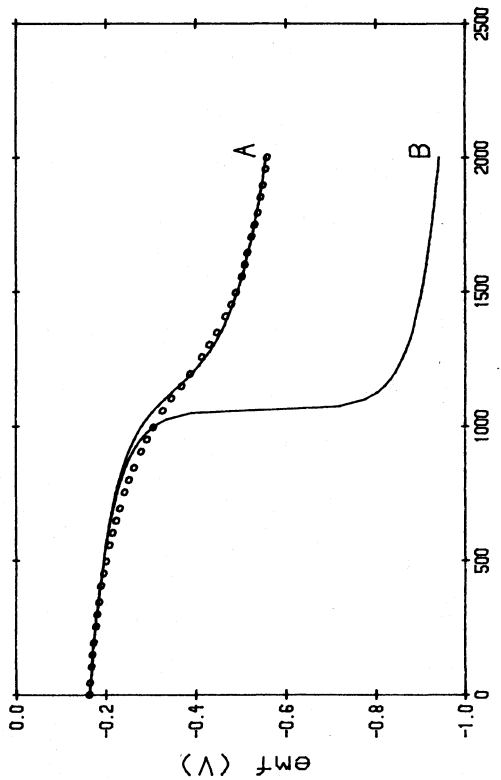

Fig. 3. Titration of $NiSO_4$ with Na_2O in molten Na_2SO_4. A. $K_{sp} = 1.51 \times 10^{-13}$, $K_{e_1} = 1.15 \times 10^{3}$, $K_{e_2} = 5.27$; B. $K_{sp} = 1.47 \times 10^{-13}$, $K_{e_1} = K_{e_2} = 0$.

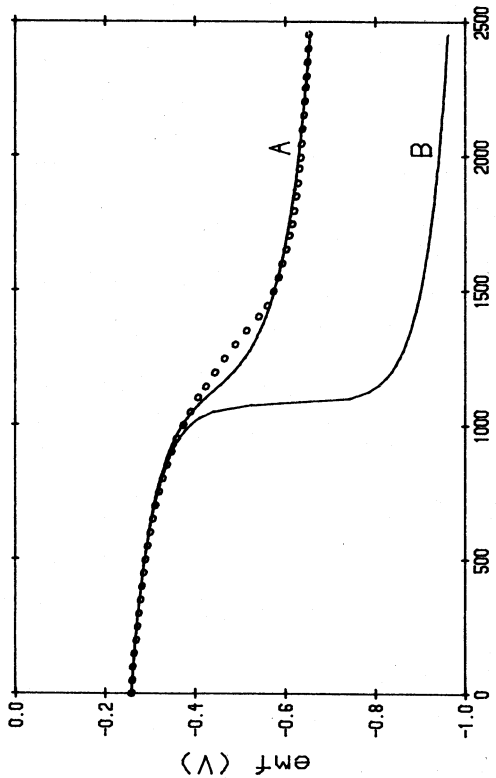

Fig. 4. Titration of $CoSO_4$ with Na_2O in molten Na_2SO_4. A. $K_{sp} = 9.24 \times 10^{-13}$, $K_{e_1} = 5.30 \times 10^{2}$, $K_{e_2} = 4.55 \times 10^{-1}$; B. $K_{sp} = 9.03 \times 10^{-13}$, $K_{e_1} = K_{e_2} = 0$.

DOI: 10.1149/198109.0393PV

CATALYTIC CHEMISTRY AND SPECTROSCOPIC STUDIES OF $SbCl_3$ MELTS CONTAINING POLYCYCLIC AROMATIC HYDROCARBONS (1)

G. Pedro Smith,* A. C. Buchanan, III,* A. S. Dworkin,*
M. Sørlie,*‡ and M. V. Buchanan†

*Chemistry Division, †Analytical Chemistry Division
Oak Ridge National Laboratory
P. O. Box X, Oak Ridge, Tennessee 37830
‡Visiting Scientist from the University of Tennessee, Knoxville, TN

Abstract

$SbCl_3$ melts have been found to catalyze internal hydrogen transfer reactions for polycyclic aromatic hydrocarbons (arenes) under low temperature, aprotic conditions. The catalytic processes are driven by redox reactions in the melt with $SbCl_3$ acting as an oxidant. Spectroscopic studies indicate that arene radical cations and carbenium ions are important reactive intermediates in the chemistry observed in these melts. Changes in the reaction behavior of arenes in molten $SbCl_3$ resulting from the addition of a few mole % of a strong chloride donor [CsCl, KCl, $(CH_3)_4NCl$] or acceptor ($AlCl_3$) are shown to result from changes in the oxidizing power of the $SbCl_3$. The reduced form of antimony in melts containing $SbCl_3$ is a dissolved lower oxidation state species.

Introduction

Our current interest in molten salt catalysis stems from the fact that molten metal halides such as SbX_3 (X = Cl, Br, I), (2) BiX_3 (X = Cl, Br), (2) AsI_3, (2) $ZnCl_2$ (3) and ZnX_2-CuX (X = Cl, I) (4) have been found to be effective catalysts for the hydrocracking of coal. Furthermore, these catalysts have been shown to have a high selectivity for the production of distillate hydrocarbons, particularly those in the boiling point range for gasoline. These molten salt hydrocracking processes are typically carried out at 350-450°C with from 1800 to 3000 psi hydrogen gas. In addition, these metal halides are usually not free from proton sources, and the catalysis is generally described in terms of proton assisted Friedel-Crafts catalysis. For example, $ZnCl_2$ has been postulated to form a Brönsted acid, $H^+ (ZnCl_2OH)^-$, with the residual water in the $ZnCl_2$ (3).

Our research is oriented towards a basic study of molten salt catalysis in an effort to understand how the catalyst functions and what types of reactive intermediates, both organic and inorganic, might be important in the catalytic process. We are presently studying the

chemistry of polycyclic aromatic hydrocarbons (arenes), which are model compounds for some of the structural units of coal, in melts in which $SbCl_3$ is the primary constituent (5,6). $SbCl_3$ melts at 73°C to form a molecular liquid with a relatively high dielectric constant (36.3 at 75°C), and it is an excellent solvent for arenes (7). The low melting point of $SbCl_3$ makes it a convenient medium in which to study the chemistry of dissolved arenes by a variety of physical methods such as nuclear magnetic resonance spectroscopy (NMR) (5,6), electron spin resonance spectroscopy (ESR) (8), and spectroelectrochemistry (9) in an effort to identify possible key reactive intermediates.

We have thus far studied the chemistry of arenes in $SbCl_3$ melts at low temperatures (80-150°C) without added hydrogen gas. Moreover, we worked with highly purified salts under carefully controlled conditions so that the starting systems are essentially aprotic. In this paper, we will summarize results which show that under these reaction conditions, it is the redox properties of molten $SbCl_3$ that drive the catalytic chemistry.

Catalytic Chemistry

We studied the reactions of arenes in $SbCl_3$ melts as a function of melt acidity by the addition of chloride ion donors or acceptors. $SbCl_3$ is itself a very weak Lewis acid from which basic melts (chloride rich) can be prepared by dissolution of a strong chloride donor such as CsCl, KCl, or $(CH_3)_4NCl$. Acidic melts (chloride deficient) can be prepared by the addition of a strong chloride acceptor such as $AlCl_3$ for which $SbCl_3$ acts as a leveling solvent (10). In addition to altering the Lewis acidity of the medium, the addition of a strong chloride ion acceptor or donor also alters the redox properties of the $SbCl_3$ since the reduction of $SbCl_3$ liberates chloride.

$$1/3\ SbCl_3 + e \rightleftharpoons 1/3\ Sb + Cl^-$$

The effect of added chloride donor or acceptor on the formal potential of the Sb^{3+}/Sb couple was measured by electrochemical methods by Bauer and coworkers, (11,12) and the results are shown in Figure 1. The melt composition is indicated along the abscissa with neat $SbCl_3$ in the center. The molar concentration units can be converted to the approximate mol % by multiplying by 10 (e.g. 0.5 M $AlCl_3 \simeq$ 5 mol % $AlCl_3$). The solid curve drawn through the experimental data points is the Nernst curve based on a model for the autoionization of neat $SbCl_3$. It is clear from the experimental points that the addition of a few mol % of a strong chloride donor (KCl) decreases the formal potential of the Sb^{3+}/Sb couple making it a weaker oxidant than in neat $SbCl_3$, while the addition of a few mol % of a strong chloride acceptor ($AlCl_3$) increases the Sb^{3+}/Sb formal potential making the couple a stronger oxidant than in neat $SbCl_3$.

On the right hand side of Figure 1, several arenes are shown along with their anodic $E_{1/2}$ values measured in $SbCl_3$ melts containing an excess chloride donor (13). The arenes shown are naphthalene (1), acenaphthene (2), pyrene (3), anthracene (4), 9,10-diphenylanthracene (5), 9,10-dimethylanthracene (6), perylene (7), and naphthacene (8). These arenes are listed in order of increasing oxidizability in the melt with naphthalene being the most difficult to oxidize and naphthacene the easiest to oxidize. For naphthalene, the oxidative $E_{1/2}$ lies beyond the anodic limit of the melt ($Sb^{3+} \longrightarrow Sb^{5+}$), but from excellent correlations with arene $E_{1/2}$ values measured in other solvents (such as acetonitrile) we estimate the $E_{1/2}$ of naphthalene to be 0.90-0.95 V. Phenanthrene, the simple polycyclic isomer of anthracene, is also very difficult to oxidize and the $E_{1/2}$ for phenanthrene is predicted to fall within this same range. We have studied extensively the reactions of many of these arenes as a function of melt composition, and Figure 1 will provide a convenient reference point for the following discussion of this chemistry.

The reaction behavior of arenes in $SbCl_3$ melts was studied by in situ ^1H NMR (80 MHz, ^2H external lock) both with and without $(CH_3)_4N^+$ as an internal chemical shift reference. Products were identified from larger scale reactions performed in Schlenk-ware under argon following separation and identification procedures which have been previously described (5,6). All material transfers were performed in a controlled atmosphere glovebox.

In neat $SbCl_3$ we found arenes 1-3 to be unreactive in the melt over the temperature range studied, 80-175°C. Although weakly bound arene-$SbCl_3$ complexes are known in the solid state (14) (and have been suggested in the molten state), the ^1H NMR of these solutions proved to be those of the molecular arenes only. An example is shown in Figure 2 for the case of naphthalene, 1, in $SbCl_3$ at 100°C. The well-resolved spectra for these unreactive arenes were closely similar to the corresponding spectra for solutions in $CDCl_3$ and gave no indication of any complexation with the $SbCl_3$ solvent.

More easily oxidized arenes such as 4, 6, and 8 were reactive in neat $SbCl_3$ and underwent a catalytic reaction (5) which is typified in Figure 3 for the case of anthracene, 4. As indicated, anthracene was found to undergo a disproportionation reaction in which some anthracene molecules were condensed to form primarily 2,9'-bianthracene (loss of two hydrogens), then anthra[2,1-a]aceanthrylene (loss of two more hydrogens). Other anthracene molecules were found to be hydrogenated to form 9,10-dihydroanthracene and then 1,2,3,4-tetrahydroanthracene. The condensation of arenes over Lewis acid catalysts (Scholl reaction) has been known for many years (15). However, it is interesting that this reaction takes place with a Lewis acid catalyst as weak as $SbCl_3$. Furthermore, in earlier Scholl chemistry, the fate of the hydrogen liberated upon condensation was not known. We were able to show that the hydrogen liberated upon the condensation of

anthracene is quantitatively transferred to unreacted anthracene molecules to form the hydroanthracene products described above. Other easily oxidized arenes such as 6 and 8 undergo an analogous catalytic hydrogen transfer reaction.

It is interesting that the addition of 3 mol % of a strong chloride donor reduces the oxidizing power of the $SbCl_3$ solvent relative to that of the neat melt. For the most easily oxidized arene, naphthacene 8, the rate of the catalytic reaction is not greatly affected by the presence of a strong chloride ion donor. These results raise the possibility that the suppression of catalytic activity upon adding a chloride donor may in some fashion be associated with a lowering of the oxidizing power of the melt.

The catalytic chemistry of arenes in acidic melts also suggests that the redox properties of $SbCl_3$ play an important role. Most of the chemistry of arenes in acidic $SbCl_3$ melts that we examined was in melts containing 8-10 mol % (~0.8 - 1.0 M) $AlCl_3$. As discussed above, this corresponds to a region where the oxidizing power of the $SbCl_3$ solvent has been enhanced. We found that arenes such as 3-8 now undergo a noncatalytic reaction which gives much insight into how the catalytic reaction proceeds. This chemistry will be described later during a consideration of the mechanism for the catalytic reactions. Recall that arenes of low oxidizability such as naphthalene, 1, and phenanthrene were completely unreactive in neat $SbCl_3$. In $SbCl_3$-10 mol % $AlCl_3$, however, they are quite reactive and undergo catalytic hydrogen transfer chemistry, but with a few new features not observed in neat $SbCl_3$. These features will now be described using naphthalene as an example.

From in situ ^1H NMR and quench and separation studies, we found that naphthalene undergoes a very complicated sequence of reactions in $SbCl_3$-10 mol % $AlCl_3$ at 130°C (again, aprotic conditions and no added hydrogen). A typical gas chromatogram of the reaction products, shown in Figure 4, was obtained on a 30 m x 0.25 mm i.d. glass capillary column coated with an OV-101 liquid phase. Many of these more than 200 products have been identified by combined gas chromatography-mass spectrometry (GC-MS) and by coelution GC studies with standards. The salient features of this complex chemistry can be summarized as follows:

(1) Naphthalene is condensed (Figure 5) to form binaphthalenes, benzo(j)-fluoranthene, benzo(k)fluoranthene, and perylene. (2) Some of the hydrogen liberated upon condensation hydrogenates unreacted naphthalene (Figure 5) molecules to form 1-methylindane, 1-methylindene, and tetralin. The presence of these rearranged products (methylindane and methylindene) indicates that the melt now has an isomerization functionality not observed in neat $SbCl_3$. (3) Most surprising of all was the finding that some of the initially formed condensed products (binaphthalenes and benzofluoranthenes) are internally hydrocracked

in $SbCl_3$-$AlCl_3$, and this is what leads to the complex product mixture shown in Figure 4. This was evidenced by the presence of products such as phenyl and alkyl substituted naphthalenes. Thus, the addition of $AlCl_3$ to $SbCl_3$ melts not only increased the catalytic activity of the melt by increasing the oxidizing power of $SbCl_3$, but it also gave the melt isomerization and cracking functionalities.

Mechanistic Considerations

The catalysis described above produced many products (particularly in $SbCl_3$-$AlCl_3$ melts) and so consisted of many individual reactions occurring both sequentially and in parallel. Taken as a whole the types of products found were those that one gets under conventional Friedel-Crafts catalysis in which strong protic acids serve as catalytic agents. This is illustrated in Figure 6 in which benzene is used to represent the arene that is undergoing condensation. The hydrogen that is liberated by condensation can end up in various places depending on the reaction details.

Arenes are protic bases albeit very weak protic bases. Thus when a strong protic acid is present, there is a fast and reversible acid-base reaction that yields a small concentration of protonated arene, an example of a carbenium ion, as shown in the first step of Figure 6. This carbenium ion is very reactive and condenses with a molecule of starting material. In this step a proton is released for catalytic recycle. The condensed product of this reaction is also reactive and goes on to form a fully aromatized stable product by a series of reactions that are lumped together in the third step. The key feature of this standard mechanism is the catalytic role of the protic acid that activates the rather inert arene by forming a reactive carbenium ion.

In the catalytic reactions that we described above there were no obvious protic acids present. In fact, we took great care to work under aprotic conditions. Nevertheless, reactions that one normally associates with protic acid catalysis took place with unusual ease. How did $SbCl_3$ catalyze these reactions? We suggested earlier in this paper that the catalysis was driven by redox reactions in the melt. However, a stock answer that is often employed in this situation is that there was an adventitious proton source present.

We might have accepted this gratuitous explanation if it were not for the discovery of an unprecedented reaction which demonstrated that $SbCl_3$ can react with arenes to generate, internally, a powerful proton source (6). This is the unusual chemistry we alluded to earlier for arenes 3-8 in $SbCl_3$-10 mol % $AlCl_3$. The experimental procedures that demonstrated this reaction are similar to those used to examine the catalytic chemistry previously described for 1 and phenanthrene in $SbCl_3$-$AlCl_3$. The major difference is that the arenes

used in the experiments we will now describe were more oxidizable than the ones used in the catalytic studies.

In a typical experiment a few mol % of an arene was dissolved in a mixture of $SbCl_3$ and 10 mol % $AlCl_3$ at 100°C. As soon as mixing was complete, ^1H NMR spectra were obtained such as those shown in Figure 7. The top spectrum, A, is that obtained for a solution in which anthracene was the starting material. This spectrum can be unambiguously assigned to anthracene protonated in the 9 position as shown. The lower spectrum, B, is that of a solution formed from naphthacene that can be unambiguously assigned to the carbenium ion formed by protonating this molecule in the 5 position as shown. As indicated earlier, similar results were obtained for arenes 3, 5, and 6. By integrating appropriate bands in these spectra with reference to $(CH_3)_4N^+$ as an internal standard, we found that in all cases 55-65% of the starting material had been protonated. Thus, protons were generated in quantities much too large to be accounted for by impurity proton sources. The protonated arenes of 4, 6, and 8 were unusually stable, and their ^1H NMR spectra remained unchanged for hours even at 130°C.

All of these arenes are very weak proton bases and can only be protonated on the massive scale that we observed by the presence of some strong protic acid (16,17). This raises the question of what the proton source for this reaction is. The complete reaction stoichiometry was elucidated from the work up of quenched melts and quantitative determination of the products not seen by NMR. A typical case is shown in Figure 8 in which anthracene was the starting material. Several condensed products were found with the one shown, anthra[2,1-a] aceanthrylene, being the major one. The number of moles of protons consumed in forming the protonated anthracene was consistent with the number of moles of hydrogen atoms that were lost upon condensation. More significantly, we recovered finely divided Sb metal, and the number of moles of metal recovered equaled 1/3 of the number of moles of protonated anthracene formed. The recovery of stoichiometric quantities of Sb metal is a clear illustration of the involvement of $SbCl_3$ as an oxidant in arene chemistry in the melt. Similar stoichiometry was observed for the other arenes that underwent this self-protonation reaction.

We also found an exception to this reaction. Perylene, 7, is oxidized but, within the times and at the temperatures used in the present study, it did not undergo the condensation/protonation reaction described above to any significant extent. This point will be examined later and a possible explanation for this behavior offered.

We shall now return to the question of how $SbCl_3$, acting as an oxidant, was able to generate a proton source strong enough to protonate a stoichiometric portion of the arene. There is an

alternative mechanism for aromatic condensation, shown in Figure 9, which suggests some possibilities (18). The initial step is the reversible oxidation of the arene (for which benzene is used as a model) to its radical cation. This is followed by an irreversible reaction of the radical cation with another radical cation (second step) or a neutral arene (third step) to form an intermediate charged condensed molecule. In each case, the ipso hydrogen on the charged ring, that is, the hydrogen next to the C-C bond that joins the rings, should be very acidic and protonate unreacted arene molecules. This reaction yields the final condensed product and the protonated starting material.

The key to the mechanism shown in Figure 9 is the ability of the arene to be oxidized to a radical cation by $SbCl_5$. We used ESR spectroscopy in an effort to find out if the predicted radical cations are in fact formed from oxidizable arenes (8). In order to do this, very dilute solutions were employed in the hope of slowing the downstream reactions of the radical cations. Figure 10 shows typical ESR spectra for three radical cations which are spontaneously formed in $SbCl_5$-rich melts at 80°C. Only one-half of the acenaphthene, 2, ESR spectrum is shown with the computer simulation of the spectrum given below. The hyperfine structure in these spectra is exceedingly well resolved so that identification of the radical cations is totally unambiguous. From the g-values and hyperfine coupling constants for these radical cations, there is no indication of any unusual medium effects, such as complexation with the solvent. Such high resolution proved to be the rule rather than the exception for the radical cations we observed in these melts.

Figure 1 provides a convenient vehicle for summarizing the ESR results and for identifying a correlation between the occurrence of arene radical cations and the oxidizing power of $SbCl_5$ as a function of melt composition. We measured the ESR spectra at 80°C of dilute solutions of the arenes shown at the right of the Figure in melts containing 8 mol % $(CH_3)_4NCl$, in pure $SbCl_5$, and in melts containing 8 mol % $AlCl_3$. In melts containing 8% $(CH_3)_4NCl$, the only arene that was oxidized sufficiently to give a strong, stable signal was the most easily oxidized arene, naphthacene, 8. Arenes 6 and 7 showed fleeting traces of radical cations. No other arene gave a detectable signal. In pure $SbCl_5$, stable radical cations were found for arenes 5-8, while only a trace of unstable radical cation was observed for anthracene, 4. Arenes 1-3 again gave no observable ESR signal. In $SbCl_5$ melts containing 8% $AlCl_3$, stable radical cations were found for arenes 3-8 while acenaphthene, 2, was weakly oxidized. Naphthalene, 1, may have been weakly oxidized in this melt but no spectrum for the parent radical cation was observed. Instead, the ESR spectrum for perylene, 7, (a downstream reaction product) was observed.

These results strongly support the view that $SbCl_5$ in these melts can oxidize arenes to their radical cations. These results also show

that the oxidizing power of $SbCl_3$ can be tuned, in qualitative agreement with the electrochemical results, by the addition of a strong chloride donor or acceptor. Furthermore, if a dilute solution of an arene in a particular melt results in the oxidation of the arene to its radical cation (stable or unstable), then more concentrated solutions of the arene in this melt will show either catalytic hydrogen transfer chemistry or condensation/protonation chemistry. The type of chemistry that is actually observed will probably depend on the degree of oxidation of the arene in the particular melt being studied. Note that the condensation/protonation reaction (in which the massive reduction of $SbCl_3$ is observed) only occurs for the most oxidizing melt (with added $AlCl_3$) and only for the most oxidizable arenes.

From what has been discussed thus far, one might assume that the arene oxidation reaction would take place at the interface between the melt and Sb metal. However, we found that antimony has lower oxidation states in between 3^+ and the metal, and these lower oxidation states form stable solutions in these melts (19). These states occur in the form of different species depending on whether the melt contains an excess of chloride donor (CsCl) or acceptor ($AlCl_3$). When the concentration of the lower oxidation state species becomes sufficiently high, or when these melts are hydrolyzed, the species becomes unstable with respect to disproportionation into metal and 3+. Thus, the oxidation of arenes by $SbCl_3$ in these melts appears to take place homogeneously.

The fact that $SbCl_3$ is reduced to a soluble species rather than the metal requires some modification in the use of Figure 1 for predicting the conditions under which radical cations will form in significant quantities. The potential of the Sb^{3+}/lower-state couple will equal that of the Sb^{3+}/Sb couple when the lower state species is at the concentration for thermodynamic disproportionation. This concentration is highly dependent on the concentration of chloride donors or acceptors, respectively (19). When the concentration of the lower state species is smaller than that for the disproportionation equilibrium, the potential of the Sb^{3+}/lower-state couple will be higher than that of the Sb^{3+}/Sb couple. Thus, an arene at a low concentration will be oxidized to a greater extent than would have been predicted from Figure 1. Furthermore, we found that in melts containing $AlCl_3$ there is a substantial kinetic barrier to the nucleation of Sb metal by disproportionation of the lower state. As a consequence one can obtain metastable solutions in which the lower state is present at a concentration much higher than that for the disproportionation reaction. For such metastable solutions the Sb^{3+}/lower-state couple will, of course, have a lower potential than that of the Sb^{3+}/Sb couple. Thus, when an arene is present at a rather high concentration, the fraction oxidized may be substantially less than would be predicted from an uncritical use of Figure 1 for two reasons: First, the concentration of reduced antimony may substantially exceed that for thermodynamic disporportionation and, second, the reduction of $SbCl_3$ releases chloride ions

that reduce the concentration of chloride acceptors or increase the concentration of chloride donors, depending on which is initially present in excess.

We are currently studying the chemical and electrochemical oxidation reactions of arenes with the aid of a fast optical multichannel analyzer. Although research is too preliminary to justify an overview at this time, we have observations that address the question of why perylene, 7, is an exceptional case. As was mentioned earlier in this paper, perylene does not undergo oxidative protonation under conditions in which other arenes of similar oxidizability undergo this reaction rapidly. We found that, by a wide margin, perylene yields the most unreactive arene radical cation that we have encountered. When perylene was dissolved in $SbCl_3$-10 mol % $AlCl_3$, oxidation took place rapidly and quantitatively (9). However, the downstream reactions of this radical cation occurred at a very slow rate in these melts in comparison with the downstream reactions of the other arene radical cations we studied. The reason for this kinetic barrier is yet to be determined.

The fact that perylene gave such a stable radical cation in the $SbCl_3$-$AlCl_3$ melt led us to try another experiment which also gave an unexpected result (9). As indicated above, the dissolution of perylene in $SbCl_3$-10% $AlCl_3$ gave the spontaneous and quantitative oxidation of perylene to its radical cation. The optical spectrum obtained for the perylene radical cation in $SbCl_3$-$AlCl_3$ at 135°C is shown in Figure 11, curve a. The radical cation was then electrochemically oxidized to give the optical spectrum shown in curve b of Figure 11, and the optical spectrum can be identified as that of the perylene dication (9). Much to our surprise, this dication is quite stable in dilute solutions in this melt. Other arene dications were also prepared in a similar fashion and, although less stable than the perylene dication, they were stable enough to allow their characterization. These findings are of fundamental importance because arene dications are among the least studied intermediates in organic chemistry. We shall investigate further the chemical properties of these arene dications in halide melts.

Conclusion

In this paper we have described the low temperature catalytic hydrogen transfer chemistry that is observed for arenes in melts in which $SbCl_3$ is the primary constituent. Under these aprotic reaction conditions, we were able to show that the driving force for the catalytic chemistry is associated with redox reactions in the melt in which $SbCl_3$ is an oxidant, and arene radical cations are important reactive intermediates. The decrease or increase in the activity of these melts as a function of added chloride donor or acceptor, respectively, is related to the decrease or increase in the oxidizing

power of the $SbCl_3$. Furthermore, combined electrochemistry and optical spectroscopy of dilute solutions of arenes in these melts appears promising for a more detailed investigation of the production and reactions of important arene cationic intermediates.

Acknowledgements

This research was sponsored by the Division of Chemical Sciences, Office of Basic Energy Sciences, U.S. Department of Energy, under contract W-7405-eng-26 with the Union Carbide Corporation. M. Sørlie is grateful for financial assistance from Norges Teknisk-Naturvitenskapelige Forskningsråd and for a travel grant from Norges Almenvitenskapelige Forskningsråd.

REFERENCES

1. This paper is the combination of two symposium presentations: (1) "Low Temperature Catalytic Hydrocracking of Naphthalene in Molten $SbCl_3$-$AlCl_3$" by A. C. Buchanan, III, M. V. Buchanan, A. S. Dworkin and G. Pedro Smith. (2) "Formation of Aromatic Hydrocarbon Cations in Molten $SbCl_3$-$AlCl_3$ Mixtures" by G. Pedro Smith, A. C. Buchanan, III, A. S. Dworkin, and M. Sørlie.

2. Wald, M. M., U. S. Patent 3 542 665, 1970.

3. Zielke, C. W.; Struck, R. T.; Evans, J. M.; Costanza, C. P.; Gorin, E. Ind. Eng. Chem. Process Des. Dev. 1966, 5, 151, 158; Zielke, C. W.; Klunder, E. B.; Maskew, J. T.; Struck, R. T., ibid. 1980, 19, 85.

4. Ida, T.; Namura, M.; Nakatsuji, Y.; Kikkawa, S. Fuel 1979, 58, 361.

5. Dworkin, A. S.; Poutsma, M. L.; Brynestad, J.; Brown, L. L.; Gilpatrick, L. O.; Smith, G. P. J. Am. Chem. Soc. 1979, 101, 5299.

6. Buchanan, A. C., III; Dworkin, A. S.; Smith, G. P. J. Am. Chem. Soc. 1980, 102, 5262.

7. The physical properties and chemistry of molten $SbCl_3$ are reviewed by E. C. Baughan, in "The Chemistry of Nonaqueous Solvents", Vol. IV, J. J. Lagowski, Ed., Academic Press, New York, 1976, pp. 129-165.

8. Buchanan, A. C., III; Livingston, R.; Dworkin, A. S.; Smith, G. P. J. Phys. Chem. 1980, 84, 423.

9. Sørlie, M.; Smith, G. P.; Norvell, V. E.; Mamantov, G.; Klatt, L. N. J. Electrochem. Soc., in press.

10. The generally accepted model has been: $SbCl_3 + AlCl_3 \rightarrow SbCl_2^+ + AlCl_4^-$. There is, however, no spectroscopic evidence for the formation of these ions [Huglen, R.; Mamantov, G.; Begun, G. M.; Smith, G. P. J. Raman Spec., 1980, 9, 188].

11. Bauer, D.; Texier, P. C. R. Hebd. Seances Acad. Sci., Ser. C 1968, 266, 602.

12. Texier, P. Bull. Soc. Chim. Fr. 1968, 4716.

13. (a) Bauer, D.; Beck, J. P.; Texier, P. Collect. Czech. Chem. Commun. 1971, 36, 940 (b) C. R. Hebd. Seances Acad. Sci, Ser. C 1968, 266, 1335.

14. Perkampus, H. H., Schönberger, E. Z. Naturforsch. 1976, 31b, 475.

15. Scholl reactions are reviewed by H. L. Jones and R. A. Osteryoung, in "Advances in Molten Salt Chemistry", Vol. III, J. Braunstein, G. Mamantov, and G. P. Smith, Eds., Plenum Press, New York, 1975, pp. 121-176, and by A. T. Balaban and C. D. Nenitzescu, in "Friedel-Crafts and Related Reactions", Vol. II, Part 2, G. A. Olah, Ed., Interscience, New York, 1964, pp. 979-1047.

16. Olah, G. A.; Staral, J. S.; Asencio, G.; Liang, G.; Forsyth, D. A.; Mateescu, G. D. J. Am. Chem. Soc. 1978, 100, 6299.

17. Koptyug, V. A.; Isaev, J. S.; Rezvukhin, A. I. Tetrahedron Lett. 1967, 823.

18. Wen, Long-Sing; Kovacic, P. Tetrahedron 1978, 34, 2723.

19. Sørlie, M.; Smith, G. P. J. Inorg. Nucl. Chem. in press.

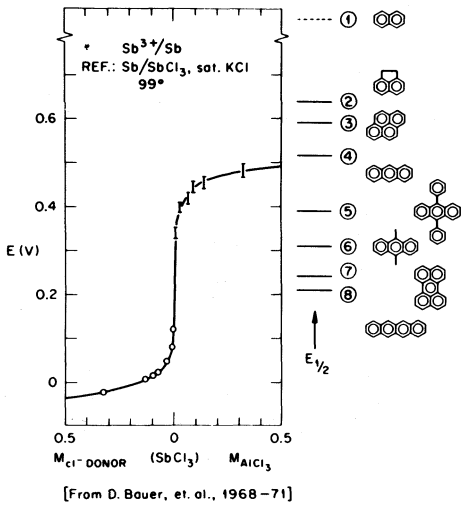

Figure 1.
Formal potential of Sb^{3+}/Sb couple as a function of melt composition, and anodic $E_{1/2}$ values for selected arenes obtained in $SbCl_3$ melts with excess chloride.

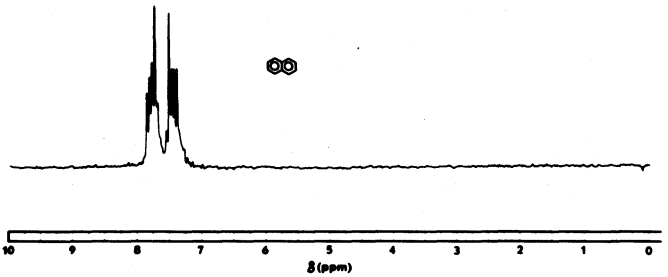

Figure 2.
^1H NMR of naphthalene in $SbCl_3$ at 100°C.

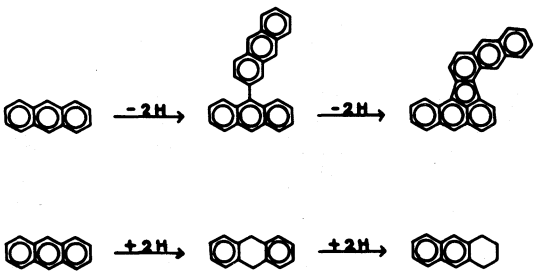

Figure 3.
Principal disproportionation route for anthracene in $SbCl_3$.

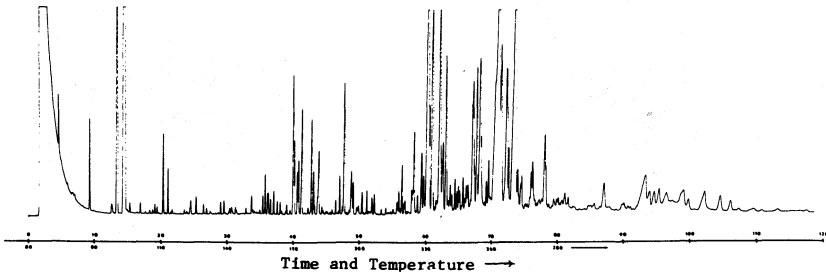

Figure 4. GC profile of the organic products, dissolved in CH_2Cl_2, from a reaction of naphthalene in $SbCl_3$-10% $AlCl_3$ (130° for 25 min).

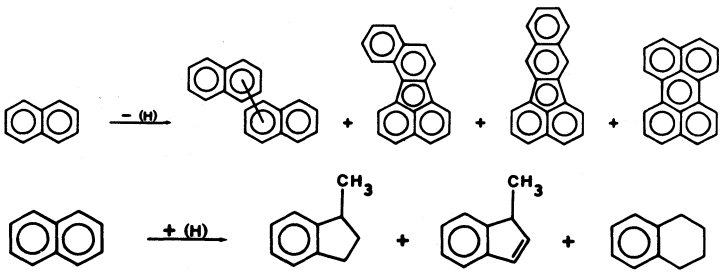

Figure 5. Principal route for condensation (upper) and hydrogenation (lower) of naphthalene in $SbCl_3$-10% $AlCl_3$.

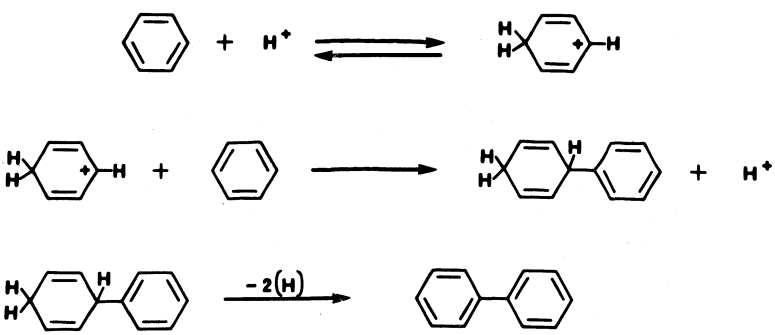

Figure 6. Proposed mechanism for proton catalyzed condensation of arenes.

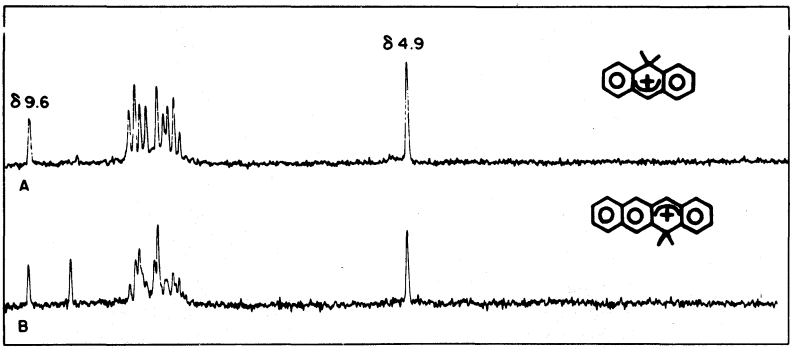

Figure 7. ^{1}H NMR of some arenium ions formed in $SbCl_3$-10% $AlCl_3$ at 100°C: (A) anthracenium; (B) naphthacenium.

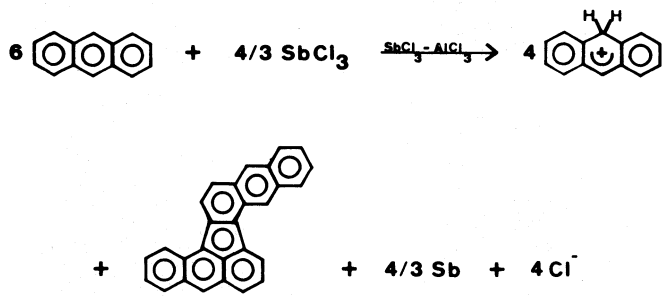

Figure 8. Condensation-self protonation reaction for anthracene in $SbCl_3$-10% $AlCl_3$ at 100°C.

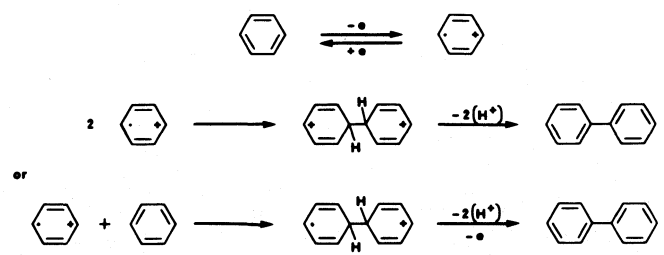

Figure 9. Proposed mechanism for redox driven condensation of arenes.

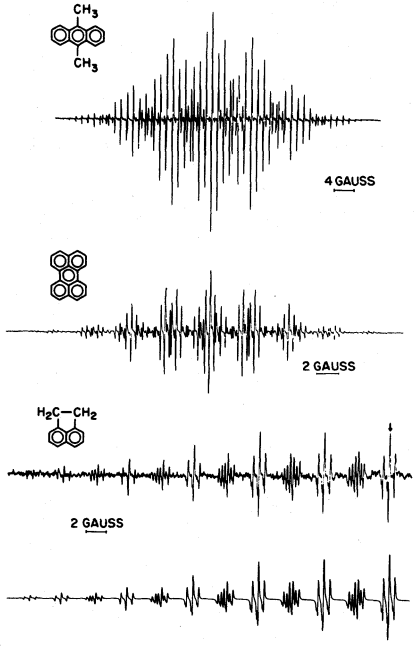

Figure 10. ESR spectra of arene radical cations in molten $SbCl_3$-8% $AlCl_3$ at 80°C.

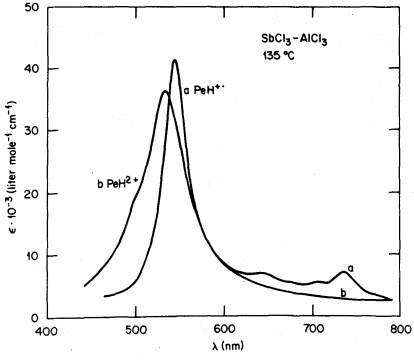

Figure 11. Optical spectrum of a solution of perylene in $SbCl_3$-$AlCl_3$ at 135°C: (a) before electrolysis showing the perylene radical cation; (b) after electrolysis showing the perylene dication.

DOI: 10.1149/198109.0408PV

PYROLYSIS OF AUTOMOBILE SHREDDER WASTE IN MOLTEN SALTS

Carey Chambers, John W. Larsen, and Robert Wiesen

Department of Chemistry
University of Tennessee
Knoxville, Tennessee 37916

ABSTRACT

The polymer containing fraction of automobile shredder waste was pyrolyzed in molten $AlCl_3/NaCl$, $ZnCl_2$, LiCl/KCl, LiCl/KCl/CuCl and $Li_2CO_3/Na_2CO_3/K_2CO_3$. Experiments were run at atmospheric pressure at temperatures of 300-575°C without added H_2. From bench scale experiments, the yields of gas, oil and solid (char) were determined for each melt. The maximum oil yield was obtained by pyrolysis of the polymer in CuCl containing LiCl/KCl at 500°C. When the pyrolysis time in this melt was increased, the fraction of oil components with a boiling point 200°C increased. The oil was highly aromatic and may be useful as a gasoline blending agent. Comparison of the rates of polymer decomposition in the different melts showed that pyrolysis in molten $AlCl_3/NaCl$ gave the most favorable rates. However, in this melt poor oil yields were obtained (∿11 % or less by weight), while a relatively large gas yield was obtained (∿30 %) which consisted primarily of isobutane. In general, the oil yields obtained by molten salt treatment of this polymer waste are comparable to yields obtained by inert gas pyrolysis of comparable materials at temperatures several hundred degrees higher. In addition, the use of molten salts offers the potential of changing the product spectrum by the appropriate selection of molten salt used for polymer pyrolysis.

INTRODUCTION

The experiments reported in this paper were designed to determine reaction conditions that would give the best yield of salable products from pyrolysis in molten salts of polymer waste obtained from an automobile shredder operation. The yields of oil and gas obtained when LiCl/KCl/CuCl melts and $ZnCl_2$ containing melts (at melt temperatures of 500°C) were used to decompose the shredder waste compare favorably with yields obtained in a rotary kiln pyrolytic recovery process (at reactor temperatures of 700°C) developed for shredder and other plastic and rubber containing waste by Colin, et al. (1). Since the oil product

obtained was found to be highly aromatic and thus has the potential for use as either a gasoline blending stock or a source of chemicals, much of the effort was spent investigating systems that showed promise in maximizing the yield of liquid products.

This investigation is being carried out in conjuction with Ford Motor Company Research, where inert gas pyrolysis of this polymer waste is being studied. The yield and composition of oil and gas products obtained from the two different processes will be compared, with the aim of deciding in which process to invest more development work.

The current practice of landfilling the polymer containing waste from automobile shredding plants is expensive, as well as a waste of a petoleum based resource. It is estimated that the average car junked in 1978 contained 80 kg plastic and non-tire rubber (2). This amount is expected to increase at a rate of 4 % per year. By 1990, a non-ferrous metal processor handling waste from two million shredded automobiles will process 200 million kilograms of plastic and rubber waste.

This investigation is an extension of work reported by Larsen and Chang on the recovery of valuable products from used tires by pyrolysis in molten $ZnCl_2$ and in a KCl/LiCl eutectic (3). It was found that treatment of scrap rubber in either of these molten salts produced efficient conversion to volatile hydrocarbons. Unlike processes using molten $ZnCl_2$ and high H_2 pressures for coal conversion, it was unnecessary to add H_2 to the system. Hydrogen was stripped from the polymer and incorporated into volatile hydrocarbons.

While a large number of investigations on the use of molten metal chlorides for hydrocracking coal and coal extracts have been reported, there are few reports on the use of molten salts in reclamation processes. Sinn and co-workers have reported some studies on the pyrolysis of plastics and used tires in molten salts (4-6). However, most of their work has been devoted to development of a reactor that utilizes the hydrocracking properties of a fluidized sand bed at temperatures of 650-850°C. A variety of other pyrolytic methods for the recovery of valuable products and/or energy from organic waste, such as plastics, automobile tires, household refuse and paper have been reported. A number of commercial and semi-commercial plants are in operation, particularly in Japan and West Germany. Several reviews of these reclamation processes have been published (7,8).

Catalytic and non-catalytic melts were examined. Molten salt systems studied included a tetrachloroaluminate melt, several cuprous chloride containing melts, zinc chloride and zinc chloride eutectics and a lithium chloride-potassium chloride eutectic. The rationale behind selection of the molten salts studied is the following: lithium chloride-potassium chloride eutectics should have no catalytic properties, but do have excellent heat transfer properties. Results

from pyrolyses carried out in a relatively inert melt can serve as controls for the method and can be used to evaluate the catalytic activity of more active salts. The use of copper chloride containing melts, particularly in combination with oxygen and chlorine, for the chlorination of hydrocarbons has been extensively reported and has been reviewed by Kenney (9-12). A cuprous chloride-potassium chloride eutectic has been shown to promote the hydrocracking of propane to smaller molecules (13). Extensive investigations on the use of zinc chloride containing melts for hydrocracking of coal and coal products have been reported (14-16). The Lewis acid properties of aluminum chloride containing melts as solvents for a number of organic reactions and as promoters for hydrocarbon isomerizations are well known (17,12).

EXPERIMENTAL

Two 55 gallon drums containing material from the first non-magnetic float fraction from Huron Valley Steel Company, Belleville, Michigan, were obtained on June 23, 1978. The two drums of material were collected 30 minutes apart to insure that the samples were from different shredded automobiles with no backmixing.

The material from each drum was hand quartered to obtain a representative sample from each drum. These two samples were course ground cryogenically (liquid nitrogen temperature) using an IMS Plastics Grinder Model #M2 without a screen. The resulting course ground material was then re-ground cryogenically using a Model 4 Thomas-Wiley laboratory hammer mill with a 4 mm screen. The fine-ground samples obtained from each drum were used in all subsequent experiments. Aliquots of the ground samples were analyzed and the range of values obtained is shown in Table 1. The heating value of the material was 7,000 cal/g. Visual inspection of the material before it was ground indicated Drum 1 contained more tire tread than Drum 2, which contained mostly rubber from hoses and tubing.

Either a pyrex or a stainless steel reaction vessel was used. The pyrex reactor consisted of a 1 liter flask equipped with a stainless steel stirrer, a thermocouple well, a neck for sample introduction and a neck leading to a water condenser through which volatile products escaped. A 316 stainless steel reactor was used for all product runs except those in $AlCl_3/NaCl$. It had 6 mm walls, was $\sim$ 14.5 cm deep and had an I.D. of $\sim$ 9.5 cm. It was also equipped with a stainless steel stirrer, a thermocouple well, a water cooled neck for sample introduction, a water cooled Claisen head with thermometer and water condenser through which the volatile pyrolysis products escaped, and an inlet for sweeping the system slowly with dry nitrogen.

Approximately 100 g shredder waste was used for each product run. It was added in $\sim$ 20 g batches to the melt. The reaction appeared complete within five minutes after each addition. Gas samples were collected and the ratios of C1 - C4 hydrocarbons determined by gas

chromatography (Poropak Q-1/4 in. X 10 ft.)

The oil and water produced were condensed, separated, and the boiling point range of the oil determined by a gas chromatographic procedure similar to ASTM D 2888-7. The oil was also analyzed on a Hewlett-Packard tandem gas chromatograph-mass spectrometer system using a 1/4 in. X 10 ft. column containing 10 % OV210 on Chromosorb W or a 1/8 in. X 15 ft. column containing 10 % SE-30 on Chromosorb W.

The residue was extracted repeatedly with water to remove the salt. The solid was isolated by filtration and dried to constant weight. Elemental analyses were obtained on the oil and solid products. Gas yields were calculated by difference. Since the weight percent of feed recovered as ash in the solid varied considerably with pyrolysis temperature and salt system used, gas yields were corrected for ash gain or loss.

In experiments to compare the rate of polymer decomposition in different melts, a 500 ml, 4-necked pyrex reaction flask was used. After the system was at temperature, the N_2 flush was discontinued, the system closed and a small (2-6 g) polymer sample dropped into the stirred reaction medium. The increase in gas volume was measured with a mercury manometer.

RESULTS

Gas, liquid and solid products were isolated from benchscale runs in which the shredder waste was decomposed in a variety of molten salts and, for comparison purposes, in stirred sand. A more complete report of these experiments is in preparation (18).

Figure 1 shows product yields obtained by treatment of the polymer waste at 450°C in a tetrachloroaluminate melt (50 mole % $AlCl_3$), in molten $ZnCl_2$ and in a LiCl/KCl eutectic (41 mole % KCl) containing 10 % by weight CuCl. Decomposition of polymer in CuCl containing melts gave the best oil yields, while the lowest oil yields were obtained when the material was decomposed in tetrachloroaluminate melts. Conversion of polymer to gaseous products was greatest in the tetrachloroaluminate melt and lowest in CuCl containing melts. At 450°C, decomposition of the polymer in molten $ZnCl_2$ produced a large amount of solid residue (char). This was probably due to enhanced solubility of large condensed aromatics in $ZnCl_2$ resulting from complex formation. This effect can be reduced by increasing the melt temperature to 500°C or above or by adding KCl to the melt to convert the molecular $ZnCl_2$ melt to an ionic melt. The large increase in oil yield that occurred when the $ZnCl_2$ temperature was increased from 450°C to 500°C is shown in Figure 2. This figure also shows the effect on oil yield of increasing the temperature of other melts studied. While the oil yields obtained when a CuCl containing LiCl/KCl melt was used were consistently higher than yields obtained in the LiCl/KCl melt, the dependence of yield on melt temperature was similar

for both. Increasing melt temperature above 500°C caused a decrease in the oil yield and increase in gas yield.

That more cracking occurred as the temperature of these melts was increased was shown by an increase in low-boiling components in the oil product and by changes seen in the gas composition. The effect of molten salt temperature on the hydrocarbon composition of the gas product is shown in Figure 3 (data from the LiCl/KCl melt are shown). At 370°C, the primary hydrocarbon component was isobutylene. As the melt temperature was increased, the relative amounts of methane and ethane increased.

The chemical composition of some of the oil products is shown in Table 2, with the corresponding solid products' composition shown in Table 3. A summary of product distributions between gas, liquid and solid products for the experiments reported in Table 2 and 3 is shown in Table 4. The H/C ratio in the oil was relatively constant, with perhaps a 10 % decrease in H/C ratio of oil produced at 570°C compared to oil produced at 400°C (treatment of polymer in CuCl containing LiCl/KCl). These data are consistent with estimates of volume % aromatics in the oils, calculated by an NMR method described by Myers, et al., which showed the $ZnCl_2$ product oils to have a higher aromatic content than other oils (31-43 % for $ZnCl_2$ product oils versus 26-31 % for LiCl/KCl or CuCl containing LiCl/KCl). (19) The char produced from this melt at temperatures above 500°C contained only 1-1.5 % H_2, limiting further volitalization of carbon remaining in the melt.

The chlorine content of some of the oils was as high as 2 %. In oil produced by low temperature treatment of polymer in LiCl/KCl, the high chlorine content probably resulted from incomplete dehydrochlorination of decomposition products of polyvinyl chloride. In oil produced in the higher temperature CuCl containing melts, increased chlorine content is probably due to chlorinated intermediates produced by the action of CuCl with oxygen containing species in the polymer. It was observed that when longer reactor residence times were used for this melt,chlorine content in the oil decreased. As expected, the chlorine content of oil produced in a carbonate eutectic (47.2 mole % Li_2CO_3; 26.6 mole % Na_2CO_3; 26.2 mole % K_2CO_3) was low.

Figure 4 shows the boiling point distributions of oil obtained from treatment of the polymer in the CuCl containing LiCl/KCl melt at 400°C and at 570°C. The fraction of oil components boiling below 200°C consistently increased as the melt temperature was increased. This figure also shows the boiling point distribution of oil obtained in the same melt, but without an inert gas sweep during pyrolysis. In this and similar experiments, after the molten salt was at temperature, the N_2 sweep was discontinued immediately before addition of polymer waste. This permitted a longer reaction chamber residence time for products and/or intermediates and produced more extensive cracking. While the total oil yield was lower than that obtained from a similar reaction with an inert gas purge, the yield of light oil with a boiling point

$\lesssim 200^{\circ}C$, obtained from the CuCl containing melts, was higher than that obtained from any other reaction conditions studied. In contrast to results reported by Perkow, the quantity of solid product (char) was not increased (6). 45.1 weight percent of the feed was recovered as solid from this pyrolysis, while 44.9 weight percent of the feed was recovered as solid product from a $520^{\circ}C$ LiCl/KCl + 10 % CuCl pyrolysis carried out with a N_2 sweep. Percent ash in the two solid products was nearly identical. Consistent with more extensive cracking occurring with the longer reaction time, the gas yield was higher in the absence of an N_2 flush. The hydrocarbon composition of the gas was similar to that of the control, but with a somewhat lower C_4 component. These data are summarized in Table 5.

These results suggest that recycling of the higher boiling components through the melt would produce further cracking. Mass spectrometric data show that the higher boiling components are primarily long chain aliphatics, with a higher hydrogen content than the lower boiling components. Because of this, excessive carbon formation should not result.

Figure 5 shows a gas chromatographic-mass spectroscopic (GC-MS) analysis on oil obtained from polymer decomposition in a CuCl containing melt at $500^{\circ}C$. Other analyses of this and other product oils on an SE-30 column that separated the isomers of C-2 and C-3 substituted benzenes showed that all the possible isomers were present. A GC-MS analysis of oil obtained by decomposing polymer in stirred sand is shown in Figure 6. Analysis conditions were identical to those used in the analysis of oil from the CuCl containing melt. The low boiling components of this oil were less aromatic than oil produced in the CuCl containing melt. Octene was a major low boiling component.

KINETICS OF GAS PRODUCTION

The kinetics of gas production resulting from decomposition of the polymer waste in molten $ZnCl_2$, $AlCl_3$/NaCl, LiCl/KCl and LiCl/KCl + 10 % CuCl, and in stirred sand, were compared. Results obtained for decomposition of polymer in molten $AlCl_3$/NaCl at $350^{\circ}C$ are shown in Figure 7. Results from four experiments showing increase in gas volume (ml) per gram of polymer is plotted versus time. Since there was considerable scatter in the volume of gas produced per gram of polymer, all the kinetic data for each set of conditions were plotted as cumulative percent of total gas produced versus time. Data from the $AlCl_3$/NaCl experiments plotted in this manner are shown in Figure 8.

For comparison of results seen under different reaction conditions, best fit curves were drawn through the plots of cumulative percent of gas produced versus time for a given set of conditions. From these curves and the average normalized total gas volume, data plotted in Figure 9 was obtained. Data shown in this figure indicate that polymer reaction rates in the tetrachloroaluminate melt at $350^{\circ}C$ are at least three times the rates in the LiCl/KCl or CuCl containing

LiCl/KCl melts and one and a half times the value measured in molten $ZnCl_2$ (all at 450°C). Reaction rates in CuCl containing LiCl/KCl are 10 % greater than in LiCl/KCl, in which rates are 10 % greater than in sand at the same temperature.

The temperature dependence of gas evolution in the less reactive systems (LiCl/KCl, LiCl/KCl/CuCl and sand) was different from that seen in $ZnCl_2$. In the less active melts at 400°C, decarboxylation to produce CO_2 (see below) was the principal reaction and gas evolution was essentially complete after 200 sec. At 450°C, a series of cracking reactions that did not occur at a measurable rate at 400°C became important and we observed a slow increase in gas volume over a much longer period of time. In $ZnCl_2$, both cracking and decarboxylation occurred at 400°C. 2200 seconds was taken as the point at which the reaction was complete; only in $ZnCl_2$ melts did a measurable reaction occur after 2200 seconds.

The average total gas volume per gram of polymer produced at 400°C in LiCl/KCl + CuCl was only 55 % of the volume produced in the same melt at 450°C. By contrast, total gas produced per gram of polymer at 400°C in $ZnCl_2$ was 85 % of the volume produced at 450°C in $ZnCl_2$. These two observations indicate that non-pyrolytic reactions are occurring in the $ZnCl_2$ melts as well as in the $AlCl_3$/NaCl melt. Further, the same kinds of reactions that occur at 450°C in $ZnCl_2$ also occur at a measurable rate at 400°C. This is probably not true in the more inert melts.

From the composition of gas samples collected from a septum near the top of the reaction flask, further comparisons of reactions occurring in the different melts can be made. Samples were obtained a number of times during the course of the experiments. Since the volume of the reaction flask was, in most cases, equal to or larger than the volume of the gas product, there was considerable backmixing of product and the gas sample collected at a particular time can not be said to be completely representative of the gas being produced at that time. However, the change in composition of gas collected at that point in the system gave useful information on the general trend in gas product composition with time. Tables 6, 7 and 8 give representative gas analysis data obtained from kinetic runs in $AlCl_3$/NaCl, LiCl/KCl and CuCl containing LiCl/KCl.

It can be seen that the reaction that occurred most rapidly, and was most important in the "inert" melts at the lower temperature studied, involved CO_2 production. The quantity of CO_2 produced per gram of polymer was approximately the same in all the melts and in sand, indicating that the source of CO_2 was probably decarboxylation of esters in the polymer mixture, rather than reaction of the polymer with oxides that might have been present in some of the melts. For example, in LiCl/KCl + CuCl at 400°C, 80-90 % of the gas product was CO_2. When the melt temperature was increased to 450°C, the first gas sample collected (time=100 sec.) contained 53 % CO_2 and 30 % isobutylene. The other

important imitial reaction that occurred in these melts at 450°C was isobutylene production. Isobutylene and other products were then cracked to smaller hydrocarbons, giving a slow increase in gas volume.

There were differences in the composition of gas produced by treatment of polymer in $AlCl_3$/NaCl melts, as compared to that obtained using any other melt. Isobutane was the largest hydrocarbon component in the gas, although at 350°C methane was formed when the product gas remained in contact with the salt. It is possible that any isobutylene produced immediately formed acid catalyzed condensation products, since the product gas was quite acidic. For the hydrocarbon analyses on all gas products, it was necessary to collect the sample over sodium hydroxide pellets to prevent acid catalyzed condensation of isobutylene. The source of HCl in gas from the "inert" melts was dehydrochlorination of polyvinylchloride. In the $AlCl_3$/NaCl melt, it is likely that additional HCl was produced from the melt itself when the polymer waste was introduced.

CONCLUSION

In the catalytic melts, $AlCl_3$/NaCl and, to a lesser extent $ZnCl_2$, the rate of polymer decomposition was more favorable than in LiCl/KCl or CuCl containing LiCl/KCl melts. However, decomposition of polymer in $AlCl_3$/NaCl gave primarily gas product. Treatment of polymer in CuCl containing LiCl/KCl at 500°C gave the best oil yield, while increasing the reactor residence time under these conditions increased the yield of liquid product with boiling point < 200°C. While there have been a number of studies on the mechanisms by which copper containing melts promote chlorination, as well as elimination reactions, the complexity of the polymer waste we worked with makes such considerations difficult in this system. Obviously there were interactions between various copper species in the melt that promoted cracking.

The oil yields obtained from molten salt treatment of this polymer waste are comparable to the yields obtained by inert gas pyrolysis of this waste at temperatures several hundred degrees higher. We conclude that molten salt treatment of highly organic waste materials has potential as a practical method of reclaiming useful products from specialized organic wastes. Oil produced in this manner from both inert melts and catalytic melts is highly aromatic. If the higher boiling components of the oil product were recycled through the melt, an even more useful oil product would result.

ACKNOWLEDGEMENT

This work was conducted under a Department of Energy-sponsored Joint Industry/University Research Program with Ford Motor Company. We are grateful for the assistance of Drs. R. L. Gealer, J. Braslow and R. C. Wingfield at Ford Research.

REFERENCES

1. Collin, G., Grigoleit, G., Michel, E., Chem.-Ing.-Tech., 51, 220 (1979).

2. Mahoney, L. R., Braslow, J., Harwood, J. J., SAE Paper No. 790299, SAE Congress, Feb. (1979).

3. Larsen, J. W., Chang, B., Rubber Chemistry and Technology, 49, 1120 (1976).

4. Menzel, J., Perkow, H., Sinn, H., Chemistry and Industry, 16, 570 (1973).

5. Sinn, H., Chem.-Ing.-Tech., 46, 579 (1974).

6. Perkow, H., Dissertation, Universität Hamburg, "Der Pyrolytische Abbau von Kunstoff in einer Salzschmelze- Massen-, Stoff- und Energiebilanzierung," 1975.

7. Sinn, H., Kaminsky, W., Janning, J., Angew. Chem. Int. Ed. Engl., 15, 660 (1976).

8. Collin, G., Grigoleit, G., Bracker, G.-P., Chem.-Ing. Tech., 50, 836 (1978).

9. Gorin, E., Fontana, C. M. Kidder, G. A., Industrial and Engineering Chemistry, 40, 2128 (1948).

10. Fontana, C. M., Gorin, E., Kidder, G. A., Meredith, C. S., Industrial and Engineering Chemistry, 44, 363 (1952).

11. Ohtsuka, Y., Tamai, Y., Journal of Catalysis, 51, 169 (1978).

12. Kenney, C. N., Catal. Rev.-Sci. Eng., 11, 197 (1975).

13. Keneshea, F. J., Yolles, R. S., Wise, H., Ind. Eng. Chem. Prod. Res. Develop., 10, 197 (1971).

14. Zielke, C. W., Struck, R. T. Garin, E., Ind. Eng. Chem., 8, 552 (1969).

15. Zielke, C. W., Klunder, E. B., Maskew, J. T., Struck, R. T., Ind. Eng. Chem. Process Des. Dev., 19, 85 (1980).

16. Nakatsuji, Y., Fujioka, S., Nomura, M., Kikkawa, S., Bulletin of the Chemical Society of Japan, 50, 3406 (1977).

17. Osteryoung, R. A., Adv. Molten Salt Chem., 3, (1974).

18. Manuscript in preparation for submission to Ind. Eng. Chem. Process Des. Dev.

19. Meyers, M. E., Stollsteimer, J., Wims, A. M., Anal. Chem., 47, 2010 (1975).

TABLE 1
ELEMENTAL COMPOSITION OF SHREDDER WASTE

% by Weight

C	H	N	Cl	O	Ash
60-70	5-7	0.4	3-5	5-15	15-20

Cu (Metallic)	Al (Metallic)	Zn (Metallic)
0.8	0.5	0.2

TABLE 2
CHEMICAL COMPOSITION OF OIL PRODUCT

Molten Salt	T °C	← % by Weight →					H/C ratio
		C	H	S	Cl	N	
LiCl/KCl	380	81.3	10.5	0.9	2.3	0.8	1.55
	405	82.0	10.7	0.9	0.4	0.6	1.57
	405	81.7	10.4	1.0	0.3	0.8	1.53
	465	83.6	11.0	NA	0.5	0.5	1.58
	500	76.6	9.6	0.8	1.1	0.1	1.50
	565	82.7	10.1	0.7	0.7	0.1	1.47
LiCl/KCl + 10 % CuCl	400	84.5	11.5	0.6	1.6	0.3	1.63
	450	83.8	10.9	0.8	0.7	0.6	1.56
	520	82.6	10.2	0.7	1.2	0.2	1.48
	570	83.5	10.2	0.8	2.1	0.1	1.47
(No N_2 Flush)	500	85.3	10.8	0.6	0.6	0.3	1.52
$ZnCl_2$	410	87.3	10.6	0.4	0.3	0.07	1.45
	430	85.3	10.0	0.5	0.4	0.08	1.41
	450	86.3	10.3	0.3	1.6	0.03	1.43
	500	86.6	11.0	0.3	1.3	0.5	1.53
$NaCl/AlCl_3$	350	86.8	11.0	0.6	1.2	0.04	1.52
	400	82.6	11.1	0.4	1.4	0.04	1.61
	450	85.6	11.1	0.4	2.1	0.6	1.56
$Li_2CO_3/Na_2CO_3/K_2CO_3$	510	84.1	10.4	0.6	0.2	0.3	1.48

TABLE 3
CHEMICAL COMPOSITION OF SOLID PRODUCT

Molten Salt	T°C	% by Weight						H/C ratio
		C	H	S	Cl	N	Ash	
LiCl/KCl	380	79.3	5.5	1.0	0.2	0.3	16.5	0.83
	405	77.2	3.9	0.9	0.3	0.4	20.0	0.61
	405	64.7	4.1	1.2	1.5	0.3	35.1	0.76
	465	73.4	2.6	NA	0.12	0.3	25.5	0.42
	500	57.2	2.0	0.9	0.2	0.1	39.8	0.42
	565	52.5	1.4	1.3	0.6	0.4	46.8	0.32
LiCl/KCl	400	78.6	4.0	1.4	1.2	0.2	18.3	0.61
+ 10 % CuCl	450	72.8	1.4	1.6	0.8	0.3	23.7	4.33
	520	78.1	1.4	1.7	0.5	0.2	18.5	0.22
	570	70.7	0.9	2.0	0.5	0.01	24.9	0.15
	*500	80.9	1.2	2.1	1.2	0.2	17.9	0.18
$ZnCl_2$	410	52.9	3.3	1.9	2.4	0.3	30.1	0.75
	430	70.5	3.5	1.3	2.2	0.4	29.9	0.60
	450	66.3	2.6	1.5	1.4	0.4	28.3	0.47
	500	50.3	1.3	1.5	3.2	0.3	44.8	0.31
$NaCl/AlCl_3$	350	65.1	2.3	0.4	9.8	0.3	15.2	0.42
	400	82.2	2.8	1.1	1.2	0.2	11.4	0.41
	450	85.1	2.5	0.4	1.5	0.5	8.3	0.35
$Li_2CO_3/Na_2CO_3/K_2CO_3$	510	57.4	1.6	1.0	0.4	0.2	14.0	0.33

* No N_2 Flush

TABLE 4
PRODUCT YIELD FROM MOTLEN SALT TREATMENT OF SHREDDER WASTE

Molten Salt	T°C	% by Weight		
		Total Oil	Solid	Gas†
LiCl/KCl	380	12.6	68.8	11.7
	405	17.4	62.5	13.4
	405	17.4	59.5	20
	465	26.1	54.4	17.4
	500	29.7	41.8	21.1
	565	29.4	42.7	24.0
LiCl/KCl	400	20.6	55.2	12.5
+ 10 % CuCl	450	33.6	45.6	12.0
	520	35.3	44.9	10.1
	570	32.2	42.8	18.3
	*500	25.0	45.1	17.2
	*500	25.0	NA	NA

TABLE 4 (Cont'd)

Molten Salt	T°C	% by Weight Total Oil	Solid	Gas†
$ZnCl_2$	410	5.7	NA	NA
	430	5.9	78.7	23
	450	17.5	63.4	20.9
	500	30.7	NA	NA
$NaCl/AlCl_3$	350	9.4	NA	NA
	400	10.4	49.9	29.5
	450	10.8	46.2	30.8
$Li_2CO_3/Na_2CO_3/K_2CO_3$	460	18.7	34.9	NA
	510	26.0	37.8	24.2

† Gas calculated by difference with correction for Ash loss or gain in solid.

* No N_2 flush

TABLE 5
EFFECT OF REACTOR RESIDENCE TIME ON PRODUCTS

Molten Salt	T°C	N_2 Flush	Yield - Wt % Total Oil	Oil BP $\lesssim$ 200°C	Solid
LiCl/KCl	500	+	29.7	6.6	41.8
	500	-	26.7	11.4	46.2
LiCl/KCl + 10 % CuCl	500	+	35.3	8.8	44.9
	500	-	25.0	11.3	45.1
	500	-	25.0	11.9	47.5
$ZnCl_2$	500	+	30.7	5.9	NA
	500	-	18.4	7.5	NA

TABLE 6
COMPOSITION OF GAS FROM KINETIC RUNS
IN $AlCl_3$/NaCl

T°C	350				300			
Sampling Time (Sec)	122	320	628	2200	114	400	670	2200
	Volume %				Volume %			
CH_4	14.7	25.0	30.6	36.2	0.7	1.6	1.5	10.0
CO_2	38.9	28.6	23.1	12.6	44.9	37.1	36.6	35.9
C_2H_4 + C_2H_6	6.3	2.8	1.7	1.4	0.7	3.0	0.9	3.1
C_3's	6.1	8.7	10.8	13.1	10.9	10.8	12.8	13.0
*C_4's	29.7	30.2	29.2	29.8	39.8	45.0	46.7	38.1

* Primarily Isobutane

TABLE 7
COMPOSITION OF GAS FROM KINETIC RUNS
IN LiCl/KCl

T°C	450				400			
Sampling Time (Sec)	93	330	684	2200	102	274	645	2200
	Volume %				Volume %			
CH_4	6.4	12.7	20.4	NA	1.6	3.5	7.4	10.0
CO_2	51.2	44.4	39.8	NA	84.0	77.0	64.5	60.4
C_2H_4	4.4	6.7	5.9	NA	6.4	5.0	6.3	6.0
C_2H_6	2.9	5.8	7.8	NA	<0.2	1.1	2.3	2.6
C_3's	6.1	8.3	9.7	NA	1.9	2.5	3.7	2.5
*C_4's	29.0	21.9	16.4	NA	4.9	9.9	15.3	18.4

* Primarily Isobutylene

TABLE 8
COMPOSITION OF GAS FROM KINETIC RUNS
IN LiCl/KCl + 10 % CuCl

$T^{o}C$	450				400			
Sampling Time (Sec)	99	324	630	2200	120	320	640	2200
	Volume %				Volume %			
CH_4	5.9	17.7	25.7	37.5	1.2	2.4	5.5	9.4
CO_2	53.4	53.8	49.0	37.6	86.4	85.2	77.7	77.9
C_2H_4	3.6	4.5	5.1	4.1	3.5	2.8	3.1	2.6
C_2H_6	2.3	4.2	4.1	6.0	<0.2	0.4	1.1	1.4
C_3's	4.3	6.1	6.8	7.9	1.7	1.1	1.6	1.5
*C_4's	30.6	13.7	9.4	6.8	7.2	7.8	11.2	7.2

* Primarily Isobutylene

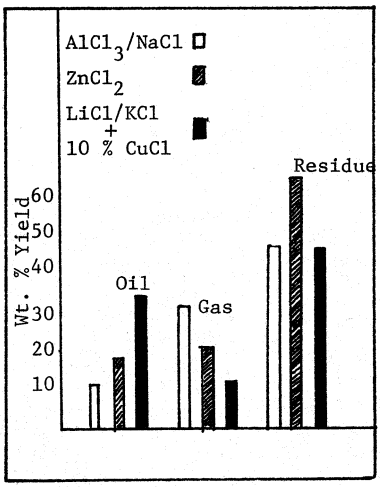

Fig. 1. Product Yield from Molten Salt Treatment of Shredder Waste at 450 C.

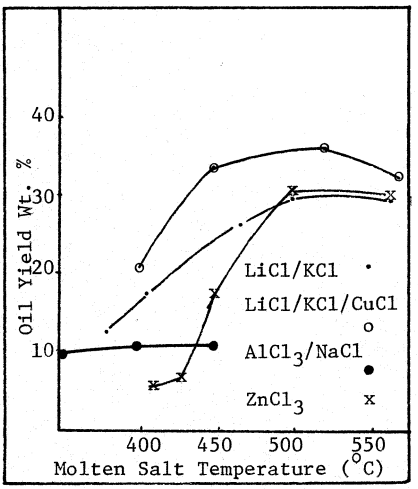

Fig. 2. Effect of Molten Salt Temperature on Oil Yield.

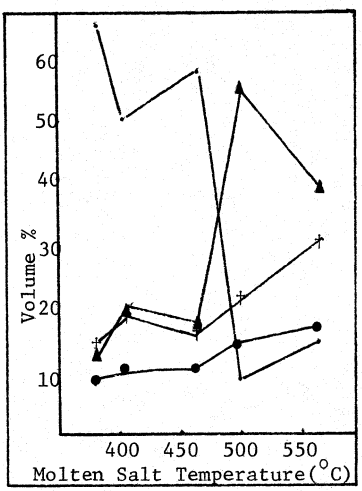

Δ Methane o Propane
† Ethane • C_4's

Fig. 3. Effect of Molten Salt Temperature (LiCl/KCl) on Hydrocarbon Composition of Gas Product.

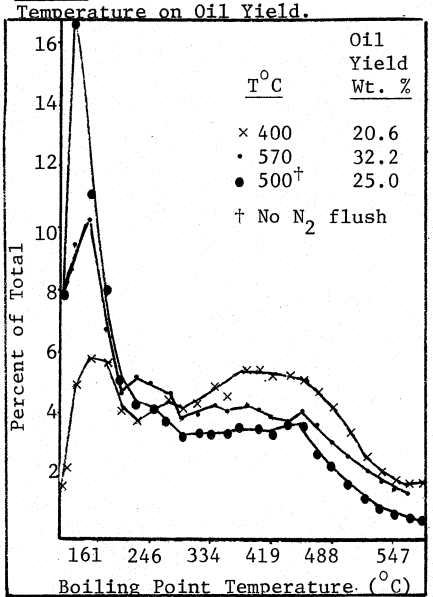

Fig. 4. Effect of Molten Salt Temperature (LiCl/KCl + 10 % CuCl) and Reactor Residence time on Boiling Point Distribution of Oil.

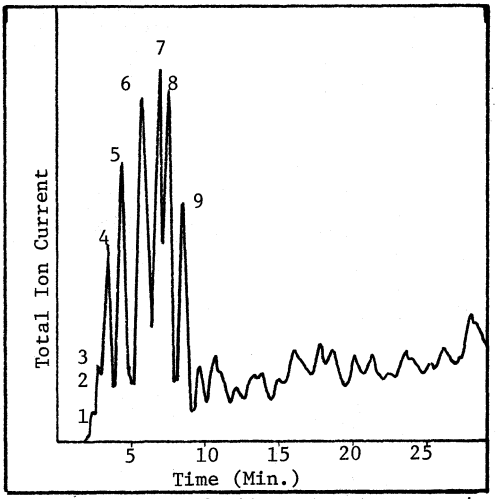

Fig. 5. GC-MS Analysis of Oil Produced in LiCl/KCl/CuCl melt; Pyrolysis Temperature 500 C. (1) C_6H_{12}; (2) C_7H_{14}; (3) Benzene; (4) C_8H_{16}; (5) Toluene; (6) Ethylbenzene; (7) Styrene; (8) Dipentene; (9) C_4-Alkylbenzene.

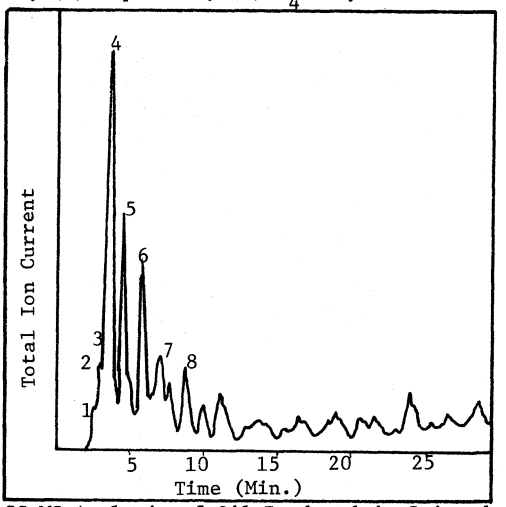

Fig. 6. GC-MS Analysis of Oil Produced in Stirred Sand; Pyrolysis Temperature 450 C. (1) C_6H_{12}; (2) C_7H_{14} (3) Benzene; (4) C_8H_{16}; (5) Toluene; (6) Ethylbenzene; (7) Styrene; (8) C_4-Alkylbenzene.

Fig. 7. Increase in Gas Product versus Time for Shredder Waste Pyrolysis in $AlCl_3$/NaCl at 350°C.

	Exp. No.	Yield t=2200 ml/g
†	1	180
•	2	170
o	3	180
Δ	4	190

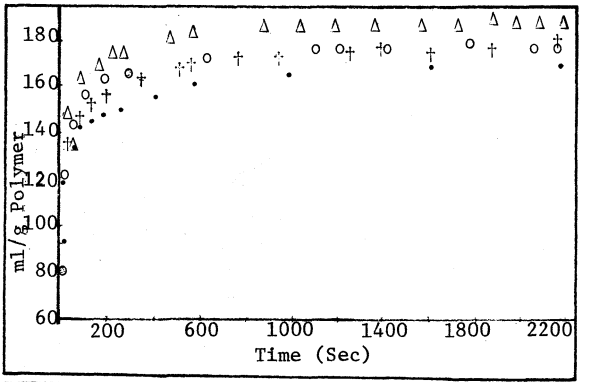

Fig. 8. Cumulative % Volume Increase in Gas versus Time for Shredder Waste Pyrolysis in $AlCl_3$/NaCl at 350°C.

	Exp. No.
†	1
•	2
o	3
Δ	4

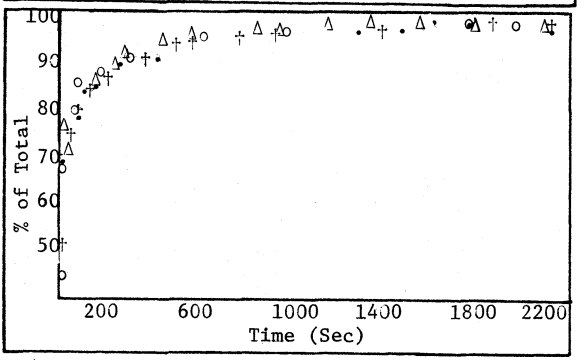

Fig. 9. Relative Rates of Gas Production in Different Molten Salts.

* $AlCl_3$/NaCl - 350°C

Δ $ZnCl_2$ - 450°C

o LiCl/KCl - 450°C

\+ LiCl/KCl/CuCl - 450°C

× Sand - 450°C

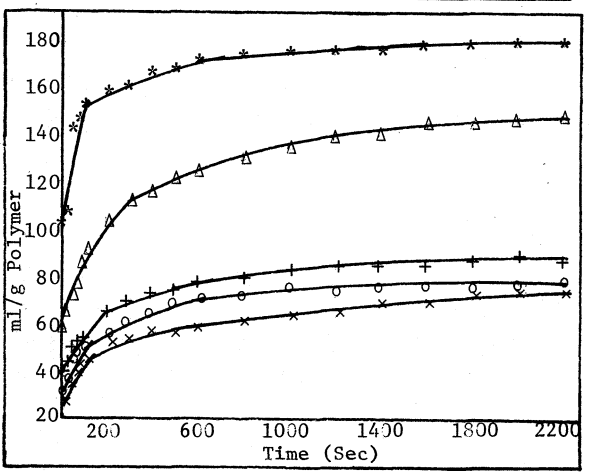

DOI: 10.1149/198109.0425PV

REACTIONS OF COAL AND MODEL COAL COMPOUNDS IN ROOM TEMPERATURE MOLTEN SALT MIXTURES

David S. Newman*[+], Randall E. Winans, Robert L. McBeth,
Chemistry Division, Argonne National Laboratory
Argonne, Illinois 60439

Abstract

A 2:1 $AlCl_3$-pyridinium chloride molten salt solution was used as the reaction medium for the alkylation of diphenyl ethane and a bituminous coal by 2-propanol. Probably accompanying the room temperature Friedel-Crafts alkylation is a Meerwein-Ponndorf-Verley reduction. Completely deuterated 2-propanol did not react at all with the pyridinium ring indicating that the pyridinium chloride serves to lower the temperature at which the $AlCl_3$ is able to catalyse the reactions. The pyridinium chloride also catalyzes the Friedel-Crafts Alkylation.

Introduction

In recent years many authors have focused their attention on alkylation reactions in molten salt mixtures containing $AlCl_3$. In particular, Osteryoung and coworkers have investigated room temperature or near room temperature melts containing $AlCl_3$ and various pyridinium salts, with the intent of finding interesting media in which to do electroorganic chemistry (1-3). Schlosberg and coworkers have recently shown that alkylation is a beneficial treatment for coal prior to liquefaction at 1500 psi and 700K, by alkylating several different coals under Friedel-Crafts conditions in an autoclave at 373-423K under N_2 atmosphere (4). At about the same time Ross and Blessing demonstrated the advantages of using isopropyl alcohol as a hydrogen donor to coal and model coal compounds in base catalyzed reactions at 600K (5), while Butler and Snelson showed that $AlCl_3$ also catalyzed the hydrogenation of coal (6).

Based on these investigations it was our contention that, by combining Friedel-Crafts conditions with Meerwein-Ponndorf-Verley conditions, we could simultaneously effect both alkylation, and reduction and depolymerization of coal and do it at or near room temperature.

The reaction medium we selected was a 2:1 mixture of $AlCl_3$ and pyridinium chloride, C_5H_6NCl, which is liquid at, or near room temperature, relatively easy to prepare and inexpensive; a very important consideration for coal chemistry. Moreover, the particular

---

+ Permanent address, Department of Chemistry, Bowling Green State University, Bowling Green, Ohio 43403

melt, as well as the pyridinium salt, is well characterized (7-9). Diphenylethane (bibenzyl) was used as our model coal compound because it has both aryl and alkyl bonds typical of those found in coals and it has been extensively studied under a variety of conditions. The coal chosen for our initial investigation was a PSOC-244 high sulfur, high volatile C bituminous coal and 2-propanol was used as an alkylating agent and hydride source.

Experimental Details

Preparation of the coal.

A 10 g sample of PSOC-244 high sulfur coal (C 55.8%, H 7.5%, N 0.95%, S 7.5%, (total), ash 19.5%, O 12% (by difference)) was ground with water in a shatter box until it formed a slurry and then demineralized using an aqueous HF/HCl solution. The demineralization was carried out by adding 100 ml con HCl to the coal slurry which had been placed in a teflon beaker. To this mixture we added 100 ml of 40% HF and allowed the system to react for 48 hours. The resulting demineralzed coal was filtered, vacuum dried and analyzed. (C 64%, H 5%, N 1.1%, S 6.23% (total), ash 3.9%, O 19.8% (by difference)). The HCl/HF treatment removed most of the silicate and other inorganic material from the coal.

Preparation of reaction media.

Reagent grade anhydrous aluminum chloride (Fisher Scientific) and reagent grade C_5H_6NCl (Eastman Kodak) which had been thoroughly dried were used without further purification because the impurities in these compounds are far fewer than impurities originating from random fluctuations in composition in any given coal sample.

In a dry box, a 2:1 mixture of the $AlCl_3$ and C_5H_6NCl was prepared by weighing the requisite amount of $AlCl_3$ into a 100 ml 3 neck flask. To the $AlCl_3$ was added the appropriate amount of C_5H_6NCl. The mixture would usually spontaneously melt forming a clear to greyish viscous liquid. We then added weighed amounts of coal or model compounds, alkylating agents and so forth to this melt. The reaction vessel was removed from the dry box, placed in a constant temperature bath and the reaction mixture stirred with a magnetic stirrer. A nitrogen atmosphere was maintained in the 3-neck flask throughout the course of the reaction.

Treatment and characterization of reaction products.

After the predetermined requisite amount of time had elapsed, the reaction was carefully quenched by first cooling the closed reaction vessel in ice water and then dropping small pieces of ice, one at a time, into the reaction vessel so as not to raise the melt's temperature substantially. After all of the $AlCl_3$ had reacted with

the water, the aqueous slurry was extracted with various organic solvents and the extracted material analyzed by high performance liquid chromatography (HPLC), gas chromatography mass spectrometry (GC/MS) (10,13), and gas chromatography-microwave plasma detector computer analysis (GC/MPD) (11).

The main feature of the GC/MPD-computer system is an Applied Chromatography System MPD-850 which is an emission spectrometer with a helium plasma source. The spectrometer is connected to a GC and is able to simultaneously detect the elements C, H, D, S, F. Cl, O or N. The output from the spectrometer is amplified and transferred to a central computer facility via a CAMAC interface. By using suitable standards we can obtain empirical formulae or detect the presence of deuterium in labeling experiments with these instruments with an accuracy of $\pm$ 5%. An inlet system allowing direct entry of solid coal into the MPD was designed to facilitate the analysis of nonvolatile coal or coal products. This inlet system or "solid probe" is shown schematically in Fig. 1a. It consists of a platinum tube which serves as a furnace and is heated directly by two leads connected to the output of a dc power supply (HP 6259 B). Both the rate and the amount of heating can be controlled by the power supply. The temperature inside the inlet tube is easily monitored by means of a thermocouple. A teflon T tube connector, attached to the inlet tube by one of its arms and to a gas source by its central channel, conducted the necessary carrier gas or gases into the system. The sample itself was held in a hollow cylinder of platinum gauze welded to a platinum rod (Fig. 1b) and inserted directly into the furnace through the unattached arm of the T tube (along the principal axis of the platinum furnace). With the sample in place and the carrier gas flowing, the furnace was heated to the desired temperature, usually 1100°C, to ensure complete pyrolysis. The pyrolysis products were fed directly into the MPD. The pyrolysis reaction of coal can be described by the equation:

$$O_2 + \text{Coal} \longrightarrow CO_2 + H_2O + SO_2 + \ldots \qquad [1]$$

The products of this reaction are atomized by the plasma and the emission spectra of the atoms analyzed by the MPD.

Results and Discussion

Model compounds and solvent system.

In order to characterize the role of the solvent and assess the extent of autoalkylation of the 2-propanol or the bibenzyl, a series of experiments were performed in which either the 2-propanol or the bibenzyl or a mixture of the two were allowed to react in the melt.

Autoalkylation of 2-propanol formed an orange red material which contained a series of high molecular weight polymers, most of which

were nonvolatile. No alkylated pyridines were identified, but some HCl was generated indicating that a small amount of aluminum alkoxide was probably forming according to the equation

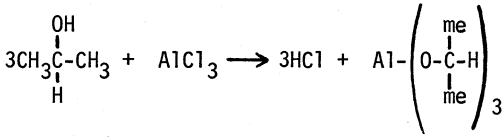

[2]

Autoalkylation of bibenzyl gave a series of polymers as well as a low yield of monomeric material. The compounds, produced by the bibenzyl reaction and identified by gel permeation chromatography and GC/MS are listed in Table I. Our results are consistant with those of Heredy and Neuworth (14) who used model compounds in phenol to show that under Friedel-Crafts conditions, methylene chains can be broken and the resulting species can alkylate other aromatic compounds. In our system, which lacked phenol or another hydrogen source, alkylation proceeded faster than bond cleavage although aryl and methylene bonds were indeed broken at the low reaction temperatures. The molecular weights of the alkylation products were determined by gel permeation chromatography and ranged from 78 (benzene) to approximately 10,000. One aspect of this reaction which deserves comment is the formation of compound 5 which was identified by its mass spectrum. For this compound to form, the aryl carbon bond of bibenzyl had to cleave even though the temperature was less than 40°C. The bond energy for this bond is 414 kj/mole which means that either the $AlCl_3$ or the C_5H_6NCl or both are catalyzing the reaction.

To discover if the pyridinium ion would react with the alkylating agent, under reaction conditions, 1.6g of 2-propanol-d and 1.8g bibenzyl were allowed to react in the 2:1 $AlCl_3$ C_5H_6NCl solution at 30°C for four hours. The reaction was quenched with water, as described previously, and extracted with hexane. The aqueous layer was neutralized with NaOH (leaving a distinct odor of pyridine) and an aliquot passed through the MPD. No deuterium was detected in the instrument's deuterium channel indicating that no ring proton exchange or alkylation of the pyridine ring occurred despite the favorable environment for alkylation reactions (12). This means the principal role of the pyridinium chloride in the melt is to lower the temperature at which the $AlCl_3$ catalyzes the various reactions. The 2-propanol-d_8 reacted with the bibenzyl to form a series of alkylated phenyl derivatives (Fig. 2) as expected. Approximately 85% of the initial bibenzyl reacted within the four hours and about 40% of its aliphatic carbon bonds were cleaved. The alkylation products were identified by GC/MPD and GC/MS. From these results we conclude that the alkylating agent prefers to alkylate bibenzyl rather than itself and bibenzyl prefers reacting with the 2-propanol to autoalkyation. The earlier experimental results, in which no deuterium was found on the pyridine ring, still did not indicate if the nitrogenic proton of

the pyridinium ion, $\geq N\text{-}H^+$, had exchanged with any of the 2-propanols' deuterium atoms. To ascertain whether or not exchange had occurred, the ^{1}HNMR spectrum of a 2:1 $AlCl_3/C_5H_6NCl$ melt was obtained on a CFT-80 NMR machine with variable temperature capability. The spectrum showed a striking nitrogen broadened triplet at 70°C (Fig. 3) indicating that in the pure melt exchange was not occurring because if it were the proton could not reside on the nitrogen long enough to couple with it, but would give a sharp singlet (8,9). Our spectrum is similar to that reported by Angell and Shuppert (7) for a similar melt at 148°C, but our ring proton resolution is not as good because of our lower temperature. This spectrum, incidentally, is excellent evidence for the fact that there are few, if any, free Cl^- ions in the melt. If a substantial concentration of free Cl^- ions were present the $\geq N\text{-}H^+$ would appear as a sharp singlet in the ^{1}HNMR spectrum (9). The dominant anionic species is probably $Al_2Cl_7^-$ as suggested by Gale and Osteryoung (22,23). The cation is, of course, the pyridinium ion, and the environment is distinctly unfavorable for exchange.

When a quantity of 2-propanol-d_8, equivalent to the C_5H_6NCl is added to the melt, the brownish-orange polymeric material formed again and remained suspended. The ^{1}HNMR spectrum changed markedly with respect to the nitrogen-broadened triplet, so prominent in the pure melt, and formed a very broad singlet peak. The integrated area under the $\geq N\text{-}H^+$ peak was reduced from approximately one sixth that of the ring proton area to approximately one twelfth, indicating that exchange was complete and the system had equilibrated. It is assumed that it was the hydroxyl deuterium that exchanged with the $\geq N\text{-}H^+$. This implies the $\geq N\text{-}H^+$ is available to catalyze various proton catalyzed reactions and broadens the scope of the $AlCl_3/C_5H_6NCl$ melt as a reaction medium.

Reactions with coal.

A sample of the HF/HCl demineralized HVC coal was added to the $AlCl_3/C_5H_6NCl$ melt and allowed to mix with it for 20 hrs at 30°C. The black slurry was then quenched and the coal separated from the melt and analyzed to assure us that no substantial elemental changes had occurred. No effort was made to distinguish between the melt soluble fraction and the melt insoluble fraction of the coal; both were combined. In another series of experiments, now underway, the solubility of coal in these melts is being investigated. The elemental analysis was substantially the same as before (C 66%, H 4.8%, N 1.25%, S 6.46% (total)). To detect changes in average molecular weight of the coal that may have occurred through bond cleavage, autoalkylation, etc., the solubility of the reacted coal in a 3:1 benzene-methanol solution was compared with that of the unreacted coal in the same solvent. The solubility of the reacted coal was 6.3% by weight and the solubility of the unreacted coal was 9.8% by weight. Considering the errors involved in recovery and the relatively low solubilities of the two coals, there is not very much difference. Nevertheless, it is

possible that some internal change, such as autoalkylation of the coal did occur while it was in the melt.

The reaction between the demineralized coal and 2-propanol is shown schematically in Fig. 4. The reaction was allowed to continue for 15 hrs whereupon it was quenched in the previously described manner. The observed increase in weight of 0.6 g by the coal is consistant with the solvent's ability to catalyze alkylation reactions and represents propyl moities added to the coal. The water insoluble alkylated coal was analyzed and found to contain 4.21% S (total) 1% N, 61% C, 5.1% H, and 13% ash. The 34% decrease in total sulfur is very likely due to the alkylation per se which increased the weight of the coal 35% and does not represent a substantial reduction in the total sulfur content. In order to show quantitatively that nothing other than alkylation (and perhaps cleaving of C-C bonds) was occurring, the C/H ratios of the coals were compared and the C/H ratio calculated if only 2-propanol were added. The C/H ratio of 2-propanol is 4.5 and the C/H ratio of the coal before alkylation is 13.8. Therefore, the expected C/H ratio is

$$\frac{1.5}{1.5 + 0.54} (13.8) + \frac{0.54}{1.5 + 0.54} (4.5) = 11.3$$

and the measured C/H ratio is 11.5. Within experimental error, these two values are the same, which means that in all likelihood alkylation of the coal is the major cause of the coal's weight increase. The increase in ash content is probably due to $AlCl_3$, together with various aluminum oxides and alkoxideds that were not removed from the coal.

The molecular weight distribution of the benzene/methanol soluble fraction of the alkylated coal was obtained by gel permeation chromatography using the HPLC instrument with the monochrometer set at 254 nm. Four u-styrogel columns were used in series for the separation. Three had 100A° nominal pore diameters and one had 500A° nominal pore diameters. The chromatogram is shown in Fig. 5. The molecular weights ranged from 4400 to less than 100 with the largest fraction being in the neighborhood of 560. Since 254 nm is the region of the spectrum in which aromatic molecules strongly adsorb light, a conclusion that can be drawn from this chromatogram is that there are either polymers containing aromatic units or double and triple bonds (which also absorb at 254 nm) dissolved in the benzene/methanol solution. These entities could not have easily originated from the alkylating agent and therefore had to come from the coal.

A portion of the benzene/methanol soluble fraction of the alkylated coal was analyzed via the solid probe of the GC/MPD and was found to contain sulfur in about the same proportion as in the original coal. This was considered proof that at least some of the original coal was dissolving. It is impossible for the sulfur to have

originated from the alkylating agent.

Comparing the solubility of nonalkylated coal in benzene/methnaol with the solubility of the alkylated coal in the same solvent, it is obvious that alkylated coal is considerably more soluble (29% vs 6.3%). If it is assumed that increased crosslinking of the coal is occurring (15) or at least is capable of occurring in the $AlCl_3/C_5H_6NCl$ melt, an obvious conclusion to be drawn from our data is that alkylation and depolymerization proceed much faster at room temperature than internal crosslinking or autoalkylation. This increases the benzene/CH_3OH solubility faster than the crosslinking-autoalkylation decreases it and suggests alkylation by 2-propanol at room temperature in 2:1 $AlCl_3/C_5H_6NCl$ is a useful technique for coal solubilization.

To further characterize the coal alkylation reaction, and prove the 2-propanol alkylated the coal rather than polymerized and attached itself to the coal's surface, we alkylated the coal with 2-propanol-d_8 and proceeded in a manner similar to that described in Fig. 4. A 1.6 g sample of 2-propanol-d_8 was allowed to react with 1.5 g of demineralized coal at 30°C for 16 hrs. The reaction mixture solidified several hours after the propanol was added, indicating 30°C is a bit too low a temperature for the reaction and 40°C is about the lowest feasible temperature to alkylate coal in the $AlCl_3/C_5H_6NCl$ melt. Again no ring proton exchange or pyridine ring alkylation occurred. The coal increased in weight by 0.16 g and the benzene/methanol soluble fraction was 0.14 g suggesting that the solubility in benzene/methanol is roughly proportional to the increase in weight. The weight increase seems to be an indication of the amount of coal alkylation that occurred.

The coal sample, after extraction with benzene/methanol, was placed in the solid probe of the MPD and monitored for deuterium on the assumption that if deuterium appeared it was final proof that the coal was alkylated. Deuterium appeared in the MPD.

Reaction Mechanisms.

The reaction mechanisms that can be given in detail and with some degree of confidence are those involved with the autoalkylation of bibenzyl and the alkylation of bibenzyl with 2-propanol. The first step in the autoalkylation of bibenzyl is protonation of the bibenzyl, the proton most likely coming from the pyridinium ion:

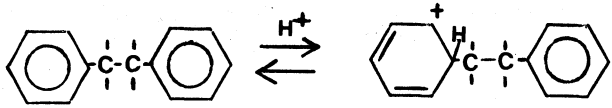

[3]

Protonation is then followed by attack on the carbonium ion by another bibenzyl:

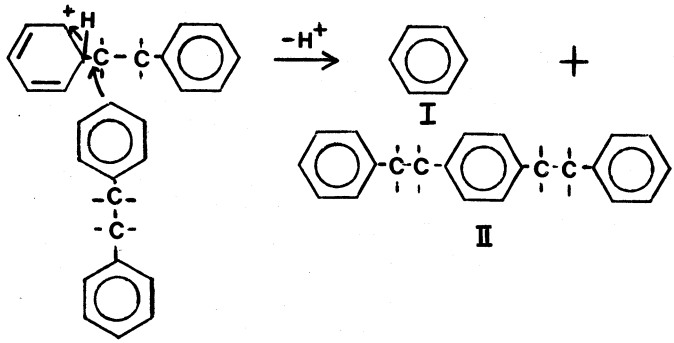

[4]

Both compound I and II have been identified by GC/MS and HPLC. The alkylation of the bibenzyl by the 2-propanol has for its initial step

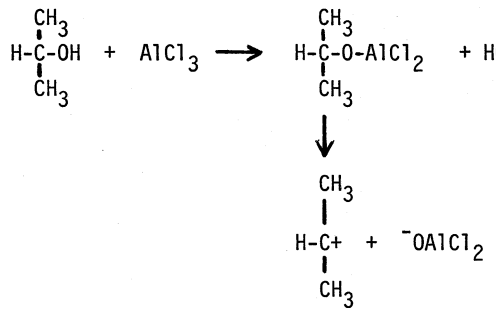

[5]

the propyl carbonium ion then attacks the bibenzyl forming the various products we have isolated.

In all likelihood the principal reaction mechanism for the coal alkylation by 2-propanol is similar to Eq. 5 with the carbonium ion then attacking aryl sites in the coal:

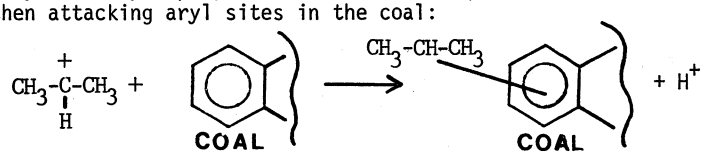

[6]

Competing with this reaction are Sholl type reactions of the form (16)

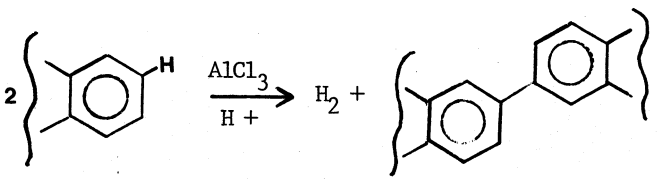

[7]

Surprisingly, Sholl reactions did not occur to any great extent in the bibenzyl-2-propanol experiments, but there was evidence for this type of reaction in the bibenzyl autoalkylation.

As a result of the formation of compounds 5 and 6 (Table I) as well as the slight decrease in the solubility of the demineralized coal in benzene/methanol, one can not rule out the possibility Eq. 7 is competing with Eq. 6. The substantial increase in the alkylated coal's benzene/methanol solubility relative to the nonalkylated coal, even taking into account that some of the soluble material, was the alkylating agent, together with the production of toluene, benzene, ethyl benzene and other reduced species in the model compound reaction, strongly suggests that a Meerwein-Pondorf-Veerly reduction is occurring. The 2-pronanol's α hydrogen is being transferred either to a carbonyl group on the coal (5) or directly to an unsaturated site. The mechanism for H^- transfer to coal is most succinctly described by Eq. [2] followed by:

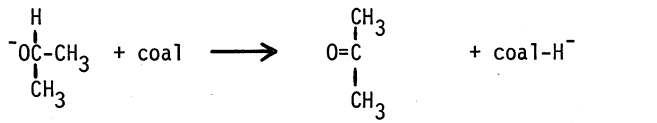

[8]

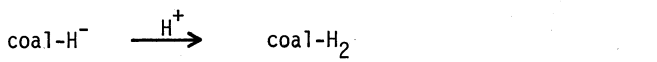

[9]

The proton in Eq. 9 comes from the pyridinium ion, another 2-propanol, or a carbonium ion originating from the Friedel-Crafts alkylation.

The exceptionally large weight increase of the alkylated coal (Fig. 4) represents the addition of approximately 15 alkyl groups per 100 carbons and is higher than that reported by Kroger (15,18,19) for the alkylation of high vitrinite coals using isopropyl chloride and $AlCl_3$ in CS_2 at 45°C. In fact, we have yet to find a more extensive coal alkylation reported in the literature. Evidence that depolymerization of the coal is accompanying the alkylation reaction stems from the fact that the average molecular weight of the benzene/methanol soluble fraction is about the same as that found by Heredy, Kostyo and Neuworth (20,21) and that the solubility of the alkylated coal is

significantly increased relative to the nonalkylated coal.

Conclusion

A 2:1 $AlCl_3/C_5H_6NCl$ solution seems to be an excellent reaction medium for both Friedel-Crafts alkylation and Meerwein-Ponndorf-Veerly reduction as well as deploymerization of coal. The low temperatures at which the reactions occur in this melt further enhance the ease of handling of the reaction products. However, a large variety of coals and model coal compounds remain to be studied before a firm conclusion as to the detailed mechanisms and scope for these intriguing reactions can be determined. It is also our opinion, in agreement with other authors, that alkylation is a beneficial treatment of coal prior to liquefaction.

Acknowledgement

This work was supported by the Office of Basic Energy Sciences, Division of Chemical Sciences, U.S.D.O.E. One of us (DSN) wishes to thank the Argonne Division of Educational Programs for awarding him a Fossil Energy Faculty Research Residency during the summer of 1980. This program is funded by the U.S. Department of Energy - Fossil Energy.

References

1. V. R. Koch, L. L. Miller, R. A. Osteryoung; J. Am. Chem. Soc. 98 5277 (1976).
2. J. Robinson, R. A. Osteryoung; J. Am. Chem. Soc. 102 4415 (1980).
3. J. Robinson, R. A. Osteryoung; J. Am. Chem. Soc. 101 323 (1979).
4. R. H. Schlosberg, R. C. Neavel, P. S. Maa, M. L. Gorbaty; Fuel 59 45 (1980).
5. D. S. Ross, J. E. Blessing; Fuel 58 (1979).
6. R. Butler, A. Snelson; Fuel 59 93 (1980).
7. C. A. Angell, J. W. Shuppert, J. Phys. Chem. 84 538 (1980).
8. V. C. Reinsborough, Aust. J. Chem. 23 1473 (1970).
9. D. S. Newman, W. Rohr, Duane Kirklin, this journal 119 798 (1972).
10. M. H. Studier, R. Hayatsu, R.E Winans, in Analytical Methods for coal and coal products, C. Carr Jr. Editor (Academic Press, New York, 1978) Vol. 2, p. 43.
11. R. E. Winans, R. G. Scott, R. L. McBeth, R. Hayatsu, Preprint 25 (No. 2) 262-267 (Div. of Petroleum Chemistry, Am. Chem. Soc.)
12. H. L. Jones, R. A. Osteryoung, Advances in Molten Salt Chemistry 3 121 (1975).
13. R. Hayatsu, M. H. Studier, L. P. Moore, E. Anders Geochim. Cosmochim. Acta 39 471 (1975).
14. L. A. Heredy, M. B. Neuworth Fuel 41 221 (1962).
15. J. W. Larsen, E. W. Kuemmerle Fuel 55 162 (1976).
16. For a review of these reactions see Balaban and Nenitzescu in Olah; "Friedel-Crafts and Related Reactions" (Interscience New

York 1963-65) Vol. 2
17. E. D. Williams, K. A. Krieger, A. R. Day J. Am. Chem. Soc. 75 2404 (1953).
18. C. Kroger, H. DeVries Liebigs Ann 35 652 (1962).
19. C. Kroger, H. B. Rabe, B. Rabe; Edrol, Kohle und Erdgas; Petrochemie 16 21 (1963).
20. L. A. Heredy, L. A. Kostyo, M. B. Neuworth Fuel 43 414 (1964).
21. L. A. Heredy, L. A. Kostyo, M. B. Neuworth Fuel 44 125 (1965).
22. R. J. Gale, R. A. Osteryoung, Inorg. Chem. 17 2728 (1978).
23. R. J. Gale, R. A. Osteryoung Inorg. Chem. 18 1603 (1979).

TABLE I - Autoalkylation Products of Bibenzyl

1. benzene
2. toluene
3. ethylbenzene
4. bibenzyl
5. 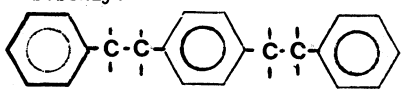
6. 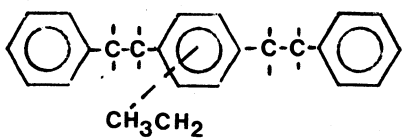

7. high molecular weight polymers

FIG 1 SOLID PROBE FOR GC/MPD

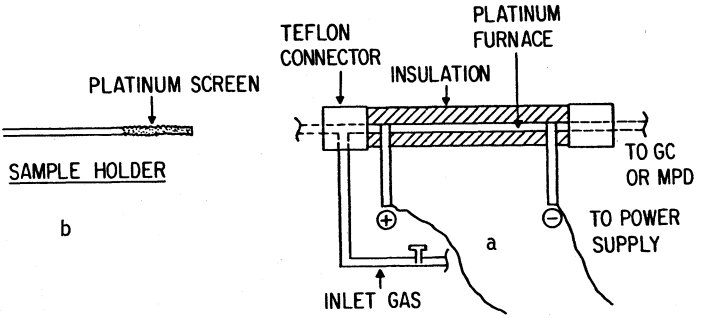

Deuterated Compounds Identified in GC/MPD

Chromatogram Peak Number	Compound	% of Total
1.	Isopropylbenzene	1.2
2.	Disopropylbenzene	2.6
3.	Triisopropylbenzene	6.1
4.	Bibenzyl	9.2
5.	Isopropyldibenzyl	7.3
6.	Diisopropyldibenzyl	18.0
7.	Unidentified	4.2
8.	Triisopropyldibenzyl	21.0
9.	Tetraisopropyldibenzyl	25.5
10.	Pentaisopropyldibenzyl	4.8
(toluene identified in HPLC)		99.9

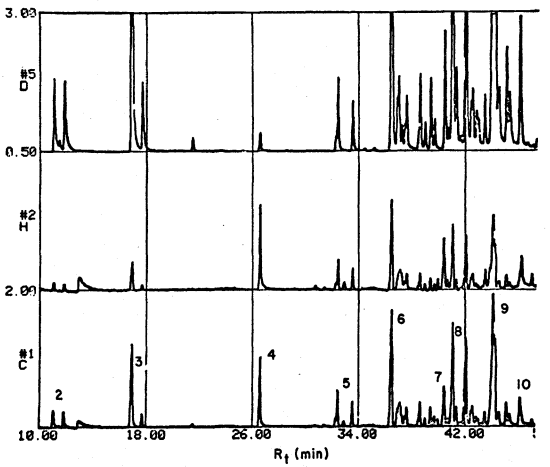

FIG 2 CHROMATOGRAM OF THE 2-PROPANOL-d_8 BIBENZYL REACTION PRODUCTS

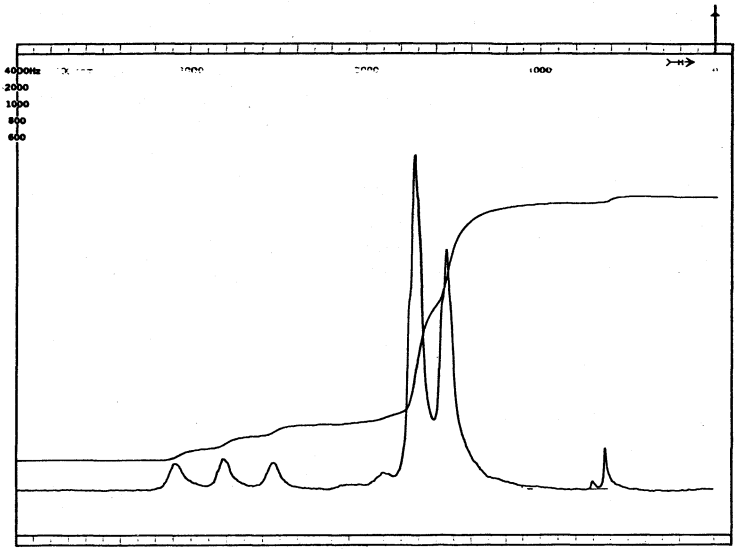

FIG 3 ^{1}HNMR SPECTRUM OF THE 2:1 $AlCl_3/C_5H_6NCl$ MELT AT 70°C

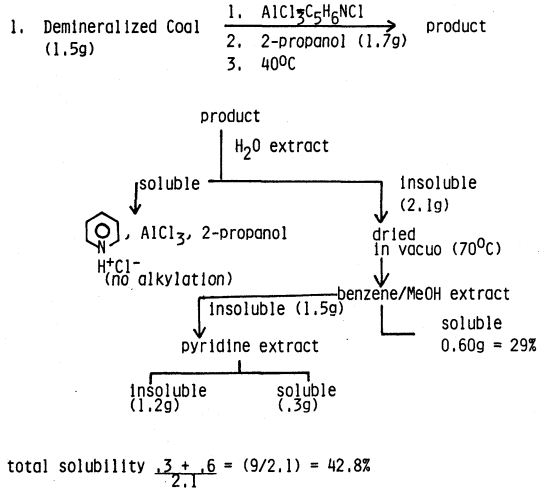

FIG 4 SCHEMATIC DIAGRAM OF THE COAL ALKYLATION REACTION

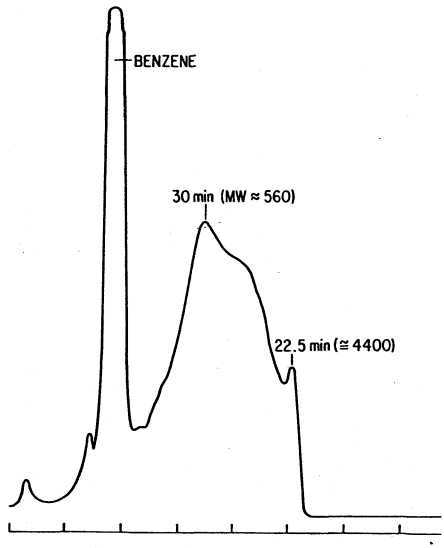

FIG 5 GEL PERMEATION CHROMATOGRAM OF THE BENZENE/METHANOL SOLUBLE PORTION OF THE ALKYLATED COAL

DOI: 10.1149/198109.0439PV

THE MOLTEN SALT COAL GASIFICATION PROCESS

S. J. Yosim

Rockwell International
Energy Systems Group
8900 De Soto Avenue
Canoga Park, California 91304

ABSTRACT

In the Rockwell Molten Salt Coal Gasification Process, coal is gasified with air or with oxygen and steam in a highly turbulent Na_2CO_3-based melt. The gasification reaction takes place at about 1800°F and at a pressure of 1 to 30 atm. A combustible gas containing CO, H_2, and CH_4 is produced. The sulfur and ash of the coal are retained in the melt. A summary of test results produced from three different size gasifiers is given. These gasifiers ranged from bench-scale gasifiers processing 2 lb/hr coal to a pilot-scale gasifier capable of processing 1-ton/hr coal.

I. INTRODUCTION

One of the processes being considered as a contender among the second-generation coal gasification processes is the Molten Salt Coal Gasification Process. In this process, the concept of which is shown in Figure 1, the coal is gasified at a temperature of about 1800°F and at pressures up to about 30 atm by reaction with air in a highly turbulent melt of sodium carbonate. The sulfur and ash of the coal are retained in the melt; a small stream is continuously processed for regeneration of the sodium carbonate, removal of the ash, and recovery of the sulfur as elemental sulfur.

This process has been under development by Rockwell International for about 8 years. The experimental program started with tests in bench-scale gasifiers processing 2 lb/hr coal. The current effort is now the operation under a DOE contract of a Process Development Unit (PDU) which is a pilot plant designed to gasify 1 ton of coal per hour. The purpose of this paper is to describe some experimental results obtained from three different gasifiers ranging in size from the bench-scale system to the PDU.

II. DESCRIPTION OF THE ROCKWELL MOLTEN SALT COAL GASIFICATION PROCESS

A generalized flow diagram of the Molten Salt Coal Gasification Process is shown in Figure 2. The diagram illustrates the production of low- or medium-Btu gas by using either air or oxygen (with steam) as the oxidant. In this process, coal is gasified in a highly turbulent

pool of sodium carbonate-based melt at a temperature of ~1800°F and at pressures up to 30 atm. The coal is injected beneath the surface of the melt together with required sodium carbonate makeup. Air is used to convey the solids pneumatically into the gasifier or, in the case of the medium-Btu version, conveying is accomplished by recycling a portion of the product gas. The ash and most of the sulfur in the coal are retained in the melt. The sulfur reacts with sodium carbonate to form sodium sulfide which has been found to have a catalytic effect on the gasification reactions.

A small stream of melt is continuously removed from the gasifier and replaced by the addition of sodium carbonate with the coal in order to prevent excessive buildup of ash and sodium sulfide. The sodium carbonate recycle rate is adjusted to maintain a steady-state ash concentration of 20% in the gasifier melt. Melt is removed from the gasifier by an overflow arrangement and is immediately quenched by contact with a water solution at full gasifier pressure. Sodium carbonate and sodium sulfide dissolve in the hot solution, while unreacted carbon and insoluble ash constituents remain as undissolved particles.

The resulting slurry is discharged from the quenching operation through a pressure reduction valve, producing low-pressure steam for use in the regeneration. The slurry is then processed to remove ash components, strip off sulfur as H_2S, and precipitate sodium bicarbonate crystals. The ash, containing about 5% unreacted carbon, is disposed of as wet filter cake, the hydrogen sulfide is converted to elemental sulfur in a conventional Claus plant, and the sodium bicarbonate crystals are calcined at about 400°F to convert them to dry sodium carbonate powder suitable for reuse.

III. TESTS CONDUCTED IN GASIFIERS OF DIFFERENT THROUGHPUTS

Tests were conducted in a bench-scale gasifier for processing 2 lb/hr of coal, a semi-pilot gasifier processing about 200 lb/hr of coal, and the PDU which gasifies up to 1-ton/hr coal.

A. BENCH-SCALE GASIFIER

1. Description

A schematic of the bench-scale molten salt gasifier is shown in Figure 3. This unit has provisions for continuously adding coal to the melt. The gasifier is a 6-in.-ID and 36-in.-high alumina tube placed in a Type 321 stainless steel retainer vessel. This stainless steel vessel, in turn, is contained in an 8-in.-ID four-heating zone electric furnace. Coal is fed to this unit at the rate of about 2 lb/hr. Additional details of the system and procedures have been presented elsewhere (1-3).

2. Results

The effects of coal rank, air/coal ratio, melt temperature, and particle size on the product gas composition were studied. Gasification experiments were performed on different types of coal ranging from low-rank lignite to high-rank anthracite. The composition of the product gas at steady state was, in general, in good agreement with that calculated from carbon, hydrogen, and oxygen balances and assuming the water-gas shift attained thermodynamic equilibrium. This is illustrated in Table 1 for the case of lignite. The heating value of the product gas in general varied from 100 to 150 Btu/scf. As expected, the heating value of the product gas increased as the air/coal ratio decreased. This can be seen in Table 2.

TABLE 1

COMPARISON OF PREDICTED AND OBSERVED PRODUCT GAS HEATING VALUES DURING GASIFICATION OF TEXAS LIGNITE IN BENCH-SCALE GASIFIER

	Product Gas Composition (vol %)	
	Predicted	Observed
CO_2	11.3	11.0
CO	22.2	23.3
H_2	19.4	15.1
CH_4	0.9*	1.8
C_2H_6	0.0	0.2
N_2	47.2	47.6
HHV (Btu/scf)	143.0	147.0

*Predicted on the basis of other experiments.

The effect of melt temperature (1650-1830°F) on the product gas composition was relatively small. This is not surprising since the temperature effect of the water-gas shift reaction is small. Increasing the coal particle size from 275 to 950 microns had little or no effect on the product gas composition.

The time from startup for the product gas to attain a heating value high enough to support combustion (~100 Btu/scf) depended on the coal rank, i.e., on the reactivity of the coal. For example, the times for the product gas to reach a heating value of 100 Btu/scf for anthracite, a medium-volatile bituminous coal, a high-volatile bituminous coal, and lignite were 50, 25, 17, and <5 minutes, respectively.

TABLE 2

EFFECT OF AIR/COAL RATIO ON PRODUCT GAS HEATING VALUE DURING GASIFICATION OF KENTUCKY NO. 9 COAL IN BENCH-SCALE GASIFIER

Air/Coal Ratio (scf/lb)	Product Gas Heating Value (Btu/scf)
77	36
55	118
44	138
39	151

The fact that the carbon monoxide concentration in the product gas and the carbon content of the melt increased with time led to the suggestion that conversion of carbon to carbon dioxide is the primary step; reduction of carbon dioxide to carbon monoxide by carbon in the melt is a secondary step.

Gasification of coal with oxygen and steam was conducted with Kentucky No. 9 coal. The Btu content of the product gas was much higher (313 Btu/scf) than with air, which was expected since the product gas is not diluted with nitrogen. Additional details of the gasification tests with the bench-scale gasifier were given in Reference 1.

B. SEMI-PILOT GASIFIER

1. Description

A photograph of the semi-pilot gasifier is shown in Figure 4. This system has provisions for continuous melt withdrawal as well as for continuous coal feeding. The molten salt vessel, 12 ft high and 3 ft ID, is made of Type 304 stainless steel and is lined with 6-in.-thick refractory blocks. It contains 1 ton of salt, which corresponds to a depth of 3 ft, with no air flow through the bed. The vessel is preheated on startup and kept hot on standby by a natural-gas-fired burner.

The salt loading is fed into the molten salt vessel through the carbonate feeder. The coal is transferred directly from the hammermill, in which it is crushed to the required size, into a feed hopper provided with a variable-speed auger, and then introduced into the air stream for transport into the vessel.

The product gases generated in the gasifier exit through refractory-lined nozzles in the vessel head to a refractory-lined mist separator, The separator traps entrained melt droplets on a baffle assembly. The gases are then ducted to a secondary combustor to burn the product gas components and then to a high-energy venturi scrubber or to a baghouse, which is used to remove any particulate matter before release to the atmosphere. An overflow discharge nozzle permits continuous removal of spent salt, thus permitting long-term tests to be carried out.

The coal feed rate in this unit is about 200 lb/hr. The air-to-coal ratio is adjusted to generate the heat required to maintain the salt in the molten state during gasification.

2. Results

A coal gasification test was conducted over 15 days of continuous operation. The test was conducted at atmospheric pressure (melt withdrawal was by overflow into open drums) and temperatures of 1700 to 1900^{o}F.

During the 15 days of coal gasification, 28.7 tons of Kentucky No. 9 coal were gasified, 34.8 tons of sodium carbonate were added to the gasifier, and 35.3 tons of spent melt overflowed into the receiving drums. The coal feed rate ranged from 100 to 240 lb/hr. The higher heating value of the product gas increased with decreasing carbonate addition up to a predicted value of about 125 Btu/scf. It is to be noted that the heating values achievable in this gasifier are limited by the high heat losses of this multipurpose gasifier.

The test demonstrated the feasibility of feeding the coal and the sodium carbonate together into the gasifier through a common feed nozzle and the satisfactory performance of the melt overflow system for continuous discharge of melt from the gasifier. The spent melt was generally collected and allowed to solidify in 55-gal drums. At various times during the test, a melt shattering and quench system was rolled under the melt discharge to allow shattering of the melt by jets of recycled liquor and quenching of the melt in this liquor. These tests provided a demonstration of the adequacy of the planned shatter and quench technique for continuous quenching of high-temperature melt in recycled liquor.

C. PROCESS DEVELOPMENT UNIT (PDU)

1. Description

The Process Development Unit (PDU)* is a pilot plant designed to process 1 ton of coal per hour at pressures as high as 20 atm. It

*The PDU program is funded by the Department of Energy.

is a completely integrated facility including systems for feeding coal and salt to the gasifier, regenerating sodium carbonate for reuse, and removing sulfur and ash in forms suitable for disposal.

The gasifier is shown in Figures 5 and 6. The gasifier is a refractory-lined vessel which has a 39.6 in. ID, is 36 ft high, and contains about 3 tons of salt. There are four downward-sloping air/solids feed nozzles. There are two drain nozzles and nine nozzles that house thermowells used for measuring the melt bed and gas temperatures.

The process flow diagram and a photograph of the site at completion of construction are shown in Figures 7 and 8, respectively. The product gas exits the gasifier vessel from the top, and a small stream of melt is continuously withdrawn through a side overflow port for ash removal, sulfur removal, and sodium carbonate regeneration. The hot melt stream falls into the quench tank where soluble components are dissolved and insoluble ash is suspended in the resulting aqueous slurry. The product gas is cooled to 350°F in a spray cooler. Its pressure is then reduced, and it is fed into the product gas combustor for disposal. The aqueous slurry from the quench tank passes through pressure reduction valves into a flash tank where steam and liquid are separated. Steam produced in the flash tank is used in a subsequent H_2S stripping step and the liquid product is pumped to a precarbonator.

The aqueous solution is sparged with CO_2 in the precarbonator to enhance ash settling and prepare the solution for H_2S stripping. The solids are removed from the system by settling and filtration. The clarified liquor is pumped to a tank which provides surge capacity at this point in the system. Liquor is pumped from the storage tank to the top of the H_2S stripper tower where it is contacted countercurrently with an upflowing stream of steam. Water is condensed from the H_2S-rich gas exiting the stripper.

In a commercial plant, this H_2S stream would then go to a Claus sulfur plant. This is not done in the PDU because Claus plants are considered to be state of the art. Instead, the H_2S gas is burned in an incinerator giving a dilute sulfur dioxide gas stream. The SO_2 is reacted with a sodium-carbonate solution in the spray dryer to produce a dry powder consisting primarily of sodium sulfite and sodium sulfate. The dry powder is removed from the gas stream by a bag filter and collected for disposal. The liquid from the H_2S stripper is pumped through a carbonator where CO_2 is absorbed to convert the sodium carbonate to sodium bicarbonate crystals. These crystals are separated from the solution, dried, and decomposed in a calciner to produce regenerated sodium carbonate. The remaining liquid is recycled to the quench tank to dissolve additional melt.

Additional details on the description of the PDU can be found in References 4-6.

2. Results

Three runs were conducted on the PDU with the gasifier at atmospheric pressure. During this series, progressively more of the plant systems were brought into operation. All sections of the plant were operated in an integrated manner during Run 3. Typical operating results for these tests are shown in Table 3. The observed HHV values of 88.6 to 96.2 Btu/scf shown in Table 3 for Runs 1 through 3 are slightly higher than predicted for a coal feed rate of 0.2 ton/hr.

TABLE 3

MOLTEN SALT COAL GASIFICATION PDU
TYPICAL OPERATING RESULTS, ATMOSPHERIC PRESSURE RUNS

Run Number	1	2	3
Feed Rates			
Coal,* lb/hr	390	328	402
Air, scfm	285	410	420
Gas Composition (average)			
CO vol %, dry basis	19.2	16.4	15.1
H_2 vol %, dry basis	6.4	10.4	5.8
CH_4 vol %, dry basis	1.1	0.9	2.1
CO_2 vol %, dry basis	8.2	11.4	8.5
N_2 vol %, dry basis	64.3	60.1	64.4
A (or O_2) vol %, dry basis	0.8	0.8	1.1
H_2S, ppm	44	-	5
Product Gas, HHV (average), Btu/scf	93.6	96.2	88.6

*Illinois No. 6 coal used for all runs. Feed contained 10% petroleum coke during Run 1.

The reason for the relatively low heating values for the product gas (89-96 Btu/scf) is the following. When operated at low pressure, the capacity of the plant is limited by the gas velocity in the gasifier vessel. This is held below 2 ft per second (and preferably close to 2 ft per second) in order to minimize carryover of entrained droplets of melt. The gas velocity limitation results in a maximum coal feed capacity of about 400 lb/hr at 1 atm gasifier operating pressure. Heat losses through the wall of the gasifier vessel are independent of throughput. As a result, at low coal feed rates, a higher percentage of the heat of combustion of the coal must be utilized to make up for gasifier heat losses and the HHV of the product gas is correspondingly reduced.

Table 4 presents data taken during a high-pressure gasification test (up to 10.5 atm). Coal feed rate during this run was approximately 75% of design and, as indicated in the table, the product gas HHV was close to the predicted value for the air-to-coal feed ratio employed during the test. Additional details can be found in Reference 6.

TABLE 4

MOLTEN SALT COAL GASIFICATION PDU
RESULTS OF HIGH-PRESSURE TEST

Operating Conditions		
Pressure, atm	10.5	
Coal Feed Rate, lb/hr	1492	
Air Feed Rate, scfm	1345	
Salt Feed Rate, lb/hr	260	
Product Gas Composition	Observed	Predicted
CO, vol % dry basis	24.8	22.9
H_2, vol % dry basis	5.2	9.0
CH_4, vol % dry basis	1.8	1.4
CO_2, vol % dry basis	5.8	7.3
N_2 (and A) dry basis	62.4	60.1
H_2S ppm	60	-
HHV (dry gas), Btu/scf	115	117

IV. FEATURES OF THE MOLTEN SALT COAL GASIFICATION PROCESS

The key advantages of the Molten Salt Coal Gasification Process are: (1) the process can handle any coal, including highly caking eastern types, (2) close sizing of coal feed is not required, (3) the product gas is essentially free of sulfur and ash, (4) negligible amounts of tar, heavy hydrocarbons, and NO_x are produced, (5) the gasifier has excellent turndown capability, (6) oxygen and steam requirements are generally low, (7) no explosion hazard occurs when coal feed is stopped, and (8) the process has a high thermal efficiency.

REFERENCES

1. S. J. Yosim and K. M. Barclay, "The Chemistry of the Rockgas Process for Coal Gasification," in Proceedings of the Second International Symposium on Molten Salts, J. R. Selman and J. Braunstein, Eds. (Pennington, NJ: Electrochemical Society, 1981) in press.

2. S. J. Yosim and K. M. Barclay, "Production of Low-Btu Gas from Wastes Using Molten Salts," in Fuels From Waste, L. L. Anderson and D. A. Tillman, Eds. (New York: Academic Press, Inc., 1977) p. 41.

3. S. J. Yosim, K. M. Barclay, R. L. Gay, and L. F. Grantham, "Disposal of Laboratory Hazardous Wastes by Molten Salt Combustion," in Safe Handling of Chemical Carcinogens, Mutagens, Teratogens and Highly Toxic Substances, D. B. Walter, Ed. (Ann Arbor, MI: Ann Arbor Science Publishers, Inc., 1980) Vol 2, p 617.

4. W. V. Botts, A. L. Kohl, and C. A. Trilling, "Low-Btu Gasification of Coal by Atomics International's Molten Salt Process," 11th Intersociety Energy Conversion Engineering Conference Proceedings, Vol 1, 280 (September 12-17, 1976).

5. A. L. Kohl, R. B. Harty, J. G. Johanson, and L. M. Naphthal, "The Molten Salt Coal Gasification Process," Chem. Eng. Prog. 74, 73 (1978).

6. A. L. Kohl, M. H. Slater, and P. H. Hsia, "Operation of the Molten Salt Coal Gasification Process Development Unit," Proceedings of the 7th Energy Technology Conference - March 24-26, 1980, edited by R. S. Hill, Published by Government Institutes, Inc., June 1980.

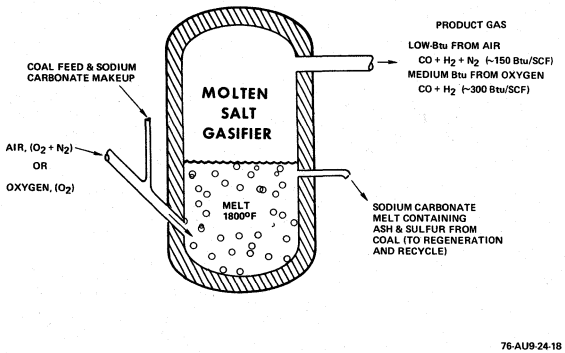

Figure 1. Molten Salt Coal Gasification Process

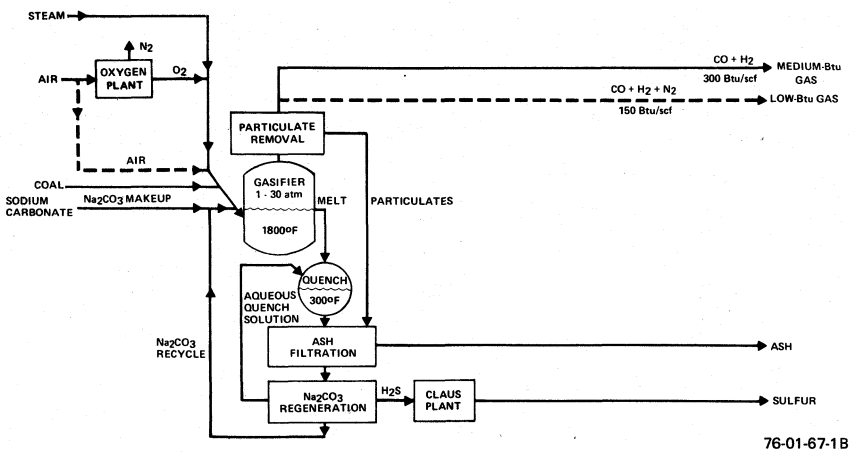

Figure 2. Molten Salt Gasification of Coal

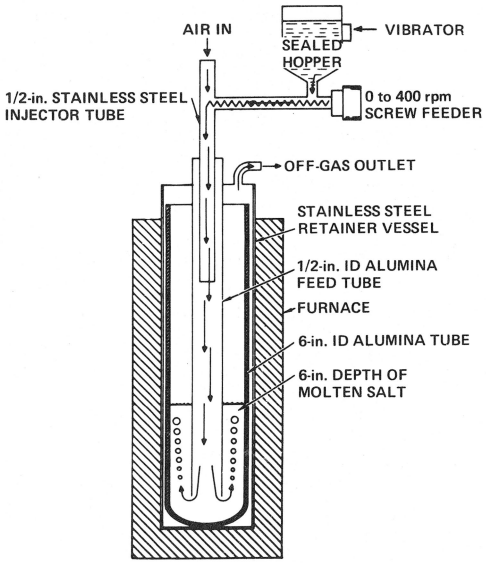

Figure 3. Bench-Scale Molten Salt Gasifier

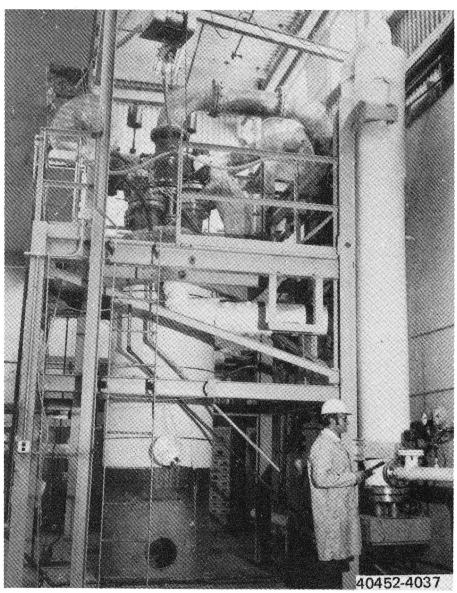

Figure 4. Semi-Pilot Gasifier

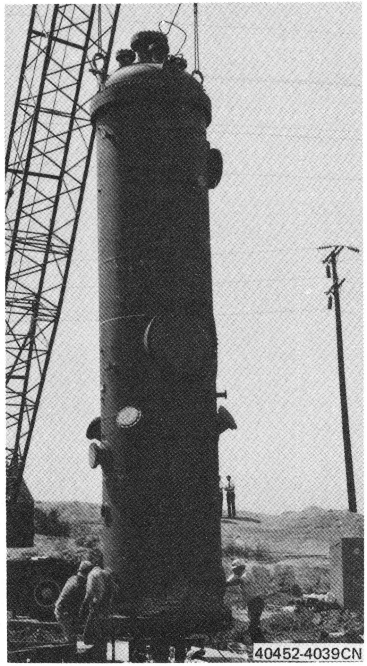

Figure 5. PDU Gasifier Vessel During Installation

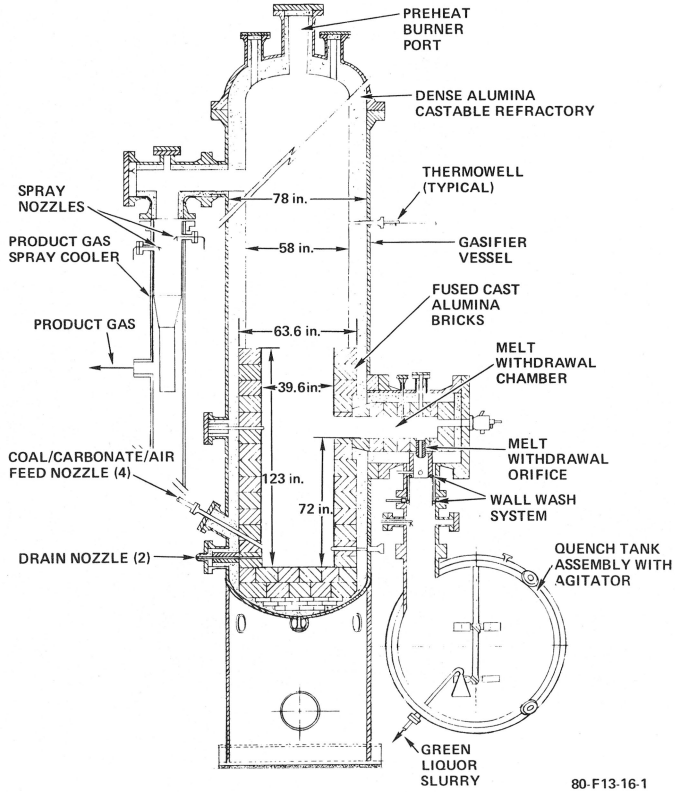

Figure 6. PDU Gasifier/Quench Assembly

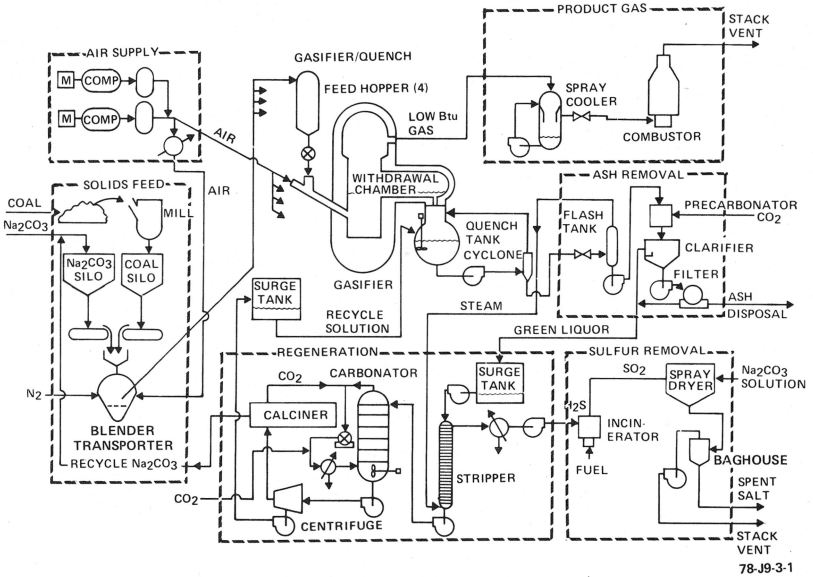

Figure 7. Process Flow Diagram of Molten Salt Coal Gasification PDU

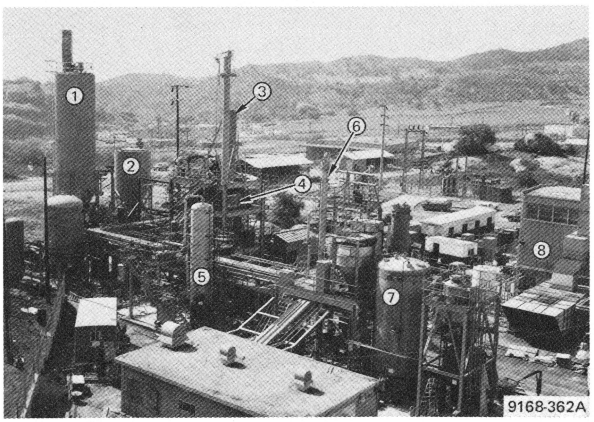

1. SODIUM CARBONATE SILO
2. COAL SILO
3. PRODUCT GAS COMBUSTOR STACK
4. GASIFIER
5. CARBONATOR
6. H_2S STRIPPER
7. GREEN LIQUOR STORAGE TANK
8. PRECARBONATOR

Figure 8. Photograph of the PDU Site

DOI: 10.1149/198109.0452PV

MOLTEN AND SOLID COMPOUNDS IN COAL AND OIL GASIFICATION

Keith E. Johnson
Chemistry Department
University of Regina
Regina, Canada
S4S 0A2

Absract

By treating coal and oil as simply carbon one can break down their gasification reactions into the redox reactions of C, CO, CO_2, H_2O, H_2 and CH_4. If the treatment of metallurgical processes presented by Ellingham in 1948 and extended to oxyanion systems in 1966 is examined with emphasis on the gaseous products rather than the reductants such as metals and sulfides, it is seen that several molten and solid oxides and oxyanion salts should act as catalysts and agents for the gasification of carbon materials.

Some examples of experiments in line with such predictions are described and the electrochemical promotion of low temperature gasification is discussed.

Introduction

About 20 years ago gas from coal was liable to mean the gas resulting from dry distillation. Such gas was formed in addition to ammonia, tars and the residual coke. This process does not utilize the energy of the starting fuel as well as gasification which was used as a starting point for liquid fuels production in Germany in the Second World War and has been in operation in South Africa for several years.

The primary coal gasification reactions can be approximated (taking coal as C rather than $\sim CH_{0.9}O_{0.1}$) as follows:

$$C + H_2O \rightleftarrows CO + H_2 \quad (1)$$
$$CO + H_2O \rightleftarrows CO_2 + H_2 \quad (2)$$
$$CO + 3H_2 \rightleftarrows CH_4 + H_2O \quad (3)$$
$$C + 2H_2 \rightleftarrows CH_4 \quad (4)$$
$$C + CO_2 \rightleftarrows 2CO \quad (5)$$
$$2C + O_2 \rightleftarrows 2CO \quad (6)$$
$$C + O_2 \rightleftarrows CO_2 \quad (7)$$

Oxygen is introduced into processes in many cases as air, leading to a product gas containing nitrogen of no fuel value. Sulfur in the coal can appear as SO_2 or H_2S at different stages.

The product gas is rated by its higher heating value (in B.t.u. per 1000 standard cubic feet) with high Btu gas being rich in CH_4,

medium Btu gas liable to contain much H_2 or CO or diluent N_2 and low Btu gas being high in N_2 and low in CH_4.

Classification of gasification reactions

It is instructive to look at the several reactions taking place in a gasifier as oxidations, reductions or hybrids. Reactions (3) and (4) are written as reductions and (6) and (7) as oxidations. Reaction (1) is the steam oxidation of carbon to carbon monoxide which is thermodynamically favored at higher temperatures and reaction (2), the water-gas shift reaction which must be promoted for hydrogen synthesis is the steam oxidation of carbon monoxide to the dioxide. The combination of (1) and (2) is an overall low temperature gasification process.

Ellingham Diagrams

The oxidation reactions in particular are familiar to the metallurgical industry where carbon in various forms has had centuries of use in the production of metals from oxides. Clear definition and representation of the conditions, particularly the temperature regime, for the successful use of carbon as a reductant was given by Ellingham (1) in the form of Gibbs free energy vs. temperature diagrams. In the course of studying the products of electrolytic reduction of several oxyanion salts (2) we found it possible and convenient to plot the corresponding Gibbs free energies of these substances on the Ellingham diagram for oxides. Figure 1 contains a few such oxide lines. The Na_2SO_4 and Na_2CO_3 lines are for the respective reactions:

$$Na_2S + 2O_2 \rightarrow Na_2SO_4 \quad (8)$$

$$Na_2O + C + O_2 \rightarrow Na_2CO_3 \quad (9)$$

The most stable oxidant at a given temperature is the one with the lowest line (corresponding to the largest $(-\Delta G°)$). Thus: CO_2 is the stable carbon oxide below ~1050°K and CO the most stable one above; C should reduce Na_2SO_4 to Na_2S and CO_2 from 900 to 1050°K and to Na_2S and CO above 1050°K; C should reduce H_2O to H_2 above ~900°K; C should reduce Na_2CO_3 to CO above ~1300°K; the reaction of C and CO_2 to produce CO should be favored above ~1050°K. Reference to more extensive Ellingham diagrams (3), (4) leads to the following postulated reactions:

$$C + CaCO_3 \rightarrow CaO + 2CO \quad (10)$$

$$C + FeO \rightarrow CO + Fe \quad (11)$$

$$Al_2O_3 + Si + 2MgO \rightarrow Al_2O_3 \cdot SiO_2 + 2Mg \quad (12)$$

$$3CaO \cdot P_2O_5 + 3SiO_2 + 5C \rightarrow P_2 + 3(CaO \cdot SiO_2) + 5CO \quad (13)$$

Implications for Gasification

Instead of restricting gasification to reactions 1-7, we can use other materials to achieve some of the conversions. Obvious examples are to carry out the oxidation of coal with sodium sulfate, a cheap mineral, to utilize coal in certain ore reductions and to deliberately process the gas, to use limestone or dolomite, which occur bearing heavy oil, to oxidise the oil and to oxidise coal and reduce water or reduce coal and oxidize water in separate compartments of an electrolytic cell - processes which might be deemed coal - depolarized water electrolysis or electrochemical coal gasification.

These electrode reactions may be written:

(a) $H^+ + e^- \rightarrow 1/2H_2$
(b) $H_2O + e^- \rightarrow 1/2H_2 + OH^-$
(c) $C + H_2O \rightarrow CO + 2e^- + 2H^+$
(d) $C + 2H_2O \rightarrow CO_2 + 4e^- + 4H^+$
(e) $C + 5OH^- \rightarrow HCO_3^- + 4e^- + 2H_2O$
(f) $C + 4H^+ + 4e^- \rightarrow CH_4$
(g) $2H_2O \rightarrow O_2 + 4H^+ + 4e^-$

and the possible resultant processes would be:

(a) + (c)	≡	(1)	$C + H_2O \rightarrow CO + H_2$	(1)
(a) + (d)	≡	(1) + (2)	$C + 2H_2O \rightarrow CO + 2H_2$	(14)
(f) + (g)			$C + 2H_2O \rightarrow CH_4 + O_2$	(15)
(d) + (f)	≡	(1) + (2) + (4)	$2C + 2H_2O \rightarrow CH_4 + CO_2$	(16)

Whether or not such an electrochemical approach would be worthwhile (assuming the processes worked) would depend on the cost of electricity, the difference in heating requirements for high temperature "conventional" gasification vs. moderate temperature electrochemical processes and any advantages of obtaining separated products by the electrolytic route.

Preliminary tests

The reaction of equal amounts of lignite and sodium sulfate at 900°C produced carbon monoxide and an ash rich in sodium sulfide while the reaction of lignite with an alkali sulfate eutectic melt at 550°C did not proceed very far - only small amounts of CO and M_2S being formed. Other laboratories (5) have demonstrated the use of Na_2CO_3 in coal gasification.

The interaction of wood charcoal and sea shells is an old source of lime and suggests the possibility of in situ gasification of heavy oil in carbonate rocks.

Electrolysis of 5 M sulfuric acid with a coal slurry anolyte was shown to yield, besides hydrogen at the cathode, carbon dioxide

containing 7% carbon monoxide at the anode (6). Raising the temperature and matching the coal density by use of a different electrolyte has increased the CO content of the anode gas to 20%.

Many efforts to convert coal to electricity in molten carbonate fuel cells (not that different from the hydrocarbon based cells of ~1960!) have led to CO_2 rather than CO formation (7) but with growing markets for H_2 and CO_2 (8) this situation may not be a problem in the case of electrochemical gasification.

Acknowledgement

This work was carried out with partial support from NSERC (Canada), Saskatchewan Research Council and Saskatchewan Power Corporation.

REFERENCES

(1) C.W. Dannatt and H.J.T. Ellingham, Dics. Faraday Soc. 4, 126 (1948).
(2) H.E. Bartlett and K.E. Johnson, Can. J. Chem. 44, 2119 (1966).
(3) K.E. Johnson, High. Temp. Tech. 493 (1969).
(4) R.H. Parker, An Introduction to Chemical Metallurgy, p. 263, Perganon (London), 1967.
(5) S.J. Yosin, This volume p.
(6) R.W. Coughlin and M. Farooque, Nature 279, 301 (1979).
(7) R.D. Weaver and L. Nanis, This volume p.
(8) K.E. Johnson, Carbon Dioxide, Report to Saskatchewan Power Corporation (1980).

Figure 1. An abbreviated Ellingham diagram

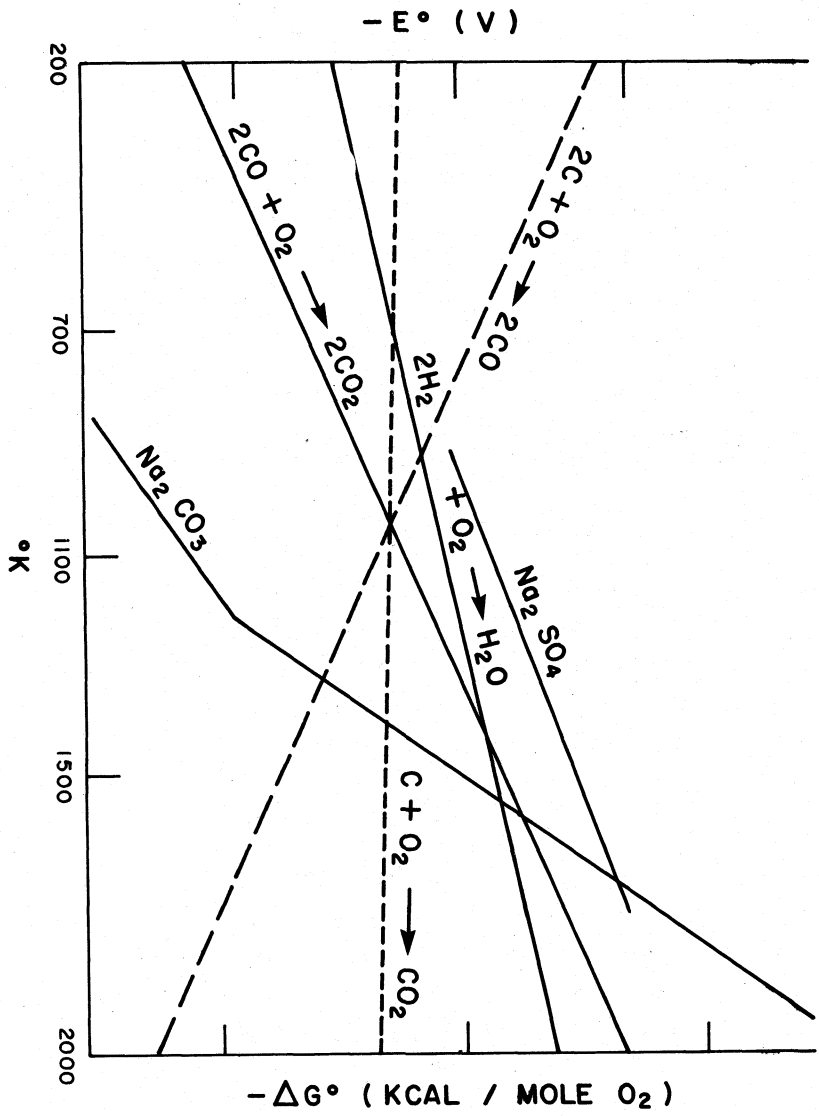

DOI: 10.1149/198109.0457PV

HEAT TREATMENT OF INDUSTRIAL MATERIALS IN MOLTEN SALTS

R. W. Foreman

Park Chemical Company
8074 Military Ave.
Detroit, Michigan 48204

A wide variety of industrial heat treating is performed in molten salts. Processing of metals includes surface hardening, brazing, anealing, coloring, descaling, and metals recovery. Nonmetallics processing includes elastomer and plastic curing, glass tempering, and plastics molding. An involved technology covering both salt and materials properties and engineering surrounds these applications. Selected examples are discussed in detail in this presentation.

Molten salts are used for heat treating a wide variety of industrial materials. Metals are the dominant material with ferrous alloys most important but curing of elastomers and plastics, and tempering of glass have been growing in recent years. Industrial use of molten salts began back in the 1860's with the carburizing of steel using molten sodium cyanide. This remained the major use until after W.W.I when neutral salts for through hardening steel and tool steels came into use. Other uses have been added in the ensuing years for such purposes as annealing steels and other non-ferrous metals, coloring the surface of steels, nitriding steels, brazing aluminum and steels, and surface cleaning of steel plus other metals. The curing of rubber and plastics and the chemical tempering of glass have been more recent applications of molten salts.

While the exact usage level is unknown, rough estimates are that upwards of 50,000,000 lbs. per year are consumed in North America for industrial heat treating.

The attractiveness of salt for heat treating stems from several favorable features. These are as follows: (1) Rapid heat up time. Salts have a high K factor and will heat up materials 4-5 times more rapidly than they can be heated in gaseous media or vacuum. (2) The heating is extremely uniform since the salt coats the entire surface and the conductivity is high. (3) Salts are capable of very precise temperature control commonly to within a degree or two centigrade. (4) Salts are relatively dense and thus provide a bouyancy effect on parts being heat treated. This minimizes distortion. (5) Salts offer a protective medium for heat treating whereas air oxidizes surfaces severely. (6) Salt has a relatively high heat capacity and thus a large amount of heat can be stored in a relatively compact space. (7) Salt is one of the most effective ways to achieve selective heat treating by partial immersion not readily done by other techniques. (8) Finally, salt is highly energy efficient and can offer significant energy savings over alternate methods of heat treating.

Salt is not without its disadvantages. Under some circumstances salt can be more corrosive towards surfaces than vacuum or inert gas atmosphere. Salt can also pose problems in removal after heat treat particularly from blind holes or highly recessed areas. Third, salt presents a potential pollution and disposal problem. However, the technology for dealing with this is well advanced and need not be a deterrent. The emphasis in this paper will be on applications of molten salts. These will be covered in approximate order of their current industrial importance as measured by the volume of salt used

for that purpose. These applications are listed in Table I.

TABLE I

Salt Bath Heat Treating: Applications

Neutral Hardening of Steel	Austenitize Marquench/Ausquench
Hi-Speed Steel Hardening	Solution treating Quenching Tempering
Liquid Carburizing	Cyanide based Non-cyanide based
Liquid Nitriding	Tool Steel "Casing" Ductrile nitriding
Aluminum Dip Brazing Aluminum Solution Treating Miscellaneous	SS Annealing Copper/Brass Brazing Ausbay Quenching Copper Annealing WC Brazing

Before proceeding to the actual applications it would be of use to discuss the equipment used for heat treating. There are a wide variety of salt bath designs which are used in industry. The earliest designs were based on gas or oil fired pots that were inserted in firing chambers usually built of brick. The more modern heat treating facilites utilize electrically heated pots at lower temperatures. These are quite often heated by resistance heaters either internally or externally located. A typical low temperature resistance heated type of pot is shown in Figure I. (Note: the figures will all be at the end of the talk) For higher temperature applications above about 500°C. It is common to use direct resistance heating of the salt in either metal lined or more commonly ceramic lined baths that are usually constructed in the square or rectangular configuration. The two most common used salt baths designs are illustrated in Figures 2 and 3. Figure 2 illustrates an over-the-side type electrode arrangement and Figure 3 illustrates the submerged electrode arrangement. The over-the-side electrode has the advantage of being easily removed and replaced when electrodes become worn or damaged but has a disadvantage that it consumes a fair amount of the working space in the bath and is also a little less efficient. The submerged electrode type bath allows the greatest working volume in the bath and is the most energy efficient design. It has the disadvantage that when repairs or replacement are needed a substantial rebuilding

is required.

The major use of molten salts is for the neutral hardening of low to medium alloy steels containing medium to high carbon. To understand the accomplishments of this process one needs to have a background in the metallurgy of steel and particularly in the microstructural forms of steel which are important to its relative hardness. Figure 4 shows an iso-thermal transformation diagram, sometimes called a time temperature transformation diagram for a typical medium carbon low alloy steel. The purpose of neutral hardening is to cool (quench) steel from high temperature rapidly to low temperatures then hold it at that temperature more or less iso-thermally to permit transformation of the steel to relatively hard structures. One of the harder structures is known as Bainite and the hardest of all is Martensite. The industrial terms used for this are Aus-Tempering or Ausquenching when it is a Bainitic structure that is desired and Martempering or Marquenching when it is a Martensitic structure that is desired. The quenching is generally done from a high temperature neutral salt down to a low temperature nitrate based salt. This must be done rapidly enough to avoid transformation to softer structures that are commonly referred to as Pearlite. At the higher elevated temperature the steel exists in a form known as Austenite and will transform rapidly at the lower temperatures to other forms as shown in the time temperature transformation diagram. The time scale here is logrithmic so the amount of time that can be tolerated to avoid Pearlitic transformation is very short, often a second or two.

The Austenitizing can be done in atmosphere and quenching in salt though this practice is not as common as the salt to salt type of quenching. There even are a few installations in which the higher temperature is accomplished in salt and the quenching done in a medium such as water or oil, but these are relatively unusual.

The types of salt baths that are used for Austenitizing are commonly referred to as neutral salts. The composition, operating range, and the commonly encountered chemical reactions in this type of bath are shown in Table II.

TABLE II

Austenitizing Salt Baths

Operating Range:	760-1000°C
Composition:	$NaCl/KCl/BaCl_2$ (optional)
Decomposition:	$NaCl + O_2 \xrightarrow{FE} Na_2O + Cl_2$
Contaminants:	Metallics, refractories, carbon, nitrate

TABLE II (cont.)

Control:	Physical:	"Razor Blade" Test
	Chemical:	pH/Acid Titration
		Insolubles (H_2O + Acid)
		I.R. or diphenylamine
Correction:		Rectification (MeCl, Si)
		Counteraction ($DiCy, CN^-$)
		Sludging

The operating temperature range indicated is readily accomplished in mixtures of sodium and potassium chloride for up to temperatures of about 875°C. If higher temperatures than this are required it is common to add barium chloride to the mixture to lend it greater stability. The volatility of sodium and potassium chloride increases substantially at temperatures above 900°C, leading to excessive fuming. Also the higher the temperature the more tendency for the reaction of the chloride with the oxides on the metals to produce metallic chlorides and sodium or barium oxides. The latter are powerful decarburizing agents even at relatively small concentrations. An important aspect of the use of this type of bath is that either a counteractant or preferably a chemical reversal of this reaction is needed and commonly used.

The quench salt baths commonly in use are outlined in Table III.

TABLE III

Quench Salt Baths

Operating Range:	150-400°C
Composition:	KNO_3, $NaNO_3$, $NaNO_2$
Decomposition:	$NaNO_2 \rightarrow Na_2O + CO_2 \rightarrow Na_2CO_3$
Contaminants:	Cl^-, $CO_3^=$, Metallics
H_2O Addition:	Low levels effective
Control:	Physical: Electrical Conductivity
	Thermal Conductivity
	Melting Point
	Wt. Loss on Drying
	Chemical: Acid Titration ($O^=$, $CO_3^=$)
	$AgNO_3$ Titration (Cl^-)

TABLE III (cont.)

Chemical: H_2O Insolubles (Metals)

Correction: Sludging (Cl^-, metallics)
Rectification ($O^=$, $CO_3^=$)
H_2O Addition

The composition of these salts is sodium and potassium nitrate with sodium nitrite commonly added. The higher the nitrite level in the salt up to about 50% the lower the melting point of that salt will be. Thus the first basis for choice of salt composition is the operating temperature that is to be used. One uses as high a melting point as one can comfortably work with since the economics and the thermal stability favor the lower nitrite, higher nitrate containing salts. The chemical changes that take place in this type of salt are numerous but the most commonly encountered problem is the accumulation of chlorides from carry-over from the austenitizing baths. These will build up and become supersaturated in the quench salt. They must be removed to maintain effective quenching. A common practice here is to crystalize out the excess chlorides and remove them by sludging or screening procedure. The formation of some sodium oxide and thus eventually carbonate can also take place though this will vary greatly with the particular type of operation. It can be readily counteracted through the use of a liquid nitrate rectifier that reacts sodium oxide and carbonate back to nitrates.

The type of equipment that is used for neutral hardening has evolved from relatively small manual transfer operations to semi-automatic and fully automatic systems. In the semi-automatic systems, parts are handled in fixtures that are transferred by over-head cranes and salt baths and wash lines are arranged in sequence. The most modern types of neutral hardening lines are capable of handling up to 2000 pounds per hour in highly automated hydraulically lifted baskets and fixtures transferred in time and sequences that are controlled by computers. Such systems are fully enclosed with good ventilation and in some cases have salt recovery systems.

The second most commonly used process that utilizes salt baths is that involving heat treatment of tool steels. Tool steel heat treating is somewhat similar to neutral hardening but tool steels are generally higher alloy and include high speed steels that contain several alloying elements such as molybdenum, chromium, nickel, colbalt, vanadium as well as carbon. In order to harden high speed steels it is necessary to heat them to

higher temperatures than are commonly used in neutral hardening. To minimize the thermal stresses and to obtain the very short exposure time at high temperatures it is common proctice to preheat in two stages. Following the solution treating at the high temperature, the tools are quenched at intermediate temperatures such as 500°C to stabilize them in the austenitic condition. They are then cooled down relatively slowly to achieve martensitic transformation. They are then taken back up for tempering sometimes two and three times for secondary hardening and to relieve stresses. The sequence and the types of baths and the temperatures ranges used commonly for high speed tool steels are shown in the Table IV.

TABLE IV

SALT BATHS FOR TOOL STEEL HARDENING

Operation	Temp. Range °C	Composition
Preheat (one or two stage)	650-930	NaCl, KCl, $BaCl_2$
High Heat	930-710	$BaCl_2$, NaCl (SiO_2)
Quench	540-650	Two Types: 1. $BaCl_2$, NaCl, $CaCl_2$ 2. Na_2CO_3, KCl, NaCN
Temper	290-590	Two Types: 1. KNO_3, $NaNO_3$ 2. $BaCl_2$, NaCl, $CaCl_2$, KCl

The kinds of salt baths used are neutral salts that are very similar to those used for neutral hardening. The high heat is generally based on barium chloride or barium chloride with a samll addition of sodium chloride. Barium chloride has the highest thermal stability and lowest volatility of commonly available chloride SaHs. The quench salt baths are commonly a neutral salt but in order to get low enough melting and fluidity ranges, these salts generally have calcium chloride added along with sodium, potassium and barium chlorides.

The kind of equipment used for tool steel hardening parallels closely that used for neutral hardening though often special designs are used where very large parts such as broaches or rolls are heat treated. There are some automated tool steel lines though not as many as used in neutral hardening.

The next most commonly used salt bath processes involve surface treatments of which carburizing is the most common with li-

quid nitriding gaining increasing favor. Table V shows the types of salt baths that are used for liquid carburizing with the operating temperatures and salient features.

TABLE V
Liquid Carurizing Processes

	Cyaniding	Light Case	Deep Case	Non-Cyanide
Temp.(°C):	760-840	815-900	870-950	870-980
Time(Hrs.):	<1	.5-3	1-6	.3-10
Case Depths (mils):	1-10	5-35	15-60	5-150
Case Compos'n:	C & N	C+Some N	Nearly all C	All C
Carbon Cover:	Little or None	Light	Heavy	Moderate (agitated)
Average Operating % Cyanide:	30	20	10	0

The most interesting of these processes today is the non-cyanide based carburizing process which has been in commercial use for less than 10 years. Table VI shows the details of the non-cyanide carburizing process. The salt bath consists of an equimolar mixture of sodium carbonate and potassium chloride into which is stirred relatively pure carbon under controlled conditions.

TABLE VI

Non-Cyanide Carburizing Salt Baths

Composition:	Alkali Carbonates/Chlorides-Proprietary Carbon.
Decomposition:	None
Contaminants:	Metallics (Fe), SiO_2/Al_2O_3
Maintenance:	Cover replenishment
Control:	Physical: C1012 Test Piece hardness; Chemical: H_2O insolubles (%C)
Correction:	Add Carbon Adjust Agitation Sludge

The rest of the details are shown in Table VI. This process is probably the most economic means for carburizing steel presently available in industry. The equipment used is very similar to the neutral hardening baths shown earlier but with important differences. The bath is operated with a layer of relatively pure carbon on the surface which requires a relatively low rpm agitator to stir the carbon into the bath on a continuing basis. The rates of carburizing are comparable to other processes and are primarily diffusion controlled. The choices of post treatment after carburizing are broader with this process than with cyanide base salts. For example, one can quench directly into nitrate salts which is unsafe with cyanide salts.

There are several commercial nitriding processes as outlined in Table VII which depend on alkali cyanates as the active ingredient.

TABLE VII

Liquid Nitriding Processes

	Conventional (Alloy Steels)	Cyanide "Ductile" (Low alloy steels)	Non-Cyanide "Ductile" (Low alloy steels)
Temp. (°F):	540-570°C	570°C	650°C
Time (hrs.):	.1-1.0	.5-3.0	.5-3.0
Case Depths (mils):	.5-1.5	15/30	15/30
Case Composition:	Fe_2N	Fe_3N + Diffused N (Fe_2S in Some)	Fe_3N + Diffused N
Average Operating % NaCN/% NaCNO:	30/15	40/50	< 4/50

The various proprietary processes differ in how the cyanate is generated. From many years this was done by oxidation of cyanide ion and many such baths are still in use. The cyanate ion reacts with the steel to generate an iron nitride surface. If done properly some nitrogen diffuses below the very thin nitride layer at the surface. At very high cyanate ion levels the nitride layer will be less brittle than at relatively lower cyanate ion levels. The non-cyanide or very low cyanide level type nitriding is accomplished in molten salts in which cyanate ion is generated from organic sources, particularly polyurea. Very little cyanide ion exists in these baths and yet the cyanate ion levels are very high.

These produce the most effective nitriding in steel. The nitriding of steel is done to produce a very wear resistant surface and has become a popular way of producing smaller size parts which have wide application in the down sizing of engines.

There are many other salt bath processes which have somewhat lesser breadth of application but are deserving of some mention here. Aluminum dip brazing is a means for joining aluminum parts of relatively complex nature through use of an aluminum alloy that melts some 25°C below the base metal. This so called braze alloy can be applied in several forms - powder, sheet or clad on the part itself. By immersion in the salt bath at a very precisely controlled temperature, the braze alloy melts and joins the base metal parts. This process is used in the aerospace and electronics industries especially. The salts as shown in Table VIII are based on sodium and potassium chlorides with fluorides and lithium chloride added.

TABLE VIII

Aluminum Dip Brazing

Temp:	585-610°C (± 3°C)
Time:	1-3 Min.
Equipment:	Ceramic Furnaces with submerged or over-the-side Electrodes.
Preparation:	Alkaline/Acid Dips Preheat to ~1000°F

Post Treatment: H_2O Cool & Thorough Wash .

Lithium chloride is a very costly but a very necessary ingredient in this process. It provides both fluidity and fluxing action and enables good brazements to be accomplished.

Another aluminum salt bath process involves solution treating. This is widely practiced in the aerospace industry and increasingly now in those industries moving to lighter weight materials. A good portion of this is done in atmosphere furnaces but salt offers considerably more uniform and rapid heat up and is used where that can be fully appreciated. Table IX lists the key features of salt bath solution treating.

TABLE IX

Aluminum Solution Treating Salt Baths

Operating Temp:	460---560°C

TABLE IX (cont.)

Composition:	KNO_3, $NaNO_3$
Decomposition:	$NaNO_3 \rightarrow Na_2O \rightarrow Na_2CO_3$ $NaNO_3 \rightarrow NaNO_2$
Contaminants:	CO_3^-, NO_2^-, metallics, Cl^-
Control:	Physical: Test Piece ---- IGA Chemical: pH/Acid Titration NO_2^- by $KMnO_4$ Titr'n. H_2O + Acid Insolubles Cl^- by Ag^+ Titr'n.
Correction:	LNR $Na_2Cr_2O_7$ (STSR)

The salts are predominantly sodium and potassium nitrates. Some miscellaneous processes that utilize salt are briefly outlined in Table X.

TABLE X

Miscellaneous Salt Bath Processes

Process	Key Salt Bath Features	Process Key Control
SS Annealing	Neutral Salts 870-980°C	Maintain Neutral
Copper Brazing	Neutral Salts 870-1095°C	Hold Slightly Alkaline
Ausbay Quench	Neutral Salt 480°C	Maintain Compos'n Remove Metallics
Copper Annealing	Neutral Salts 700-870°C	Maintain Neutral Remove Metallics
WC Brazing	Neutral Salts High Heat/Quench	Controlled Alkalinity

The entries are self-explanatory.

A few non-heat treating type applications are worthy of mention. Most notably are those that involve cleaning salts. These remove undesirable coatings from the metal. For example, high alloy steels,

stainless steels for example, are descaled utilizing salts that are either oxidizing, reducing, or can have electrolysis imposition to assist the cleaning. In this case the scale is either conditioned for later removal by pickling or can be reduced or electrolytically removed in the salt bath.

Another form of cleaning involves removal of organic matter from steel parts such as extrusion dies, which can be rapidly and quickly cleaned in a caustic base salt having some oxidizing power through addition of nitrates. Likewise the removal of paint racks can be accomplished in caustic nitrate mixtures. The devestment of casting sand from steel castings utilizes a caustic base salt. All of these processes commonly operate at around 500°C. The salts have somewhat different compositions but generally involve caustic, chlorides, and sometimes fluorides and nitrates.

Finally a few non-metallic heat treating processes deserve mention. One of the fastest growing areas for use of salt bath lies is their use for curing elastomers and various heat resistant plastics. A number of extruded rubber parts are immersed in salt baths at temperatures around 200°C to effect a rapid and uniform cure within one to two minutes. This is more economic and produces a more reproducible cure on rubber than ovens or autoclaves. Likewise certain plastics can be foamed and/or cured in direct contact with salt and in some cases by indirect heating where the plastic is cured by immersion of the mold in the molten salt.

Glass can be chemically tempered at around 420°C in potassium nitrate or a potassium plus sodium nitrate mixture. This involves an ion exchange at the surface of the glass to generate a surface under tension. It is widely used now to make ophthalmic glass much stronger than can be accomplished by thermal tempering.

All of these non-metallic heat treating processes utilize nitrate/nitrite mixtures. The principles that apply to quench salts and neutral hardening apply fairly well in this type of application. However, the salt baths themselves are generally in very different designs because of the needs for handling the work going through the bath. Thus a rubber extrusion line might be very long, narrow and be relatively shallow. Immersion type heaters along the length of the bath are usually used.

In conclusion, the use of molten salts for the heat treating industrial products is steadily growing and expanding to new uses and involves a very wide variety of applications. The choice of salts is heavily dependent upon the temperature range in which they operate and in some cases on the chemistry that can be evolved for that particular mixture. The advantages listed earlier in this talk are fully realized in most situations. The disadvantages can be readily overcome through salt recovery, wash water treatment, and proper handling systems.

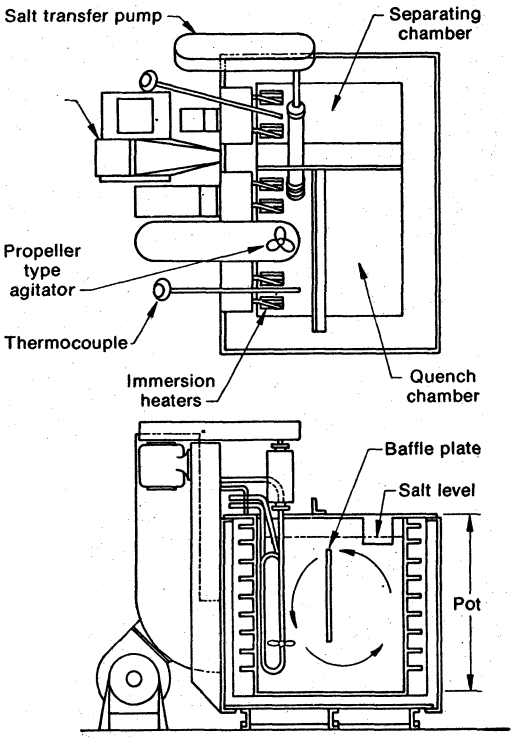

Figure 1. Typical isothermal quench furnace.

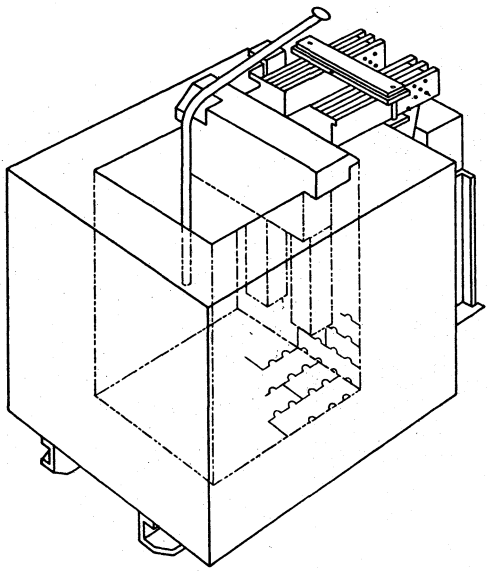

Figure 2. Salt bath furnace featuring a ceramic pot and over-the-top electrodes.

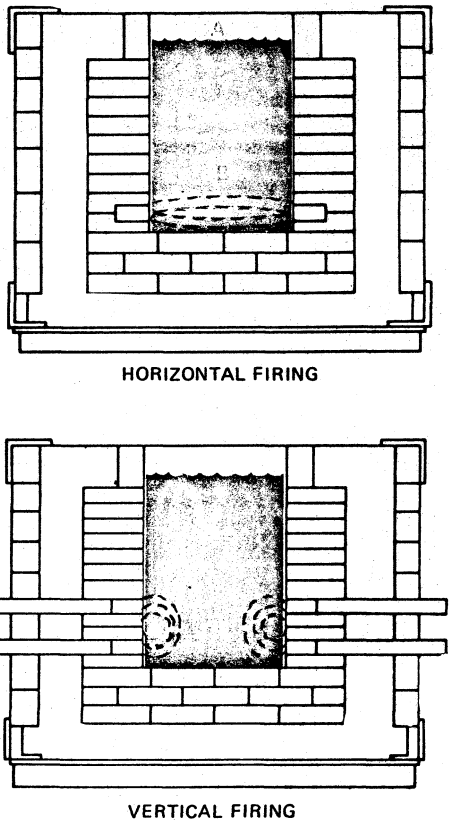

Figure 3. Submerged Electrode Salt Bath Furnaces.

Figure 4.

TTT CURVE

Low Alloy-Medium Carbon Steel

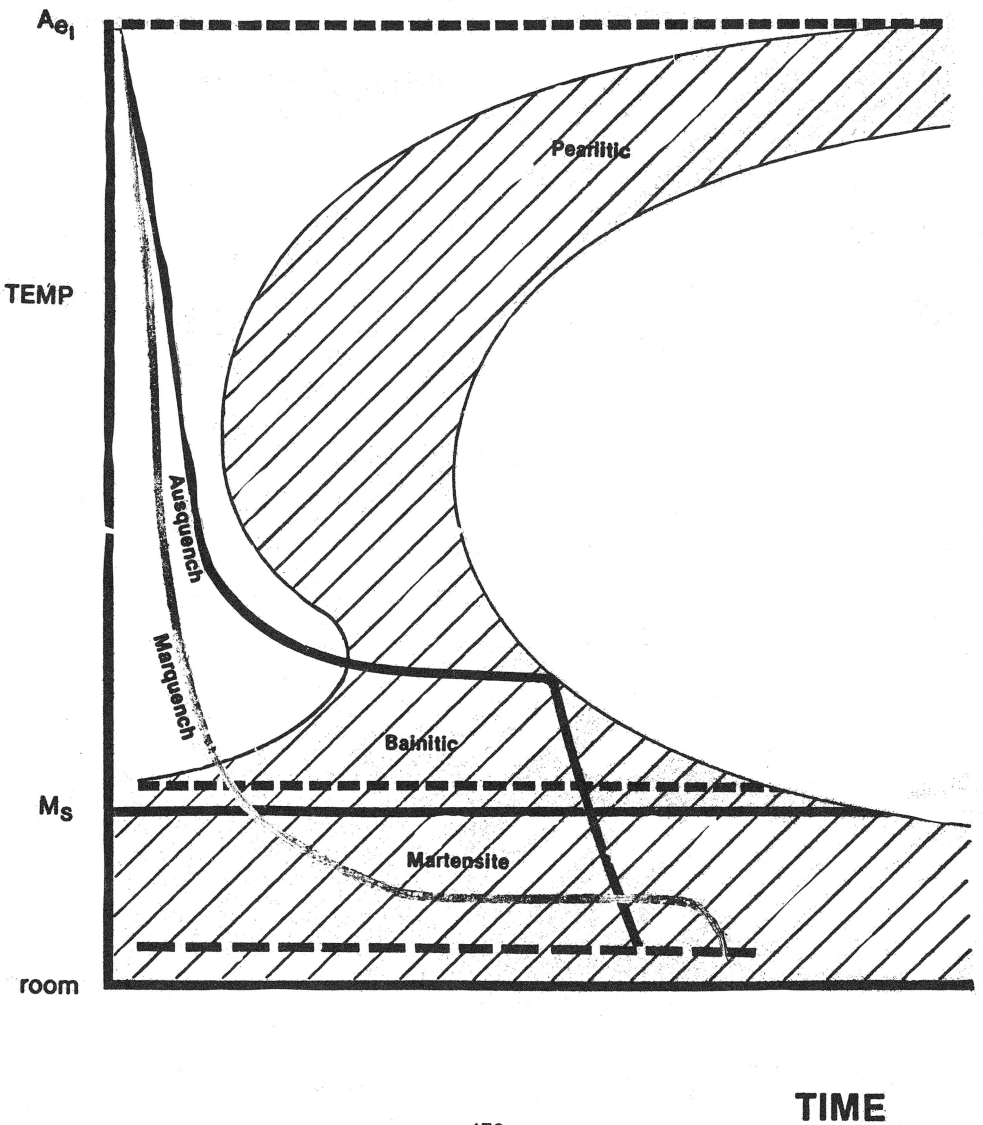

DOI: 10.1149/198109.0473PV

THE APPLICATION OF MOLTEN SALTS TO SOLAR LARGE POWER SYSTEMS*

Raymond W. Mar
Robert W. Carling
Sandia National Laboratories
Livermore, CA 94550

Abstract

Various solar thermal power concepts in which the end product is electricity (for utility use) are described. It is shown that molten nitrate salts are leading candidates for the heat transfer and thermal energy storage fluids. Selected research problems and current results are described concerning the decomposition and corrosion characteristics of nitrate salts.

*This work supported by the United States Department of Energy under contract DE-AC04-76DP00789.

Introduction

Molten salts have been used for many years in the chemicals and metals industries. Common applications include removing heat from exothermic reactors and providing heat to processing equipment such as evaporators and concentrators (1). They have also found widespread use as a bath medium for the heat treatment of metals (2). Recently interest in molten salts has heightened because of their proposed use in solar energy systems (3) and the purpose of this paper is to review the application of salts to such systems.

Various solar energy concepts in which molten salts may be used as the fluid for heat transfer and thermal energy storage will be reviewed. Fluid requirements and conditions of operation will be discussed and it will be shown that molten nitrate salts are leading candidates. Several examples of current research and current technical problems will be given.

Solar Energy Systems

This paper concerns the solar large power concept where the end product is electric power. The four components of the system, shown in Figure 1, are the heliostat, the receiver, the thermal energy storage system, and the electric generation system. Solar energy is incident on a field of heliostats, computer driven mirror reflectors, and is focused onto a central receiver. There the energy is absorbed by a heat transfer fluid which is then diverted to the thermal energy storage system. The storage system serves two purposes, to extend the time of operation beyond which there is adequate solar insolation, and to buffer the electrical generation equipment from the thermal cycles inherent in a solar energy source. By means of a secondary water/steam heat transfer loop, the thermal energy storage system is used to convert water to superheated steam which is then used to drive the electric generating turbines of a steam Rankine cycle. As an alternative path for the heat transfer fluid from the receiver, the energy may be used directly to generate electricity. In this case a secondary heat exchange loop is of course necessary to generate the steam if the primary heat transfer is not water/steam

There are numerous variations of the concept illustrated in Figure 1. One option is to have a system of dispersed point focusing collectors, each collector having its own small receiver situated at its focal point. Line focus systems have also been proposed in which the solar energy is focussed along a line. A central receiver line focus system consists of a field of heliostats all directing solar energy to the same linear receiver. Another variation is the dispersed line focus system comprised of many different collectors each with its own linear receiver.

There is a need for fluids to serve as the heat transfer and energy storage media in all of the systems discussed above, and it is for this purpose that molten salts have been proposed.

Fluid Requirements and Selection

Fluid Requirements

Regardless of the system design and configuration, the requirements of the heat transfer and energy storage fluids are essentially the same. Fluid temperatures range from 350-600°C and the fluid must be thermally stable, non-corrosive, and possess suitable thermal properties in this temperature range. Fluid flow rates will reach values of 3-3.3 m/s through receiver tubes. While the intrinsic behavior of the fluid is probably not altered by flow rate, the corrosion processes may be affected. Parts of the system will be thermally cycled; there will be diurnal cycling upon which shorter term transients will be impressed due to such things as cloud coverage. While the fluid properties will probably not be strongly affected by cycling, the fluid/containment material interaction may be. For example, protective oxide scales may be breached upon thermal cycling. The fluid/containment material interaction may also be affected by the mechanical state of the alloy. Thermal transients discussed above cause thermal stresses which may accelerate crack growth mechanisms. Stresses may also develop as a result of the combined effects of thermal gradients (due to asymmetric heat fluxes and one sided receiver tube heating) and constrained motion. The synergistic effects of thermal, mechanical, and chemical environments must be considered in the fluids selection process.

There are several other considerations which greatly influence system and hardware designs and are as important as the operational requirements discussed above. The fluid should be non-reactive with air in order to eliminate the need to design, operate and maintain an air-tight leak-proof system. Similarly, fluids with a high vapor pressure are undesirable because of the costs associated with a high pressure containment system. Because large quantities of fluid are required for thermal energy storage, the fluid must be inexpensive, and readily available in abundant quantities.

Fluid Selection

Typical classes of fluids proposed for heat transfer and energy storage are oils, water/steam, molten salt, and liquid metal (3). The Barstow pilot plant (4) design calls for water/steam as the heat transfer fluid and a mixture of oil and rocks as the energy storage medium. Costs can be saved in second generation (after Barstow) solar thermal power systems if the same fluid is used for heat

transfer and energy storage. This requires a liquid with a lower vapor pressure over a large temperature range (350 to 600°C). Molten salt and liquid metal satisfy that criterion. Sodium has an extensive data base from which to draw information and has been used as a heat transfer fluid at high temperatures in nuclear reactor applications. However, sodium is expensive and requires elaborate safety precautions. For this reason, molten salt appeared to have potential cost savings. But which salt?

There are, of course, numerous salts and salt mixtures that could potentially be used in a solar thermal power system. However, after screening the possibilities and excluding such things as lithium salts (too expensive), sulfates and phosphates (too corrosive), and carbonates and fluorides (melting points too high) one is left with such common materials as nitrates, chlorides, and bromides of the alkali metals and alkaline earths to choose from. After more careful scrutiny chlorides and bromides can be excluded because of melting points and cost. Based on this rather straightforward reasoning alkali metal nitrates appear to have the best chance of the salts considered for success in a solar thermal power system.

The merits and shortcomings associated with each class of fluid are listed in Table I. In preparing Table I the comments pertaining to molten salt are made assuming the chemical composition to be drawsalt, an equimolar mixture of $NaNO_3$ and KNO_3. From this table it is clear that no class of fluid materials is obviously superior to the others.

In order to determine the most attractive fluid for use in a central receiver system one should take a plant design using the fluid in question, and conduct a cost analysis. The most important criterion is the cost of energy, and the projected energy cost should be the key constituent in determining the most attractive class of fluid material. Recent cost studies have been carried out (5) and the details of the studies are outside of the scope of this paper. Suffice it to say the potential for the lowest cost energy system resides with using nitrate salt for heat transfer and energy storage.

Salt Composition

The nitrate/nitrite salts of sodium and potassium are of greatest interest because of suitable temperature ranges of liquid formation, nonreactivity to air, and low cost. The salt composition most prominantly used in industry is the three component mixture of 40% $NaNO_2$-53% KNO_3-7% $NaNO_3$ by weight. This mixture is marketed by Coastal Chemicals under the trade name HITEC and by Park Chemical under the name Partherm 290. It is known that the nitrite constituent is not stable at high temperatures, and if heated in air to the

TABLE I

ADVANTAGES AND DISADVANTAGES OF VARIOUS FLUIDS
PROPOSED FOR HEAT TRANSFER AND THERMAL ENERGY STORAGE APPLICATIONS

Fluid	Advantages	Disadvantages
• Water/Steam	- Extensive user experience - Direct coupling of receiver to power generation system	- High pressure containment - Sealed system - Low gas phase heat transfer coefficient - Low gas phase energy density
• Liquid Metal (Na)	- Extensive data base - Low vapor pressure - Excellent thermal properties - Hardware development	- High materials costs - Sealed system - Fire hazard
• Molten Salt (nitrates)	- Inexpensive chemicals - High energy transfer density - Low vapor pressure - Excellent thermal properties - Open system design	- Minimal user experience at peak operating conditions - Thermal stability and corrosion issues unresolved
• Oil	- Relatively non-corrosive	- Extensive decomposition at higher temperatures

temperatures of interest for solar power applications the nitrite readily converts to nitrate. Therefore, compositions of interest for solar power systems lie along the $NaNO_3$-KNO_3 binary.

Drawsalt is nominally an equimolar mixture of $NaNO_3$ and KNO_3 at the eutectic composition. Drawsalt is marketed by several companies including Park Chemical as Mixture AL-2. Due to cost considerations it is desirable to use $NaNO_3$ rich off-eutectic compositions; the $NaNO_3$ constituent is less expensive than KNO_3. $NaNO_3$ rich binary mixtures are marketed commercially by Park Chemical in the form of Partherm 430, a 60% $NaNO_3$-40% KNO_3 by weight mixture. While many of the solar projects have adopted the Partherm 430 composition as baseline, the choice of fluid is not restricted to current market items as tailormade compositions could easily be prepared. Nevertheless, it is clear that the greatest promise for a viable fluid is a $NaNO_3$-KNO_3 mixture, rich in the $NaNO_3$ constituent.

Recent Developments

While it is comforting to have such an extensive amount of industrial experience backing up the use of nitrate salts, it is also important to realize there are some major differences between current industrial usage and intended solar applications. Industrial experience has generally been at temperatures lower than 600°C. Furthermore, many of the heat transfer applications are for constant operation isothermal reactors. Industrial uses are designed to avoid thermal and mechanical cycling, two conditions which will definitely be present in portions of solar power systems. Finally, 25-30 year lifetimes as desired for solar energy systems are not typical design goals for current industrial equipment. Because of these differences, many studies are being carried out to develop a better understanding of molten nitrate salt behavior. To date these studies have indicated no insurmountable problems. However, the data base needed for reliable lifetime predictions is far from complete. Several examples of current research to generate this data base are given below.

Thermal Decomposition

When heated the nitrate salts undergo numerous reactions (6-10). The nitrate ion may decompose to nitrite and oxygen and the nitrite ion may undergo subsequent decomposition to an oxide species with the release of N_2, O_2, and/or NO_x. Direct vaporization to complex nitrate gas species has also been proposed (11). The preponderance of information in the literature suggests the most important reaction to consider is

$$\text{nitrate} \rightarrow \text{nitrite} + \text{oxygen} \quad .$$

It is often proposed that this reaction alone is sufficient to represent the decomposition chemistry. In an operating system, the salt composition will attain a fixed nitrate to nitrite ratio as determined by the oxygen partial pressure. Once this composition is reached, further changes in the salt will not occur. The operational characteristics and the thermal properties of the salt will not be significantly affected by these composition changes.

Recent studies by Kramer (12) have shown, however, that there are conditions under which the nitrate/nitrite/oxygen reaction is not the most important; in fact, conditions have been found where this reaction does not appear to be operative. The decomposition of $NaNO_3$ and KNO_3 into a vacuum has been studied by thermogravimetric and simultaneous evolved gas analysis techniques. The objectives were to determine the intrinsic decomposition processes and rates for the nitrate, i.e., the decomposition of the nitrate without recombination reactions due to interactions from gaseous species. The evolved gas species when heating to temperatures of less than 350°C were N_2 and NO. No evidence of O_2 was observed. Heating to higher temperatures also produced N_2 and NO species; however, after an induction period, O_2 was seen. The oxygen was clearly a less abundant species than N_2 and NO. It is emphasized that Kramer's studies were carried out at conditions quite different from those anticipated in solar power systems. Nevertheless, the results provide mechanistic insight into decomposition mechanisms which may be operative at higher temperatures and atmospheric pressures.

Corrosion

Nitrate salts are very strong oxidizers. In selecting alloys for containment a logical starting point is with alloys developed to withstand gaseous oxidizing environments. These alloys, for example stainless steel, withstand oxidation by the formation of passive protective oxides. The corrosion behavior of 316 stainless steel immersed in drawsalt is shown in Figure 2. It is seen that the rate of weight gain decreases with time, indicative of a corrosion process involving protective product layers.

Recent research carried out by Bradshaw (14) and Keiser et al. (15) have shown there are conditions under which deviations from protective oxide formation behavior are seen. As an example, preliminary results generated by Bradshaw (14) are shown in Figure 3 in which the weight changes of Incoloy 800 coupons suspended in a convection test loop with drawsalt as the fluid are shown. At the three temperatures studied there was an initial weight gain, caused by the formation of oxides on the sample coupons. With time all samples experienced weight losses. The weight loss was so significant at high temperatures that the net sample weight change was negative. The weight losses did not occur solely as a result of

oxide flaking and spalling. Microstructural analysis revealed that the oxide thickness increased steadily with time. A working hypothesis has been formulated in which the corrosion process is assumed to be comprised of several simultaneous processes, the formation of adherent oxide layers, and the selective dissolution of chromium from the alloy and the loss of oxide. Current studies are in progress to develop a complete qualitative and quantitative understanding of these processes. To put everything in proper perspective, it is noted that significant alloy depletion is observed only at temperatures greater than the anticipated operating temperatures in solar power plants. All studies to date suggest uniform corrosion will not be a detrimental problem in operating plants as long as the temperature is maintained at temperatures less than 600°C.

The extent to which the mechanical state of an alloy affects the corrosion behavior is as yet undetermined. Preliminary results generated by Goods (16) are shown in Figure 4, in which the oxide corrosion products formed on Incoloy 800 tubes under several different conditions are shown. Figure 4a shows the oxide formed while the alloy is held in drawsalt at 650°C for 550 hours while being strained to a maximum strain of 10%. The amount of oxide formed can be contrasted with that shown in Figure 4b, where the same alloy was heated in the identical salt for the same period of time at the same temperature, only without being strained. It is clear the amount of oxide had increased when strained. To complete the comparison, Figure 4c shows the amount of oxide formed when exposed to air. Comparing Figure 4b and 4c shows the nitrate salt environment to be a much more aggressive oxidizer than air. The experiments used to generate the results shown in Figure 4 are clearly an overtest of solar conditions, as the metal parts in an actual system will not experience 10% total strain and will not reach temperatures exceeding 600°C. Currently, long term experiments are underway to evaluate the corrosion processes taking place under realistic conditions, including stress and thermal cycling.

Summary

Various concepts have been proposed for the generation of electric power from solar energy. Such systems require the focusing of solar energy, and point focus and line focus designs have been proposed. As an additional design option, central receiver or dispersed receiver configurations are possible. Regardless of the specific system design, fluids are needed for heat transfer and thermal energy storage. It has been shown that molten nitrate salts are the most attractive choice for use as a fluid. The greatest interest lies with $NaNO_3$-KNO_3 mixtures of compositions on the $NaNO_3$ rich sides of the equimolar eutectic. Numerous research activities are being carried out to further the development of solar large power

systems using nitrate salts. While it is too early to predict the future of such systems, it is clear the impetus exists for developing a better understanding of nitrate salt behavior. Recent results concerning decomposition and corrosion characteristics have been described above.

REFERENCES

1. B. W. Watt and D. H. Kerridge, Chem. in Britain, 15, 78 (1979).
2. R. W. Foreman, "Heat-Treatment of Industrial Materials in Molten Salt" presented at the Third Int'l Symp. on Molten Salts, 158th Electrochemical Soc. Mtg, Hollywood, Fla., October 8, 1980.
3. T. N. Tallerico, "A Description and Assessment of Large Solar Power Systems Technology,"Sandia Laboratories Report #SAND79-8015, August, 1979.
4. A. C. Skinrood, Solar Age, 24, June, 1978.
5. K. W. Battleson, P. De Laquil III, J. D. Fish, H. F. Norris, and J. J. Iannucci, "1980 Solar Central Receiver Technology Evaluation," Sandia Laboratories Report SAND80-8235, October, 1980.
6. R. F. Bartholemew, J. Phys. Chem. 70, 3442 (1966).
7. E. S. Freeman, J. Phys. Chem. 60, 1487 (1958).
8. E. S. Freeman, J. Am. Chem. Soc. 79, 838 (1957).
9. G. D. Sirotkin, Russ. J. Inorg. Chem. 4, 1180 (1959).
10. B. D. Bond and P. W. M. Jacob, J. Chem. Soc. A, 1265 (1966).
11. A. Buchler and J. L. Stauffer, J. Phys. Chem. 70, 4092 (1966).
12. C. M. Kramer (Sandia National Laboratories, Livermore, CA 94550) private communication.
13. T. R. Tracey, "Conceptual Design of Advanced Central Receiver Power System, Phase I" Martin Marietta final report for DOE contract EG-77-C-03-1724.
14. R. W. Bradshaw (Sandia National Laboratories, Livermore, CA 94550) private communication.
15. J. R. Keiser, J. H. deVan, E. J. Lawrence, J. Nucl. Mat. 85, 294 (1979).
16. S. H. Goods (Sandia National Laboratories, Livermore, CA 94550) private communication.

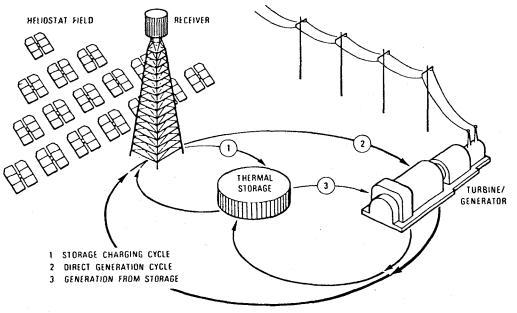

Figure 1. A schematic illustration of a solar central receiver system for the generation of electricity.

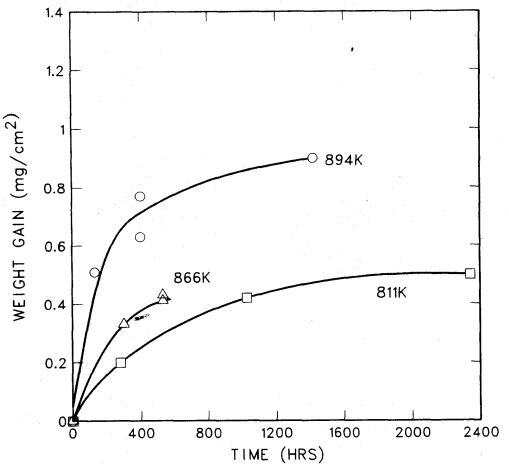

Figure 2. The corrosion behavior of 316 stainless steel coupons immersed in Partherm 430 (60% $NaNO_3$-40% KNO_3 by weight) (13).

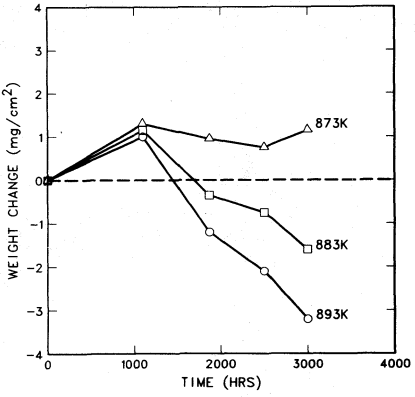

Figure 3. The corrosion behavior of Incoloy 800 samples suspended in a thermal convection loop with a Partherm 430 working fluid (14).

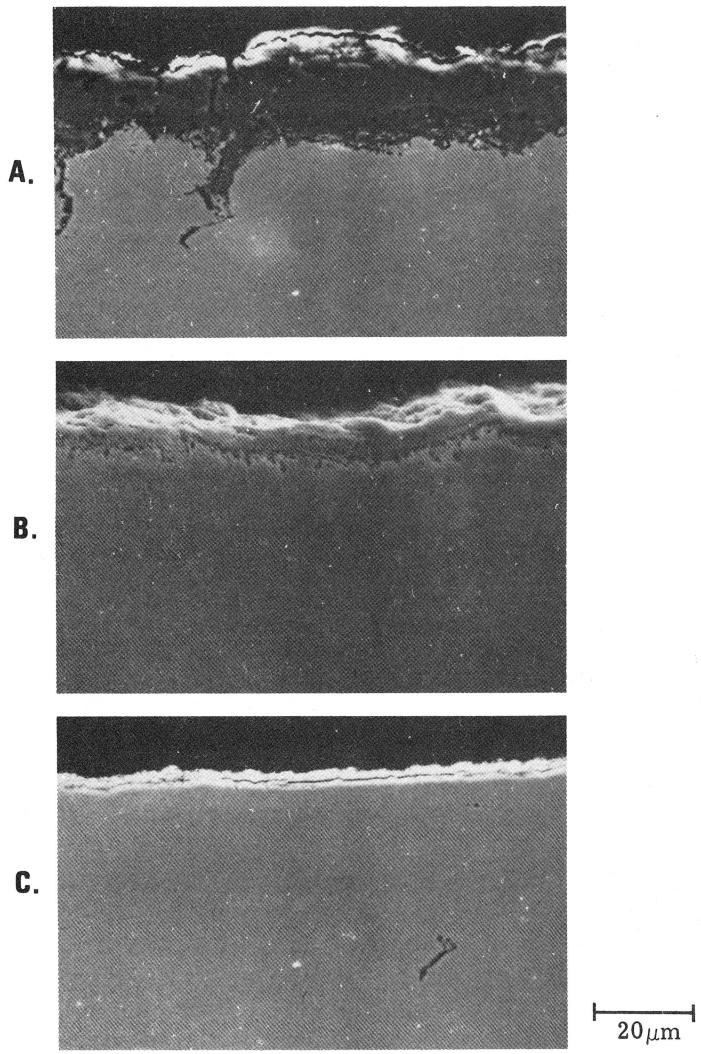

Figure 4. Oxide corrosion products found on Incoloy 800 tubes exposed at 650°C for 550 hours: (A) in contact with Partherm 430 and strained to 10%, (B) in contact with Partherm 430 and undeformed, (c) in contact with air and undeformed.

DOI: 10.1149/198109.0485PV

HEAT CAPACITIES OF $NaNO_3$, KNO_3 AND $(Na,K)NO_3$*

R. W. Carling
Sandia National Laboratories
Livermore, CA 94550

Abstract

Some current designs of solar central receivers employ molten nitrate salts as the heat transfer and storage medium. The salt of most interest is nominally a 50/50 molar mixture of $NaNO_3$ and KNO_3. The temperature range of interest for the central receiver application is 623 to 873 K. Available heat capacity results are disparate and incomplete over this temperature range. However, such data are important in terms of thermal modeling of the receiver system and for determining the quantity of energy storage. Therefore, an experimental program was undertaken to measure the heat capacity of $NaNO_3$, KNO_3, and a mixture of $NaNO_3$ and KNO_3. Heat capacities were measured from 350 to 740 K for $NaNO_3$, 350 to 800 K for KNO_3, and 330 to 700 K for a mixture of $NaNO_3$ and KNO_3. The desired temperature limit of 873 K was not obtained because of experimental difficulties. The experimental results are presented and compared with previous investigations.

Introduction

Some current designs of solar central receivers employ molten nitrate salts as the heat transfer and storage medium. The salt of most interest is a 50/50 molar mixture of $NaNO_3$ and KNO_3, often referred to as drawsalt. Work has focused on this salt mixture because it has good physical and chemical properties relative to other salt mixtures over the temperature range of a central receiver (623 to 873 K). Some of these properties are low cost, chemically stable, non-corrosive, low melting point, and high heat capacity. Although many of the physical and chemical properties of $NaNO_3/KNO_3$ are known at low temperatures, there are relatively little data available in the temperature range of interest. The property of interest in this paper is the heat capacity. The heat capacity is an important parameter for the designers and engineers of the heat transfer and storage systems. Data are available up to 773 K, but not beyond (1). While it is often assumed that the heat capacity of a molten salt does not change with temperature, the heat capacity of molten $NaNO_3/KNO_3$ decreases by about 10 percent from 510 to 770 K (1). The main thrust of this work was to extend the heat capacity to 873 K.

*This work supported by U.S. Department of Energy, DOE, under contract DE-AC04-76DP00789.

The heat capacities of $NaNO_3$ and KNO_3 were also measured in this study. The reasons for this work were two-fold. First, since the heat capacities of $NaNO_3$ and KNO_3 have been measured previously (1-12), the previous work would provide a means for assessing the accuracy of the technique used here. Secondly, the validity of the additive rule was determined. One can calculate a heat capacity by adding the heat capacities of $NaNO_3$ and KNO_3 in the appropriate proportions of the mixture (2). If the experimentally derived heat capacity and that obtained by adding the Cp's of the components agree, then the heat capacity of any mixture of KNO_3 and $NaNO_3$ could be determined simply.

Experimental

Heat capacity measurements were made with a Perkin-Elmer differential scanning calorimeter, DSC-2. All measurements were made with the samples sealed in gold or stainless steel capsules. Sapphire was used as the heat capacity reference material. Heat capacity measurements were made at a heating rate of 10 degrees/min with range settings of 1.25 to 5.00 J/min. The salts were reagent grade material, recrystallized from water and dried at 425 K for at least 48 hours in vacuum. The salts, prepared in this manner, were stored over $CaSO_4$ until use.

Control and operation of the DSC were through a Hewlett Packard 9825 desk-top calculator. Measurements were typically taken over temperature ranges of 100 degrees. Temperature ranges were overlapped and scanned several times. The heat capacity results are, therefore, the average of several measurements at each temperature. Accuracies in the solid regions were estimated to be 2% by comparison with previous heat capacity results.

A major problem developed in the liquid region of each salt. The gold sample pans cracked and leaked molten salt within the DSC sample pan holder. The gold pans cracked adjacent to the hermetic seals and it is thought to be due to residual H_2O vapor and/or O_2 generated as the salt decomposed to nitrite and oxygen. The stainless steel pans did not work any better. The stainless steel pans were closed without the Viton O-rings provided and hence leaked for lack of proper sealing. The O-rings were omitted because Viton will not take the temperatures over which measurements were to be made.

Results and Discussion

The heat capacity results for $NaNO_3$, KNO_3, and $(Na,K)NO_3$ are illustrated in Figures 1 to 3 and tabulated in Table 1. The results do not extend to 873 K as desired. The upper temperature was limited due to salt leakage from the sample pans as described in the previous section. The heat capacity results of the solids agree well with

previous investigations (3,5-7). Comparisons of the results are not shown in the figures to avoid confusion. It can also be seen in Table 1 that the additivity rule for heat capacities holds for $NaNO_3$ and KNO_3 (2).

Temperatures and enthalpies and entropies of transition and fusion of $NaNO_3$, KNO_3, and $(Na,K)NO_3$ are presented in Table 2. As can be seen the values in this work agree well with previous investigations. These results are presented to further support the accuracy of the technique up to the melting points. However, the accuracy of the heat capacity results obtained above the melting are in doubt. The heat capacity values have considerably more scatter in the liquid region than in the solid region. Although the results from this work tend to agree reasonably well with a few previous investigations they are in serious disagreement with some very recent publications (11,12). The discrepancies of the pure liquid components will be discussed separately from the mixture.

$NaNO_3$ and KNO_3 (Liquid)--Some of the literature derived heat capacity values for liquid $NaNO_3$ and KNO_3 are in serious disagreement with this work. The results obtained in this work indicate a decrease in heat capacity as the temperatures increase above the melting point. The heat capacities measured were in the range of 130 to 140 J K^{-1} mol^{-1} at temperatures up to 200 kelvins past the melting points. Two previous investigations support these results for KNO_3 (1,4). Other investigations suggest that the heat capacity results from this work are too low. They suggest heat capacities of about 150 to 160 J K^{-1} mol^{-1} at temperatures slightly above the melting point (1,4,6). A decreasing heat capacity in the liquid region is also supported by one other investigator (6). However, two very recent publications put the heat capacities of $NaNO_3$ at 160 to 180 J K^{-1} mol^{-1} (12) and 212 J K^{-1} mol^{-1} (11) and KNO_3 at 180 to 210 J K^{-1} mol^{-1} (12) and 233 J K^{-1} mol^{-1} (11) just above the melting points. Further, one (reference 12) suggests an increasing heat capacity with temperature. Unfortunately, at this point it is difficult to rationalize any set of results as better than another. Each of the techniques used have serious drawbacks. The results from this work up to the melting point would suggest accuracies of 2-3% in the heat capacity measurements. The increased scatter and the experimental difficulties due to leaking sample pans obviously decreases the accuracy of the heat capacities in the liquid region. Therefore, the heat capacities in this work may be too low as a result of the experimental difficulties described above. However, previously reported heat capacity values were measured at the melting point and not into the liquid region. If the salt had not completely melted heat capacity values much too high could be measured. The conclusion at this stage is that the heat capacities of each salt are in the range of 140 to 150 J K^{-1} mol^{-1} in the liquid region. Also, the heat capacities certainly decrease but probably don't change much in the liquid region until the salts begin to decompose (24).

$(Na,K)NO_3$ (Liquid)--There are only two previous investigations on the heat capacity of the 50:50 molar mixture. One shows the heat capacity decreasing with the temperature from 167.3 J K^{-1} mol^{-1} at 510 K to 138.6 J K^{-1} mol^{-1} at 770 K (1). The other gives a value of 142 J K^{-1} mol^{-1} just above the melting point of 494 K (11). This latter result, although not necessarily wrong, is about 35 percent lower than their results for pure $NaNO_3$ and KNO_3 as liquids. It is difficult to reconcile such a difference. Again, the techniques for measuring heat capacities in the temperature range of interest have serious drawbacks as described above. At this point it is not possible to arrive at recommended values for the heat capacity of the liquid.

Summary

The heat capacities of $NaNO_3$, KNO_3 and $(Na,K)NO_3$ have been measured well into the liquid range of each salt. The solid heat capacities agree very well with previous investigations as do the transition and melting points. However, serious experimental difficulties were encountered in the liquid regions of the salts. Methods to resolve the experimental difficulties are being explored. Future experiments will clarify the disparate heat capacity results obtained to date.

REFERENCES

1. G. J. Janz, C. B. Allen, N. P. Bansal, R. M. Murphy, and R. P. T. Tompkins, "Physical Properties Data Compilations Relevant to Energy Storage. II. Molten Salts: Data on Single and Multi-Component Salt Systems," NSRDS-NBS 61, April 1979.

2. T. B. Douglas, ASME Trans., 79, 23 (1957).

3. V. C. Reinsborough and F. E. W. Wetmore, Aust. J. Chem., 20, 1 (1967).

4. H. M. Goodwin and H. T. Kalmus, Phys. Rev., 28, 1 (1909).

5. J. C. Southard and R. A. Nelson, J. Am. Chem. Soc., 55, 4865 (1933).

6. Mustajoki, A., Ann. Acad. Scient. Fenn. A VI, 5 (1957).

7. Mustajoki, A., ibid., 99 (1962).

8. V. A. Sokolov, V. A. Palkin, and N. E. Schmidt, Invest. Sektora Fiz.-Khim. Anal., Inst. Obscheĭ i Neorg. Khim., Akad. Nauk S.S.S.R., 25, 134 (1954) CA 49:14463.

9. V. A. Sokolov and N. E. Schmidt, ibid., 26, 123 (1955). CA 50:3060.

10. V. A. Sokolov and N. E. Schmidt, ibid., 27, 217 (1956). CA 50:15200.

11. P. Nguyen-Duy and E. A. Dancy, Thermochim. Acta, 39, 95 (1980).

12. T. Asahina, M. Kosaka, and H. Taoda, (Gov. Ind. Res. Inst., Nagoya, Japan). Nagoya Kogyo Gijutsu Shikensho Hokoku, 29, 25 (1980).

13. M. G. Lowings, K. G. McCurdy, and L. G. Hepler, Thermochim. Acta, 23, 365 (1978).

14. C. N. R. Rao, B. Prakash, and M. Naturajan, "Crystal Structure Transformations in Inorganic Nitrites, Nitrates, and Carbonates," NSRDS-NBS 53, May 1975.

15. D. I. Marchidan and C. Telea, Rev. Roumaine Chim., 13, 1291 (1968).

16. P. Franzosini and C. Sinistri, Ricerca sci., 33, 411 (1963).

17. H. C. Ko, T. Hu, J. G. Spencer, C. Y. Huang and L. G. Hepler, J. Chem. Eng. Data, 8, 364 (1963).

18. T. Hu, H. C. Ko, and L. G. Hepler, J. Phys. Chem., 68, 387 (1964).

19. G. J. Janz and T. R. Kozlowski, J. Phys. Chem., 67, 2857 (1963).

20. E. R. Van Artsdalen, J. Phys. Chem., 60, 173 (1956).

21. D. M. Speros and R. L. Woodhouse, J. Phys. Chem., 67, 2164 (1963).

22. O. J. Kleppa and F. G. McCarty, J. Chem. Eng. Data, 8, 331 (1963).

23. R. P. Clark, J. Chem. Eng. Data, 18, 67 (1973).

24. O. Kubaschewski and C. B. Alcock, "Metallurgical Thermochemistry," Pergamon Press, New York, 1979.

TABLE 1

HEAT CAPACITIES OF $NaNO_3$, KNO_3, AND $(Na,K)NO_3$

$\frac{T}{K}$	$\frac{C_p}{J\ K^{-1}\ mol^{-1}}$		
	$NaNO_3$	KNO_3	$(Na,K)NO_3$
300	92.2	95.6	
325	96.3	96.6	
350	100.7	98.8	104.7
375	105.6	105.1	109.4
400	111.3	111.3	110.9
425	118.0	124.2	119.9
450	125.6	124.3	122.7
475	134.6	125.5	126.1
500	150.1	126.7	a
525	182.2	128.6	138.9
550	a	131.7	137.0
575	a	138.4	141.5
600	140.0	a	141.9
625	140.6	140.6	139.9
650	141.2	139.1	141.2
675	141.4	138.1	137.6
700	140.8	137.3	134.6
725	139.5	136.4	
750	137.3	135.1	
775		133.1	
800		130.1	

[a]Solid-solid transition or melting region.

TABLE 2

SUMMARY OF TRANSITION AND MELTING IN $NaNO_3$, KNO_3, and $(Na,K)NO_3$

Compound	T_t / K	T_m / K	ΔH_t / kJ mol^{-1}	ΔH_m / kJ mol^{-1}	ΔS_t / J K^{-1} mol^{-1}	ΔS_m / J K^{-1} mol^{-1}	Reference
$NaNO_3$	550	583	4.42	15.1	8.03	26.0	This Work
				15.1			13
	549		4.3				14
				15.1			15
		579		15.6		26.8	16
		579		15.0			9
				15.1			17
		606		15.4			4
				14.9			18
				14.7			19
	549	579	3.95	14.6	7.19	25.2	6
				15.9			20
				14.8			21
		583		15.5			22
KNO_3	406	612	5.64	10.5	13.8	17.2	This work
		610		10.0		16.4	23
	401	607	5.10	9.6			10
		607		10.0		16.7	16
		610		10.1			22
		611		10.7			4
	402		5.42				7
	403		5.02				14
$(Na,K)NO_3$	383	494	3.5	10.2	9.2	20.5	This work
		495		13.4			15

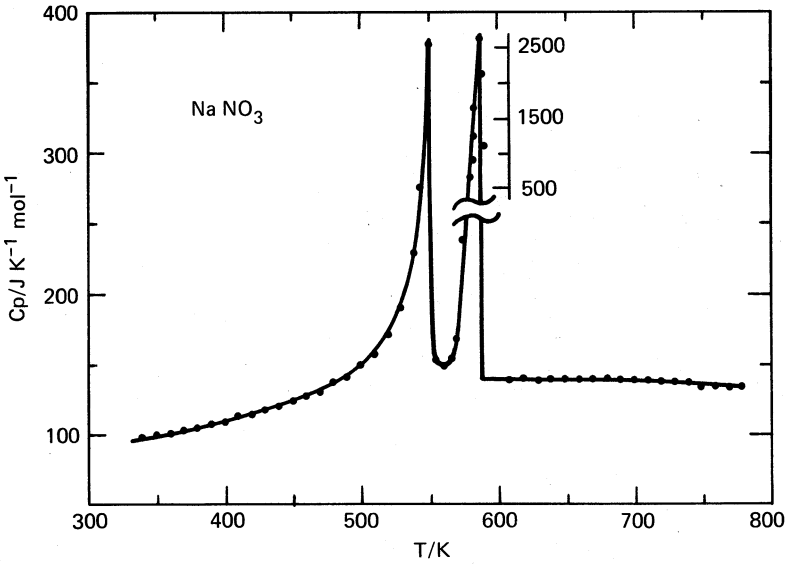

Figure 1. Heat Capacity of $NaNO_3$

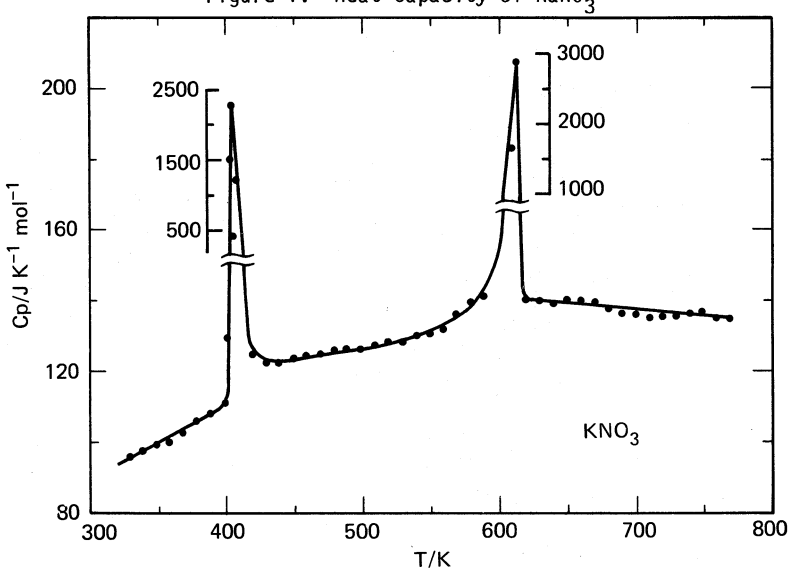

Figure 2. Heat Capacity of KNO_3

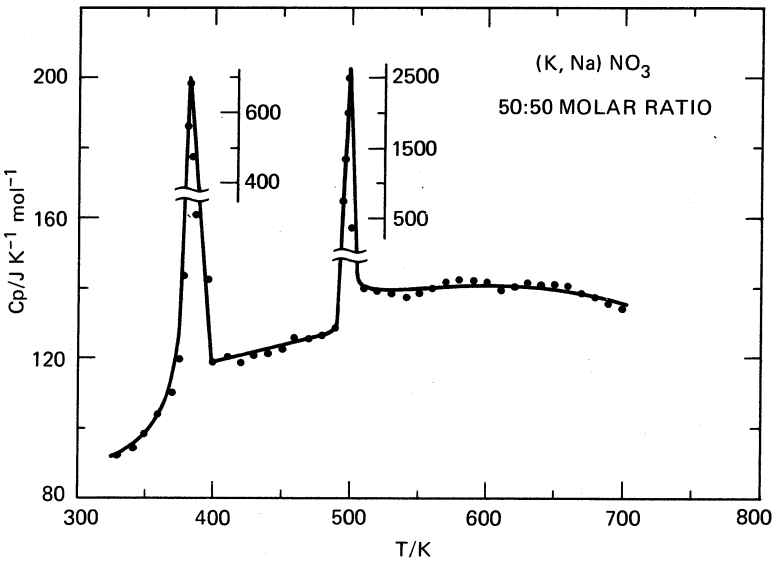

Figure 3. Heat Capacity of a 50:50 Molar Mixture of $NaNO_3$ and KNO_3

DOI: 10.1149/198109.0494PV

THERMAL DECOMPOSITION OF $NaNO_3$ AND KNO_3*

C. M. Kramer
Chemistry Division
Naval Research Laboratory
Washington, D.C. 20375

and

Z. A. Munir
Materials Science Division
Mechanical Engineering Department
University of California
Davis, California 95616

ABSTRACT

Mixtures of sodium nitrate and potassium nitrate have potential applications as high temperature heat transfer fluids and thermal storage media in solar thermal electric power plants. High temperature salt stability is an important characteristic for these applications; therefore the decomposition of the nitrates was studied to elucidate the mechanisms by which nitrates decompose. To this end, the decomposition of sodium nitrate and potassium nitrate was studied isothermally in vacuum at temperatures ranging from 620-750 K using simultaneous thermogravimetric analysis and mass spectrometry. Decomposition in vacuum was observed as low as 620 K. Nitrogen, nitric oxide, and oxygen were observed to be products of nitrate decomposition.

Introduction

Solar electric power plants use thermal energy from the sun to generate steam for turbines that generate electrical power. The sun's rays are focused by a field of heliostats (sun-tracking mirrors), onto an elevated receiver, through which a heat transfer fluid is pumped to absorb the energy. The hot fluid is pumped to a heat exchanger to generate steam to turn a turbine (1).

*This work was performed at Sandia National Laboratories, Livermore, CA, and was supported by the U.S. Department of Energy under Contract DE-AC 04-76DP00789.
+National Research Council Cooperative Research Associate at NRL.

Economic use of insolation for electrical power generation necessitates energy storage. Ideally the heat transfer fluid that generates steam would also be the sensible heat thermal storage medium (1,2). The criteria for a single heat transfer and themal energy storage fluid are: melting point less than 523 K, thermal stability to 873 K, high specific heat, low vapor pressure, compatibility with structural materials, and low cost (3). Satisfying these criteria are mixtures of sodium nitrate, $NaNO_3$ and potassium nitrate, KNO_3 (3,4). An important characteristic of sodium and potassium nitrate is their chemical stability in air (5,6) which can greatly simplify the design of the solar power plant.

In various applications the molten nitrates have been heated to as high as 873 K, the exact temperature depending on the duration of use and economic factors (6). At elevated temperatures, the nitrates may undergo a number of reactions (7-10) including decomposition to nitrite ($NaNO_2$) or oxide (Na_2O), and vaporization (11):

$$NaNO_3 \longrightarrow NaNO_2 + 1/2\ O_2 \qquad (1)$$

$$2\ NaNO_3 \longrightarrow Na_2O + 5/2\ O_2 + N_2 \qquad (2)$$

$$NaNO_3(l) \longrightarrow NaNO_3(g) \qquad (3)$$

The chemical behavior of $NaNO_3$ and KNO_3 is complex because of the multiple conjugate, consecutive, and reversible reactions that occur. In particular, Reaction (2) is an overall reaction that may proceed by various steps involving N_xO_y gas species (7). Recent work has shown that the oxide product in Reaction (2) is unstable in the nitrates (12). The oxide reacts with nitrate or oxygen to form peroxide and superoxide ions in the molten nitrates. The congruent vaporization of nitrates occurs as low as 623 K, according to Hardy and Field (11). Also, the nitrite produced in Reaction (1) may undergo decomposition reactions that obscure the behavior of the nitrates alone (7).

Experimental Technique

A mass spectrometer and microbalance were combined into one system to study Reactions (1-3). The essential elements of the thermogravimetry and mass spectrometry (TG/MS) system are the microbalance, furnace, gas inlet system, mass spectrometer, vacuum system, and data acquisition system. The TG/MS system was housed in a stainless steel vacuum system. A Cahn R-H microbalance was used which has a minumum detectable weight change of 10 μg and a maximum weight limit of 10 g. The furnace was a 1.9 cm diameter stainless steel tube that was heated externally by a kanthal heater.

The furnace in which the sample was suspended was coupled to the mass spectrometer using a leak valve. A disadvantage of this gas sampling arrangement was that vapor species that are condensible at room

temperature could not be detected. These vapors condensed on the circuitous and relatively cold route the gases must take to the mass spectometer; therefore species from nitrate or nitrite vaporization (Reaction (3)) were not studied by mass spectrometry in this work.

The mass spectrometer was an Extranuclear Laboratories quadrupole mass spectrometer and had an axial ionizer and a Cu-Be detector. To facilitate comparisons of experiments, the electron optics were adjusted so that the ion intensities were insensitive to small changes in the lenses and all experiments were performed with identical mass spectrometer settings.

A data acquisition system was incorporated into the TG/MS system for collecting thermogravimetric data. The balance output voltage was fed into a digital voltmeter. A microprocessor unit read the digital voltmeter and a digital chromel-alumel thermocouple located beneath the sample. The thermocouple readings and the voltmeter output were read into a CDC 6600 computer so that kinetic analysis could be performed.

The TG/MS apparatus was used to study molten $NaNO_3$ and KNO_3 in isothermal decomposition experiments under vacuum over the temperature range 620-750 K. The nitrate samples were prepared in the following manner. The salts were dissolved in hot distilled water. Small (<10 mg) samples of salt were precipitated from the hot salt water solutions onto flat gold coupons as the salt solutions cooled. The samples were dried with a hot air gun and suspended in the furnace by thin gold wires. When melted, the salt samples covered the entire coupon surface. Since the samples of salt were small, they did not form pendant drops on the coupon; therefore, the salt thickness was uniform over the surface of the coupon. Precipitated salt samples were submitted to infrared absorption analysis which showed that the $NaNO_3$ and KNO_3 samples were unchanged by precipitation from the salt water solutions.

The heating schedule for the decomposition experiments was as follows. The furnace was heated from room temperature to 330 K and held for 180 minutes; the furnace was then heated at 25 K per minute to the isothermal test temperature and held at that temperature for 360 minutes; the furnace was then turned off to cool.

A unique method of comparing the evolved gases was employed. From preliminary experiments, masses 28, 30 and 32 (N_2, NO, and O_2) were the only gases evolved from $NaNO_3$ and KNO_3. To compare the amounts of each gas that were evolved, the mass range 27-33 was quickly and repeatedly scanned with the mass spectrometer. The mass spectra were recorded on a strip chart recorder. The resulting record gave discrete peaks that formed an envelope for each mass. After each experiment was finished a planimeter was used to measure the area under each envelope for each mass. The kinetic analysis of the weight changes and the evolved gases are given in Tables 1 and 2 for $NaNO_3$ and KNO_3, respectively.

Table 1

Thermogravimetry and Mass Spectrometry Experiments with $NaNO_3$ in Vacuum

Trial	Temperature (K)	NO/N_2*	O_2/N_2*	O_2/NO*	b($mg\text{-}cm^{-2}\text{-}min^{-1}$)
50	752	<0.85	<0.23	<0.28	$-1.628(10^{-1})$
55	745	<0.52	<0.08	0.15	$-1.171(10^{-1})$
56	744	0.31	0.15	0.49	$-1.198(10^{-1})$
49	636	0.52	0.0	0.0	$-1.105(10^{-3})$
54	627	0.086	0.0	0.0	$-1.765(10^{-3})$
55	631	0.066	0.0	0.0	$-1.721(10^{-3})$
74	676	0.91	0.057	0.063	$-5.572(10^{-3})$
75	650	0.51	0.042	0.12	$-2.884(10^{-3})$
76	715	0.77	0.27	0.35	$-3.045(10^{-2})$

*When the ratio is indicated to be less than the value shown, the mass spectrometer was saturated during peak production of the gases.

Table 2

Thermogravimetry and Mass Spectrometry Experiments with KNO_3 in Vacuum

Trial	Temperature (K)	NO/N_2	O_2/N_2	O_2/NO	$b(mg\text{-}cm^{-2}\text{-}min^{-1})$
66	747	*	*	*	$-1.938(10^{-1})$
72	743	0.56	0.062	0.11	$-1.924(10^{-1})$
80	737	0.27	0.16	0.58	$-1.908(10^{-1})$
81	717	*	*	*	$-3.994(10^{-2})$
82	671	0.21	0.086	0.041	$-9.742(10^{-3})$
83	741	0.42	0.189	0.45	$-2.382(10^{-1})$
84	650	0.087	0.0	0.0	$-4.981(10^{-3})$
85	624	0.047	0.0	0.0	$-1.950(10^{-3})$
86	623	0.035	0.0	0.0	$-1.863(10^{-3})$
87	621	0.025	0.090	0.11	$-2.455(10^{-3})$

*Not available.

Results and Discussion

The nitrates were completely decomposed and vaporized within 100 minutes at 750 K. In contrast to previous work by Freeman (8,9), the weight losses did not arrest at a weight corresponding to 100% oxide formation. We observed that nitrates vaporized and condensed in cooler areas outside the furnace. These results indicate that decomposition, vaporization of the nitrates and nitrites, and vaporization of the decomposition products occur simultaneously.

The nitrates evolved N_2, NO, and O_2 as they decomposed, but not NO_2. Nitrogen dioxide has been reported in the literature (8,9); however, it is possible that the NO_2 that was observed was actually oxidized NO. Nitrogen, oxygen, and nitric oxide were observed by Brown et al (13) in a Knudsen cell filled with $NaNO_3$ above 570 K.

The relative amounts of the evolved gases (N_2, NO, and O_2) are shown for $NaNO_3$ and KNO_3 as a function of inverse temperature in Figures 1 and 2. The amount of NO relative to N_2 increased at higher temperatures for both $NaNO_3$ and KNO_3. Although there is significant scatter in the data in Figure 1, the ratios of NO to N_2 were greater for $NaNO_3$ than for KNO_3. The O_2 to N_2 ratios (Figure 2) were also higher at higher temperatures and were greater for $NaNO_3$ compared to KNO_3.

These three gases may arise from several reactions. Oxygen is a product of Reaction (1) and (2). Nitrogen may arise from (2) and nitric oxide from (4) due to decomposition to oxide.

$$2\ NaNO_3 \longrightarrow Na_2O + 2\ NO + 3/2\ O_2 \qquad (4)$$

Since superoxide and peroxide are considered to be stable in the nitrates, it is possible that Reactions (5-7) occur producing superoxide (O_2^-) and peroxide (O_2^{-2}) and releasing N_2 and NO.

$$2\ NO_3^- \longrightarrow 2\ NO + 2\ O_2^- \qquad (5)$$

$$2\ NO_2^- \longrightarrow 2\ NO + O_2^{-2} \qquad (6)$$

$$2\ NO_2^- \longrightarrow N_2 + 2\ O_2^- \qquad (7)$$

The nitrite in Reactions (6) and (7) is a product of Reaction (1). The O_2 to N_2 and the NO to N_2 ratios varied depending on the salt at the temperature which indicated that the rates of Reactions (1-7) were different for $NaNO_3$ compared to KNO_3 and at 750 K compared to 620 K.

The thermogravimetric data were analyzed as a function of time and temperature. A computer program was written that performed a least squares analysis for the weight per unit surface area (W) as a function of time, t. The equation to which the thermogravimetric data were

fitted was:

$$W = a + bt + ct^2 \qquad (8)$$

where a, b, and c are constants. The computer program calculated the best values of a, b, and c for each experiment. The data from one of the experiments are shown in Figure 3. The data points were connected by straight lines and a marker was drawn periodically. The least squares fit to the data using Eq. (8) was also drawn and the fit to the data was very good.

The initial rate of decomposition is b. The values of b for each experiment are given in Tables 1 and 2. The initial rates were assumed to have an Arrhenius temperature dependence, i.e.,

$$b = \exp(\Delta S^*/R)\ \exp(-\Delta H^*/RT) \qquad (9)$$

Where ΔS^* and ΔH^* are the entropy and enthalpy of activation for a reaction. The computer program also determined the least squares fit of ln(b) versus 1/T and determined ΔS^* and ΔH^* for a given series of experiments. The least squares fit and the individual values of the initial rates of weight loss are shown in Figure 4. The rates span two orders of magnitude over 120 K. The activation enthalpies for $NaNO_3$ and KNO_3 are 153 and 146 kJ-mole^{-1} (± 21 kJ-mole^{-1} for a 90% confidence limit). Within experimental error, the temperature dependencies for the two nitrates are the same. These temperature dependencies are lower than those reported by Freemen (8,9) or Bond and Jacobs (10) in Table 3. Of course, the present experiments were performed at lower temperatures and in vacuum where other reactions may prevail.

Table 3

Temperature Dependence of Salt Decomposition

Reaction	ΔH^* kJ-mole^{-1}	Reference
$KNO_3 \longrightarrow KNO_2 + 1/2\ O_2$	274	9
KNO_3 evaporation	146 ± 21	This work
$NaNO_3 \longrightarrow NaNO_2 + 1/2\ O_2$	187	8
$NaNO_3 \longrightarrow NaNO_2 + 1/2\ O_2$	169	10
$NaNO_3$ evaporation	153 ± 21	This work
$2NaNO_2 \longrightarrow Na_2O + N_2 + 3/2\ O_2$	179	10

The initial rates of weight loss from KNO_3 were higher than those for $NaNO_3$, although the differences between the $NaNO_3$ and KNO_3 rates were always less than a factor of two. Potassium nitrate is considered to be more stable (7-9) than $NaNO_3$; therefore one would expect the rates for KNO_3 decomposition to be less than $NaNO_3$ rates at the same temperature. However, the rates in Figure 4 are weight losses and not molar fluxes. Molar fluxes could not be calculated because all of the vaporizing species and their relative contributions were not known. Since potassium is heavier than sodium, the higher rates for KNO_3 samples may simply reflect the larger molecular weight of KNO_3 compared to $NaNO_3$.

Summary and Conclusions

Sodium and potassium nitrate were decomposed in vacuum from 620-750 K. The intrinsic gaseous decomposition products were N_2, NO and O_2 for both $NaNO_3$ and KNO_3. The initial rates of weight loss were approximately 0.0015 and 0.002 mg-cm^{-2}-min^{-1} for $NaNO_3$ and KNO_3, respectively, at 620 K. The activation enthalpies were 153 for $NaNO_3$ and 146 kJ-mole^{-1} for KNO_3 (± 21 kJ-mole^{-1}) over the given temperature range. More oxygen and nitric oxide (relative to nitrogen) were evolved at higher temperatures and from $NaNO_3$ compared to KNO_3. The decomposition process in vacuum was a complex series of overlapping reactions that occur concurrently with nitrate vaporization and decomposition product vaporization.

Acknowledgements

We are grateful to Joanne Volponi for her tremendous contributions to the experimental sections and to Dr. Kurt H. Stern for his thoughtful reviews and suggestions.

References

1. L. N. Tallerico, "A Description and Assessment of Large Solar Power Systems Technology," Sandia Laboratories Report, SAND79-8015 (1979).

2. L. Radosevich, "Thermal Energy Storage for Advanced Solar Central Receiver Power Systems," Sandia Laboratories Report, SAND78-8821 (1978).

3. A. Borucka, "Survey and Selection of Inorganic Salts for Application to Thermal Energy Storage," Borucka Research Co., Livingston, NJ (1975).

4. H. P. Voznick and V. W. Uhl, Chem. Eng., 70, 135 (1963).

5. B. W. Watt and D. H. Kerridge, Chem. in Brit., 15, 78 (1979).

6. J. Alexander and S. G. Hindin, Ind. Eng. Chem., 39, 1044 (1947).

7. K. H. Stern, J. Phys. Chem. Ref. Data, 1, 747 (1972).

8. E. S. Freeman, J. Phys. Chem., 60, 1487 (1956).

9. E. S. Freeman, J. Amer. Chem. Soc., 79, 838 (1957).

10. B. D. Bond and P. W. M. Jacobs, J. Chem. Soc., Lon. A (9), 1265 (1966).

11. C. J. Hardy and B. O. Field, Chem. Soc. J., Pt 4-5, 5131 (1963).

12. D. R. Flinn and K. H. Stern, J. Electroanalyt. Chem., 63, 39 (1975).

13. R. W. Brown, J. H. Lippiatt, D. Price and D. C. A. Izad, Intl. J. Mass Spec. and Ion Phys., 16, 101 (1975).

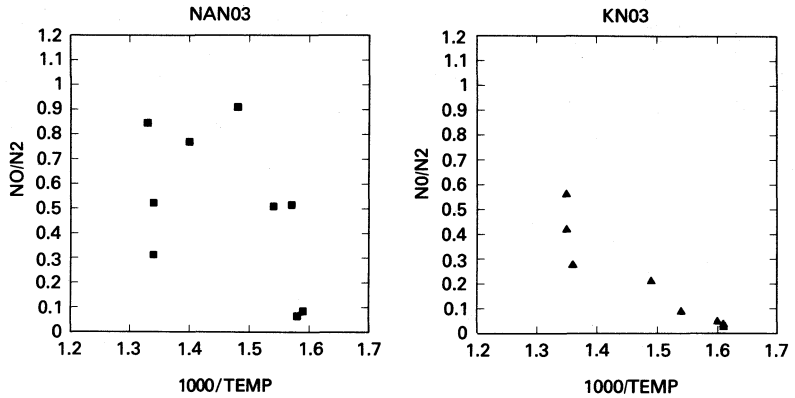

FIGURE 1. DECOMPOSITION GASES - NO/N_2 AS A FUNCTION OF TEMPERATURE

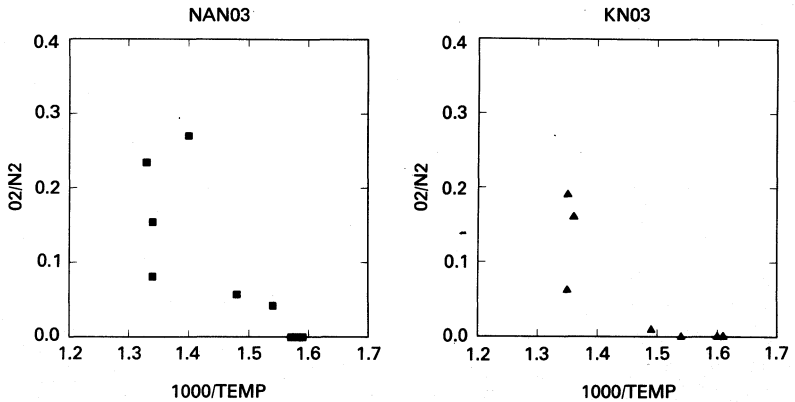

FIGURE 2. DECOMPOSITION GASES - O_2/N_2 AS A FUNCTION OF TEMPERATURE

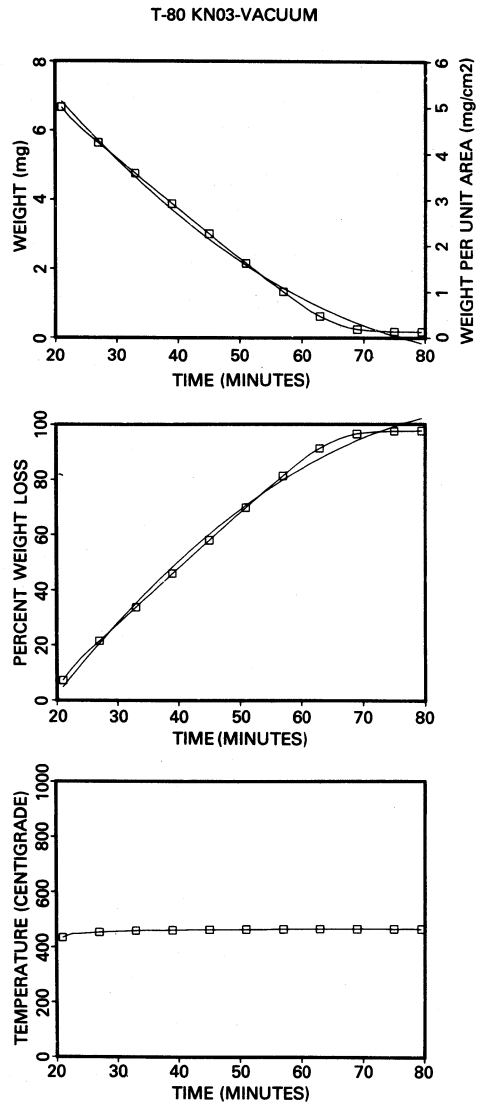

FIGURE 3. DATA FROM A TG/MS DECOMPOSITION EXPERIMENT

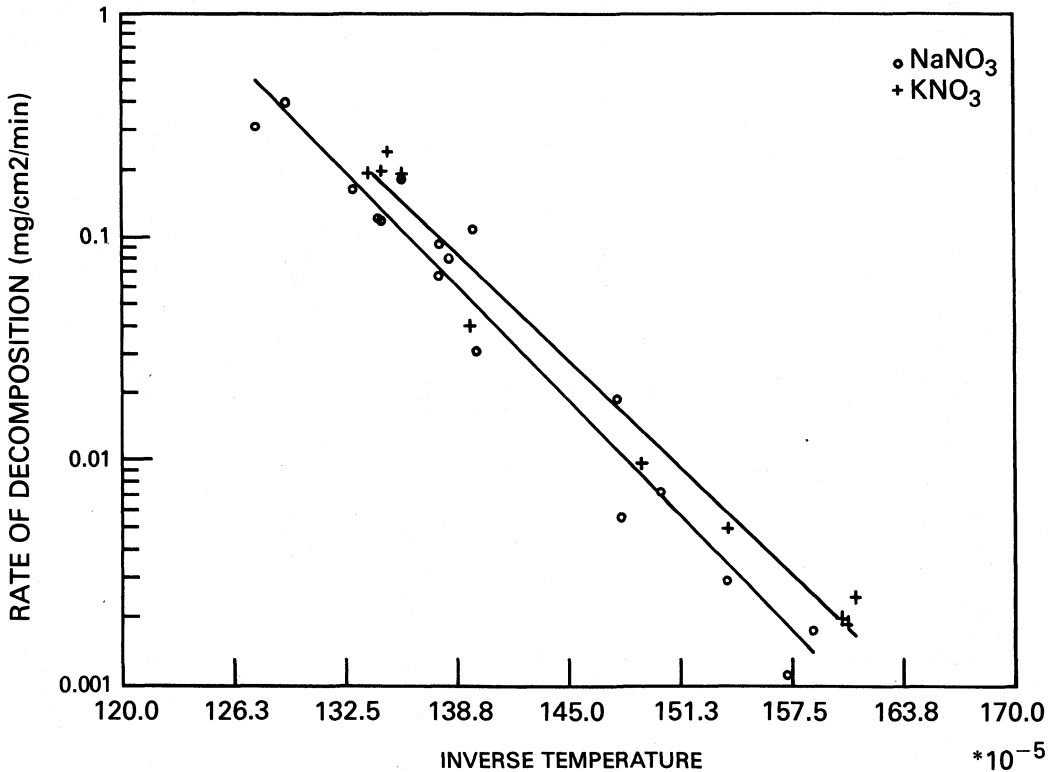

FIGURE 4. INITIAL RATES OF WEIGHT LOSS IN VACUUM

DOI: 10.1149/198109.0506PV

THERMAL ENERGY STORAGE USING LATENT HEAT STORAGE OF MOLTEN SALTS : STUDY AND REALISATION OF A DYNAMICAL EXCHANGE WITH A VERY HIGH EFFICIENCY*

P. Cerisier, J. Pantaloni, R. Santini, R. Occelli,
L. Tadrist, G. Finiels

Laboratoire de Dynamique et Thermophysique des Fluides
Université de Provence, rue H. Poincaré
13397 Marseille, cedex 4 - France

The heat produced by solar energy or by nuclear energy is stored with Hitec (eutectic $NaNO_3$, $NaNO_2$, KNO_3). For the recovery of the heat the molten salt is injected into an organic oil. The influence of temperatures and velocities of molten salt and oil on the average diameter of particles is studied. All the experimental results can be correlated with a single dimensionless number giving the efficiency of the apparatus.

1. INTRODUCTION

In order to use new forms of energy it is necessary to store it. Indeed some sources as nuclear energy yield a continuous out put,some others, as solar energy, are essentialy intermittent, and finally energy consumption essentially fluctuates. In order to lower costs and to save energy, one has to put in reserve the energy during low consumption periods or over production to carry it over for times when conditions are reversed.

Different ways of storage can be considered. At the present time the thermal energy storage with molten salts is probably one of the most interesting processes. These generally exhibit a good temperature stability, they have high heat capacities and latent heat, they do not require equipment under pressure (as is the case for water).

Two kinds of thermal storage can be considered :

- storage by sensible heat

Some industrial achievements already exist : for instance the experimental solar plant called "Themis" (1) and solar houses at Le Havre (2) in France. But this process presents some drawbacks. To store a large amount of energy one has two possibilities,either to increase the temperature and so, new technological problems occur (like the

* This study has been undertaken in the frame of a research on the solar habitat (A.T.P. PIRDES 3297).

corrosion, the efficiency of solar captors at high temperature, etc...) or to increase the volume of storing fluid which has other problems (volume of apparatus, price...). Finally the apparatus does not work at the constant temperature level generally imposed by a thermodynamic chain.

- storage by latent heat of fusion $\overset{\rightarrow}{\leftarrow}$ solidification

In this case the stored heat is important : for instance with NaCl, the heat stored by latent heat is the same as is stored by sensible heat over 418°. In this case the use of the change of state avoids using a wide range of temperatures.

With the eutectic mixture (7% $NaNO_3$ - 40% $NaNO_2$ - 53% KNO_3) named Hitec the latent heat corresponds to an interval of 54° and its use allows lower temperature operation for solar collectors. In both cases technological problems are simplified. In conclusion the storage by latent heat exhibits undeniable advantages but heat recovery is difficult. Two kinds of recovery can be considered.

- Static recovery, which can be described as a heat exchanger tube in a vessel. The molten salt can be either in the vessel or in the tube. But in both cases the salt crystallizes on the exchange wall, and this hampers the thermal transfer on account of the bad thermal conductivity of the solid crust (3-4); the efficiency is bad.

- Dynamic recovery. In order to increase to a maximum value the exchange surface between the molten salt and the heat transfer fluid, the former is sprayed into the latter. The two liquids can go in the same way or countercurrent. But the chief difficulty is to find two fluids which are totally inert chemically and not soluble at all within each other. These conditions can be achived with only a few systems :

  - metal-molten salt (5-6)
  - gas-molten salt (7)
  - organic oil-molten salt (4)

In this work, we present a study of experimental results obtained with an exchanger using the couple Hitec-gilotherm (organic oil).

2. DYNAMICAL EXCHANGER

It is described in detail in another paper (8). The apparatus is described in Fig.1. Initially the salt (solid) is in the storage tank, 1, then it is heated to the liquid state close to the melting temperature by Joule effect ; at the same time the oil is heated in the tank, 2, to the temperature chosen. The circuits between differents tanks are pre-heated in order to avoid obstruction and thermal loss - all the tanks and circuits are thermally insulated.

Then the molten salt is injected into the flow of organic oil in the exchange column, 3, where the heat of salt (mainly the latent heat) is transfered to the oil. The resulting mixture is liquid-liquid at the top and solid-liquid at the bottom. It is received in the tank, 4, where a sample of crystallites is taken off for a gra-

nulometric study.

Then the salt is melted, the mixture is driven toward the tank, 1. There the oil is pumped into, 2. In order to determine the thermal balance we measure :

- molten salt temperature T_i
- oil temperature T_h
- mixture temperature T_m (at the bottom of 3)
- oil flow ψ_h
- molten salt flow ψ_i

In all experiments the diameter of injection and T_i were kept constant.

3. AVERAGE SIZE OF CRYSTALLITES

The size of crystallites is measured with different gauged bolts. The distribution of mass vs size is determined.

We also showed that the average size of a particle only depends on the relative speed $\Delta v = v_i - v_h$ of the jet with respect to oil at the injector level ; Δv governs jet fracture.

The temperature difference $\Delta T_h = T_i - T_h$ which governs the agregation between droplets (if ΔT is large there is no recombination ; if ΔT is small, the coalescence is important)

The average size $\langle\phi\rangle$ is given by

$$\mathrm{Ln}\langle\phi\rangle = (a+b\Delta T_h)+(c+d\Delta T_h)\mathrm{Ln}\Delta v = A + B\mathrm{Ln}\Delta v \qquad (3.1)$$

where a,b,c are constant and characteristic of the apparatus and of the liquids. Knowledge of $\langle\phi\rangle$ is important to calculate the efficiency as we shall see in the next paragraph.

4. HEAT TRANSFER EFFICIENCY

The efficiency coefficient K is defined as the ratio of thermal power actually obtained P_r to the thermal power P_p which would be achieved had the exchange been perfect.

$$K = \frac{P_r}{P_p} \quad , \qquad (4.2)$$

If T_p is the final temperature of the mixture for perfect exchange

$$P_p = \psi_h \int_{T_h}^{T_p} C_h dT = \psi_i \left[C_\ell (T_i - T_c) + L_c + C_s (T_c - T_p) \right] \qquad (4.2)$$

with

C_ℓ = molten salt heat capacity
C_s = solid salt heat capacity
C_h = oil heat capacity
L_c = melting latent heat

and

$$P_r = \psi_h \int_{T_h}^{T_m} C_h dT \qquad (4.3)$$

The direct determination of K provides scattered points because of an important uncertainty, e.g. for 0.5° in T_h and T_m and 1ℓ/m in flow, it reaches 15%. So we calculate K by another way. Indeed we observe that oil-oil injection under the same conditions as with molten salt provides unit efficiency. So the apparatus is good and the differences from one are not due to the quality of exchange (thermal losses for instance). We admitted that the molten salt is not completely crystallized at the exit of the exchange column. Some quantity of molten salt remains inside the droplet and we assume they are at the melting temperature. Considering the average size it is possible to evaluate the average diameter of liquid phase and to know the energy still stored in a crystallite. Using $R=\frac{<\phi>}{2}$, R_ℓ : average radius for the liquid phase, ρ_i : density of molten salt, we obtain for a perfect exchange

$$E_p = \frac{4}{3}\pi R^3 \rho_i \left[C_\ell (T_i - T_c) + L_c + C_s (T_c - T_p) \right] = \frac{4}{3}\pi R^3 \rho_i \frac{P_p}{\psi_i} \quad (4.4)$$

and for the energy not exchanged :

$$E_r = \frac{4}{3}\pi R^3 \rho_i \left[L_c + C_s (T_c - T_p) \right] \quad (4.5)$$

The efficiency is $K = \frac{E_p - E_r}{E_p}$ and the average size of a liquid part is:

$$\frac{<\phi_\ell>}{<\phi>} = \left[(1-K) \frac{P_j}{\psi_i (L_c + C_s (T_c - T_p))} \right]^{1/3} \quad (4.6)$$

The study of $<\phi_\ell>/<\phi>$ shows (fig.2) that this ratio only depends on $<\phi>$ with a good approximation. So from this graph we deduce $<\phi_\ell>$ for a measured $<\phi>$ and we calculate K from (4.6).

5. INFLUENCE OF DIFFERENT PARAMETERS

As is usual in hydrodynamics this synthetic approach of problems requires dimensionless numbers.
Let us start from Peclet's number :

$$P_e = \frac{\tau_{th}}{\tau_{ec}} = \frac{\ell^2}{\chi} \frac{V}{\ell} \quad (5.1)$$

(V : speed and ℓ : length of outflow, χ thermal diffusivity) which compares the characteristic times of thermal transfer and of flow
if $\tau_{th} >> \tau_{ec}$: the stay time of a drop is too short ; it cannot give up all its heat
if $\tau_h << \tau_{ec}$: the drop yields all its heat before it leaves the column.

But in the experimental case we have to take into account partial solidification. Applying Fourier's law to the heat flow through a drop of diameter $<\phi>$ we obtain :

$$\frac{dq}{dt} \simeq \frac{\lambda (T_i - T_f)}{<\phi>} \simeq \frac{<\phi>^3 \rho_i C_\ell (T_i - T_c) + L_c + C_s (T_c - T)}{<\phi>^2 \tau_{th}} = \frac{<\phi>^3 \rho_i P_p}{\psi_i} \quad (5.2)$$

and

$$\tau_{th} \simeq \frac{\langle\phi\rangle^2 \rho_i P_p}{\lambda \psi_i (T_i - T_p)} \qquad (5.3)$$

The number characteristic of this phenomenon is

$$P'_e = \frac{\rho_i \langle\phi\rangle^2 \langle v\rangle P}{\lambda \psi_i (T_i - T_f) \ell}$$

The variations of K $v_s P'_e$ are represented on fig.3. It shows that with an excellent precision K only depends on P'_e. As expected the efficiency is good when P'_e is small.

6. CONCLUSION

It must be noticed that it is possible to realize a dynamical exchanger at direct contact with very good efficiency. All the experimental results can be correlated with a single dimensionless number, giving the efficiency of the apparatus. One may achieve a genuine optimization of the system and carry out an a priori calculation of the characteristics of an exchanger.

REFERENCES

(1) Maison Solaire - Le Havre, E.D.F. ED. 1978
(2) La Centrale solaire expérimentale THEMIS, EDF-CNRS Ed. 1978
(3) J. Pantaloni, O. Favre, R. Bailleux, G. Finiels, J. Marchisio - Rev. Phys. Appl. 14, 113, 1979.
(4) O. Favre - Thèse de doctorat de spécialité, Marseille 1978.
(5) J. Le Queré - Diplôme d'Etudes Supérieures, Marseille 1978.
(6) J. Marchisio, J. Le Quéré, J. Pantaloni, O. Favre - Rapport contrat EDF, 1978.
(7) J. Pantaloni, M. Larini, H. Guenoche, M. Desaulty, J. Boyer, J.P. Petit, J. Huetz - Rev. Gén. Therm. Fr. 212-213, 1979.
(8) J. Pantaloni, P. Cerisier, R. Santini, R. Occelli, L. Tadrist, G. Finiels - Rev. Gén. Therm. Fr. in press (1981).

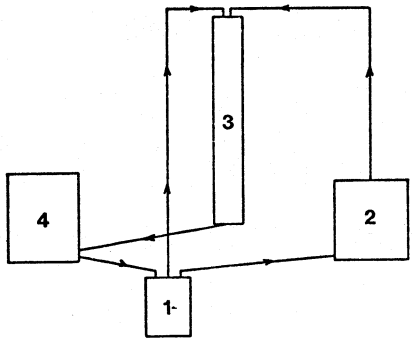

FIGURE 1 : Schema of apparatus

FIGURE 2 : Variation of diameter of liquid core as a function of average diameter of a drop.

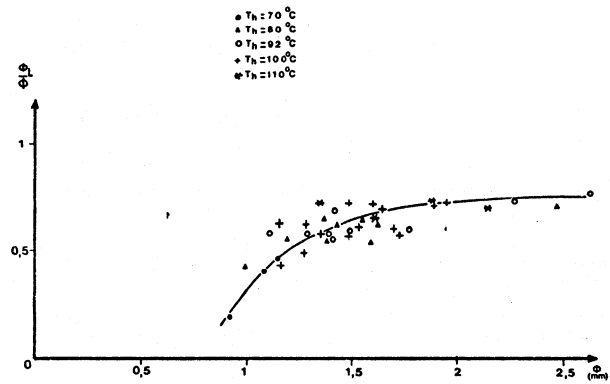

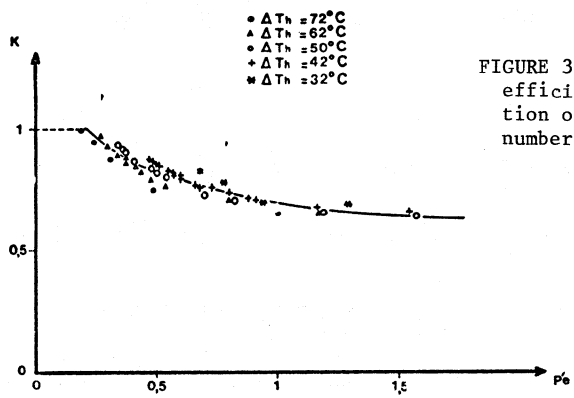

FIGURE 3 : Variation of efficiency K as a function of the dimensionless number P'_e.

DOI: 10.1149/198109.0512PV

LOCATION AND ASSIGNMENT OF ALL SPIN ALLOWED AND FORBIDDEN BANDS OF Ni(II), Cr(III) AND Fe(III) COMPLEXES IN FUSED (Na,K,Al)(SO_4,Cl)

Trevor R. Griffiths and Keith King*

Department of Inorganic and Structural Chemistry,
The University, Leeds LS2 9JT, England

*Present address: Shell Research Limited,
Thornton Research Centre, PO Box 1,
Chester CH1 3SH, England

ABSTRACT

Our first contribution described a new spectroscopic technique for measuring hot corrosion: this contribution shows how computer treatment of the digitised spectra therein recorded can yield considerable information concerning the corrosion products, transition metal complex ions, dissolved in the molten salts. The spectra of nickel(II), chromium(III) and iron(III) in the system (Na,K,Al)SO_4 with added chloride between 580 and 740°C were recorded, and their second and fourth differentials carefully computed by various methods, with total consistency. Consequently all the spin-allowed and spin-forbidden bands (and no more) were assigned, and the geometries, basically octahedral or tetrahedral, of the transition metal complex ions were identified. Many of the spin-forbidden bands, particularly for Fe(III) complexes, have not previously been located. Chloride was added, to study its effects, because coals with higher than usual chlorine content are becoming available, and hot corrosion generally increases markedly with only small increases in chlorine content.

INTRODUCTION

Once a spectrum has been digitised a number of mathematical manipulations and analyses can be performed in a mainframe computer. Two such processes, smoothing and resolution by higher derivative analysis will be first discussed, and then the results of these treatments on the spectra of nickel(II), chromium(III) and iron(III) in

molten $(Na,K,Al)SO_4$ with added chloride will be given and discussed in terms of the transitions assigned and the geometries of the various complex ions identified. This fundamental study was initiated because coal from new coalfields, with higher-than-average chlorine content, is expected to increase significantly the rate of hot corrosion.

SMOOTHING OF SPECTRA

Pen noise is inherent in all spectral measurements. Although it cannot be eliminated, it is possible to reduce noise by a number of methods.

Experimentally, noise can best be reduced by taking the average of a number of recordings of a particular spectrum. This method is both time-consuming and inappropriate when dealing with samples which change with time or are not stable over long time periods. Furthermore, improvement in the signal-to-noise (S/N) ratio increases only with the square root of the number of spectra averaged.

Mathematical smoothing may be applied to digitised spectra. Methods involving a simple moving average, or non-linear triangular and exponential smoothing functions have been discussed by Savitzky and Golay (1). Such methods were discounted by these authors, since they lead to distortion and reduction in intensity of the peaks. Instead, Savitzky and Golay evaluated an exact least-squares method, from a procedure derived theoretically by Worthing and Geffner (2). This method involves the fitting of a polynomial, of degree n (n = 2 to 6), to an array of data points, recorded at equal sampling intervals, to obtain the smoothed value for the datum point at the center of the array. The data set is then moved forward by one point, and the process repeated until the whole spectrum has been smoothed. This operation is referred to as an "x point convolute", where $x = 2m + 1$, and m is the number of data points preceeding and following the datum point at the center of the array.

This convolution method has the advantage that it is non-iterative, and therefore requires very little computing time. The degree of noise reduction is proportional to the square root of the number of points used in the convolution. Spectra characterised by insufficient data points may suffer degradation as a result of this smoothing procedure. This is most common when large digitising intervals are used to record narrow absorption bands. The spectra in

this study were digitised at 1 nm intervals, and no degradation of the broad d—d bands was observed.

The tables of convolution coefficients given by Savitzky and Golay (1) contain a number of mistakes resulting from an error in their reasoning. This was noted by Steinier et al. (3), who published the corrected coefficients. We have available a computer program that determines from first principles the convolution coefficients for any value of x and n, the number of points in the convolute and degree of the polynomial to be used, respectively (4).

RESOLUTION OF SPECTRA BY HIGHER DERIVATIVE ANALYSIS

The convolution method of Savitzky and Golay (1) may also be applied to the calculation of the derivatives of a spectrum, by using the appropriate set of coefficients. Indeed, smoothing should more properly be regarded as a special case of a general method to calculate the n^{th} derivative of a polynomial fitted to the digitised data at each particular point: for smoothing, n = 0, i.e. the zeroth order derivative.

In Figure 1, the first four derivatives of a simulated absorption profile are shown. The ordinate scales of the plots are not comparable, and the figure does not therefore reflect the true ratios of the peak heights. The first derivative is of limited value for curve resolution. It is zero at observed peak maxima (and also minima), but may be used to locate such maxima precisely. The second and fourth derivatives are similar in shape (the second derivative being inverted) to the original band, but much sharper, as can be seen from Figure 1. In the case of Gaussian bands, the second and fourth derivatives have half-widths (i.e. the full width at half-height) which are 53 and 41%, respectively, of the original band half-width. For a Lorentzian band, the corresponding values are 33 and 20%.

An observed spectrum is the envelope resulting from the summation of the bands which comprise the spectrum. If these component bands are overlapping to any significant extent, the observed maxima will not correspond to the positions of the maxima of the constituent bands. Indeed, overlap may be such that no maxima are observed for one or more of the components. The second (or fourth) derivative of the observed spectrum is the sum of the second (or fourth) derivative bands of the constituents. However, because these derivative bands are sharper than the

originals, individual maxima will now be observed for previously unresolved combinations.

This is the basis of this resolution method. It is particularly useful when only the positions and relative intensities of the bands need to be known. It has an advantage over curve-fitting methods in that no assumptions need to be made regarding the heights, half-widths, mathematical functions (e.g. whether the bands are Guassian, Lorentzian, or log-normal etc.), or, indeed, the number of component bands.

The other important feature concerning second and fourth differential spectra of a profile containing several bands is that the derivative of the largest and broadest band is essentially lost, the height of this band is now considerably less, often two orders of magnitude less than the derivative heights of smaller and narrower bands in the original profile. In practise, for transition metal spectra this means that, in general, charge-transfer spectra essentially disappear upon even-order differentiation, but spin-allowed transitions become clearly identified, and spin-forbidden bands now appear with approximately the same heights as the spin-allowed bands.

COMBINED SMOOTHING AND DIFFERENTIATION

Since experimental noise is magnified by the differentiation process, it is desirable to smooth spectra before differentiation. It is not necessary to carry out two separate, successive convolutions, since the two sets of convolution coefficients can be used to generate a third set, which will carry out the smoothing and differentiation simultaneously (1). This latter method was used to differentiate spectra in this study. The coefficients for this purpose we calculated using a subroutine (COEFFS) written by Dr. P. Gans, in our department (4). Thus a $(m + 1)$ point smoothing, combined with a $(n + 1)$ point differentiation results in a $(m + n + 1)$ point combined smoothing and differentiation. For best results n should equal m: the best value for n needs to be determined by trial and error.

Our procedure was therefore to compare the differential spectra of a profile as n (and m) were steadily increased from around 15. A persistant pattern of a constant number of peaks always appearing at the same place soon emerged, and the optimum value for n to give maximum resolution was soon identified. All other (usually small) peaks were

therefore due to random noise. In addition, second and fourth differential spectra were compared. Good agreement between the peak positions obtained separately from the second and fourth derivatives was taken to indicate that the band in question was neither spurious nor grossly distorted from its true position.

MELT SPECTRA OF Ni(II), Cr(III) AND Fe(III): A REVIEW

There are relatively few reports in the literature of the spectra of transition metal ions in sulfate melts, and none for such ions in aluminum-containing sulfate melts. The spectra in chloride systems (including those containing $AlCl_3$) are more widely reported. There are, however, no reports for mixed sulfate-chloride melts.

Of the three transition metal ions in question, Ni(II) has been the most extensively studied. Johnson and Piper (5) recorded the spectrum of this ion in the $(Li,Na,K)SO_4$ eutectic at 550°C. They concluded that a distorted octahedral nickel complex was formed, and suggested that three bidentate sulfate ligands were present in the complex. Duffy et al. (6,7) compared the spectra of Ni(II) in the $(Li,Na,K)SO_4$ melt, concentrated H_2SO_4, K_2SO_4-$ZnSO_4$ and $(Na,K)HSO_4$ glasses, and molten $(Na,K)HSO_4$. They found essentially octahedral coordination in all cases, but distinguished between bidentate sulfate and ligands in $(Li,Na,K)SO_4$ and monodentate sulfates in concentrated H_2SO_4 and $(Na,K)HSO_4$ glass. The K_2SO_4-$ZnSO_4$ glass containing nickel(II) has also been investigated by Narasimham and Rao (8), and again octahedral coordination was found over the entire composition range.

Chlorides generally form lower melting mixtures than sulfates, and so much more work has been performed on chlorides. Boston and Smith (9) originally studied the spectrum of nickel(II) in the (Li,K)Cl melt, and found it temperature and composition dependent, and with at least two species present. Gruen and McBeth (10) observed tetrahedral $NiCl_4^{2-}$ complexes in fused pyridinium chloride, CsCl, and in Cs_2ZnCl_4 crystals: spectra obtained in fused LiCl were thought to result from tetragonally distorted $NiCl_4^{2-}$ species.

Øye and Gruen (11) investigated nickel(II) in molten $AlCl_3$ at 227°C: octahedral coordination was identified. The spectrum of nickel(II) in a $ZnCl_2$-KCl mixture has been examined (12) over the whole composition range, and between 250 and 900°C. A two-species equilibrium was found, between octahedral and distorted tetrahedral symmetries. High

temperatures favored the four-fold coordination, while octahedral complexes were favored by high zinc content.

Brynestad *et al.* (13-16) have studied nickel(II) in a wide range of melts. In the (Li,K)Cl system, with temperatures in the range 363-1070°C, an equilibrium between tetrahedral and octahedral species was observed, in which the tetrahedral form was favored by increasing temperature and KCl content. The outer shell of the tetrahedral complex was thought to be principally of K^+ ions, while that of the octahedral form contained largely Li^+ ions. Similar behaviour was found when lithium was replaced by magnesium, in the $KCl-MgCl_2$ system. In the $CsCl-ZnCl_2$ system, however, distorted tetrahedral nickel(II) species were identified for a $ZnCl_2$ content of 50 mol %. As the $ZnCl_2$ content was increased, conversion to octahedral coordination took place, and was virtually complete beyong 72 mol % $ZnCl_2$. The nickel ions in this complex were thought to be incorporated in a chlorozincate polymer network. In molten $CsAlCl_4$, the chloride ion concentration is dependent on the equilibrium $2AlCl_4^- \rightleftharpoons Cl^- + Al_2Cl_7^-$, and can be increased or reduced by adding CsCl or Al_2Cl_6, respectively. In a melt containing a substantial excess of chloride ions, $NiCl_4^{2-}$ was formed. A reduction in chloride ion concentration, or temperature increase, resulted in the progressive replacement of $NiCl_4^{2-}$ by a second chloronickel complex. Although this complex was not identified, its spectrum indicated that it approximated to neither octahedral nor tetrahedral symmetry.

Turning to chromium(III) in molten salts, we find very much less reported work. Johnson *et al.* (17) recorded the chromium(III) spectrum in the (Li,Na,K)SO_4 melt at 600°C. This indicated an octahedral species, which they proposed as $Cr(SO_4)_3^{3-}$, with three bidentate sulfate ligands. The Cr(III) spectrum in the (Li,K)Cl eutectic was recorded by Harrington and Sundheim (18), who noted slight changes on increasing the temperature from 392 to 444°C. The $CrCl_6^{3-}$ species was proposed, and the observed changes attributed to thermal perturbations. Gruen and McBeth (19) also examined this system, and extended the temperature range to 1000°C. Even at the highest temperature the spectrum could still be interpreted on the basis of $CrCl_6^{3-}$ octahedra, with no indication of an octahedral-tetrahedral equilibrium.

Iron(III) is a d^5 ion and thus d—d transitions are both Laporte and spin-forbidden. Consequently, the bands are very weak, and their observation is further limited by a very strong charge transfer edge which dominates the

iron(III) spectrum in molten systems. There are no reported spectra of iron(III) in sulfate melts. Harrington and Sundheim (88) obtained the spectrum in the (Li,K)Cl eutectic. It comprised a strongly absorbing shoulder below 400 nm on the side of an edge rising sharply at approximately 250 nm. An increase in temperature caused the shoulder to diminish. Comparison of this spectrum with others of iron(III) in a variety of non-aqueous solvents led the authors to propose a tetrahedral $FeCl_4^-$ species. Silcox and Haendler (20) recorded the uv spectrum of iron(III) in the NaCl-KCl-$MgCl_2$ eutectic at 430°C. Again, a rising absorption edge was found, but this time containing possible indications of weak bands. No identification of the iron(III) species was attempted.

Although no studies have been made for mixed sulfate-chloride systems a spectrophotometric study of nickel(II) in mixed nitrate-chloride melts (21) identified various chloro-nitrato nickel(II) complexes, and an octahedral-tetrahedral equilibrium, and indicated appropriate approaches.

EXPERIMENTAL

Spectra were recorded on an Applied Physics Cary 14 H spectrophotometer. No modifications were made to the optics for this study and a conventional isothermal furnace was employed. It was not possible to prepare a melt of given chloride content and investigate the temperature variation of the spectrum, since Al_2Cl_6 was continually lost from the melt, and significant composition changes would have occurred in the time required for thermal equilibration at each temperature. The chosen procedure was therefore that the temperature was kept constant and chloride added in approximately 5 mol anion % increments as (Na,K)Cl pellets. At the end of each experiment, the chloride content of a solidified melt sample was obtained by titration with mercury(II) nitrate (22), a method not susceptible to interference by sulfate. In all cases the chloride content was within $\pm$ 2 mol anion % of the expected value.

Chloride additions to the $(Na,K,Al)SO_4$ melt encouraged gradual decomposition of the melt, evidenced by the formation of a precipitate, shown to be Al_2O_3 upon micro-analysis. Thus at the highest temperature (730°C), chloride additions were limited to 45 mol anion % for nickel, since a larger wavelength scan range was required for this ion, and thus each spectrum took longer to record.

NICKEL(II)

Results

The variation of the nickel(II) spectrum with chloride content from 0 to 35 mol anion % was recorded over the temperature range 587-720°C, although at 587°C the system was very near its melting point and too opaque for recordings at chloride content below 15 mol anion %. The variation with chloride content at 600°C is shown in Figure 2 and at 720°C in Figure 3.

The spectrum of nickel(II) in the $(Na,K,Al)SO_4$ melt (i.e. no chloride) is similar to that in the $(Li,Na,K)SO_4$ melt (5), except that the shoulder on the low energy side of the main band is much more pronounced in the aluminum-containing melt. The effect of increasing temperature is to shift the whole spectrum to slightly lower energy and introduce a second shoulder on the low energy side of the main band. The progressive broadening of bands with increasing temperature tended to mask these effects.

The addition of chloride ions has a dramatic effect on the spectra at all temperatures. As the chloride content is increased, the original main band diminishes and the spectra become dominated by bands emerging at lower energies. The addition of chloride is also accompanied by the establishment of a number of isosbestic points at approximately 10,000, 12,000, 20,000 and 25,000 cm^{-1}. However, not all the curves pass through these points and there is an apparent improvement in the convergence with increasing temperature. The relatively poor definition of the 25,000 cm^{-1} isosbestic point results, in part, especially at the higher temperatures, from the onset of precipitation of alumina (spectra were recorded from high to low wavelengths). The appearance of isosbestic points has generally been taken as evidence for the presence of a two-species equilibrium. However, this is not always so, and a more rigorous analysis, based on internal linearity theory, must be performed. We therefore report at this time that with chloride concentrations greater than around 20 mol anion % we have found, and will describe elsewhere, that two species predominate in solution, $NiCl_4^{2-}$ (with probably a distorted rather than regular tetrahedral geometry) and $NiCl_2(SO_4)_x^{2x-}$ (an octahedral complex, in which the number of sulfate ligands is uncertain, since these ligands could be either mono or bidentate, but we favor x = 2, with two bidentate sulfates).

To establish the effect of complete replacement of sulfate by chloride in the melt, the spectrum of nickel(II)

chloride in the (Na,K,Al)Cl melt, having the same cation ratios as the (Na,K,Al)SO_4 system, was recorded at 692°C. This is shown in Figure 4, along with the spectra for chloride additions to the sulfate melt at that temperature. The spectrum in (Na,K,Al)Cl is very similar to that for nickel(II) in fused CsCl at 800°C, reported by Smith (23).

Higher Derivative Analysis

Both second and fourth derivative analyses were performed, and good agreement between the two found. Simultaneous smoothing and differentiation was utilized, equivalent to a 49 point differentiation of a 49 point smooth spectrum, fitting a fifth order polynomial. The uncertainty in the energies of the band positions obtained was estimated as 200 cm^{-1}.

For the spectra in the (Na,K,Al)(SO_4,Cl) system, up to six bands were identified. Representative second and fourth derivatives are shown in Figure 5. The variation of the energies of the resolved bands with chloride content was investigated at six temperatures, examples being given in Figure 6.

Discussion

In the spectrochemical series for molten salts, reported by Johnson (24), sulfate appears directly above chloride. We should therefore expect a slight shift to lower energies if sulfate ligands were replaced by chloride in the nickel coordination sphere. The interpretation of the mixed sulfate-chloride spectra is aided by the results from the analysis of nickel(II) in (Na,K,Al)Cl, and so this is considered first.

The similarity of the nickel(II) spectra in fused CsCl and in a crystal of Cs_2ZnCl_4 doped with Cs_2NiCl_4, in which nickel ions are known to be tetrahedrally coordinated, led Smith (23) to conclude that nickel complexes of T_d symmetry were present in the CsCl melt. The same conclusion may be drawn here, regarding nickel(II) in the (Na,K,Al)Cl melt. Assuming a Dq value of 370 cm^{-1} for the $NiCl_4^{2-}$ complex (23), the bands at 14,300, 15,800 and 17,500 cm^{-1} may be assigned to the $^3T_1(F) \rightarrow {}^3T_1(P)$ transition. Three distinct bands have been observed as a result of splitting of the triplet states by spin-orbit coupling (23). The band at 13,400 cm^{-1}, which is much less pronounced than the rest, may be assigned to the spin-forbidden transition $^3T_1(F) \rightarrow {}^1E(D)$ or $^1T_2(D)$.

Of the six transitions identified in the spectra of the mixed sulfate-chloride melts, four may be associated

with the above bands found in the (Na,K,Al)Cl melt. The remaining two, around 22,000 and 24,000 cm^{-1}, depending upon the temperature and mol anion % chloride, may be assigned to transitions of an octahedral complex. The main band, at 22,000 cm^{-1}, corresponds to the $^3A_{2g} \rightarrow {}^3T_{1g}(P)$ transition, while the weak band may be assigned to a spin-forbidden transition to the $^1A_{1g}$ or $^1T_{1g}$ state, from the ^1G free ion term.

Thus, in the mixed sulfate-chloride melts we have both octahedral and tetrahedral nickel(II) species. The octahedral complex clearly commences as $Ni(SO_4)_3^{4-}$ (strictly, it has D_3 symmetry, but the crystal field of the metal ion may be taken as O_h), with three bidentate sulfate ligands. This has been observed in sulfate melts by other workers (5). The steady shift to lower energies as chloride concentration is increased implies that chloride is progressively being substituted for sulfate. The most likely course is for one sulfate ligand to become monodentate as one chloride ligand enters, and then this sulfate is replaced by a second chloride, forming a cis-dichlorosulfato nickel(II) complex.

The tetrahedral species are more rapidly converted to $NiCl_4^{2-}$ as shown by the positions of the four bands tending to constant energies above around 20 mol anion % chloride. Below this concentration various tetrahedral chlorosulfato complexes are present, but because of the greater distance to be spanned by a bidentate sulfato ligand in a tetrahedral complex, compared with an octahedral complex, we anticipate that here all sulfato ligands are monodentate.

In the case of nickel(II) in pure sulfate melts the ligand field spectra have previously been interpreted in terms of only an octahedral nickel complex present, $Ni(SO_4)_4^{4-}$ (5). The spectrum of nickel(II) in $(Li,Na,K)SO_4$ at 640°C (Figure 7) compares well with the featureless spectrum reported at 550°C by Johnson and Piper (5). The composite non-Gaussian nature of the principle visible band has been pointed out (23) and the possibility of distortion from pure octahedrality raised. A reinvestigation of this spectrum (25), including a test of Beer's law in the range 5-25 x 10^{-3} M, confirmed most of the original features but showed a more pronounced shoulder on the low energy side of the main band, and a slight saddle at the maximum of the band at 10,000 cm^{-1}. The resolution of the spectrum into Gaussian components gave neither a unique nor a decipherable result, but additional bands at 18,000 and 19,500 cm^{-1} were reported. These are more clearly seen in our aluminum-containing sulfate melt (Figure 7).

Examination of our second and fourth differential spectra of nickel(II) in $(Na,K,Al)SO_4$ all showed two bands in this region: at 600°C they were at 18,100 and 19,600 cm^{-1}. This is consistent with the mixed chloro-sulfato melts, where the data extrapolated back to bands in this region in the absence of chloride. Thus we can explain the observed asymmetry: sulfate melts containing nickel(II) have both octahedral and tetrahedral sulfato complexes. The latter is attributed to $Ni(SO_4)_4^{6-}$, all the sulfate ligands being monodentate.

CHROMIUM(III)

Results

The effect of chlorides on the spectrum of Cr(III) in $(Na,K,Al)SO_4$ is comparatively small and virtually temperature independent in the range examined (610-730°C). An example is given in Figure 8, which also includes the spectrum of Cr(III) in the (Na,K,Al)Cl melt.

The effect of increasing temperature upon the spectrum in the pure sulfate melt is to produce a slight shift to lower energy. Additionally the doublet at approximately 14,000 cm^{-1} becomes less pronounced, due to thermal broadening.

Chloride additions also cause a shift to lower energy, but of greater magnitude than that due to increasing temperature. The effect on the smaller band of the spectrum is interesting in that chloride addition appears to increase the intensity of the lower energy component of the doublet which comprises this band.

In the $(Na,K,Al)SO_4$ melt, the Cr(III) spectrum is at lower energy than when recorded in the mixed sulfate-chloride system, with sharper, more intense bands. After a few hours, and especially at the higher temperatures, chromium(III) ions begin to decompose, in both $(Na,K,Al)SO_4$ and in the presence of chloride. The absorption edge around 24,000 cm^{-1} increases, and the d—d bands decrease. A green precipitate is formed in the melt, identified as Cr_2O_3 by elemental analysis. If synthetic flue gas, containing both SO_2 and SO_3, is passed over the melt the rate of decomposition is reduced.

Higher Derivative Analysis

The analysis chosen as best for the chromium spectra was equivalent to a 47 point differentiation of a 47 point smoothed spectrum, with a fifth order polynomial. A

typical result is shown in Figure 9. The bands obtained were closely spaced and therefore not always resolved by the second derivative. However, in cases where resolution was possible, good agreement between second and fourth derivatives was obtained. When a band was not clearly resolved in the second derivative, the value obtained from the fourth derivative alone was used. Small separations of the component bands sometimes led to failure to locate all bands present.

Up to ten bands, initially designated A-J, were obtained, and examples of the variation of their energies with chloride content is shown in Figure 10, together with their assignments. For the spectrum in the (Na,K,Al)Cl melt, the corresponding energies of the corresponding bands are, in descending order: A, 18,400; B, 17,600; C, 16,700; D, not observed; E, 16,000; F, 15,200; G, 14,400; H, 13,600; I, 12,800; and J, 11,700 cm^{-1}.

Discussion

The chromium(III) ion is highly stabilized in octahedral site symmetry, and we may therefore conclude that the species $Cr(SO_4)_3^{3-}$ is present in the $(Na,K,Al)SO_4$ melt. The two main bands in the spectra may therefore be assigned to the transitions $^4A_2 \rightarrow {}^4T_{2g}(F)$ and $^4A_2 \rightarrow {}^4T_{1g}(F)$. A third band, at higher energy, due to the transition $^4A_2 \rightarrow {}^4T_{1g}(P)$, is in this case masked by the charge transfer absorption edge. The values for Δ (10Dq), the crystal field splitting parameter, for octahedral $Cr(SO_4)_3^{3-}$ and for $CrCl_6^{3-}$ are similar, 12,000 and 14,300 cm^{-1} respectively, and thus using the Tanabe and Sugano diagram for d^3 octahedral species the spin-forbidden transitions, $^4A_2 \rightarrow {}^2T_1(G)$ and $^2E(G)$, are expected between the two main bands. Differentiation is therefore expected to resolve both main bands into the three components of their triplets, and the spin-forbidden bands into three and two components, respectively. The spin-forbidden triplet is likely to resolve into a doublet and a singlet, the separation in the doublet possibly being small. Since both spin-forbidden transitions are not well separated according to the Sugano and Tanabe diagram assignment of some of the bands identified by differentiation is not unambiguous.

However, we can assign bands A-C to the $^4A_2 \rightarrow {}^4T_{1g}(F)$ transition, and by careful comparison of the recorded and the differentiated spectra we can, with reasonable confidence, assign bands H-J to the $^4A_2 \rightarrow {}^4T_{2g}(F)$ transition. This leaves the four intervening bands D-G. Since the $^2E(G)$ transition is expected at lower energy than the $^2T_1(G)$ band G is assigned to the lower energy component

of the $^2E(G)$ doublet. We suggest that the other component of this transition is band F, and that bands D and E are, respectively, the singlet and unresolved doublet of the $^2T_1(G)$ transition.

It may be observed in Figure 8 that the two main bands in the sulfate melt are broader than in the chloride melt. This is the result of distortion from octahedral symmetry. Whole both $CrCl_6^{3-}$ and $Cr(SO_4)_3^{3-}$ are both octahedral complexes the former has O_h symmetry and the latter D_3 symmetry. This results in splitting the O_h levels as follows (26):

$$A_{2g}(O_h) \rightarrow A_2(D_3) \text{ i.e. unchanged,}$$
$$T_{2g}(O_h) \rightarrow E(D_3) + A_1(D_3),$$
$$\text{and } T_{1g}(O_h) \rightarrow E(D_3) + A_2(D_3).$$

These splittings are greater in magnitude than those due to spin-orbit coupling, discussed above, and thus result in the observed broadening of the sulfate main bands, and also in the appearance of the doublet just discernible in the lower energy band in Figure 8: this doublet is better resolved at lower temperatures.

The effect of chloride additions on the spectrum is far less dramatic than in the case of nickel. This is to be expected, since for the chromium(III) ion no change in coordination occurs and, as already mentioned, chloride is directly below sulfate in the spectrochemical series for molten salts (24). Figure 8 also shows that the spectrum for the melt containing 45 mol anion % chloride, the maximum employed, is not shifted even half-way towards that for the $CrCl_6^{3-}$ ion in the (Na,K,Al)Cl melt. Thus although we obviously now have a mixed chloride-sulfate coordination sphere around the chromium(III) ion, the bidentate sulfate is here clearly the more strongly held and a less readily displaced ligand, unlike in the nickel situation.

A measure of the ratio of chloride-to-sulfate ligands may be obtained from the values of the crystal field splitting parameter, Δ_o, the energy of the $^4A_2 \rightarrow {}^4T_{2g}(F)$ transition, reported above. (The value of 14,300 cm^{-1} for $Cr(SO_4)_3^{3-}$ was taken as the center of the doublet.) It is clearly difficult to locate the center of this transition for the 45 mol anion % chloride spectrum, and strictly its energy is no longer precisely equal to Δ_o (see below), but a value of 13,500 cm^{-1} may be taken as a reasonable approximation. This gives an oxygen-to-chlorine ratio of 4:2 in the coordination sphere,

corresponding to $Cr(SO_4)_2Cl_2^{3-}$, with two bidentate sulfates. Although the complex could be $Cr(SO_4)_3Cl_2^{5-}$, with two mono and one bidentate sulfate ligands, this is unlikely on charge and steric considerations. Thus $Cr(SO_4)_2Cl_2^{3-}$ is a cis-complex, it being improbable that in the formation of this complex one or both of the two remaining sulfates would rearrange one of their coordination sites. Further evidence to support a cis-complex is now given.

An examination of the addition of chloride upon the energies of the resolved bands (Figure 10) shows that bands A-C, the components of the $^4A_2 \rightarrow {}^4T_{1g}(F)$ transition decrease in energy, but the components of the $^4A_2 \rightarrow {}^4T_{2g}(F)$, bands H-J, decrease only slightly. Bands D-E are essentially independent of chloride concentration, as the spin-forbidden transitions to $^2T_1(G)$ and $^2E(G)$ are field-independent, and thus no shift is here expected on reducing Δ_o. Now since the $^4T_{1g}(F)$ band is shifted more than the $^4T_{2g}(F)$ band, this must be explained in terms of symmetry changes on going from a $[CrA_6]$ complex to one represented by $[CrA_4B_2]$ (26). Here A and B represent the ligand atoms occupying the six coordination sites, and here A represents oxygen and B, chlorine, in a cis-complex. Such a complex has C_{2v} symmetry, and this results in the splitting of the original $T_{2g}(F)$ and $T_{1g}(F)$ terms into components, viz.,

$$T_{1g} \rightarrow B_2,\ A_2 \text{ and } B_1,$$
$$\text{and } T_{2g} \rightarrow B_2,\ A_2 \text{ and } A_1.$$

Both pairs of levels are at lower energies than the terms from which they arose, but the shifts for the B_2, A_2 and B_1 levels of the T_{1g} term are greater than those for the B_2, A_2 and A_1 levels from the T_{2g} term. Thus, the change in configuration has a greater effect (superimposed upon the overall shift resulting from a reduction in Δ_o) on the levels originating from T_{1g} than those from T_{2g}. The net result is that, as observed, the higher energy band is shifted to a greater degree than the lower energy peak.

IRON(III)

Results

The spectrum of iron(III) in the $(Na,K,Al)SO_4$ melt is dominated by a strong ligand-to-metal charge transfer edge, which completely swamps the weak, spin-forbidden d—d transitions. The effect of chloride addition is to shift this edge progressively to lower energy (Figure 11).

Increasing the temperature has the same effect. Additionally, weak bands begin to appear on the rising edge, (Figure 12), though they are never of sufficient intensity to form a well-defined shoulder. The spectrum of iron(III) in the (Na,K,Al)Cl melt is also shown in this Figure. With the complete replacement of sulfate by chloride the edge is shifted further into the visible region. The weak bands evident at lower chloride contents are no longer apparent.

No decomposition of the iron(III) species was observed during the few hours lifetime of these experiments. Neither was decomposition of iron(III) observed in molten (Na,K,Al)SO_4, held at 805°C for six hours. However, as discussed in our previous contribution, deposition of Fe_2O_3 is believed to be slow.

Higher Derivative Analysis

Second and fourth derivative analyses were performed, and the optimum derivatives were obtained using a 35 point derivative of a 35 point smoothed spectrum, with a polynomial of order five. A large number of weak, closely spaced bonds were identified. First impressions might be that these bands could be noise and thus spurious, but their number, and peak positions are self-consistent among all the iron(III) spectra recorded. The bands can be identified in sets of spectra and at different temperatures: spurious noise bands would be randomly distributed. Further, their derivative intensities are comparable with, but slightly less than, those of the bands found in the spectra of nickel(II) and chromium(III), and, as we shall show, satisfactory crystal field assignments can be made for these observed bands.

The variation of the band energies with chloride content was small, and temperature independent. A representative plot is shown in Figure 13. Typical second and fourth derivative spectra are shown in Figure 14. Initially we label the bands alphabetically, in order of decreasing energy. Since temperature and chloride content increase shifts the charge transfer band edge to lower energies, bands A-C cannot always be located. In the pure chloride melt, (Na,K,Al)Cl, the following bands were identified (energies in cm^{-1}): D, 18,800; E, 18,300; F, 17,700; H, 16,900; I, 15,900; K, 15,100; and M, 13,200. Bands corresponding in the mixed sulfato-chloro melts to G, J and L were not located, and as expected, the bands A-C were beyond the absorbance range of the spectrophotometer and could therefore not be detected.

Discussion

Since all the d—d transitions for a d^5 ion are spin-forbidden, their intensities are generally too low for bands to be detected unless enhanced by derivative analysis.

The pattern of crystal field splitting for a d^5 ion is the same in both octahedral and tetrahedral fields. Thus the only changes expected as a consequence of coordination change would be those resulting from a variation in Δ, since $\Delta(\text{tet}) = -4/9\Delta(\text{oct})$. Since chloride and sulfate have adjacent postions in the spectrochemical series for molten salts (24) and the energies of the resolved bands are virtually independent of chloride concentration it is concluded that no coordination change takes place with increase in chloride content.

For a d^5 ion there is no net change in crystal field stabilization energy on going from octahedral to tetrahedral coordination. Electrostatic factors will favor four-fold coordination. We may therefore assumed that $FeCl_4^-$ ions are present in (Na,K,Al)Cl. And consequently, in the pure sulfate melt a tetrahedral complex of iron(III) will be present, viz., $Fe(SO_4)_4^{5-}$. We again anticipate that a bidentate sulfate cannot span the distance between two adjacent tetrahedral sites.

The degree of sulfate replacement by chloride as chloride concentration is increased is difficult to gauge. The shift of the absorption edge to lower energy on the addition of chloride indicates chloride participation in the ligand-to-metal charge transfer process, since its lower electronegativity reduces the energy of the transition. However, the absorbance of the charge transfer band at some fixed wavelength is not generally as sensitive an indicator of coordination sphere composition as the crystal field splitting, which in this case shows no discernible trends.

The observed bands may be assigned with reference to the spectrum of $FeCl_4^-$ in acetone at room temperature (27), and in the solid pyridinium salt $(PyH)_3Fe_2Cl_9$ at 20 K (28). The bands reported were identified by eye.

The assignments for the $FeCl_4^-$ spectrum are complex. Balt (27) has discussed possible assignments of the bands, taking account of the pronounced nephelauxetic effect known to exist in this ion. The bands in the spectrum of iron(III) in our sulfate and chloride melts have been identified on the basis of these assignments. The results are presented in Table 1.

Table 1. Comparison of Maxima (cm^{-1}) of Resolved Bands from Iron(III) Spectrum in $(Na,K,Al)SO_4$ and (Na,K,Al)Cl Melts with the Reported Maxima of $FeCl_4^-$.

Band	Assignment	$FeCl_4^-$ in acetone at 300 K	$FeCl_4^-$ in $(PyH)_3Fe_2Cl_9$ at 20 K	Fe(III) in (Na,K,Al)Cl at 972 K	Fe(III) in $(Na,K,Al)SO_4$ at 1003 K
A	$^4T_1(^4P)$	22,000[a]	22,100	nf[b]	21,500
B		nf	nf	nf	20,900
C		nf	nf	nf	20,000
D	$^2\Gamma$	nf	19,750	nf	19,500
E	$^4E(^4D)$	18,760	18,800	18,800	18,700
F		nf	nf	18,300	18,300
G	$^2\Gamma$	nf	17,800	17,700	17,600
H	$^4T_2(^4D)$	16,700	16,500	16,900	16,700
I	$^4A_1(^4G)$	16,150	16,150	15,900	16,200
J	$^4E(^4G)$	nf	15,650	nf	15,600[c]
K		nf	nf	15,100	15,100
L	$^4T_2(^4G)$	14,600	14,600	nf	14,400
M	$^4T_1(^4G)$	13,700	13,700	13,200	13,400

a, 883 K; b, nf = not found; c, 943 K.

Assignments designated $^2\Gamma$ by Balt represent transitions to unspecified doublet terms, arising from the ^2I free ion state. These were observed in the solid state $FeCl_4^-$ spectrum but not in solution. Bands B, C, F and K observed in this work have not been detected in the acetone or solid state spectra of $FeCl_4^-$. They may be assigned to further sextet-doublet transitions, or possibly splitting of the quartet term states. It is to be expected that more bands would be identified in this study than were found previously since, as already mentioned, previous identifications relied solely on examination by eye of the recorded spectrum. Band A was not found in the pure chloride melt because it was out of the absorbance range of the spectrophotometer. The value reported for A in the sulfate melt was obtained in low temperature melts only.

It is also to be expected that the $FeCl_4^-$ spectrum observed at 20°K would reveal more bands than the number seen at ambient temperatures. We would point out that from our spectra, recorded nearly 1000°C higher, were found these low temperature bands, and more. We also note that most of the band maxima identified for $FeCl_4^-$ in molten $(Na,K,Al)SO_4$, generally within experimental error the same as those reported at 20 K, were also generally at slightly lower energy, shifted in the direction expected with temperature increase.

Comparison of the peak maxima identified in the sulfate and chloride melts reveals that, for tetrahedral complexes of iron(III), sulfate and chloride have identical, rather than adjacent (24), positions in the spectrochemical series for molten salts, in contrast to our chromium results.

Thus in the case of iron(III), differentiation of observed spectra has been shown to be a powerful and sufficiently precise technique for identifying spin-forbidden bands, even when broadened by high temperatures. Differentiation of the spectrum of $FeCl_4^-$ at 20 K should therefore reveal the additional bands we now report, plus possibly some more, such that the at present unassigned bands can be identified with sextet-doublet transitions, or splittings of quartet term states, or vibronic transitions.

CONCLUSION

We have shown that various chloro-sulfato complexes of the transition elements nickel, chromium and iron are formed when chloride is added to $(Na,K,Al)SO_4$ melts containing these metals. The implication for power

generation plant turning to high-chlorine coals is that, where chlorine-containing complex ions are readily formed at low chloride concentrations (the chlorine content of, say, superheater tube salt deposits is not expected to exceed a few mole %) then corrosion will be increased. This will apply to the corrosion of nickel and iron, but not to chromium, where sulfate ligands are not readily replaced by chloride. The basic reason for accelerated corrosion is that these complexes are smaller than sulfato complexes and will thus diffuse faster across the thermal gradient.

It must be stressed that confirmation is awaited, and is expected from our present determinations of corrosion rates for these three elements as a function of chloride concentration. We would caution that determinations of corrosion rates for various stainless steels in molten $(Na,K,Al)SO_4$, and with added chloride using our technique, described in our earlier paper, are also required before any quantitative predictions of corrosion rates can be attempted.

We can however say that the development of our new technique has shown such determinations a ready reality, and our computer treatment of spectra has revealed a considerable body of information concerning the nature, properties and geometries of the corrosion products that will be formed.

ACKNOWLEDGMENTS

We thank Dr. P. Gans for valued discussions. K.K. acknowledges a CASE Research Studentship with the Science Research Council and the Central Electricity Generating Board, Harrogate, West Yorkshire.

REFERENCES

1. A. Savitzky and M.J.E. Golay, Anal. Chem., 36, 1627 (1964).
2. A.G. Worthing and J. Geffner, 'Treatment of Experimental Data', Wiley and Sons, New York (1948).
3. J. Steiner, Y. Termonia and J. Deltour, Anal. Chem., 44, 1906 (1972).
4. Dr. P. Gans, private communication.
5. K.E. Johnson and T.S. Piper, Discuss. Faraday Soc., 32, 32 (1961).
6. J.A. Duffy, F.P. Glasser and M.D. Ingram, J. Chem. Soc. A, 551 (1968).

7. J.A. Duffy and W.J.D. MacDonald, J. Chem. Soc. A, 977 (1970).
8. P.S.L. Narasimham and K.J. Rao, Proc. Indian Acad. Sci., 87A, 275 (1978).
9. C.R. Boston and G.P. Smith, J. Phys. Chem., 62, 409 (1958).
10. D.M. Gruen and R.L. McBeth, J. Phys. Chem., 63, 393 (1959).
11. M.A. Øye and D.M. Gruen, Inorg. Chem., 3, 836 (1964).
12. C.A. Angell and D.M. Gruen, J. Phys. Chem., 70, 1601 (1966).
13. J. Brynestad, C.R. Boston and G.P. Smith, J. Chem. Phys., 47, 3179 (1967).
14. J. Brynestad and G.P. Smith, J. Chem. Phys., 47, 3190 (1967).
15. G.P. Smith, J. Brynestad, C.R. Boston and W.E. Smith, in 'Molten Salts, Characterization and Analysis', Ed. G. Mamantov, Marcel Dekker, New York (1969).
16. W.E. Smith, J. Brynestad and G.P. Smith, J. Chem. Phys., 52, 3890 (1970).
17. K.E. Johnson, R. Palmer and T.S. Piper, Spectrochim. Acta, 21, 1697 (1965).
18. G. Harrington and B.R. Sundheim, Ann. N.Y. Acad. Sci., 79, 950 (1960).
19. D.M. Gruen and R.L. McBeth, Paper for the Seventh International Conference on Coordination Chemistry, Stockholm (June 1962).
20. N.W. Silcox and H.M. Haendler, J. Phys. Chem., 64, 303 (1960).
21. T.R. Griffiths and P.J. Potts, Inorg. Chem., 14, 1039 (1975).
22. A.F. Colson, Analyst (London), 90, 35 (1965).
23. G.P. Smith, in 'Molten Salt Chemistry', Ed. M. Blander, Wiley and Sons (1964).
24. K.E. Johnson, Electrochim. Acta, 11, 129 (1966).
25. J.R. Dickinson, Ph.D. Thesis, University of Saskatoon (1969).
26. H.L. Schläfer and G. Gliemann, 'Basic Principles of Ligand Field Theory', Wiley Interscience, London (1969).
27. S. Balt, Recl. Trav. Chim. Pays-Bas Belg., 86, 1025 (1967).
28. A.P. Ginsberg and M.B. Robin, Inorg. Chem., 2, 817 (1963).

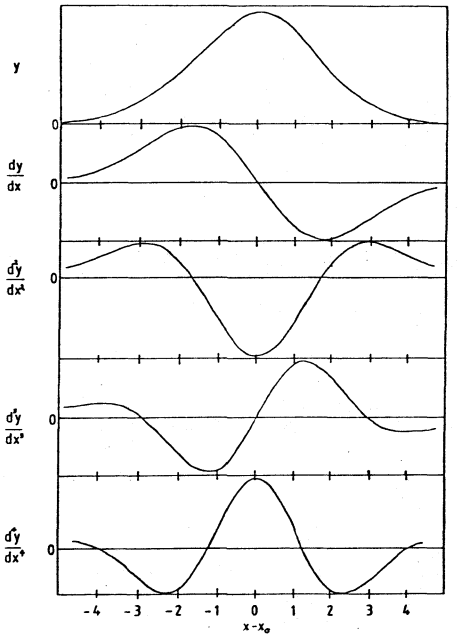

Figure 1. First four derivatives of a simulated Gaussian absorption profile (ordinate scales not comparable).

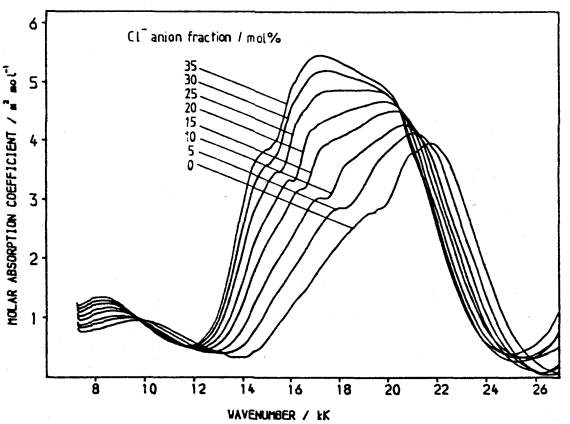

Figure 2. Variation of nickel(II) spectrum in (Na,K,Al)(SO_4,Cl) with chloride content at 600°C (49 point smoothing; fifth order polynomial).

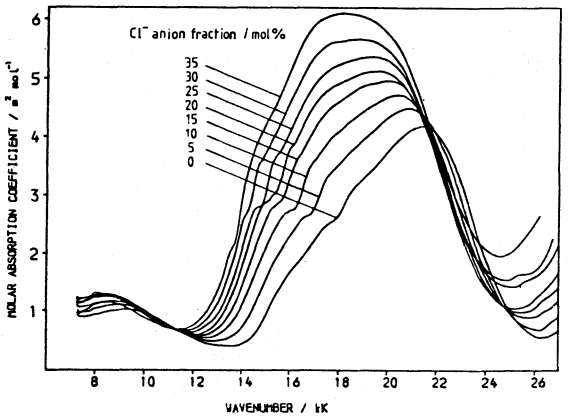

Figure 3. As for Figure 2, at 720°C.

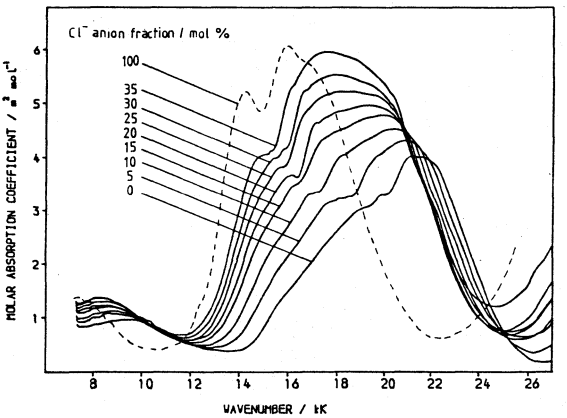

Figure 4. As for Figure 2, at 692°C. Dashed line, (Na,K,Al)Cl melt.

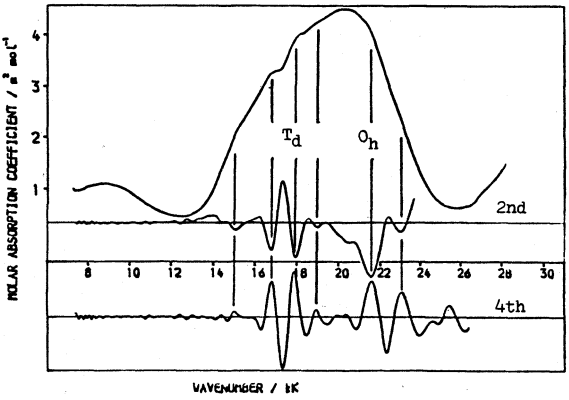

Figure 5. Spectrum of nickel(II) in (Na,K,Al)(SO_4,Cl), containing 10 mol anion % chloride at 692°C and its second and fourth derivative.

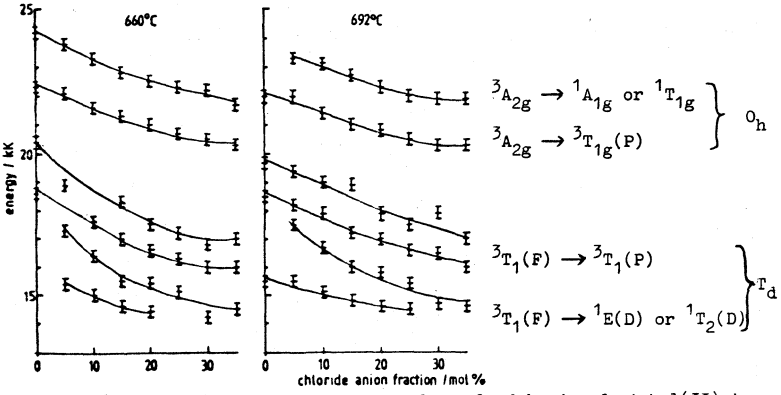

Figure 6. Variation and assignments of resolved bands of nickel(II) in (Na,K,Al)(SO_4,Cl).

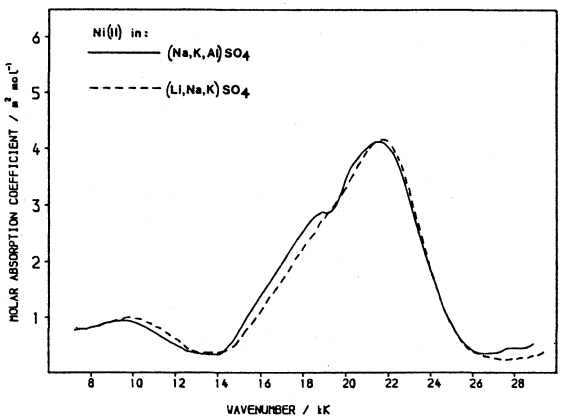

Figure 7. Comparison of nickel(II) spectra at 640°C.

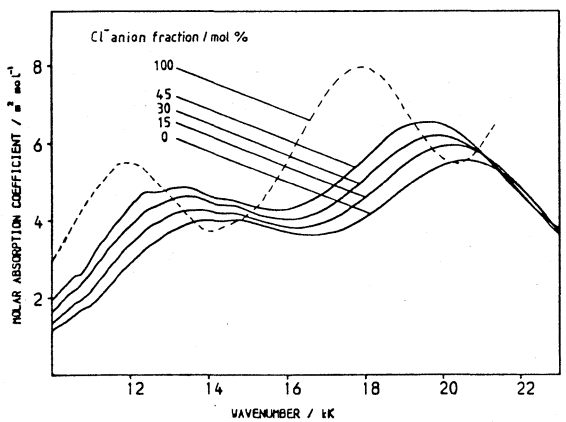

Figure 8. Effect of chloride addition on chromium(III) spectrum in $(Na,K,Al)SO_4$ at 695°C (47 point smoothing, fifth order polynomial.

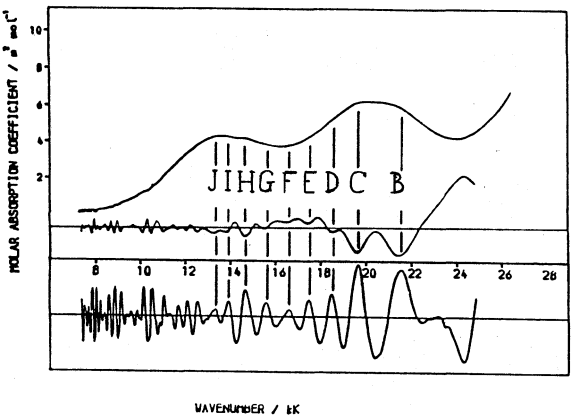

Figure 9. Spectrum of chromium(III) in (Na,K,Al)(SO_4,Cl) containing 20 mol anion % chloride at 640°C and its second and fourth derivative.

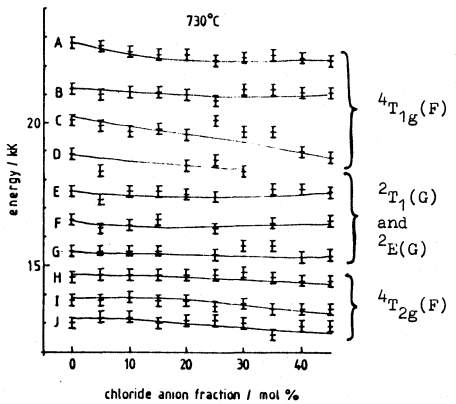

Figure 10. Variation and assignments of resolved bands of chromium(III) in (Na,K,Al)(SO_4,Cl).

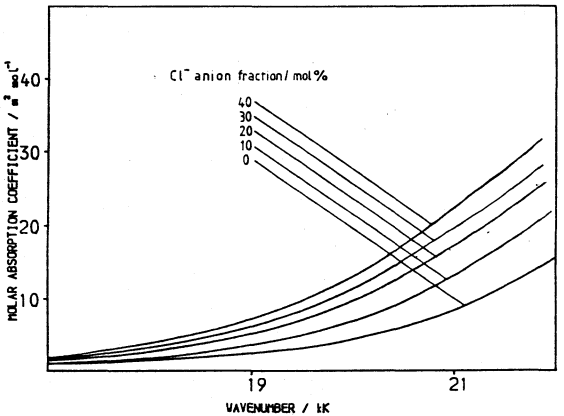

Figure 11. Effect of chloride addition on iron(III) spectrum in $(Na,K,Al)SO_4$ at 610°C (35 point smoothing, fifth order polynomial).

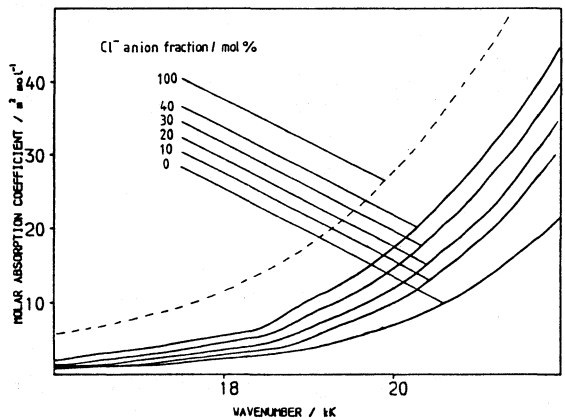

Figure 12. As for Figure 11 at 699°C (47 point smoothing, fifth order polynomial). Dashed line, (Na,K,Al)Cl melt.

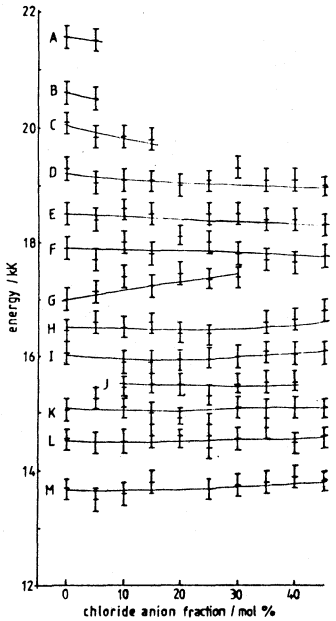

Figure 13. Variation of resolved bands of iron(III) in (Na,K,Al)(SO_4,Cl) at 610°C.

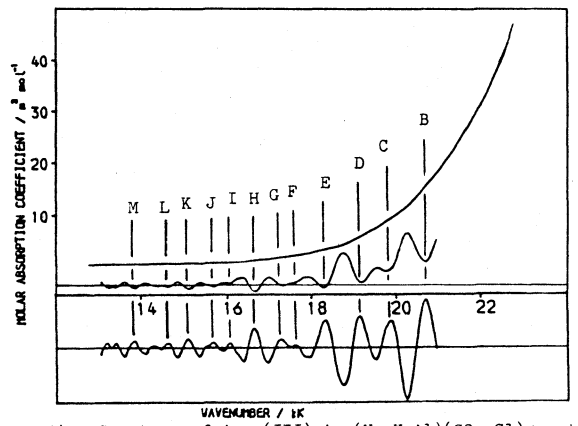

Figure 14. Spectrum of iron(III) in (Na,K,Al)(SO_4,Cl) containing 20 mol anion % chloride at 640°C and its second and fourth derivative.

DOI: 10.1149/198109.0539PV

NEW DEVELOPMENT IN MOLTEN SALT ANODISING

David G. Lovering, Alan K. Turner and Kevin P. D. D. Clark

R.M.C.S., Shrivenham, SWINDON SN6 8LA U.K.

ABSTRACT

A small number of studies has been carried out using mainly molten nitrates for anodically growing oxide films on various metals. The present study demonstrates that the presence of dissolved water in the melt sharply influences the structure of the oxide film as determined by microscopical, particle diffraction and scattering and electrochemical transient investigations. The anodising temperature is also critical. Previous claims of improved s.c.c. resistance, if confirmed, may arise from bulk material recrystallization. Most recent work suggests that new, very low temperature melts may prove useful as non-aqueous anodising media. Applications in the electronics, solar conversion and materials protection fields are envisaged.

Table I reminds us why anodising procedures are of commercial and military importance.

Table II suggests reasons why molten salt anodising procedures might be particularly unique and attractive.

Table III indicates that most of the traditionally anodised metals have been processed in a range of melt systems at various temperatures. In Japan, the bisulphate bath is apparently used on a commercial scale for aluminium anodising (18), (19). A few other metals including copper have also been anodised in this way (20). Most of these investigations have been carried out within the last decade.

Unfortunately a number of problems and criticisms arises from some of these previous studies; these fall into the general categories shown in Table IV.

In some cases, aluminium alloys have been anodised in nitrate melts at temperatures up to 300°C, for example (1), (2), (3), (4), (5).

Rather poor grey, brown or black films have resulted. These have unsatisfactory mechanical and dielectric properties and overaging of the alloy itself occurs. In other studies, melts have been subjected to adequately rigorous drying procedures, followed by utilization in cells open to the atmosphere (6), (10), (11)! Moreover, the application of cathodic current pulses in a cyclic anodic-cathodic train to aluminium specimens in nitrate melts is potentially hazardous (11). Complex phenomena accompany the reduction of nitrate ions and the still uncharacterised active intermediate could react explosively with the metal.

In yet further examples, corrosion studies have been somewhat "ad hoc" in nature. Treated specimens have been tested in the "raw" anodised condition, i.e. without being subjected to full specification chromating and paint finishing (6).

As a result of these difficulties attending the interpretation of previous investigations, a more fundamental and systematic study of the anodising of super-pure aluminium in molten alkali metal nitrates was instigated. Most of this work was carried out at 140°C but lower temperatures were also employed. Table V shows the melts and conditions generally employed, although the most recent work has centered on lower melting nitrate and organic substance systems. In particular, the possible role of water dissolved in the melt upon the nature of anodically-grown oxide films was of interest. In this work, films were normally grown at constant applied voltages in the range ~5-80, (occasionally 100), in order to establish process-selective conditions. The techniques of scanning electron microscopy (S.E.M.), transmission electron microscopy (T.E.M.), with appropriate shadowing and replication procedures, ultramicrotomy, x-ray diffraction and Rutherford (deuteron) backscattering were employed to characterise the oxide films prepared. Firstly, specimens were anodised in both the as-rolled and then electropolished condition in the anhydrous melt. In separate series of experiments, similar specimens were anodised in melts containing water (usually ~0.2 molal, which represented an "equilibrium" concentration achieved by continuous purging with water-saturated N_2).

In anhydrous $LiNO_3$-KNO_3 melts at 140°C, thin transparent, barrier films were formed. These were reasonably coherent at forming voltages of 7.5 and ≥50. Some local flaking occurred at 15V and 30V, with slight cracking apparent along the rolling lines of the as-rolled specimens; this cracking increased with increasing voltage above ~30. Epitaxial growth was evident. Smooth, thin, continuous transparent films were obtained on electropolished specimens; these exhibited very few small protrusions and short cracks whose densities increased with anodising time and voltage.

Transmission electron micrographs of ultramicrotomed sections showed these oxide films to be structureless and to have a sharp metal-oxide interface. Selected-area diffraction showed them to be composed of amorphous alumina. Thicknesses of the films were typically ~0.3-0.4μm, corresponding to a very high anodising ratio of ~80Å.V^{-1}. The effect of time and voltage on these thicknesses was uncertain, but small. The current density time curves recorded during preparation of these films (Fig.1) showed an exponential decay of current with time reflecting the growth of the film and decrease of the field gradient within the film.

In contrast, current density time curves obtained in melts containing water (Fig.1) were more complex. Apart from current densities being an order of magnitude greater, peaked functions (7.5V and 15V) and rising transients were observed. It is not clear whether these wholly reflect filmgrowth current utilization, changes in surface area accompanying this type of film growth (vide infra) or some other mechanism of growth operating.

When water is present dissolved in the melt, two distinct film-types can be identified. For 10>V>50, patchy, thin films are obtained, not unlike those observed in anhydrous systems. However for 15<V<40, then thick, milky-white, inadherent flaky films are produced. The corresponding S.E.M. of films grown onto as-rolled aluminium at these voltages show the development of hillock-shaped protrusions having a layered structure. Where the apex of a hillock has become detached, a rough but continuous oxide film can be noted growing underneath. This suggests that growth occurs primarily from the substrate boundary outwards and can account for the layering of the oxide film. As a result of studies conducted as a function of time at the fixed applied voltage of 15, it appears most likely that nucleation of the crystalline oxide phase is the slow process and that it occurs at the high energy sites (along rolling lines, for example). Some improvement in the definition of the various features was noted when electropolished specimens were employed, but, otherwise, no significant differences were evident.

Ultramicrotomy and selective-area diffraction of films formed at 50V showed them to be thin (~0.3-0.4μm), amorphous structures similar to those obtained from anhydrous melts. Some difficulty was encountered in characterising films formed at 30V, by ultramicrotomy; the oxide layers tended to become detached and break up regardless of the cutting direction. Thicknesses were assessed by S.E.M. of the surface of specimens retained in the resin block after slicing in the microtome and shadowing with Au/Pd alloy. These were ~2-3μm i.e. an order greater than those obtained in the anhydrous melt. Films formed at 15V and 30V were also stripped by the amalgamation

technique and subjected to T.E.M. and selective-area diffraction. Although not necessarily truly representative of the whole film, the presence of both α-Al_2O_3 and $Al_2O_3.H_2O$ was detected.

Two important questions arise. Why does water in the melt induce electrocrystallization? Why does this only occur at <50V? Hydrolytic and precipitation reactions could be associated with the formation of $Al_2O_3.H_2O$, whilst the different mobilities of the doubly charged O^{2-} ion and singly charged OH^- ion in the steadily decreasing field gradient might result in different oxide growth mechanisms. Clearly further work in this area is called for.

An interesting feature of films grown at 50V and 70V was revealed by bulk x-ray diffraction of anodised specimens. Whereas films formed at 15V and 30V exhibited diffuse rings indicating a polycrystalline structure, those formed at the higher voltages showed considerable break up of the rings and the emergence of a not quite random spot pattern. This was demonstrated not to be an artefact e.g. due to heat treatment. It would seem that the surface layers of the aluminium substrate had become reorganized, probably a result of induced stress due to the growing oxide layer. It might be that the claims for improved s.c.c. resistance (1), (6), (10), (11) for molten salt anodised films actually arise from this change in the metal itself.

Results obtained with $NaNO_3$-NH_4NO_3 and $LiNO_3$-NH_4NO_3 melts at 140°C were broadly similar to those described above for $LiNO_3$-KNO_3 melts. However, the $LiNO_3$-NH_4NO_3 system with its lower melting temperature, permitted experiments to be carried out at 110°C, also. Surprising, at this lower temperature, uniform, thick, adherent, milky-white films were formed in the presence of dissolved water; the films were substantially flaw-free. Detailed examination of these films was not undertaken, but their possible commercial value was not overlooked. In view of this result, most recent work has centered on the application of even lower melting systems, mainly comprised of an inorganic nitrate and an organic substance. Some of these new melt systems remain liquid at room temperature, and in one case, below 0°C. Apart from promising preliminary anodising experiments carried out in these media, they suggest applications in a diversity of other fields.

Currently, these new melts are being employed to anodise titanium specimens for applications in photoelectrochemical cells and other devices. As in aqueous anodising of the refractory metals, all the

interference colours can be obtained on titanium by adjusting the anodising voltage. Some thicker films have been prepared both by stepwise increasing of the anodising voltage and by extending the anodising time, in some cases. The particular feature of films prepared by this method is that they are exceptionally uniform and are not hydrated. Further work in these directions is now in progress.

REFERENCES

1. L Campanella, Plating 56, 813 (1969); 57, 807 (1970); 59, 575 (1972)

2. E. L. Krongauz, V. D. Kascheev, and V. B. Busse-Machukas, Soviet Electrochem. 8, 1219 (1972).

3. A. Conte, A. Borello, and A. Cabrini, J. Appl. Electrochem. 6, 293 (1976).

4. V. Saifullin and F. F. Faizullin, Sb. Aspir. Rob. Kazan. Gos. Univ. Estecto. Nauki Khim. 25, (1973).

5. L. Campanella and A. Conte, J. Electrochem. Soc. 116, 144 (1969).

6. R. E. Herfert, Tech. Rep. AFML-TR-76-142 USAF (1976).

7. A. K. Turner and D. G. Lovering, Final Report to MOD(PE) on contract AT/2160/027 MAT (1978).

8. A. K. Turner and D. G. Lovering, Trans. Inst. Met. Finish. in press (1980).

9. A. K. Turner, thesis, London (1978).

10. G. L. Holleck, F. H. Cocks, D. R. Cogley and I. W. Frutkoff, Tech. Rep. AFML-TR-72-191 USAF (1978).

11. F. H. Cocks, D. R. Cogley, G. H. Hurley, and C. R. Mitchell, Corrosion 32, 135 (1976).

12. S. Ikonopisov, Electrodep. Surf. Treat. 2, 303 (1973-4).

13. A. Yamashita and H. Hagiwara, J. Electrochem. Soc. 112 279 (1965).

14. L. Campanella, Trans. Inst. Met. Finish. 51, 97 (1973).

15. R. K. Nigam and I. K. Arora, Electrochim. Acta 17, 2133 (1972).

16. R. K. Nigam and R. S. Chaudhary, Indian J. Chem. 8, 343 (1970).

17. R. K. Nigam and R. S. Chaudhary, Electrochim. Acta 17, 1765 (1972).

18. S. Tajima, M. Soda and T. Mori, Electrochim. Acta 1, 205 (1959).

19. S. Tajima, Y. Tanabe, M. Shimura and T. Mori, Electrochim. Acta 6, 127 (1962).

20. A. J. Arvia and N. R. de Tacconi, Thin Solid Films 43, 173 (1977).

TABLE I
DECORATIVE FINISH
ELECTRONICS INDUSTRY - CAPACITORS, MICROCIRCUITS, ETC.
ENHANCED CORROSION RESISTANCE
IMPROVED ADHESIVE BONDING

TABLE II
ELEVATED TEMPERATURE → THICKER FILMS
NON-AQUEOUS ENVIRONMENT → ANHYDROUS FILM
HIGH CONDUCTIVITY ELECTROLYTE → GOOD "THROWING POWER"
PROTECTIVE FILM OF SOLID MELT → AVOIDS ATMOSPHERIC CONTAMINATION
UNIFORM TEMPERATURE, GOOD WETTING → UNIFORM FILM
LOWER VOLTAGES → LOWER POWER REQUIREMENTS?
EXTREMELY OXIDISING MEDIA → LACK OF PIN-HOLE FLAWS

TABLE III

Melt	M.Pt. °C	Anodising Temperature Range °C	Metals Anodised	References
$NaNO_3$-KNO_3	220	250-300	Al, Ti, Zr	1,2,3,4
$LiNO_3$-KNO_3	133.5	140-260	Al, alloys	5,6,7,8,9,10
$LiNO_3$-NH_4NO_3	∿ 98	110-140	Al	7,9
$NaNO_3$-NH_4NO_3	121	140	Al	7,9
$LiNO_3$-KNO_2	108	110-120	Al, alloys	11
$NaNO_2$-KNO_2		227-352	Al	12
$NaNO_3$-$Ca(NO_3)_2$		330-370	Ti	13
KNO_3	337	400-450	Al, Ti	1,14
$NaNO_3$-$NaNO_2$-KNO_3	142	150-200	Zr	3
$LiNO_3$-$NaNO_3$-KNO_3	125	217-340	Al, Ta	15,16,17
$Ca(NO_3)_2.4H_2O$	42.7	50-100	Al, Zr	1,3
$NaHSO_4$-$KHSO_4$	∿125	130-180	Al	18,19
NH_4HSO_4		184-207	Al	
$NaHSO_4$		178-207	Al	

TABLE IV	
PROBLEMS WITH PREVIOUS INVESTIGATIONS	
MELT TOO HOT	- OVERAGING OF ALLOYS.
MELT TOO WET	- PICK-UP OF ATMOSPHERIC MOISTURE.
POORLY OR UN-CHARACTERISED FILMS	- DOUBLE REPLICATION, WEIGHT CHANGE, EDDY CURRENT METHODS UNRELIABLE.
OPERATION AT CONSTANT CURRENT	- NOT PROCESS SELECTIVE - MAY PASS THRO' SEVERAL VOLTAGE REGIMES.
CURRENT-REVERSAL EMPLOYED	- POTENTIALLY DANGEROUS IN CATHODIC REGION FOR NITRATE MELTS.
FEW FUNDAMENTAL ELECTROCHEMICAL STUDIES	- MOST INTEREST FOCUSSED ON RESULTS.
FEW MEANINGFUL CORROSION STUDIES	- MANY "AD HOC" TRIALS.

TABLE V			
SYSTEM	STATE	COMPOSITION	MELTING TEMPERATURE
$LiNO_3$-KNO_3	Anhydrous	32.2% (wt) $LiNO_3$	133.5°C
$LiNO_3$-KNO_3	Containing Water	45.3% (wt) $LiNO_3.3H_2O$	. ∿ 120°C
$LiNO_3$-NH_4NO_3	Containing Water	44.6% (wt) $LiNO_3.3H_2O$	∿ 80°C
$NaNO_3$-NH_4NO_3	Containing Water	20.1% (wt) $NaNO_3$	121°C

Figure 1.

Current density versus time curves for anodising as-rolled aluminium foil in molten $LiNO_3$-KNO_3 at 140°C, both in the anhydrous and "wet" state (primed).

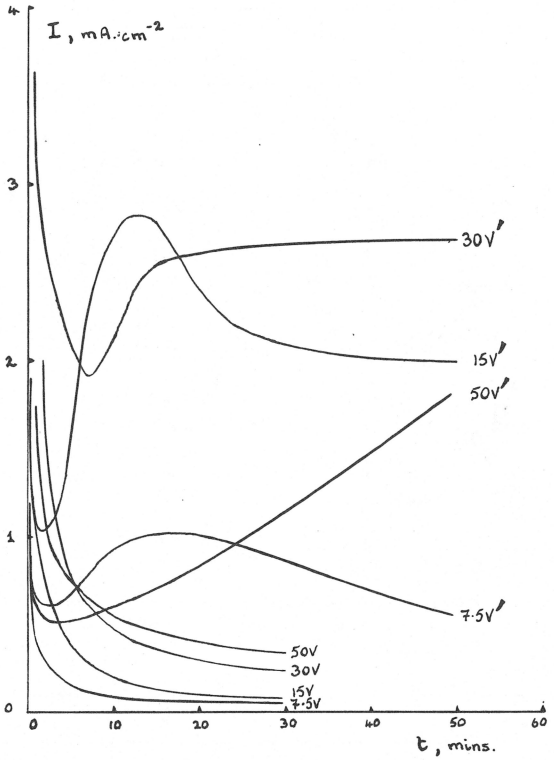

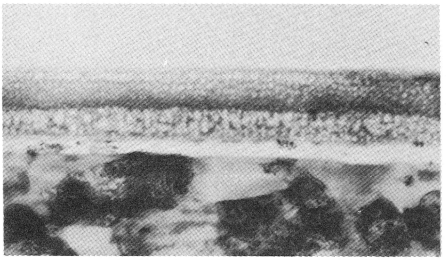

Figure 2. T.E.M. of ultramicrotomed section of electropolished Al foil anodised at 50V. for 1hr. in anhydrous molten $LiNO_3$-KNO_3 eutectic at 140°C.

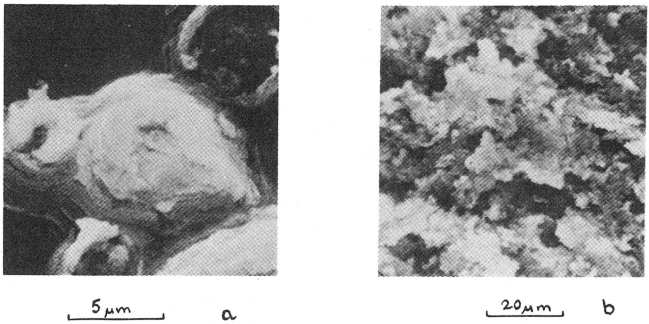

Figure 3. S.E.M. of electropolished Al foil anodised at (a) 15V. (b) 30V. for 30mins. in molten $LiNO_3$-KNO_3 eutectic containing water at 140°C.

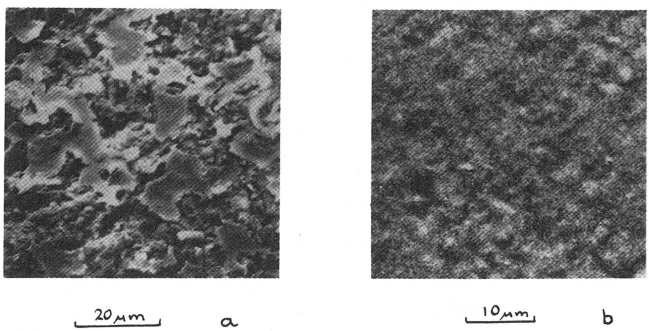

Figure 4. S.E.M. of electropolished Al foil anodised at 50V. for 30mins. in molten $LiNO_3$-NH_4NO_3 eutectic containing water at (a) 140°C (b) 110°C.

DOI: 10.1149/198109.0550PV

ELECTRODEPOSITION OF SILICON FROM MOLTEN SALTS

T. L. Rose, T. O. Hoover, R. A. Boudreau, S. H. White and R. D. Rauh
EIC Laboratories, Inc.
55 Chapel Street
Newton, Massachusetts 02158

Cyclic voltammetry was used to study the reduction of silicon ions on silver substrates in FLINAK and LiF:KF (1:1) molten salts at 550-800°C. Two overlapping cathodic waves were obtained which start about -1.9 V vs the Ag/Ag(I) reaction of the working electrode used as an internal reference. The potential, shape, and intensity of the reduction peaks and the corresponding stripping peak indicated that a complicated reduction process is occuring. Quantitative electrochemical measurements were difficult to perform because of the lack of a stable reference electrode, the sensitivity to impurities, the possible existence of several silicon complexes in the melt, and the high reactivity of silicon in forming alloys.

Background. Recently there has been a surge of interest in the electrodeposition process as a low cost method of production of photovoltaic grade silicon (1-6). This work was preceded by the studies of Cohen (7-10), Bøe et al. (11), and Monnier and Giacometti (12). The best results have been obtained from molten salts containing fluoride ions which act to stabilize the silicon precursor. Silicon deposits up to 3 mm thick with purity of 99.999% have been reported on silver substrates at 750°C from FLINAK [LiF (46.5 m/o), KF (42 m/o), and NaF (11.5 m/o), m.p. 454°C] (3). Potassium fluorosilicate (K_2SiF_6) was used as the silicon precursor. Silicon pieces from 1-3 mm with transition metal impurities <10 ppm were deposited on a molten tin cathode from molten solutions of Na_3AlF_6:LiF:SiO_2 at 860°C (2). In both cases the high purity material was obtained after pre-electrolysis purification of the melts.

Although the successful reduction to high purity silicon has been obtained, there is relatively little understanding of the electrochemical processes involved. Most of the depositions were done galvanostatically in two electrode systems (2,3,6). Rao, et al., (3) report the reduction of silicon ions in FLINAK at 750°C occurs at -0.74 ± 0.1 V vs a Pt quasi-reference for K_2SiF_6 concentrations of 4-6 m/o. The suitability of Pt as a reference electrode, however, has been questioned (1). The Stanford group has also calculated that stable growth of a silicon deposit on a solid substrate is limited to deposition current below 40 mA/cm^2 corresponding to 45 μm/hr (13). Nevertheless, the relationship between the quality of the deposit and the current density, plating potential, substrate material, and purity

of the melt is still poorly understood. This information will become increasingly important as the electroreduction technique is refined, quality control procedures are developed, and attempts are made to dope the material in situ.

Those electrochemical studies that have been made deal mostly with the reduction of silicon species introduced as SiO_2 in molten cryolite (4,14,15). From this work the conclusion is that two or more silicon species are in equilibrium. One of these is electroactive and is reduced to silicon in a fast, four electron step. Schematically these reactions can be represented by

$$\text{Silicon complex I} \underset{k_b}{\overset{k_f}{\rightleftharpoons}} \text{Silicon complex II}$$

$$\text{Silicon complex II} + 4e^- \rightarrow Si^\circ + \text{anions}$$

Frazer & Welch found $k_f + k_b$ to be 31 and 23 sec^{-1}, respectively, in a Na_3AlF_6:SiO_2 melt at 1020°C for the preceding chemical dissociation step (14).

Delimarskii has studied the kinetics of reduction of silicon from Na_2SiF_6 dissolved in KCl:NaCl(1:1) melts with various concentrations of NaF (16). At 700°C the expected alloying with the platinum working electrode to form Pt_2Si was observed with an $E_{1/2}$ of -0.83 V vs a Pt quasi-reference in melts containing 10 w/o NaF and 1.0 w/o Na_2SiF_6. A second peak was observed at $E_{1/2}$ = -1.35 V and was attributed to deposition of Si on the alloy with a limiting current determined by diffusion of the silicon electroactive species. Polarization measurements on a pyrolytic graphite electrode where no alloying took place resulted in a single wave with a half-wave potential of -1.28 V under similar melt conditions. Increased concentrations of NaF lead to more cathodic values of $E_{1/2}$, indicating increased stabilization of the silicon electroactive species by the fluoride ion, i.e.,

$$SiCl_6^{2-} + xF^- = SiF_xCl_{(6-x)}^{2-}.$$

This contribution presents preliminary cyclic voltammetry measurements in FLINAK and LiF:KF(1:1) molten salts at temperatures in the range 550-750°C with and without K_2SiF_6 added as the silicon precursor.

Experimental. Most of the experiments were conducted in a high temperature apparatus consisting of a closed end quartz outer jacket, a quartz inner sleeve to align the crucible, and a water cooled, brass cap in which the electrodes and gas inlet and outlet ports were mounted (1). A vitreous carbon crucible with a volume of 87 ml was used to contain the

melt. In some earlier experiments a smaller apparatus was used with a quartz tube, pressed graphite crucible of 25 ml, and an air cooled stainless steel lid.

The working and quasi-reference electrodes were silver or platinum wires 0.5 mm in diameter immersed in the melt between 5 and 10 mm. The counter electrode was either a piece of vitreous carbon or p-type single crystal silicon or, in the smaller cell, the graphite crucible. The electrodes were supported by Ni rods. To maintain the highest purity of the melt, the Ni rods were sheathed in silica tubing and terminated with pure silver connecting pieces. The silica tubing as well as the quartz outer jacket had to be replaced periodically when they became badly corroded and structurally weakened.

Generally the reagents used were obtained from Alfa Division of Ventron Corporation although some experiments were done using Fisher ACS certified reagents or high purity LiF and KF from Cerac. The LiF from Alfa was puratronic grade, KF and NaF ultrapure grade and KHF_2 99+%. The purity of the K_2SiF_6 was 99.7% with chloride reported as the major impurity. The salts were stored over P_2O_5 in a dessicator. All operations of filling the cell were done in a dry box. The cell was then transferred to the oven, evacuated, and slowly heated until the mixture melted. After melting, the cell was backfilled with dry argon. When the electrodes were admitted or removed from the cell, a positive pressure of argon prevented atmospheric contamination of the melt. In some runs, 5-10 m/o KHF_2 was substituted for the equivalent amount of KF. KHF_2 reportedly reduces the oxide contamination by reducing the oxides with HF, liberated by its decomposition above 350°C (10). In the present experiments, however, no marked improvement of melt purity was observed when the KHF_2 treatment was used.

The cyclic voltammograms (CV) were measured with an Amel Model-551 potentiostat modulated by a wave form generator constructed in the laboratory. A Hewlett-Packard X-Y recorder (Model 7015B) was used to record the CV's.

Results and Discussion. Figure 1 shows the CV for a FLINAK melt at 700°C to which no silicon precursor had been added. The major feature is the large cathodic peak at -2.75 V vs Ag/Ag(I). The cathodic limit at -2.90 V is close to the value of -3.01 V calculated for unit molarity for the reduction of K^+ (17). The potentials are reported versus the Ag/Ag(I) potential of the working electrode used as an internal standard because the potential of the quasi-reference platinum electrode changed with time and concentration of the silicon precursor (1). The peak at -2.75 V is attributed to an alloying reaction of the alkali with the silver. A similar peak was observed on a pyrolytic graphite electrode in FLINAK at 500°C (18). When a tungsten electrode was substituted for the silver, no major cathodic peak was observed

until the alkali cathodic limit was reached. Tungsten does not form alloys with the alkali metals.

A cyclic voltammogram with 5 m/o K_2SiF_6 run at high sensitivity is shown in Fig. 2. Several peaks are observed before the major reduction peak for silicon ions at -2.0 V. The arrows indicate the standard reduction potentials of several metal ions at unit mole fraction calculated from the Gibbs free energy (17). The potentials of these impurities can be compared with those reported in FLINAK by Clayton, et al. (18). Their small impurity thought to be iron at about -0.7 V vs the unit mole fraction Ni(II)/Ni electrode would be before our silicon peak but too cathodic to be iron. A more likely possibility for iron is the reduction peak in Fig. 2 at about -1.30 V vs Ag/Ag(I). The larger impurity Clayton observes at -0.9 V and attributes to chromium is exactly where we observe the silicon reduction. K_2SiF_6 is a major impurity in the KF obtained from Fisher and may be present in fluorides from other suppliers as well. The reagents from Alfa, however, have reported impurities of Si of less than 30 ppm.

A series of cyclic voltammograms at different scan rates was run on a "pure" LiF-KF melt at 550°C to which no silicon had been added. The two overlapping waves shown in Fig. 3 whose peaks are separated by about 0.12 V are certainly due, however, to silicon. The waves are too close to treat as independent waves; nevertheless the trends seen in Table 1 for the cathodic peak potential for the two waves, $E_p(1)$ and $E_p(2)$, their difference, and the peak currents for the first peak $i_p(1)$ are

Table 1. Cathodic Peak Potentials and Currents for Silicon Reduction on Silver in LiF:KF(1:1) at 550° C

Scan Rate, ν (mV/sec)	$E_p(1)$* (V)	$E_p(2)$* (V)	ΔE_p (mV)	$i_p(1)$ (mA)	$i_p(1)\nu^{-1/2}$ ($mAV^{-1/2}s^{1/2}$)
30	-2.02	-2.13	110	9.5	55
100	-2.06	-2.17	130	14.0	44
200	-2.07	-2.20	130	17.5	39
300	-2.09	-2.24	150	20.0	37

* Versus Ag/Ag(I) potential of the working electrode

interesting. The peak potentials shift cathodically with increasing rate speed, and the difference between the peak potentials increases. The last column in Table 1 is the peak current normalized to the square root of the scan rate. The value is clearly not constant and is consistent with a chemical equilibrium process proceeding the reduction rather than a simple diffusion limited mass transfer process (14). The

areas under the cathodic and stripping peaks are equal within the experimental error indicating that all the deposited silicon is reoxidized. The very large shift between the cathodic and anodic peak potential, however, is not consistent with a simple reversible electrode reaction. Finally it should be remembered that there are metallic impurities in the melt which are reduced prior to the silicon and alloying reactions between the silicon and the deposited metals may be occurring.

Another example of the complexity of the silicon reduction process is illustrated by Figure 4. The two cyclic voltammograms were run in melts of identical composition and histories. The differences in the reduction and stripping curves are remarkable. The dashed curve exhibits a much broader reduction peak and an over-potential of 0.3 V. The double stripping peak on the anodic sweep indicates that when deposition occurs at the more cathodic potentials, alloying reactions may occur with the deposited silicon or the impurities deposited before the silicon. Reversing the sweep leads to a peak anodic of the expected stripping reaction of Si since the alloys should form more readily than reduction of the pure elements.

The striking differences between the two CV's in "similar" melts emphasizes the importance of impurities, substrate preparation, alloying, etc., in determining the electrochemistry associated with the silicon reduction process leading to silicon electrodeposition. Our results indicate that the deposition on silver is not a simple process. In addition to SiF_6^{-2}, there may be additional Si precursors such as polymeric silicon fluorides or an oxyfluoride which is reduced at different potentials. Additional electrochemical studies are needed before the mechanism of silicon reduction in fluoride melts will be understood.

Acknowledgement: This work was supported in part by The Department of Energy under contract No. DE-AC03-79ET23046.

REFERENCES

1. R. D. Rauh, T. L. Rose, S. H. White, R. A. Boudreau, T. O. Hoover, and D. L. Natwig, Final Report Under DOE Contract DE-AC03-79ET23046, EIC Laboratories, December 1980.

2. J. M. Olson, Abstract No. 28, The Electrochemical Society Meeting, Los Angeles, CA, October 14-19, 1979.

3. G. M. Rao, D. Elwell, and R. S. Feigelson, J. Electrochem. Soc., 127, 1940 (1980).

4. G. M. Rao, D. Elwell, and R. S. Feigelson, Abstract No. 378, The Electrochemical Society Meeting, Hollywood, FL, October 5-10, 1980.

5. R. C. DeMattei, D. Elwell, and R. S. Feigelson, Abstract No. 377, ibid.

6. W. R. Gass, I. E. Kanter, and R. W. Witkowski, Quarterly Report No. 3 under DOE Contract EG-77-C-01-4042, Westinghouse R & D Center, August, 1980.

7. U. Cohen and R. Huggins, J. Electrochem. Soc., 123, 381 (1976).

8. U. Cohen, U.S. Patent 4,142,947 (1977).

9. U. Cohen, J. Electron. Mater., 6, 607 (1977).

10. U. Cohen, Ph.D. Dissertation, Stanford University, 1978.

11. G. Bøe, K. Grjotheim, K. Matiasovsky, and P. Fellner, Can Met. Quart., 10, 281 (1971).

12. R. Monnier and J. C. Giacometti, Helv. Chim. Acta, 47, 345 (1964).

13. R. C. DeMattei and R. S. Feigelson, J. Crystal Growth, 44, 115 (1978).

14. E. J. Frazer and B. J. Welch, Electrochimica Acta, 22, 1179 (1977).

15. K. Grjotheim, K. Matiasovsky, P. Fellner, and A. Silny, Can Met. Quart., 10, 79 (1971); G. Bøe, K. Grjotheim, K. Matiasovsky and P. Fellner, ibid., 10, 179 (1971).

16. Yu. K. Delimarskii, N. N. Storchak, and R. V. Chernov, Electrokhimiya, 9, 1443 (1973).

17. W. J. Hamer, M. S. Malmberg and B. Rubin, J. Electrochem. Soc., 112, 750 (1965).

18. F. R. Clayton, G. Mamantov, and D. L. Manning, ibid., 120, 1193 (1973).

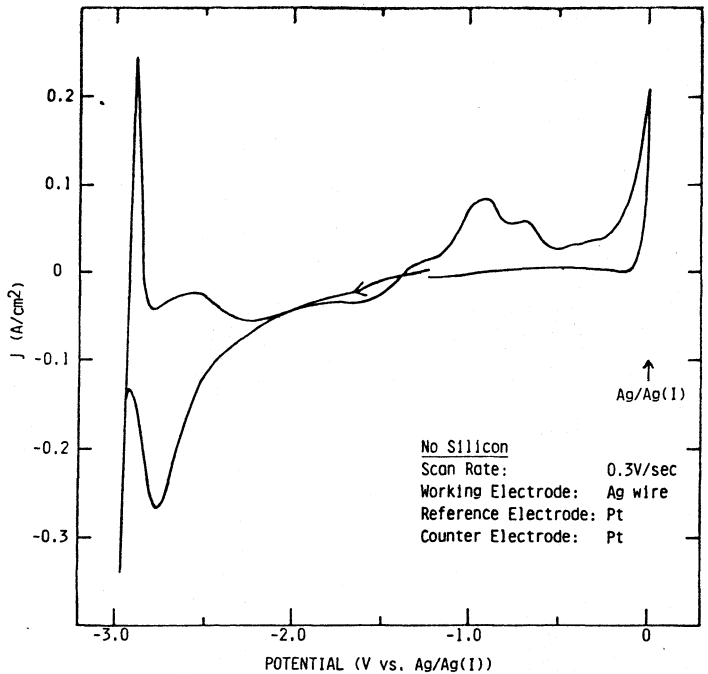

Fig. 1. Voltammogram of FLINAK at 700°C to which no silicon has been added showing alloying reaction with silver substrate at -2.8V.

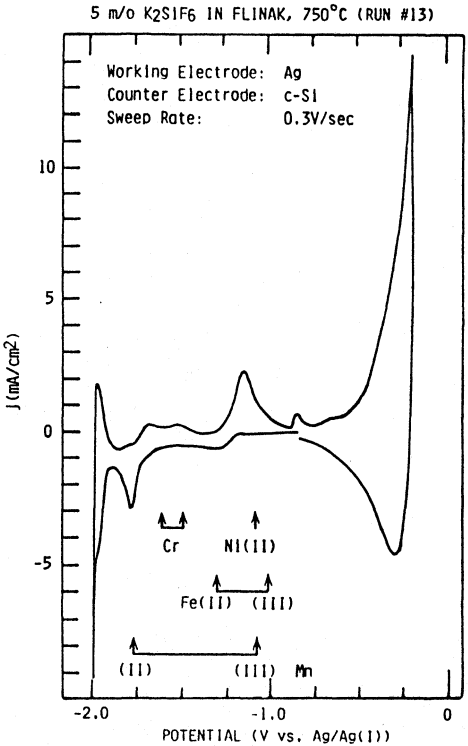

Fig. 2. Voltammogram at high sensitivity showing impurity peaks before Si reduction at -2V.

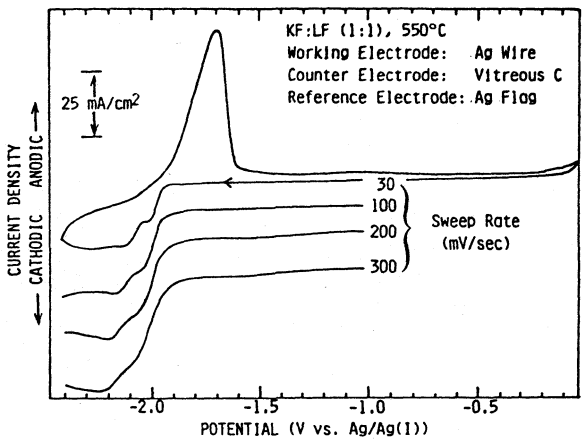

Fig. 3 (Above). Effect of sweep rate on voltammograms for reduction of silicon in molten KF:LiF at 500°C.

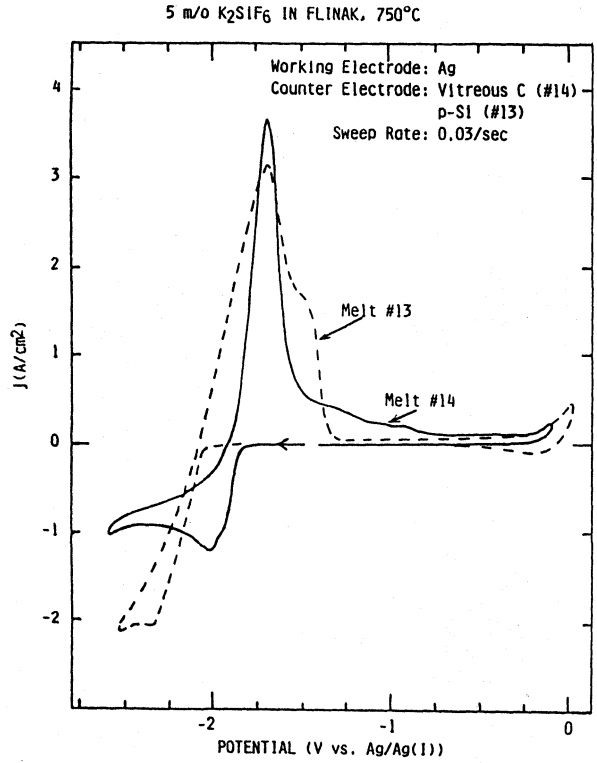

Fig. 4 (Right). Voltammograms for reduction and stripping of silicon (5 m/o) at similar conditions for two different samples of FLINAK.

DOI: 10.1149/198109.0558PV

ELECTRODEPOSITION OF TANTALUM AND TANTALUM-CHROMIUM ALLOYS ON STAINLESS STEEL AND COPPER FROM FLINAK

I. Ahmad

U.S. Army Armament Research and Development Command
Benet Weapons Laboratory
Watervliet, New York 12189

W. A. Spiak and G. J. Janz

Rensselaer Polytechnic Institute
Cogswell Laboratory
Troy, New York 12181

ABSTRACT

As a part of a program to develop erosion resistant coatings for advanced gun barrels, electrodeposition of tantalum and tantalum-chromium alloys from fused FLINAK has been investigated. Tantalum-chromium alloys containing 2-6% chromium were obtained by codepositing tantalum and chromium from an electrolyte containing 10 wt% TaF_5 and 0.5-1.5% Cr at 800°C. The alloy coatings are smooth and columnar in structure. The microhardness of these coatings increases with the increase of chromium content. With chromium-rich alloys, an equiaxed alloy structure is observed, with a hardness greater than for pure tantalum or chromium.

KEYWORDS: Gun Erosion, Refractory Metals, Tantalum, Tantalum-Chromium Alloys, Chromium, Coating, Fused Salt Electrolyte, Electrodeposition, FLINAK

Introduction

As a part of a program to develop erosion resistant coatings for advanced gun barrels, electrodeposition of tantalum and tantalum-chromium alloys from fused FLINAK is being investigated.

As background to this approach, it is of interest to examine briefly the elements involved in gun barrel erosion, the magnitude of the problem, and some of the approaches to minimizing erosion.

In Figure 1 are illustrated the salient elements involved in the process of erosion of a gun.

When the gun is fired, the propellant burns and develops high temperature (2500-3800°K) and high pressure (20-80,000 psi) due to the formation of large volume of gases which propel the projectile and give it the required muzzle velocity.

The CO/CO_2 ratio for single-base propellants is $\sim$ 2-3, while for double-base propellants, the ratio is $\sim$ 1, i.e., single base propellants are more reducing than double base propellants. The reducing nature of the gases thus favors the transition metals (Cr, Mo, Ta,...) as candidate materials for limiting erosion in gun barrels.

In the small caliber guns the residence time may be a fraction of a millisecond, in large caliber guns, this may be 20 milliseconds. For example, a 20 mm M61 (rapid fire machine gun) has a fatigue life between 3000-12000 rounds, but the erosion life is not more than 500-2000 rds. With a projectile travel time of $\sim$ 1 millisecond, and if the gun is condemned after 1200 rounds due to fatigue, its useful life is only 12 seconds; due to erosion it would fail after $\sim$ 0.5 to 2 seconds, i.e., small rapid fire guns are, in general erosion limited. The severity of conditions to which the bore surface is exposed is illustrated in Figure 2, in which a temperature profile of the bore surface is shown for a 76.2 mm gun after a single shot, and with repeated firing. The heat transferred from the hot gases to the bore surface causes rapid (and extreme) temperature excursions in the first few mils of the bore surface.

The resulting progressive damage of the bore surface of a 105-M68 gun barrel as a result of firing is shown in Figure 3.

Gun barrel erosion thus is defined as the progressive damage to the bore surface and the enlargement of the bore, by normal firing. Ultimately it results in losses in muzzle velocity, range, and accuracy, and therefore in the effectiveness of the weapon. It is sufficient, in summary, to note that erosion is a result of the combined action of thermal, mechanical, and chemical processes. For additional information see Ahmad (1).

Obvious approaches to minimizing erosion include:

- reduction of bore surface temperature

- development of propellants with lower flame temperature and less erosive gases

· improvements in the rotating band design and band material to minimize the engraving stresses without losses in obturation

· development of coatings or liners in gun barrels which are resistant to all the three main causes of erosion

With reference to the latter, to protect the bore surface, the liner or coating should have a m.p. higher than gunsteel and good high temperature strength [2]. It should also be resistant to the reactive propellant combustion gases and thermo-mechanically compatible with the main gunsteel body. In case of a coating, it should also be well bonded to the substrate, and the thickness should be optimized for protection of the gunsteel from the effects of heat which is the main cause of degradation of its mechanical strength.

The present investigation is part of a program to develop erosion resistant coatings for various metal substrates, such as gunsteels, through electrodeposition of refractory metals from molten salts.

The nine transition elements of groups IVB, VB, and VIB of the periodic table, known as the refractory metals because of their high melting points and the refractory nature of their compounds, are strong candidate materials for the present needs.

	IVB	VB	VIB
	Ti	V	Cr
m.(K)	1950	2190	2176
	Zr	Nb	Mo
m.(K)	2125	2770	2890
	Hf	Ta	W
m.(K)	2495	3270	3650

With the exception of chromium, aqueous electrodeposition can be discounted. Presently chromium electroplates (from aqueous solutions) are being used in large and small caliber guns, but these have serious limitations, i.e., microcracks, brittleness, and bonding. After a certain number of firing rounds, such plates chip and flake off, adversely affecting the performance of the guns. Of the other possible metal cladding routes, such as chemical and physical vapor deposition, diffusion coating processes such as metalliding, plasma spray deposition, and electrodeposition from fused salts, the last one appears the most promising for application in gun barrel liners.

Figure 4 shows a magnified view of a transverse section of a tantalum coated rifling achieved by fused salts electrodeposition. The uniform thickness of the tantalum coating on both the lands and grooves illustrate the excellent throwing power that is possible in the fused salts approach. Because exposure of gunsteel to the plating temperatures (750-900°C) is undesirable, the approach here is to use a short liner insert which can be coated independently of the main gun tube. Such liners have been tested [3] with severe firing schedules in the M24A1 gun. As shown in Figure 5 the erosion resistance appeared quite superior. The coating is found to swage by the engraving stresses of the projectiles, and this is undoubtedly due to softness of high purity tantalum (180-250 KHN).

An interest of the present investigation was to explore the modifications of the hardness properties and structures of such coatings through the addition of chromium to such electrolytes. Results are reported for a series of tantalum-rich chromium alloys obtained as increasing amounts of chromium were added to the Flinak tantalum plating bath.

Electroplating Assembly and Procedures

The electrolytic cell assembly was designed after that of Mellors and Senderoff [4]. The lower 16 cm of the plating cell was placed in a Lindberg crucible furnace. The hot zone temperatures were controlled with a time proportioning temperature controller (± 10°C). The plating cell was loaded with the FLINAK electrolyte contained in the nickel crucible and with the preweighed electrodes suspended above the crucible. The assembly was evacuated and back filled with argon. Maintaining a steady flow of the inert gas, the electrolyte was heated to 450°C for six hours and the temperature was then raised to the deposition temperature (∿ 800°C). Preweighed amounts of the solute (e.g., K_2TaF_7, K_3CrF_6,...) were next added under argon atmosphere to the melt and allowed to equilibrate for 48-72 hours. The anode was then positioned in the melt and a pre-electrolysis step (at 40-50 ma/cm^2 for ∿ one hour) was used to remove trace impurities. The cathode coupon was then replaced and the plating was carried out at the predetermined current density.

On the completion of the plating experiment, the coupon was withdrawn, ultrasonically washed in distilled water for ∿ 1-3 hours to remove adherent salts, and weighed. The area of the deposit was measured and the plate thickness calculated. The coupon was then sectioned and polished for metallographic examination, electron microprobe analysis (EPMA) and microhardness measurements using the standard techniques.

Details on the composition of the electrolytes, and associated plating parameters will be published elsewhere [5] and it is sufficient for the present to note the results of the tantalum and tantalum-chromium alloy coatings thus plated from FLINAK.

Tantalum

Dense, columnar and high purity coatings (indicated by the microhardness similar to that of high purity bulk Ta) were obtained as illustrated in Figure 6.

Tantalum Rich-Chromium Alloys

In three series of runs, SB, SC, SD, chromium to the extent of 0.5, 1.0, and 1.5% as K_3CrF_6 was added to the FLINAK bath containing 10 wt% of TaF_5 and K_2TaF_7.

A transverse section of a typical alloy is shown in Figure 7 which indicates a dense columnar structure, rather similar to those of Ta coatings. Figure 8 shows the hardness and composition profile of a Ta-Cr alloy specimen. An EPMA profile of tantalum at 2 micron intervals across the interface is shown in Figure 9, indicating a diffusion zone of about 10 microns. As seen from inspection of Figure 10, the chromium distribution in the alloy is good. The sensitivity of the measurement of chromium by EPMA technique was ± 0.5%.

Figure 10 also shows that the concentration of Cr is the highest at the coating-substrate interface (i.e., at the start of electrodeposition) and then it gradually decreases. The decrease in hardness at corresponding positions is undoubtedly due to this.

The chromium content in the alloy appears to be a linear function of the chromium added to the electrolyte. This is illustrated in Figure 11. The hardness of the alloy increases with chromium content, as illustrated in Figure 12. It appears possible to increase predictably the hardness of tantalum through addition of chromium.

Chromium and Chromium Rich Alloys

A limited number of trials were undertaken to explore the feasibility of plating Cr and Cr-Ta alloys. Copper coupons were used as cathodes. The electrolyte was FLINAK containing 6 wt % CrF_3. For Cr-Ta alloys, in addition to CrF_3, 0.05 wt % TaF_5 and K_2TaF_7 were also added. For pure chromium deposition, current densities in the range 0.8-49.9 ma/cm^2 and melt temperatures of 800-835°C were selected. In these runs some anodic dissolution of nickel (from the basket containing the chromium metal) was noted. The coatings obtained were mostly dendritic and porous and the current efficiency was, in general, low. However, the hardness values in the nonporous areas of these deposits were in the range of 137-205 KHN indicating high purity chromium. The purity of Cr was confirmed by EPMA. Addition of 0.05 wt % TaF_5 gave coherent dense coatings such as shown in Figure 13 which was obtained at a c.d. of 25.8 ma/cm^2. The average microhardness of the coatings was found to be 294 KHN, i.e., higher than pure chromium or tantalum. The

presence of Ta in this coating could not be confirmed by the EPMA technique (detection limit $\sim$ 0.5% Ta), and it is assumed that the alloy contained Ta only in trace amounts. A further noteworthy feature of this coating is the grain structure. Inspection of Figure 13 shows that it is almost equiaxed instead of the more general columnar structure. The very fine grain size of the equiaxed structure would be expected to confer superior mechanical properties. Such alloy structures appear a desirable feature for the erosion resistant coatings required for the present applications. Investigations of the electrodeposition of chromium and chromium-rich alloys are being extended.

Acknowledgements

The micrographs and microhardness for the specimens were made at the Benet Weapons Laboratory by Theresa Brassard and Joe Barranco. This is acknowledged with pleasure. Dr. R. A. Bailey (RPI) is thanked for continued interest and helpful discussions.

References

1. I. Ahmad, "The Problem Of Gun Barrel Erosion - A Overview", Plenary Lecture, Tri Services Symposium on Wear and Erosion of Gun Barrels, Dover, N.J. (1977).

2. I. Ahmad, P. Greco, G. D'Andrea, and J. Barranco, "Potential Erosion Resistant Refractory Metal (And/Or) Alloy Coatings For Gun Tubes", Proceedings 1978 Triservice Conference on Corrosion MAC-79-40, May 1979, pp. 203-217.

3. R. Cullinan and G. D'Andrea, "Erosion Study of Tantalum Coated Gun Barrels", to be presented at 1980 JANAF Meeting.

4. S. Senderoff et. al., J. Electrochem. Soc., 101, 16 (1954); 112, 266, 840 (1965); 113, 60, 66 (1966).

5. I. Ahmad, G. J. Janz, and W. A. Spiak, J. Applied Electrochemistry (submitted, 1980).

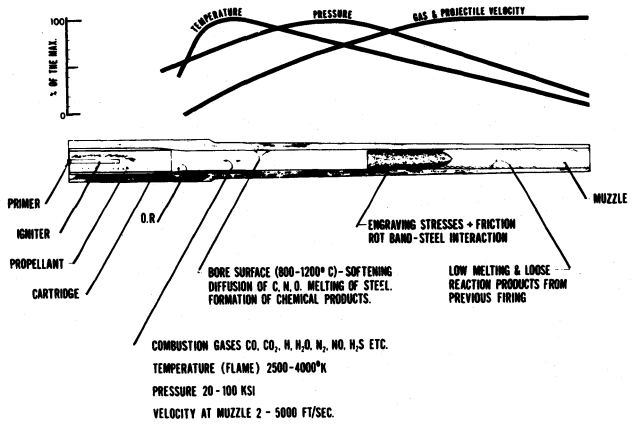

Figure 1. Elements involved in the process of erosion of a gun barrel.

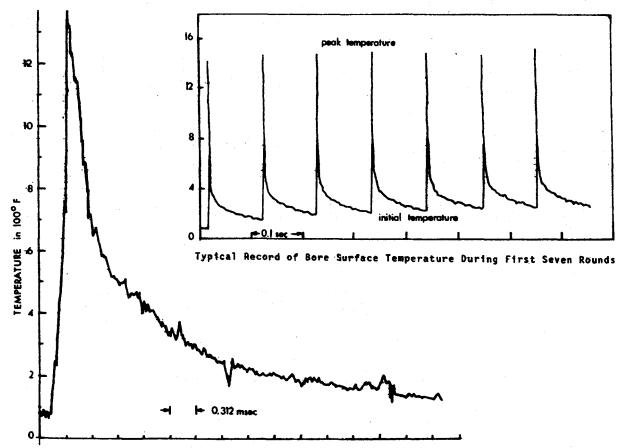

Figure 2. Temperature profile of a bore surface of a 76.2 mm gun as a result of a single shot and after repeated firing.

Figure 3. Damage to the bore surface of a 105 M68 barrel in the O. R. region as a result of firing.

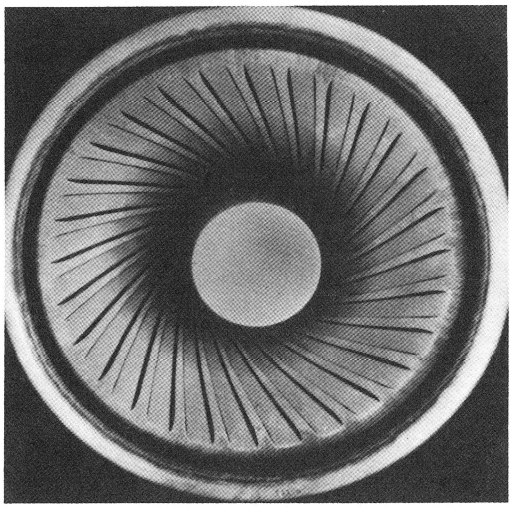

(a) initial appearance (unused barrel surface).

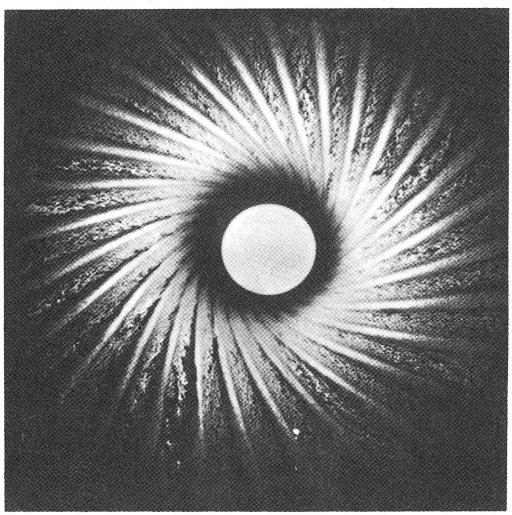

(b) after firing 1744 rounds.

Figure 4. Transverse section of a rifling land showing uniformity of the tantalum coating thickness achieved from fused salts electrodeposition.

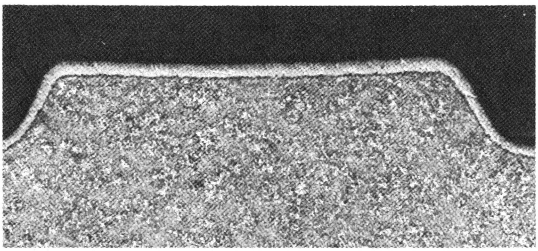

Figure 5. Comparison of an uncoated and tantalum coated bore surface in the O. R. region of an M68-105 mm gun

(a) Uncoated gunsteel surface after 2000 rounds

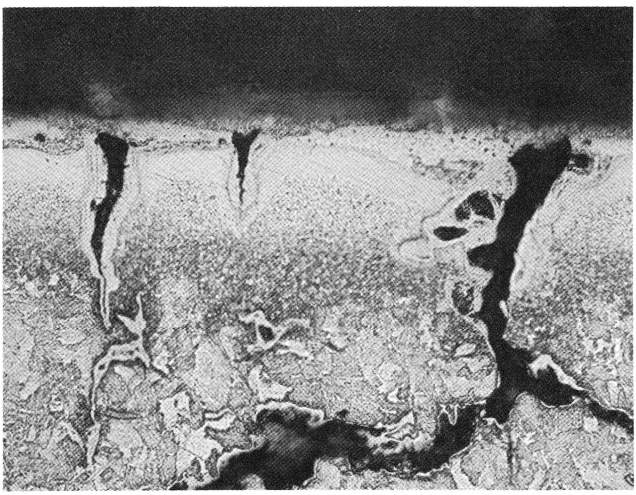

(b) tantalum gunsteel surface after 5000 rounds.

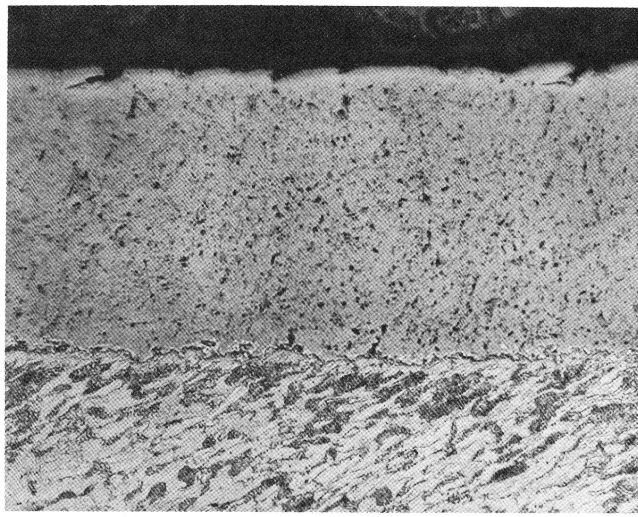

Figure 6. (a)Transverse section of a typical tantalum coating (X200).
(b) Microhardness profile.

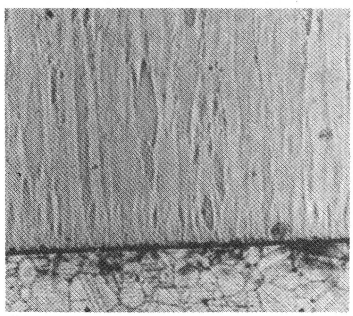

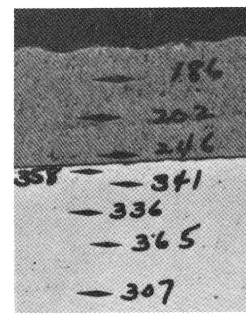

Figure 7. Transverse section of a typical Ta-Cr alloy coating. (a) SB-6, Specimen: 0.5 Cr (X100); (b) hardness profile.

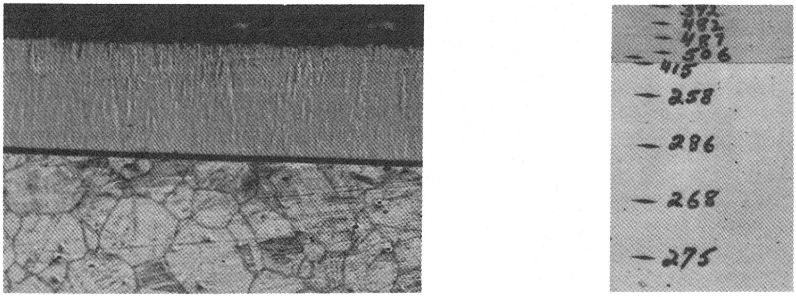

Figure 8. Hardness and Cr composition profile of a selected coating SD-3 (interval between data points 20 microns).

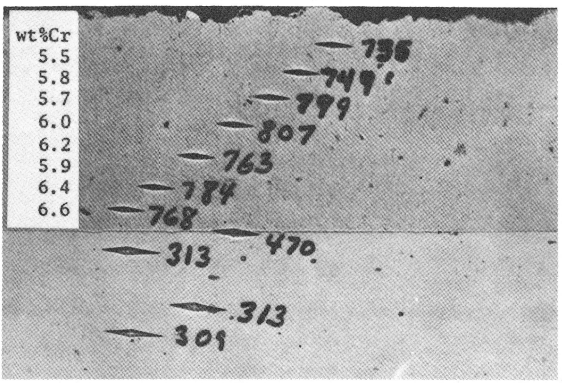

Figure 9. EPMA profile of Ta-Cr/steel interface in SD-3 specimen.

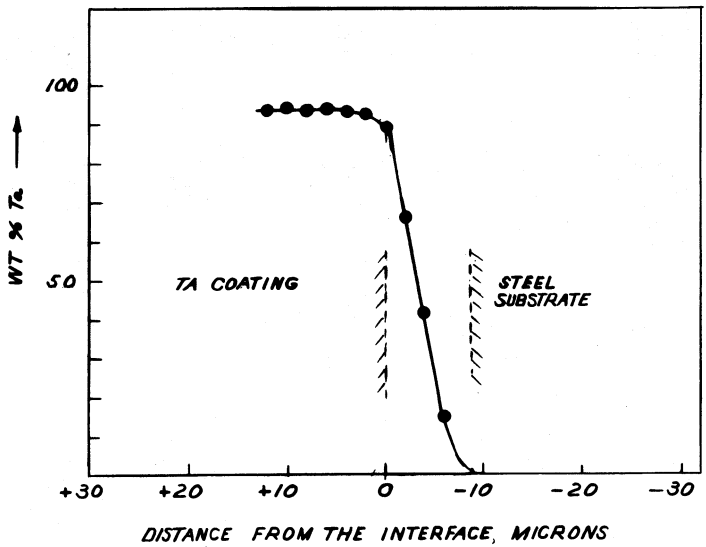

Figure 10. Variation of chromium in SB-6, SC-3, and SD-3 coatings.

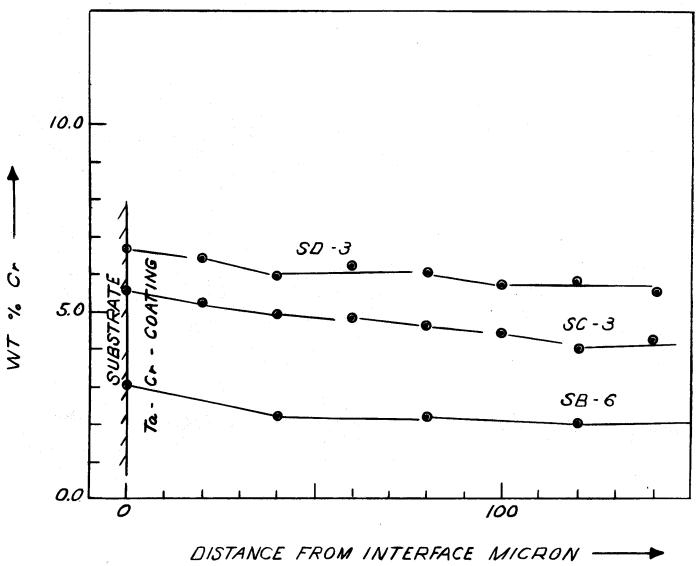

Figure 11. Variation of Cr in the coating as a function of Cr added as CrF_3 in the melt.

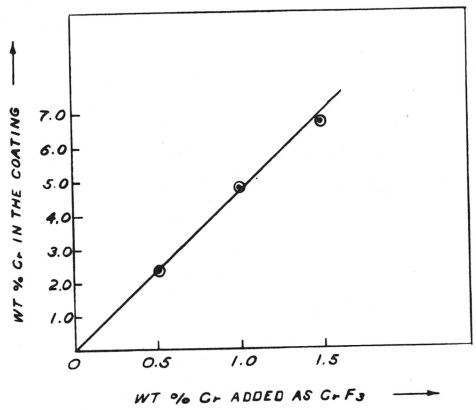

Figure 12. Variation of hardness of tantalum alloy with the chromium content.

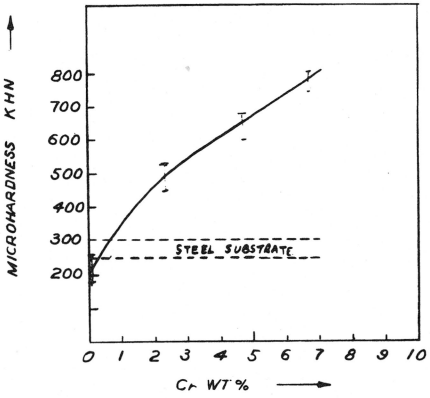

Figure 13. Cr-rich Ta alloy, showing the equiaxed grain structure (X1000).

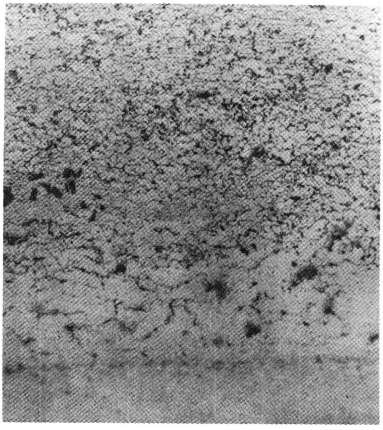

DOI: 10.1149/198109.0571PV

COMPRESSIBILITY OF MOLTEN SALTS MIXTURES WITH A MISCIBILITY GAP

P. Cerisier, B. SY

Laboratoire de Dynamique et Thermophysique des Fluides
Université de Provence - Rue H. Poincaré
13397 Marseille cedex 4 - France

The velocities of ultrasonic waves of frequency 4MHz in the reciprocal mixture K,Tℓ//NO_3,Br have been measured by a pulse method. In the miscibility zone the ultrasound velocity may be predicted using the equation of state of Buehler. It is concluded that the reciprocal mixture is far from ideality for high concentrations in KNO_3. In the immiscibility zone the ultrasound velocity is well calculated assuming a mixture of two phases. Finaly the isothermal compressibility may be predicted on the basis of cellular theory if the mixture is not too far from ideality.

1. INTRODUCTION

Since the first measurements of ultrasound speeds in molten salts of Bockris and Richards (1) numerous studies were carried out* but it seems that no study has been published, to our knowledge, concerning the reciprocal mixtures involving a polyatomic anion and an halide ion until the recent paper on (NaK//$BrNO_3$) by our group (2). Contrary to liquids like silicates, molten salts such as nitrates, sulfates, halides of metals do not exhibit a strong tendency to immiscibility : some miscibility gaps have been reported in a few binary mixtures with BeF_2. However numerous reciprocal systems of molten salts exhibit a miscibility gap between two liquids, although subsidiary binaries are miscible at any concentration. Generally the components are halides, nitrates or sulfates. Therefore, we thought it might be of interest to conclude our study on nitrates, together with their binary, ternary, quaternary and reciprocal mixtures (without a miscibility gap) by a study of the reciprocal mixture (KTℓ//$BrNO_3$) with such a gap. The latter was chosen because the experimental investigation of the miscibility zone is precise and complete (3). The stable diagonal we studied is KNO_3+TℓBr. The temperature of monotectic and upper consolute point are respectively 444°C and 543°C. The width of the gap at 444°C goes from 15,5 to 92.5 TℓBr mole per cent, the molar fraction corresponding to upper consolute point is 0.57.

* For an extended bibliography see ref.(2).

2. EXPERIMENTAL

The apparatus used was described in detail previously (4). Some minor modifications were made of the furnace. The vapour pressure of TlBr is important (71mmHg at 630°) and our method prohibits the use of a closed vessel. Therefore, in order to reduce vaporization out of the cell the oven was constructed with no temperature gradients. In this case the vaporization remains slight during the experiment.

A pulse method was used. The ultrasonic waves of 4MHz passed through the melt and silica rods. The velocity was measured directly from the transit time of the wave through a known thickness of molten salt.

The salts used were pure grade as supplied by Prolabo (RP) or Merck. After a stay of several days in a drying oven, they were set into the measuring cell and heated for several hours under an overpressured and dry argon atmosphere.

The temperature zone studied (above 444°C) was above the melting temperature of KNO_3 (337°C) and even more above that of $TlNO_3$ (206°C). In order to avoid a strong decomposition of the nitrates, we had to limit ourselves to comparatively low temperatures : a few tenth of degrees around the demixing zone.

3. RESULTS

The ultrasonic velocities in KNO_3 and KBr were determined previously (5). Those of $TlNO_3$, TlBr and (KNO_3+TlBr) are shown respectively on fig.1,2,3 and well represented by a linear polynomial as a function of temperature u=a-bt (table I) as well in the miscibility zone as in the immiscibility gap, for the mixture.

TABLE 1 - TEMPERATURE VARIATION OF ULTRASONIC SPEED IN FUSED SALTS KNO_3 + TlBr

	miscibility zone			immiscibility zone		
x_K	a $m.s^{-1}$	b $m.s^{-1}°C$	Temperature range (°C)	a $m.s^{-1}$	b $m.s^{-1}°C$	Temperature range (°C)
0.09	1380	0.653	460-480	1380	0.65	460-480
0.15	1502	0.908	503-525	2059	2.02	450-490
0.30	1475	0.764	540-570	1662	1.21	485-540
0.43	2076	1.710	545-565	2186	1.89	490-540
0.76	2035	1.295	510-550	2096	1.34	460-500
0.82	2128	1.320	467-495	2147	1.36	440-465
$TlNO_3$	1808.7	0.718	220-300			
TlBr	1367.0	0.627	480-510			

4. CALCULATION OF ULTRASOUND VELOCITIES

The first goal of this work is to calculate the ultrasound velocity in order to reduce the number of experiments and to know if the mixture is close to ideality.

a. Miscibility zone

Starting from the Buehler equation:

$$PV(1-\phi) = RT$$

with $\phi = (V^*/V)^{1/3}$ where V^* and V are respectively the molar covolume and volume it was shown (6) that the ultrasound speed is given by :

$$u = \left[(1-\phi) \frac{\alpha M}{R} - \frac{MT\alpha^2}{C_p} \right]^{-1/2} \qquad (3.1)$$

α is the expansion coefficient, C_p the molar heat capacity, M the molar mass. If the mixture is ideal, M, V, V^*, α and C_p are easely calculable from the data of the four pure components from a such expression

$$M = \sum_i x_i M_i \quad \text{etc...} \qquad (3.2)$$

The data V_i^* were calculated from (3.1) and ref.(5) ; V, C_p are extracted from Jänz's book (7). All these values, which are valid to about a hundred degrees above the melting point, were extrapolated to the studied range (for the nitrates it is higher than the melting point, for the bromides it is lower). The variation of u as a function of temperature is presented in fig.3 and as a function of mole fraction in fig.4. The deviation from experimental values is at most 7% and is generally smaller (near high concentrations of Tℓ). In the reciprocal mixture ($NaK//NO_3Br$) it is only 0.5%. So we can conclude that the reciprocal system ($KTℓ//NO_3Br$) is not ideal (at least as far as V, V^*, α and u are concerned) even if a part of the 7% must be attributed to the numerous more or less justified extrapolations. But it is close to ideality. The excess volume of $KBrNO_3$ was estimated as a few thousandths (2), that one of $KTℓNO_3$ is 3‰ (8).

Noticing that the excess volumes of mixtures (alkali nitrate + thallous nitrate) are larger than those of alkali nitrates only (8) and that replacing one Br^- ion by an NO_3^- ion leads to very small volume variation in ($NaK//BrNO_3$)(2), the non ideal behavior can be attributed to the presence of $Tℓ^+$ and its partially covalent character. This fact is confirmed when we compare the constant velocity curves for ($KNa//BrNO_3$)(fig.5a) and for ($KTℓ//BrNO_3$)(fig.5b) as calculated from equation (3.1) at a given temperature. For the first mixture the velocity changes chiefly with the anion concentration and the difference is about 140m/s, for the second mixture the velocity is governed by the cation concentration and the difference is four times more important, about 550m/s.

In conclusion, the excess volumes of mixtures with $Tℓ^+$ (ie KTℓBr, $TℓBrNO_3$) which are unknown, are larger than a few thousandths, as

those of the alkali ions.

b. Immiscibility zone

Let us label all the quantities for the first phase with a prime and for the second phase with a double prime. We get two obvious relations :

$$t = t' + t'' \tag{3.3}$$

$$ut = u't' + u''t'' \tag{3.4}$$

and a third one

$$\frac{u't'}{u''t''} = \frac{x'V'}{x''V''} \tag{3.5}$$

whereby the ultrasonic waves go through lengths proportional to the volume of each phase (V' and V'' are molar volumes of each phase, x' and x''=1-x' give the number of moles in the two phases).

Let x be the molar fraction of TℓBr in the quasi binary (TℓBr+KNO_3), and X', X'' the mole fraction of TℓBr in the two phases, hence:

$$\frac{x''}{x'} = \frac{x-X'}{X''-x} \tag{3.6}$$

and, combining (3.3),(3.4), and (3.5) :

$$u = \frac{u'\left(1 + \frac{x''V''}{x'V'}\right)}{1 + \frac{u'}{u''}\frac{x''V''}{x'V'}} \tag{3.7}$$

X' and X'' are given by the data in ref.(3), V' and V'' can be calculated from the molar volume of the reciprocal system (2) which may be expressed as

$$V = \sum_{i=1}^{2}\sum_{k=3}^{4} x_i x_k V_{o,ik} + \frac{4}{3}\sum_{i=1}^{4}\sum_{\substack{j=1 \\ i\neq j\neq h}}^{4}\sum_{h=1}^{4} x_i x_j x_k V^E_{ijk} \tag{3.8}$$

where 1 and 2 stand for cations, 3 and 4 for anions, $V_{o,ij}$ is the molar volume of pure salt (ij), and V^E_{ijk} the excess molar volume for an equimolar binary mixture (ijk). The value of excess volume of ($KT\ell NO_3$) was given by Cleaver (8). For the three other binaries, we ascribed the values 4.10^{-2}, 5.10^{-3}, 7.10^{-2} respectively for $T\ell NO_3Br$, KNO_3Br and KTℓBr. The values of u' and u'' are the limiting values of speed in a miscible mixture at the demixing temperature. The variations of u', u'' and u with temperature are shown on fig.3. The difference between experimental and calculated values is at most 8%. The discrepancies may be ascribed chiefly to a possible decomposition of salts, to extrapolations, to estimations of u' and u'' and above all of V' and V'' and not to the physical state of mixture (drops or two superposed liquids).

5. COMPRESSIBILITY

The isothermal compressibility was obtained by using the classical equation :

$$\beta_T = (V/Mu^2)\left[1+(MT\alpha^2u^2/C_p)\right] \qquad (4.1)$$

Where all the symbols have their usual significance. Similarly the compressibility of ideal mixtures, as defined by

$$\beta_{Ti} = (1/V) \sum_{j=1}^{2} \sum_{k=3}^{4} x_j x_k V_{o,jk} \beta_{ik} \qquad (4.2)$$

was calculated. Both are shown in fig.6. It must be noticed that some "experimental" points are, in fact, extrapolated, but it seems it can be concluded, in spite of uncertainties, that the liquid is quasi ideal for T&Br rich mixtures, and it departs from ideality when x_{KNO_3} increases (the discrepancy was 8%).

In previous works (2)(9) we proposed a model to calculate the isothermal compressibility. The agreement between experimental and calculated values was surprisingly good for associated mixtures (binaries, quaternaries, etc...) and for the reciprocal system (NaK// NO_3Br). But to take into account the "S shape" of β_T (fig.6)it is necessary to get a negative and dissymetric excess volume. This needs an experimental verification before asserting that our model is valuable for a reciprocal mixture far from ideality.

REFERENCES

(1) J. O'M. Bockris, N.E. Richards, Proc. Roy. Soc. 241, 244, 1958
(2) P. Cerisier, G. Finiels, J. Chem. Thermodynamics, to be published Janv. 1981.
(3) C. Sinistri, P. Franzosini, A. Timidei, M. Rolla, Z. Naturforschg. 20a, 561, 1965.
(4) J. Marchisio, G. Salvini, Y. Doucet, J. Chem. Phys. 7-8, 1165,1973
(5) P. Cerisier, G. Finiels, Y. Doucet, J. Chim. Phys. 6, 836, 1974
(6) P. Cerisier, Y. Doucet, J. Chim. Phys. 9-10, 815, 1976
(7) G. Janz, Molten Salts Handbook, Academic Press, New-York, London, 1967.
(8) B. Cleaver, B.C.J. Neil, Trans. Farad. Soc. 65, 11, 2860, 1969.
(9) P. Cerisier, G. Finiels, Y. Doucet, J. Chim. Phys. 7-8, 895, 1975.

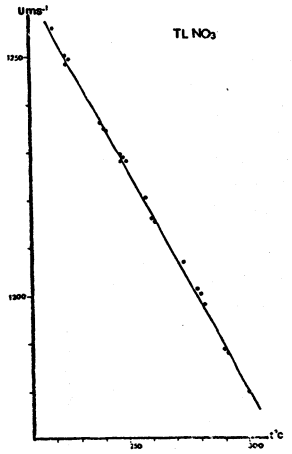

FIGURE 1. Ultrasonic speed in $T\ell NO_3$

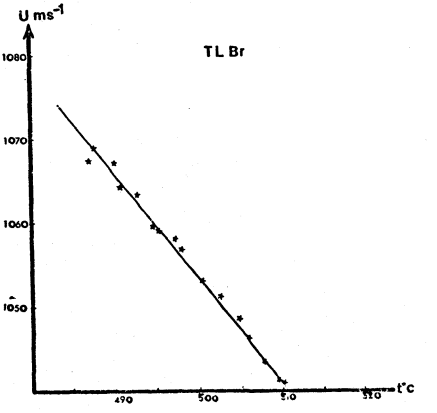

FIGURE 2. Ultrasonic speed in $T\ell Br$

FIGURE 3

Ultrasonic speed in $T\ell Br+KNO_3$ at constant molar fraction in KNO_3

□ 0.09 ● 0.43
■ 0.835 X 0.15
+ 0.76 o 0.30
△ 0.82

The full lines represent the calculated ultrasonic speed from Eq.(3.1)

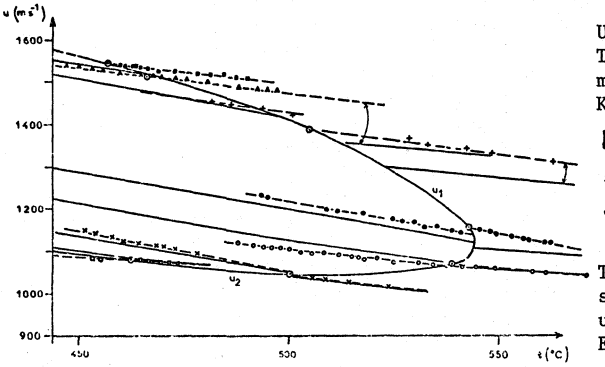

FIGURE 4. Calculated and experimental ultrasonic speed at 545°C as a function of molar fraction in KNO_3 X extrapolated point, • measured point (1) calculated from (3.1), (2) experimental

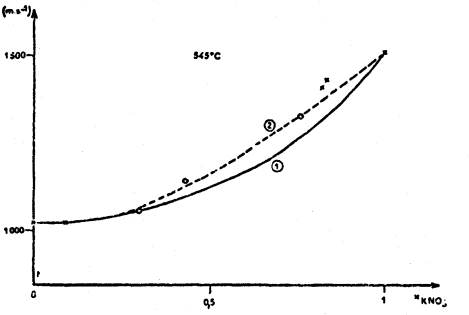

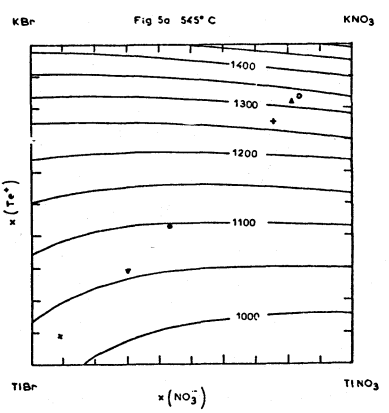

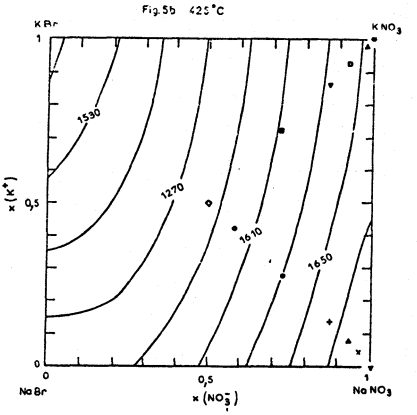

FIGURE 5. Ultrasonic constant speeds calculated from equation (3.1)

a) ($KT\ell//NO_3Br$) experimental speeds ($m.s^{-1}$) X 1024 ▼1059 ●1144 o 1436 Δ1409 +1329

b) ($KNa//NO_3Br$) experimental speeds ($m.s^{-1}$) ▽ 1688 ✕1680 Δ 1674 +1660 ●1630 o1600 ✳1658 ▲1652 □ 1648 ∇ 1636 ■1615 ◇1585

FIGURE 6. Isothermal compressibility à 545°C

(1) ideal from (4.2) ✗ extrapolated point o measured point